Thesis submitted for the

Degree of Doctor of Philosophy,

University of Oxford

GEOLOGY OF THE NORTHEAST SACRAMENTO MOUNTAINS, CALIFORNIA

by

V. L. Pease



Wolfson College and Department of Earth Sciences

University of Oxford

Trinity 1997

ABSTRACT

Geology of the northeast Sacramento Mountains, California

V. L. Pease
Wolfson College

A multidisciplinary investigation into the timing, distribution, and intensity of tectonothermal events has resulted in an understanding of the tectonic evolution of the northeast Sacramento Mountains, in particular, and of the northern Sacramento Mountains in general. The application of geologic, structural, geochemical, and thermochronologic techniques has provided the relative and absolute timing of crustal and tectonic processes, leading to the development of a petrogenetic model for the evolution of the Sacramento Mountains metamorphic core complex.

The metamorphic core complex was uplifted and cooled during Miocene detachment faulting (~23-12 Ma). The Eagle Wash Intrusive Complex, a calc-alkalic granodioritic intrusion, was emplaced during detachment faulting at ~20 Ma, at ~3 kb and ~680°C. The EWIC records rapid cooling and uplift following emplacement, at rates of >100°C/Ma and 1.5-3 km/Ma, respectively. The EWIC was below ~100°C (the closure temperature of fission tracks in apatite) by 15 Ma.

The structural and thermal history for the syntectonic intrusive suite is best explained via an evolving simple shear zone. The EWIC was intruded into, or proximal to, a mylonitic shear zone. The SW dip of the myonitic foliation in the EWIC could represent a primary feature of the shear zone, or the capture of a relatively older feature by a younger detachment fault splay. The later interpretation is consistent with the thermochronologic data, which suggests that faulting continued in the east after its termination in the west.

Using the thermochonologic data to develop a thermal profile of the crust, the angle of faulting was calculated to be <30°C. The slip-rate associated with the detachement fault, though poorly constrained, was determined to be ~4 mm/yr. This value is about half that determined from other core complexes and suggests that extension was slower here than elsewhere in the region.

TABLE OF CONTENTS

Acknowledgements viii

Extended Abstract x

List of Inserts

Geologic map and cross-section, 1:24,000
Data/sample locations, northeast Sacramento Mountains, 1:24,000
Data/sample locations, northwest Sacramento Mountains, 1:48,000 (1:24,000 base)

Chapter 1. Introduction

1.1 Metamorphic core complexes and continental extension 1
1.2 Models for continental extension 3
Observations and considerations 3
The "pure shear" model 4
The "simple shear" model 5
The "rolling hinge" model 7
The role of magmatism 8
1.3 The Sacramento Mountains 9
Colorado River extensional corridor 9
Regional geologic setting 11
Previous work and local geologic setting 16
Terminology 19
1.4 Objectives 20

Chapter 2. Lithologies of the Northeast Sacramento Mountains

2.1 Introduction 21
2.2 Quaternary and Pliocene units 22
Overview 22
Qg, Pleistocene (?) Colorado River gravel and sand deposits 22
Tbo, Pliocene calcareous clay, silt, sand, and marl 22
2.3 Allochthonous units 22
2.4 Autochthonous units 24
Overview 24
Tr, Miocene rhyolitic dykes 26
Tu, Miocene dykes, undifferentiated 26
Tcb, Miocene chloritic breccia 30
cbz, chloritic breccia zone 33
Tdy, Miocene diorite 34
Tlg, Miocene leucogranite 34
Tgd, Miocene granodiorite 39
Tgd amphibole compositions 39
Tgd plagioclase compositions 44
Td, Miocene (?) diorite 47
Yg, Middle Proterozoic porphyritic granite 51
Xgn (Xmgn), Early Proterozoic gneiss, schist, and migmatite 51
2.5 Discussion 52

Chapter 3. Structure of the Footwall in the Northeast Sacramento Mountains

3.1 Introduction 56
3.2 Tertiary brittle deformation (D3) 57
High-angle faults 57
Fractures, joints, and tension gashes 62
Dykes 64
Low-angle faults 64
Temperature, pressure, and age of formation 69

3.3 Tertiary ductile deformation (D2) 70
Mesoscopic structures 70
Asymmetric meso- and microstructures 74
Temperature, pressure, and age of formation 76
3.4 Pre-Tertiary deformation (D1) 80
3.5 Structural evolution 82
Stress regime during D3 82
Stress regime during D2 85
3.6 Synthesis 87
Evolution of the footwall 87
Correlation between footwalls 91
Summary 96

Chapter 4. Geochemistry of the EWIC
4.1 Introduction 98
4.2 Variation diagrams 100
4.3 EWIC element characterization 101
Major element geochemistry 101
Trace element geochemistry 105
4.4 Preservation of a magmatic signature 114
Loss on ignition 115
Element mobility in mylonites 115
4.5 EWIC isotopic characterization 118
Initial lead geochemistry 118
Rubidium and strontium geochemistry 120
Samarium and neodymium geochemistry 122
4.6 Magma genesis 125

Chapter 5. Age and Thermal Evolution of the Northern Sacramento Mountains
5.1 The application of thermochronology 133
5.2 Thermobarometry of EWIC emplacement 134
Amphibole-plagioclase thermometry 136
Al-in hornblende barometry 136
Thermobarometric results 138
5.3 High-temperature history 142
U/Pb and common lead technique 142
U/Pb and common lead results 143
5.4 Medium-temperature history 154
$^{40}Ar/^{39}Ar$ technique 154
$^{40}Ar/^{39}Ar$ results 154
5.5 Low-temperature history 157
Fission track technique 157
Fission track results 157
5.6 Discussion 162
Northwest Sacramento Mountains 162
Northeast Sacramento Mountains 165
Summary 166

Chapter 6. Angle of Faulting the Northern Sacramento Mountains
6.1 Calculating the angle of the fault 170
Premise 170
Assumptions 172
6.2 Barometry/slip rate 175
6.3 Spacing of isotherms 175
6.4 Age variation down-dip 176
Slip rate 176
Angle of faulting 178

6.2 Summary 180

Chapter 7. Conclusions and Synthesis
7.1 Tectonogenesis of the northeast Sacramento Mountains 181
7.2 The role of magmatism during detachment faulting 185
7.3 Detachment faulting in the northern Sacramento Mountains 186
7.4 Future investigations 189

References 190

Appendices
A. X-Ray Flourescence Analytical Techniques and Analyses 207
B. Electron Microprobe Analytical Techniques and Analyses 217
C. Mineral Separation Techniques 231
D. Isotopic Analytical Techniques and Analyses 233
U/Pb and common lead analytical techniques 233
$^{40}Ar/^{39}Ar$ analytical techniques and analyses 234
Fission track analytical techniques and analyses 236

LIST OF FIGURES

Chapter 1. Introduction

Figure 1.1 Characteristics of a metamorphic core complex 2
Figure 1.2 Symmetric "pure" shear 5
Figure 1.3 Evolving "simple" shear 6
Figure 1.4 Development of the "rolling-hinge" 7
Figure 1.5 Regional features 9
Figure 1.6 Colorado River extensional corridor 10
Figure 1.7 Generalised stratigraphy of the extensional corridor 15
Figure 1.8 Simplified geology of the northern Sacramento Mountains 18

Chapter 2. Lithologies of the Northeast Sacramento Mountains

Figure 2.1 Bouse Formation (*Tbo*) 23
Figure 2.2 Allochthonous units (aerial view) 24
Figure 2.3 Rhyolite dyke (*Tr*) 27
Figure 2.4 Rhyolite dyke with spherulites (*Tr*) 27
Figure 2.5 Multiple generations of mafic/intermediate dykes (*Tu*) 28
Figure 2.6 Leucogranite (Tlg) cross-cutting sheared dykes (*Tu*) 29
Figure 2.7 Static recrystallization of sheared horizontal dyke (*Tu*) 29
Figure 2.8 Dynamic recrystallization of sheared horizontal dyke (*Tu*) 30
Figure 2.9 Composite dyke (*Tu*) 31
Figure 2.10 Magma mixing (*Tu*) 31
Figure 2.11 Undeformed vertical dyke (*Tu*) 32
Figure 2.12 Deformed vertical dyke (*Tu*) 32
Figure 2.13 Microbreccia of the SMDF (*Tcb*) 33
Figure 2.14a Diorite pluton (*Td*) 35
Figure 2.14b Microphotograph of diorite pluton (*Td*) 35
Figure 2.15 Leucogranite sheets (*Tlg*) 36
Figure 2.16 Leucogranite dykes (*Tlg*) 37
Figure 2.17 S-C planes in leucogranite (*Tlg*) 37
Figure 2.18 Precambrian xenolith in leucogranite (*Tlg*) 38
Figure 2.19 Granodiorite (*Tgd*) cross-cutting leucogranite (*Tlg*) 38
Figure 2.20 Sketch of heterogeneities within granodiorite (*Tgd*) 40
Figure 2.21 Compositional variation within granodiorite (*Tgd*) 41
Figure 2.22 Minor strain within granodiorite (*Tgd*) 42
Figure 2.23 Moderate strain within granodiorite (*Tgd*) 42
Figure 2.24 High strain within granodiorite (*Tgd*) 43
Figure 2.25 S-C planes in granodiorite (*Tgd*) 43
Figure 2.26 *Tgd* amphibole compositions 44
Figure 2.27 *Tgd* amphibole genesis 45
Figure 2.28 *Tgd* plagioclase compositions 45
Figure 2.29 Magma mixing of diorite (*Td*) and granodiorite (*Tgd*) 46
Figure 2.30 Net-vein mixing of diorite (*Td*) and granodiorite (*Tgd*) 47
Figure 2.31a Magma mingling between granodiorite (*Tgd*) and leucogranite (*Tlg*) 48
Figure 2.31b Magma mingling between granodiorite (*Tgd*) and leucogranite (*Tlg*) 48
Figure 2.32 Xenoliths in granodiorite (*Tgd*) 49
Figure 2.33 Xenoliths with reaction rims in granodiorite (*Tgd*) 49
Figure 2.34 Xenoliths with reaction rims in granodiorite (*Tgd*) 50
Figure 2.35 Amphibole from diorite (*Td*) intergrown with leucocratic vein 51
Figure 2.36 Alignment of megacrysts in deformed Proterozoic granite (*Yg*) 52
Figure 2.37 Contact between EWIC and Proterozoic gneiss (*Xmgn*) 53
Figure 2.38 Subhorizontal layering of granodiorite (*Tgd*) and Proterozoic gneiss (*Xmgn*) 53
Figure 2.39 Cretaceous (?) megacrystic granite 54
Figure 2.40 Cretaceous (?) megacrystic granite 54

Chapter 3. Structure of the Footwall in the Northeast Sacramento Mountains
Figure 3.1a Vertical strike-slip fault 58
Figure 3.1b Horizontal strike-slip striae 58
Figure 3.2a Vertical dip-slip fault 59
Figure 3.2b Near vertical dip-slip striae 60
Figure 3.3a Stereonet of fault orientations 61
Figure 3.3b Stereonet of fault striae orientations 61
Figure 3.4 Protocataclasite associated with strike-slip faulting 62
Figure 3.5 Stereonet of fracture and joint orientations 63
Figure 3.6 Near-vertical, *en echelon* tension gash 63
Figure 3.7a Stereonet of dyke orientations 65
Figure 3.7b Stereonet of dyke foliation and lineation orientations 65
Figure 3.8a SMDF near Browns Camp 66
Figure 3.8b Sense of motion near Browns Camp 66
Figure 3.9a SMDF in Hacienda Wash 67
Figure 3.9b Striae on SMDF at Hacienda Wash 68
Figure 3.10 Secondary low-angle fault gouge 69
Figure 3.11 Stereonet of D2 mylonitic fabric in *Tgd* 70
Figure 3.12 Stereonet of D2 mylonitic fabric in *Tlg* 71
Figure 3.13 Stereonet of D2 mylonitic fabric in *Td* 71
Figure 3.14 Microphotograph of D2 overprinting all lithologies 73
Figure 3.15 Stereonet of contact orientations 73
Figure 3.16 Drag folds in EWIC 75
Figure 3.17 Stereonet of fold axes 75
Figure 3.18a Histogram of shear sense associated with D2 by lithology 77
Figure 3.18b Histogram of shear sense associated with D2 by geographic distribution 77
Figure 3.19 Extensional microfractures in amphibole associated with D2 in *Tgd* 78
Figure 3.20 Low-temperature plasticity of plagioclase associated with D2 in *Tgd* 79
Figure 3.21 Stereonet of D1 (and D2) fabric in *Xmgn* 80
Figure 3.22 Relict, high temperature recrystallization of amphibole associated with D1 81
Figure 3.23 Relict, high temperature recrystallization of plagioclase associated with D1 81
Figure 3.24 Relict sillimanite associated with D1 in *Xmgn* 82
Figure 3.25 Principal stress axes associated with normal and strike-slip faulting 83
Figure 3.26 Strike-slip faulting in a nearly uniaxial stress field 84
Figure 3.27 Foliation trajectory of extension-perpendicular fold 88
Figure 3.28 Formation of back-dipping mylonites 89
Figure 3.29 Schematic representation of three generations of detachment faults 91

Chapter 4. Geochemistry of the EWIC
Figure 4.1a Alkalic versus sub-alkalic 102
Figure 4.1b Tholeiitic versus calc-alkalic 102
Figure 4.2 Metaluminous versus peraluminous 103
Figure 4.3 Oxides versus silica 103
Figure 4.4 Potassium group elements versus silica 107
Figure 4.5 Potassium group element correlations 108
Figure 4.6a Contamination versus fractionation (logNi *vs.* logRb) 109
Figure 4.6a Contamination versus fractionation (Nb/Y *vs.* Rb/Y) 109
Figure 4.7 MORB normalized multi-element variations 111
Figure 4.8 MORB normalized multi-element reference patterns 113
Figure 4.9 Chondrite normalized multi-element variations 114
Figure 4.10 Secondary alteration and loss on ignition versus silica 116
Figure 4.11 Element mobility during mylonitization 117
Figure 4.12 Contamination versus fractionation (Pb isotopes) 119
Figure 4.13 Contamination versus fractionation (Sr isotopes) 122
Figure 4.14 Contamination versus fractionation (Nd isotopes) 124
Figure 4.15 Possible source reservoirs (ε_{Nd} *vs.* $^{87}Sr/^{86}Sr$) 125

Figure 4.16 Binary mixing and source reservoirs (ε_{Nd} *vs.* $^{87}Sr/^{86}Sr$) 127
Figure 4.17 Tectonic discrimination diagram (Rb *vs.* Y + Nb) 130

Chapter 5. Age and Thermal Evolution of the Northern Sacramento Mountains
Figure 5.1 Thermobarometric sample locations 135
Figure 5.2 Temperatures and pressures EWIC emplacement 139
Figure 5.3 Thermochronologic sample locations 146
Figure 5.4 U/Pb concordia diagram, VP94-129 (ion probe) and VP94-127 146
Figure 5.5 U/Pb concordia diagram, VP94-069b 149
Figure 5.6 U/Pb concordia diagram, VP94-138 and VP94-140a 150
Figure 5.7 Hornblende argon data 154
Figure 5.8 Biotite argon data 156
Figure 5.9 Zircon fission track data 158
Figure 5.10 Apatite fission track data 159
Figure 5.11 Apatite compositions 162
Figure 5.12 Cooling history of the Northern Sacramento Mountains 163
Figure 5.13 Age versus distance down-dip 164
Figure 5.14 Thermal profile of Northern Sacramento Mountains 167

Chapter 6. Angle of Faulting in the Northern Sacramento Mountains
Figure 6.1 Geometric relationship between normal faulting and ages younging 171
Figure 6.2 Geometric relationship between the paleogeothermal profile and faulting 172
Figure 6.3 Perturbation of the geotherm as a result of normal faulting 174
Figure 6.4 Sample distribution and younging to the northeast 177
Figure 6.5 Geometric relationships which control the angle of faulting 178
Figure 6.6 Angle of faulting from the "Age versus distance down-dip" technique 179

Chapter 7. Conclusions and Synthesis
Figure 7.1 Tectonogenesis of the northern Sacramento Mountains 182

LIST OF TABLES

Chapter 3. Structure of the Footwall

Table 3.1 Summary of foliation and lineation data associated with D2 72
Table 3.2 Correlation of deformational events in the Sacramento Moutains 92

Chapter 4. Geochemistry of the EWIC

Table 4.1 Summary of geochemical samples 99
Table 4.2 EWIC correlation coefficient matrix for major element oxides 101
Table 4.3 EWIC correlation coefficient matrix for trace elements 106
Table 4.4 Summary of initial lead analytical data 118
Table 4.5 Rb/Sr and Sm/Nd analytical data, and derived parameters 121
Table 4.6 Summary of end-member compositions 126
Table 4.7 Evidence for the petrogenesis of EWIC 131

Chapter 5. Age and Thermal Evolution of the Northern Sacramento Mountains

Table 5.1 Mineral closure temperatures 134
Table 5.2 Results from amphibole-plagioclase thermometry and Al in hornblende barometry 138
Table 5.3 U/Pb analytical data, conventional and ion probe 144
Table 5.4 Initial lead isotope analytical data 145
Table 5.5 Summary of $^{40}Ar/^{39}Ar$ analytical results 153
Table 5.6 Summary of fission track analytical results 160

ACKNOWLEDGEMENTS

Many people and organisations have assisted me one way or another and I am especially indebted to the Department of Earth Sciences at Oxford, the U.S. Geological Survey in Menlo Park, the Bureau of Land Management in Needles, and the Natural Environment Research Council (NERC). In Oxford, Professor John Dewey approved the project, was willing to have me as a student, and has been a continuous source of support and encouragement. Dr. Dave Waters and Dr. Ed Young both provided invaluable feedback/discussion. Field-assistance was provided via Burdett Coutts funding and Jason Bletcher (thanks Dr. J!). I learned a lot from many folks in Oxford: Keith Parrish for XRF techniques, Norman Charnley for microprobe techniques, Steve Wyatt for helping with so many things, Matthew Turnbull for help with the mass spectrometer, Steve Baker and Richard MacAvoy for their assistance with microphotographs and photographs, Roy Goodwin for too many things to mention in so short a treatise, and Steve Usher for trouble shooting computer difficulties. Thanks also to my office mates, who put up with my cleanliness! I do hope that I haven't neglected anyone, but if I have, just refresh my memory and I'll stand you a pint the next time I'm in town.... The NERC generously funded this work via a research studentship; I would also like to mention my deep appreciation to NERC for providing extra funding due to a medical emergency.

The U.S.G.S. provided both technical and academic support. The former included my 4WD vehicle each season, my mylar base map and various topographic and orthophoto maps, general office support, and fantastic laboratory and intellectual support. The later was principally in the form of Dr. Keith Howard, who was always interested, giving of both his time and his knowledge. Dr. Joe Wooden generously provided me with access to his U/Pb laboratory, while Chuck Holdsworth showed me "the ropes" associated with U/Pb mineral separation and column chemistry. Betty Hamachi introduced me to the principals of heavy liquid mineral separation and facilitated my own work under restrictive time limitations, for which I am very grateful. I am especially indebted to Dr. Jack Hillhouse, for facilitating U.S.G.S. support.

The Bureau of Land Management, Needles, was practically my home for six months, a haven for both business and social needs. There is a great bunch of people at that office, all generous with their time and willing to help whenever they can. I was kindly allowed access to drafting tables, email, colour air

photographs, doughnuts, BBQs, etc. Special thanks go to Elaine Downing and Jim Foote for various services too numerous to list here...

The argon and fission track work was performed in Melbourne, at La Trobe University under the auspices of Dr. Dave Foster and the Australian Research Council. I was allowed access to Dave's laboratory for one month, using valuable machine time and resources, and mere words seem insufficient in expressing my gratitude to Dave and his facility! Paul O'Sullivan introduced me to fission track counting, which could not be mastered in the short time allowed, and so special thanks go to Paul for counting all my tracks!

Special thanks also go to Barbara John for sparing her expertise and time in the field, to John Argent and Erin Campbell for stimulating discussion about life *and* the field area, and to Martin Whitehouse for his emotional and financial support. (I should like to point out that this is the *second time* that Martin has been through a higher degree with me, surely a fate that no-one should have to endure twice!) Finally, my gratitude to the Museum of Natural History, Sweden, for logistical support while I was writing up.

EXTENDED ABSTRACT

Geology of the northeast Sacramento Mountains, California

V. L. Pease
Wolfson College

In order to understand the tectonic evolution of the northeast Sacramento Mountains metamorphic core complex, a multidisciplinary investigation into the geology, structure, geochemistry, age, and thermal history of region was undertaken. The combination of detailed mapping, structural analysis, petrography, and geochemistry has lead to a petrogenetic understanding of crustal evolution in the range. By combining this information with thermobarometry and thermochronology, the timing, distribution, and intensity of tectonothermal events is revealed.

The syntectonic Eagle Wash Intrusive Complex (EWIC) intruded during detachment faulting ~20 million years ago (U/Pb zircon, monazite, sphene, and SHRIMP zircon). Using the amphibole-plagioclase thermometer and total aluminum in hornblende barometer, the temperature and pressure of emplacement (crystallisation) for the EWIC was determined to be 680 ± 19°C and 3.3 ± 0.75 kb, respectively. The EWIC is predominantly granodiorite, with lesser amounts of diorite, granite, and leucogranite. Major and trace elemental data indicate that the EWIC is a calc-alkaline intrusive complex. Isotopic data are variable ($^{87}Sr/^{86}Sr$ = 0.708-0.716, $^{143}Nd/^{144}Nd$ = 0.51172-0.51240, $^{206}Pb/^{204}Pb$ = 17.72-18.53, $^{207}Pb/^{204}Pb$ = 15.54-15.60, and $^{208}Pb/^{204}Pb$ = 38.68-39.07) and suggest that the source for the EWIC was either heterogeneous and/or involved variable degrees of assimilation.

Low Mg numbers (~45) for the least fractionated members of the diorite suite (*Td*) preclude equilibration with a mantle source containing olivine or pyroxene, suggesting that the "primitive" compositions in this study (*Td*) are themselves derivatives of an unseen parent. The most likely composition of this unseen parent in the southern Basin and Range Province is either the depleted mantle or an enriched subcontinental lithospheric mantle. Enriched LIL and HFS elements, relative to MORB, favour an enriched mantle source. Using the enriched mantle signature observed in Miocene age basalts from the region, EWIC trends cannot be successfully modelled. In order to derive EWIC lithologies from an enriched mantle source, the enriched mantle would need to have an $^{87}Sr/^{86}Sr$ ratio > 0.707. This is not a composition

observed in the region and suggests that the parent magma to EWIC *plutonic* lithologies involved a greater component of crustal assimilation than their possible *extrusive* equivalents.

Binary mixing models do not successfully reproduce the observed isotopic trends of the EWIC. This implies that a more complex AFC-type process(es) was involved in EWIC genesis. Mafic phases of the EWIC (*Td* and *Tgd*) were not generated by the assimilation of supracrustal material, but instead require a more mafic (lower Sr), less radiogenic (lower $^{87}Sr/^{86}Sr$), and older (negative ε_{Nd}) crustal component. The highly evolved leucogranites (*Tlg*) could not be the result of mixing, and it is considered more likely that they represent variable degrees of partial melting of upper-crustal material. This interpretation is consistent with the evolved neodymium ($^{143}Nd/^{144}Nd$ = 0.5117-0.5121) and strontium ($^{87}Sr/^{86}Sr$ > 0.716) data, and with the highly variable trace element abundances (at any given silica content) for *Tlg*.

The elemental and isotopic data indicate that the petrogenetic evolution of the EWIC involved 1) an enriched subcontinental lithospheric mantle source, 2) the assimilation of heterogeneous crustal material (both middle- and upper-crust) with *variable degrees* of partial melting, and 3) concurrent fractional crystallisation. Individual contributions of each of these processes could not be quantified, particularly because the composition of both the enriched subcontinental lithosphere and the lower- to middle-crust in the region are not well-constrained, but also because of the decoupling of major elements, trace elements, and isotopic ratios during anatexis and assimilation.

Three distinct episodes of deformation (D1, D2, and D3) can be identified in the northeast Sacramento Mountains, with D1 representing pre-Tertiary (or pre-detachment faulting) deformation, D2 representing mid-Tertiary (or syn-detachment faulting) deformation, and D3 representing mid- to late-Tertiary (or late- to post-detachment faulting) deformation. D2, the dominant fabric, is mylonitic and Miocene in age. It shallows from west (S2, ~155°, 25SW) to east (S2, ~135°, 15SW). This variation is not seen in the mineral stretching lineation (L2), which has a consistent orientation of ~240°, 15°SW. Older D1 fabrics are rotated into parallelism with D2 to the east. S-C fabrics are predominantly top-to-the-northeast, consistent with the inferred direction of hanging wall displacement. These structural relationships are interpreted to represent an evolving shear zone, with the SW dip of S2 being attributed to the rotation of the mylonitic fabric during its "capture" by a younger splay of the detachment fault system.

The youngest deformational event (D3) includes the apparently *synchronous* development of both strike-slip and near-vertical faulting. These structural features could not have resulted from the same stress regime and suggest a three dimensional strain existed in the region during their development. Vertical, NW and NE strike-slip fault motions associated with D3 indicate E-W extension with a component of horizontal, N-S directed shortening. The near vertical orientations of normal faults associated with D3 suggest that $\sigma_1 > \sigma_2 \approx \sigma 3$. The dominant stress in the northeast Sacramento Mountains alternated between σ_1 and σ_3, i.e.- between $\sigma_3 < \sigma_2 \approx \sigma_1$ and $\sigma_1 > \sigma_2 \approx \sigma_3$. Assuming an initial condition of an inclined plane with $\sigma 1 = \sigma 2 = \sigma 3$ = lithostatic load, σ_1 and σ_2 would have been roughly equal during detachment faulting. Variations in vertical stress arising from differential tectonic unroofing, buoyant forces associated with an uncompensated undulatory crustal root, or magmatic inflation could have resulted in the alternation of the dominant stress direction. The alternation of the dominant stress direction is promoted by the episodic nature of magmatic intrusion and detachment faulting in space and time.

The dominant fabric (D2) is well-developed in the EWIC and is thought to have formed during the cooling and uplift of the pluton, at temperatures ≤500°C. Evidence of higher temperature, magmatic fabrics is not expected to have survived the lower temperature, sub-solidus deformation. In the NE Sacramento Mountains, younging of ages in the tectonic transport direction is consistent with normal faulting. After intrusion at ~20 Ma, very rapid cooling of the EWIC from magmatic temperatures to below ~100°C (T_c of fission tracks in apatite) occurred by 15 Ma. This requires cooling rates of >100°C/Ma and exhumation rates of 1.5 - 3 km/Ma. Tectonic denudation associated with Miocene detachment faulting is interpreted to be the cause of such rapid exhumation.

In the northwest Sacramento Mountains, Late Cretaceous ages associated with the T_c of zircon and sphene (≥600°C), as well as with the T_c of biotite (~325 °C), require cooling rates on the order of 100°C/Ma. Post-Late Cretaceous cooling in the northwest Sacramento Mountains slowed to ~1-6°C/Ma (the difference between biotite and zircon (FT) ages). Lastly, the northeastern-most region of the northwest Sacramento Mountains records more rapid cooling of 38-53°C/Ma (through the T_c associated with biotite, zircon (FT), and apatite) to ambient surface temperatures, between ~20 and 15 Ma. The high temperature portion of the cooling curve for the northwest Sacramento Mountains is consistent with cooling of the crust

by thermal conduction, but the sudden increase of the cooling rate to 38-53°C/Ma between 20 and 15 Ma again suggests that tectonic denudation (unroofing) as a result of detachment faulting was the driving mechanism for the final cooling of the northwest Sacramento Mountains.

The fundamental premise in applying thermochronologic data to calculate the angle of faulting is that as normal faulting proceeds, the footwall is progressively unroofed, and minerals from deeper crustal levels in the footwall and along the fault surface pass through their closure temperatures later in time. This results in ages younging down-section/down-dip. In the NW Sacramento Mountains, samples appear to record the movement of the fault block through the closure temperatures of biotite and zircon (FT) and in the NE Sacramento Mountains, the movement of the fault block is recorded by the closure temperatures associated with hornblende and biotite. The angle of faulting, calculated using several techniques dependant upon theromochronologic data, was consistently low-angle: $\leq 30°$. This solution is robust inasmuch as the angle of faulting is likely to be less than 30°, within error at the 95% confidence level and whether a linear or non-linear geothermal gradient is assumed. Furthermore, a slip rate along the Sacramento Mountains detachment fault of ~4mm/yr is also obtained. This slip rate suggests that extension was slower here than elsewhere in the extensional corridor.

A tectonogenetic model for the evolution of the Sacramento Mountains, consistent with the above data, emphasises the importance of syntectonic (pre-tectonic?) magmatism for core complex development. Magmatism is necessary to i) thermally soften the crust prior to faulting, ii) contribute to upward buoyancy of the crust during faulting, iii) raise the local (regional?) geotherm, facilitating the development of mylonites, and iv) facilitate the development of a variable stress field. Thus, the uplift and cooling of core complexes is primarily driven by the combination of *magmatism and tectonic denudation* via detachment faulting. It is suggested that theoretical fault mechanics inadequately accounts for rotation of the stress field in an extending crust, which can lead to the development of low-angle faulting.

Chapter 1

Introduction

1.1 Metamorphic core complexes and continental extension

The study of metamorphic core complexes has revolutionised our understanding of continental extensional processes. Recognised in the North American Cordillera since the late 1970's (e.g., Crittenden et al., 1980), metamorphic core complexes have come to be recognised the world over as major features associated with extensional tectonics (e.g., Hetzel et al., 1995; Jolivet et al., 1991; Hossack, 1984). Most of the models developed to explain the evolution of metamorphic core complexes have been based on field studies in the Basin and Range province of the western United States, an area of well-documented extension. Despite intensive research efforts in metamorphic core complexes within the Colorado River extensional corridor (Howard and John, 1987), several ranges remain largely unexplored, including the northeast Sacramento Mountains. Thus, research efforts focused on the northeast Sacramento Mountains metamorphic core complex are likely to provide insights into the crustal evolution and tectonic processes operating in the development of such core complexes.

Metamorphic core complexes are characterised by a ductilely deformed *footwall* composed of mid- to lower-crustal, high-grade metamorphic rocks, juxtaposed against a brittlely deformed *hanging wall* of

upper-crustal, low-grade or unmetamorphosed rocks, along a low-angle, normal (*detachment*) fault (Fig. 1.1). These faults are large, regionally extensive structures that form traceable, continuous surfaces, accommodate significant extension, and excise large (10-15 km) amounts of crustal section (Davis, 1988). One of the commonly observed features associated with metamorphic core complexes is the *doming* of the detachment fault surface, the footwall, and the mylonitic foliation usually present in the footwall (e.g., Reynolds and Lister, 1990). The mylonitic fabric associated with core complexes typically displays a regionally consistent mineral stretching lineation. Pre-, syn-, and post-tectonic plutonism may also be present. The detachment fault surface is commonly preserved as a microbreccia "ledge" with a polished slip-surface. Striations on the fault surface are generally concordant with the mineral stretching lineation in the mylonites of the footwall. Directly below the detachment fault surface, to depths of 5-30 m, is a zone of pervasively brecciated and altered rocks, commonly known as the "chloritic breccia zone" (Schweitzer, 1991; Lister and Davis, 1989).

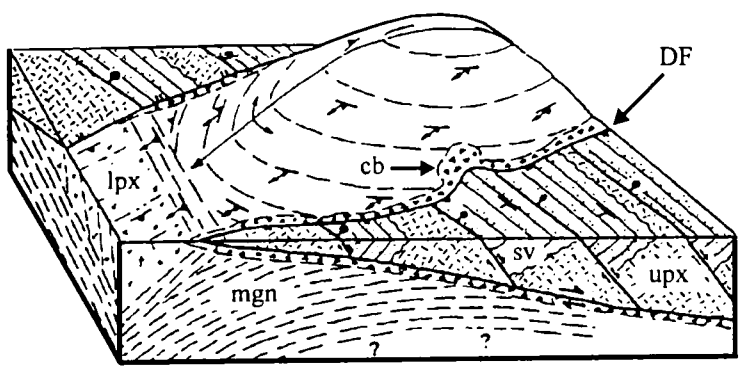


Figure 1.1 Characteristics of a metamorphic core complex (after Davis and Lister, 1988). Note dome of lower-plate basement surrounded by detachment fault. Lower-plate crystalline rocks (lpx), Upper-plate crystalline rocks (upx), mylonitic gneiss (mgn), detachment fault (DF), Miocene sediments and volcanic rocks (sv), and chloritic breccia (cb).

The *doming* of the core complex is thought to be the response of a flexing crust to isostatic rebound following denudation (Spencer, 1984) or due to magmatic inflation (Lister and Baldwin, 1993). It is

typically the result of the superposition of two upright fold sets (e.g., Yin and Dunn, 1992; Yin, 1991; Spencer, 1982). One of these fold sets comprises long-wavelength folds with axes that trend perpendicular to the movement direction. Most workers agree that this folding of the fault zone occurs in response to tectonic denudation and isostatic rebound of the footwall (Reynolds and Lister, 1990; Bartley et al., 1990; Wernicke and Axen, 1988; Hamilton, 1988; Buck, 1988; Spencer, 1984). These structures clearly overprint mylonitization and active displacement across the fault zone. The second set of fold axes are related to shorter-wavelength folds oriented parallel to the movement direction. Some workers interpret these folds to form as primary corrugations on the fault (Spencer and Reynolds, 1991; John, 1987). Others argue that the movement-parallel folds result from secondary folding of an originally sub-planar fault zone (Fletcher and Bartley, 1994; Yin and Dunn, 1992; Yin, 1991; Spencer, 1982).

1.2 Models for continental extension

Observations and considerations A number of models have been proposed to explain the evolution of metamorphic core complexes and detachment faults. A *successful* unifying model must explain a number of observations common to most metamorphic core complexes: i) extensive brittle deformation of hanging wall rocks above detachment faults, ii) overprinting of ductile fabrics by brittle deformation in footwall rocks (the inevitable consequence of bringing rocks from deeper in the crust to the surface), iii) uniform shear sense indicators which suggest unidirectional transport of the hanging wall relative to the footwall (Hetzel et al., 1995), iv) detachment faults present as the youngest structures (Scott and Lister, 1992), v) rapid exhumation of footwall rocks (John and Foster, 1993), and vi) the presence of pseudotachylites associated with detachment faults, suggesting that these faults were seismogenic (John and Foster, 1993).

Two important considerations associated with developing a unifying model to explain the evolution of metamorphic core complexes have to do with 1) how to bring mylonitic rocks from original depths of 10-15 km to the surface *rapidly*, and 2) the geometry and mechanics of detachment faults. With respect to 1), $^{40}Ar/^{39}Ar$ and fission track thermochronologic data indicate that mid-crustal mylonitic rocks associated with metamorphic core complexes have cooled quickly as a result of tectonic exhumation. Cooling rates as high as 100°C/Ma, but generally around 50°C/Ma, have been documented in the Chemehuevi, Whipple, and Ruby Mountains (John and Foster, 1993; Foster et al., 1990; Davis, 1988; Dallmeyer et al., 1986; Dokka et

al., 1986). Assuming a constant geothermal gradient of 30°C/km, upward rates of motion of 4 km/Ma are implied. Additionally, barometric studies on syn- and post-tectonic intrusive rocks indicate exhumation rates of 1.3-2.3 km/Ma (Anderson, 1988).

With respect to 2) above, the issue is whether these faults were initiated and active at higher angles and were subsequently rotated to their present low-angle configuration, or were initiated and active at low angles. This quandary arises because theoretical fault mechanics predicts that active normal faults near the Earth's surface should be oriented 45-75° from horizontal (Anderson, 1951). Fault plane solutions for large continental normal faults world-wide have shown that most earthquakes nucleate at depths of 6-15 km on faults dipping 30-60°, with seismic faults dipping <30° being rare (Thatcher and Hill, 1991; Jackson and White, 1989; Jackson, 1987; Jackson and McKenzie, 1983). There are, however, a few notable examples of low-angle fault plane solutions (Johnson and Loy, 1992; Abers, 1991; Allmendinger et al., 1983) and Wernicke (1995) has proposed that the absence of low-angle fault plane solutions may be a function of recurrence interval. He suggests that low-angle detachment faults, perhaps due to their significantly greater efficiency in absorbing elastic strain associated with horizontal extension, fail less frequently but with larger magnitude events.

That *some* of the structural features associated with metamorphic core complexes must be related to continental extension, is a common theme of *all* of the models proposed to explain the evolution of metamorphic core complexes and detachment faults. Whether rotated higher-angle faults or originally low-angle features, these two scenarios have become "end-members" in detachment fault geometry and are represented by the "pure shear" model and the evolving "simple shear" zone, respectively. These models differ primarily in the vertical distribution of strain within the lithosphere.

The "pure shear" model - In the "pure shear" model (Gans et al., 1985; Miller et al., 1983; Eaton, 1982; Rehrig and Reynolds, 1980; Proffett, 1977), the detachment fault is assumed to mark a brittle-ductile transition, with "domino" style block rotation in the brittle, upper-crust along high-angle faults (Fig. 1.2). As deformation progresses in the hanging wall, high-angle faults are rotated to shallow angles to conserve volume, become mechanically unstable, and the next generation of mechanically stable high-angle faults are initiated. Deformation below the detachment fault is via ductile, coaxial (pure) shear. The detachment fault is considered to be the surface (decollement) where brittle deformation ends and ductile deformation begins.

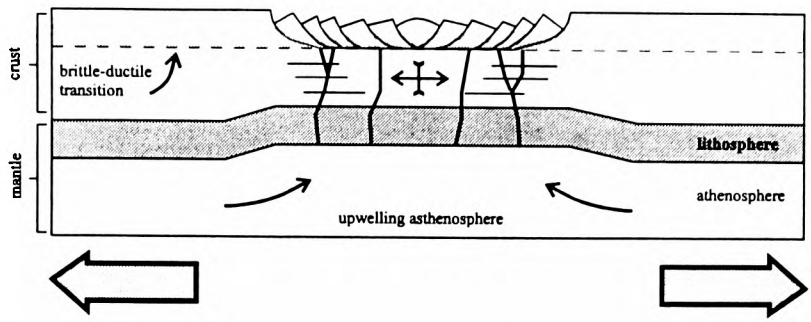


Figure 1.2 Symmetric "pure" shear. Note synchroneity of brittlely deforming upper-plate with ductilely deforming lower-plate. Ductile deformation in the lower-plate is the result of bulk, coaxial extension as the entire lower lithosphere uniformly stretches (after Lister and Davis, 1989).

The model predicts synchronous coaxial deformation of the upper- and lower-plates, until the upper-plate passes into the brittle regime. A consistent sense of shear would be absent in the lower plate, but the upper- and lower-plates would have parallel directions of maximum extension. This model agrees well with theoretical fault mechanics, which predicts dips of 45-75° for upper-crustal normal faults (Anderson, 1951), and with earthquake focal mechanism data which indicate that most seismically active normal faults dip 30-60° (Thatcher and Hill, 1991; Jackson and White, 1989; Jackson, 1987; Jackson and McKenzie, 1983). It is difficult, however, to produce the sharp juxtaposition of metamorphic grade and to promote the rapid uplift/exhumation of mid-crustal rocks observed in core complexes with this model. Furthermore, there is no a priori reason for the decollement to remain the brittle-ductile transition as it is exhumed through successively higher structural levels during extension.

The "simple shear" model - The evolving "simple shear" zone (Lister and Davis, 1989; Wernicke, 1981) is characterised by an active low-angle fault that evolves into a crustal-scale shear zone with depth (Fig. 1.3). As the crust extends, lower-plate rocks are drawn upwards and out from beneath a hanging wall subject to brittle extension. Mylonites formed within the ductile shear zone at depth are transported to higher structural levels, where they are subsequently cataclastically deformed.

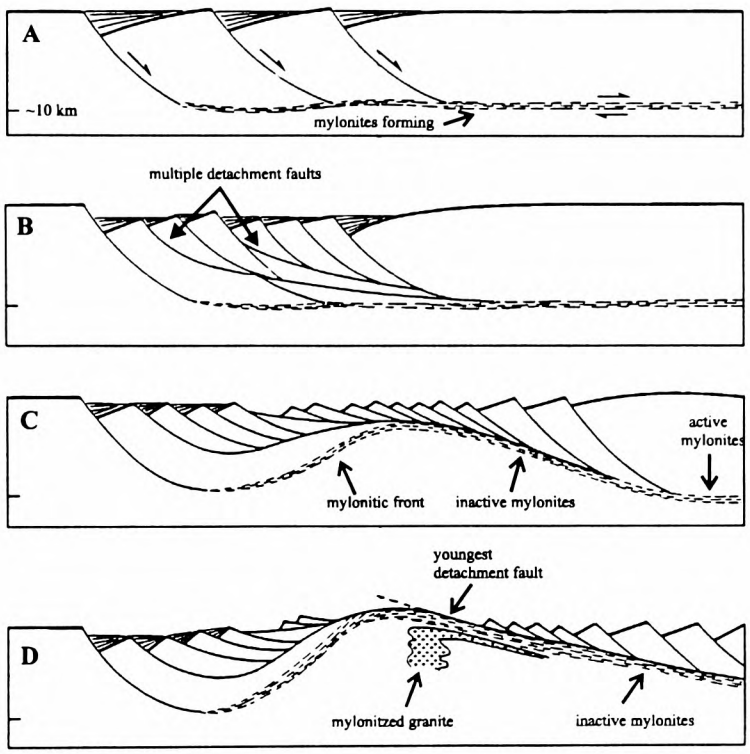


Figure 1.3 Evolving "simple" shear zone (after Lister and Davis, 1989). With increasing depth (~10 km), rocks are deformed in a flat-lying, ductile shear zone (A and B). As normal faulting progresses, ductilely deformed rocks are transported upwards in the footwall (C) and are overprinted by brittle fabrics. In D), the metamorphic core complex is finally exposed beneath younger detachment faults.

This model predicts that the contact between brittle and ductile deformation is gradational and characterised by a broad zone of simple/general shear, with intracrustal laminar flow forming mylonites. The sense and direction of shear in the mylonites would be the same as those associated with the detachment fault because they are kinematically related. This model explains the sharp contact between rocks of different metamorphic grade, large lateral displacements of structural markers observed across detachment faults, and can accommodate the rapid uplift/exhumation of mid-crustal rocks. The model, however, is not consistent with theoretical fault mechanics, which does not favour low-angle orientations for active normal faults (Anderson, 1951), nor with earthquake focal mechanism data suggesting that most seismically active normal faults dip 30-60° (Thatcher and Hill, 1991; Jackson and White, 1989; Jackson, 1987; Jackson and

McKenzie, 1983). The existence of low-angle faults are, however, substantiated by a small number of fault planes and are corroborated by seismic reflection profiles (Johnson and Loy, 1992; Abers, 1991; Smith and Bruhn, 1984; Allmendinger et al., 1983).

The "rolling-hinge" model - Other models also employing non-coaxial shear have been proposed. The most notable of these, the "rolling-hinge" model (Buck, 1988; Hamilton, 1988; Wernicke and Axen, 1988), combines the additional element of flexural rotation with isostatic uplift of the footwall (Fig. 1.4). In the "rolling-hinge" model, moderate- to high-angle faults are rotated to low angles. This rotation is in response to isostatic forces in the footwall, resulting from the tectonic denudation of the hanging wall. New, higher-angle faults are propagated when the rotated faults can no longer overcome frictional resistance. The "hinge" which separates rotated and shallow from unrotated and steeper fault segments, "rolls" through the footwall, migrating towards the tectonically denuding hanging wall.

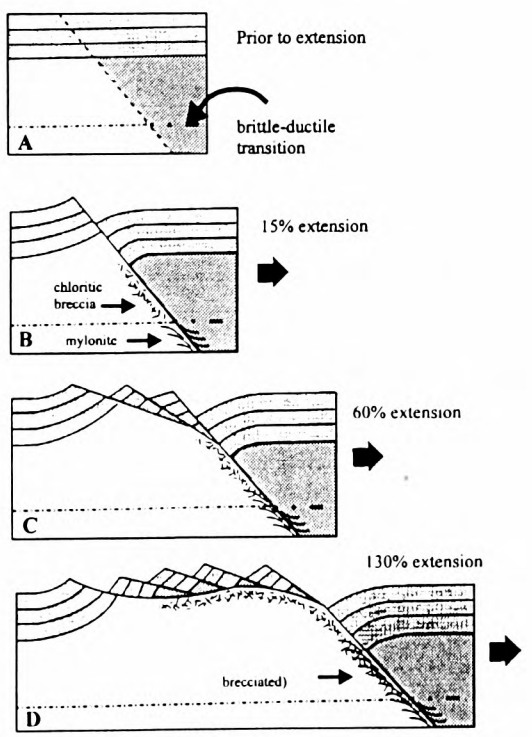


Figure 1.4 Development of the "rolling hinge" (after Buck, 1988; Hamilton, 1988; and Wernicke and Axen, 1988). Originally moderate- to steeply-dipping normal faults are progressively rotated to mechanically inactive, lower angles (C). Younger, active faults continue to form near the hanging wall. This results in younging of structural features in the direction of tectonic transport (D).

The deformational structures predicted by this model include i) a detachment fault consisting of a series of smaller fault segments, which progressively young from shallower- to higher-angles and towards the tectonic transport direction, and ii) a footwall where the upper portion displays post-mylonitic, extensional brittle deformation, overprinted by contractional brittle deformation oriented perpendicular to the direction of extension. As a result of progressive faulting, the footwall moves into the extensional brittle regime and, as the hinge migrates, the upper part of the footwall should experience late contraction along the previous extension direction (Bartley et al., 1990; Manning and Bartley, 1994). This model is consistent with seismic data and theoretical fault mechanics, and provides a mechanism for the rapid uplift/exhumation of mid-crustal rocks. Some aspects of the model, however, are contrary to the well-established field observations which show that low-angle faults are commonly the youngest structures (cross-cutting high-angle faults), and that synextensional sediments are often juxtaposed against detachment faults without major tilting.

The role of magmatism The role of magmatism associated with crustal stretching in the extensional corridor is poorly understood, though the spatial and temporal coincidence between magmatism and core complex development suggest that these processes may be associated phenomena. That volcanism, extensional faulting, and core complex development were contemporaneous in the Colorado River extensional corridor is well documented (Spencer et al., 1995; Armstrong and Ward, 1991; Gans et al., 1989; Davis, 1988). Only recently, however, with the development of high resolution ion-probe technology, have numerous Tertiary *plutonic* suites within the extensional corridor been recognised (this investigation - Chapter 5; Foster et al., 1996; Lister and Baldwin, 1993). Parsons and Thompson (1993) have suggested that magmatic inflation during intrusion may affect the local stress field. If intrusion occurs at rates higher than those associated with extension, the horizontal compressive stress must increase, which has the effect of locally rotating the principal stress field. Furthermore, thermal softening at these mid-crustal levels, coupled with vertical magmatic inflation, allows for a more mobile isostatic doming of the core complex. The thermal perturbation of the geothermal gradient associated with plutonism has a transient effect on the brittle-ductile transition, effectively raising the transition zone to higher crustal levels (Lister and Baldwin, 1993), such that core complex formation may be the direct result of pluton emplacement at depth.

1.3 The Sacramento Mountains

Colorado River extensional corridor The Sacramento Mountains are located in the Basin and Range province of the western United States, which has a long and complex history of deformation including Proterozoic extension and Mesozoic contraction, followed by pronounced Cenozoic extension (Fig. 1.5). During the Miocene, the southern Basin and Range experienced moderate to extreme (~100%) crustal extension in the region known as the Colorado River extensional corridor (Howard and John, 1987). Miocene extension is responsible for the development of metamorphic core complexes and the landscape seen in the region today.

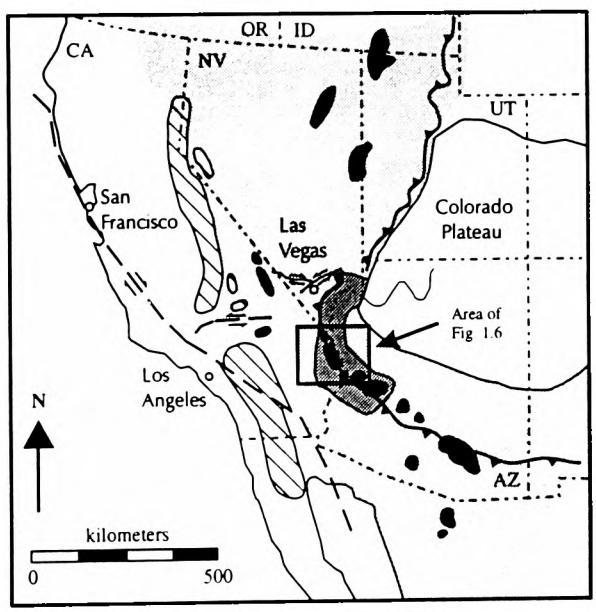


Figure 1.5 Location and tectonic setting of metamorphic core complexes and the Colorado River extensional corridor. Core complexes are shown in black, the greater Basin and Range province in light shading, the extensional corridor in dark shading, the eastern edge of the Mesozoic fold and thrust belt with teeth and the Mesozoic plutonic arc with hatchure.

The extensional corridor includes parts of California, Nevada, and Arizona (Fig. 1.6). Extension was accommodated along a regional scale, shoaling detachment fault system with its headwall in the eastern Old Woman and Homer Mountains (Howard and John, 1987). The fault system roots downward to the northeast, beneath the Hualapai Mountains at the edge of the Colorado Plateau. Detachment faults of this

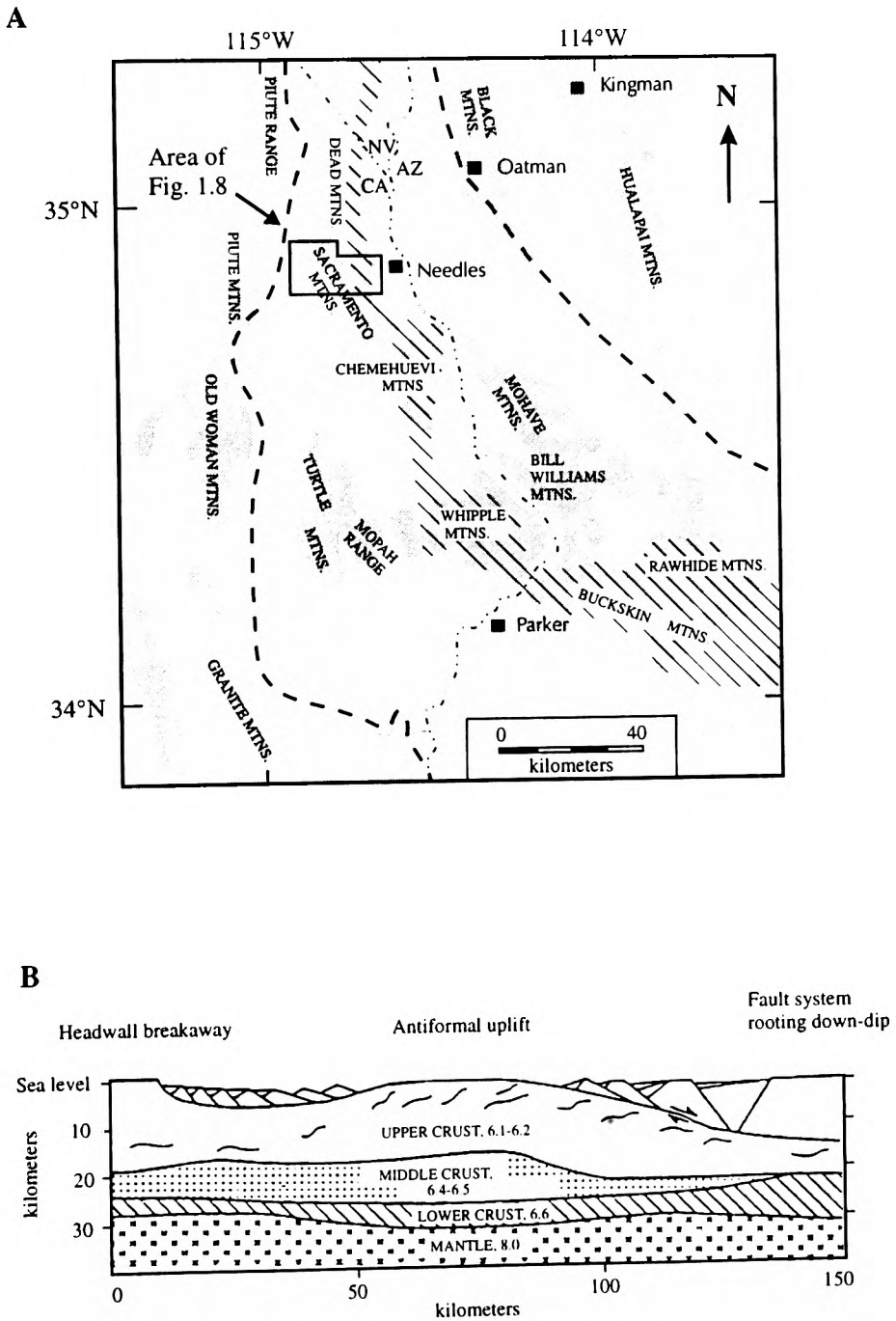


Figure 1.6 - The Colorado River extensional corridor (after Howard and John, 1987). A) The dashed line shows the limits of the corridor and hatchure patterns represent the central region of core complexes. B) Schematic crustal section across the extensional corridor with seismic velocities in km/sec. (after Spencer, 1984, and McCarthy et al., 1991).

system are exposed along the flanks of the Homer, Dead, Sacramento, Chemehuevi, Whipple, and Buckskin Mountains. Cumulative slip on the fault system increases to the northeast across the region and totals 40-70 km (Spencer and Reynolds, 1991; Davis, 1988; Howard and John, 1987). The width of the corridor increases from 50 to 120 km, north to south. Numerous hanging wall fault blocks, with southwest dipping synextensional sedimentary and volcanic rocks, have been displaced consistently to the northeast and rotated top-to-southwest (Spencer, 1985; Howard et al., 1982; John, 1982; Davis et al., 1980). Higher-angle, block bounding faults strike perpendicular to the tectonic transport direction. Exposed in the central part of the corridor are the isolated mountain ranges which form the metamorphic core complexes of the region.

Regional geologic setting Prior to the Mesozoic, southeastern California was part of the stable North American craton (Bennett and DePaolo, 1987). Proterozoic basement gneisses experienced granulite to upper-amphibolite facies metamorphism at 1.7 Ga (Foster et al., 1992; Wooden and Miller, 1990). Intrusion of the regionally extensive Fenner Gneiss was contemporaneous with this metamorphism (Bender et al., 1990; Hazzard and Dosch, 1936) and was followed by the intrusion of 1.4 Ga granitic plutons (Anderson, 1983) and 1.1 Ga diabase sills (Elston and McKee, 1982). Miogeoclinal sediments from the craton margin began to be deposited in the Late Precambrian, and sedimentation continued during the Cambrian through the Devonian (Burchfiel and Davis, 1981).

In the Old Woman-Piute Mountains, to the west of the Sacramento Mountains and the headwall to the extensional corridor (Fig. 1.6), Proterozoic metamorphism is preserved and records pressure and temperature conditions ~9 kb and ~700°C (Foster et al., 1992). The relict mineral assemblage of orthopyroxene + hornblende + plagioclase suggests that Proterozoic rocks were once at granulite facies conditions. Proterozoic metamorphism in the Old Woman Mountains area apparently occurred at higher pressures than in other parts of the eastern Mojave Desert and southern Nevada. Low-pressure granulite facies conditions are recorded in the McCullough Range (Young et al., 1989) and at Gold Butte, Nevada (Thomas et al., 1988), where Proterozoic rocks experienced 3-4 kb and 590-750°C. Proterozic upper-amphibolite facies metamorphism (2-4 kb and 620-680°C) also affected rocks exposed in the Whipple Mountains (Thomas et al., 1988).

Proterozoic gneisses in the Old Woman-Piute and Big Maria Mountains are unconformably overlain by 1-2 km of predominantly carbonate sediments, which range from Paleozoic through early

Mesozoic in age (Stone et al., 1983). Within the extensional corridor, these sediments have been eroded and outcrops of pre-Tertiary sediments are rare. This thick succession of sediments reflects the stable passive margin setting which existed along the western edge of the North America.

In the mid-Jurassic the western margin of North America changed from a passive margin to an active subduction zone (Burchfiel and Davis, 1981). This transition resulted in the reactivation of the old continental crust across the western United States, accompanied by intense deformation, arc magmatism and associated regional and contact metmorphism. Jurassic arc magmatism of the Sierra Nevada is located ~100 km west of the extensional corridor (Fig. 1.6). Jurassic deformation and metamorphism is widespread and well documented in southwest Arizona and in southern California (Tosdal et al., 1990; Hoisch et al., 1990), but pre-Cretaceous plutons are relatively scarce within the extensional corridor: A potassic granitic pluton in the Ship Mountains, potassic granitic dykes in the Old Woman-Piute Mountains and Kilbeck Hills (Howard et al., 1987), and a synkinematic granodioritic pluton in the Clipper Mountains (Howard et al., 1995).

Thrusting and crustal thickening of the Paleozoic sequences and Proterozoic gneisses accompanied magmatism and metamorphism throughout the Cretaceous. In the Old Woman Mountains, the Scanlon Nappe consists of a series of ductile thrusts placing Proterozoic basement gneisses above metamorphosed Paleozoic and Triassic sedimentary strata (Hoisch et al., 1988). Cretaceous plutonism, and attendant metamorphism and deformation, is common throughout the extensional corridor. Cretaceous plutonic rocks have been identified in almost every range, with the greatest volumes located in the Stepladder Mountains, Old Woman-Piute Mountains and Chemehuevi Mountains. In the Old Woman-Piute Mountains, Cretaceous contact metamorphism reached upper amphibolite facies (>650°C at 3.5-5.0 kb). This contrasts with the ambient retrograde greenschist facies metamorphism associated with pre-Cretaceous basement in the Ship Mountains, which were part of the upper crust by Cretaceous time (Foster et al., 1992, 1990). Cretaceous plutonic rocks within the extensional corridor are weakly peraluminous to metaluminous granite and granodiorite, with Sm/Nd and Pb/Pb isotopic compositions indicative of crustal derivations (Anderson and Cullers, 1990; John and Wooden, 1990).

Burchfiel and Davis (1981) suggested that these Mesozoic structures link the Cordilleran foreland fold and thrust belt of Nevada and western Utah to southern Arizona, where brittle thrusts thicken the

Paleozoic and Mesozoic passive margin sediments. In the extensional corridor, however, thrusting involved mostly basement lithologies and appears to have been controlled by thermally-induced ductility of mid-crustal levels. This ductility resulted from plutonism, reflecting deeper levels of the orogen (Howard et al. 1987; Haxel et al, 1984; Burchfiel and Davis, 1981). This certainly appears to be the case in the Chemehuevi Mountains, where the development of mylonitic deformation is associated with the intrusion of the ~68 Ma Chemehuevi Mountains plutonic suite (John and Mukasa, 1990). A period of conductive cooling, facilitated by local tectonic denudation, followed Cretaceous thrusting and plutonism (Foster et al., 1992). Most of the Old Woman-Piute Mountains region had cooled to below 300°C by about 70 Ma. Parts of this region were within a few kilometres of the surface before the onset of Cenozoic extension.

The western margin of North America was once again reorganised at ~40 Ma, when Mesozoic compressional deformation ended (Dickinson, 1979). Between 20 and 30 Ma, the East Pacific Rise came into contact with the North American plate, resulting in the development of the northwest trending dextral transform boundary active today (Christiansen and Lipman, 1972; Atwater, 1970). The change from subduction to transform tectonics corresponded with the diachronous development of magmatism and extensional deformation in the Cordillera (Eaton, 1984; Glazner and Bartley, 1984). The development of core complexes related to detachment faulting began in the northern Cordillera in the Eocene and in the southwest United States during the Oligocene to mid-Miocene (Spencer and Reynolds, 1986; Glazner and Bartley, 1984). Extension occurred while the regional horizontal least principal stress was oriented WSW-ENE (Zoback et al., 1981). Thus Tertiary extension was parallel to the direction of shortening associated with Mesozoic compression.

Within the extensional corridor, extension of the upper and middle crust was accomplished along an imbricate, east-dipping detachment fault system (Howard and John, 1987; Fig. 1.6). Single detachment splays of the greater fault system can be traced for tens of kilometres, e.g., Whipple detachment fault (Davis and Lister, 1988) and Chemehuevi detachment fault (John, 1987). The development of multiple generations of detachment faults have been recognised in the Sacramento Mountains (Spencer and Turner, 1983; McClelland, 1981), Chemehuevi Mountains (John, 1987), the Whipple Mountains (Davis and Lister, 1988), and the Dead Mountains (Howard, unpublished mapping). Correlation of detachment fault systems between

ranges is difficult because of the absence of outcrop in the Pliocene to Holocene basins surrounding the ranges and the surprisingly different lithologies in each range.

The asymmetric geometry of the extensional corridor, the consistent southwest dipping syntectonic deposits, and northeast dipping faults suggest non-coaxial shear failure of the continental crust (Wernicke, 1984). Seismic studies (McCarthy et al., 1991), however, suggest that the deepest part of the crustal section has a symmetric geometry (Fig. 1.6), compatible with models of crustal extension dominated by coaxial shear (McKenzie, 1978). The "mid-crustal bulge" at a depth of 10 km has been interpreted to represent magmatic inflation and inward intracrustal flow in response to tectonic denudation during extension (Wilson et al., 1991; McCarthy et al., 1991; Block and Royden, 1990). This is consistent with structural and thermobarometric studies which suggest uplift of the footwall from a depth of 10-15 km during extension (this study; Anderson, 1988).

The onset and cessation of Cenozoic extension in the Colorado River extensional corridor is relatively well constrained. Extension began ~24-26 million years ago, based on K-Ar ages of the oldest volcanic units in synextensional Tertiary basins (Nielson and Beratan, 1995; Spencer and Reynolds, 1991; Howard and John, 1987; Brooks and Martin, 1985), crystallisation ages of the oldest synextensional plutons in the lower plate of core complexes (Foster et al., 1990; Anderson et al., 1988), and the oldest $^{40}Ar/^{39}Ar$ cooling ages directly related to denudation of footwall rocks (Foster et al., 1990). The ages of untilted volcanic rocks, thermochronology, and flatlying sediments in Miocene basin deposits suggest that rapid extension had ceased between ~9-14 Ma (Nielson and Beratan, 1995; John and Foster, 1993; Simpson et al., 1991; Richard et al., 1991; Davis and Lister, 1988; Howard and John, 1987).

Detachment faulting was accompanied by mid- to late-Tertiary deposition in isolated, interior-drainage basins (Nielson and Beratan, 1995). The base of the syntectonic Tertiary stratigraphy is marked by an arkosic sandstone deposited upon pre-Tertiary crystalline rocks. In the Castaneda Hills, a basal arkose deposited on pre-Tertiary crystalline rocks is interbedded with an airfall tuff dated at 26.4 ± 0.2 Ma (whole rock K/Ar; Lucchitta and Suneson, 1993, recalculated by J. Spencer, 1994 - refer to Nielson and Beratan, 1995). This basal arkose is thought to have been deposited prior to the onset of Tertiary extension. The basal arkose is succeeded by a thick sequence of syntectonic mafic to silicic volcanic flows interspersed with minor incursions of fluvial sandstones, silts, and lacustrine muds and limestones. Syntectonic

sediments and interstratified volcanic rocks in the Whipple and Buckskin are early Miocene in age (Davis et al., 1980). In places, these volcanic rocks interfinger with landslide megabreccia deposits. The sequence of volcanic rocks is capped by the 18.5 ± 0.2 Ma Peach Springs Tuff (Nielson et al., 1990). Following the deposition of the Peach Springs Tuff, syntectonic sedimentation continued with coarse clastic deposition into the opening basins.

At least three unconformities in the synextensional sedimentary sequence (Fig. 1.7) can be correlated across the extensional corridor (Nielson and Beratan, 1995). These unconformities represent episodes of tilting within the extensional corridor, recording episodic movement along the detachment fault system. Extension is considered to have stopped in the corridor between 9-12 Ma (Davis and Lister, 1988), but sedimentation continued with the deposition of untilted alluvial fans and local basaltic to andesitic flows (Nielson et al., 1990).

After detachment faulting had ceased in the extensional corridor, a 45° clockwise rotation of the least principal stress axis occurred in the Basin and Range at ~10 Ma, in response to an increase in the relative motion between the Pacific and North American Plates (Zoback et al., 1981). At this time, ongoing

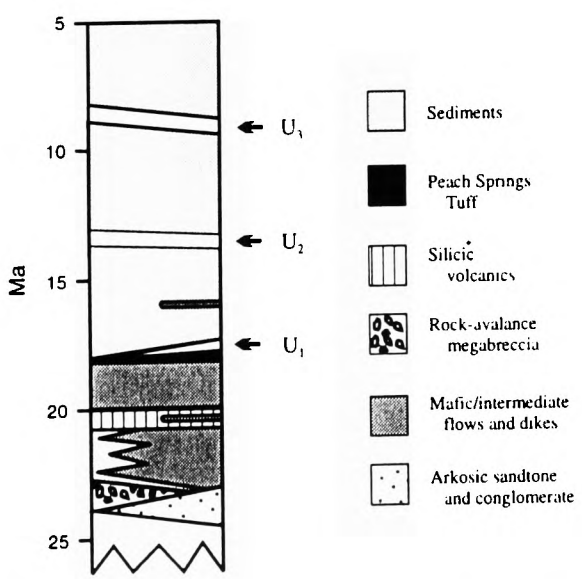


Figure 1.7 Generalised stratigraphic section illustrating the three regional unconformities in synextensional deposits within the extensional corridor (after Nielson and Beratan, 1995). The unconformities represent episodes of tilting and uplift during detachment faulting.

extension occurred by high-angle normal faulting (Spencer and Reynolds, 1986; Zoback et al., 1981). Since the latest Miocene/Pliocene, the tectonic history of the extensional corridor has been *relatively* quiescent, dominated by basin subsidence related to the development of the proto-Gulf of California and subsequent transform-related subsidence under the modern tectonic regime (Buising, 1990).

Previous work and local geologic setting The first documented description of the Sacramento Mountains geology is a brief mention from the United States Geological Survey's exploratory expedition along the proposed Santa Fe railroad route, which was to extend from the state of Kansas, through Missouri, and into California (Darton, 1915). The region was mined for gold by independent prospectors during the 1920's (recorded by claims from the state of California) and has been mined intermittently, both commercially and independently, since the 1940's to the present day. In the 1960's the Southern Pacific Mineral Land Company of Santa Fe performed a mineral resource survey of the eastern Mojave Desert and the first major geologic maps of the northeast Sacramento Mountains were produced (Bonham, 1960; Collier, 1960). These earlier investigations focused on the economic potential of the region, which was primarily associated with hydrothermal mineralization along faults. Consequently, detailed geologic mapping of footwall rocks in the northeast Sacramento Mountains, the structural fabrics associated with them, their geochemistry and petrogenesis, as well as their age and thermal history, was not assessed.

Footwall rocks of the Sacramento Mountains form topographic highs, while hanging wall rocks lie in intervening basins. Detachment faults exposed in this region are typically subhorizontal or domed, dip at low angles (10-30°), and separate upper-plate Tertiary rocks and their depositional basement from footwalls of deeper-seated crystalline rocks (e.g., Armstrong, 1982; Coney, 1980; Davis et al., 1980). The Sacramento Mountains detachment fault forms part of the imbricate, east-dipping, mid-Tertiary asymmetric shear system which underlies the extensional corridor (Howard and John, 1987; Davis and Lister, 1988).

Our current understanding of the local geologic setting of the Sacramento Mountains is based on the contributions of ongoing and past studies. The Sacramento Mountains conveniently divide into the southern, central, and northern regions. The northern Sacramento Mountains are separated into the northwestern and northeastern regions by hanging wall rocks of predominantly Tertiary volcanic and sedimentary origin. The geology of the southern Sacramento Mountains is currently being investigated by E. Campbell, University of Wyoming. The geology of footwall rocks in the central Sacramento Mountains

was studied by Schweitzer (1991). Upper plate rocks in the northern Sacramento Mountains were investigated by McCelland (1983) and Spencer and Turner (1983). Spencer (1985) addressed the tectonic evolution of footwall rocks in the northwest Sacramento Mountains and this has been evaluated in greater detail by Argent (1996). Simpson et al. (1991) re-evaluated the relationship between the Eagle Peak rhyolite and the Sacramento Mountains detachment fault (SMDF). A handful of age and barometric data from the Sacramento Mountains focused the direction of this research in the northeast Sacramento Mountains (Foster et al., 1990; J. Wooden, unpublished data; Anderson, 1988).

In the northeast part of the range (Fig. 1.8), the Sacramento Mountains detachment fault (SDMF) separates upper-plate, hanging wall rocks (Tertiary volcanic and sedimentary rocks and their depositional crystalline basement) from a footwall of Proterozoic gneisses, Cretaceous granites, and Miocene plutonic rocks (this study; Argent 1996; McClelland, 1983; Spencer and Turner, 1984). The extrusion of the 14.3 Ma Eagle Peak rhyolite onto the exhumed fault surface of the SMDF (Simpson et al., 1991) and the untilted 14.6 Ma andesite of Flattop Mountain (Spencer, 1985), define the end of low-angle faulting on the west side on the northeast Sacramento Mountains.

Lower-plate crystalline rocks in the NE Sacramento Mountains comprise Precambrian and Cretaceous(?) gneisses to the north and a syntectonic intrusive complex to the south. The gneisses are thought to be similar in age and composition to those exposed in the NW Sacramento Mountains, where Argent (1996) inferred that Proterozoic rocks were once at granulite facies conditions based on the relict mineral assemblage of orthopyroxene + hornblende + plagioclase. The Eagle Wash Intrusive Complex (EWIC after Schweitzer, 1991) is dominated by granodiorite, with lesser amounts of leucogranite, diorite, and granite. Zenoliths and rafts of Cretaceous (?) and Precambrian material are abundant in the EWIC and show various degrees of resorbtion. The age of the EWIC is about 20 Ma (U-Pb sphene, this study; U/Pb SHRIMP zircon, Foster, unpublished).

A pervasive mylonitic foliation is preserved in the EWIC (ductile deformation of quartz and brittle deformation of feldspar). This fabric shows a consistent orientation striking 130°, dipping 14°SW, and is sub-parallel to the detachment fault (within 10°). The shape-preferred orientation of amphibole and a biotite stretching lineation define a well-developed and consistent lineation trending 241°, 14°SW. Shear sense indicators (σ and δ porphyroclasts, S-C fabrics, deformed veinlets, parasitic folds) all show top-to-the-

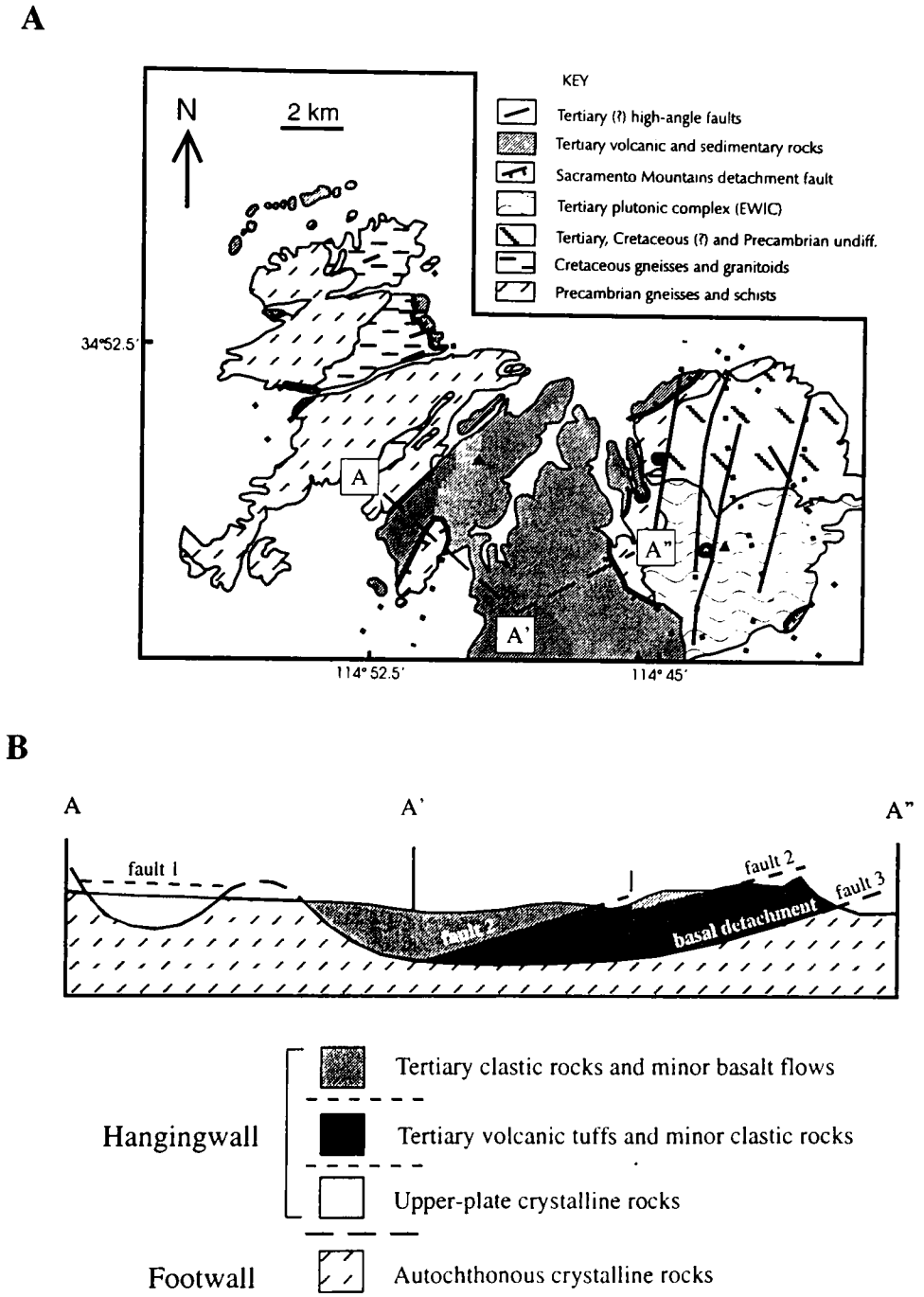


Figure 1.8 A) Simplified geology of the northern Sacramento Mountains. Northwest and northeast parts of the range are separated by a hanging wall of Tertiary volcanic and sedimentary rocks. Triangles indicate local peaks. From mapping in this study and by Argent (1996). B) Schematic cross-section of the Sacramento Mountains detachment fault system showing multiple, imbricate splays (after Spencer, 1985).

northeast motion, consistent with the regional tectonic transport direction (N60E). Taken together, the radiometric ages and structural information suggest that the EWIC was intruded during detachment faulting.

Terminology As advances are made in the understanding of geologic processes, existing terminology survives as relics from previous work, or may be modified and used in different ways. This is certainly true for two concepts critical to this investigation, i.e.- *detachment faulting* and *mylonitization*. The term *detachment fault* has been used inconsistently in the past (c.f. Reynolds and Spencer, 1985; Carr and Dickey, 1976; Pierce, 1973). I use the term synonymously with *low-angle normal fault*, which implies a knowledge of fault orientation and shear sense during slip, conveying significant information regarding the geometry of faulting.

In the original definition of *mylonite*, Lapworth (1885) considered such rocks to be the products of grain size reduction due to clastic milling and breakage. More recently, however, they have come to be recognised as the products of ductile flow, syntectonic crystal-plastic grain size reduction, and dynamic recrystallization (Tullis et al., 1982; Bell and Etheridge, 1973). Mylonitic rocks are highly strained rocks which, as a result of continuous deformation, have been tectonically reduced in grain size and have developed a penetrative foliation and/or lineation (Tullis et al., 1982). Shear displacement in mylonites is accommodated by continuous volumetric straining. Mylonitic rocks form in a variety of settings and are believed to be characteristic of ductile fault zones at middle and lower crustal depths (Sibson, 1977). Using the nomenclature of Wise (1984) and Sibson (1977), mylonitic rocks can be classified into three categories (protomylonite, mylonite, and ultramylonite), where the proportion of porphyroclasts decreases with increasing mylonitization and the relative proportion of porphyroclasts to matrix material defines the gradational boundaries between protomylonites, mylonites, and ultramylonites. This is the usage I have adopted in this investigation. Ductilely deformed rocks in the northeast Sacramento Mountains range from modestly strained to ultramylonites, with protomylonites and mylonites predominating.

Geographic subdivisions (NE, NW, SW, and SE) of the footwall in the northeast Sacramento Mountains used throughout this investigation refer to specific regions. These regions are defined by township and range boundaries on U.S. Geological Survey topographic quadrangles, i.e.- the township boundary between T9N and T8N, and the range boundary between R21E and R22E. The topographic N-S high dividing the western and eastern regions is coincident with this range boundary (Insert 1).

1.4 Objectives

Multidisciplinary investigations are becoming increasingly necessary in order to develop a precise knowledge of the relative and absolute timing of crustal and tectonic processes (e.g., Karlstrom et al., 1993). The combination of detailed mapping, structural analysis, petrography, and geochemistry can lead to a petrogenetic understanding of crustal evolution. In combining this information with thermobarometry and thermochronology, the potential for unravelling the timing, distribution, and intensity of tectonothermal events becomes possible.

In order to understand the tectonic evolution of the northeast Sacramento Mountains metamorphic core complex, a multidisciplinary investigation into the geology, structure, geochemistry, and age and thermal history of region was undertaken. The EWIC was intruded during detachment faulting, consequently focusing on the EWIC will provide information about conditions at the time of detachment faulting and about magma genesis associated with detachment faulting. Little work has been done in the footwall rocks of the northeast Sacramento Mountains, consequently detailed investigations evaluating the timing and evolution of this metamorphic core complex may provide broad insights into detachment faults and the tectonogenesis of continental crust in extending environments.

The work presented in this dissertation was undertaken over a three year period (1994-1996). Field work, carried out over six months, was used to produce a 1:24,000 scale geologic map (Insert 1 and Chapter 2) and to collect samples (Inserts 2 and 3) for structural (Chapters 3 and 6), geochemical (Chapter 4), and thermobarometric and thermochronologic (Chapter 5) analyses. Oriented thin-sections were used for micro-structural analysis. X-ray fluorescence and electron microprobe analyses were used to determine major and trace element abundances (Appendices A and B, respectively) and mass spectrometry was used to determine isotopic abundances (Appendix D). The results of this investigation are synthesized in Chapter 7.

Chapter 2

Lithologies of the Northeast Sacramento Mountains

2.1 Introduction

A geologic map and cross-section of footwall lithologies and macrostructures in the northeast Sacramento Mountains has been compiled at a scale of 1:25,000 (Insert 1). Abbreviated lithologic descriptions of footwall rocks included on Insert 1 have been derived from the following lithologic descriptions. These descriptions are based on field appearance, mineral assemblages, and petrographic evaluation. In some instances, mineral compositions have been determined by electron microprobe analyses (refer to Appendix C). Lithologic contacts are based on field observations over the course of three mapping seasons (6 months total), as well as aerial photograph interpretation. Radiometric dating, combined with cross-cutting relationships observed in the field, have been used to determine absolute or relative age relationships (Chapter 5). Field location numbers are summarised on Insert 2 and are specified for type localities of lithologic units, structural data, all photographs, and/or sample locations, throughout this thesis. Field locations are indicated by the abbreviation "Loc."

2.2 Quaternary and Pliocene units

Overview - Undeformed Quaternary and Pliocene sedimentary deposits overlie allochthonous units in the northeast Sacramento Mountains. Two generations of Quaternary alluvium (*Qa* and *Qoa*) have been mapped. These units have been described previously by McClelland (1983), Bonham (1960), and Collier, (1960) and summaries of these descriptions are included on Insert 1. Additionally, two units previously unidentified in the region were found. Colorado River gravels and sands (*Qg*) (Metzger and Loeltz, 1973) were identified in the northeastern-most region of the study area. Also a marl was found in low-lying areas above Tertiary volcanic rocks and underlying Quaternary alluvium in the southeast and in the north of the study area. This marl may be correlative with the Mio-Pliocene Bouse Formation (*Tbo*) of Buising (1990). This is the first documentation of these two units in the northeast Sacramento Mountains and their lithologic descriptions and UTM locations are given below (Zone 11, meters).

Qg, Pleistocene (?) Colorado River gravel and sand deposits - River gravels consist of rounded cobbles of quartzite, limestone, and rare volcanic material. River sand is buff coloured, well sorted silty-sand, poorly consolidated, laminated, and flat-lying. Mud clasts and rip-ups are not present. The sand is composed of quartz and feldspar grains. Both sands and gravels interfinger with modern alluvial fans to the west. (Loc. 429, N. 3859777, E. 714132; Loc. 430, N. 3859536, E. 712355.)

Tbo, Pliocene calcareous clay, silt, sand, and marl - Thin layers (0.3-5 m) of discontinuous, poorly indurated marl comprise the dominant facies (Fig. 2.1). Samples were collected and analysed in the laboratory for composition: 85 wt.% of the original carbonate material dissolved in a 10% HCl solution and the remaining fraction was 14 wt.% clay minerals and 1 wt.% grain fragments (presumably of detrital origin) of muscovite, biotite, chlorite, quartz, potassium feldspar, tiny rare garnets, and oxide (?) alteration material. (Loc. 159, N. 3851505, E. 710338; Loc. 162, N. 3861402, E. 705749.)

2.3 Allochthonous units

Hanging wall rocks in the western region of the study area have been mapped previously (Spencer and Turner, 1983; McClelland, 1984). These maps were field-checked and are accurate with respect to location, lithologic subdivisions, and structural information. Consequently they have been used to compile hanging wall units in the western region of the study area. Additionally, the reinterpretation of Simpson et al. (1991) of the Sacramento Mountains detachment fault (SMDF) near Eagle Peak is also



Figure 2.1 - Bouse Formation (*Tbo*). Thin layers (0.3-5 m) of discontinuous, poorly indurated marl (Loc. 160).

accepted. In this reinterpretation, the ~14.3 Ma Eagle Peak rhyolite was erupted onto the exhumed fault surface of the SMDF and thus provides a constraint for the lower limit of detachment faulting in the Sacramento Mountains area.

The hanging wall units are summarised as comprising three allochthonous plates of syntectonic deposits and their depositional basement (Spencer, 1985; McClelland, 1984; Spencer and Turner, 1983). The lowest structural plate includes depositional basement of Precambrian gneisses and schists, the middle plate is dominantly Miocene felsic volcanic rocks, and the highest structural plate is primarily Miocene terrigenous clastic sediments with minor basaltic flows (Fig. 2.2). These allochthonous plates are capped by the flat-lying, 14.6 ± 0.2 Ma (K-Ar whole rock; Spencer, 1985) andesite of Flattop Mountain, which also constrains the cessation of detachment faulting in the Sacramento Mountains.

Geologic correlation of hanging wall rocks between the various regions of the Sacramento Mountains is made, based on field-checks, and is shown on Insert 1. Small areas of unmapped hanging wall



Figure 2.2 - General aspect of hanging wall units. View looking south towards Eagle Peak. Tertiary volcanic units dip moderately to the southwest.

rocks occurred, generally at the boundaries between different workers, e.g., in the northern/northwestern and southeastern regions. My mapping in these regions follows the lithologic nomenclature of Spencer and Turner (1983).

2.4 Autochthonous units

Overview - The autochtonous units in the northeast Sacramento Mountains comprise footwall rocks to the main detachment fault. Using field-checks, correlations between footwall units in the various regions of the Sacramento Mountains are made and are shown on Insert 1. Map units are based on sample identification in the field; field names are used throughout this thesis and are not necessarily the same as rock names derived strictly from petrography or analytical chemistry (Chapter 3). The Eagle Wash intrusive complex (EWIC; after Schweitzer, 1991) comprises ~50% of the footwall rocks exposed in the northeast Sacramento Mountains and is directly correlative with rocks exposed in the central region of the Sacramento Mountains, just south of Eagle Pass road (c.f. Schweitzer, 1991).

The EWIC is a syntectonic, intrusive suite of dominantly granodioritic composition. Lesser volumes of diorite, granite, and leucogranite also form part of the EWIC. Composition and deformation are notably heterogeneous, though it is typically deformed (from protomylonite to ultramylonite) and generally has a well-developed subhorizontal to shallow dipping foliation and lineation. Samples of the granodioritic phase of the EWIC were collected for thermobarometry and thermochronology (Chapter 5). Thermochronologic results suggest a Miocene age for the EWIC of ~20 Ma.

The northernmost region of the northeast Sacramento Mountains is predominantly Precambrian gneiss and schist, with lesser amounts of amphibolite, possible Cretaceous (?) rocks (gneiss and gabbro), and variable amounts of EWIC lithologies. At the given map scale (Insert 1), these subhorizontal units are interlayered at too fine a scale to subdivide (< 20 metres in thickness) and instead their *relative* abundance has been indicated on Insert 1, e.g., *Tlg* > *Tgd*. Similar rocks may be exposed adjacent to the EWIC in the central Sacramento Mountains (C. Simpson, 1994, pers. comm.; Schweitzer, 1991). It is very likely that these Precambrian gneisses and schists are correlative with those of Argent (1996), which are exposed in the northwest Sacramento Mountains.

In the northeast Sacramento Mountains, the transition between the main body of EWIC and the older rocks to the north-northeast, is a relatively thin zone of complex folding and migmatization immediately adjacent to the intrusive complex. This deformed zone grades into a larger region (kilometres) of subhorizontal layering and interfingering (on the scale of tens of metres) of all footwall rock types (see cross-section, Insert 1). The uppermost contact of the EWIC, just below the SMDF and Precambrian (?) units, is a high-strain domain characterised by fine-scale (≤ 0.5 m), subhorizontal layering of microdiorite, granodiorite, and leucogranite; this "banded" appearance is distinctive and was used as a "marker" unit. The following units comprise the EWIC and are considered to be relatively contemporaneous in age: *Tdy*, *Tlg*, *Tgd*, and *Td*.

Throughout the region, younger, near-vertical dykes and high-angle faults trend north-south to northeast-southwest. The dykes range in composition from rhyolite to basalt, and can contain xenoliths of the country rock or have magma mixing textures. The dykes often use the faults as conduits and show variable degrees of shear, indicating that they were sometimes contemporaneous with faulting. There are a few, small rhyolitic dykes in the northeasternmost part of the study area with northwest-southeast

orientations which have quenching textures. Lithologic descriptions of these autochthonous units are presented below.

Tr, Miocene rhyolitic dykes Porphyritic sanidine, quartz, biotite, and plagioclase rhyolitic dykes are probably correlative with the Eagle Peak rhyolite. (Fig. 2.3). Simpson et al. (1991) report concordant biotite and sanidine ages for the Eagle Peak rhyolite of ~14.3 Ma. One of these dykes intrudes across the study area from north to south, cross-cuts a mafic dyke, and is parallel to the major high-angle fault trends in the region. If this dyke is correlative with the Eagle Peak rhyolite, it suggests that the high-angle, north-south faults are also at least ~14.3 Ma. Some of these rhyolitic dykes are spherulitic (Fig. 2.4). Spherulitic rhyolite dykes are only found in the north-northeastern-most region of the study area and have atypical northwest trends. These quenched, northwest trending dykes may represent the waning stages of volcanism in the study area, with dyke intrusion into relatively cool country rock occurring late in the exhumation history of the northern Sacramento Mountains.

Tu, Miocene dykes, undifferentiated Aphanitic to porphyritic, basaltic to rhyodacitic, undifferentiated dykes. These undifferentiated dykes were not mapped systematically. They comprise both horizontal, highly sheared, and highly altered mafic dykes, as well as vertical, north-northeast trending dykes of wide compositional variation which can be undeformed to highly sheared (Fig. 2.5). These dykes generally cross-cut all units in the study area except the rhyolite dykes. Other units, however, are occasionally seen cutting *Tu* (Fig. 2.6), suggesting that these dykes probably represent multiple intrusion events over time.

Horizontal, foliated dykes can be divided into two categories on the basis of petrographic textures. Group A dykes show complete strain recovery, whereas group B dykes are dominated by unrecovered strain features. Both groups are holocrystalline, generally fine grained, and have a typical mineral assemblage of plagioclase + amphibole ± biotite + accessory minerals of sphene, zircon, and opaque oxides. The foliation is defined by a strong mineral alignment of amphibole porphyroclasts. Group A dykes have microscopic textures which show complete static recrystallization at amphibolite grade conditions (Fig. 2.7). Group B dykes record dynamic recrystallization ranging in intensity of deformation from protomylonite to ultramylonite (Fig. 2.8).

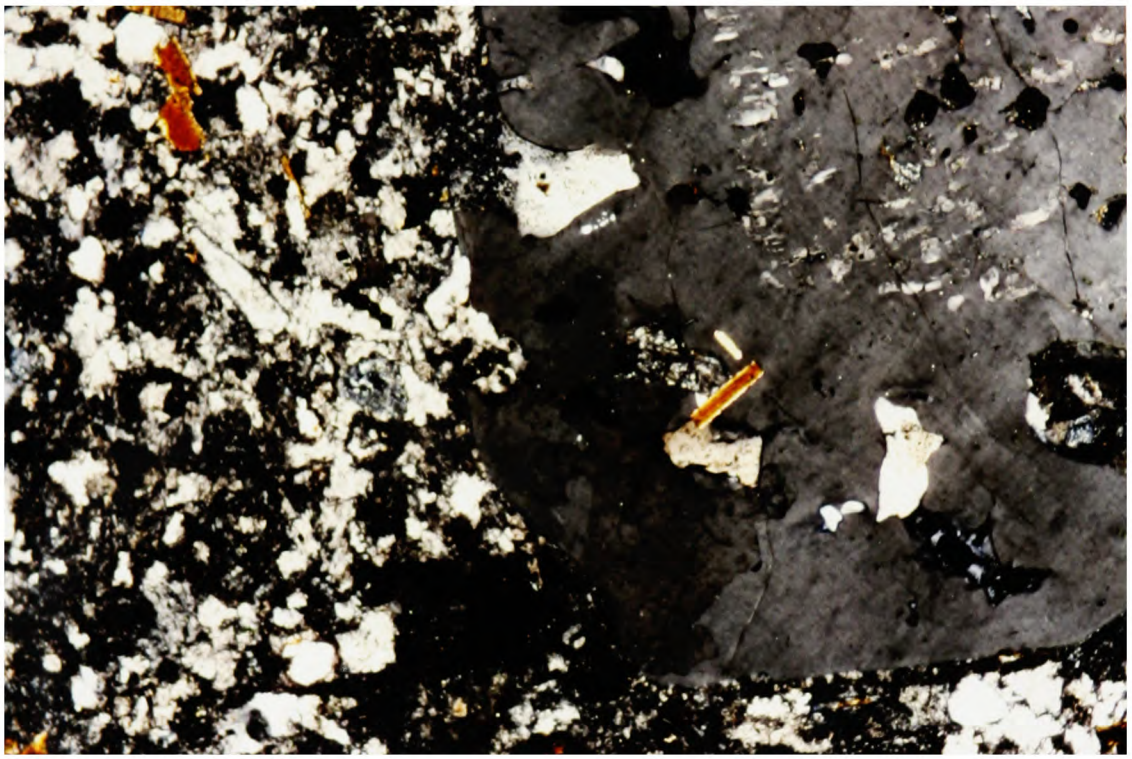


Figure 2.3 - A rhyolite dyke (*Tr*), probably correlative with Eagle Peak rhyolite. Porphyritic, embayed sanidine, quartz, biotite, and plagioclase visible. Field of view 3.5 mm (Loc. 002, VP94-003).

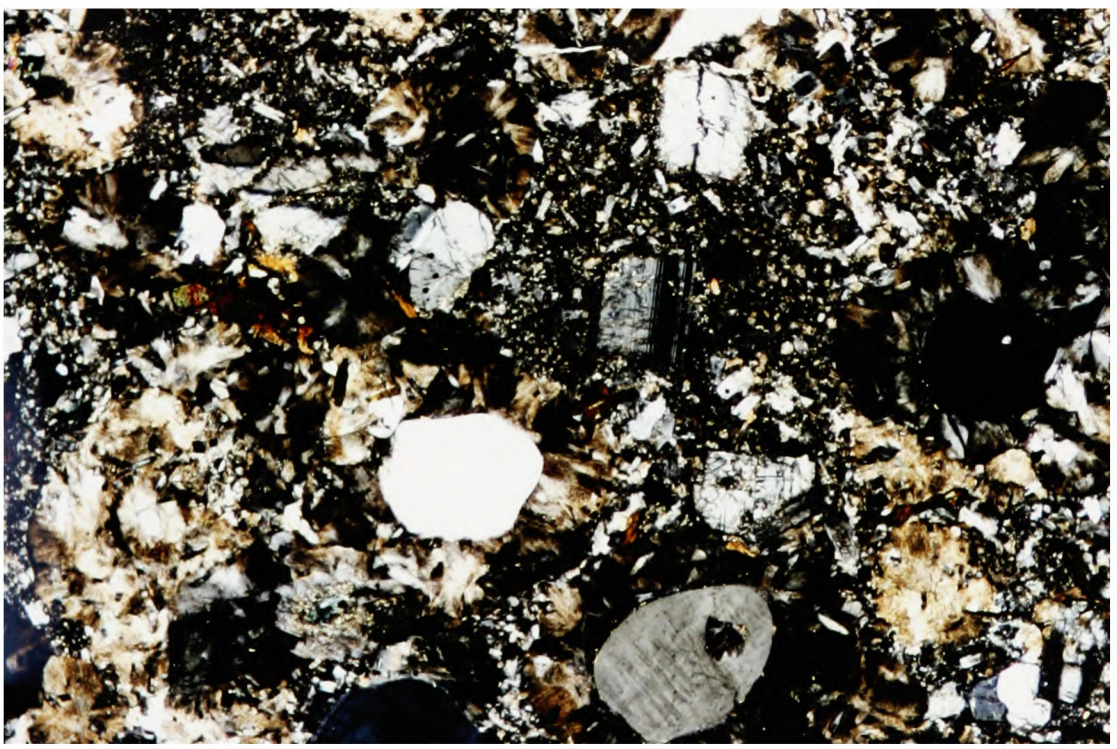


Figure 2.4 - Spherulitic rhyolite dykes (*Tr*) only occur in the northeast of the study area. Field of view 3.5 mm (Loc. 94, VP94-111).

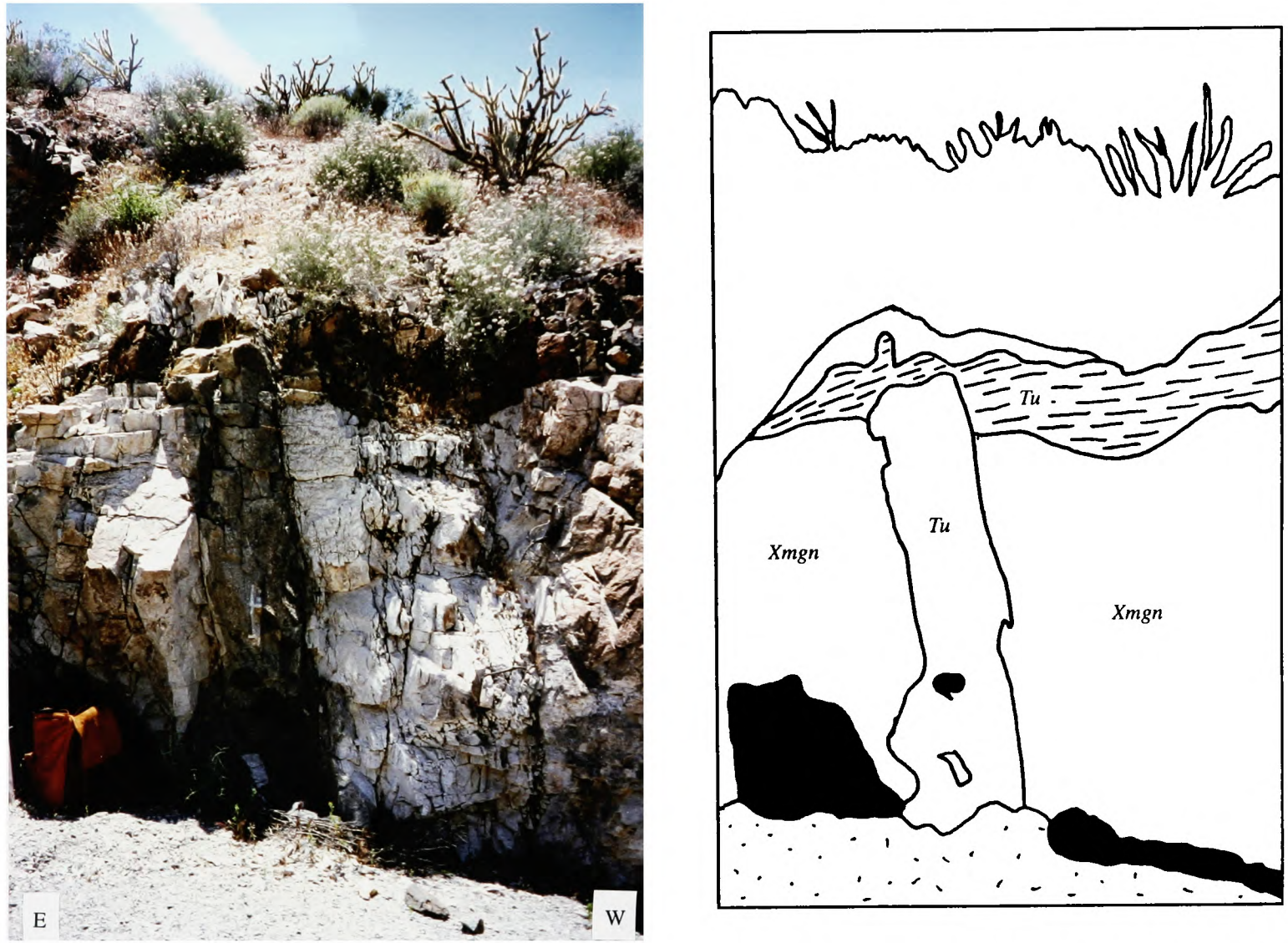


Figure 2.5 - Multiple generations of *Tu*. Note sheared horizontal dyke and xenoliths in undeformed vertical dike. Daypack for scale (Loc. 225).



Figure 2.6 - Sheared *Tu* cross-cut by *Tlg*. Hammer for scale (Loc. 440).

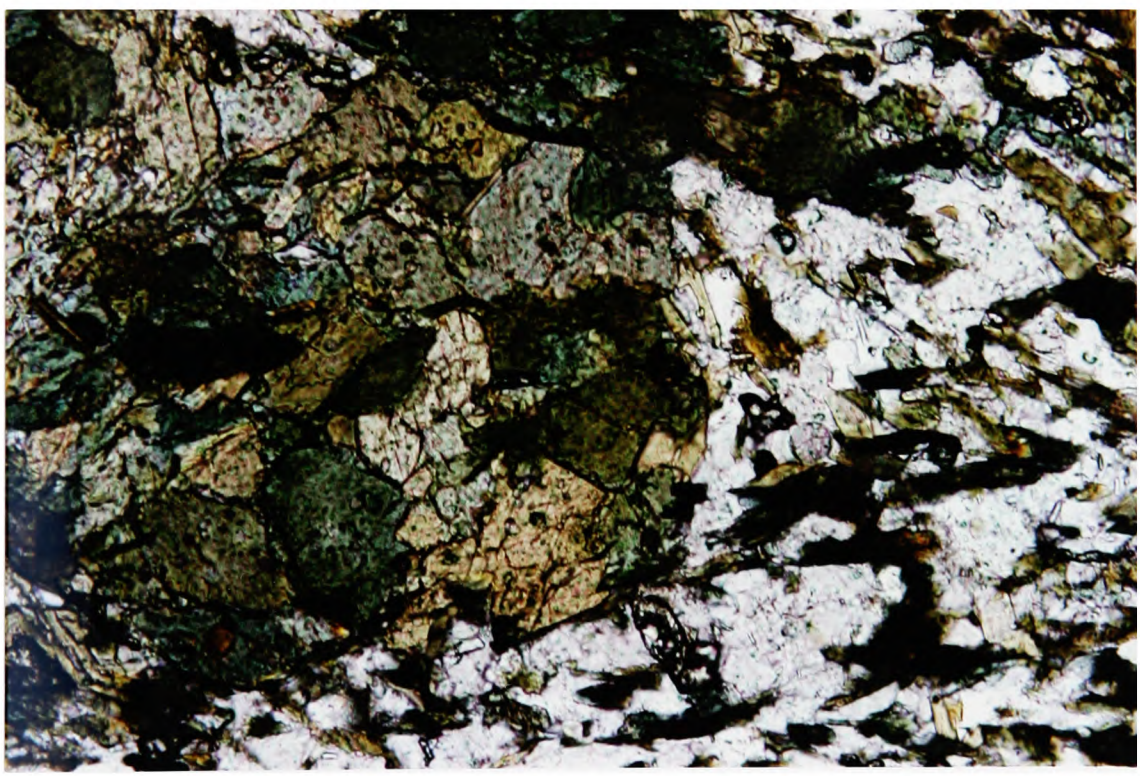


Figure 2.7 - Static recrystallization, amphibolite grade, of *Tu*. Field of view 1.35 mm (Loc. 15, VP94-019).

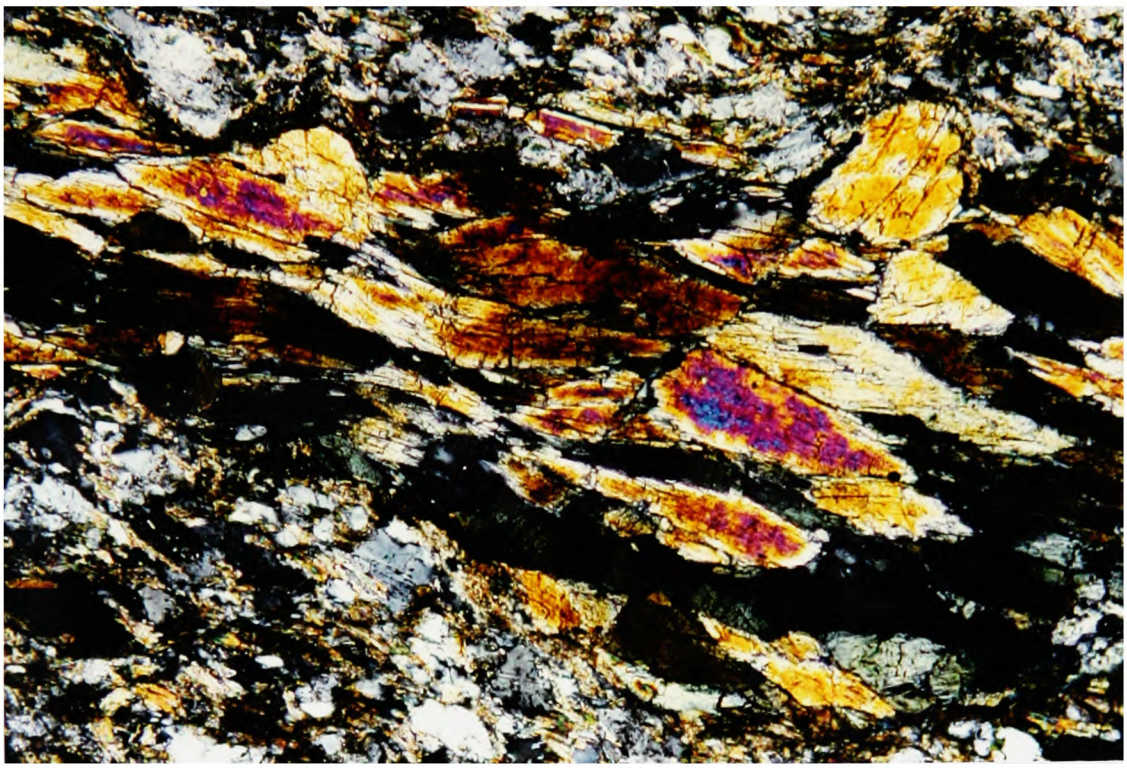


Figure 2.8 - Dynamic recrystallization of *Tu*. Field of view 1.35 mm (Loc. 70, VP94-084).

Near vertical to vertical dykes can be sheared or undeformed, composite (Fig. 2.9), have granitic xenoliths (see Fig. 2.5), or have pronounced magma mixing textures (Fig. 2.10). Basaltic dykes weather to dark greenish-black and are generally fine to medium grained. In the undeformed mafic dykes, plagioclase is the dominant phenocryst and pyroxene is subophitic in the groundmass (Fig. 2.11). Andesitic to dacitic dykes weather grey to reddish-tan and have variable phenocryst mineralogy, including plagioclase, hornblende, biotite, and potassium feldspar. These dykes, when deformed, record dynamic recrystallization from protomylonite to ultramylonite, characterised by S-C fabrics, serrate feldspar and quartz grain boundaries, elongation of quartz grains, as well as subgrain development in quartz, feldspar and biotite. Typically, the finer grained groundmass deforms ductilely, while the larger porphyroclasts deform brittlely (Fig. 2.12). Chill margins may or may not be present.

Tcb, Miocene chloritic breccia - Dark greenish-black to red, fine grained to aphanitic microbreccia of the Sacramento Mountains detachment fault. This cataclasite is exposed directly below the basal detachment fault surface, when it has not been eroded away or buried by talus or alluvium, and is easily seen



Figure 2.9 - Composite dyke (*Tu*). Hammer for scale (Loc. 155).



Figure 2.10 - Magma mixing in intermediate dyke (*Tu*). Map case for scale (Loc. 104).



Figure 2.11 - Undeformed, mafic dyke (*Tu*). Field of view 3.5 mm (Loc. 83, VP94-105).



Figure 2.12 - Intermediate dyke (*Tu*) with plagioclase phenocrysts deforming brittley and groundmass deforming ductiley. Field of view 1.35 mm (Loc. 211, VP95-216).

on aerial photographs. It is best preserved in the north of the study area near locations 187, 188, 229 (just south of I-40) and 405, but is also preserved in the southwest of the study area (south and southwest of Loc. 234). Where present, it has a maximum thickness of ~5 m and is so extensively brecciated and mineralised that it is impossible to determine the protolith (Fig. 2.13). The breccia typically contains crushed quartz and feldspar, and an alteration assemblage of chlorite + hematite + sericite + opaque oxides ± epidote. This breccia grades downward into a zone of sheared, brecciated, and chloritized lower-plate rocks (*cbz*).

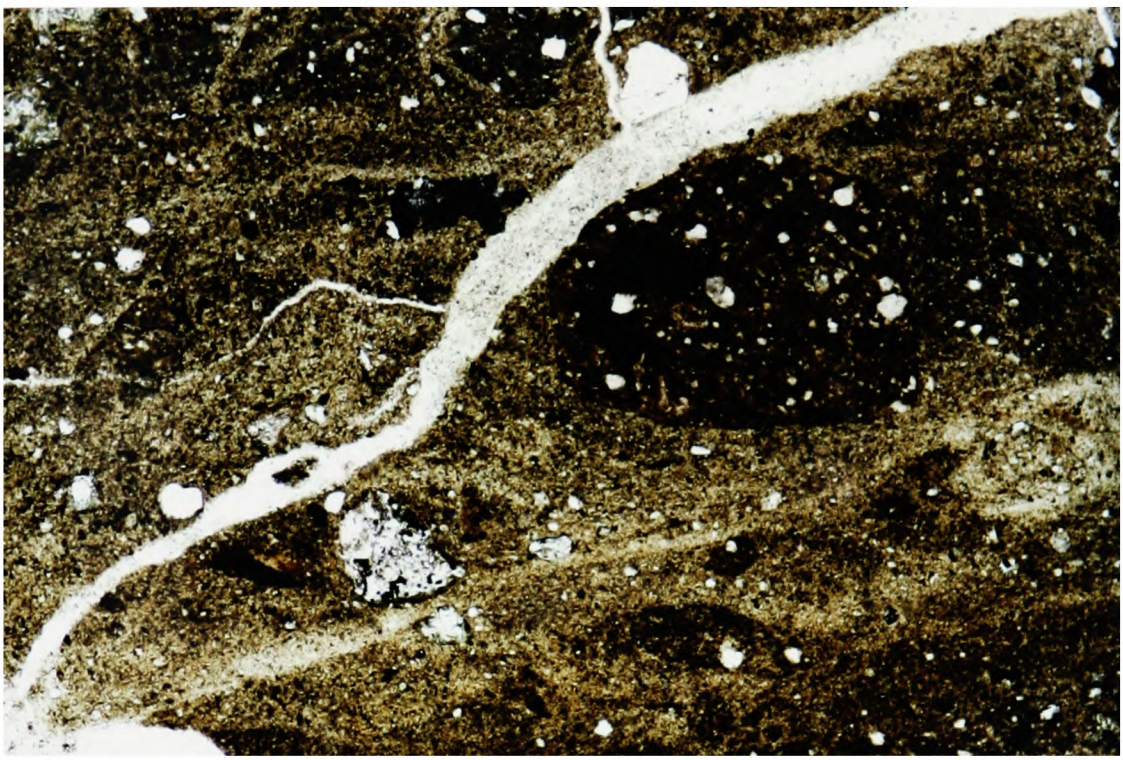


Figure 2.13 - Microbreccia of the SMDF (*Tcb*). *Tcb* typically composed of crushed quartz and feldspar, and an alteration assemblage of chlorite + hematite + sericite + opaques oxides ± epidote. Field of view 3.5 mm, plane polarised light (Loc. 229, VP95-231).

cbz, chloritic breccia zone - A zone of chloritic alteration and brecciation below the SMDF, which decreases with increasing distance from the fault. Rocks in this zone possess the associated lower-greenschist, secondary mineral assemblage of chlorite + hematite + sericite + opaques oxides ± epidote ± calcite. The SMDF and *cbz* provided a conduit for hydrothermal fluid migration and some of the breccias are rich in hematite and calcite, while mineralization in the *cbz* and along the SMDF includes quartz, copper-oxides (chrysocolla, malachite, chalcocite), barite, fluorite, and iron oxides. Fracture intensity in the

cbz increases towards the fault surface, without systematic orientation or displacement. This zone is ≤100 m thick in the northeast Sacramento Mountains.

Tdy, Miocene diorite A fine to medium grained, sphene-hornblende diorite which intrudes Tlg (Fig. 2.14a) and is present in relatively small volumes. The youngest intrusive manifestation of the EWIC is *Tdy*. It is protomylonitic to undeformed, equigranular, and is strongly affected by hydrothermal (deuteric?) alteration (Fig. 2.14b). The mineral assemblage is plagioclase + amphibole + sphene + apatite + accessory (biotite, opaque oxides, zircon) and alteration (chlorite, hematite, calcite) minerals. The amphibole is subhedral to anhedral (≤ 2 mm), displays well-developed twins and exsolution lamellae, and the cores are pervasively altered to chlorite. Plagioclase is interstitial to amphibole, with irregular grain boundaries. Sericitization of plagioclase is pervasive, but some Carlsbad and albite twins are preserved and allow the plagioclase composition to be determined via the Michel-Lévy method: An_{55} (five grains).

Tlg, Miocene leucogranite A fine to coarse grained, mylonitic to ultramylonitic, biotite leucogranite, ± muscovite ± garnet. Rare (seen only twice) tourmaline, with a well-defined mineral stretching lineation, can be present. This unit is gradational in composition from granite to leucogranite, with leucogranite as the volumetrically dominant composition. It typically occurs as subhorizontal, 10-40 m thick, sheets (Fig. 2.15) or as subhorizontal or cross-cutting dykes and dykelets (Fig. 2.16). It usually has a well-defined fabric, ranging from a lineated tectonite to a lineated and foliated tectonite. Whether *Tlg* is only lineated or both lineated and foliated appears to be determined by biotite content. The foliation may be difficult to discern in the field but is readily visible in thin-section (Fig. 2.17). Potassium feldspar with patchy extinction and fractures, and lesser amounts of plagioclase with concentric zoning and simple twins, form porphyroclasts in a dynamically recrystallized matrix of quartz + feldspar + biotite + opaque oxides. *Tlg* always has a well-defined northeast-southwest biotite stretching lineation and often possesses a well-defined S-C fabric, indicating top-to-northeast shear sense (Fig. 2.17). Xenoliths of *Xgn* and *Tgd*, when present, are aligned parallel to the foliation (Fig. 2.18). Xenoliths of *Td* are not seen in *Tlg*. While *Tlg* cross-cuts most of the other compositional phases of the EWIC (Fig. 2.16), it is also *intruded* by *Tgd* (Fig. 2.19) and this mutually intrusive relationship suggests that the intrusion of *Tlg* and *Tgd* overlapped in time.



Figure 2.14a - Small (~65 m across) hornblende diorite pluton (*Tdy*) intruding *Tlg* (Loc.156).

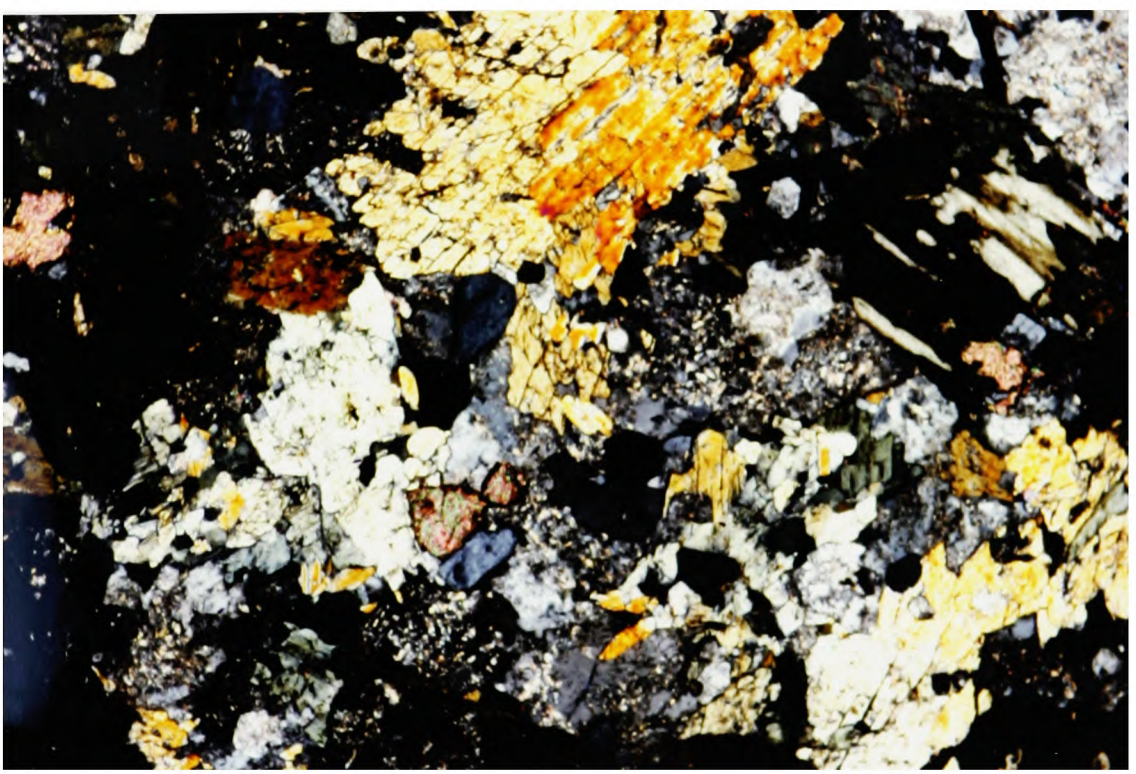


Figure 2.14b - Sphene-hornblende diorite (*Tdy*). Field of view 3.5 mm (Loc. 156, VP95-174).



Figure 2.15 - Sheets of leucogranite (*Tlg*). Hammer for scale (Loc. 56)



Figure 2.16 - Leucogranite (*Tlg*) as dykes/dykelets. Maximum *Tlg* thickness ~0.3 m (Loc. 105).

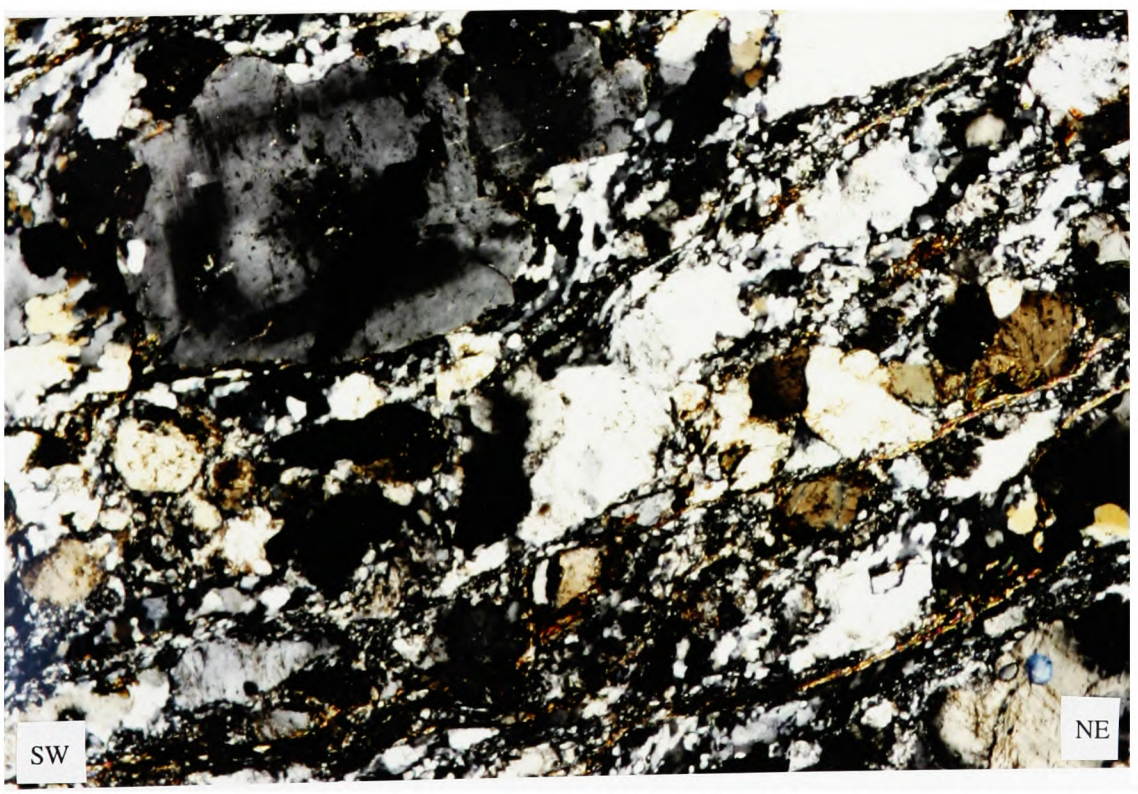


Figure 2.17 - S-C fabric in *Tlg* (top-to-northeast shear). Field of view 3.5 mm (Loc. 37, VP94-046).



Figure 2.18 - Xenoliths of *Xgn* (biotite schist) in *Tlg*. Notebook for scale (Loc. 147).



Figure 2.19 - Two varieties of granodiorite (*Tgd*) intruding *Tlg*. Note shear along dyke margins in lower right corner. Hammer for scale (Loc. 37).

Tgd, Miocene granodiorite The most abundant compositional phase of the EWIC is a sphene-bearing granodiorite. The term "granodiorite" is a loose field name, intended to encompass the broad and gradational compositional heterogeneity from mafic granodioritic (quartz monzodiorite) to leucocratic granodioritic (granite) phases within this unit. *Tgd* also generally shows pronounced textural (coarse to fine grained, rarely porphyritic) and structural (proto- to ultramylonitic) variations. Some of these variations are illustrated in figures 2.20 and 2.21, where such changes occur over ~5^3 m.

Small domains of *Tgd* are preserved which exhibit *comparatively* little strain and a relative intrusive sequence *within Tgd* can be established, e.g., Loc. 105 (Figs. 2.20 and 2.21). Even in these relatively strain-free zones, however, interstitial quartz shows an alignment of subgrains (Fig. 2.22). More commonly, *Tgd* displays a range of fabrics, reflecting relatively moderate to large amounts of strain (Fig. 2.23 and 2.24). Regardless of the relative amount of strain, *Tgd* usually has a pronounced northeast-southwest lineation and S-C planes with consistent top-to-the-northeast shear sense (Fig. 2.25). The lineation is defined by a shape preferred orientation of amphibole and the foliation by millimetre-scale segregation of tabular plagioclase and amphibole. Plagioclase (and occasionally potassium feldspar) phenocrysts form visible porhyroclasts, both microscopically and macroscopically, in a matrix of calcic amphibole, quartz, ± potassium feldspar, ± biotite, with accessory sphene, magnetite, apatite, and zircon. Sphene often exhibits a mineral stretching lineation. In altered samples, a second generation of globular sphene is present as mantles surrounding magnetite and magnetite can also be mantled by red hematite.

Tgd amphibole compositions: Amphiboles from *Tgd* were analysed using an electron microprobe (Appendix B) in order to determine the temperature and pressure of emplacement associated with the EWIC (Chapter 5). Mineral compositions determined from these data are presented here. The electron microprobe cannot distinguish between ferrous and ferric iron. These two cations occupy different sites in the amphibole mineral structure and are critical in determining A-site occupancy. The Fortran program RECAMP of Spear and Kimball (1984) was used to recalculate electron microprobe analyses of amphiboles into amphibole structural formulae. In this program, ferric iron is estimated on the basis of stoichiometric constraints of amphibole crystal chemistry. All recalculations that obey both chemistry and stoichiometry are calculated, however Cosca et al. (1991) demonstrated that only the 13-cation normalization procedure

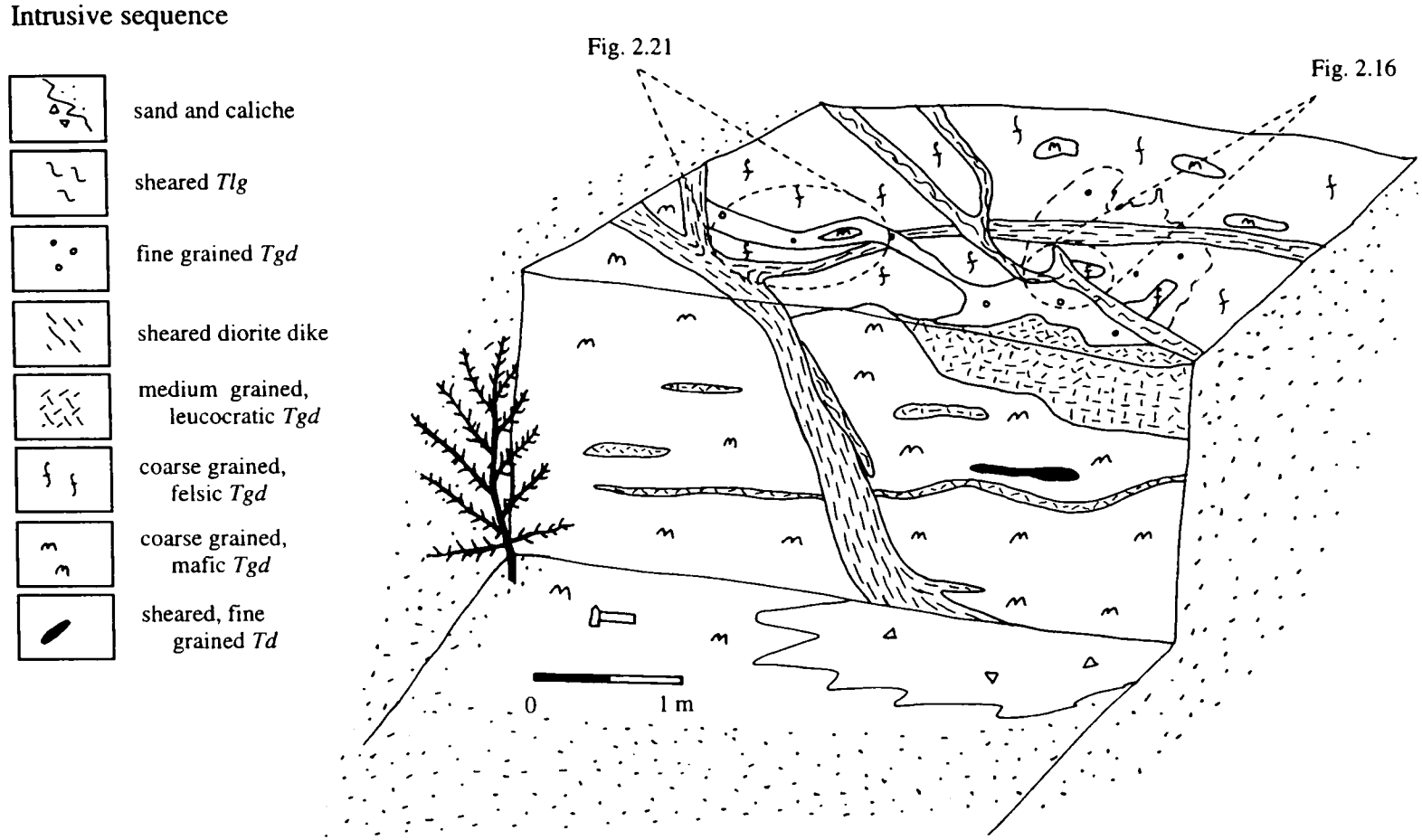


Figure 2.20 - Compositional and textural variations within *Tgd*. Relatively undeformed "type" outcrop (Loc. 105). Scale indicated.



Figure 2.21 - Compositional variation of coarse grained, mafic to leucocratic *Tgd* (Loc. 105).



Figure 2.22 - Strained quartz in relatively undeformed *Tgd*. Note "horizontal" alignment of quartz subgrains just right of central plagioclase. Field of view 3.5 mm (Loc. 105, VP94-123a).



Figure 2.23 - Moderate to high strain in *Tgd*. Field of view ~0.5 m (Loc. 394).



Figure 2.24 - Variation from high to extreme (shear zones) strain in *Tgd*. Pencil for scale (Loc. 31).

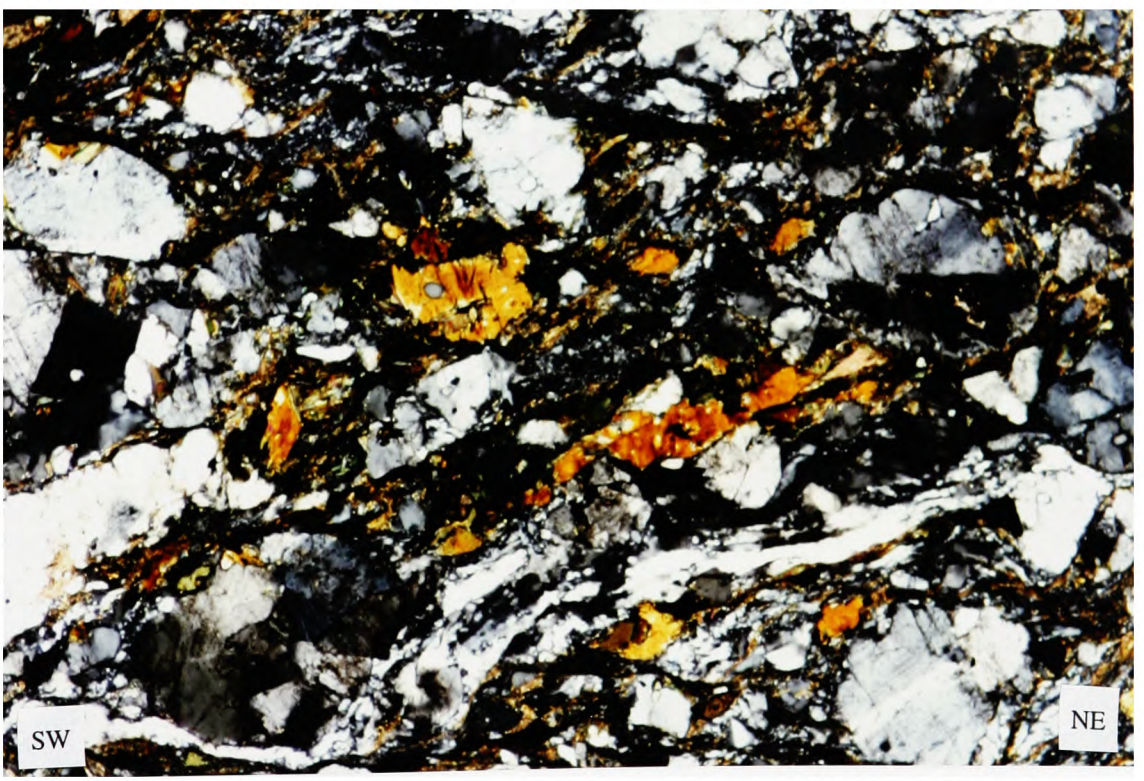


Figure 2.25 - S-C fabric in *Tgd* (top-to-northeast shear). Field of view 3.5 mm (Loc. 31, VP94-042).

closely predicts site occupancies for amphiboles in which FeO and Fe_2O_3 were determined by titration. Consequently, only the 13-cation output from RECAMP was used to determine amphibole compositions.

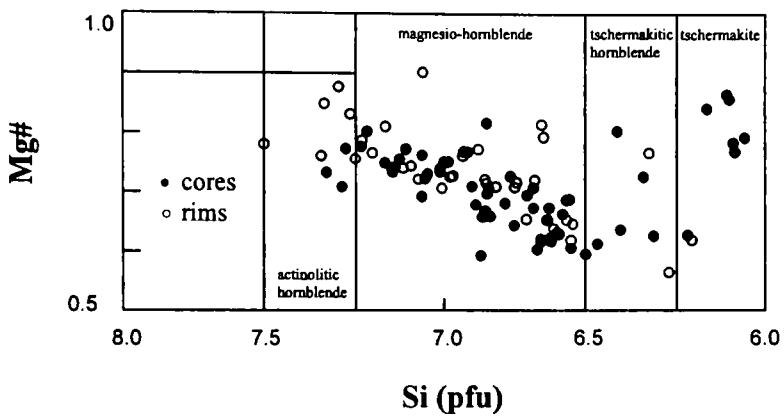


Figure 2.26 - *Tgd* calcic amphibole classification, with $(Na + K)_A < 0.5$ and $Ti < 0.5$ (after Leake, 1978). The majority of amphiboles are magnesio-hornblendes. Si cations per formula unit (pfu), for 23 oxygens.

The majority of *Tgd* amphiboles are magnesio-hornblendes, with about 12% being actinolitic or tschermakitic hornblendes, and 3% being edenitic hornblendes (Fig. 2.26). Using the empirical criterion of Fleet and Barnett (1978), the $^{[4]}Al/^{[6]}Al$ ratio can distinguish unaltered igneous calcic amphiboles from low-pressure and high-pressure metamorphic calcic amphiboles. Amphiboles with $^{[4]}Al/^{[6]}Al$ greater than 3.3 are considered to be the products of crystallisation from a melt. From figure 2.27, it is clear that the majority of amphiboles from the granodioritic phase of the EWIC, both rims and cores, fall within the igneous field of Fleet and Barnett (1978).

Tgd plagioclase compositions: Plagioclases from *Tgd* were analysed using an electron microprobe (Appendix B) in order to determine the temperature and pressure of emplacement associated with the EWIC (Chapter 5). Mineral compositions determined from these data are presented here (Fig. 2.28). Plagioclases from *Tgd* exhibit complex normal, reverse, and oscillatory zoning, even in highly strained samples. They exhibit a range of compositions, with cores from An_{27-57} and rims between An_{20-62}. Only one (altered) sample gave rim analyses between An_{10-20} (Loc. 1, VP94-001).

Occasionally globules of *Td* (*Tdy*?) in a matrix of *Tgd*, or in a net-vein relationship, record magma mixing (Fig. 2.29 and 2.30). Lobate, serrated, and wispy protrusions suggest, however, that magma

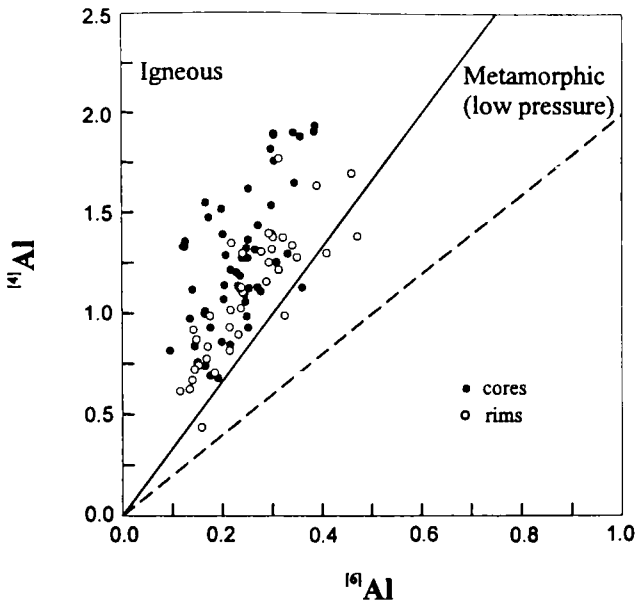


Figure 2.27 - *Tgd* amphibole genesis. The majority of *Tgd* amphiboles lie in the igneous field of Fleet and Barnett (1978). The dashed line separates low pressure and high pressure metamorphic compositions; none of the *Tgd* amphiboles lie in the high pressure field.

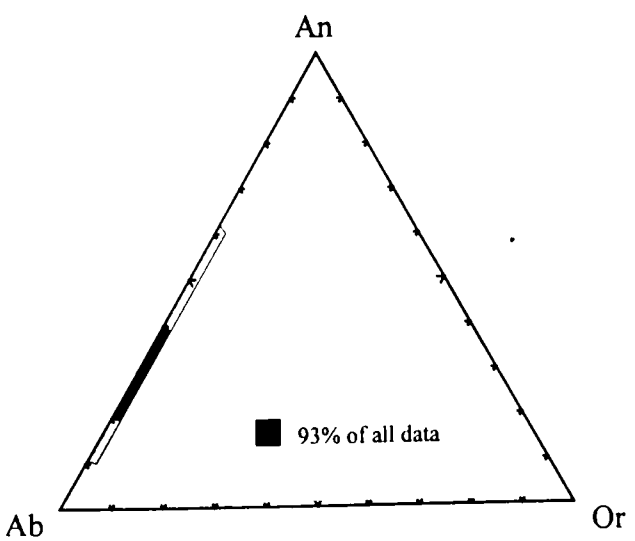


Figure 2.28 *Tgd* plagioclase compositions (from electron microprobe analyses). Compositions range from An_{10-63}, with 93% of the data between An_{20-40}. *Tgd* plagioclases exhibit complex zoning patterns (refer to text).



Figure 2.29 - Magma mixing with globules of *Td* in felsic *Tgd*. Hammer for scale (Loc. 203).



Figure 2.30 - Net-vein complex of *Td* (*Tdy?*) intruding and mobilising *Tgd*. Hammer for scale (Loc. 269).

mingling is much more prevalent between *Tgd* and *Tlg* (Fig. 2.31). Intimate mingling of *Tlg* and *Tgd* suggests that these units are contemporaneous. Xenoliths of *Tu*, *Tlg*, *Td*, and *Xgn* are all present, generally subparallel to the foliation, and reaction rims are common (Figs. 2.32, 2.33, and 2.34). Concordant zircon (U/Pb) and hornblende ($^{40}Ar/^{39}Ar$) dates suggest a Miocene crystallisation age for *Tgd* (Chapter 5).

Td, Miocene (?) diorite - Xenoliths (millimetres) and rafts (metres) of microdiorite and diorite pegmatite are preserved only in *Tgd*. The relative age relationship suggests that *Td* is older than *Tgd*, but it may be related to EWIC, in which case it would be regarded as Miocene in age. Pegmatitic diorite is



Figure 2.31a - Intimate magma mingling between *Tgd* and *Tlg*. Hammer for scale (Loc. 37).



Figure 2.31b - Magma mingling with wispy *Tlg* in medium grained *Tgd*. Field of view ~0.5 m (Loc. 68).



Figure 2.32 - Xenoliths of *Td* and fine grained *Tgd* in a weakly foliated matrix of *Tgd*. Note subangular to subrounded xenoliths are aligned with the foliation. Pencil for scale (Loc. 45).



Figure 2.33 - Xenolith of *Td*, with reaction rim, in matrix of *Tgd*. Hammer for scale (Loc. 14).



Figure 2.34 - Xenolith of mafic dyke (*Tu*), with reaction rim, in *Tgd*. Pencil for scale (Loc. 45).

restricted in occurrence to the main north-south drainage (south of Nomento Peak, in the southwest of the study area), where a large raft of hornblende diorite pegmatite is preserved (Locs. 12 and 14). In the pegmatite, amphibole grows into leucocratic veins, suggesting that this diorite and the leucocratic melt (sweat?) are cogenetic (Fig. 2.35). The pegmatite is typically chloritized, with amphibole pervasively altered to chlorite and minor epidote present. Xenoliths of *Td* are generally aligned with the foliation of *Tgd*, and reaction rims around enclaves are occasionally preserved (Figs. 2.33 and 2.34).



Figure 2.35 - Amphibole of *Td* growing into leucocratic vein. Hammer for scale (Loc 2).

Yg, Middle Proterozoic porphyritic granite. Tan to pale-red, coarse-grained, porphyritic biotite granite. Tabular potassium feldspar megacrysts (≤ 3 cm), typically rimmed by plagioclase, occur in a matrix of plagioclase, quartz, potassium feldspar, biotite, magnetite, and sphene. When present in the upper-plate, *Yg* is the depositional basement for Tertiary volcanic rocks (in the southwest, near Loc. 189), has a pronounced red oxidation, weathering stain, and lacks ductile deformation. As a lower-plate footwall rock in the northeast region of the study area (Loc. 288), it has a pronounced fabric, with rotation and parallel alignment of megacrysts (Fig. 2.36). This granite may be correlative with 1.4-1.5 Ga anorogenic rocks of Anderson (1983).

Xgn and Xmgn, Early Proterozoic gneiss, schist, and migmatite. Heterogeneous, non-mylonitic (*Xgn*) and mylonitic (*Xmgn*), amphibolite-facies crystalline rocks which include migmatites, amphibolites, schists, orthogneisses, and paragneisses. These rocks are best exposed in the northeast of the study area and are highly deformed near the EWIC intrusive contact (Fig. 2.37). This contact is irregular on a millimetre scale and more planar at outcrop scale. Away from the contact a subhorizontal, planar or anastamosing layering, with layer-parallel isoclinal folding, is regionally developed; this is sometimes concordantly



Figure 2.36 - Deformed *Yg*, with alignment of megacrysts. Pencil for scale (Loc. 288).

interlayered with the lithologies of the EWIC (Fig. 2.38). In the northeasternmost region of the study area, *Xmgn* is intruded by *Yg*. The biotite schist in contact with the EWIC (Loc. 112) has yielded concordant zircon SHRIMP U/Pb ages of 1.6-1.7 Ga (Chapter 5).

2.4 Discussion

The absence of Cretaceous rocks in the northeast Sacramento Mountains is notable, given their relatively ubiquitous and proximal occurrence elsewhere in the region. In the northwest Sacramento Mountains, for example, Cretaceous gneiss (or an older gneiss reworked at amphibolite grade during the Cretaceous), as well as small volume, Late Cretaceous granitic plutons (deformed and undeformed), intrude into the Precambrian basement (Argent, 1996; this thesis, Chapter 5). In the Chemehuevi Mountains, to the south, John and Mukasa (1990) report Cretaceous U/Pb ages for the voluminous Chemehuevi Mountains plutonic suite, which intrudes older basement rocks.

Minor occurrences of coarse grained, granitic rocks are also present in the northeast Sacramento Mountains (Fig. 2.39), but these units are not extensive and their contact relationships are either gradational



Figure 2.37 - Contact between EWIC and *Xmgn*. Sledge hammer for scale (Loc. 109).



Figure 2.38 - Subhorizontal interlayering of *Xmgn* (biotite schist) and *Tgd*. Hammer for scale (Loc. 314).

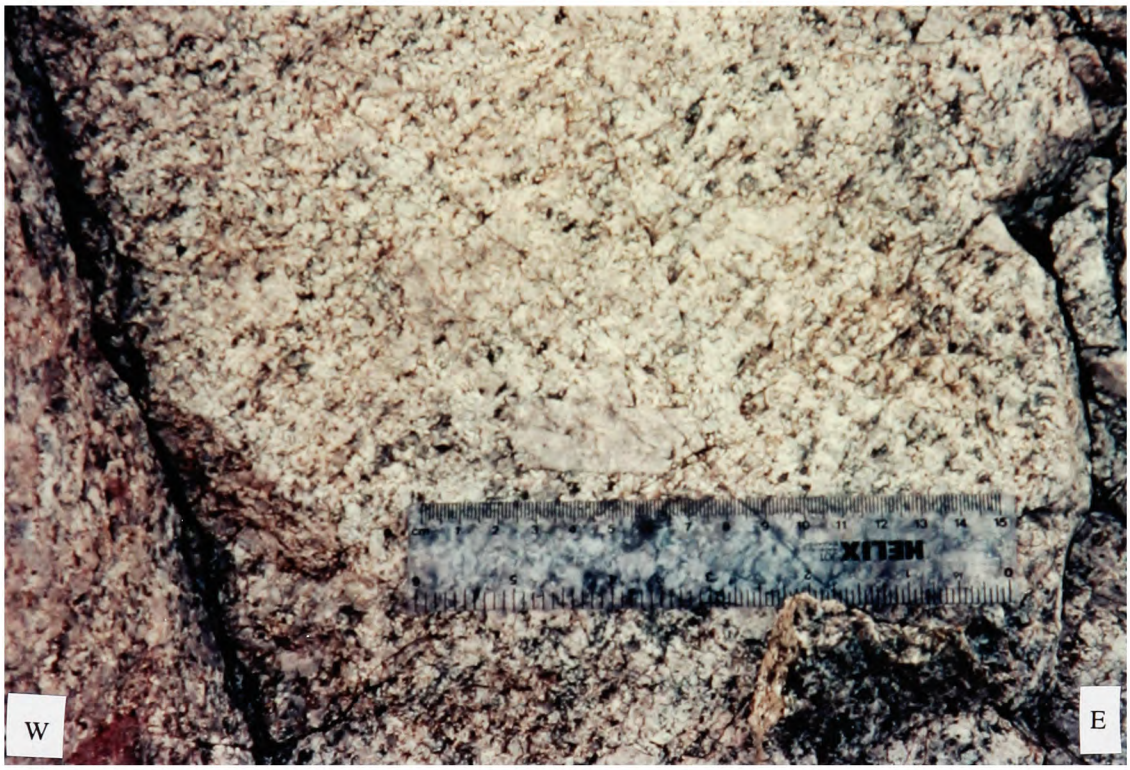


Figure 2.39 - Foliated, megacrystic granite. Ruler for scale (Loc. 32).



Figure 2.40 - Foliated, porphyritic granite. Pencil for scale (Loc. 29).

(resorbed?) with EWIC granodiorite or are now parallel with the pervasive mylonitic foliation, inhibiting relative age determinations. These unique granites are always foliated, with potassium feldspar phenocrysts (porphyroclasts) often rotated into relative parallelism with each other and typically exhibiting brittle deformation fabrics (cleaving along twin planes; Fig. 2.40). These rocks are undated and may be equivalent to Cretaceous granitic rocks found in nearby regions.

It is also possible that some of the leucogranite in the northeast Sacramento Mountains may be pre-Miocene in age. In particular, the age of the coarse grained, thick sheets of leucogranite found in the eastern region of the study area is poorly constrained. Again, the parallelism of contacts resulting from the strong, mylonitic fabric makes determining relative ages problematic. While it is clear, from cross-cutting relationships in the lesser deformed regions of the study area, that some leucogranite is, in fact, younger or contemporaneous with *Tgd*, there in no a priori reason to assume that all the leucogranite present in the northeast Sacramento Mountains represents a single generation of magmatism. That said, there are a number of Miocene ages recently reported from the Dead Mountains to the north and from the southern Sacramento Mountains, indicating that Tertiary granitic plutonism in the region is much more prevalent than previously believed (Howard et al., 1996; Foster et al., 1996). Furthermore, a similar absence of Cretaceous rocks has been noted in the footwall of the southern Sacramento Mountains (Campbell and John, 1996), and this may also be true in the Dead Mountains immediately adjacent to the study area in the north.

Chapter 3

Structure of the Footwall in the Northeast Sacramento Mountains

3.1 Introduction

The structural geology of the northeastern Sacramento Mountains is dominated by the Tertiary Sacramento Mountains detachment fault (SMDF) system and a pervasive mylonitic deformation of footwall rocks. "Footwall" here is considered to be the autochthonous basement beneath the basal surface of the SMDF system. The SMDF system in the northeast Sacramento Mountains juxtaposes Miocene volcanic/sedimentary rocks and their crystalline basement against mylonitically deformed Tertiary, Cretaceous (?), and Precambrian igneous and metamorphic rocks (this study; Schweitzer, 1991; Spencer, 1985; McClelland, 1982). Unlike elsewhere in the region, i.e. the northwest and southern Sacramento Mountains, the ductile fabric of footwall deformation in the northeast (and central) Sacramento Mountains appears to be a function of an elevated thermal regime resulting from the emplacement of the syntectonic, Miocene Eagle Wash Intrusive Complex (EWIC) (c.f. Chapter 5). After emplacement of the EWIC and the onset of cooling and uplift of the footwall, intrusion by basaltic to rhyolitic dykes and high-angle faulting occurred. These dykes are inferred to be Miocene in age and are cut by the SMDF system. Other dykes, also inferred to be Miocene in age, appear to be coeval with later high-angle, north-south faults. Some of

these high-angle faults cut the SMDF and some are cut by the SMDF, illustrating their relative contemporaneity. During and after detachment faulting, the northeast Sacramento Mountains was undergoing *rapid* cooling and uplift associated with tectonic denudation of hanging wall rocks (Chapter 5).

Three distinct episodes of deformation (D1, D2, and D3) can be identified in the northeast Sacramento Mountains, with D1 representing pre-Tertiary (or pre-detachment faulting) deformation, D2 representing mid-Tertiary (or syn-detachment faulting) deformation, and D3 representing mid- to late-Tertiary (or late- to post-detachment faulting) deformation. Due to the pervasive mylonitic fabric associated with the rocks in the northeast Sacramento Mountains, it is logical to approach the structural evolution of the region by evaluating the youngest, best preserved fabrics, and progressing towards the oldest, least-preserved/over-printed fabrics. By combining the spatial and temporal relationships associated with each deformation, the structural evolution of the region can be evaluated and a deformational model developed.

The stereonets presented are equal-area, lower-hemisphere projections. Planar data (foliation, bedding, etc.) are plotted as poles, and linear data (lineations, fold axes, etc.) are plotted as points (dip direction, dip). Eigen vectors and/or Fisher statistics (Fisher, 1953) have been calculated when appropriate and the primary eigen vector *(primary vector)*, the 95% circle of confidence (α_{95}), and the precision parameter kappa (κ) are reported. For clarity, only the first 3 or 4 contours are shown on sterionet figures.

3.2 Tertiary brittle deformation (D3)

High-angle faults The youngest structural feature in footwall rocks of the northeast Sacramento Mountains is the regionally unique, north-south to northeast-southwest trending, near-vertical faults. These faults define the unusual north-south physiographic trend of the northeast Sacramento Mountains, and continue into the Dead Mountains to the north (Spencer, 1985; K. Howard, 1997, pers. comm.) and into the central Sacramento Mountains to the south (Schweitzer, 1991), but are absent elsewhere in the extensional corridor. These faults cut the SMDF in the northwest and cut other low-angle faults in the study area, clearly constraining their development to post-detachment faulting. Occasionally intruded by dykes inferred to be Miocene in age, it is likely that these faults are, in part, also Miocene in age. Last-motions from slickensides indicate that these faults represent strike-slip, oblique -slip, and normal dip-slip fault motions (Figs. 3.1 and 3.2). When relative motion can be determined on strike-slip and oblique-



Figure 3.1a - Vertical, north-south fault. Fault zone ~ 1 m wide (Loc. 396).



Figure 3.1b - Near-horizontal striae indicate strike-slip motion. Pencil for scale (Loc. 396).



Figure 3.2a - Steep, dip-slip normal fault. Mineralised breccia zone ~ 1 m wide (Loc. 100).

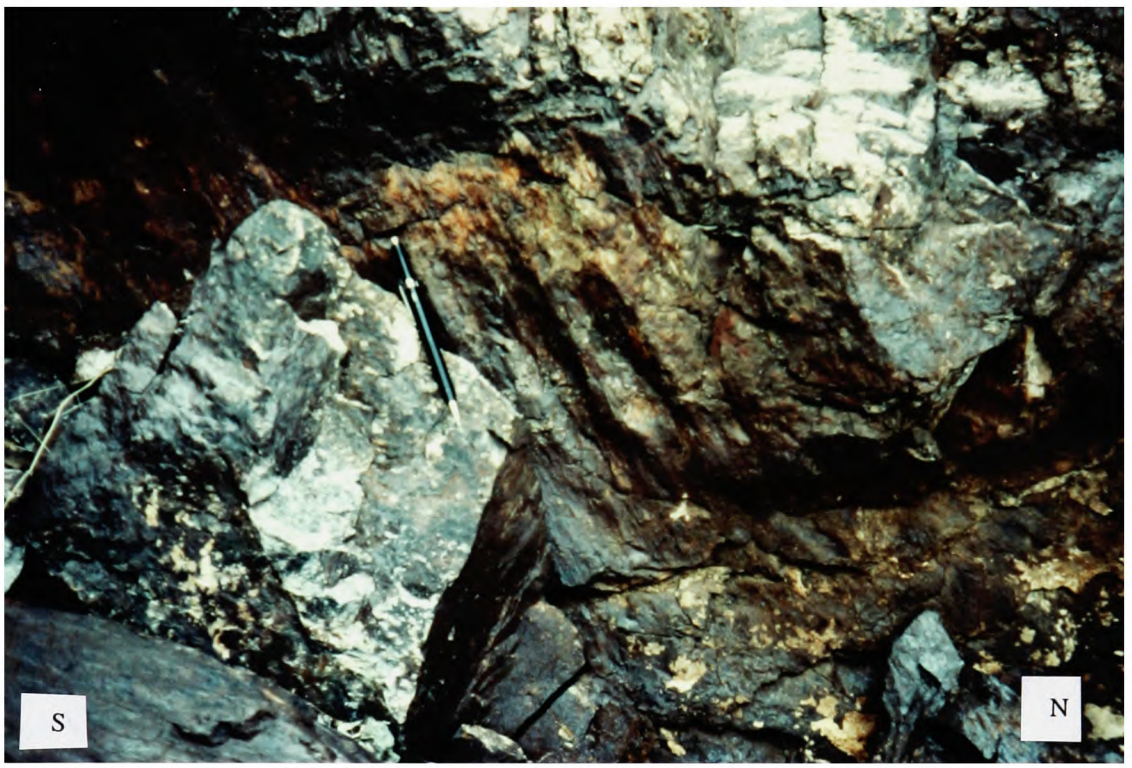


Figure 3.2b - Near-vertical striae indicate dip-slip motion. Pencil for scale (Loc. 100).

slip faults using offset markers, "smooth direction" on striae, or drag folds, it is dominantly right-lateral (dextral) with small displacements (< 20 m). Sinistral strike-slip faults are also developed, though to a much lesser extent. The relative motion on dip-slip faults is typically down-to-the-east, east of the range axial-high, i.e.- roughly east of Nomento Peak, and down-to-the-west, west of the range axial-high, suggesting that domal uplift was occurring, or had already occurred, at the time of high-angle faulting. The maximum relative motion along normal dip-slip faults observed was ~100 m. This figure is consistent with the depth of Quaternary gravel on the east side of the range front (east of Loc. 381, at labelled elevation 964'), reported by a homesteader who had a water-well drilled (330', oral comm.).

Figure 3.3 summarises the orientations and slip-directions of faults in the study area. Dominant fault populations can be seen to define three groups: 1) Shallow poles in the southwest to northwest quadrant of the stereonet indicate near-vertical faults striking north-northwest to northeast; 2) intermediate poles in the southwest quadrant define moderately northeast-dipping, northwest-southeast trending faults; and 3) steep poles clustered about the centre of the stereonet define shallow dipping normal faults (Fig. 3.3a). Fault

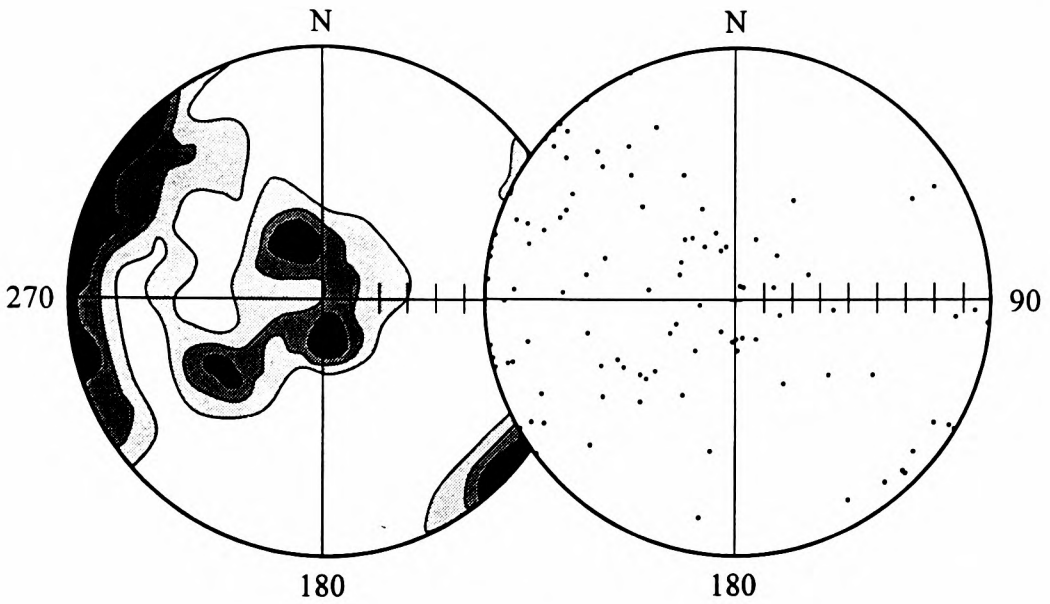


Figure 3.3a - Fault trends (N=105). Contours = 1% per 1% area. Note several populations: 1) steep, NW-SE to NE-SW trending faults; 2) moderately NE-dipping, NW-SE trending faults; and 3) low-angle faults.

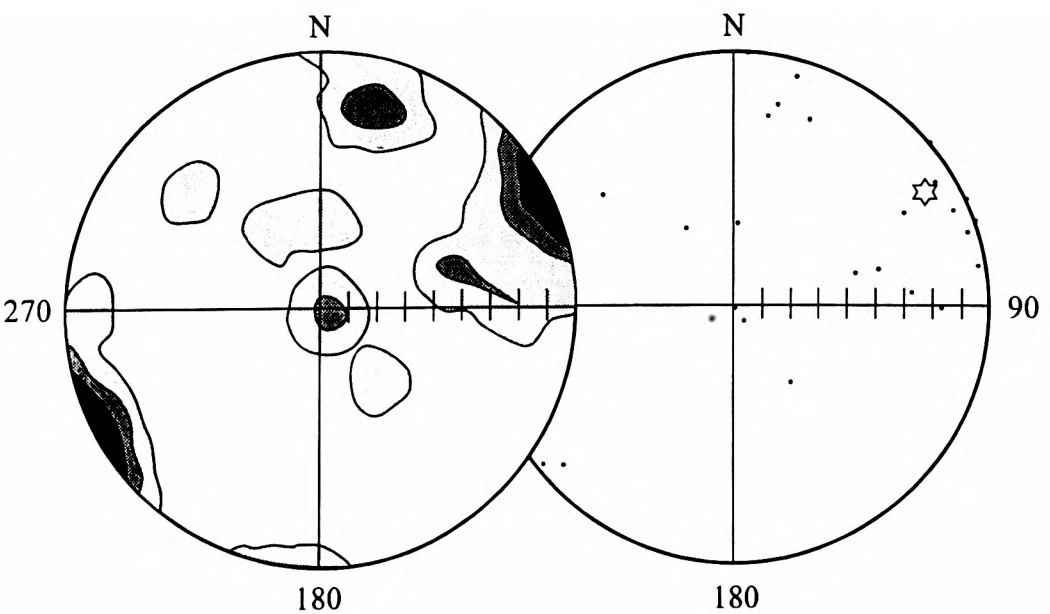


Figure 3.3b - High-angle fault lineations (N=29). Contours = 4% per 1% area; primary vector = 59.0°, 14.0°. The dominant, subhorizontal population indicates NE-SW strike-slip faulting. Note ancillary N-S, subhorizontal, strike-slip faulting and steeper lineations indicative of dip-slip and oblique-slip fault motions.

striae also define several types of fault motion, with the dominant group indicating northeast-southwest, strike-slip faulting (Fig. 3.3b).

Fault gouge, breccia, and/or protocataclasite (up to a meter thick) is common (Fig. 3.4). Secondary hydrothermal mineralization is also pervasive. Secondary minerals include quartz, copper-oxides (chrysocolla, malachite, chalcocite), barite, fluorite, iron oxides, and calcite, and indicate that the high-angle faults acted as conduits for hydrothermal circulation. Secondary hydrothermal mineralization is most abundant in the northeast of the study area.



Figure 3.4 - Protocataclasite of granite along N-S fault. Pencil for scale (Loc. 340).

Fractures, joints, and tension gashes - Fractures and joints define populations similar to those associated with faults (Fig. 3.5). A near-vertical, north-south to northeast-southwest trending population is the dominant fracture set. A second near-vertical, east-west, direction is weakly defined, as are intermediate and shallow-dipping fractures. The joints seldom form conjugate arrays. Occasionally, near-vertical *en echelon* tension gashes develop with motion synthetic to nearby major faults (Fig. 3.6).

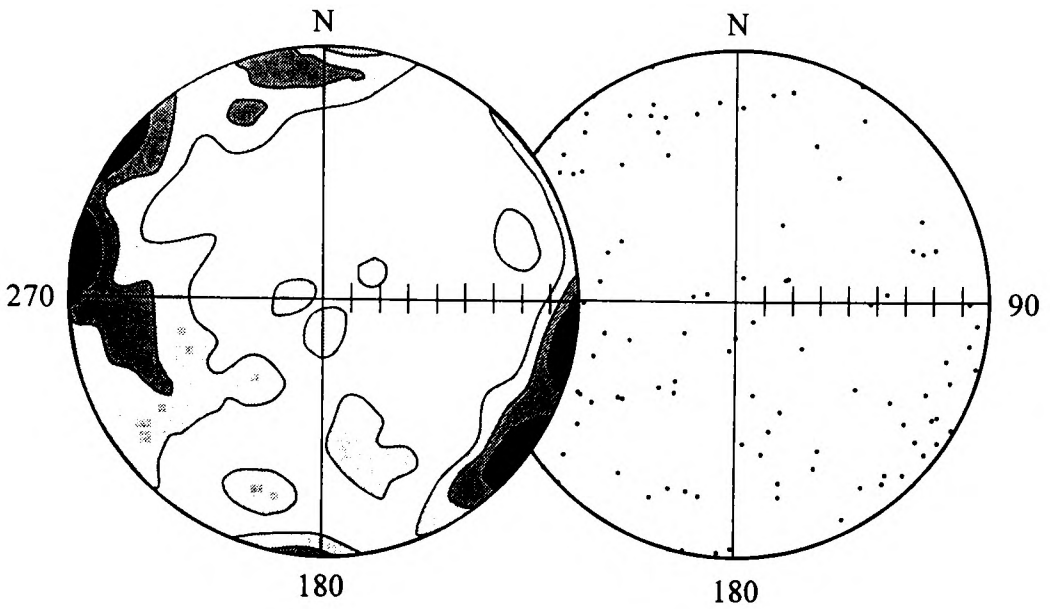


Figure 3.5 - Fracture trends (N=138). Contours = 1% per 1% area; primary vector = 288.3°, 7.6°. Note several populations: 1) steep, N-S to NE-SW trending fractures; 2) steep, E-W trending fractures; and 3) moderate- and shallow-dipping fractures.

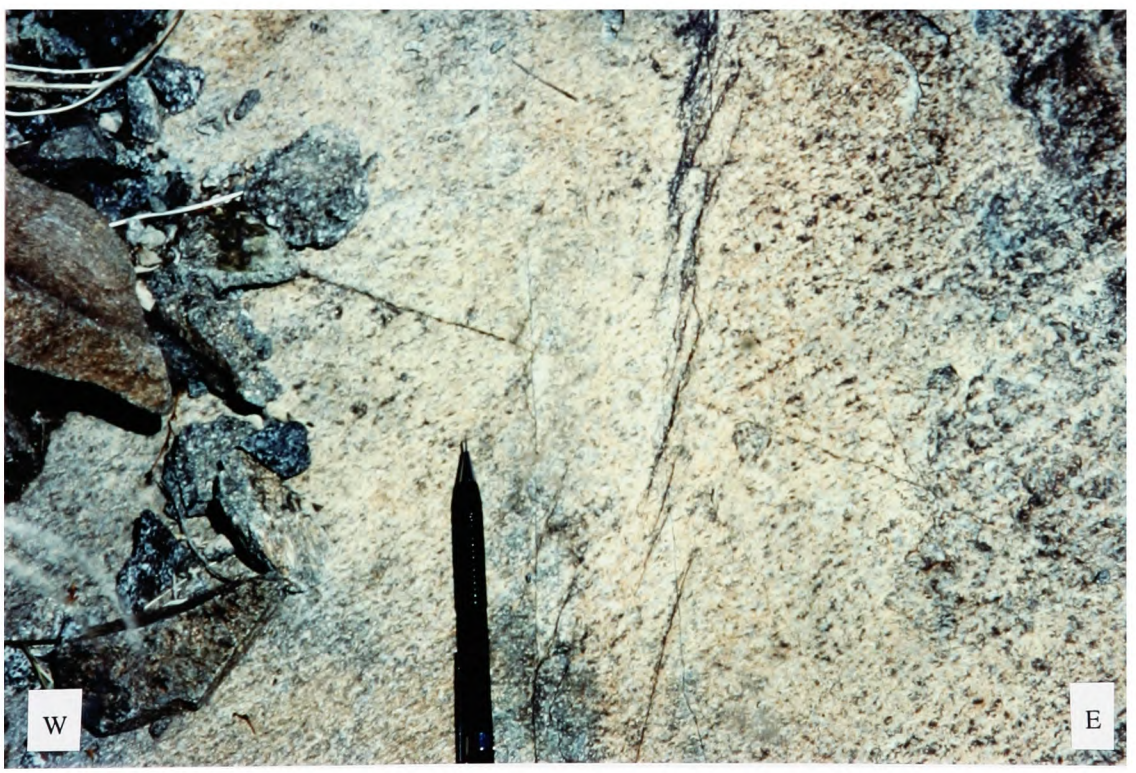


Figure 3.6 - *En echelon* tension gash, motion synthetic to nearby fault. Pencil for scale (Loc. 26).

Dykes - Dyke trends define populations similar to those associated with faults in the study area (Fig. 3.7a) and in some cases the faults are clearly used as magma conduits. Though the total number of measurements is small, a near-vertical, northwest-southeast to northeast-southwest trending population is well-defined. The similarity of fault and dyke orientations suggests a structural control on dyke emplacement. A single, N-S rhyolitic dyke which cuts the footwall of the northeast Sacramento Mountains is correlative with the Eagle Peak rhyolite (Simpson et al., 1991) and is truncated by the SMDF. Foliations and lineations from deformed dykes are also shown (Fig. 3.7b) and appear to record the syntectonic, ductile deformation associated with D2 (see Section 3.3).

Low-angle faults - Low-angle faults can be divided into two categories which comprise 1) the main SMDF, juxtaposing Tertiary volcanic and sedimentary rocks against higher-grade igneous and metamorphic rocks, and 2) secondary, within plate, low-angle faults of minor displacement. Pseudotachylites, thought to be generated by frictional melting during seismogenic faulting (Sibson, 1977), are absent from the study area. Both the SMDF and the ancillary low-angle faults are cut by younger, near-vertical faults.

1) The SMDF is best exposed to the west of the northeast Sacramento Mountains, near Browns Camp and in Hacienda Wash, where it currently dips $\leq 25°$ Browns Camp is outside the study area, located in Section 6 of the U.S. Geological Survey 7.5' Flattop Mountain quadrangle. At this location, ~500 m west of Browns Camp, the detachment fault juxtaposes hanging wall conglomerates against footwall gneisses (Fig. 3.8). The gouge zone is ~1 m thick. Principal and conjugate Riedel fractures and synthetic shears are developed and are consistent with top-to-the-northeast transport of the hanging wall relative to the footwall. Striations on the fault surface trend to the northeast and dip gently to the northeast (061°, 17°; Argent, 1996).

In Hacienda Wash (Loc. 55), the SMDF juxtaposes pink Miocene volcanic and sedimentary rocks against severely fractured Precambrian rocks (Fig. 3.9). The lineation exposed on the indurated fault surface trends southwest and dips gently to the southwest (230°, 10°). The trend of striations on the SMDF are consistent with those found on major detachment faults in the Whipple Mountains (Davis and Lister, 1988), Chemehuevi Mountains (John, 1986), and central Sacramento Mountains (McClelland, 1984), which indicate the northeastward transport of the hanging wall rocks relative to the footwall across the Colorado River extensional corridor.

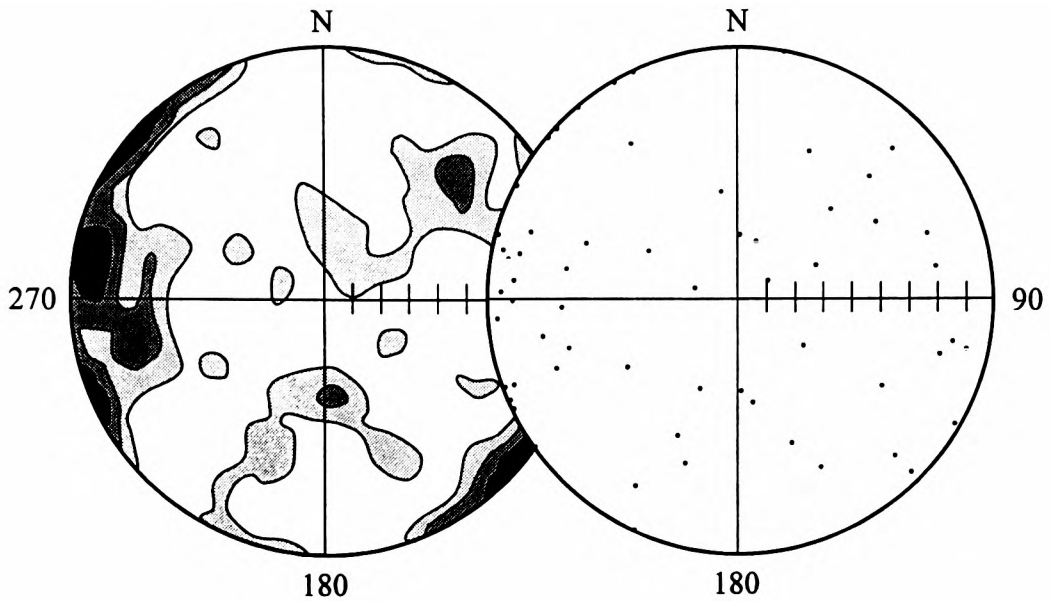


Figure 3.7a - Dyke trends (N = 65). Contours = 2% per 1% area. Note that most dykes are steep and trend NW-SE to NE-SW.

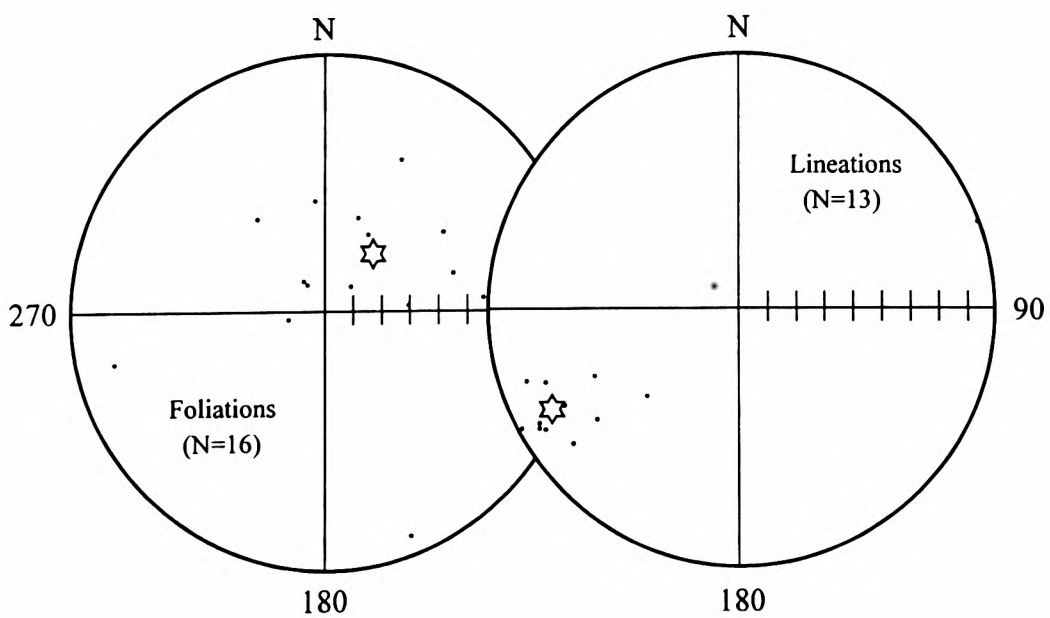


Figure 3.7b - Foliation and lineation data from sheared dykes. Primary vector for foliations = 35.3°, 67.4°, and for lineations = 242.6°, 16.3°.



Figure 3.8a - SMDF near Browns Camp (Flattop Mountain quadrangle). Person for scale.

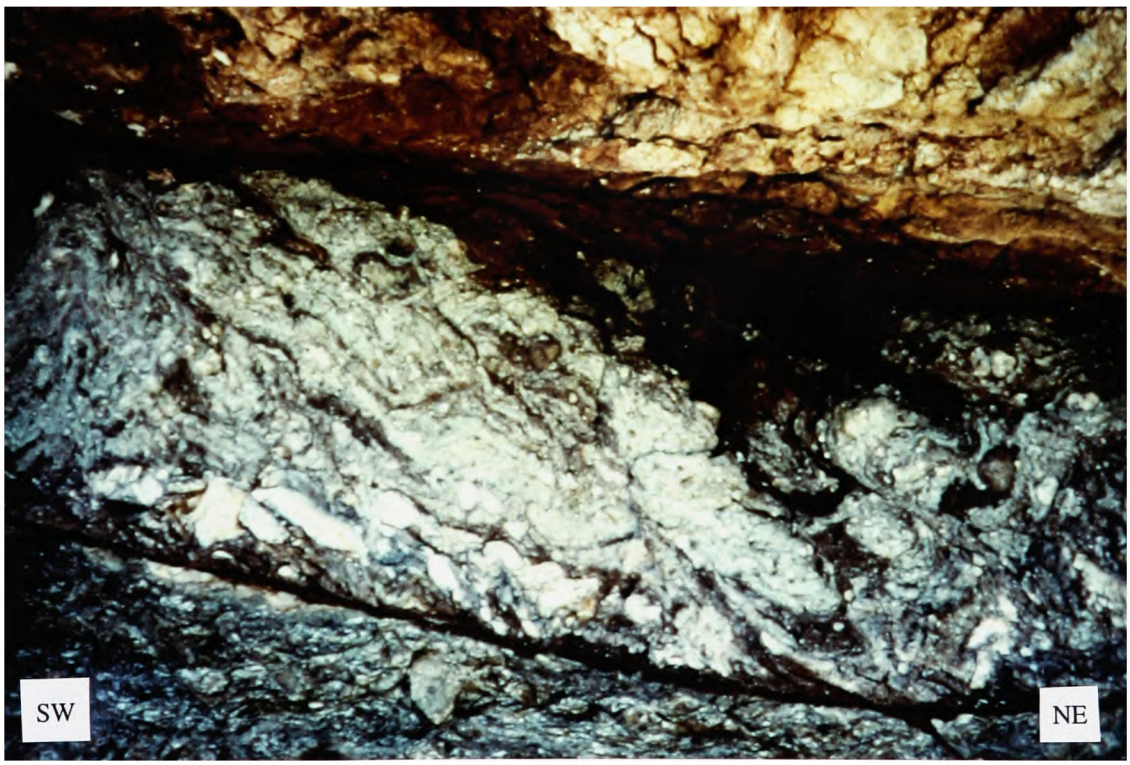


Figure 3.8b - Close-up of 3.8a showing Riedel structures in the SMDF zone near Browns Camp.



Figure 3.9a - SMDF in Hacienda Wash. Map case for scale (Loc 55).



Figure 3.9b - Striae on SMDF at Hacienda Wash. Pencil for scale (Loc 55).

Rocks within the SMDF breccia zone form incoherent fault gouge, microbreccia, breccia, and cataclasites. Using the classification of Sibson (1977), these fault rocks represent a depth-dependent series of shallow (0-5 km - gouge and breccia) to intermediate crustal levels (5-10 km - breccia and cataclasite). Cataclastic fault rocks are best preserved in the north and northwest of the study area and consist of recrystallized quartz and feldspar in a matrix of hematite + chlorite ± epidote ± albite (?) ± sericite ± copper oxides. The similarity of secondary minerals associated with the SMDF and the near-vertical faults suggests that the SMDF also acted as a conduit for post-detachment hydrothermal mineralization.

2) The secondary low-angle faults have motions synthetic to the SMDF (determined from "smooth direction" on striae and/or drag folds). Though absolute displacements on these faults could not be determined, overall displacements are thought to be small because the fault zones are narrow and the associated fault rocks are thin, generally < 1 m wide/thick (Fig. 3.10). Fault rocks associated with secondary low-angle faults consist entirely of microbreccia and gouge, suggesting formation at < 5 km



Figure 3.10 - Close-up of secondary low-angle fault gouge. Pencil for scale (Loc. 45).

crustal depths (Sibson, 1977). Hydrothermal fluid migration along these faults has altered the primary mineral assemblage and the secondary mineral assemblage includes hematite, chlorite, calcite, ± epidote ± sericite ± albite ± copper oxides. These ancillary faults are presumed to be younger than the SMDF, though a cross-cutting relationship between the two was never seen, for the following reasons: i) cataclasite is associated with the SMDF and not with the ancillary low-angle faults, suggesting that the SMDF was active at greater depth relative to the ancillary low-angle faults; and ii) the SMDF is now domed, whereas the ancillary low-angle faults are flat-lying. This suggests that these secondary low-angle faults were active at shallower crustal levels, and post-date the deformation of the SMDF.

Temperature, pressure, and age of formation - The development of D3 had started by ~15 Ma and may have continued after this time. This interpretation is supported by the following: i) the similarity of dyke and fault orientations suggest that dyke emplacement was structurally controlled, and ii) the N-S rhyolite dyke which transects the entire footwall of the northeast Sacramento Mountains, is correlative with the ~14 Ma Eagle Peak rhyolite, so that the structural control on dyke orientation was established prior to

~14 Ma. Furthermore, biotite ($^{40}Ar/^{39}Ar$), zircon and apatite (fission track) thermochronologic data (Chapter 5) show that the northeast Sacramento Mountains cooled rapidly at ~15-14 Ma, when all three of these mineral systems yield similar ages. This cooling event is thought to result from the tectonic exhumation and uplift of these rocks and this timing is consistent with the low temperatures (<350°C) required for development of brittle (as opposed to ductile) deformational fabrics. The temperatures associated with late propylitic alteration developed in many core complexes, from oxygen isotope and fluid inclusion studies, range from 200-370°C (Hyndman and Meyers, 1988; Kerrich, 1988; Kerrich and Hyndman, 1986). Consequently, low temperature and pressure is associated with the development of D3, which occurred late in the history of detachment faulting about 14 to 15 million years ago. It is unlikely that this deformation occurred later than 14 Ma, because the thermochronologic data (Chapter 5) indicate that the range has been below ~100°C since then and the propylitic alteration associated with D3 could not have developed.

3.3 Tertiary ductile deformation (D2)

Mesoscopic structures - D2 is characterised by a well-developed subhorizontal, southwest dipping foliation (S2) and a well-developed subhorizontal, southwest dipping stretching lineation (L2). Lithologies of the EWIC (*Tgd*, *Tlg*, and *Td*) consistently display this fabric (Figs. 3.11, 3.12, and 3.13). There appears

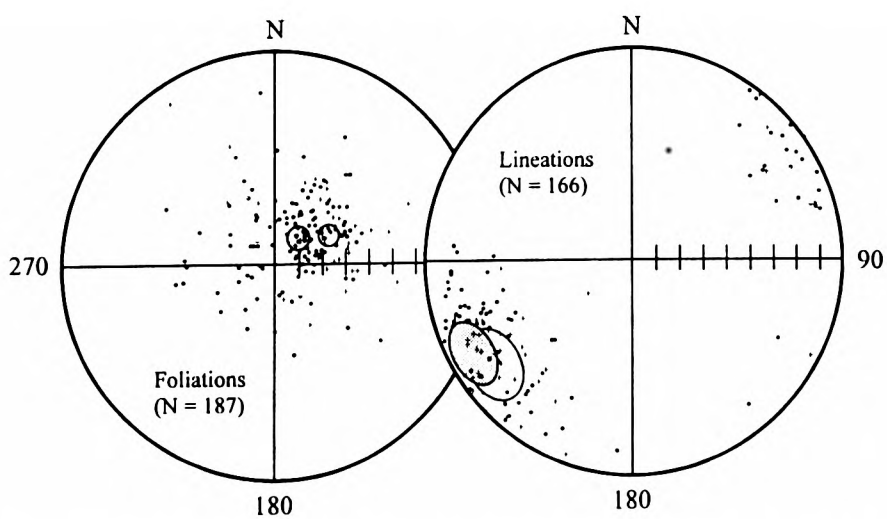


Figure 3.11 - Foliation and lineation data from granodiorite (*Tgd*). Data from the west side is represented by crosses and the open α_{95}, the east side by circles and the shaded α_{95}. Note that the foliations shallow to the east, while the lineations are indistinguishable (primary vector = 239.4°, 13.2°).

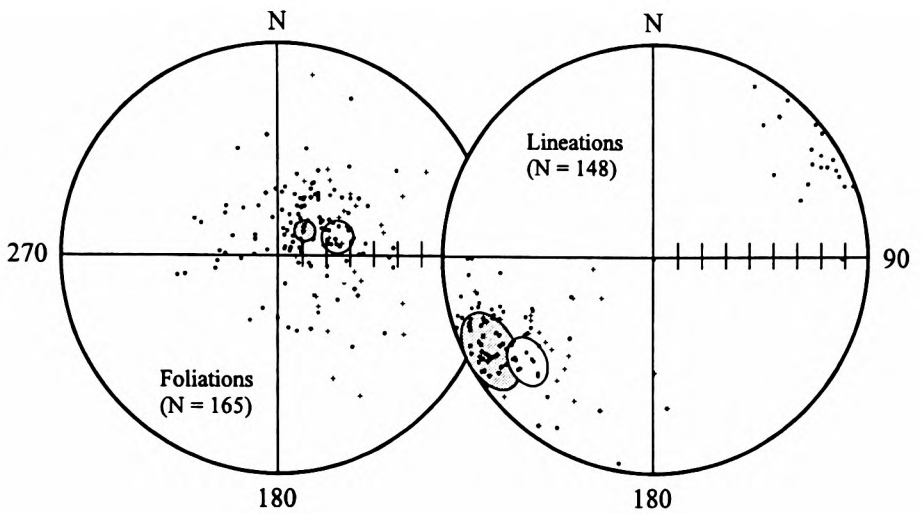


Figure 3.12 - Foliation and lineation data from leucogranite (*Tlg*). Data from the west side is represented by crosses and the open α_{95}, the east side by circles and the shaded α_{95}. Note that the foliations shallow to the east, while the lineations are indistinguishable (primary vector = 240.4°, 15.3°).

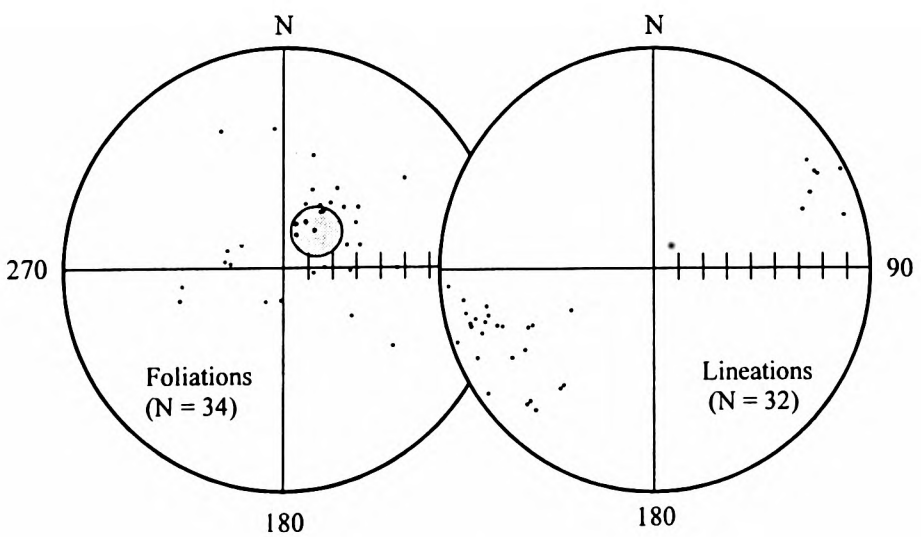


Figure 3.13 - Foliation and lineation data from *Td*. Primary vector associated with foliations = 36.5°, 73.2° and with lineations = 245.5°, 13.4°.

to be a slight directional difference of D2 between the eastern and western regions of the study area. In the east, S2 strikes NW-SE (130°-140°) and dips gently (15°) to the SW. In the west, S2 is oriented 150-160°, 25°SW, defining a slightly steeper and more NNW-SSE striking foliation. Note that this difference is not shown in *Td* because of the small number of measurements. The number of measurements is a direct reflection of the much smaller volume of *Td* (relative to *Tgd* and *Tlg*) present in the study area. This directional variation is not mirrored by the mylonitic lineation associated with D2 (though L2 generally has a larger α_{95} and smaller κ, indicating a greater directional dispersion), which consistently trends 240° and dips ~15° across the study area. Note that L2, given its rather large dispersion, is concordant with S2, i.e.- the orientation of L2 is parallel with the "dip direction, dip" of S2 (see summary Table 3.1).

Table 3.1 - Summary of foliation and lineation data associated with D2.

Unit	West				East			
	no.	primary vector	a95	k	no	primary vector	a95	k
Tgd_f	51	150, 23SW	5.7	13.3	136	129, 14SW	3.4	13.5
Tlg_f	51	162, 24SW	6.5	10.5	128	137, 14SW	3.7	12.2
Td_f - all	34	126, 17SW	9.0	8.4				
PC_f	46	173, 29W	8.1	7.7	30	152, 9SW	8.5	10.5
Tu_f - all	16	125, 23SW						
Contacts	40	151, 26SW	7.7	9.7	30	132, 12SW	7.3	13.9
Tgd_l	40	235, 18	11.8	4.6	126	241, 12	10.0	2.6
Tlg_l	43	232, 25	8.5	7.6	115	241, 21	11.4	2.3
Td_l - all	32	246, 13	21.8	2.3				
PC_l	32	229, 15	18.4	2.9	32	246, 10	27.9	1 8
Tu_l - all	13	243, 16						
Fold axes					38	311, 8	26.4	1.8

Note: f = foliation data, given as strike and dip; l = lineation data, given as trend and plunge; where "all" is indicated, the number of total measurements is too small to divide into West and East populations; contacts given as strike and dip; fold axes given as trend and plunge.

Using the nomenclature of Wise (1984) and Sibson (1977), D2 in the northeast Sacramento Mountains consists of a pervasive protomylonitic to ultramylonitic fabric. This mylonitic deformation affects all rocks in the study area, overprinting structures associated with pre-Miocene rocks to variable degrees (i.e.- D1, see Section 3.4). Strain in the region is notably heterogeneous, with the regions of highest relative strain concentrated at lithologic contacts or along "within unit" ultramylonitic shear zones. In both cases, the structure is parallel to the foliation (Figs. 3.14 and 3.15). Small scale folds are also present within



Figure 3.14 - Photograph of large thin-section showing D2 developed in all lithologies in the study area, with fabric and contacts parallel. Shear sense: top-to-NE. Darker regions are ultramylonites with abundant biotite. Horizontal dimension = 2 cm, vertical dimension = 4 cm (Loc. 230, VP95-232).

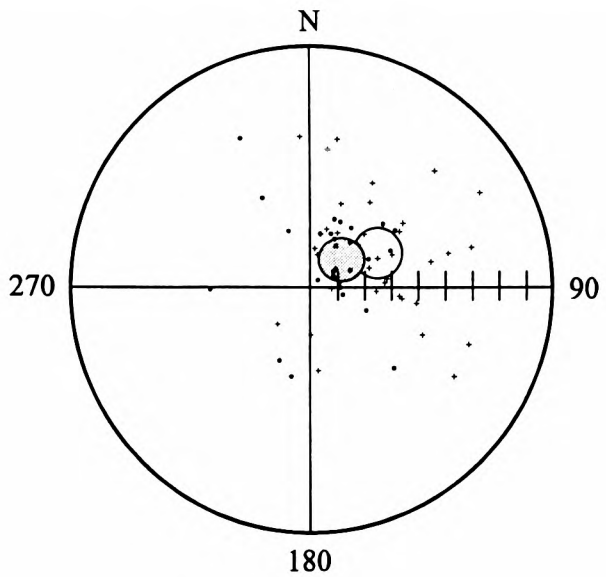


Figure 3.15 - Orientations of contacts (N=70). Data from the west side is represented by crosses and the open α_{95}, the east side by circles and the shaded α_{95}. Note that contacts may shallow to the east.

the EWIC. These are generally recumbent and tight to isoclinal (Fig. 3.16). Fold axes are subhorizontal and perpendicular to L2 (Fig. 3.17, Table 3.1), suggesting that these folds are drag features associated with the development of D2 (see also Fig. 2.22b).

Asymmetric meso- and microstructures - Several types of kinematic indicators defined by Hanmer and Passchier (1991), Passchier and Simpson (1986), and Lister and Snoke (1984) were used to investigate the sense of shear associated with the mylonitic rocks in the northeast Sacramento Mountains. These include i) shape fabrics or foliations (e.g., continuous shear zones, inclined quartz ribbons, S-C relationships, and asymmetric extensional shear bands), ii) inclusions and appendages (e.g., σ and δ prophyroclasts, "mica fish", and obliquity of pressure shadows), and iii) deformed veins, veinlets, and broken grains. Folds can develop during bulk simple shear (Bell and Hammond, 1984), but fold vergence was *not* used to determine shear sense: Continued folding of the mylonitic foliation during deformation can generate opposing shear sense in different fold limbs (Krabbendam and Leslie, 1996; Hanmer and Passchier, 1991).



Figure 3.16 - Drag folds in EWIC. Pencil for scale (Loc. 27).

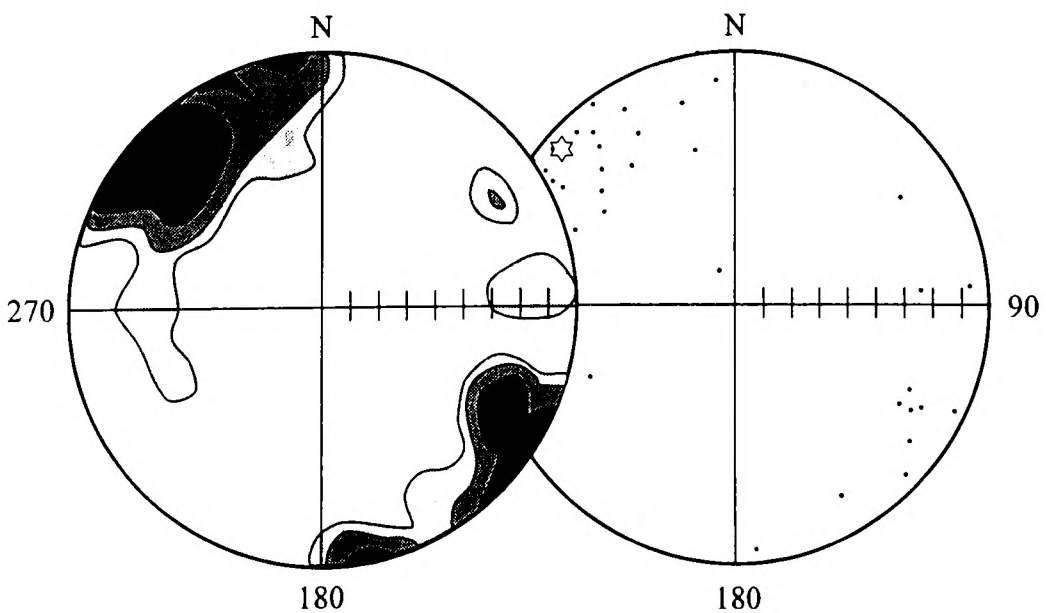


Figure 3.17 - Fold axes (N = 38). Contours = 2% per 1% area; primary vector = 311.0°, 8.0°. Note that fold axes are perpendicular to the tectonic transport direction.

The majority of shear sense indicators (77%) display top-to-the-northeast relative motion. Less than 1% (5 of 415) of the samples evaluated had top-to-the-SW shear sense. The shear direction could not be determined for a significant proportion (22%) of the samples, due to either i) grain-to-grain interference resulting in poorly defined fabrics, or ii) the presence of opposing shear directions. As can be seen from figure 3.18, top-to-the-northeast directed shear is the dominant shear direction regardless of lithology or geographic distribution.

Temperature, pressure, and age of formation - The temperature and pressure associated with the emplacement of the granodioritic phase of the EWIC, presented in Chapter 5, has been determined to be 680°C (± 19°) at 3.3 kb (± 0.75 kb). Age data for the EWIC from zircon (SHRIMP and conventional U-Pb), sphene (conventional U-Pb), and hornblende (incremental heating $^{40}Ar/^{39}Ar$) analyses also presented in Chapter 5, suggest that the EWIC was intruded at ~20 Ma. Biotite ($^{40}Ar/^{39}Ar$), zircon and apatite (fission track) data indicate that the EWIC was cooled to temperatures below ~325°C by ~15 Ma, below the temperatures necessary for pervasive mylonitic fabric development. D2 is well-developed in the EWIC, consequently D2 must have formed at temperatures and pressures equal to, or less than, those determined to be syn - to post-emplacement for the EWIC, but prior to the onset of brittle deformation, i.e.- after 20 Ma ago, but prior to 15 Ma.

The mineralogy of rocks in ductile shear zones typically reflect the characteristics of the metamorphic facies under which mylonitization occurred. The conditions of mylonitization can be inferred by comparing phase mineralogy and fabrics from the deformed rocks to their undeformed equivalents preserved in low-strain zones (Anderson, 1988). In undeformed *Tgd*, the stable mineral assemblage is hornblende + plagioclase + biotite ± potassium feldspar + accessory sphene, magnetite, apatite, and zircon. Thus, undeformed *Tgd* reflects crystallisation consistent with amphibolite facies conditions. The primary mineralogical difference in mylonitic *Tgd* is that hornblende may be intergrown with biotite and an alteration assemblage of epidote, chlorite, and sericite may be present; both of these mineral associations are interpreted to reflect retrograde conditions. Thus the mylonitic mineral phase assemblage of the EWIC is similar to that associated with undeformed *Tgd* or records slightly lower-temperature (retrograde) conditions.

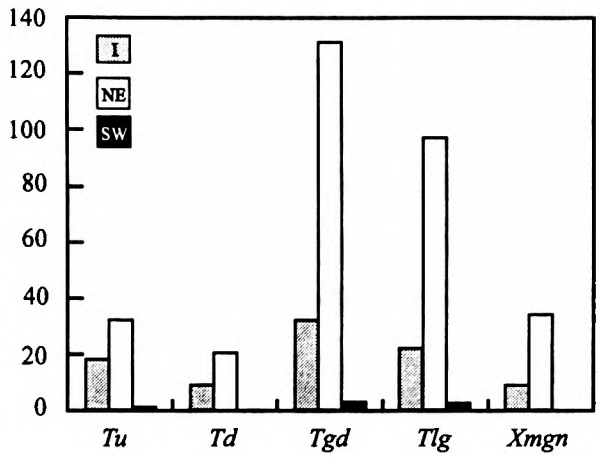


Figure 3.18a - Histogram of shear sense by lithology. Indeterminate directions (I) shaded, top-to-SW (SW) black, and top-to-NE (NE) unfilled.

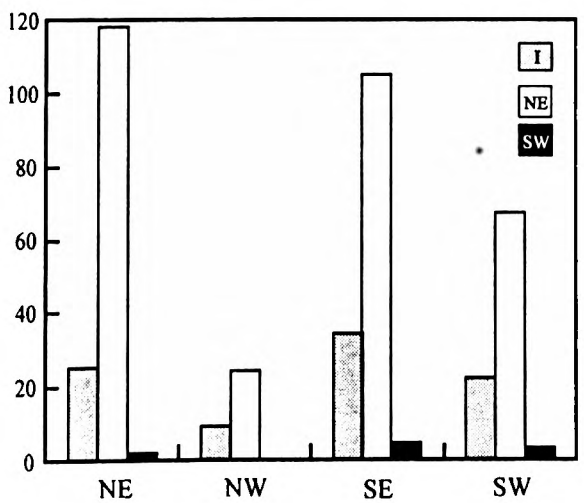


Figure 3.18b - Histogram of shear sense and geographic distribution (NE, NW, SE, SW). Indeterminate directions (I) shaded, top-to-SW (SW) black, and top-to-NE (NE) unfilled.

Deformational effects associated with D2 are typical of upper- to mid-greenschist through lower-greenschist facies mylonitization, with deformation apparently occurring entirely in the sub-solidus field. Amphibole is typically fractured parallel to (011), shows sliding along grain-boundaries, and is sometimes bent or kinked (Fig. 3.19, see also Fig. 2.23). Cataclastic fabrics in hornblende are widespread up to 600°C (Brodie and Rutter, 1985). Undulose extinction, deformation bands, and subgrain recrystallization along deformation bands in plagioclase (Fig. 3.20) suggest temperatures in excess of 450°C (Simpson, 1985; Brodie and Rutter, 1985). Deformation associated with D2 appears to record upper- to middle-greenschist facies conditions, i.e.- 450°C (plagioclase) < x < 600°C (hornblende).

These features are overprinted by variably developed brittle fracturing of feldspar, sphene, and apatite. These extensional microfractures are perpendicular to the long crystallographic axes, which are aligned parallel to the stretching lineation. Microfractures are typically filled with quartz or sometimes epidote. Quartz generally displays well-developed dynamic recrystallization fabrics (see Fig. 2.25). Fine grained ribbons, undulose extinction, parallel and elongate subgrains, etc., indicate temperatures in excess of 350°C, but can also occur under lower-greenschist conditions (Simpson, 1985; Tullis, 1983). This brittle deformation seems to have occurred at mid- and lower-greenschist conditions.

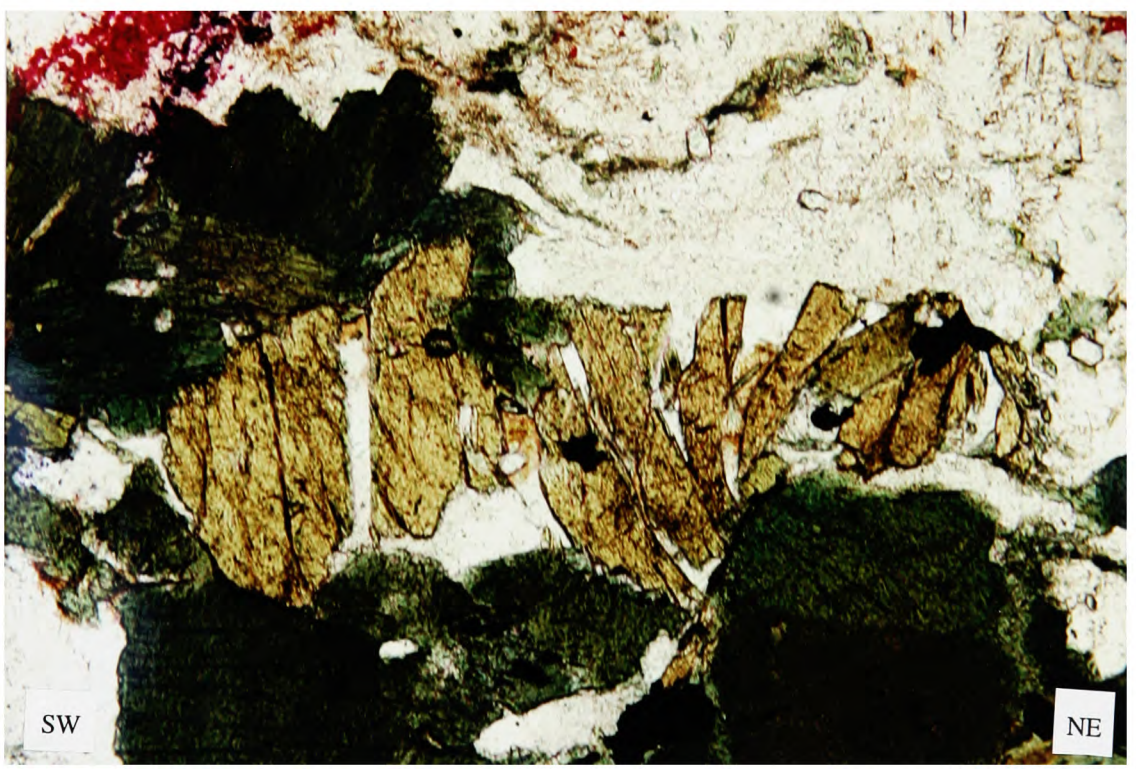


Figure 3.19 - Extensional microfractures in amphibole of *Tgd*. Field of view 1.35 mm (Loc. 44, VP94-057).

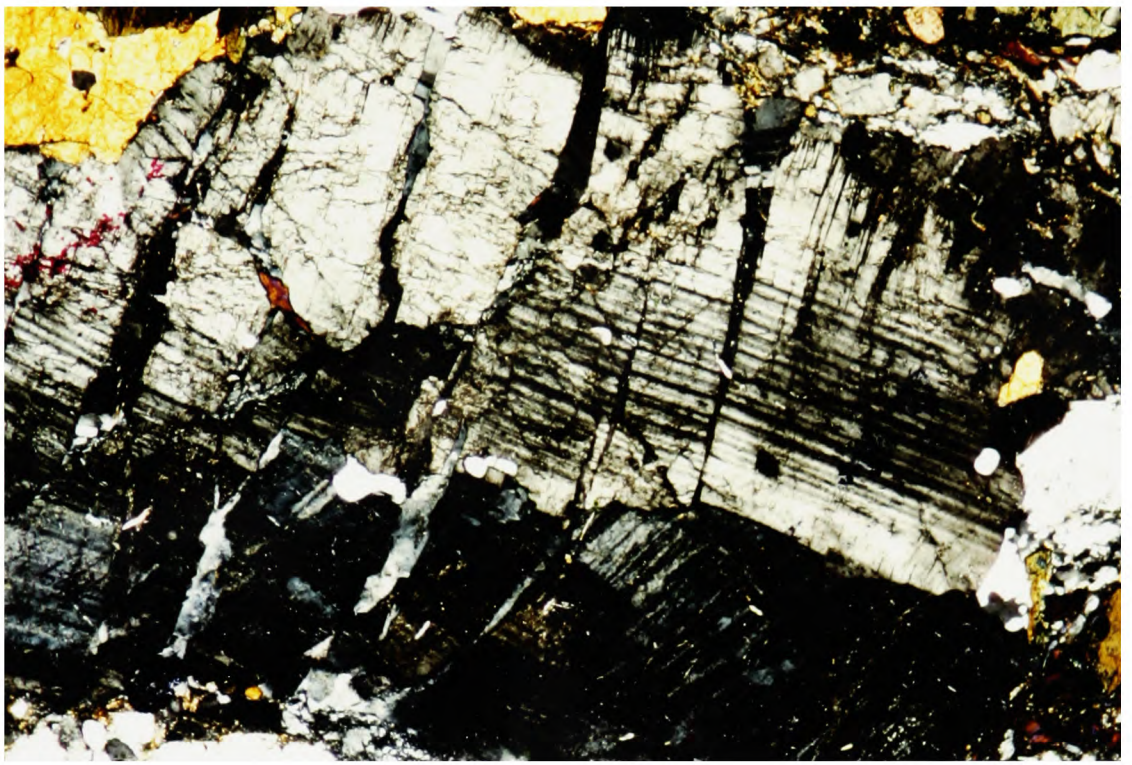


Figure 3.20 - Low-temperature plasticity of plagioclase in Tgd. Field of view 3.5mm (Loc. 44, VP94-057).

The transition from higher grade to lower grade conditions associated with D2 can be perceived in terms of a thermal continuum, rather than discrete deformational episodes, though in fact the uplift and cooling history of the northeast Sacramento Mountains may have been episodic. Detachment faulting in the range appears to have progressed from the southwest to the northeast through time, as evidenced by the younging of ages to the northeast (Chapter 5). Under such circumstances, ductile deformation could have been occurring in the northeast, while rocks in the southwest were undergoing lower-temperature deformation. Furthermore, given the presence of syntectonic magmatism, it seems reasonable that a range of deformational fabrics would be associated with the progressive cooling of the intrusive suite. This appears to be in agreement with plagioclase displaying both upper- to mid-greenschist (low-temperature plasticity) and lower-greenschist (brittle) deformation fabrics.

3.4 Pre-Tertiary deformation (D1)

The mylonitic deformation associated with D2 (above) followed an unknown number of earlier events. A pre-Tertiary deformation (D1) associated with Precambrian (and Cretaceous?) lithologies in the northeast Sacramento Mountains is present. D1 is manifest as a transposed schistosity or gneissic layering (Fig. 3.21) with Precambrian rocks on the west side of the study area recording the steepest and most N-S strike of S1 (170°, 30°W; Table 3.1). Though the number of measurements is small, this fabric in the *eastern* region has the same orientation as D2 and is parallel to the EWIC lithologies, i.e.- 152°, 9°SW (Table 3.1). This sub-parallelism with D2 is manifest by the *gradual transposition* of the N-S and NNW-SSE striking, more steeply dipping mylonitic foliation, to the shallower dipping, NW-SE striking orientation, from west to east. This is interpreted to reflect the rotation of an older fabric into alignment with D2, though the original orientation of the fabric is no longer preserved in the study area.

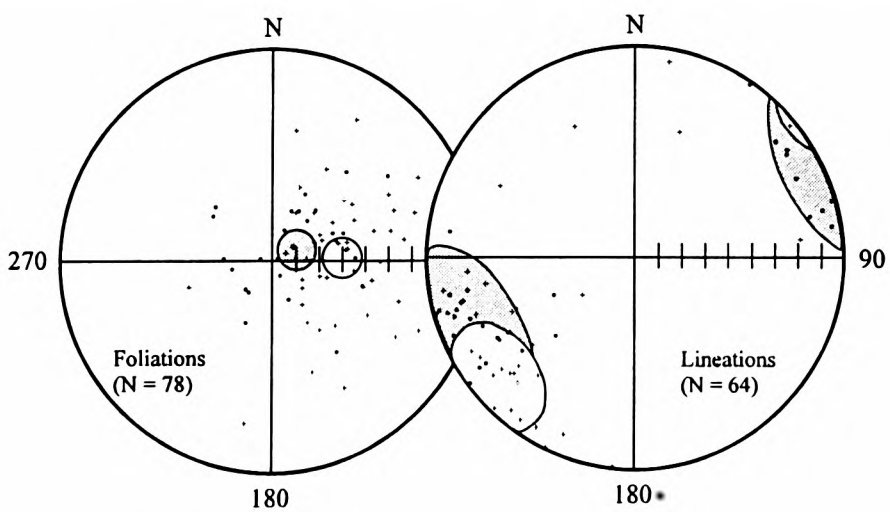


Figure 3.21 Foliation and lineation data from Precambrian rocks (*Xmgn*). Data from the west side is represented by crosses and the open α_{95}, the east side by circles and the shaded α_{95}. Note that the foliations shallow to the east, while lineations are indistinguishable (primary vector = 239.3°, 12.9°).

Though the original orientation of this fabric is no longer preserved, the mineralogy associated with its higher metamorphic grade can be recognised. D1 appears to be a high temperature (upper-amphibolite grade), recrystallization fabric with obvious polygonization of amphibole, plagioclase, and quartz (Figs. 3.22 and 3.23). Pelitic rocks preserve a relict upper amphibolite facies assemblage of sillimanite + biotite +

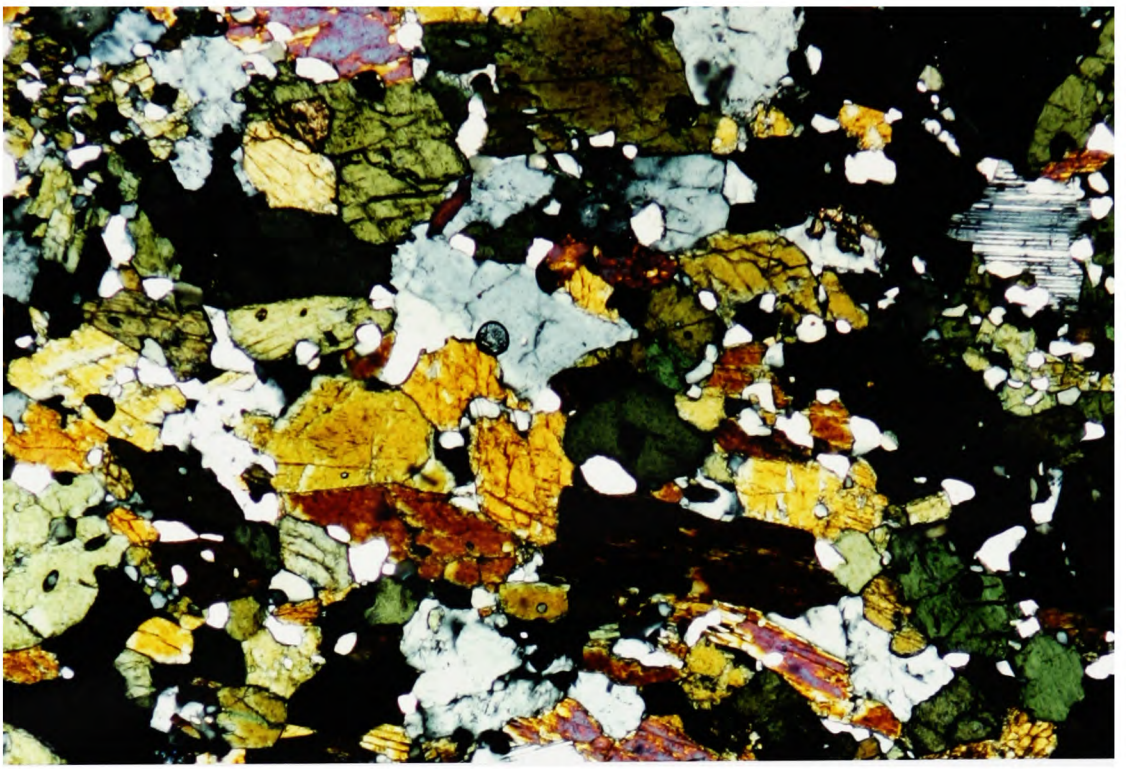


Figure 3.22 - Polygonal subgrain boundaries in amphibole associated with D1. Cretaceous (?) amphibolite dyke, field of view 3.5 mm (Loc. 80, VP96-281).

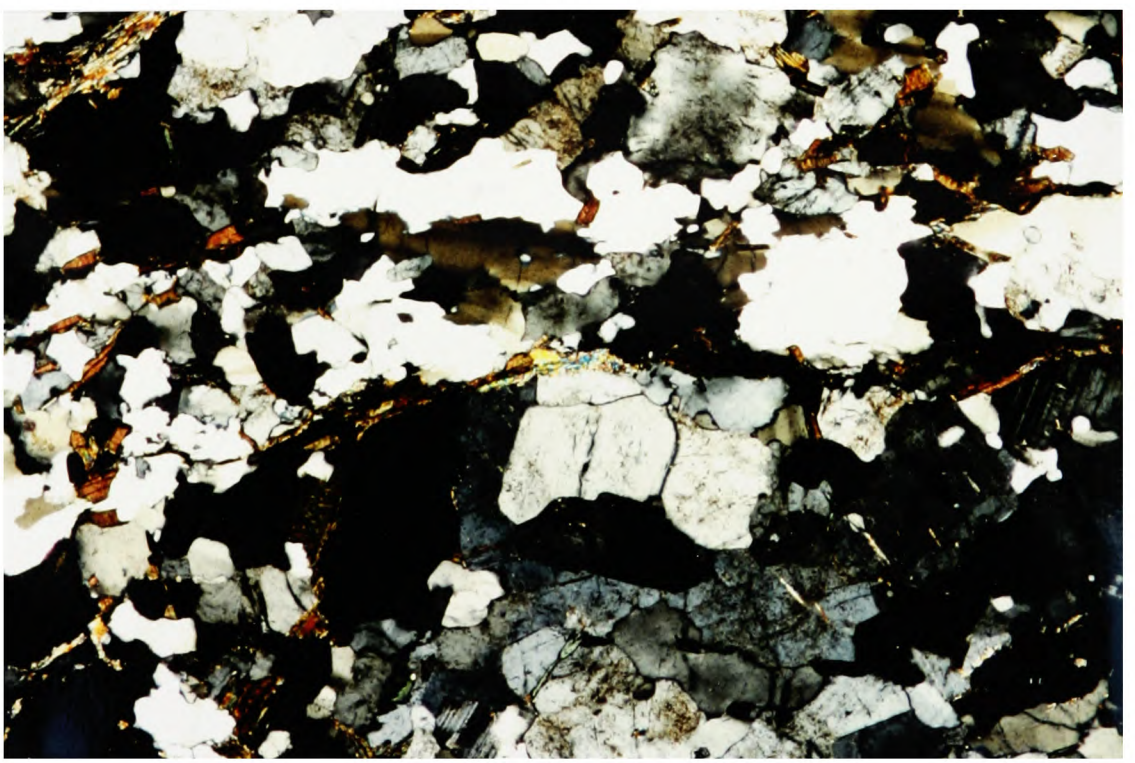


Figure 3.23 - Polygonal grain boundaries in plagioclase (bottom centre) associated with D1. Felsic layer in Precambrian schist, field of view 3.5 mm (Loc. 314, VP96-270).

garnet + quartz + plagioclase (Fig. 3.24). Whether this assemblage represents original Proterozoic P/T conditions or a later (Mesozoic) thermotectonic event is unknown (Foster et al., 1992; Hoish et al., 1988). Sillimanite porphyroclasts in ultramylonites are probably relict grains and are not indicative of the conditions associated with mylonitization. Also preserved in regions of low strain are relict textures which record a more complex, multi-stage deformation history, e.g., small scale (<5 m) folded folds or irregular and ptygmatic folds in outcrop, recrystallized quartz veins microscopically, etc. Pre-Miocene, amphibolite facies fabrics are preserved in the northwest Sacramento Mountains (Argent, 1996) and in the central Sacramento Mountains (Schweitzer, 1991).

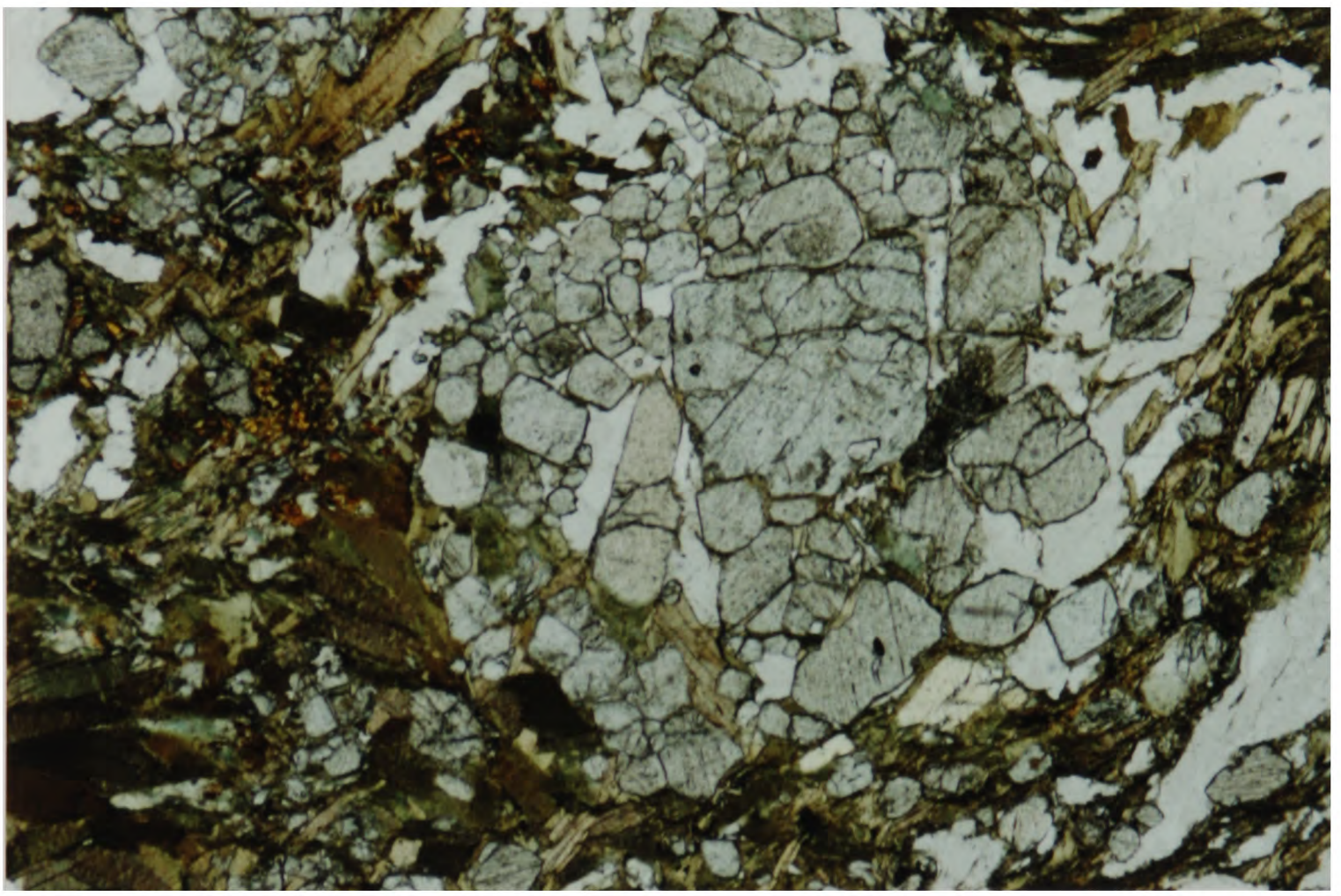


Figure 3.24 - Relict high-temperature sillimanite associated with D1. Precambrian sillimanite, garnet schist, field of view 3.5 mm (Loc. 217, VP95-244).

3.5 Structural evolution

Stress regime during D3 - The configuration of the stress field associated with deformational events can be reconstructed from the orientations of deformational structures, inasmuch as the instantaneous strain axes approximate the principal stress axes. In the northeast Sacramento Mountains, D3 includes the

apparently *synchronous* development of both strike-slip and near-vertical faulting. These structural features could not have resulted from the same stress regime.

According to Anderson (1951), the orthogonal principal stress axes (σ_1, σ_2, and σ_3, where σ_1 is the maximum principal stress and σ_3 is the least principal stress) for normal faulting are oriented such that σ_1 is vertical and both σ_2 and σ_3 are horizontal. Normal faults should dip ~60° and dykes will intrude perpendicular to the least principal stress, σ_3 (Fig. 3.25). During strike-slip faulting, the maximum and minimum principal stress axes should lie in the horizontal plane and the faults will be vertical (Fig. 3.25).

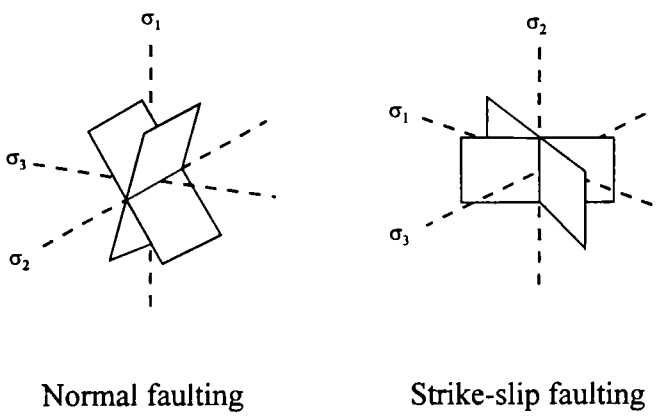


Figure 3.25 - Orientation of principal stress axes for normal and strike-slip faulting (after Anderson, 1951).

Strike-slip faulting is also possible in an extending environment with a nearly uniaxial stress configuration, if the fault zone is *inclined* to the principal stress axes (Fletcher and Bartley, 1994; Yin, 1991). McGarr (1988) proposed that a hydrostatic state of stress ($\sigma_1 = \sigma_2 = \sigma_3$ = lithostatic load) is the most stable configuration in the crust. According to Anderson (1951), normal faulting will occur if one of the horizontal compressive stress axes is reduced, i.e.- σ_3 In this case, the resulting stress field is nearly unaxial ($\sigma_3 < \sigma_2 \approx \sigma_1$), with σ_1 and σ_2 equal to the lithostatic load. Nearly uniaxial stresses are commonly inferred from fault-slip and earthquake focal mechanism data in many extensional terranes throughout the Basin and Range (Zoback, 1989). This is consistent with the need to develop shear stress in order to generate displacement. The normal stress acting on a horizontal layer lying in the plane of σ_2 and σ_3, is σ_1 and deformation resulting from compression along σ_2 can not occur (Fig. 3.26). If the horizontal layer

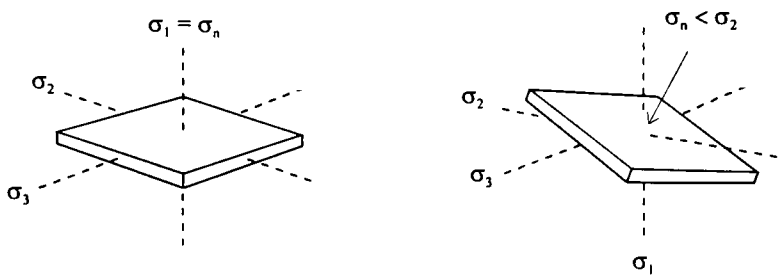


Figure 3.26 Strike-slip faulting in a nearly uniaxial stress regime (after Fletcher and Bartley, 1994). Normal stress on layer parallel to the σ_2/σ_3 plane is equal to σ_1 and compression in response to σ_2 is impossible. Normal stress on an *inclined* layer, or shear zone, is less than σ_1 (or σ_2) and compression in response to σ_2 may be possible.

is *inclined* to the stress field, however, the resolved normal stress across this layer (or shear zone) will be less than σ_1 (and σ_2), therefore strike-slip faults perpendicular to the extension direction may be possible in such a fault zone and in any inclined layering in the extending region. Of course, other compressional features might also be expected to form as a result of subhorizontal crustal shortening along σ_2 of an inclined layer or shear zone, such as L-tectonites and buckle folds with axes parallel to the extension direction, as well as conjugate strike-slip faults (Fletcher and Bartley, 1994). Even when the formation of movement-parallel folds is mechanically unfavourable (due to the orientation of the inclined layering), it will be possible to generate strike-slip faults in a nearly uniaxial stress field because the stress difference which drives strike-slip faulting ($\sigma_2 - \sigma_3$) is identical to the stress difference that drives normal faulting ($\sigma_1 - \sigma_3$).

The vertical, NW and NE strike-slip fault motions associated with D3 indicate E-W extension with a component of horizontal, N-S directed shortening. Shortening perpendicular to the extension direction in the footwall of detachment faults is well documented (Fletcher et al., 1995; Fletcher and Bartley, 1994; Yin and Dunn, 1992; Reynolds and Lister, 1990). In some core complexes, the youngest syntectonic sediments are also folded, suggesting that shortening perpendicular to the extension direction may have outlasted displacement across the fault zone, e.g., Duebendorfer and Simpson (1994), Yin and Dunn (1992).

The near vertical orientations of normal faults associated with D3 suggest that $\sigma_1 > \sigma_2 \approx \sigma 3$. The orientation of these structures are difficult to explain. They are not *true* normal faults in the sense that they have not accommodated *crustal extension*, but appear to be accommodating vertical uplift during lateral confinement.

Strike-slip and dip-slip faulting were apparently *contemporaneous* in the northeast Sacramento Mountains (this work) and in the central Sacramento Mountains (Schweitzer, 1991), but could not have formed in the same stress regime. If the region was subject to a three dimensional strain then stress could be partitioned in space, or oscillate in time, in such a way as to produce the observed strain. A three dimensional strain, for example, is seen in Tibet today, e.g., Burchfiel et al. (1992) and Molnar and Lyon-Caen (1989).

In a regime dominated by E-W horizontal extension, the dominant stress in the northeast Sacramento Mountains alternated between σ_1 and σ_3, i.e.- between $\sigma_3 < \sigma_2 \approx \sigma_1$ and $\sigma_1 > \sigma_2 \approx \sigma_3$. Assuming an initial condition similar to that shown in Fig. 3.26, σ_1 and σ_2 would have been roughly equal in magnitude prior to D3. Variations in vertical stress could arise from differential tectonic unroofing between the extending terrane and its lateral margin (Spencer, 1984, 1982), or from buoyant forces associated with an uncompensated undulatory crustal root or magmatic inflation (Yin, 1991). Magmatic inflation and motion along the detachment fault have the effect of decreasing the vertical compressive stress. The combined effects of syntectonic plutonism and episodic tectonic denudation in the northeast Sacramento Mountains suggests that a heterogeneous vertical stress would have developed. When the vertical stress is reduced, horizontal compression perpendicular to σ_3 is facilitated; as the denuded footwall is isostatically compensated, or as plutons solidify, the vertical stress is restored and vertical compression dominates. This alternation of the dominant stress is then directly related to the episodic nature of magmatic intrusion and detachment faulting in space and time. Both Spencer (1985) and John (1987) have argued for rapidly changing states of stress in the Homer Mountains to the west and in the Chemehuevi Mountains to the south (respectively) in order to explain the simultaneous intrusion of vertical and horizontal dykes.

Stress regime during D2 - Inasmuch as the stretching lineation in the footwall, the tectonic transport direction of the hanging wall, and striae on the SMDF surface are co-linear, the footwall rocks of the

northeast Sacramento Mountains record non-coaxial ductile shear (D2) that is kinematically related to brittle extension above the SMDF. Though such similarities do not in themselves *prove* a genetic relationship between brittle and ductile deformation (e.g., John and Mukasa, 1990), thermochronologic data from the EWIC (Chapter 5) link these two processes in the Sacramento Mountains and confirm that they are Miocene in age. The instantaneous stretching axis (hence σ_3) must have been oriented NE-SW, i.e. towards 060°, during it's formation. Whether or not σ_3 was horizontal, however, is unconstrained.

It is assumed here that low-angle faulting occurs in the northeast Sacramento Mountains (Chapter 6) and elsewhere, e.g., Axen (1993), Dokka (1993), Scott and Lister (1992),Yin and Dunn (1992). The *mechanics* associated with the development of low-angle faults, however, is enigmatic. Andersonian fault theory assumes that one principal stress is vertical and that the other two principal stresses are horizontal. If the maximum principal stress (σ_1) is vertical in an extending environment, then moderately dipping normal faults are predicted. It is possible for normal faults to form at low-angles, however, if the greatest principal stress is not vertical. For example, if σ_1 is rotated 45°, normal faults will form dipping 0-25° Consequently, rotation of the stress field is favoured as a mechanism for the generation of low-angle faults.

Rotation of the stress field has been variously attributed to crustal flexure (Spencer and Chase, 1989), stress refraction across lithologies of differing viscosities (Bradshaw and Zoback, 1988), stress/material property heterogeneities within the lithosphere (Forsyth, 1992), detachment below the brittle-ductile transition (Davis and Lister, 1988), viscous flow of deep crust against the seismogenic layer (Melosh, 1990), high fluid pressure (Axen, 1992; Davis and Lister, 1988), and igneous dilation at depth (Parsons and Thompson, 1993). Of these mechanisms, material property heterogeneities within the lithosphere exist (Insert 1) and igneous dilation (magmatism) occurred in the northeast Sacramento Mountains (Chapter 5). Other mechanisms may have occurred, but these cannot be assessed directly. The effect of syntectonic plutonism is to locally elevate deviatoric stress around the margins of magma body. Furthermore, an increase in fluid pressure associated with magmatism decreases frictional resistance, as well as the effective normal stress (Axen, 1992). The effect of magmatism, with or without tectonic denudation, could have produced an inhomogeneous stress regime/rotated the stress field, leading to the development of detachment faulting in the northeast Sacramento Mountains.

A regional gravity and magnetic high occurs along the axis of the extensional corridor (Mickus and James, 1991; Simpson et al., 1990). The presence of Miocene intrusive rocks and their spatial correlation with the gravity peaks suggests that the two are related, but the documented surface exposure of these rocks is insufficient to account for the anomaly (Mickus and James, 1991; Simpson et al., 1990). Thus, the source of the anomaly has been attributed to the presence of concealed dense, mafic material (Campbell and John, 1996; Simpson et al., 1990). As a regional analogue to the northeast Sacramento Mountains, the concealed mafic root of the magnetic anomaly could represent rotation of the stress field due to mafic magmatism on a regional scale, resulting in detachment faulting across the entire extensional corridor during the Miocene.

3.6 Synthesis

Evolution of the footwall The broad, antiformal arch of detachment faults in nearly all core complexes consists of a limb which dips in the same direction as the active shear zone and one tilted through horizontal showing a dip opposed to the direction of upper-plate transport. Following Reynolds and Lister (1990), these are referred to as the fore- and back-dipping limbs, respectively. It is clear that a "dome" *sensu stricto*, e.g., Lister and Davis (1989), is not defined in the northeast Sacramento Mountains (see Fig. 1.1 and Insert 1). Though a very small portion of the SMDF and the mylonitic foliation associated with D2 dip away from the range along the west and northwest fault contact, across most of the study area D2 defines a relatively planar fabric which dips ~30° SW on the west side of the range and shallows to ~20° SW across the centre and east side of the range. Foliation and lineation data of all rock types across the range are parallel to subparallel and have a consistent top-to-NE shear sense. Relative strain increases to the east and affects all lithologies. Transport-parallel folds are not present, though there is a single, small scale (3 m wide, 5 m long, 4 m high) mullion with it's long axis parallel to the tectonic transport direction (near Loc. 257). This ductile deformation is overprinted by strike-slip faults and vertical dip-slip faults. Low-angle faults, which cut D2, are also present and were active entirely in the brittle regime. Various models related to core complex development can be assessed within the framework of these observations.

The steepening of the mylonitic fabric to the west may represent the "back-dipping limb" of a transport-perpendicular fold. The hypothetical northeast-dipping limb is no longer present. Given the dip variation over the exposed area of the limb (10°/8 km), and assuming a *symmetric* structure, this transport-perpendicular fold would have had a wavelength of ~50 km and an amplitude of ~2.5 km (Fig. 3.27).

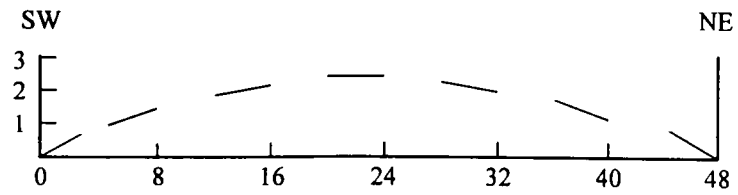


Figure 3.27 - Foliation trajectory for a symmetric, extension-perpendicular fold (fold axis into the page). The projection assumes a 10°/8 km change in dip, derived from observed data in the northeast Sacramento Mountains, i.e. - 30° SW to 20° SW over ~8 km. (Axes units in kilometers.)

Known transport-perpendicular structures have wavelengths of 10-50 km and amplitudes of ~1 km (Spencer, 1982). Such folds are typically *asymmetric*, however, and the foliation trajectory technique used, therefore, overestimates the dimensions of the "dome". If an asymmetric trajectory were used, the final dimensions are likely to be more consistent with the scale of existing transport-perpendicular structures.

If a dome existed in the northeast Sacramento Mountains, then the fore-dipping limb has been tectonically removed. Down-to-the-east faulting is common on the east side of the range (Section 3.2). Immediately adjacent to exposures of basement gneiss (Loc. 381), *Qoa* is 100 m deep, suggesting the presence of an unexposed, steep, down-to-the-east, range-bounding fault on the east side of the northeast Sacramento Mountains. In order to account for the missing vertical section of ≤ 1 km (rough estimate, assuming that an asymmetric dome will not reach the elevation projected in Fig. 3.27), displacement on such a fault would be an *order of magnitude* greater than any observed offset in the study area and therefore seems unlikely.

Alternatively, in the central Sacramento Mountains Schweitzer (1991) noted steepening of the relatively planar mylonitic fabric to the west and attributed it to rigid-body rotation by multiple, NW-trending, east-dipping normal faults. There is little evidence to support such an interpretation for the northeast Sacramento Mountains. For example, the majority of faults in the northeast Sacramento Mountains are oriented N-S or NE-SW and would not be able to accommodate top-to-the-southwest rotations. Also, such rotations do not account for the greater transposition of fabrics associated with D1.

A better explanation for the variation in orientation of fabric associated with D2 may be that it represents a primary feature associated with the detachment shear zone. The progressive increase in the non-coaxial ductile deformation from west to east is consistent with the tectonic denudation (Chapter 5). The SMDF system was inactive on the west side of the northeast Sacramento Mountains by ~14.5 Ma (the time of emplacement for the Eagle Peak rhyolite and the Flattop Mountain andesite), but probably continued to be active to the east as indicated by the younging of ages in that direction (Chapter 5). This would also account for the greater transposition of fabric associated with D1 to east: The east side of the range would have experienced greater cumulative deformation. Detachment faults in the extensional corridor, however, are thought to have originally dipped gently to the NE or E. Consequently, a mechanism to explain the back-dipping configuration across the range is still needed.

Reynolds and Lister (1990) proposed various models to explain the formation of back-dipping mylonite zones, two of which may be relevant to the northeast Sacramento Mountains (Fig. 3.28). In a simple shear zone, finite strain decreases towards the shear zone boundary. As in figure 3.28a, this decrease in finite strain towards the bottom of the shear zone is reflected by variation of the foliation orientation. In

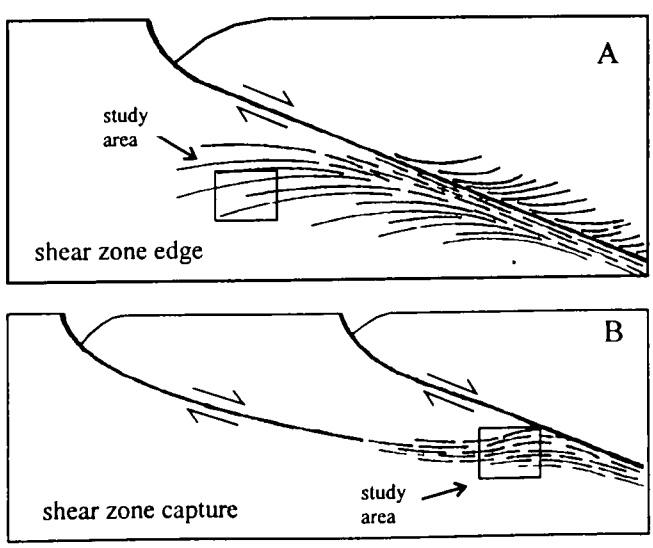


Figure 3.28 Back-dipping mylonite formation (after Reynolds and Lister, 1990). In A, the foliation steepens towards the shear zone margin due to a decrease in finite strain. In B, the foliation is rotated due to motion on the capturing detachment fault.

this case, the intensity of fabric development should decrease away from the shear zone (both upward and downward), and this variation should accompany the change in foliation orientation. Furthermore, C-surfaces associated with S-C fabrics should remain constant, i.e.- parallel to the shear zone, regardless of foliation variations. In the study area, S-C fabrics parallel the foliation, though the 10° variation in foliation orientation and the increase in strain to the east are consistent with the northeast Sacramento Mountains representing the edge of a simple shear zone.

Alternatively, this back-dipping mylonite zone may represent the "capture" of a *relatively* older fabric associated with an earlier splay of the same detachment fault system (Fig. 3.28b). In this case, the older fault and associated mylonites are intersected by a younger fault splay. The "older" mylonites are rotated from their original, gently northeast-dipping orientations by their upward transport in the footwall of the younger fault. In this model a consistent sense of shear will be associated with multiple splays of a single detachment system. A regional variation in relative strain, however, is not expected, though Lister and Davis (1989) suggest that deformation is likely to be more penetrative with depth. Furthermore, the "capture" scenario could account for the missing fore-dipping limb: As the detachment fault system in the northeast Sacramento Mountains continued to evolve, the fore-dipping limb could have been transported in the hanging wall of an even younger fault splay.

As illustrated in figure 3.29, such an evolution for the back-dipping myonites in the northeast Sacramento Mountains requires at least three episodes of major faulting. Initially, D2 would have formed in a horizontal or gently northeast-dipping orientation. It then had to be "captured" and rotated by an unseen splay. Whether this occurred prior to, or after, D2 fabrics were truncated by the currently flat-lying, low-angle fault(s) associated with D3 is unconstrained, but because these flat-lying faults were active in an entirely brittle regime, it seems likely that the "capture" of D2 occurred prior to flat-lying normal faulting. This would be consistent with the presence of an older, underlying fault. Nevertheless, *at least* three episodes of low-angle faulting occurred in the region: 1 = formation of D2, 2 = rotation of D2, 3 = truncation of D2 by currently flat-lying normal faults, and 4 = removal of the fore-dipping limb (?). This evolution for the footwall structure is consistent with three generations of detachment faults recognised in the Tertiary volcanic and sedimentary hanging wall rocks in the Sacramento Mountains (McClelland, 1984; Spencer and Turner, 1983).

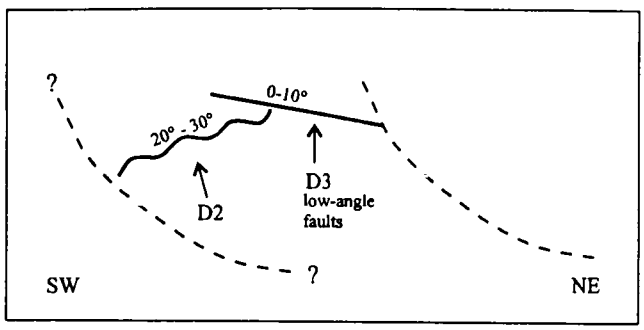


Figure 3.29 - Schematic representation of at least three generations of detachment faults in the footwall of the northeast Sacramento Mountains.

Correlations between footwalls - A series of deformational events recording decreasing temperature and a corresponding change from ductile through brittle behaviour in footwall rocks has been recognised in the northeast Sacramento Mountains. Similar series have also been recognised in the footwalls of the northwest Sacramento Mountains (Argent, 1996) and the central Sacramento Mountains (Schweitzer, 1991). Correlations between the internal deformation of the footwalls in the Sacramento Mountains can be made on the basis of timing, metamorphic grade, and fabric orientation (Table 3.2).

Deformational events common to the central, northeast, and northwest Sacramento Mountains include an older amphibolite facies deformation, Miocene upper- to lower-greenschist facies deformation related to detachment faulting, Miocene lower-greenschist facies deformation related to the exhumation of these footwall rocks, and post-detachment strike-slip deformation. Pre-Miocene deformational events are best preserved in the northwest Sacramento Mountains, where these rocks have not been thermally overprinted by syntectonic Miocene plutonism (Pease et al., 1995; Chapter 5). Two distinct fabrics of differing metamorphic grade, orientation, and age have been identified in the northwest Sacramento Mountains (D1 and D2 of Argent in Table 3.2). The younger of these is associated with Late Cretaceous granitic plutons (Pease et al., 1995; Chapter 5) and the older is constrained to be pre-Late Cretaceous in age as it is cut by the Late Cretaceous plutons. Both fabrics show pronounced strain recovery textures such as polygonization. Such fabrics are only cryptically preserved in the central and northeast Sacramento

Table 3.2 - Correlation of deformational events in the Sacramento Mountains.

Schweitzer (1991)	Pease, this study	Argent (1996)
Miocene (~24-14 Ma) brittle shear zones, middle- to lower-greenschist facies cataclasis and hydrothermal mineralization.	~15-14 Ma brittle shear zones, middle- to lower greenschist facies cataclasis and hydrothermal mineralization.	Post-14 Ma brittle shear zones with strike-slip faulting.
D3 • top to NE detachment faulting and cataclasis • brittle fracturing • chloritic breccia formation • NE sinistral strike-slip faulting • NNW and NE trending faults with dip-slip and oblique-slip motion	**D3** • brittle fracturing • hydrothermal mineralization • NW to NE, dextral and sinistral strike-slip, oblique-slip, and dip-slip, vertical faulting	• E-W sinistral strike-slip faults **D4**
Tertiary (?) greenschist facies mylonitic deformation.	~20-15 Ma, transitional upper- through middle-greenschist facies mylonitic deformation.	~24-14 Ma, transitional ductile through brittle extensional shear zones, lower greenschist facies.
• SW dipping foliation • SW lineation, plunging 20° **D2** • dynamic recrystallization of quartz • top-to NE shear • cataclastic deformation of feldspar • no strain recovery	• SW dipping foliation **D2** • SW lineation, plunging 20° • NNE-SSW dyke intrusion • a continuim in feldspar of ductile through brittle deformation • dynamic recrystallization of quartz • no strain recovery • top-to NE shear	**D3** • top to NE detachment faulting and cataclasis • brittle fracturing • E-W dyke intrusion • SW dipping foliation • SW lineation, plunging 30° • no strain recovery
Pre-Tertiary amphibolite facies deformation.	Pre-Tertiary amphibolite facies deformation.	Late Cretaceous (~72 Ma) greenschist facies mylonitic deformation.
• SW dipping foliation **D1** • SW lineation, dipping 20° • strain free quartz and feldspar ribbons. • rare refolded folds	• SW dipping foliation **D1** • SW lineation, dipping 20° • strain free quartz and feldspar ribbons. • rare refolded folds	**D2** • NW dipping foliation • NE lineation, dipping 30° • minor asymmetric similar folds • granitic intrusion
		Cretaceous or earlier (Pre- 72 Ma) amphibolite facies gneissic foliation (locally mylonitic). **D1** • NW dipping foliation • N-S horizontal lineation • rare isoclinal folds • boudinage • granodioritic gneiss intrusion

Mountains, where they have been rotated into parallelism with a younger, overprinting mylonitic deformation (D2 of both Schweitzer and Pease in Table 3.2).

D2 is well-correlated in the central and northeast Sacramento Mountains, though it seems that D2 in the northeast Sacramento Mountains occurred at slightly higher temperatures (upper- to mid-greenschist facies, producing low-temperature plasticity in feldspar). Lacking absolute geochronology, Schweitzer (1991) suggested that D2 in the central Sacramento Mountains could be Tertiary in age based on preliminary $^{40}Ar/^{39}Ar$ data from Foster et al. (1990). A Miocene age for this deformational event has been well-substantiated using SHRIMP ion probe, conventional U/Pb, and $^{40}Ar/^{39}Ar$ techniques (Chapter 5). The preservation of magma mixing and mingling textures in domains of low strain suggest that EWIC lithologies were intruded and then subjected to sub-solidus deformation. This deformation, however, occurred prior to the exhumation of the footwall, at temperatures between ~450°C (low-temperature plasticity in feldspar) and ~600°C (brittle deformation of hornblende).

It is worth noting that the strongest textural evidence for the syntectonic emplacement of plutons is the preservation of a continuous transition from submagmatic to high-temperature solid-state deformation (Patterson et al., 1990). Many plutons emplaced during regional deformation do not, however, preserve such evidence because of the transitory nature of the submagmatic state and the obscuring effects of post-emplacement deformation (Miller and Paterson, 1994). Miller and Paterson (1994) suggest that syntectonic fabrics are most likely preserved in plutons cooled at slow to moderate rates, deformed at high strain rates during emplacement, or intruded during the waning stages of regional deformation. The EWIC was intruded relatively early during the regional deformation and then cooled rapidly (Chapter 5), circumstances not conducive to the preservation of syntectonic fabrics.

In the northwest Sacramento Mountains, the correlative deformation event (D3 of Argent in Table 3.2) was spatially restricted to dykes intruded into the deepest portion of a relatively cool (~400°C) footwall (Chapter 5). The thermal regime associated with Miocene mylonitic deformation in this region allowed only the formation of discrete ductile through to brittle shear zones (Argent, 1996) and pervasive mylonites are not present. The orientation of foliation and lineation data of ductilely deformed dykes in the northwest Sacramento Mountains is not consistent with D2 in the central and northeast Sacramento Mountains.

Furthermore, dyke orientations in the northwest are E-W, suggesting an instantaneous stretching axis oriented N-S (Argent, 1996).

There is an apparent dichotomy in the Sacramento Mountains associated with the orientation of the stress regime during D2 deformation. In the northwest Sacramento Mountains (as well as in the Homer Mountains and in the southern Piute Range to the northwest; Spencer, 1985) extension was directed N-S, but in the central and northeast Sacramento Mountains (and in the Dead Mountains to the north; Spencer, 1985) extension occurred in a NE-SE to E-W direction. Spencer (1985) has argued that the E-W extension and uplift associated with the Newberry, Dead, and northeast/central Sacramento Mountains in the Miocene resulted in the synformal warping of an "upper plate" domain (which included the northwest Sacramento Mountains) to the west (Fig. 3.30). He regarded the lower plate basement rocks of the northwest Sacramento Mountains as structurally anomalous because they occurred in his region of "synformal upper plate". The thermochronologic data presented in Chapter 5 suggests that the northwest Sacramento Mountains is a tilted crustal block (top-to-the-southwest), which was rotated ≥20° prior to the intrusion of

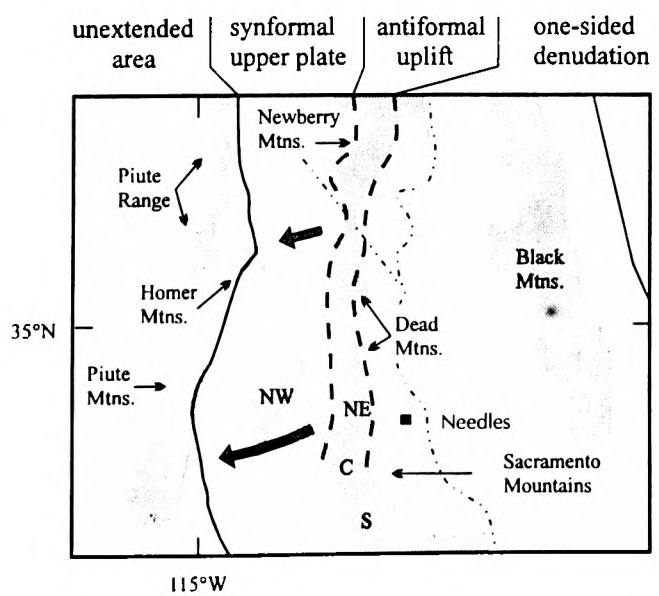


Figure 3.30 - Structural domains in the Sacramento Mountains region (modified from Spencer, 1985). The Sacramento Mountains divide into the northwest (NW), northeast (NE), central (C), and southern (S) regions. The *antiformal uplift* domain coincides with the axial core of the extensional corridor. Differential rates/directions of extension (indicated by the large arrows) could result in a dextral transtensive regime. Solid lines define the limit of the extensional corridor.

the regional dyke swarm. Thus, basement rocks of the northwest Sacramento Mountains do, in fact, represent an "upper plate" segment of crust and Spencer's (1985) structural domains are internally consistent.

According to Spencer (1985), the domain of synformal flexure was under E-W compression due to the uplift of the axial high to the east. Dykes oriented E-W were intruded when the N-S stress (σ_{NS}) was less than both the vertical stress (σ_V) and E-W directed stress (σ_{EW}). Argent (1996) argued that the E-W dykes were intruded under conditions of dextral transtension, in order to explain the discordance in orientation between the regional tectonic transport direction (N060E) and the instantaneous stretching axis (recorded by N-S stretching lineations). Argent (1996) invoked the "no slab window" of Dokka and Ross (1995) as the driving mechanism for this regime of dextral transtension. There is no evidence for dextral transtension, however, in the adjacent axial high to the east, i.e.- the central and northeast Sacramento Mountains, Dead Mountains, and Newberry Mountains (this study; Schweitzer, 1991; Spencer, 1985). Consequently, another driving mechanism (or combination of mechanisms) is necessary to adequately explain the structural evolution of the region.

Spencer (1985) suggested that differential rates of (or directions in) extension within the corridor could result in secondary components of convergence or divergence to the regional extension direction. Alternatively, if extension were diachronous, rotations of unextended regions would occur in which arcuate vectors describing the extensional and rotational movement would also produce secondary convergence or divergence. Such a mechanism would also allow for regimes of dextral or sinistral transtension, depending of the direction and relative rates of movement. For example, if extension south of the Sacramento Mountains were more rapid than north of the Sacramento Mountains, then deformation in the Sacramento Mountains area could have had a component of dextral, oblique extension (Fig. 3.30). Furthermore, this would be consistent with the slower slip-rate determined for the Sacramento Mountains detachment fault (Chapter 6), relative to detachment faults to the south.

Spencer (1985) also argued that the E-W directed extension along this axial high (in the Newberry, Dead, and northeast Sacramento Mountains) was due to the development of single-sided denudation. One-sided denudation in the northeast Sacramento Mountains is supported by the thermochronologic data

(Chapter 5), which suggests that detachment faulting continued in the east after it had ceased in the west. Recent radiometric ages (Howard et al., 1996) suggest that this axial high would also have been facilitated by syntectonic magmatism.

Thus the dichotomy between the direction of extension in the northwest and northeast Sacramento Mountains is one of primarily structural level. The "upper plate domain", which includes the northwest Sacramento Mountains, was subject to secondary dextral shear probably due to increased rates of extension to the south. The "uplift" domain, including the northeast Sacramento Mountains, reflects laterally unconfined (one-sided) northeast directed extension, combined with plutonic intrusion.

Younger, entirely brittle structures are recognised both in the central and northeast Sacramento Mountains (D3 of both Schweitzer and Pease in Table 3.2). The metamorphic grade and type of faulting associated with D3 (Schweitzer and Pease in Table 3.2) correlates well, though it appears to be slightly younger in the northeast Sacramento Mountains. This would be consistent with relatively higher temperatures in this region, as suggested by low-temperature plasticity of feldspar associated with D3 (this study). Later fabrics in the northwest Sacramento Mountains consist entirely of brittle antithethic shear zones (some D3 structures of Argent in Table 3.2). The orientation of these structures are consistent with hanging wall displacement to the NE (as in the central and northeast Sacramento Mountains), however antithetic structures appear to be absent in the latter regions. Moreover, post-14 Ma, E-W sinistral strike-slip faults are found only in the northwest Sacramento Mountains.

Summary In the northeast Sacramento Mountains, the EWIC intruded into already deformed basement at ~20 Ma. The EWIC's dominant mylonitic fabric was acquired sub-solidus ~18 million years ago, at a temperature of ~500°C. The variation in orientation of this fabric across the range is likely to be a primary feature associated with a detachment shear zone. Its back-dipping configuration is consistent with its "capture" by a younger splay of the SMDF system at a later time. Younger, entirely brittle, low-angle faulting indicates that detachment faulting continued during the uplift of the range into the brittle regime. The missing fore-dipping limb would have been transported to the east in the hanging wall of a younger splay of the SMDF system, which is more consistent with the existing geometry and timing of detachment faulting in the region than by its removal due to steep, down-to-the-east normal faulting.

During uplift and cooling of the northeast Sacramento Mountains, the dominant compressive stress varied from vertical to N-S horizontal. This variation was likely due to tectonic denudation, combined with ongoing magmatic intrusion. Exhumation and cooling of the range was complete by ~ 15 Ma on the west side and by ~14 Ma on the east side. This diachroneity is consistent with detachment faulting continuing to the east. This series of deformational events, recording decreasing temperature and a corresponding change from ductile through brittle behaviour in footwall rocks, are recognised in the northwest Sacramento Mountains (Argent, 1996) and the central Sacramento Mountains (Schweitzer, 1991), and can be correlated on the basis of timing, metamorphic grade, and fabric orientation.

Chapter 4

Geochemistry of the Eagle Wash Intrusive Complex

4.1 Introduction

Magmatic intrusion is assumed to have an important role in continental extensional processes, though the causal relationships between extension and magmatism remain poorly understood. In the Colorado River extensional corridor, magmatism and extreme extension were approximately coincident in time and space. Volcanism, extensional faulting, and doming were concentrated temporally between ~14-23 Ma (Spencer et al., 1995; Armstrong and Ward, 1991; Gans et al., 1989; Davis, 1988). Though the presence of voluminous unexposed mafic roots is suggested by long (150-200 km), northwest trending gravity and magnetic highs (Simpson et al., 1990), Miocene plutons have only recently been recognised within the extensional corridor (Howard et al., 1996; Foster et al, 1996). This has generally been due to a lack of age data, though the recognition of syntectonic plutonism appears to have been hindered by their misidentification as gneisses, resulting from the development of strong mylonitic fabrics.

Previous geochemical work in the extensional corridor focused predominantly on Tertiary extrusive rocks and on Mesozoic plutonic suites. Throughout the Basin and Range province, when studied in detail, intrusive bodies and thick lava accumulations are coincident in time and are essentially coextensive

(Armstrong and Ward, 1991). Given the importance of magmatism to Tertiary extensional models, e.g. Parsons and Thompson (1993), Lister and Baldwin (1993), Miocene plutons have as yet received minimal attention. The Eagle Wash intrusive complex (EWIC) in the northeast and central Sacramento Mountains is one of a few recognised examples within the extensional corridor of syntectonic plutonism. Other examples occur in the southern Sacramento Mountains (Foster et al, 1996), the Whipple Mountains (Davis, 1988), and the Dead and Newberry Mountains (Howard et al., 1996). The EWIC provides an opportunity to evaluate the petrogenetic and magmatic processes associated with syntectonic plutonism in the extensional corridor and to place some constraints on models related to Tertiary extension.

Samples collected for major and trace element, and isotopic, analysis are summarised in Table 4.1. They are predominantly from the EWIC (~75%) and represent the compositional range of the suite, i.e. leucogranite (*Tlg*), granodiorite (*Tgd*), and diorite (*Td*). Samples from the "banded" unit represent the upper contact of the intrusion (c.f. Chapter 2, Section 2.3) and are also considered part of the EWIC suite. The remaining samples from the NE Sacramento Mountains are cross-cutting, mafic dykes (*Tu*); it is assumed that these mafic dykes record a lesser degree of crustal contamination and were collected in order to provide a geochemical reference of "uncontaminated" mafic melt. Samples of known Cretaceous granites and Precambrian gneisses and schists are mostly from the NW Sacramento Mountains; these samples were also collected in order to provide geochemical reference signatures.

Table 4.1 - Summary of geochemical samples

Precambrian & Cretaceous rocks	Banded unit	EWIC*			Mafic dykes
		Td	Tgd	Tlg	
VP94-129§	VP95-237§	VP94-020c§	VP94-002	VP94-060b	VP95-163§
VP94-130b§	VP95-238	VP94-057b	VP94-016b	VP94-069b	VP95-164§
VP94-138	VP95-239	VP94-123a	VP94-020a	VP94-133	VP95-165§
VP94-139b	VP95-240	VP94-123b§	VP94-020b	VP94-136	VP95-168
VP94-140a§	VP95-246§	VP94-123c§	VP94-119a§	VP95-160§	VP95-170
VP94-140b§	VP95-247§	VP94-124§	VP94-119b§	VP95-214	
VP94-141	VP95-248§	VP94-130a§	VP94-127	VP95-234b	
VP94-142	VP95-253	VP94-135§	VP94-128	VP95-242	
VP94-143	VP95-254	VP95-198	VP94-132	VP95-243	
VP94-144	VP95-255	VP95-256§	VP94-137	VP95-250	
VP94-145			VP94-139a	VP95-252	
VP94-146			VP95-159§	VP95-258§	
			VP95-185		
			VP95-251		
			VP95-249§		

Note: * = lithologic subdivisions are derived from field appearance and mineralogy (c.f. Chapter 2, Section 2.1).
§ = samples used for isotopic analysis; samples from the banded unit represent Tlg and Tgd.

Major and trace element analyses were performed using X-ray fluorescence techniques. Machine specifications, operation conditions, sample preparation, as well as the limits of determination, precision, and accuracy, are presented in Appendix A. The procedure used to calculate CIPW normative mineralogy is also presented in Appendix A, along with all of the XRF analytical results. Isotopic analytical techniques are presented in Appendix D. Sample locations are shown on Inserts 2 and 3. Note that all values for major element abundances in the text and figures which follow are recalculated to 100% (volatile free).

4.2 Variation diagrams

Silica content consistently and significantly correlates with other elements in EWIC samples and consequently is chosen as a convenient abscissa for illustrating variations in major and trace element concentrations. Linear trends from igneous rocks on diagrams of the form A *vs.* B (where A and B represent different elements) are the result of mixing *sensu lato*, whether mixing of two magmas, the addition and/or subtraction of solid phases during contamination or fractional crystallisation, or mixing due to the addition of melt increments during partial melting.

Ratios of incompatible trace elements (with similar bulk partition coefficients) and isotopes are indicative of source compositions because they do not change appreciably during either melting or fractionation. Variations in such ratios reflect heterogeneity of the source, either as a result of magma mixing, crustal contamination/partial melting, or some combination of the two. Allègre and Minster (1978) have shown that within-suite variations of trace element compositions can be used to distinguish between fractional crystallisation, batch partial melting, and magma mixing (*sensu stricto*). Fractional crystallisation is the only differentiation process which causes trace elements to follow Rayleigh distillation patterns, resulting in *exponential* changes in the concentration of elements in residual liquids. Consequently, concentrations determined by fractional crystallisation define straight lines on *log-log* diagrams, whereas concentrations determined by non-exponential processes (batch melting or mixing) lead to curves. Batch melting and mixing processes are best distinguished on log-log plots using a highly incompatible element as the abscissa and a compatible element as the ordinate: Concave-up curves are due to fusion, whereas concave-down curves are due to mixing (Gill, 1981). The data presented here should constrain the petrogenetic process(es) involved in the genesis of the EWIC.

4.3 EWIC element characterisation

Major element geochemistry The major element oxide correlation coefficient matrix for EWIC samples is presented in Table 4.2. The EWIC defines a calc-alkaline plutonic suite (Fig. 4.1), dominantly composed of granodiorite (*Tgd*), with lesser volumes of diorite (*Td*) and leucogranite (*Tlg*). It is extremely variable in composition, with silica ranging in weight percent from ~50 to ~76 and a possible gap between 61-63 wt.%. Field nomenclature is more generalised than classification by strict chemistry due to the *gradational* compositional variation within the EWIC: *Td* incorporates gabbroic and dioritic rocks, and *Tgd* encompasses both granodioritic and granitic rocks (nomenclature of Wilson, 1989). The EWIC is generally metaluminous (Fig. 4.2).

Table 4.2 - EWIC correlation coefficient matrix for major element oxides

	SiO_2	TiO_2	Al_2O_3	FeO	Fe_2O_3	MnO	MgO	CaO	Na_2O	K_2O
TiO_2	-0.97									
Al_2O_3	-0.43	0.35								
FeO	-0.98	0.99	0.30							
Fe_2O_3	-0.96	0.96	0 53	0.94						
MnO	-0.95	0.93	0.24	0.96	0.90					
MgO	-0 91	0.90	0.02	0.95	0.80	0 93				
CaO	-0.97	0.94	0 24	0.97	0.88	0.95	0 96			
Na_2O	0 26	-0.32	0 63	-0.38	-0 15	-0.42	-0 57	-0 41		
K_2O	0.86	-0 82	-0 47	-0.83	-0 81	-0.78	-0.76	-0.86	0.00	
P_2O_5	-0 87	0.92	0 05	0.92	0 81	0.91	0 92	0.90	-0.49	-0.71

Note: Correlation coefficients calculated as product-moments, i e - Pearson-type Standard error (2σ) when N=47, r = 0 9 ⇒ 0 004, r = 0.5 ⇒ 0 016, r = 0.1 ⇒ 0 021 (Marsal, 1987)

Major element oxides show linear, curva-linear, and non-linear trends (Fig. 4.3). The EWIC is typically high in K which, though displaying significant scatter, is positively correlated with silica. Compatible elements (Ti, Fe, Mn, Mg, Ca, and P) show strong negative correlations with silica (though MnO in ~10% of these samples is at the precision limits of the technique c.f. Appendix B). Notable inflections at ~57 wt.% SiO_2 are apparent in Al and Na, with general enrichment of both elements changing to flat or negitive correlations. Such inflections may indicate the entry of a new phase during crystal fractionation or the loss of a phase during partial melting; for example, the crystallisation and removal of Al- and Na-poor minerals could result in the *enrichment* of Al and Na in the melt, and the inflection at ~57 wt.% SiO_2 might reflect the loss of this phase from the crystallising assemblage. Less-evolved EWIC samples (*Td*) are typically hypersthene + diopside + olivine normative. With increasing silica (*Tgd*), quartz replaces olivine in the norm, until quartz + hypersthene + diopside is replaced by quartz + hypersthene. At the

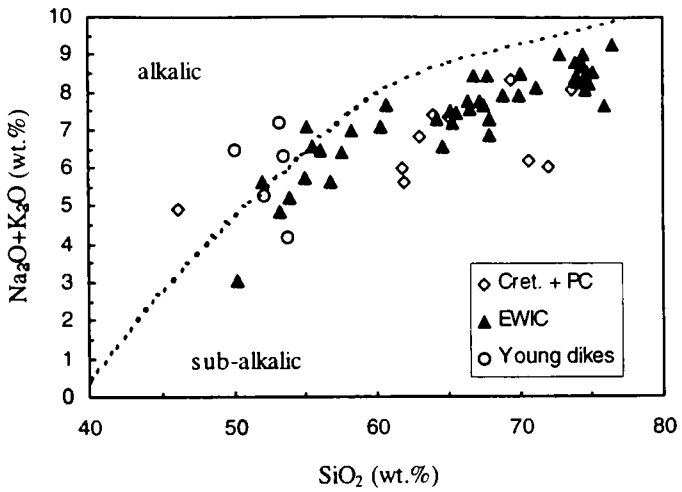


Figure 4.1a - Chemical classification of the EWIC. The complex is sub-alkalic (Irvine and Baragar, 1971) and includes gabbro, diorite/syeno-diorite, granodiorite, and granite to alkali granite (nomenclature of Wilson, 1989).

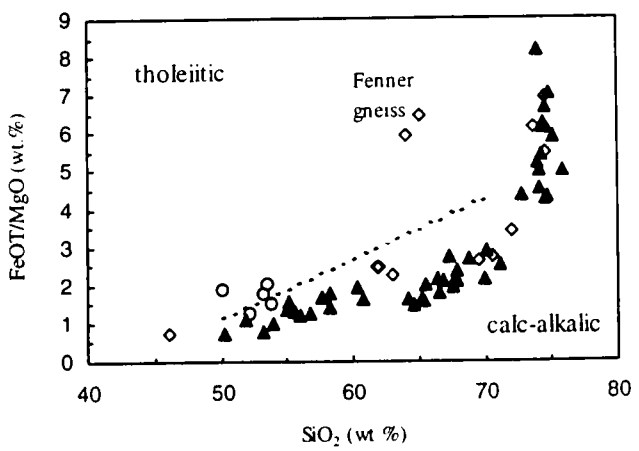


Figure 4.1b - Subdivision of sub-alkalic field into tholeiitic and calc-alkalic fields (Miyashiro, 1974). The EWIC is calc-alkalic, whereas the younger dykes may be transitional to tholeiites (symbols as above).

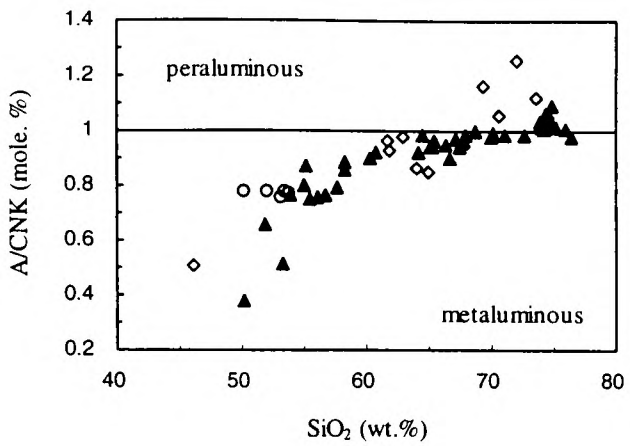


Figure 4.2 - Chemical features associated with the EWIC. SiO_2 vs. molecular percent $Al_2O_3/(CaO + K_2O + Na_2O)$ indicates the complex is compositionally expanded and metaluminous (to weakly peraluminous in the silica-rich end-members). Symbols as in figure 4.1.

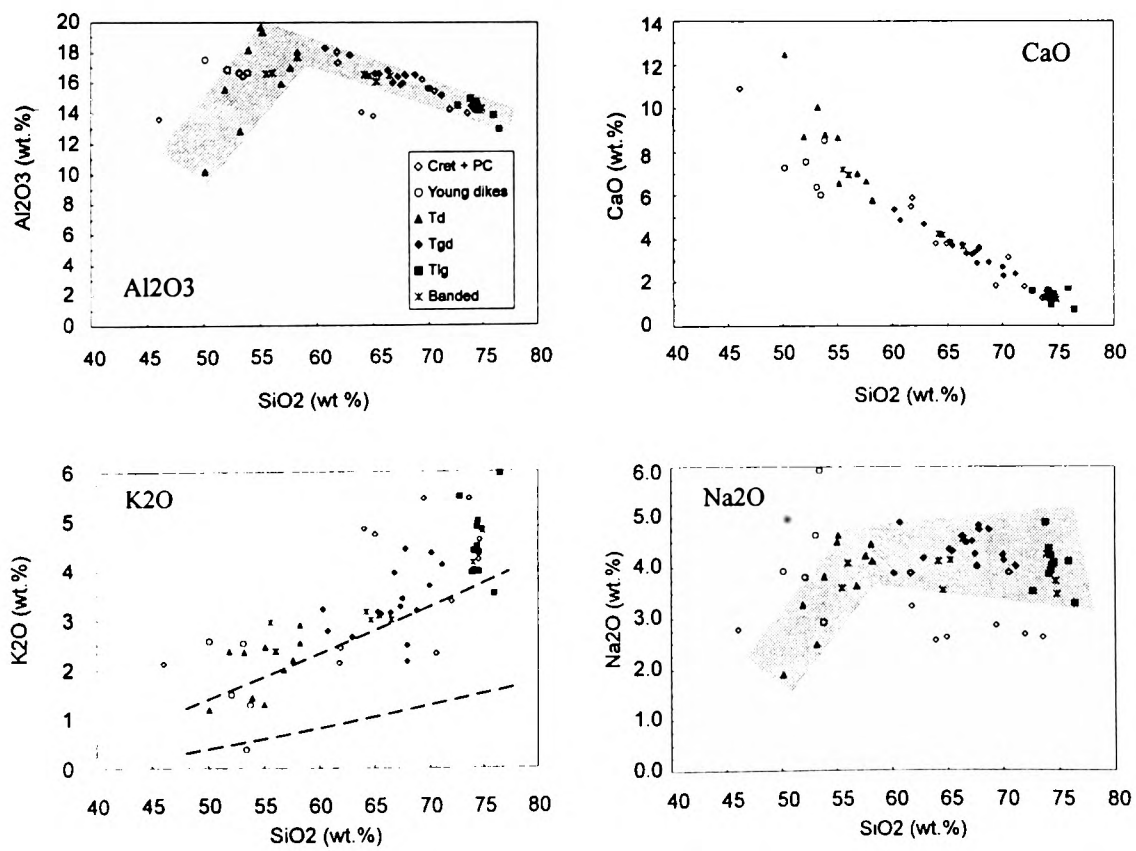


Figure 4.3 Major element bivariate plots. Symbols defined in Al_2O_3 inset. High, medium, and low potassium fields in K_2O plot after LeMaitre et al. (1989). Shading is used to emphasise EWIC trends in Al_2O_3 and Na_20, and older lithologic trends in FeO and MnO.

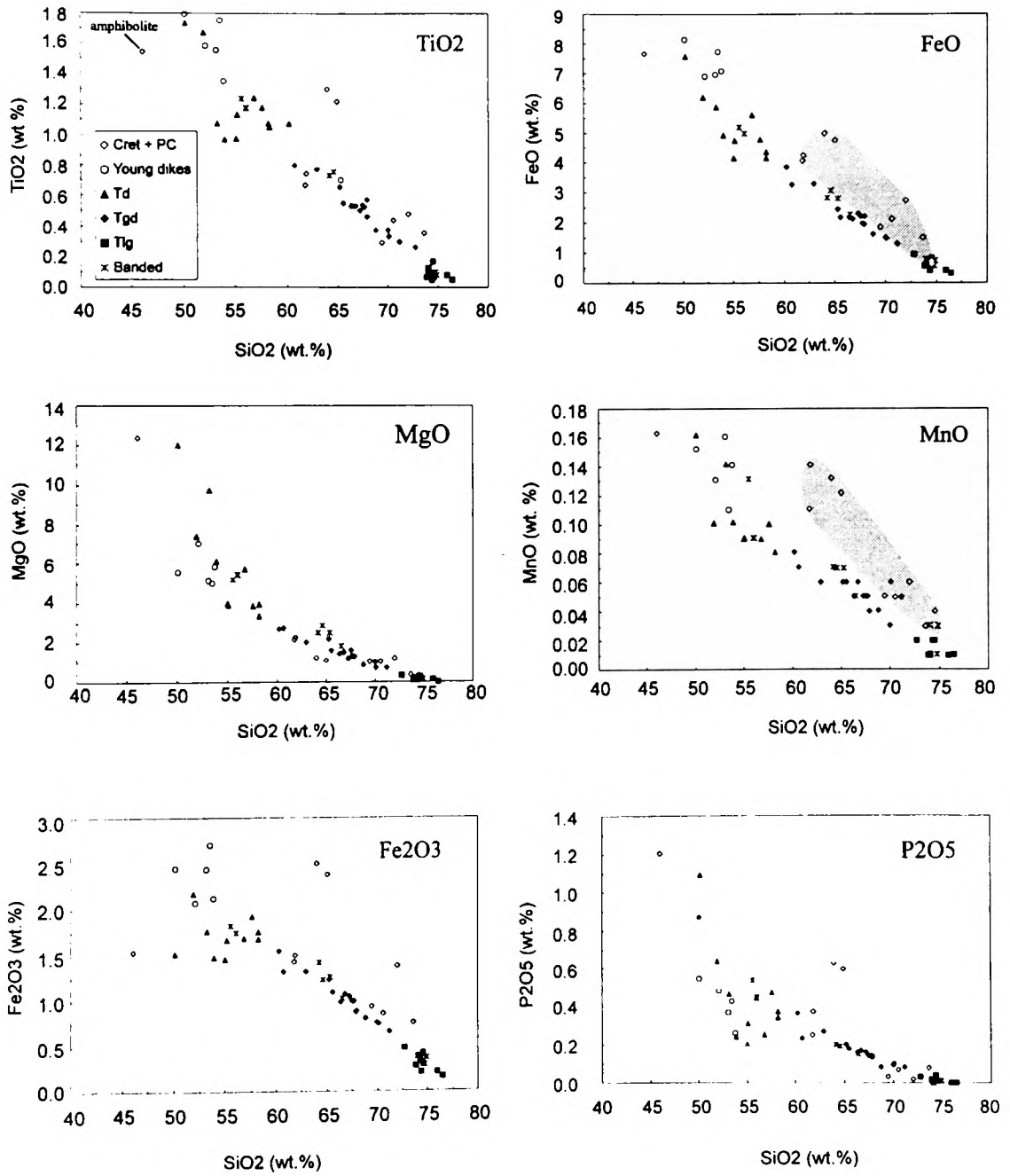


Figure 4.3 con't.

highest silica contents, i.e. - *Tlg*, the samples become corundum normative and slightly peraluminous (Fig. 4.2). It should be noted that neither olivine or pyroxene occur as mineral phases in the EWIC.

The "banded" unit represents the highly strained, upper contact of the EWIC. The banded unit comprises thin (≤ 0.3 m), alternating layers of diorite, granodiorite, and leucogranite. This compositional variation was sampled at three different locations and in general there is very good agreement in major element compositions, both between sites and to the EWIC sample suite.

In contrast to the EWIC, later cross-cutting dykes (*Tu*) may be transitional to tholeiites (Fig. 4.1b): They have low Mg numbers (30-45) and are variably nepheline + olivine or diopside + hypersthene normative. These dykes, however, are altered, have high LOIs (see Section 4.3 below), and their major element chemistry may not be representative of magmatic compositions. The older samples of Cretaceous or Precambrian lithologies, though calc-alkaline, are generally more iron-rich than EWIC rocks. Variations between the EWIC and the older lithologies show notable enrichments of Fe and Mn, and a relative depletion of Na in the Cretaceous and Precambrian samples. The Cretaceous and Precambrian rocks are also slightly more peraluminous than the EWIC (Fig. 4.2). A/CNK values of 1.0 to 1.15 (molecular percent) are typical of Cretaceous plutons in the extensional corridor (John and Wooden, 1990; Anderson and Cullers, 1990). The Cretaceous and Precambrian granites are quartz + corundum + hypersthene normative, whereas the Precambrian gneisses have quartz + diopside + hypersthene in the norms. The two Precambrian samples which appear to lie in the tholeiitic field (Fig. 4.1b) are Fenner Gneiss (Argent, 1996), a regional, mafic granitoid of Proterozoic age (Bender et al., 1990). The most "primitive" sample from the northern Sacramento Mountains, with respect to SiO_2 and Mg #, is a Cretaceous (?) amphibolite dyke (VP94-140b).

Trace element geochemistry - The trace element correlation coefficient matrix for EWIC samples is presented in Table 4.3. Most elements correlate negitively with silica. Only Rb and Pb show the strong positive correlations indicative of incompatible element behavior, consistent with the absence of K-feldspar from the fractionating mineral assemblage. The EWIC is rich in barium (500-1500 ppm) and strontium (400-1400 ppm). Inflections at ~57 wt.% SiO_2 in Rb, Sr, and Ba (Fig. 4.4) mirror those in Al and Na. Again, such inflections may indicate the entry of a new phase during crystal fractionation or the loss of a phase during partial melting, however, the extremely high concentrations of these elements suggests that

partial melting is the mechanism by which these elements were preferentially partitioned into the relatively less-evolved melt phases of the EWIC.

Table 4.3 - EWIC correlation coefficient matrix for trace elements

	Ga	Zn	Cu	Ni	Co	Cr	V	Ba	Rb	Sr	Y	Zr	Nb	Pb	Th	U
SiO2	-0.60	-0.89	-0.31	-0.72	-0.69	-0.56	-0.91	0.10	0.71	-0.76	-0.70	-0.62	-0.44	0.87	0.10	-0.07
TiO2	0.60	0.91	0.29	0.71	0.71	0.56	0.93	-0.06	-0.68	0.75	0.70	0.61	0.50	-0.86	-0.08	0.10
Al2O3	0.76	0.42	0.49	-0.20	-0.16	-0.37	0.31	0.01	-0.24	0.73	0.13	0.51	-0.06	-0.36	-0.22	-0.07
FeO	0.53	0.89	0.25	0.77	0.75	0.63	0.93	-0.08	-0.71	0.70	0.72	0.57	0.48	-0.87	-0.09	0.08
Fe2O3	0.72	0.91	0.38	0.58	0.59	0.37	0.90	0.00	-0.64	0.84	0.64	0.68	0.44	-0.84	-0.08	0.06
MnO	0.47	0.88	0.27	0.80	0.71	0.69	0.86	-0.04	-0.66	0.67	0.71	0.61	0.59	-0.81	-0.02	0.11
MgO	0.29	0.78	0.10	0.90	0.84	0.80	0.86	-0.13	-0.70	0.49	0.71	0.43	0.47	-0.80	-0.04	0.08
CaO	0.41	0.83	0.19	0.82	0.79	0.71	0.89	-0.14	-0.78	0.65	0.70	0.51	0.44	-0.86	-0.10	0.09
Na2O	0.34	-0.18	0.22	-0.64	-0.59	-0.68	-0.34	0.10	0.16	0.23	-0.36	0.07	-0.36	0.22	-0.25	0.00
K2O	-0.53	-0.78	-0.22	-0.61	-0.59	-0.50	-0.76	0.07	0.86	-0.76	-0.52	-0.50	-0.28	0.80	0.33	-0.06
P2O5	0.38	0.83	0.20	0.82	0.74	0.75	0.82	-0.03	-0.61	0.56	0.70	0.53	0.62	-0.76	-0.01	0.12
Ga		0.73	0.50	0.10	0.13	-0.11	0.58	0.00	-0.30	0.83	0.29	0.66	0.18	-0.46	-0.08	0.14
Zn			0.41	0.67	0.57	0.50	0.88	0.08	-0.61	0.85	0.69	0.73	0.56	-0.80	-0.10	0.12
Cu				0.04	-0.07	-0.07	0.24	0.10	-0.10	0.48	0.14	0.53	0.13	-0.19	0.12	0.04
Ni					0.77	0.93	0.69	-0.07	-0.64	0.34	0.69	0.38	0.58	-0.68	0.07	0.08
Co						0.69	0.78	-0.16	-0.68	0.35	0.58	0.17	0.27	-0.65	-0.03	0.18
Cr							0.50	-0.09	-0.56	0.15	0.57	0.25	0.58	-0.54	0.09	0.11
V								-0.13	-0.67	0.72	0.78	0.50	0.42	-0.87	-0.10	0.14
Ba									-0.04	0.21	-0.04	0.36	0.13	0.00	0.00	-0.40
Rb										-0.63	-0.41	-0.43	-0.18	0.71	0.14	-0.06
Sr											0.48	0.76	0.32	-0.72	-0.15	0.05
Y												0.43	0.64	-0.78	-0.08	0.03
Zr													0.56	-0.57	0.28	-0.03
Nb														-0.52	0.23	0.11
Pb															0.12	-0.04
Th																0.20

Note Correlation coefficients calculated as product-moments, i.e.- Pearson-type. Standard error (2σ) when N=47, r = 0.9 ⇒ 0.004, r = 0.5 ⇒ 0.016, r = 0.1 ⇒ 0.021 (Marsal, 1987)

Systematic correlations can be seen between Rb, Sr, and Ba (Fig. 4.5). Notable variations between Rb and Sr include i) a pronounced negative correlation in the older lithologies, ii) an apparent positive correlation within *Tu*, iii) a wide range in Sr at relatively constant Rb in *Tlg*, and iv) a lack of correlation within *Td* and *Tgd* (Fig. 4.5a). In contrast, there are generally no correlations between Rb and Ba (Fig. 4.5b). Younger dykes (*Tu*) and the older lithologies are highly variable, whereas *Td*, *Tgd*, and the banded unit define a relatively tight cluster. *Tlg* is more variable, but appears to define a weak negative correlation of Rb with increasing Ba.

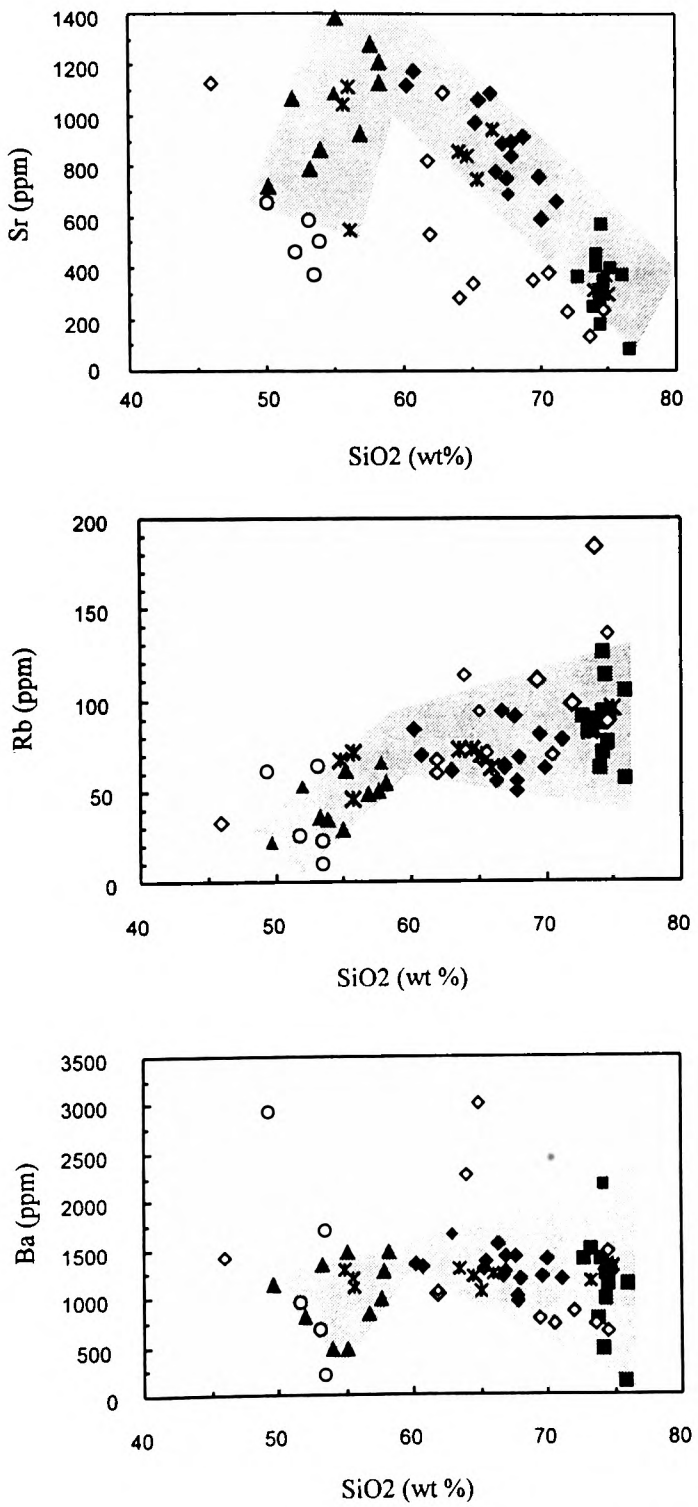


Figure 4.4 - K-group elements versus silica (symbols as in Fig. 4.3). Shaded region emphasises trend of EWIC lithologies (including the banded unit).

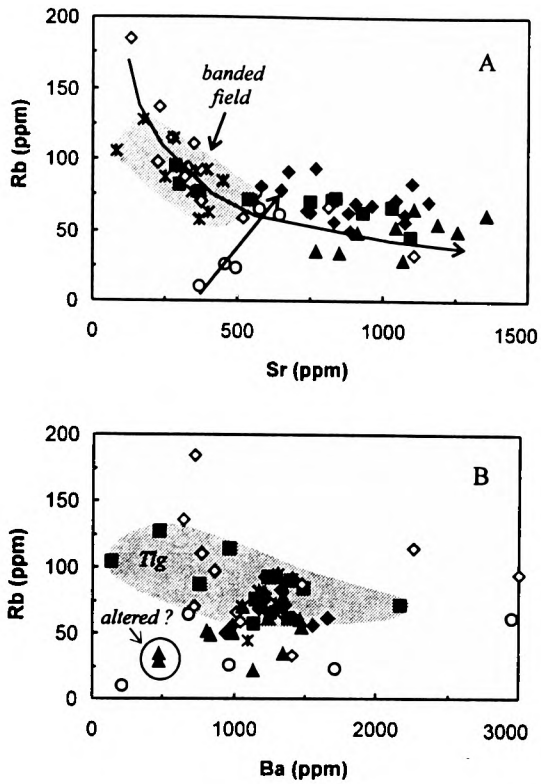


Figure 4.5 Apparent correlations between Rb, Sr, and Ba. A) More mafic EWIC lithologies (*Td* and *Tgd*) show greater variability than Tlg or the banded unit (shaded region). Apparent trends can be seen in younger dykes (*Tu*, short arrow) and older lithologies (long arrow). B) *Td*, *Tgd*, and the banded unit define a relatively tight cluster, whereas *Tu* and older lithologies show wide variations. *Tlg* may show a negative correlation between Rb and Ba (shaded field). Symbols as in figure 4.3.

On a logarithmic scale plot of an incompatible element versus a compatible element, Gill (1981) has shown that concentrations determined by fractional crystallisation define straight lines with steep (but *not* vertical) slopes, whereas mixing and partial melting are defined by curves with specific shapes. From figure 4.6a, Rb *vs.* Ni (incompatible and compatible, respectively, in mafic melts), it is clear that the overall concave-down curves defined by EWIC lithologies suggests that magma mixing (*not* partial melting, which generates concave-up curves on this diagram) had a dominant role in the genesis of the intrusive complex (Gill, 1981). Other processes are likely to be responsible for the range in Rb at any given Ni content, but it

is not possible to determine whether partial melting or fractional crystallisation was the principal mechanism responsible for this variation from this data.

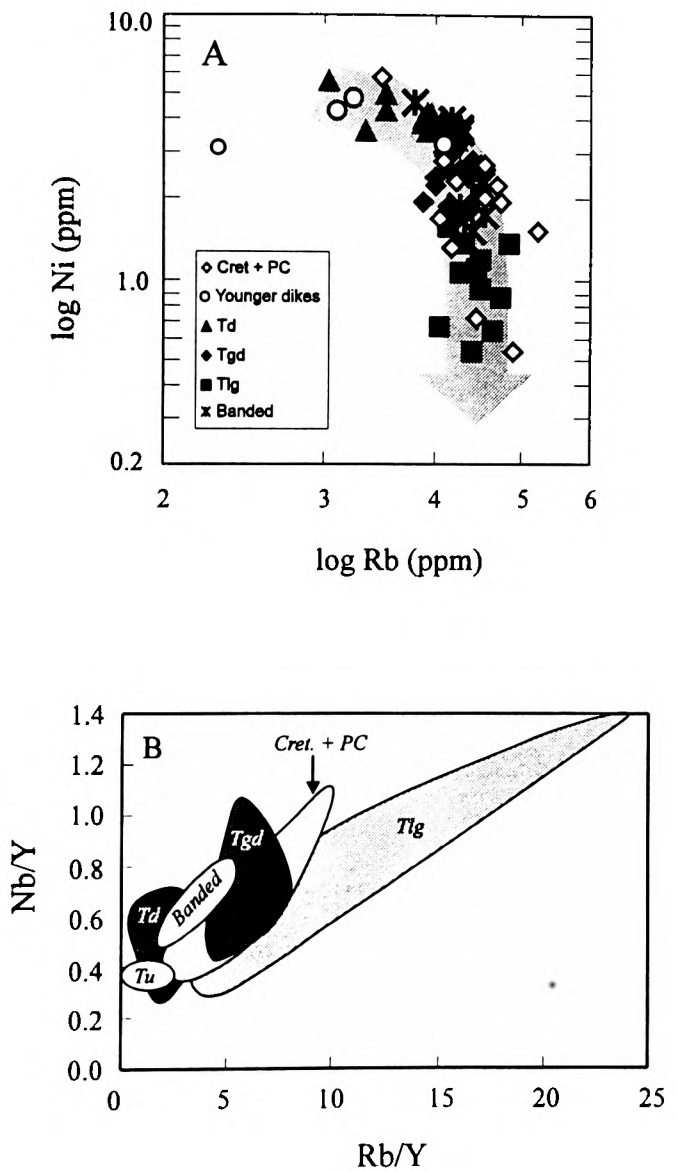


Figure 4.6 - Contamination versus fractionation using trace elements. A) On a log Ni *vs.* log Rb plot, EWIC lithologies define a typical concave-down parabola, suggesting that magma mixing dominated over crystal fractionation or partial melting (after Gill, 1981). B) A source distinct from the upper-crustal lithologies exposed in the region was involved in the genesis of *Tlg* (and by inference, *Td* and *Tgd*), as illustrated by Nb/Y *vs.* Rb/Y.

Plots of incompatible element ratios (using the same denominator) also identify mixing trends as straight lines and can be useful in identifying different sources (Gill, 1981). *Tlg* samples define a linear array in Nb/Y *vs.* Rb/Y space, with variable, but consistently high, Rb/Nb ratios of 9 to 25 (Fig. 4.6b). These high Rb/Nb ratios indicate involvement of an evolved (crustal) component in their genesis (Leeman and Hawksworth, 1986) and the ratio variability is consistent with variable degrees of partial melting. The linear array defined by mafic phases of the "banded" unit (*Td* and *Tgd*) is parallel to the *Tlg* trend, though based on a small number of samples. Mafic phases of the "banded" unit have variable Rb/Nb ratios (5-14), but suggest the involvement of *both* crustal and non-crustal material. Both *Td* and *Tgd* lack systematic variation in figure 4.6b and have limited Rb/Nb ratios (*Td* 1 to 6 and *Tgd* 5 to 11), indicating the increasing involvement of crustal material with fractionation. Older lithologies from the northern Sacramento Mountains (Cretaceous and Precambrian samples) define a distinct array, with a wide range of Rb/Nd ratios (2-12) also suggestive of the involvement of crustal and non-crustal sources. The divergence of this trend from that of *Tlg* suggests that the upper-crustal Cretaceous and Precambrian lithologies currently exposed in the area were not involved in the genesis of *Tlg*. Though the younger dyke "array" (*Tu*) is defined by a very limited data-set (three analyses), it has Rb/Nb ratios of 1-5, consistent with a *minimal* amount of crustal material involved in their genesis.

Multi-element diagrams for lithologies of the Sacramento Mountains are shown in Fig. 4.7. Element compositions have been normalized to average mid-ocean ridge basalt (MORB) using the values of Pearce (1983). It is apparent that EWIC lithologies are enriched in large ion lithophile (LIL) elements and depleted in high field strength (HFS) elements, relative to MORB. The most mafic EWIC lithology (*Td*) defines a coherent trend showing a peak at Ba, with MORB-like values for Nb and relatively depleted abundances for P, Zr, Ti, and Y. As EWIC lithologies become more evolved (*Tgd*), the overall pattern remains broadly similar, but with increased LIL enrichment and more pronounced HFS depletion.

The most notable variations are associated with P and Ti, especially in the more evolved units (Tgd, Tlg, and their equivalents in the banded unit). Phosphorous and titanium are generally regarded as incompatible elements, but can be compatible due to their preferred partitioning into accessory phases. Accessory phases become increasingly important in more evolved systems, i.e.- *Tlg*. For example, Ti and Nb are partitioned into titanomagnetite, rutile, or sphene, and P and Y are partitioned into apatite. The

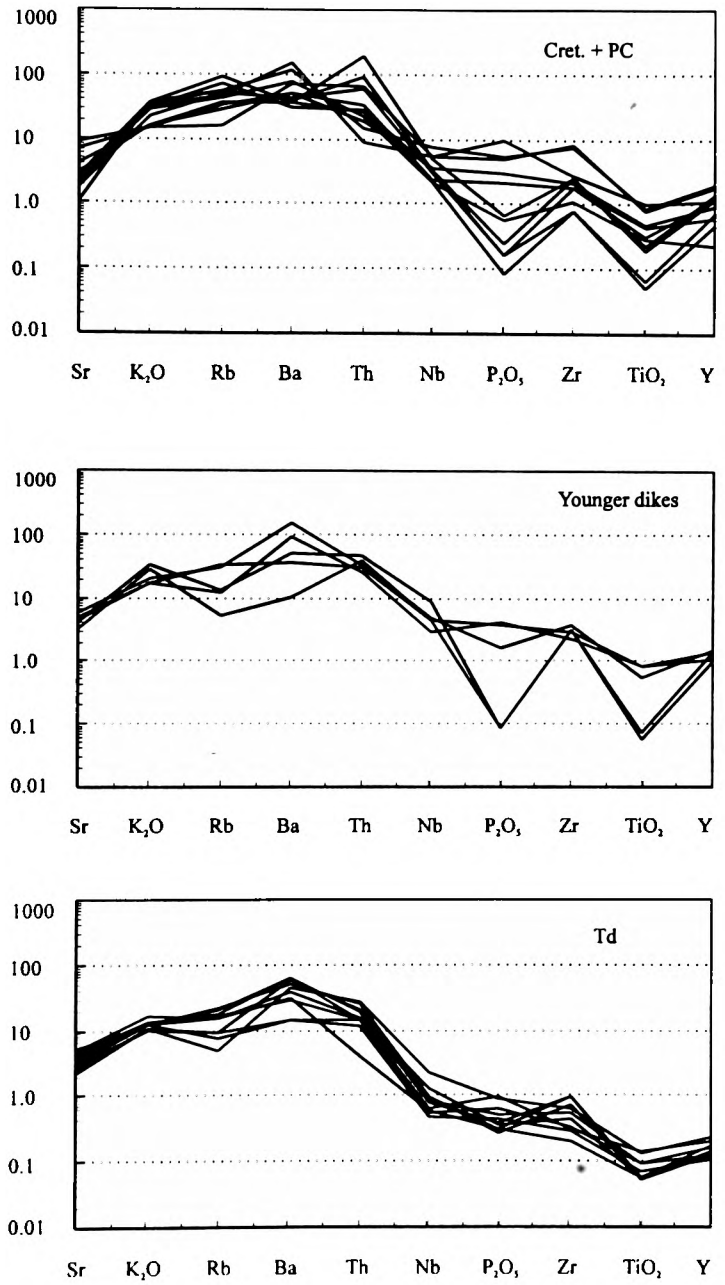


Figure 4.7 Multi-element variation diagram, normalized to MORB (Pearce, 1982). Large ion lithophile (LIL) elements are to the left of Th and high field strength (HFS) elements are to the right of Ba. LIL elements are generally mobile, whereas HFS elements are considered immobile.

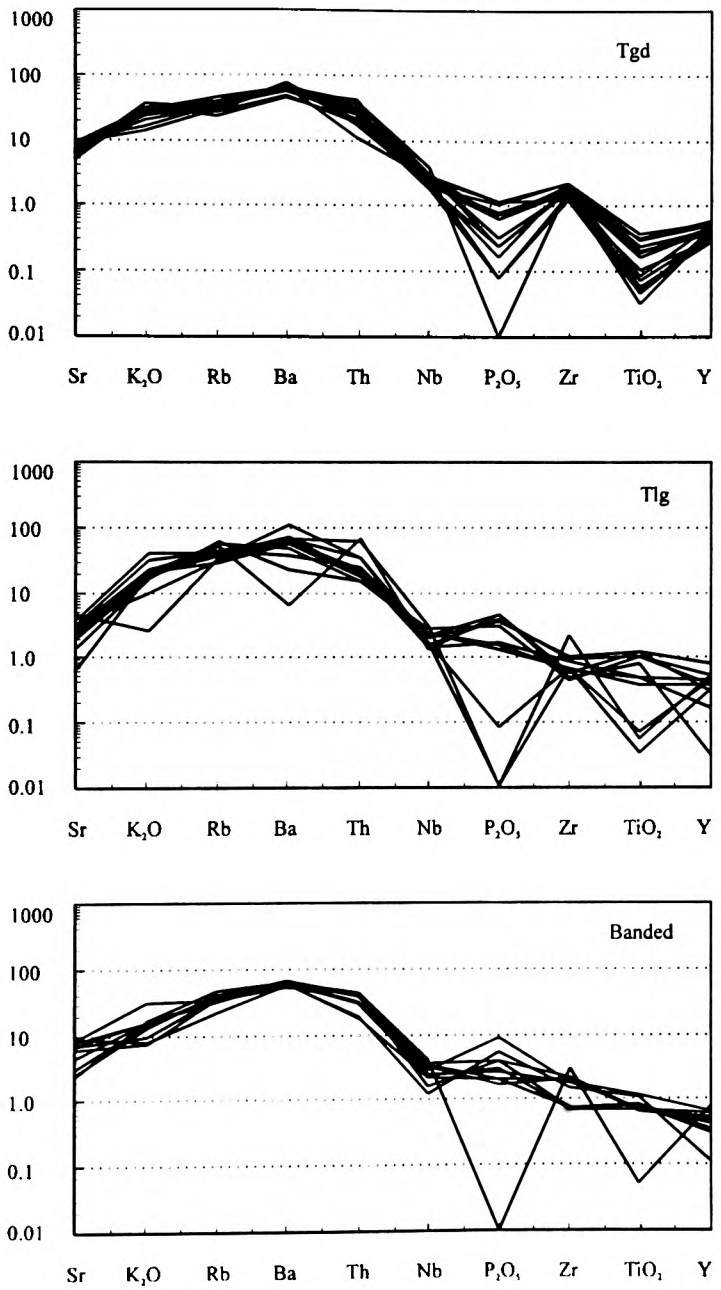


Figure 4.7 continued...

EWIC is typically sphene-, (titano?)magnetite-, and apatite-bearing. That said, the complementary depletion of Y from *Td* through *Tlg* is consistent with apatite fractionation, but a similar depletion associated with Nb is lacking. On the contrary, Nb appears to be more enriched with increasing silica. For comparison, broadly similar trends are seen in the Cretaceous and Precambrian lithologies. The gneisses generally lack pronounced P and Ti depletions, while the granites have trends which are very similar to *Tlg*. These older lithologies typically have higher HFS enrichments (10 x MORB) than EWIC lithologies.

Patterns of element variation associated with EWIC lithologies can be compared to reference curves for "typical" rock types, in an attempt to constrain the petrogenetic evolution of the intrusive complex (Fig. 4.8). Upper continental crust (UCC), lower continental crust (LCC), and ocean island basalt (OIB) are all LIL enriched, relative to MORB. Of these three reference materials, OIB is unique in displaying a rather uniform enrichment of HFS elements. The primary distinctions between the average

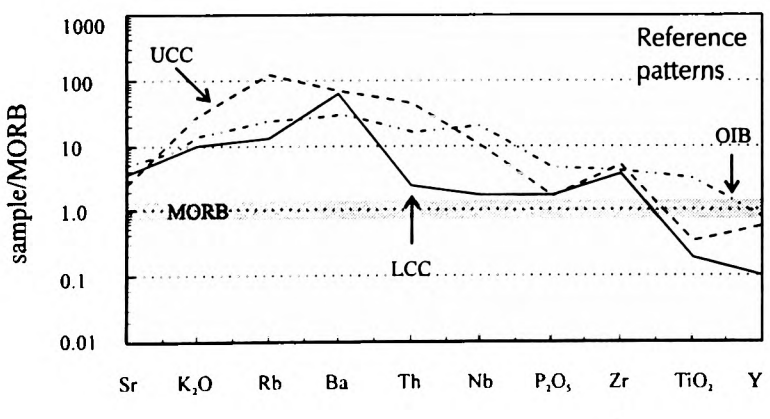


Figure 4.8 Reference multi-element patterns for typical upper continental crust (UCC), lower continental crust (LCC), and ocean island basalt (OIB). The MORB reference line will always plot at 1 (shaded region). (Figure modified from Rollinson, 1993).

geochemical signatures of UCC and LCC are related to the more mafic composition of the latter. Pronounced element enrichment occurs in Ba and Zr, with depletions of Ti and Y in the LCC. The UCC is generally more enriched than the LCC in LIL elements, as well as in the HFS elements Th and Nb. Depletions of Ti and Y occur in the UCC, but are less dramatic than in the LCC. EWIC element patterns

show some similarities with both UCC and LCC, but also show dramatic differences. The pronounced Ba peak and the general lack of a Rb peak in EWIC lithologies is representative of typical LCC. The overall enrichment of LIL elements, however, is more representative of typical UCC. Additionally, EWIC lithologies display marked depletions in HFS elements which are inconsistent with either UCC, LCC, OIB, or MORB reference patterns, and which show a notable decrease in HFS enrichment with increasing SiO_2, i.e.- from *Td* to *Tlg*.

LIL and HFS element concentrations from the EWIC are enriched relative to chondrite, though the enrichment of LIL elements is much more dramatic than the HFS elements (Fig. 4.9). Subcontinental mantle lithosphere is thought to be enriched in trace elements (Menzies et al., 1983; Waters and Erlank, 1988). Consequently, EWIC LIL and HFS element concentrations may be consistent with derivation from an enriched (metasomatized) source.

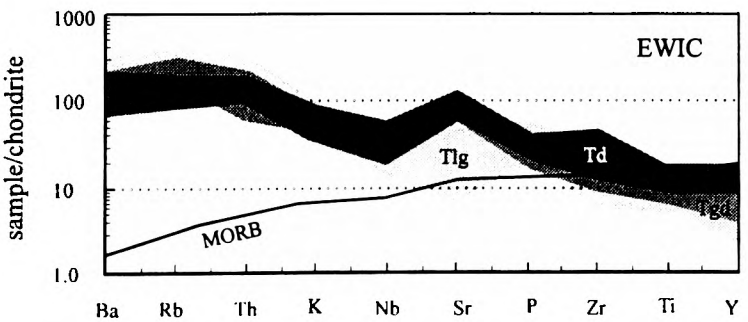


Figure 4.9 Reference multi-element patterns for MORB and EWIC lithologies, normalized to chondrite. Chondrite values from Thompson (1982) and MORB from Saunders and Tarney (1984). Note that EWIC lithologies are enriched in LIL and HFS elements relative to chondrite and that with increasing evolution, samples become increasingly depleted in HFS elements. (Element ordering from left to right indicates increasing compatibility in small melt fractions of the mantle.)

4.4 Preservation of a magmatic signature

The older lithologies in this investigation have experienced pre-detachment faulting metamorphism and deformation, and EWIC lithologies are variably mylonitized. It is therefore important to consider whether the original magmatic compositions of these rocks are preserved, before using their elemental data

to make inferences regarding magmatism, extension, and crust-forming processes. Alteration observed in metamorphic core complexes is generally the result of retrograde hydration, hydrothermal fluid migration, and/or the presence of a fluid phase during deformation and metamorphism.

Loss on ignition (LOI) - Secondary alteration is readily apparent from the loss of structurally bound water (H_2O+) during geochemical analysis (LOI, refer to Appendix B). In metamorphic core complexes severe retrograde alteration occurs in the chloritic breccia zone, e.g. Davis et al. (1980), and samples were *not* collected from this zone. In the northeast Sacramento Mountains, there is petrographic evidence below this zone for *local* pervasive alteration of plagioclase to sericite and of biotite to chlorite. This type of alteration is most pronounced in the younger dykes (*Tu*) and in the older diorite (*Td*). In *Tu* this alteration is probably post-emplacement (secondary), as indicated by accessory calcite. In *Td*, however, the alteration may be deuteric (primary) and related to associated intrusive phases of the EWIC.

The younger dykes (*Tu*) have unusually high H_2O+ contents indicative of secondary alteration (Fig. 4.10). Re-evaluation of thin-sections show that calcite and chlorite are present in the interstitial groundmass of these samples. Consequently, petrogenetic extrapolations using the geochemical analyses from these dykes must be evaluated with caution. EWIC lithologies show a general decrease in H_2O+ with increasing silica, consistent with the overall decrease of hydrous mineral phases in more evolved compositions. A break in slope at ~55 wt.% SiO_2, suggests that the earliest intrusive phase of the EWIC (*Td*) had a higher H_2O+ content than later compositional phases. Only two *Td* samples (VP95-256, H_2O+ ~2.5 wt.% and VP94-130a, H_2O+ ~1.9 wt.%) show evidence of secondary alteration in thin-section. All of the other samples of *Td* are pristine, in as much as there is no petrographic evidence of secondary alteration. This is also true for the Cretaceous (?) amphibolite dyke. Equilibrium experiments on synthetic granitic systems by Naney (1983) indicate that hornblende is only stable in plutons emplaced at 2 kb when water contents exceed 4 wt% (higher pressures, i.e.- 8 kb, require at least 3 wt% water). The EWIC was intruded at 3-4 kb (Chapter 5), suggesting water contents of 3-4 wt.% (Naney, 1983). Therefore, the relatively high H_2O+ contents (~1.5-2 wt.%) indicated by some *Td* samples is thought to be primary.

Element mobility in mylonites Element mobility during deformation and metamorphism is dominantly controlled by mineral changes and/or the presence of a fluid phase. Changes in elemental abundances have been noted in associated with myonitization (Glazner and Bartley, 1991; O'Hara and

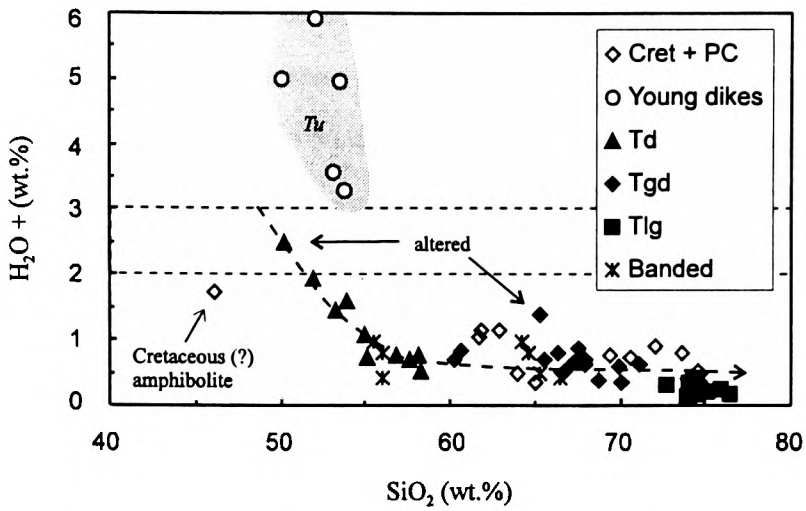


Figure 4.10 - Loss on ignition (LOI) of structurally bound water (H_2O+) as an indication of secondary alteration. The trend of EWIC lithologies (dashed arrow) is consistent with the overall decrease of hydrous mineral phases in more evolved compositions. Dashed lines indicate experimental limits on water contents in shallow, hornblende-bearing granitic systems (Naney, 1983). *Tu* samples are altered (shaded field).

Blackburn, 1989). In deformed EWIC lithologies, porphyroclasts retain igneous compositions (Chapter 2), in spite of some subsolidus recrystallization of plagioclase. Simpson (1985) has shown that under upper- to middle-greenschist facies conditions, recrystallization of plagioclase results in a slight reduction of An content (from An_{35} to An_{27}) and notes that the recrystallization of orthoclase is isochemical. Groundmass recrystallization in EWIC lithologies has resulted in partial subsolidus re-equilibration of principally biotite and quartz. In the Whipple Mountains, similar reactions have been attributed to closed-system behaviour (Anderson, 1988). This appears to be substantiated in the northern Sacramento Mountains by well-defined bivariate elemental trends (Figs. 4.3 and 4.4), though the greater scatter shown by the more mobile elements such as K and Ba may indicate minor disturbance.

Glazner and Bartley (1991) noted that the depletion of K, Rb, Si, and Ba and the enrichment of Zr, Mg, Ti, and Fe, accompanied mylonitization of granodiorite in the Mojave Desert. This pattern of depletion and enrichment can be explained by assuming that either i) all elements were mobile and partitioned into an infiltrating fluid, or ii) the relatively immobile HFS elements were concentrated as a result of bulk volume loss during deformation. Glazner and Bartley (1991) concluded that bulk volume loss was responsible for

element migration within the mylonitized granodiorite and that element depletion in the footwall was consanguineous with silicification and potassium metasomatism within the hangingwall. A similar conclusion was reached by O'Hara and Blackburn (1989), invoking volume loss to explain the substantial elemental enrichments (in Ti, P, Zr, Y, and V) and depletions (in silica and alkalis) in the mylonitic equivalent of a granodioritic gneiss in the Appalachians.

Multi-element data from undeformed and mylonitized samples of the mafic phases of the EWIC (*Td*, *Tgd*) are show in figure 4.11. After Glazner and Bartley (1991), the data has been normalized to a representative analysis of an undeformed, unaltered sample (VP94-135). Mobile elements are plotted to the left and immobile elements to the right. Note that more obvious *depletions* in P and Ti in the mylonitized samples are due to 1) the compositional variation represented by the samples, and 2) the larger number of samples associated with the deformed population. This analysis utilizes a restricted compositional subset of 31 *Td* and *Tgd* analyses. This data subset includes all samples from 50-65 wt.% SiO_2. The upper limit is somewhat arbitrary, but balances the need to compare samples which are similarly evolved with the need to have a large enough number of samples to be representative. The technique requires normalization to an undeformed sample which, in this case, has ~55 wt.% SiO_2 (VP94-135). Consequently, the expanded compositional range of the data subset likely reflects element partitioning associated with accessory phases in the more evolved samples, i.e.- apatite and magnetite. Furthermore, 8 out of 31 samples are undeformed,

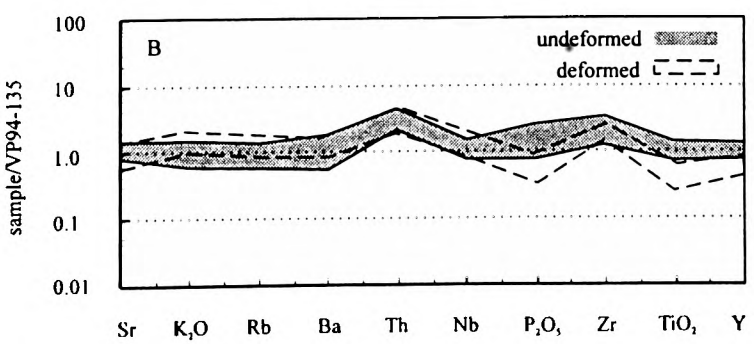


Figure 4.11 - Element mobility during mylonitization. Significant element mobility is not indicated in the mylonitic equivalents of undeformed EWIC lithologies (*Td* and *Tgd*). Analyses have been normalized to representative, undeformed *Td* (VP94-135). Oxides are in weight percent and elemental data in parts per million.

so the undeformed population may be under represented. Even with these caveats, is obvious that there is little difference in composition between undeformed and deformed samples. Certainly, the "expected" variation of HFS element *enrichment* and LIL *depletion* is not apparent. Thus, the majority of elements, and especially the immobile/HFS elements, are thought to represent magmatic compositions and can be utilised to determine the magmatic processes operating during the genesis of the EWIC.

4.5 EWIC isotopic characterisation

Representative samples of lithologies from the northern Sacramento Mountains were selected for isotopic analysis. The techniques used focus on the highly immobile and long-lived isotopes of samarium (Sm) and neodymium (Nd) to evaluate source signatures, and on the more mobile isotopes of strontium (Sr) and rubidium (Rb) to assess crustal involvement in the generation of EWIC magmas. Additionally, some initial lead (Pb) isotopic data is available from U/Pb radiometric dating (Chapter 5). Strontium and lead isotopes are particularly useful in identifying crustal components, while neodymium isotopes can discriminate between mantle signatures (Moorbath and Taylor, 1988). Analytical results are presented in Tables 4.4 and 4.5.

Table 4.4 - Summary of initial lead analytical data

Unit	$^{206}Pb/^{204}Pb$	$^{207}Pb/^{204}Pb$	$^{208}Pb/^{204}Pb$
EWIC, Tgd	18.27-18.53	15.60-15.61	39.05-39.07
EWIC, Tlg	17.72-18.01	15.54-15.59	38.68-39.05
Precambrian + Cretaceous rocks	17.51-18.30	15.51-15.59	38.28-39.05

Initial lead geochemistry In order to obtain the initial lead correction for U/Pb radiometric dating, feldspar was analysed for initial lead isotopic composition (Table 5.4, Chapter 5). These results are summarised in Table 4.4. Samples from the Sacramento Mountains exhibit significant variation in lead isotopic composition. EWIC lithologies have $^{206}Pb/^{204}Pb$ ratios of 17.72 to 18.53, $^{207}Pb/^{204}Pb$ of 15.54 to 15.60, and $^{208}Pb/^{204}Pb$ of 38.68 to 39.07. Country rocks show similar variations, with Precambrian lithologies ranging in $^{206}Pb/^{204}Pb$ from 17.51 to 18.30, $^{207}Pb/^{204}Pb$ from 15.51 to 15.59, and $^{208}Pb/^{204}Pb$ from 38.40 to 39.05.

The distribution of feldspar lead isotopic ratios suggest that the lead source for EWIC lithologies had variable, but typically low, U/Pb ratios when compared to upper-crust (Fig. 4.12). EWIC lithologies also have reduced Th/Pb ratios, albeit not as dramatic as U/Pb ratios. Magmatic differentiation processes do not result in lead isotopic fractionation. The variability in lead data within, and between, the compositional phases of the EWIC cannot, therefore, have been derived through fractionation of magma, but imply heterogeneity either inherited from the source or acquired by contamination. That *Tlg* analyses plot in, or trending towards, the present-day average lower-crustal array suggests that they were derived at least in part from lower-crustal material.

The lower U/Pb and Th/Pb ratios suggest that the source (s) for the EWIC experienced an ancient, variable depletion in U, apparently accompanied by a more modest depletion in Th. Such depletions are generally attributed to very high grade metamorphism and imply that the source was in part high-grade (upper-amphibolite to granulite facies) lower crust (Tilton and Barreiro, 1980). Time-averaged Th/U ratios calculated for the source rocks from *Tlg* and *Tgd* are high (>4.5), indicating stronger retention of Th than U, also typical of lower crustal granulites. This data is consistent with the strontium and neodymium data presented below.

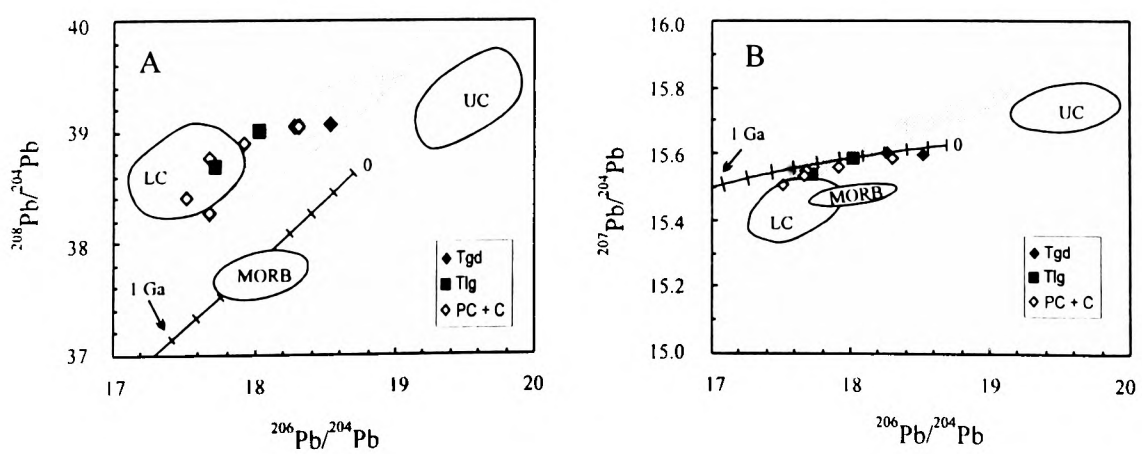


Figure 4.12 Feldspar lead isotopic compositions from the northern Sacramento Mountains. Reference fields: present-day average lower-crust (LC), mid-ocean ridge basalt (MORB), and upper-crust (UC) from Zartman and Doe (1981). Mesozoic feldspar lead data from southeastern California indicated by shaded region (Wooden et al., 1988). Stacey and Kramers (1975) lead evolution curve for average crust shown in 100 Ma increments.

The lead data from the EWIC may lie within the Mesozoic plutonic array of Wooden et al. (1988) for rocks in southeastern California and western Arizona (Fig. 4.12). It appears, then, that Tertiary plutonic rocks in this region, which interact strongly with Mesozoic crust, may not generate *distinct* isotopic signatures. Wooden and coworkers concluded that the Mesozoic intrusives were largely derived from the melting of, and interaction of magmas with, Proterozoic basement. They suggest that these lead isotopic compositions are typical of rock suites formed by the reworking of continental crust, rather than by subduction at the plate margin. These conclusions appear to apply to Cenozoic intrusions as well.

Rubidium and strontium geochemistry Lithologies in the northern Sacramento Mountains have variable $^{87}Sr/^{86}Sr$ ratios (Table 4.5). Within the EWIC, *Td* and *Tgd* ratios generally range from 0.70863 to 0.71121, with *Tlg* showing higher $^{87}Sr/^{86}Sr$ ratios from 0.71633 to 0.71967 (if the sample of *Tlg* from the "banded" unit is included). Older Cretaceous (?) and Precambrian rocks show much greater variability ranging from 0.70746 to 0.75056, reflecting the greater range of lithologies within this group (amphibolite, granite, and biotite schist). Typical *initial* $^{87}Sr/^{86}Sr$ ratios for Miocene plutons in the extensional corridor range from 0.706 to 0.710 (Falkner et al., 1995; Davis et al., 1982). Typical initial $^{87}Sr/^{86}Sr$ ratios for Cretaceous plutons in the extensional corridor range from 0.706 to 0.719 (John and Wooden, 1990; Miller et al., 1990; Davis et al., 1982), and pre-Mesozoic sialic upper-crust has $^{87}Sr/^{86}Sr$ ratios of ~0.72 (Gill, 1981).

Initial $^{87}Sr/^{86}Sr$ ratios ($^{87}Sr/^{86}Sr_i$), i.e.- the ratio corrected for the amount of ^{87}Sr produced by ^{87}Rb decay since the formation of the rock, are plotted against 1/Sr, Sr, and SiO_2 in figure 4.13. The age of the EWIC (~20 Ma; Chapter 5) is used to calculate the initial ratio of $^{87}Sr/^{86}Sr$. On this figure, horizontal trends may represent crystal fractionation (the dashed line in Fig. 4.13b), while non-horizontal trends may indicate mixing processes (the solid line on Fig. 4.13b). If these processes have occurred, then the expected variations on "companion" plots (Langmuir et al., 1978) should be seen. For example, a corollary to non-horizontal lines equating with mixing in A/B *vs.* 1/B plots (Fig. 4.13b), is that mixing should define a parabolic curve on plots of A/B *vs.* B. Secondly, crystal fractionation processes would be expected to correlate with silica, whereas mixing processes probably would not. The samples which define an apparent "mixing" trend in A/B *vs.* 1/B space (solid line in Fig. 4.13b), do not define a parabolic curve in A/B *vs.* B space (Fig. 4.13c). Furthermore, the samples which define an apparent crystal fractionation trend in A/B *vs.*

1/B space (dashed line in Fig. 4.13b), generally correlate with silica (Fig. 4.13d), suggesting that crystal fractionation processes dominated over mixing process. Unless the rubidium and strontium isotope systematics in the EWIC have been disturbed, the variable $^{87}Sr/^{86}Sr_i$ ratios and the high Sr content in EWIC samples are indicative of either an isotopically heterogeneous source region or crustal contamination. The elevated $^{87}Sr/^{86}Sr_i$ ratios imply that the EWIC was derived from, or contaminated by, quartzo- feldspathic

Table 4.5 - Rb-Sr and Sm-Nd analytical data, and derived parameters

Sample	Rb (ppm)	Sr (ppm)	$^{87}Rb/^{86}Sr$	$^{87}Sr/^{86}Sr$	Sm (ppm)	Nd (ppm)	$^{147}Sm/^{144}Nd$	$^{143}Nd/^{144}Nd$	ε_{Nd} (0 Ga)	t_{CHUR} (Ga)	t_{DM} (Ga)
Precambrian and Cretaceous samples											
VP94-129	97.4	223.2	1.268	0.75056	9.264	58.52	0.0957	0.511517	-21.9	1.68	2.05
VP94-130b	60.8	1074	0.164	0.71030	6.557	41.86	0.0947	0.512056	-11.4	0.870	1.33
VP94-140a	66.0	810.2	0.236	0.71009	11.69	69.89	0.1011	0.512376	-5.1	0.419	0 971
VP94-140b	32.9	1109	0.086	0.70746	19.15	115.3	0.1004	0.512392	-4.8	0.390	0.940
EWIC samples, Td											
VP94-020c	54.2	1188	0.132	0.71018	7.920	46.03	0.1040	0.512063	-11.2	0.945	1.42
VP94-123b	34.2	850.4	0.116	0.70914	5.068	26.77	0.1144	0.512275	-7.1	0.674	1.26
VP94-123c	60.5	1358	0.129	0.71119	8.563	49.71	0.1041	0.512017	-12.1	1.02	1.50
VP94-124	34.8	771.6	0.131	0.70906	10.89	61.12	0.1077	0.512369	-5.3	0.462	1.04
VP94-130a	51 8	1044	0.144	0.70975	98.74	464.2	0.1286	0.512100	-10.5	1.20	1 80
VP94-135	48.5	912.3	0.154	0.71090	6.67	30.98	0.1302	0 511984	-12 8	1 50	2 05
VP95-256	20.8	706.6	0.085	0.70863	18.97	106.8	0.1074	0.512400	-4.6	0.407	0 99
EWIC samples, Tgd											
VP94-119a	62.0	750.0	0.239	0 71112	3.998	25.90	0.0933	0.511961	-13.2	0.998	1 44
VP94-119b	69 9	1156	0.175	0.71114	7 274	45.21	0.0973	0.511981	-12.8	1.01	1.46
VP95-159	80 4	582.7	0.399	0.71121	4 468	32.38	0.0834	0.512026	-11.9	0.823	1.25
VP95-249	61 9	878.7	0 204	0.71031	5.759	37.93	0.0918	0.511971	-13.0	0.969	1.41
EWIC samples, Tlg											
VP95-160	84 1	451.0	0.540	0.71633	2.710	15.70	0.1043	0.511718	-18.0	1.52	1.93
VP95-258	113.7	280.4	1.174	0.71661	2.505	12.67	0.1195	0.511738	-17.6	1.77	2.21
EWIC samples, Banded unit											
VP95-237	61.8	930.1	0.192	0.71046	4.442	26.98	0 0995	0.512032	-11.8	0.950	1 42
VP95-246	72.0	822.3	0.253	0.71038	5.382	30 51	0 1067	0.512042	-11.6	1.01	1 50
VP95-247	72 6	834.8	0 252	0.71018	6 389	39.31	0.0982	0.512082	-10.8	0.861	1.34
VP95-248	94 7	290.3	0.945	0.71967	4 405	24 47	0.1088	0 511715	-18.0	1.60	2.02
Young dykes, Tu											
VP95-163	22.8	496.1	0.133	0.71100	5.630	28.31	0.1202	0.512106	-10.38	1.060	1.62
VP95-164	61.2	645.0	0.274	0.71091	8.518	46.45	0.1109	0.512136	-9.79	0.891	1 42
VP95-165	64 5	577.5	0.323	0.71137	7.369	39.67	0.1123	0 512165	-9.22	0.854	1.40

Note: Chemical separation for whole rock samples followed standard ion-exchange procedures (Whitehouse et al., 1996; Turnbull et al., 1996). Rb and Sr ppm determined by XRF on pressed powder pellets (Pankhurst and O'Nions, 1973); error on $^{87}Rb/^{86}Sr$ ratios is *c.* ± 2% (2σ). Sr-isotopic ratios were determined on a VG Micromass 30 mass spectrometer and corrected for within-run mass fractionation by normalisation to an $^{88}Sr/^{86}Sr$ ratio of 8.37521; replicate analyses of Eimer and Amend $SrCo_3$ standard yielded ratios systematically biased from the accepted value of 0.70800 and samples ratios were corrected accordingly. External precision on $^{87}Sr/^{86}Sr$ ratios is *c.* ± 0.01%. Decay constants follow the convention of Steiger and Jäger (1977) and Lugmair and Marti (1978)

Sm and Nd ppm determined by isotope dilution; error on $^{147}Sm/^{144}Nd$ ratios is *c.* ± 0.1% Nd-isotopic ratios were determined on a VG 54E mass spectrometer and corrected for within-run mass fractionation by normalisation to a $^{146}Nd/^{144}Nd$ ratio of 0.7219, replicate analyses of La Jolla standard yielded 0.511858 ± 0.000029 (0.0056%, 2σ). ε_{Nd} parameters calculated relative to CHUR using values of Jacobsen and Wasserburg (1984), depleted mantle model age (t_{DM}) assumes the model of DePaolo et al. (1991)

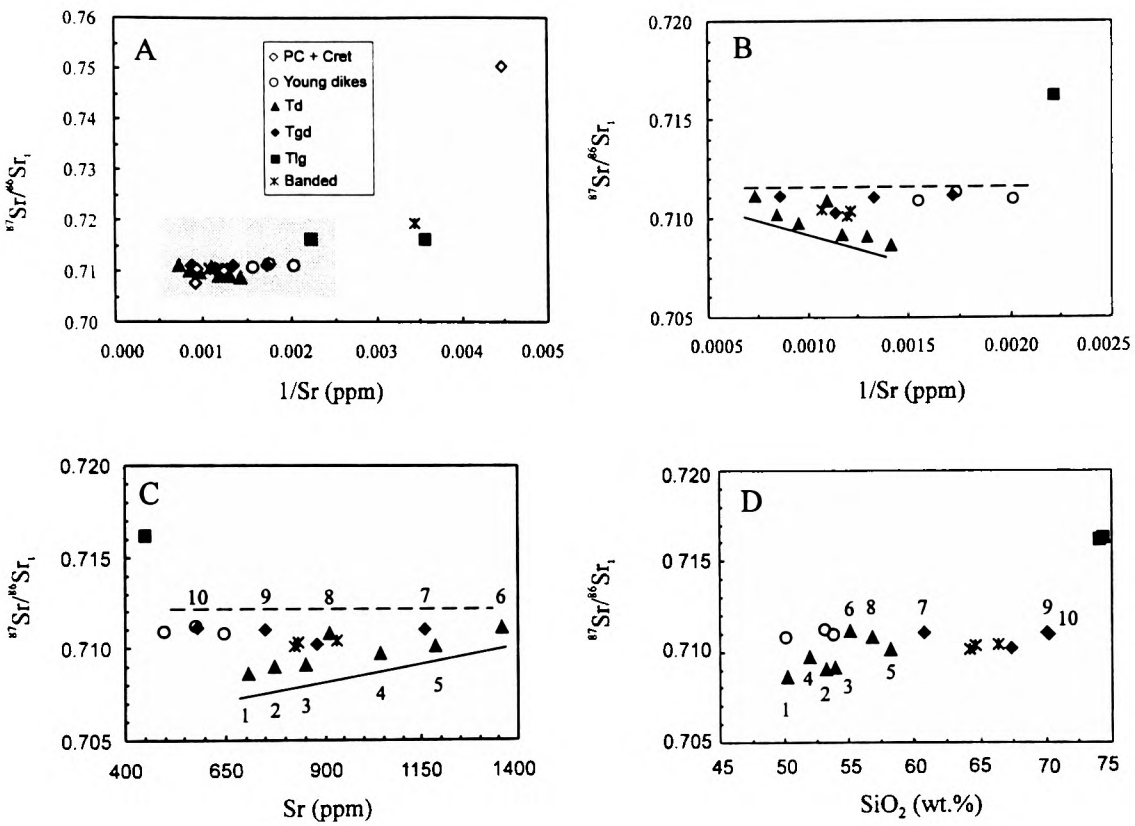


Figure 4.13 Contamination versus fractionation using strontium isotopes. A) Lithologies in the northern Sacramento Mountains have variable initial $^{87}Sr/^{86}Sr$ ratios (where t = 20 Ma). B) Magnification of shaded region in A) showing *Td*, *Tgd*, banded unit, and younger dykes (*Tu*). Horizontal, linear trends may indicate crystal fractionation, while non-horizontal, linear trends may indicate mixing processes. C) Companion plot to B) with $^{87}Sr/^{86}Sr_i$ plotted against Sr. Simple binary mixing is generally indicated by a parabolic curve; note linear trends. D) Companion plot to B) with $^{87}Sr/^{86}Sr_i$ plotted against SiO_2. In general, a predictable relationship of relatively constant $^{87}Sr/^{86}Sr_i$ with increasing silica is suggestive of crystal fractionation (samples numbered 6-10 in Fig. 4.13d). All symbols as in A).

crust with a high content of radiogenic ^{87}Sr. Furthermore, fractional crystallisation appears to be responsible for some of the trends seen in the EWIC data. Magma mixing and mingling textures, and upper-crustal xenoliths, are preserved in EWIC lithologies and, together with evidence for crystal fractionation, suggest that an AFC-type process was involved in the genesis of the intrusive complex.

Samarium and neodymium geochemistry - Lithologies in the northern Sacramento Mountains have variable ε_{Nd} values (Table 4.5). ($^{144}Nd/^{143}Nd$ ratios are typically expressed in epsilon notation (ε_{Nd}), which is $^{144}Nd/^{143}Nd$ normalized to chondrite, such that the chondrite uniform reservoir (CHUR) is equal to zero.)

Within the EWIC, *Td* and *Tgd* ε_{Nd} values generally range from about -5 to -13, with *Tlg* showing more restricted ε_{Nd} values of about -18 (including the sample of *Tlg* from the "banded" unit). Compared to the mafic phases of the EWIC (*Td* and *Tgd*), the younger mafic dykes also show a more restricted and generally evolved value of about -10. Older lithologies show the greatest range in ε_{Nd} values from about -22 (Precambrian biotite schist) to about -5 (Cretaceous amphibolite).

Similar to rubidium and strontium trends, Sm-Nd data for the EWIC appear to define linear arrays in a plot of ε_{Nd} *vs.* 1/Nd (dashed lines in Fig. 4.14a). The subhorizontal, parallel trends in figure 4.14a suggest that discrete mixing episodes occurred in the evolution of the EWIC, which involved variable amounts of crustal contamination or a heterogeneous source (ε_{Nd} ca. -5 to -14). Also consistent with rubidium and strontium, these trends are maintained in the "companion" plot of ε_{Nd} *vs.* Nd (dashed lines in Fig. 4.14b), though they are not maintained when ε_{Nd} is plotted against silica (Fig. 4.14c). In spite of the lack of systematic correlation with Nd content to silica on a per-sample basis, there is a general trend of decreasing ε_{Nd} with increasing silica for EWIC samples. This suggests that as the EWIC became more evolved it was interacting with older and more mafic continental crust characterised by more negative ε_{Nd} values. The neodymium isotopic data indicate that discrete mixing events, involving a mafic lower-crust, were important in the genesis of the EWIC.

Variable depleted mantle model ages (t_{DM}) from EWIC samples in the northern Sacramento Mountains of ~1 to 2 Ga (Table 4.5) are not wholly consistent with the expected values of 2.0-2.3 Ga for the region from Bennett and DePaolo (1987). *Td* and *Tgd* samples show a wide range of model ages, with a maximum of ~2 Ga, a minimum of ~ 1 Ga, and a pronounced 1.4 Ga signature. *Tlg* samples have consistently older t_{DM}s (including the banded unit sample) of 1.9-2.0 Ga. This variability suggests that EWIC samples were derived from a very heterogeneous crustal source and/or involved variable amounts of mantle material.

The source reservoirs for the EWIC can be evaluated using neodymium and strontium isotopes. All of the data from the northern Sacramento Mountains is shown in figure 4.15a. An enlarged region of the data (omitting VP94-129) is shown in figure 4.15b, with various possible source reservoirs superimposed. Data from the EWIC and younger dykes (*Tu*) lie to the right of the projected oceanic mantle array (Fig.

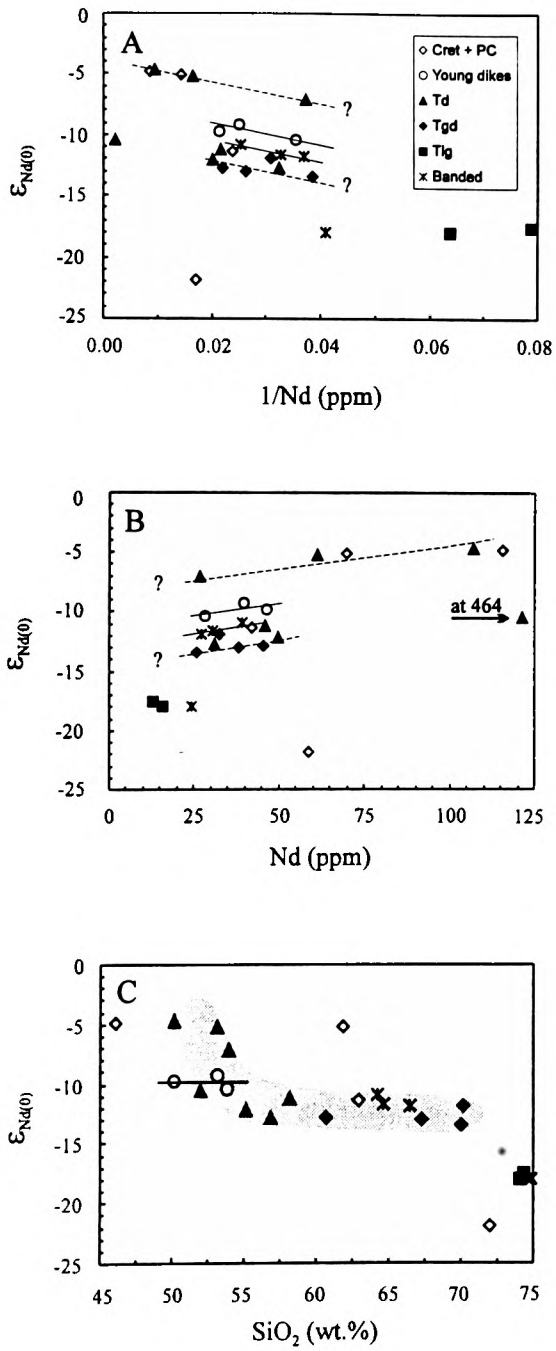


Figure 4.14 - Contamination versus fractionation using neodymium isotopes. A) Lithologies in the northern Sacramento Mountains have variable ε_{Nd} values, though some linear trends are present which appear to be reflected in the "companion" plots (dashed lines). B) Companion plot to A), with ε_{Nd} plotted against Nd. Note a lack of parabolic trends, but the persistence of linear trends apparently correlable with A). C) Companion plot to A), with ε_{Nd} plotted against SiO_2. Note the apparent decrease in ε_{Nd} with increasing SiO_2 (shaded field).

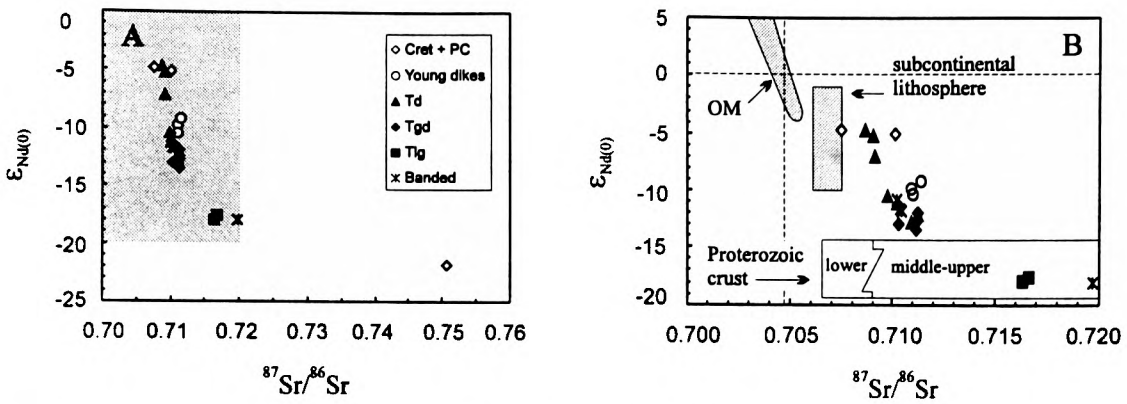


Figure 4.15 Source reservoirs for the EWIC. A) All $^{144}Nd/^{144}Nd$ (using ε notation) and $^{87}Sr/^{86}Sr$ data from the northern Sacramento Mountains. B) Magnification of shaded region in A), with possible isotopic source reservoirs for the EWIC. Reference fields: oceanic mantle (OM) after DePaolo (1981), subcontinental lithosphere after Farmer et al. (1989), Proterozoic crust after Miller and Wooden (1993) and Young et al. (1992).

4.15b), signifying crustal contamination (DePaolo, 1988), with the dykes showing the greatest shift. *Tlg* samples (including the banded unit sample) clearly show their derivation from partial melting of sialic Proterozoic continental crust (ε_{Nd} -18). The spatial association of *Tlg*, *Td*, and *Tgd* in the upper-contact of the EWIC (the "banded" unit), suggests that heat from the more mafic magmas may have lead to the *in situ* partial melting of Proterozoic country rock to generate *Tlg*. From the associated t_{DM}s, it can be inferred that this Proterozoic crust was ~2 Ga old. Binary mixing between subcontinental lithospheric derived magma and older continental lithosphere is suggested by both the strontium and neodymium isotopes (Figs. 4.13, 4.14, and 4.15).

4.6 Magma genesis

Part of the problem associated with plutonic suites containing several compositional phases is determining whether these phases are genetically related to a single parent and, if so, what is the nature of the source from which the parent was generated. Binary mixing calculations (Langmuir, 1978), using various parents and crustal end-members, were performed in an attempt to constrain the source of EWIC magmas. The end-member compositions used are given in Tables 4.5 and 4.6.

Table 4.6 - End-member compositions used in binary mixing

Components	Sr (ppm)	$^{87}Sr/^{86}Sr$	Nd (ppm)	$^{143}Nd/^{144}Nd$
Proterozoic (young, <1.7Ga)[1]	400	0.72	80	0.51172
Proterozoic (mean)[2]	300	0.73	50	0.51172
Mesozoic granite[3]	500	0.711	35	0.51207
pre-Tertiary (mean)[4]	350	0.719	45	0.51182
depleted mantle[5]	700	0.703	35	0.51315[a]
enriched mantle[6]	1100	0.707	65	0.51218[a]

Notes: 1 Miller and Wooden (1993); 2 - Miller and Wooden (1993), Young et al. (1992); 3 - Miller and Wooden (1993); 4 - Miller and Wooden (1993); 5 - Glazner et al. (1991), Farmer et al. (1989); 6 - Farmer et al. (1989); a, re-calculated using CHUR values of Jacobsen and Wasserburg (1984)

Mixing between the local upper-crustal component (VP94-129 1.6 Ga biotite schist; SHRIMP age, see Chapter 5) and the most primitive *Td* sample (VP94-256) does not reproduce the observed EWIC trends (Fig. 4.16a). It is clear that the mafic phases of the EWIC (*Td* and *Tgd*) were not generated by the assimilation of this supracrustal material, but instead require a more mafic (lower Sr), less radiogenic (lower $^{87}Sr/^{86}Sr$), and older (negative ε_{Nd}) crustal component. It is also obvious that the highly evolved leucogranites (*Tlg*) could not be the result of such mixing, and it is considered more likely that they represent variable degrees of partial melting of upper-crustal material. This is certainly consistent with the neodymium and strontium data (Fig. 4.15b), and with their highly variable trace element abundances for any given silica content (Fig. 4.6).

The low Mg numbers (~45) for the least fractionated members of the diorite suite (*Td*) preclude equilibration with a mantle source containing olivine or pyroxene, e.g., Frey et al. (1978). Vaniman et al. (1982) showed that fractionation of amphibole can explain low Mg numbers and low Ti concentrations in evolved hawaiite magmas, relative to their parental magmas. This suggests that the "primitive" compositions in this study (*Td*) are themselves derivatives of an unseen parent. The most likely composition of this unseen parent in the southern Basin and Range Province is either the depleted mantle or an enriched subcontinental lithospheric mantle (Bradshaw et al, 1993; Farmer et al., 1989). Consequently both of these compositions have been used in modelling binary mixtures of mantle and crust (Figs. 4.16b and 4.16c, respectively).

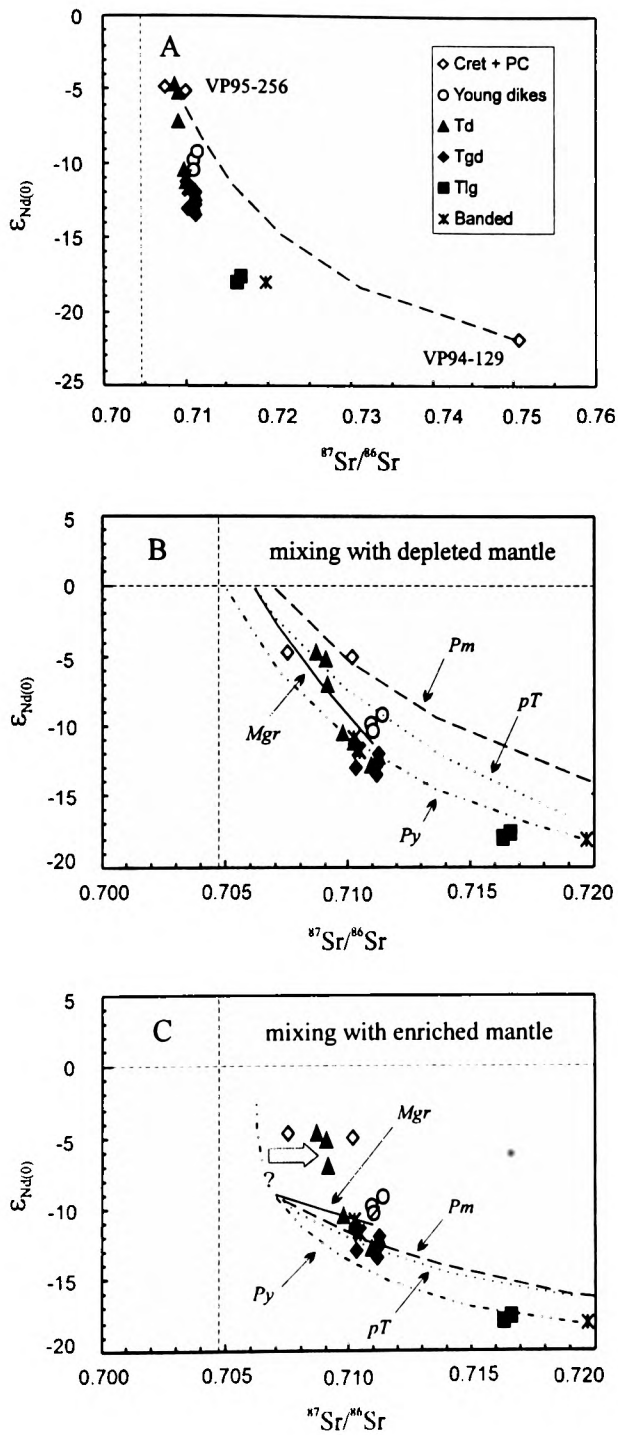


Figure 4.16 Binary mixing and EWIC genesis. A) The observed data cannot be derived from upper-crustal material (*Td*, VP94-256; 1.6 Ga biotite schist, VP94-129). B) Enlarged area of A) showing binary mixing of *depleted mantle* with various crustal end-members. C) Enlarged area of A) showing binary mixing of *enriched mantle* with various crustal end-members. End-members: *Pm*, Proterozoic (mean); *Py*, Proterozoic (young mean, <1.7 Ga -); *Mgr*, Mesozoic granite; *pT*, pre-Tertiary mixed crust (*Pm* + *Mgr*). End-member values and references given in Table 4.6. ε_{Nd} parameter normalized to CHUR (Jacobsen and Wasserburg, 1984).

Neither mixing scenario satisfactorily model's the observed EWIC trends. If the *depleted mantle* was the parent to EWIC lithologies, the calculations suggest that a heterogeneous crust was being assimilated in variable quantities (Fig. 4.16b). *Td* appears to be derived from ~ 50% assimilation of a pre-Tertiary crust composed of Mesozoic granite and Proterozoic rocks, while *Tgd* and *Tlg* are derived from the assimilation of young Proterozoic (<1.7 Ga) crustal material (~60% and 100%, respectively). Model ages (t_{DM}s, Table 4.5) for *Tlg*, however, suggest that it was derived from 2.0 Ga crust (though t_{DM}s could be unreliable if fractionation occurs, i.e.- assimilation of accessory phases like monazite or zircon). If an *enriched mantle* was the parent to EWIC lithologies (as suggested by trace element geochemistry, Section 4.3), *Tlg* is apparently derived from 80-100% assimilation of young Proterozoic crust, again in contradiction to t_{DM}s. *Tgd* is apparently derived from ~40% assimilation of either average Proterozoic, or mixed Proterozoic and Mesozoic, crust, while *Td* cannot be derived from the enriched mantle composition used (Fig. 4.16c).

The enriched mantle is typically low in $^{143}Nd/^{144}Nd$ with *variable* $^{87}Sr/^{86}Sr$ ratios (Zindler and Hart, 1986). In order to derive EWIC lithologies from an enriched mantle source, this would need to have a higher $^{87}Sr/^{86}Sr$ ratio, i.e.- the mixing trend needs to be shifted to the right (shaded arrow in Fig. 4.16c). Such a composition is not observed in Miocene age basalts from the region (Bradshaw et al, 1993; Farmer et al., 1989), though it is not unreasonable theoretically and suggests that the parent magma to EWIC *plutonic* lithologies involved a greater component of crustal material than their possible *extrusive* equivalents.

Thus far, it is clear that simple binary mixing fails to reproduce the observed EWIC trends, confirming that complex AFC-type processes were involved in EWIC magma genesis. The petrogenetic evolution of the EWIC involved 1) an enriched subcontinental lithospheric mantle source, 2) the assimilation of heterogeneous crustal material (both middle- and upper-crust) with *variable degrees* of partial melting, and 3) concurrent fractional crystallisation. The net result is that it is difficult to quantify the individual contributions of each of these processes, particularly because the composition of both the enriched subcontinental lithosphere and the lower- to middle-crust in the region are not well-constrained. Identifying specific source materials for granitoid rocks is difficult. Crustal source regions are usually heterogeneous and magmas show the imprint of such diversity (c.f. Miller et al., 1988). This complexity increases if there is material input from juvenile subcrustal magmas (possibly important in the genesis of the

EWIC). Even if a single, homogeneous source can be assumed, it is rarely clear what, if anything, within a granitoid complex represents a liquid composition. The best candidates are generally the most evolved and therefore the least useful for assessing sources. The least evolved rocks are typically cumulate-rich, and thus also of limited usefulness.

Another important consideration has to do with the differing behaviour of major elements, trace elements, and isotopic ratios during anatexis and assimilation. The trace element content of a rhyolitic liquid produced by anatexis of a granitoid is controlled by the percentage of melting and by the phases present in the residue (presence or absence of zircon, etc.), whereas major element concentrations are controlled by the phase equilibria of the granitoid. For example, a liquid produced by 5 wt.% melting of a granitoid source region will have a significantly different trace element signature than a liquid produced by 20 wt.% melting of the same source region, yet both liquids will be rhyolitic. Thus, major and trace elements are decoupled during anatexis and mixing. Furthermore, major elements and isotopic ratios are also decoupled during anatexis and mixing. For example, the present-day $^{87}Sr/^{86}Sr$ ratios of Precambrian granitioids in the Mojave Desert generally exceed 0.78 (Glazner et al., 1988) and are much greater than present-day ratios from Mesozoic granitoids (~0.71), yet both will generate a rhyolitic liquid during anatexis. Silicic components derived from the crust cannot, therefore, avoid being heterogeneous, especially in their isotopic and trace element compositions. Consequently, coherent major element trends and scatter in trace element and isotopic trends are predicted by generalised mixing models (Glazner, 1990).

Furthermore, the effect of mixing dioritic and granodioritic magmas, combined with crystal fractionation, results in magmatic compositions with many of the characteristics of calc-alkaline suites formed during plate convergence (Fig. 4.17). This relationship has also been noted for the ~16 Ma Aztec Wash pluton in the El Dorado Mountains to the north (Falkner et al., 1995) and in the Lake Mead region by Smith et al. (1990). Factors controlling such geochemical signatures appear to be three-fold. First, mixing of mafic (*Td*) and comparatively felsic (*Tgd*) melts inhibit the tholeiitic iron enrichment trend and lead instead to a calc-alkaline trend. Second, EWIC magmatism reprocessed lithosphere that had been strongly affected by arc and collisional processes. The majority of the crust, and probably the lithospheric mantle, was formed and reworked in the Early Proterozoic (Wooden and Miller, 1990) and during Mesozoic arc magmatism, e.g., Miller and Wooden (1993). Basalts invading the mid-Tertiary crust were probably

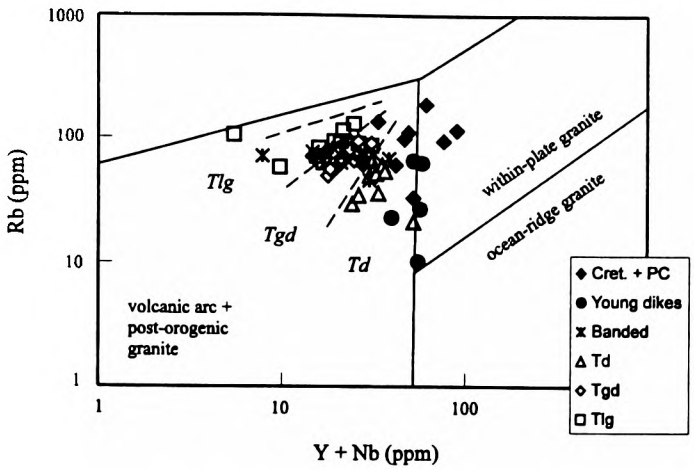


Figure 4.17 Tectonic discrimination diagram (after Pearce et al., 1984). EWIC lithologies move towards the syn-collisional granite fields with increasing evolution (silica). Discrete mixing fields (dashed lines) are identified for each compositional phase (*Td*, *Tgd*, and *Tlg*).

derived from the subcontinental lithospheric mantle and would have been contaminated by crust which included both arc and collisional components. Third, bimodal volcanism is well-documented in extensional settings (Armstrong and Ward, 1992). Volcanism before and during the initiation of detachment faulting, however, is mainly calc-alkalic or alkalic-calcic, with basaltic andesite, andesite, and dacite predominating, e.g., Eaton (1982), Otton (1982), Smith (1982). Bimodal volcanism may be a function of the tectonic structure of the crust, rather than of some primary petrogenetic process (Smith et al., 1990). Smith et al. (1990) suggest that steep faults facilitate extrusion of bimodal magmas without significant mixing, whereas low-angle faults encourage magmas to spread laterally, accumulate, and mix, generating magmas of intermediate composition. Consequently, both the chemical nature and structural state of the pre-existing lithosphere has a strong influence on magma genesis and contributes to the resulting geochemical signature.

The geochemical data presented (summarised in Table 4.7) suggest a complex evolution for the EWIC, in which admixing of lower- to middle-crustal material with magma derived from a subcontinental lithosphere dominated over fractional crystallisation. Lower-crustal assimilation occurred prior to the genesis of *Tlg*, which was largely generated by the partial melting of upper-crustal material. Thus, the following sequence for the genesis of the EWIC is suggested. A "parent" magma, not necessarily seen in the

northern Sacramento Mountains, was generated from the enriched subcontinental lithospheric mantle. This parent magma ponded at the base of the lower-crust, assimilating old (Proterozoic), mafic (granulitic) crust, generating *Td*.

Table 4.7 - Evidence for the petrogenesis of the EWIC

Fractional crystallisation	Assimilation/partial melting	Magma mixing
• Plagioclase fractionation	Upper crust	• Scatter in element concentrations of *Td*
• Apatite fractionation	• High LIL elements, Sr, Ba, Rb/Nb ratios	
• Decreasing HFS elements with increasing silica	• Variable HFS element at a given silica and Pb isotopes (*Tlg*)	• Scatter in ratio plots of *Td*
• Decreasing ε_{Nd} with increasing silica	• Parabola in log/log plot (Fig. 4.6)	• Scatter in log/log plot of *Td*
• Consistent trends of Sr in companion plots (Fig. 4.12)	• Lines in ratio plots (Fig. 4.13)	
	Lower (to middle) crust	
	• Low HFS elements, $-\varepsilon_{Nd}$, high Th/U ratios	

The assimilation of sialic Proterozoic crust from present-day exposures is not favoured (Fig. 4.16). Proterozoic rocks from present-day exposures in the eastern Mojave Desert region (Wooden and Miller, 1990) have average Sr concentrations of 246 ppm, Rb/Sr ratios of 0.42, and high $^{87}Sr/^{86}Sr$ ratios (> 0.73). This composition is typical of felsic crust. The composition needed to generate EWIC evolutionary trends (*Td*) should have low time-averaged Rb/Sr ratios of ~0.04 (*Td*). Furthermore, lead isotopes suggest that the source for the EWIC experienced an ancient (Proterozoic) high-grade, U-depleting event. Both the Rb/Sr ratios and ε_{Nd} ratios suggest that *ancient, mafic* crust was involved in the genesis of EWIC lithologies.

The contaminated magma (*Td*) ascended to higher crustal levels and ponded at the base of the detachment shear zone, where it spread laterally, assimilating, mixing, and crystallising, generating magmas of intermediate composition (*Tgd*). This evolutionary stage probably involved multiple intrusive phases (magma batches), as well as separate magma chambers/conduits, as indicated by i) magma mixing between *Td* and *Tgd* (Chapter 2) and ii) diorite forming both the oldest and youngest intrusive lithologies (Chapter 2) in the northern Sacramento Mountains.

Once emplaced at higher structural levels, small volume partial melts of Proterozoic *sialic upper-crust* (*Tlg*) were generated. Again, multiple intrusive phases are suggested by the various generations (compositions) of *Tlg*. After the final stages of crystallisation, the still hot, semi-plastic mush began to deform as the result of motion along the detachment fault. Continued and progressive deformation of the EWIC by detachment faulting, from sub-magmatic/sub-solid-state temperatures to low-temperature brittle deformation, was responsible for the final structural fabrics preserved in the EWIC and the current morphology of the Sacramento Mountains (Chapter 3).

Chapter 5

Age and Thermal Evolution of the Northern Sacramento Mountains

5.1 The application of thermochronology

Unravelling the thermal history of the footwall in the northern Sacramento Mountains is important for understanding the tectonic evolution of the region, especially that associated with Tertiary detachment faulting. Using thermobarometry to constrain the pressure and temperature of emplacement for the EWIC, the depth and temperature of origin of the crystalline assemblages which comprise the lower-plates of detachment faults can be assessed. Furthermore, in combining this information with thermochronology (the use of temperature-sensitive dating techniques), it is possible to determine the exhumation and cooling history of the EWIC in the northeast Sacramento Mountains and to calculate the original orientation of the basal Sacramento Mountains detachment fault (see Chapter 6).

Fundamental to the application of thermochronometers is the concept of *closure temperature* (T_c). Dodson (1973) defined closure temperature and, with regards to geochronology and isotopic systems, formalised the mathematics associated with closure theory. At relatively high temperatures, the daughter isotope diffuses out of the mineral as fast as it is produced by radioactive decay and does not accumulate - the mineral is an "open" system. As the mineral system cools, it passes through a temperature at which

diffusion of the daughter isotope is inhibited and it begins to accumulate, i.e.- the mineral behaves as a "closed" system, and this temperature is regarded as the mineral's T_c . Dodson (1973) showed that T_c is influenced by the cooling rate and effective grain size of the sample, with faster cooling rates and larger grain sizes yielding higher T_c. In this investigation, samples were collected for uranium/lead (U/Pb), argon/argon ($^{40}Ar/^{39}Ar$), and fission track (FT) analyses. These radioactive systems, applied to a variety of mineral separates, define a set of closure temperatures ranging from magmatic to sub-solid state conditions (Table 5.1 below). The granodioritic phases of the EWIC possess most of the minerals in Table 5.1 and are well suited to documenting the thermal history of the region, though the sample suite is consequently compositionally biased.

Table 5.1 - Closure temperatures for minerals used in this study

U/Pb*			$^{40}Ar/^{39}Ar$†		FT§	
zircon	monazite	sphene	hornblende	biotite	zircon	apatite
>800°C	≈700°C	≈600°C	550-500°C	345-310°C	250-170°C	120-80°C

Note: * = T_c from Heaman and Parrish (1991).
† = T_c from Harrison (1981) and Harrison et al. (1985) for cooling rates ~70-100°C/Ma (Pease et al., 1995).
§ = T_c from Wagner and Van den Haute (1992).

Samples were collected for thermobarometric and thermochronologic investigations of the northeast Sacramento Mountains and sample locations are shown on Insert 2. In order to evaluate whether the northwest and northeast Sacramento Mountains represent a continuous crustal section, samples were also collected for thermochronology in the northwest Sacramento Mountains (Insert 3). Samples in both regions were collected along northeast trending transects, parallel to the inferred tectonic transport direction, in order to determine whether the crust is tilted, with deeper structural levels being exposed to the northeast.

5.2 Thermobarometry of EWIC emplacement

Although contact metamorphic rocks may contain mineral assemblages appropriate for emplacement barometry, applying the various techniques may be difficult in pervasively intruded terranes because of extensive thermal overprinting. In contrast, refractory igneous phases are commonly less affected by younger thermal events. Even in mylonites, porphyroclasts can retain compositions related to igneous crystallisation (Anderson, 1988). Consequently, samples from the EWIC were used for thermobarometric

determinations. Sample locations are summarised in figure 5.1. Analytical results from other workers are reported for comparison, i.e.- a single analysis from Anderson (1988), indicated by A., '88 in figure 5.1.

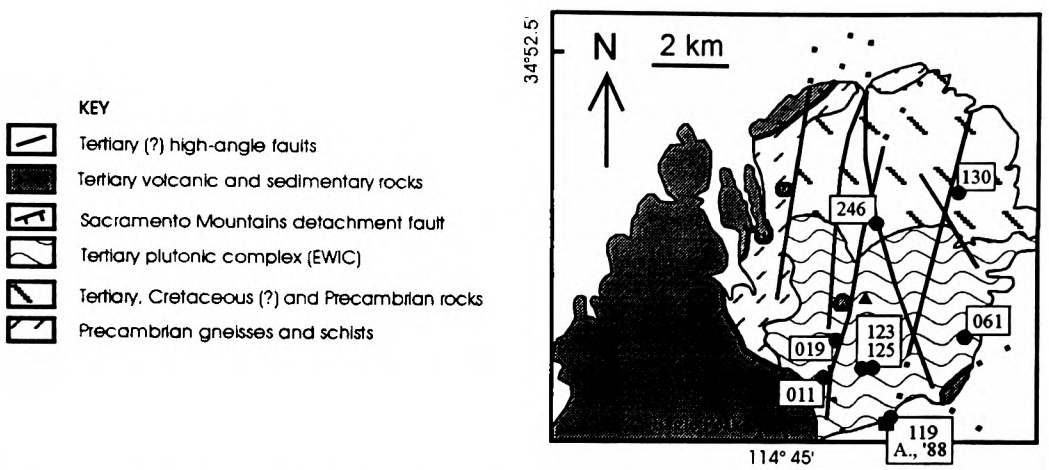


Figure 5.1 Thermobarometric sample locations in the NE Sacramento Mountains. Circles represent samples from this investigation and the square is from Anderson (1988). Triangles identify local peaks.

To estimate the temperature of crystallisation, the amphibole-plagioclase thermometer of Blundy and Holland (1990) was used with the revised calibration of Holland and Blundy (1994). The pressure-dependent solubility of total aluminum in hornblende (e.g., Hammarstrom and Zen, 1986; Hollister et al., 1987) was used with the revised calibration of Anderson and Smith (1995) as the barometer. Using an electron microprobe, five to ten mineral pairs were analysed per thin-section. The resulting compositional data is presented in Chapter 2. A brief discussion of the electron microprobe analytical technique and associated errors is presented in Appendix C, along with the mineral analyses of hornblende and plagioclase. The Fortran program RECAMP of Spear and Kimball (1984) was used to recalculate electron microprobe analyses of amphiboles into amphibole structural formulae. In this program, ferric iron is estimated on the basis of stoichiometric constraints of amphibole crystal chemistry. All recalculations that obey both chemistry and stoichiometry are calculated, however Cosca et al. (1991) demonstrated that only the 13-cation normalization procedure closely predicts site occupancies for amphiboles in which FeO and Fe_2O_3 were determined by titration. Consequently, only the 13-cation output from RECAMP was used for thermobarometry. The chosen normalization scheme does not significantly affect calculated Al_{tot} or

pressure, but it does affect calculated $^{[4]}$Al and $^{[6]}$Al, and this can affect the calculated temperatures (see below). Non-stoichiometric results and analyses which do not meet the compositional requirements outlined below are not included in data synthesis.

Amphibole-plagioclase thermometry Crystallisation temperatures were calculated, using the equations of Holland and Blundy (1994), by assuming a given pressure; these temperatures were then substituted into the revised equation of Anderson and Smith (1995) in order to calculate pressures. The resulting, calculated pressures were then used to solve for the crystallisation temperatures, and this iterative process was continued until convergence in the value of both temperature and pressure was achieved (typically three iterations). Both equation A (T_a) and equation B (T_b) of Holland and Blundy (1994) were used to calculate the crystallisation temperature of quartz-bearing and marginally quartz-bearing samples (CIPW qtz-norms of ~0-5%, see Appendix B), whereas only T_b was used for non-quartz bearing samples.

For these thermometers, the 13-cation normalization procedure used to determine site occupancy in amphiboles influences the calculated $^{[4]}$Al and $^{[6]}$Al, which in turn affects the calculated temperatures. For the mineral compositions used in this study, the effect is minor, generally $\leq$ 20°C. The error associated with these temperature determinations is ± 35-50°C (1σ; Holland and Blundy, 1994), including the analytical uncertainties associated with electron microprobe determinations of silica in amphibole and anorthite contents. For the compositions in this study (X_{ab} = 0.6 - 0.8 and Si per formula unit in amphibole = 6.5 7.2), the 2σ uncertainty is ± 75°C (see discussion of errors and uncertainties in Blundy and Holland, 1990). It should be noted, however, that the associated error may be larger for samples whose compositions vary from that of the calibration data set, i.e.- $\mathbf{T_a}$: T = 400-900°C, amphiboles with $^{[A]}$Na > 0.02 per formula unit (pfu), $^{[6]}$Al < 1.8 pfu, Si = 6.0-7.7 pfu, and plagioclases with X_{an} < 0.90; $\mathbf{T_b}$: T = 500-900°C, amphiboles with $^{[M4]}$Na > 0.03 pfu, $^{[6]}$Al < 1.8 pfu, Si = 6.0-7.7 pfu, and plagioclases with 0.1< X_{an} < 0.9.

Al in hornblende barometry - This approach assumes that the phase compositions represent near-emplacement conditions, i.e.- that crystallisation occurs near the H_2O-saturated solidus, thus rim compositions are most likely to reflect emplacement conditions. This barometer is commonly applied to rocks with the restricted mineral assemblage used in the experimental calibration: quartz + alkali feldspar + plagioclase + hornblende + biotite + iron titanium oxide + sphene + liquid. The granodioritic phases of the

EWIC usually contain the full buffering assemblage, though quartz and potassium feldspar can be absent in the more mafic phases. There is some evidence to suggest that the full buffering assemblage may not be necessary: Anderson and Smith (1994) found that the absence of potassium feldspar and sphene did not significantly affect pressure determinations. It is also common practice to apply the barometer to restricted mineral compositions. Anderson and Bender (1988) showed that the barometer fails for Proterozoic anorogenic granitoids in which Fe contents in the hornblendes are higher than those used in the original calibration, therefore use of the barometer is restricted to amphiboles with $Fe^{tot}/(Fe^{tot} + Mg)$ between 0.4 0.65 and $Fe^{3+} / (Fe^{3+} + Fe^{2+}) > 0.2$. Also, plagioclase compositions of ~An_{25-35} were used in the original calibration, thus the application of the barometer in this study is restricted similarly. Anderson and Smith (1995) estimate a total error of ± 1.5 kb (2σ) for their revised calibration of this barometer. This figure includes the 2σ variation associated with regression of the calibration data sets (± 0.6 kb), the propagation of 2σ uncertainties associated with temperature determinations (± 50°C ⇒ ± 0.8 kb), as well as an analytical precision associated with electron microprobe analyses of Al_2O_3 (±1% ⇒ ± 0.1 kb). The analytical precision associated with the determination of Al_2O_3 is well within the range of analyses from this investigation (Appendix B) and its contribution to the total error is relatively minor, but the contribution from the temperature determination is underestimated. The error contribution from the temperature determination should be evaluated using ± 75°C (2σ). This increases the error contribution associated with temperature determination to ± 1.1 kb. Consequently, the best figure for uncertainty associated with this barometer is ± 1.8 kb (2σ).

The Al in hornblende barometer assumes that emplacement conditions reflect crystallisation near the H_2O-saturated solidus. Amphiboles are known to be susceptible to sub-solidus alteration. Consequently, amphibole compositions from granodioritic phases of the EWIC were evaluated, prior to the application of the barometer, to determine whether sub-solidus alteration had occurred (Chapter 2). The majority of calcic amphiboles are magnesio-hornblendes, with about 15% being actinolitic or tschermakitic, and edenitic hornblendes (Chapter 2, Fig. 2.25). Using the empirical criterion of Fleet and Barnett (1978), the $^{[4]}Al/^{[6]}Al$ ratio indicates that most amphiboles from the granodioritic phases of the EWIC, both cores and rims, represent calcic, igneous compositions and not low- or high-pressure metamorphic amphibole compositions

(Chapter 2, Fig. 2.26). Consequently, the thermobarometric results which follow are likely to represent the emplacement temperature and pressure of the EWIC at solidus conditions.

Thermobarometric Results - The results of thermobarometric calculations are shown in Table 5.2 and are summarised in figure 5.2. Attrition due to unacceptable microprobe analysis, non-stoichiometric hornblende compositions, or mineral compositions outside the calibration data set resulted in generally three to five grain-pairs per thin-section comprising the sample means quoted in Table 5.2. Only T_h was applied to non-qtz-bearing samples and because qtz was not present in the buffering assemblage, pressures calculated using these temperatures should be evaluated with caution (see discussion below).

Table 5.2 - Results from amphibole-plagioclase thermometry and Al in hornblende barometry

	Rim					Rim			
Sample ID	T_a	T_h	P_a	P_h	Sample ID	T_a	T_h	P_a	P_h
VP94-011c 1-r		660		4.9	VP94-123c 3-r		726		3.8
VP94-011c 2-r		633		3.5	VP94-123c 4-r		699		4.1
VP94-011c 3-r		674		3.4	VP94-123c 5-r		759		3.7
VP94-011c 4-r		683		2.9	**Mean**		**728±43**		**3.9±1.0**
VP94-011c 5-r		656		1.3					
Mean		**661±34**		**3.2±0.8**	(VP94-124 1-r		641		1.6)
VP94-019 4-r		691		1.9	VP94-125 1-r		685		5.0
VP94-019 5-r		677		1.8	VP94-125 2-r		654		4.7
VP94-019 6-r		646		0.6	VP94-125 4-r		663		4.0
Mean		**671±43**		**1.4±1.0**	VP94-125 5-r		666		4.4
					Mean		**667±38**		**4.5±0.9**
VP94-061 1-c*	680	652	3.6	3.8					
VP94-061 3-c*	648	687	1.8	1.6	VP94-130b 1-r	638	647	3.2	3.2
VP94-061 4-c*	725	691	3.9	4.4	VP94-130b 2-r	681	677	3.4	3.5
VP94-061 4-r *	707	697	3.4	3.5	VP94-130b 3-r	681	656	3.4	3.6
VP94-061 5-c*	723	718	3.9	4.0	VP94-130b 4-r	(787)	(734)	(4.7)	(5.9)
VP94-061 5-r *	670	669	3.6	3.6	VP94-130b 5-r	651	646	3.0	3.0
Mean	**692±31**	**685±31**	**3.4±0.7**	**3.5±0.7**	**Mean**	**663±38**	**660±38**	**3.3±0.9**	**3.3±0.9**
Overall Mean		**689±31**		**3.4±0.7**	**Overall Mean**		**662±38**		**3.3±0.9**
VP94-119b 1-c*	740	707	3.7	4.2	VP95-246 1-r	714	704	4.5	4.6
VP94-119b 2-c*	724	709	3.5	3.7	VP95-246 2-r	727	707	4.3	4.6
VP94-119b 3-c*	768	733	2.5	3.2	VP95-246 3-r	685	689	4.9	4.8
VP94-119b 5-c*	776	735	2.4	3.2	VP95-246 4-r	690	683	4.2	4.3
VP94-119b 5-r*	782	718	2.3	3.5	VP95-246 5-r	708	702	4.3	4.4
Mean	**758±34**	**720±34**	**2.9±0.8**	**3.6±0.8**	**Mean**	**705±34**	**697±34**	**4.4±0.8**	**4.6±0.8**
					Overall Mean		**671±34**		**4.5±0.8**
VP94-123b 1-r		667		2.6					
VP94-123b 2-r		646		1.9					
VP94-123b 3-r		644		1.2					
VP94-123b 4-r		655		2.5					
VP94-123b 5-r		653		3.0					
Mean		**653±34**		**2.2±0.8**					

Note T_a and T_h, temperature in °C, for silica-saturated and unsaturated samples, respectively (Holland and Blundy, 1994). P_a and P_h pressure in kilobars, calculated using T_a and T_h, respectively (Anderson and Smith, 1995). Error (2σ) of individual analyses: T± 75°C, P ± 1.8 kb. Sample ID includes field sample number and grain-pair number (cross reference Appendix B) Numbers in parentheses are not included in the mean (see text). P_hs should be evaluated with caution, as compositional criteria may not be met *= fine grained, no real distinction between rim and core.

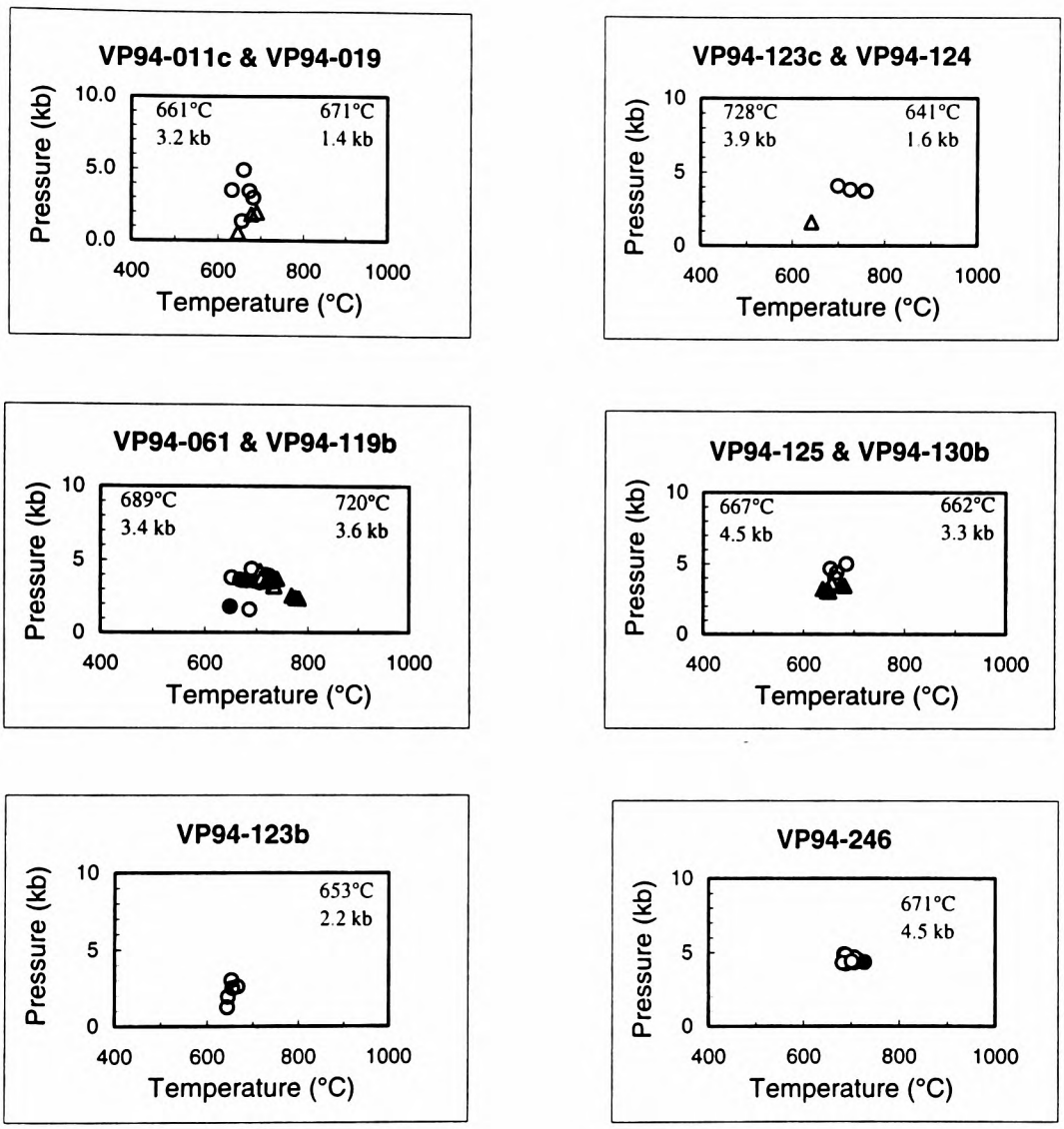


Figure 5.2 Calculated temperatures and pressures of EWIC emplacement (from the granodioritic phases). Thermometer of Holland and Blundy (1994) and barometer of Anderson and Smith (1995). The first samples is represented by circles, and the second by triangles; Ta represented by solid symbols; Tb represented by open symbols. Error (2σ) of individual analyses: T ± 75°C, and P ± 1.8 kb. Sample means shown (first sample on left and second sample on right).

Two samples require special mention, VP94-124 and VP94-119b. The various causes of attrition (outlined above) resulted in only a single acceptable analysis of VP94-124. The result is reported in Table 5.2, but is not statistically representative and, consequently, is not used in the final calculations. Though the

temperature results from T_a and T_b are the same (within 2σ error), VP94-119b has a consistently higher T_a than T_b, combined with a consistently lower P_a than P_b. This is typical for samples which are silica undersaturated (Holland and Blundy, 1994). Upon further investigation, this sample proved to be only nominally silica saturated at ~6% normative quartz (Appendix A), whereas the other samples in this investigation are clearly quartz-normative (>10%) or lacking in normative quartz. This suggests that only equation B should be applied to this sample. Subsequently, only T_b from VP94-119b is used in the final calculations.

There is little difference (≤8°C) between the calculated temperatures, when compositional criteria allow both equation A and B to be applied (Table 5.2; samples VP94-061, VP94-130b, and VP94-246). The within-sample temperature variation from these analyses is generally between 30°C and 70°C, within the 2σ error of ± 75°C quoted for the technique. (The notable exception is VP94-130b, where grain-pair-4 is outside the grouping of analyses. Grain-pair-4 is regarded as an outlier, perhaps an inherited crystal, and is not included in the sample mean.) The individual grain analyses are averaged to produce **sample means** for T_a and T_b (Table 5.2). Sample means for T_a and T_b are within 2σ analytical error and can be averaged together to represent an **overall mean** for the sample. The overall sample means show rim temperature variations within the suite of ~30°C, from 660 - 690°C and the weighted average of the overall means for the temperature of emplacement ($\mathbf{T_1}$) is 676 ± 19°C.

When compositional criteria allow *only* equation B to be used, the calculated temperature of emplacement ($\mathbf{T_2}$) is nearly identical to $\mathbf{T_1}$ above (within 2σ analytical error, using VP94-011c, VP94-019, VP94-119b, VP94-123b, VP94-123c, and VP94-125). Sample mean temperatures (using equation B only) vary ~75°C, from 655-730°C, with a resulting weighted average for $\mathbf{T_2}$ = 683 ± 31°C. These two temperatures are the same, within error, thus the temperature of emplacement of the granodioritic phase of the EWIC is taken to be 680 ± 19°C.

The Al in hornblende barometer was calibrated experimentally with a quartz-bearing assemblage (quartz + alkali feldspar + plagioclase + hornblende + biotite + iron titanium oxide + sphene + liquid; see Hammarstrom and Zen, 1986, and Hollister et al., 1987). The application of this barometer to non-quartz-bearing assemblages is, *sensu-stricto*, inappropriate, i.e. samples with *only* P_bs in this study (see Table

5.2). By comparing the results of Si-saturated samples ($\mathbf{P_a}$) with non-Si-saturated samples ($\mathbf{P_b}$), the validity of using non-quartz bearing, EWIC rocks to calculate pressures using the Al in hornblende barometer can be assessed. The pressures calculated using *Si-saturated* samples (VP94-061, VP94-130b, and VP94-246) show excellent agreement between P_a and P_b, allowing the average of these **sample means** to represent the pressure of emplacement for each sample (the **overall mean**). The resulting weighted average of the overall means ($\mathbf{P_1}$) is 3.7 ± 1.4 kb.

P_b s from *non-saturated* samples show a greater range of pressure variation than those from saturated samples. Using the six reliable non-saturated samples, an overall mean of 3.1 kb ± 1.2 ($\mathbf{P_2}$) is generated. This value is indistinguishable (within error) from the Si-saturated mean of 3.7 ± 1.4 kb ($\mathbf{P_1}$ above). Over 50% of the non-saturated samples yield results in excellent agreement with $\mathbf{P_1}$ and it is interesting to note that VP94-125 yields one of the highest pressures calculated for the EWIC (4.5 kb). Silica undersaturated minerals are entirely absent from the non-saturated samples; it may be that the activity of Si (a_{Si}) of these samples, though low, is *close* to unity, and the pressure calculation continues to yield accurate results. Consequently, it would seem that in some instances samples without normative quartz can be used to determine pressure with the Al in hornblende barometer. This kind of application, however, requires an "external" pressure determination to verify the results or an independent check on a_{Si} on a "per sample" basis. Finally, because $\mathbf{P_1}$ and $\mathbf{P_2}$ are within error and can be combined, the pressure of emplacement for the granodioritic phase of the EWIC is calculated to be 3.3 ± 0.8 kb.

Anderson (1988) used the same techniques on a sample of EWIC from the quarry along Eagle Pass road: The same location as the biotite-hornblende granodiorite, VP94-119b (Fig. 5.1). The results of his four rim pairs, recalculated using Anderson and Smith (1995) for pressure and Holland and Blundy (1994) for temperature (Anderson, 1996), are 700 ± 9°C and 4.3 ± 0.5 kb. These errors seem overly precise given the discussion above on cumulative errors associated with the technique. Nonetheless, these results compare well to those from VP94-119b (T_b = 720 ± 34 and P_b = 3.6 ± 0.8) and would seem to verify the reproducibility of this thermobarometric technique. The 2σ errors associated with Anderson's data can be recalculated and the results combined with those from VP94-119b, yielding a mean of 711 ± 25°C and 3.9 ±

0.6 kb for the quarry site in the northeast Sacramento Mountains. Though at the upper limit of the temperature variation, these values are in good agreement with the overall results shown in Table 5.2.

Anderson (1988) also reports additional pressure determinations for two samples of garnet, two-mica granite adjacent to the EWIC granodiorite in the central Sacramento Mountains, south of the study area. The granite has foliations and lineations which are concordant with the granodiorite, but the granite is thought to be younger than the granodiorite (Anderson, 1996, pers. comm.). He was able to derive both igneous and metamorphic conditions from the same samples using porphyroclast and matrix phases. Anderson's (1996) recalculated data from igneous porphyroclasts is 2.9 ± 0.7 kb (using the garnet + plagioclase + muscovite + biotite barometer of Ghent and Stout, 1981) and 748 ± 20°C (using the garnet-biotite reformulation of Ganguly and Saxena, 1984). The pressure determination for the mylonitic phase is ≤ 2.5 kb (using phengite barometry). Porphyroclast data from the garnet, two mica granite is similar to (within 2σ), or possibly lower than, the results from the granodioritic phases of the EWIC. This suggests that the granite (probably correlative with *Tlg*) shared the same decompression history as *Tgd*, or was intruded after decompression had begun in the Sacramento Mountains. The lower pressures from the mylonitic matrix suggest that mylonitization occurred while decompression of the footwall was already under way.

5.3 High-temperature history

U/Pb radiometric dating technique "Conventional" U/Pb geochronology involves the chemical isolation of uranium and lead from an accessory mineral and analysing the isotopic composition of these purified elements using a solid-source thermal ionisation mass spectrometer. This procedure uses populations of grains (by size, colour, magnetic susceptibility, etc.) and is distinct from either ion microprobe or evaporation techniques, which are based on single grain analysis. The data presented in this investigation are from conventional analyses of zircon, monazite, and sphene, with the exception of VP94-129: VP94-129 is the only sample analysed by the ion microprobe technique, due to having a uniformly small (<63μm) zircon population (refer to Appendix C for mineral separation techniques and population specifications, and to Appendix D for analytical techniques and chemical separation procedures).

U has two unstable nuclides, ^{238}U and ^{235}U, that decay through a series of unstable intermediate daughter products to the stable daughter isotopes of ^{206}Pb and ^{207}Pb, respectively. For each U/Pb analysis, therefore, three apparent U/Pb ages are obtained ($^{206}Pb/^{238}U$, $^{207}Pb/^{235}U$, and $^{207}Pb/^{206}Pb$), offering an internal check on whether a mineral has behaved as a closed system with respect to the gain or loss of parent or daughter product. If the three ages are identical, then the mineral has behaved as a closed system and the ages are regarded as concordant. It has been known for some time that there is often a negative correlation between grain size and the amount of discordance (e.g., Silver and Deutsch, 1963) and a positive correlation between magnetic susceptibility and the amount of discordance (Silver, 1963). By selecting mineral fractions with slight differences in magnetic susceptibility or grain size, it is possible to generate a series of analyses that are co-linear on a concordia diagram ($^{206}Pb/^{238}U$ versus $^{207}Pb/^{235}U$). The best-fit line through the co-linear, discordant analyses (the discordia or mixing line) defines an upper and lower intercept which may have geologic significance. Clearly, for multi-stage systems, a discordia can be misinterpreted if viewed in terms of only two age stages.

Ion microprobe analysis can avoid this complication in multi-component populations, by analysing single grains. It has the additional benefit, since no chemical preparation is required, of not completely destroying the sample. Currently, however, access to such microprobes is restrictive and costly. The single microprobe analysis done in this investigation was performed using the Australian National University SHRIMP (Sensitive High Resolution Ion MicroProbe).

U/Pb results - All thermochronologic (U/Pb, Ar, FT) sample locations are summarised in figure 5.3. Details on analytical procedures and errors are presented in Appendix D. Analytical results are presented in Tables 5.3 and 5.4. Concordia diagrams of results are shown in figures 5.4, 5.5, and 5.6. Analytical results from other workers are reported for comparison, e.g., a sphene U/Pb age from J. Wooden (pers. comm., 1995), sample number JW89-140, and an unpublished zircon SHRIMP analysis of D. Foster (pers. comm., 1996), sample number SM95-10.

The ion microprobe results from VP94-129 are shown in figure 5.4. This biotite schist, near the north-central intrusive contact of the EWIC (Fig. 5.3), is associated with amphibolite and minor migmatite. It has a homogeneous population of zircon grains, in as much as they are uniformly small and euhedral, typical of high-grade metamorphic zircons. Several grains are concordant from 1.6 1.7 Ga, while the

Table 5.3 - U-Pb analytical data, conventional and ion-probe

Sample (fraction/grain.spot)	[U] ppm	[Pb] ppm	$^{207}Pb/^{235}U$	±2σ (%)	$^{206}Pb/^{238}U$	±2σ (%)	$^{207}Pb/^{206}Pb$	±2σ (%)	Age estimates (Ma) $^{207}Pb/^{235}U$	$^{206}Pb/^{238}U$	$^{207}Pb/^{206}Pb$	$^{206}Pb/^{204}Pb$
VP94-069												
zircon												
80-100 µm	433.1	56.75	1 7370	0.05	0.13084	0.03	0.09629	0.04	1022	793	1515	14498
100-130 µm	386.51	51.26	1.7572	0.04	0.13214	0.03	0.09645	0.02	1030	800	1557	12658
130-163 µm	370.3	51.1	1.8353	0.07	0.13690	0.06	0.09723	0.03	1058	827	1572	8000
>163 µm	349.9	50.27	1.9139	0.04	0.14183	0.03	0.09787	0.03	855	1086	1584	12048
VP94-069b												
monazite												
100-130 µm	1087	84.11	0.06271	0.72	0.00706	0.07	0.06440	0.66	62	45	755	123.2
130-163 µm	1154	82.11	0 05793	0.53	0.00678	0.07	0.06199	0.49	57	48	674	122.1
>163 µm	811	172.3	0.29247	0.14	0.02446	0.05	0.08674	0.12	261	156	1355	461.7
VP94-127												
zircon												
<100 µm	340.4	40.43	1.57076	0.07	0.11640	0.05	0.09787	0.04	959	710	1584	9050
>100 µm	273.4	37.23	1.78662	0.04	0.13211	0.03	0.09808	0.02	1041	800	1588	8330
VP94-127												
sphene												
	2.38	53.86	0.0193	5.9	0.002926	0.30	0 0484	5.6	19.4	18.8	91.3	23 1
VP94-138												
zircon												
63-80 µm	353 4	55 86	2.0616	0.03	0.15735	0.02	0.09502	0.02	1136	942	1528	6579
80-100 µm	318.8	50.6	2 0590	0.07	0.15701	0.03	0.09511	0.05	1135	940	1530	9000
100-130 µm	279.9	44.62	2 0579	0.06	0.15678	0.05	0.09520	0.01	1135	939	1532	6040
>130 µm	209.8	29.42	1.7901	0.10	0.13606	0.03	0.09542	0.09	1042	822	1536	4975
VP94-138												
monazite												
	594.7	105.0	0.1618	1.3	0.01782	0.13	0.0659	1.2	152	114	801	110 4
VP94-140a												
zircon												
<63 µm	245.7	7.9	0.33128	0.44	0.02970	0.06	0.08088	0.40	291	189	122	1324
63-80 µm	233.85	12.38	0.62035	0.14	0.05027	0.11	0.08951	0.08	490	316	141	3871
100-130 µm	196.1	21.19	1.3626	0.15	0.10293	0.04	0.09602	0.13	873	632	1548	5747
130-163 µm	195.4	22.2	1.4419	0.07	0.10875	0.04	0.09616	0.05	907	666	1551	6426
VP94-140a												
sphene												
	52 59	1.95	0.07270	1.1	0.01097	0.08	0.04808	1.1	71.3	70.3	103.1	42 4

TABLE 5.3 - con't.

Sample (fraction/grain.spot)	[U] ppm	[Th] ppm	[Pb] ppm	$^{207}Pb/^{235}U$	±1σ	$^{206}Pb/^{238}U$	±1σ	$^{207}Pb/^{206}Pb$	±1σ	Age estimates (Ma) $^{207}Pb/^{235}U$	$^{206}Pb/^{238}U$	$^{207}Pb/^{206}Pb$	$^{204}Pb/^{206}Pb$
VP94-129 (ion-probe)													
zircon													
1.1	1071	15	261	3.503	0.105	0.2575	0.0066	0.0987	0.0013	1528 ± 24	1477 ± 34	1599 ± 25	1.0*
2.1	533	93	135	3.495	0.090	0.2562	0.0062	0.0989	0.0006	1526 ± 20	1470 ± 32	1604 ± 10	2.4*
3.1	220	35	72	5.368	0.160	0.3281	0.0085	0.1187	0.0014	1880 ± 26	1829 ± 41	1936 ± 21	8.8*
4.1	1469	30	358	3.481	0.083	0.2573	0.0060	0.0981	0.0004	1523 ± 19	1476 ± 31	1589 ± 7	3.2*
5.1	1677	29	400	3.290	0.078	0.2522	0.0058	0.0946	0.0003	1479 ± 18	1450 ± 30	1521 ± 6	0.4*
6.1	326	198	104	4.477	0.175	0.2892	0.0088	0.1123	0.0024	1727 ± 32	1637 ± 44	1837 ± 39	2.8*
7.1	5559	607	1554	3.917	0.090	0.2864	0.0065	0.0992	0.0002	1617 ± 19	1624 ± 33	1609 ± 3	-
8.1	2054	64	496	3.378	0.080	0.2538	0.0059	0.0965	0.0003	1499 ± 19	1458 ± 30	1558 ± 6	1.1*
9.1	630	190	163	3.065	0.088	0.2575	0.0069	0.0863	0.0007	1424 ± 22	1477 ± 35	1346 ± 15	3.4*
10.1	2923	56	962	5.003	0.353	0.3448	0.0163	0.1052	0.0049	1820 ± 60	1910 ± 78	1719 ± 89	-
11.1	749	111	224	4.321	0.471	0.3038	0.0190	0.1032	0.0084	1697 ± 90	1710 ± 94	1682 ± 159	5.6*

Note: Conventional analyses reported at 2σ precision, whereas ion-probe data is reported at 1σ. Ion-probe zrn U/Pb analyses were performed on the SHRIMP II (Sensitive High-Resolution Ion Micro-Probe) instrument at the Australian National University, Canberra, using previously described analytical techniques (Compston et al., 1984; Williams and Claesson, 1987). Ion-probe analyses are denoted by grain number.spot number. Errors in age estimates quoted at the 1σ level. Conventional data for zrn, mnz, and spn was obtained following techniques described by Whitehouse et al., 1992, mineral size fractions given in μm and only non-magnetic fractions were used. All ages calculated using the decay constants of Steiger and Jäger (1977).

* 204/206 ratio $x10^{-5}$ (for ion probe data only).

Table 5.4 - Initial lead analytical data

Sample	206/204	207/204	208/204
VP94-069b	17.715	15.538	38.681
VP94-127	18.532	15.599	39.069
VP94-138	17.665	15.534	38.279
VP94-140a	17.510	15.505	38.404
VP94-140b	18.304	15.585	39.054
VP94-141	17.910	15.560	38.896
VP94-142	17.675	15.548	38.762
VP94-159	18.268	15.605	39.053
VP94-160	18.013	15.589	39.021

Note: Initial lead ratios obtained following techniques described by Whitehouse et al., 1992

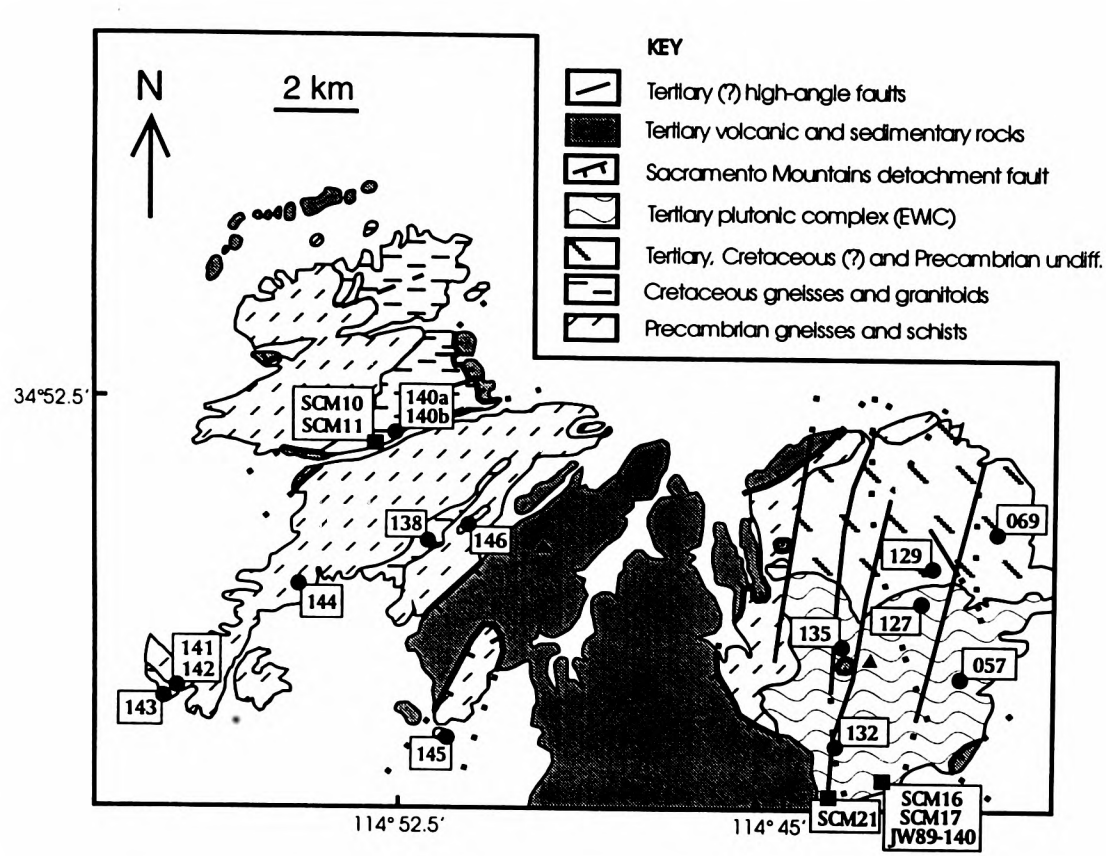
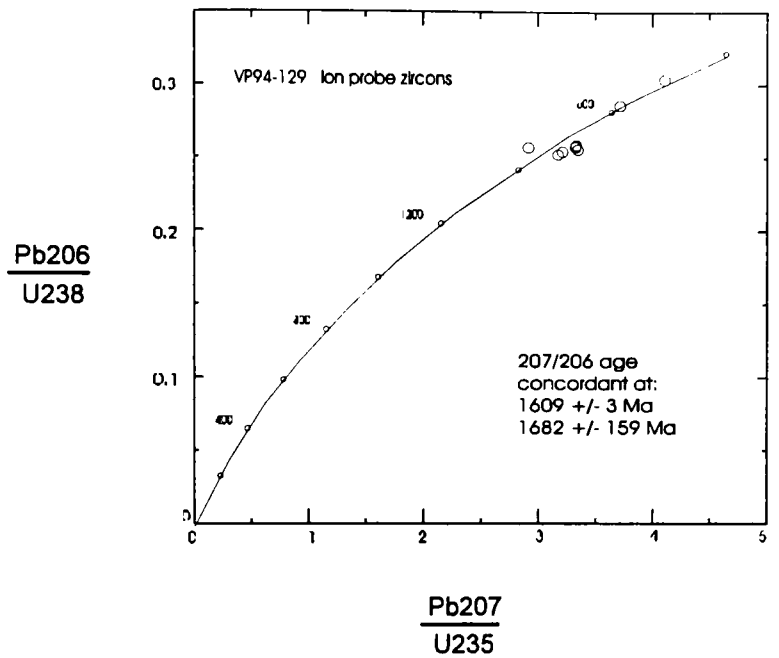


Figure 5.3 - Thermochronologic sample locations (U/Pb, argon, and fission track), sample numbers, and simplified geology. Circles represent samples in this study, squares from published and unpublished data of others (refer to text). Triangles identify local peaks. Geology in NW after Argent (1996).



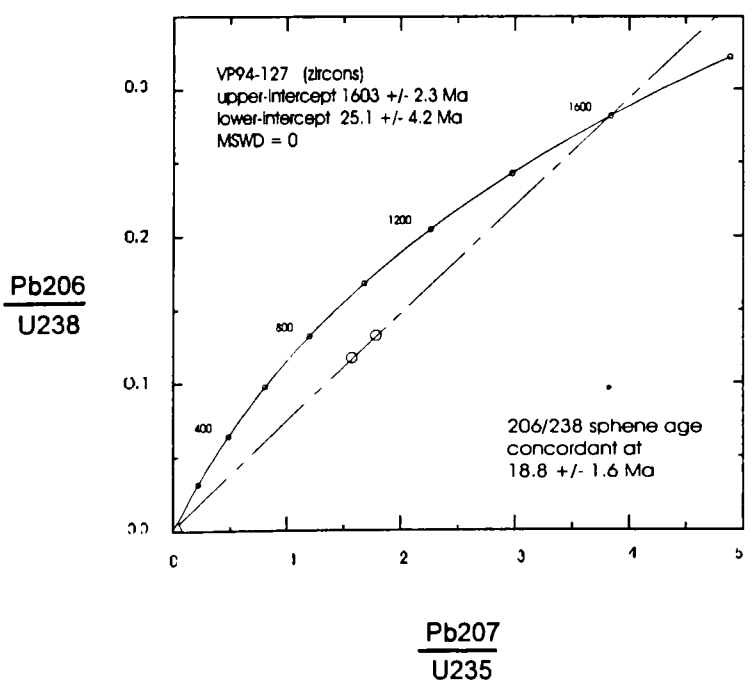


Figure 5.4 - U/Pb concordia diagram of VP94-129 (ion probe, zircon) and VP94-127 (zircon and sphene). Zircon represented by circles and sphene by triangles. Only zircon data used in fitting discordia.

remainder show 5-10% discordance, possibly associated with high temperatures from the amphibolite-grade metamorphic event or from contact metamorphism associated with the emplacement of the EWIC. The variation in concordant ages from 1.6 to 1.7 Ga likely reflects heterogeneity in the source rock, preserved in spite of the amphibolite grade metamorphism.

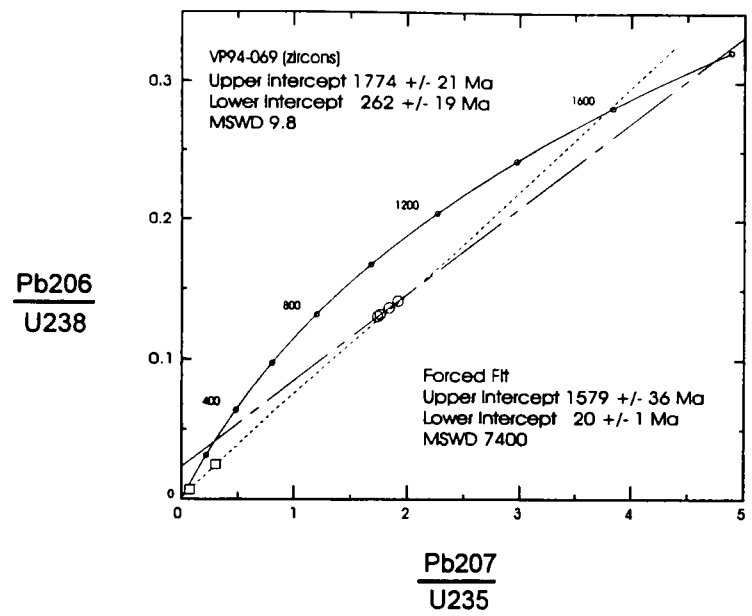
VP94-127 is from a medium grained, moderately deformed (mylonitic), granodioritic phase of the EWIC (Fig. 5.3), adjacent to the biotite schist sample (VP94-129). In VP94-127, the zircon population is varied in size, colour (clear, smoky, and pink), and shape (euhedral to subhedral, variable aspect ratio), suggesting that inheritance has occurred. The zircon discordia is defined by two points which have a limited spread in U/Pb composition, resulting in imprecise age information (Fig. 5.4); nevertheless, a Middle Proterozic upper intercept (~1.6 Ga) and a lower intercept of ~25 Ma can be defined. Given the range of zircon grains present and visible xenoliths of biotite schist in the field (of known Proterozoic age, see VP94-129 above), this data is interpreted to reflect simple binary mixing between an inherited Pb component (resorbed from Proterozoic country rock) and a younger, non-inherited Pb component from the EWIC granodioritic magma. Thus the upper intercept is in agreement with the known age of resorbed material and the lower intercept suggests an Oligocene/Miocene age for the EWIC. Sphene data from VP94-127 is concordant (Fig. 5.4), and yields a $^{206}Pb/^{238}U$ age of 18.8 ± 1.6 Ma. This age is in good agreement with unpublished data from the granodiorite at the quarry site on Eagle Pass road (J. Wooden, pers. comm., 1995), where a concordant sphene age of 19.2 ± 0.6 Ma was obtained (sample JW89-140). Combining these two sphene data, the best age for the granodiorite at the closure temperature for sphene (~600°C, see Table 5.1) is calculated to be 19.0 Ma ± 0.6 (2σ). Viewed in conjunction with this sphene data, it would seem that the lower intercept of the zircon discordia, though poorly constrained, is not unreasonable, and suggests a crystallisation age for the granodiorite of about 20 Ma. This interpretation is consistent with i) a bimodal population of Middle Proterozoic (1.35 Ga) and Miocene (~19 Ma) zircons from the granodiorite at the quarry site on Eagle Pass road (unpublished data of D. Foster, pers. comm., 1996: concordant zircon SHRIMP analyses, sample SM95-10), and with ii) the igneous origin of the EWIC having a solidus temperature of 680°C (see *Thermobarometry* above).

Sample VP94-069b is from a coarse grained, mylonitic leucogranite which is thought to represent the leucocratic phase of the EWIC. The sample, however, is not from within the EWIC "proper", which is

dominantly in the southern part of the range (Fig 5.3). Figure 5.5 shows the concordia diagram for the zircon and monazite populations for this sample. Both data are discordant. The zircon upper intercept is ~1.8 Ga and the lower intercept is ~260 Ma. The lower intercept, having no known geologic significance in this region, appears unreasonable and may be a function of the very narrow range of U/Pb composition exhibited by these zircon populations. Consequently, the discordia was forced through a 20 Ma lower intercept and recalculated. The 20 Ma intercept is used because it is a known thermal event, the time of EWIC intrusion. The upper intercept resulting from the forced fit agrees well with the known age of surrounding country rocks (1.6-1.7 Ga), though the MSWD is poor.

Monazite results from this sample (also shown in Fig. 5.5) have an upper intercept of ~1.5 - 1.6 Ga and a lower intercept of 29 ± 7.5 Ma. The monazite data are somewhat poorly constrained because the discordia is essentially a two-point line. In two-stage scenarios, these data can be interpreted as i) a mixing line between an inherited Pb component (from Proterozic country rock) and a younger, non-inherited Pb component (the ~20 Ma EWIC), or ii) reworking of Proterozic crustal material during a high-grade(amphibolite) event in the Oligocene/Miocene. There are no known high temperature, thermal events (igneous intrusion/metamorphism) of Oligocene age known in this region, but there is the intrusion of the Miocene EWIC, as well as other Miocene intrusive and extrusive rocks, in the immediate vicinity (Howard et al., 1996; Nakata et al., 1990; Nielson and Beratan, 1990; Spencer, 1985, Spencer, 1984; Spencer and Turner, 1983; Davis et al., 1982, 1980). Consequently, the former interpretation is favoured. Recent studies have shown that monazite, similar to zircon, can be inherited or xenocrystic (e.g., Copeland et al., 1988; Parrish, 1990; Harrison et al., 1995). The general agreement between the zircon (forced fit) and monazite data from this leucogranite suggests an upper intercept of ~1.6 Ga and a lower intercept as young as ~22 Ma for this sample. This data is consistent with that from VP94-127 and suggests a temporal relationship with the main body of EWIC to the south. (An additional sample of leucogranite was collected in an attempt to increase the compositional range and, consequently, improve the age statistics, but it proved to be monazite-free.)

In figure 5.6, the concordia diagram for samples VP94-138 (zircon and monazite) and VP94-140a (zircon and sphene) are presented. Both of these samples are from the northwest Sacramento Mountains (Fig. 5.3). VP94-138 is a sample of a medium grained, undeformed two-mica granite and was collected



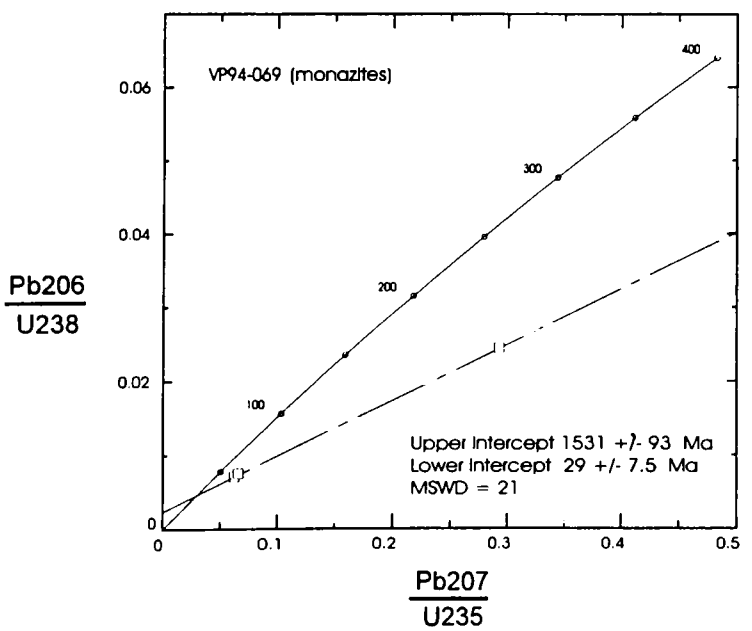
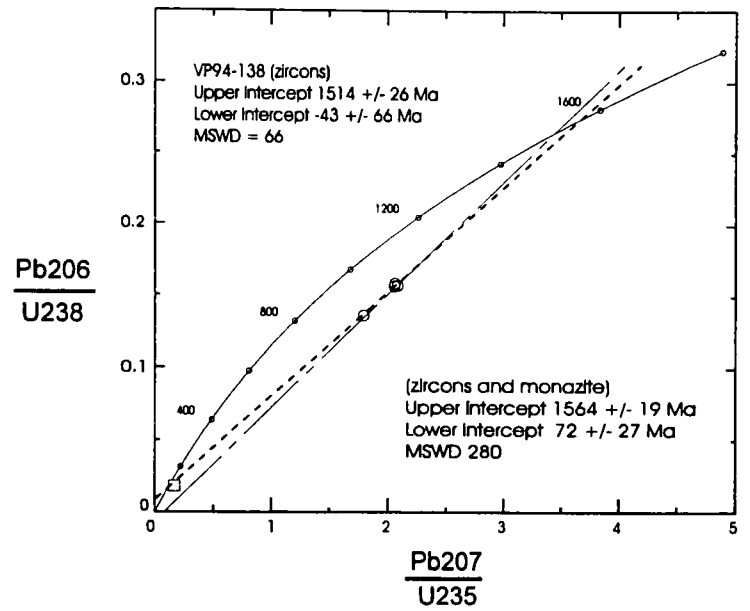


Figure 5.5 - U/Pb concordia diagram of VP94-069b (zircon and monazite). Zircon represented by circles. Fine dashed line represents forced fit; monazites represented by squares and shown only for reference on zircon plot (not used in line-fits).



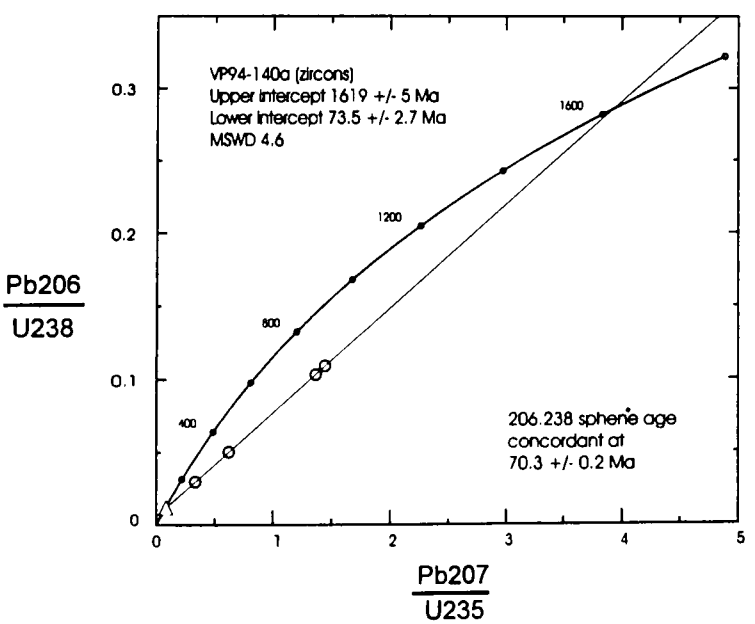


Figure 5.6 - U/Pb concordia diagram of VP94-138 (zircon and monazite) and VP94-140a (zircon and sphene). Zircon represented by circles, monazite by a square, and sphene by a triangle. Fine dashed line is fit using zircon and monazite. Otherwise, only zircon is used in the line fit.

because intrusive relationships suggested it was Cretaceous or younger. The zircon population varied in size, shape, and colour, suggesting that inheritance was likely. The zircon data are discordant, defining essentially a two-point discordia with an upper intercept of 1514 ± 26 Ma. The lower intercept is -43 ± 66 Ma. These data define a limited range in compositional space, thus the relatively poor line-fit. Only one monazite population was analysed (the other was lost during column chemistry) and if it is combined with the zircon data, then an upper intercept of 1564 ± 19 Ma and a lower intercept of 72 ± 27 Ma are obtained. The data suggest i) the presence of a large component of inherited Pb (xenocrystic mid-Proterozoic zircon), or ii) significant, high temperature reworking of a mid-Proterozoic terrane. The lack of deformation in this granite favours the former interpretation. The lower intercept of the combined data supports a Late Cretaceous age for this pluton. This is consistent with the presence of Cretaceous plutonism throughout the region which was derived, in part, by the partial melting/assimilation of "continental" country rocks (Anderson and Cullers, 1990; John and Wooden, 1990; Miller et al., 1990). A Late Cretaceous age of ~72 Ma is supported by $^{40}Ar/^{39}Ar$ (see following section).

The results from VP94-140a are also discordant and are shown in figure 5.6. This is a medium to coarse grained, sphene-bearing granodioritic gneiss sample of unknown age, in sharp contact with Precambrian augen gneiss and intruded by an undeformed Late Cretaceous two-mica granite (VP94-138 above). The zircon population varied in size, shape, and colour, suggesting that inheritance was likely. The zircon data define a discordia with an upper intercept of 1619 ± 5 Ma and a lower intercept of 73.5 ± 2.7 Ma. Sphene is concordant at 70.3 ± 2.7 Ma. Thus this sample appears to represent i) syntectonic Late Cretaceous magmatism with a large component of inherited Pb (mid-Proterozoic zircons), or ii) Proterozoic crust which experienced significant high-temperature reworking at ~70 Ma. Argent (1996), using structural arguments and rock fabrics, identified three episodes of deformation in the northwest Sacramento Mountains: an older amphibolite facies deformation, Cretaceous greenschist facies deformation, and Miocene lower-greenschist deformation. Both of the older fabrics are present in this unit. Cretaceous greenschist to amphibolite grade metamorphism, resulting from Laramide compression (thrusting and magmatism), is well documented in the region (Foster et al., 1992; John and Mukasa, 1990; Burchfield and Davis, 1981). This information is consistent with the interpretation that this gneiss represents older crust

reworked under amphibolite-grade conditions in the Cretaceous, and intruded by post-kinematic Late Cretaceous plutons.

5.4 Medium-temperature history

$^{40}Ar/^{39}Ar$ technique - Information about the thermal history of these samples can be inferred from the form of age spectra (see McDougall and Harrison, 1988, for a review). In principle, the $^{40}Ar/^{39}Ar$ technique is capable of distinguishing between disturbed and undisturbed samples, identifying the presence of excess argon, and of recovering the crystallisation age or reheating age of a sample that has experienced a thermal or chemical perturbation if argon loss is less than 15-20% (Harrison, 1983). Age gradients revealed by step-heating analysis of hornblende may result from slow cooling, partial argon loss due to reheating, or from the presence of excess radiogenic argon. Samples that yield flat age spectra, referred to as "plateaus", have traditionally been regarded as undisturbed since cooling (for example, Fleck et al., 1977). In some cases, however, these plateau may result from experimental artefacts such as homogenisation of gas in minerals that are unstable in the vacuum furnace (Harrison et al., 1985; Gaber et al., 1985). Non-ideal forms such as saddle-shaped spectra (Lanphere and Dalrymple, 1976) and large-domain-trapped-argon-effect spectra (Foster et al., 1990b) result from incorporation of trapped argon with a non-atmospheric composition. Isochron analysis is commonly an effective method to reveal both the trapped $^{40}Ar/^{39}Ar$ and the ages of samples so affected (Roddick, 1978; Heizler and Harrison, 1988). Isochron analyses have been performed on samples analysed with the incremental heating technique, but were not feasible for samples analysed with the laser (too few data points). In the case of laser analyses, concordant steps from replicate analyses were used to generate weighted mean ages, or maximum/minimum ages have been assigned in the case of disturbed spectra. Generally, greater confidence can be placed in plateau and isochron ages than in weighted mean and minimum/maximum ages. Closure temperatures are as specified in Tables 5.1 and 5.5.

$^{40}Ar/^{39}Ar$ results A discussion of the analytical techniques, uncertainties, etc., is presented in Appendix D. The release spectra data table and release spectra/isochron plots are also presented in Appendix D (Table D2 and D3, respectively). Argon analytical results are summarised in Table 5.5 and Figs. 5.7 and 5.8. The overall quality of the data is good, in as much as it is possible to determine a time/age associated with each mineral's T_c for 80% of the analyses. Samples in the northeast Sacramento Mountains are predominantly from a medium grained, granodioritic phase of the EWIC. The two

exceptions are VP94-129, which is a sample of Precambrian biotite schist, and VP94-069, which is a coarse-grained, mylonitic leucogranite thought to be correlative with the leucocratic phase of the main EWIC body to the south. Samples from the northwest Sacramento Mountains are predominantly from medium to coarse grained Precambrian and Cretaceous gneisses, and medium grained, undeformed, granitic intrusions. One sample (VP94-140b) is from a later cross-cutting granodioritic dike, part of the Miocene dike swarm in the region (Argent, 1996; Spencer and Turner, 1983) and possibly correlative with the EWIC in the NE. Results from other workers are reported for comparison, e.g., hornblende and biotite $^{40}Ar/^{39}Ar$ data from Foster et al. (1990), sample numbers SCM10, SCM11, SCM16, and SCM17.

Hornblende samples from the northeast Sacramento Mountains were analysed by the incremental heating technique and the results are summarised in Table 5.5 and in figure 5.7 (refer to Fig. 5.3 for sample locations). These samples yield isochron or plateau ages of 20 -21 Ma (Appendix D, Table D3), with all

Table 5.5 - Summary of $^{40}Ar/^{39}Ar$ analytical results

Sample No.	Mineral separated	Age (Ma) ± 2σ	Distance* (km)	Closure T† (°C)	Type§
Northeast Sacramento Mountains					
VP94-057b	hornblende	20 1 ± 0.5	16.5	550-500	i(4)
VP94-069b	biotite	na	20.3	345-310	na
VP94-127	hornblende	20 6 ± 0 5	16.75	550-500	i(4)
	biotite	14.0 ± 0.6	16.75	345-310	w(5)
VP94-129#	biotite	13.0 ± 0.2	17 0	345-310	w(4)
VP94-132	hornblende	21.3 ± 0 4	12.5	550-500	p(5)
	biotite	14 2 ± 0.4	12.5	345-310	w(3)
VP94-135	hornblende	20.8 ± 0.8	14.25	550-500	i(5)
	biotite	13 4 ± 1 4	14 25	345-310	m(1)
Northwest Sacramento Mountains					
VP94-138	biotite	16 4 ± 0.3	8 7	345-310	p(8)
VP94-140a	hornblende	≤69 0	7.6	550-500	m(2)
	biotite	~15?	7.6	345-310	tf(2)
VP94-140b	hornblende	≤22.6	7.6	550-500	m(1)
VP94-141	biotite	70 2 ± 1.0	0.5	345-310	w(3)
VP94-142	biotite	70.6 ± 0 6	0 5	345-310	w(3)
VP94-143	biotite	68.2 ± 0.7	0.4	345-310	w(3)
VP94-144	hornblende	≥77	4 3	550-500	m(1)
	biotite	~70?	4 3	345-310	na
VP94-146	hornblende	≤62.8	10.3	550-500	m(1)
	biotite	25.8 ± 0.6	10.3	345-310	w(3)

Note: See Appendix E, Table E1, for release spectra data, and Table E2, for plots and isochrons.

* Distance down-dip from an arbitrary reference line (the NW-SE steel tower transmission line road), perpendicular to the transport direction.

†Closure temperatures from Harrison (1981) and Harrison et al. (1985), using cooling rate of 70-100°C/Ma (Pease et al., 1995).

§ Type of age where p = plateau age, i = isochron age, w = weighted mean age, m = maximum or minimum age; tf = total fusion age, with the number of steps used in parentheses; na, not applicable.

Sample from Precambrian biotite schist at the intrusive contact.

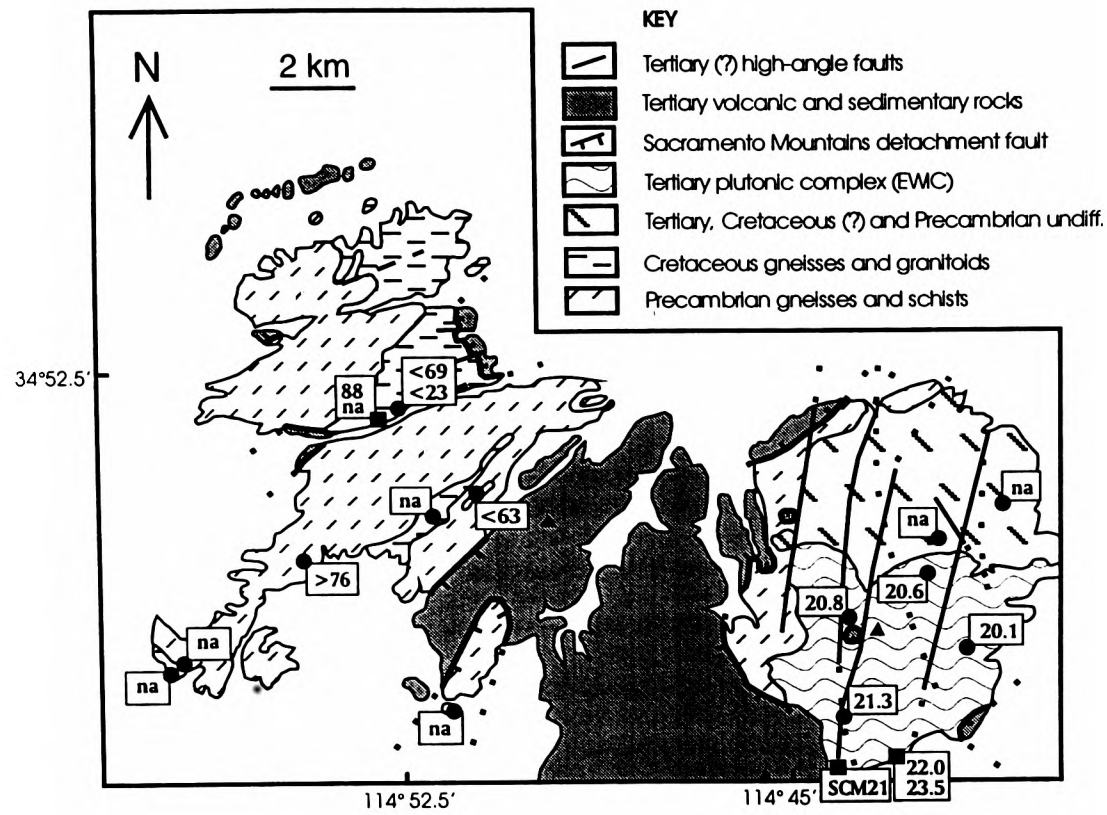


Figure 5.7 - Hornblende 40Ar/39Ar ages (Ma). Circles represent data from this study, squares published and unpublished data of others (refer to text). Not applicable (na) shown where the mineral is not present in the sample or age data is uninterpretable.

samples displaying saddle-shaped (concave) spectra. Isochron analysis of VP94-057b indicates that the sample contains excess radiogenic argon ($^{40}Ar/^{36}Ar$ intercept ~330), which may explain the spectra shape (Lanphere and Dalrymple, 1976). The surrounding Precambrian country rock provides a likely source for this older, non-atmospheric component of ^{40}Ar. Biotite samples from this region (all analysed by the laser fusion technique) display more irregular degassing patterns, with some flat spectra (VP94-127 and VP94-132), as well as irregular spectra (VP94-069b, VP94-129, and VP94-135). Biotite results are summarised in Table 5.5 and presented in figure 5.8. VP94-069b is the only uninterpretable sample and the remaining biotite ages are similar at 13-14 Ma.

Hornblende samples from the northwest Sacramento Mountains were all analysed by the laser fusion technique and display concave and convex spectra (Appendix D, Table D3). Where replicate analyses show reproducibility, data have been averaged to produce weighted mean ages. In the case of curved spectra, maximum or minimum ages assigned on the basis of the shape of the release spectra, i.e.- where the concave curve of saddle-shaped spectra result from the presence of excess argon, maximum ages are derived from the curve minimum; where the convex curve of release spectra result from slow cooling or argon loss, minimum ages are derived from the curve maximum. The resulting ages from the northwest vary, from ~50-80 Ma (Table 5.5 and Fig. 5.7). Biotite samples from this region (all analysed by the laser fusion technique) display degassing patterns similar to those from the northeast, with flat and variable release spectra. Biotite ages range from ~15-75 Ma (Table 5.5 and Fig. 5.8). Replicate analyses of sample VP94-144 (biotite) did not produce the same results (within 2σ errors). The hornblende separate from this sample yields an age of $\geq$77 Ma, has a release curve indicative of slow cooling or argon loss, and suggests that, because of the lower T_c associated with biotite, the biotite age should be less than 77 Ma. Therefore, an imprecise but reasonable estimate for this biotite age is 65-75 Ma and this is supported by one of the analyses. A younging trend to the NE is not well-defined in the hornblende ages from the northwest. The biotite ages in the northwest Sacramento Mountains, however, show a well-defined younging in the direction of tectonic transport (Figs. 5.7 and 5.8), with a sharp transition between Late Cretaceous ages and Tertiary (mostly Miocene) ages.

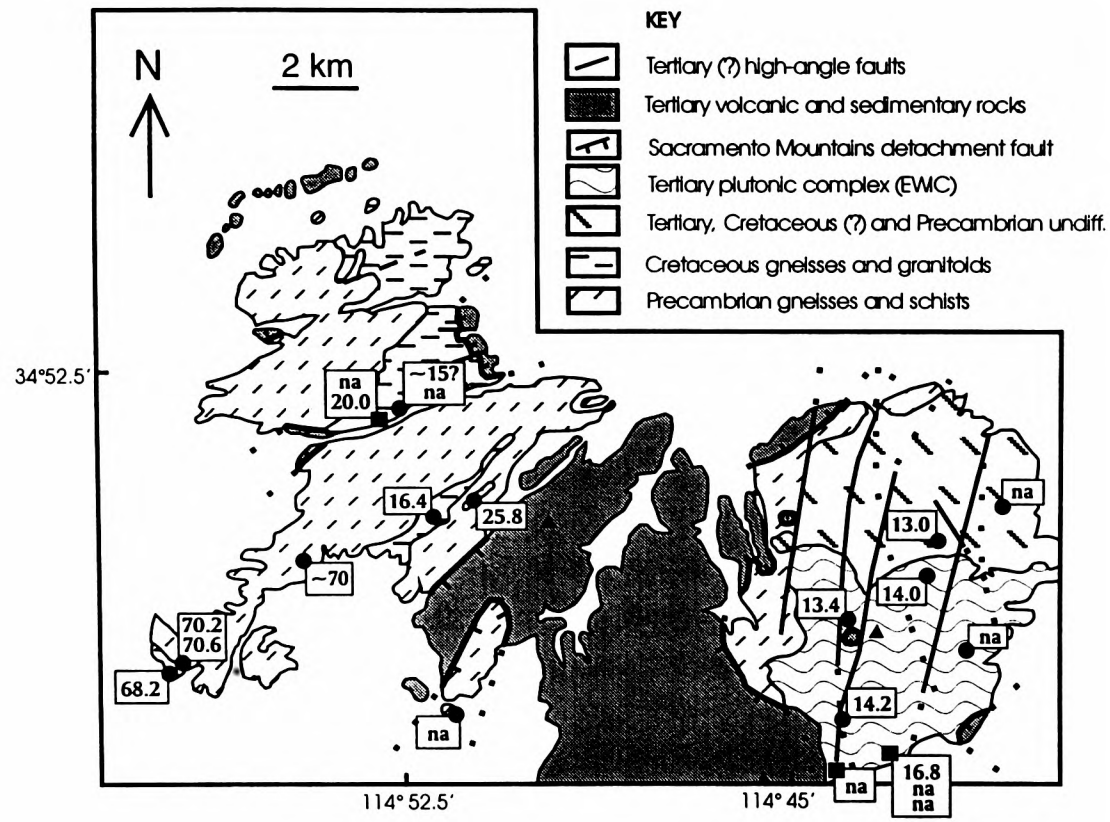


Figure 5.8 - Biotite 40Ar/39Ar ages (Ma). Circles represent samples from this study, squares published and unpublished data of of others (refer to text). Not applicable (na) shown where the mineral is not present in the sample or age data is uninterpretable.

5.5 Low-temperature history

Fission track technique Fission track dating of zircon and apatite provide a measure of rock thermal histories below about 260°C. This method relies on the temperature-dependent annealing of fission tracks that results in complete erasure of tracks in zircon and apatite at temperatures of ~240-300°C and ~60-120°C, respectively, for 10^6 to 10^7 year time scales (Naeser, 1979; Green et al., 1989; Brandon and Vance, 1992; Yamada et al., 1995). Below these temperatures, track annealing rates decrease progressively with lower temperature. The temperature interval bounded by the point of total annealing and the point of effective track stability where annealing occurs at very slow rates is known as the partial annealing zone, PAZ, e.g., Fitzgerald and Gleadow (1990). This interval for common compositions of apatite spans temperatures of ~100-50°C, while that for zircon is less well constrained at ~260-175°C (see summary in Brandon and Vance, 1995). The temperatures recorded by apparent zircon and apatite ages are a function of the cooling rate through, and the subsequent time-temperature path within, the PAZ.

Fission track results Fission track results are summarised in Table 5.6. A discussion of the analytical techniques, uncertainties, etc., is presented in Appendix D. The counting statistics for each sample are also presented in Appendix D (Table D4). The overall quality of the data is good, in as much as it is possible to determine the relative time associated with these samples passing through the closure temperatures of the respective minerals. Confined track lengths in these apatite grains are generally around 14 ± 1 (1σ) microns (see Appendix D, Table D4), providing some degree of confidence that these samples have not resided in the PAZ for a significant period of time and that these dates, in spite of the relative dispersion in the data-set, reflect geologically meaningful ages. Analytical results from other workers are reported for comparison, e.g., apatite FT data from Foster et al. (1991) and pers. comm. (1996), sample numbers SCM11 and SCM21.

The three zircon FT dates from the northeast Sacramento Mountains can be regarded as similar at ~18 Ma (within 2σ error). There are too few data to determine whether a correlation exists between age and geographic distribution, i.e.- with the tectonic transport direction (Fig. 5.9). Apatite dates in the northeast Sacramento Mountains are similar, having a mean Miocene age of 17.2 ± 1.6 Ma (within 2σ error) and no correlation between age and geographic distribution (Fig. 5.10).

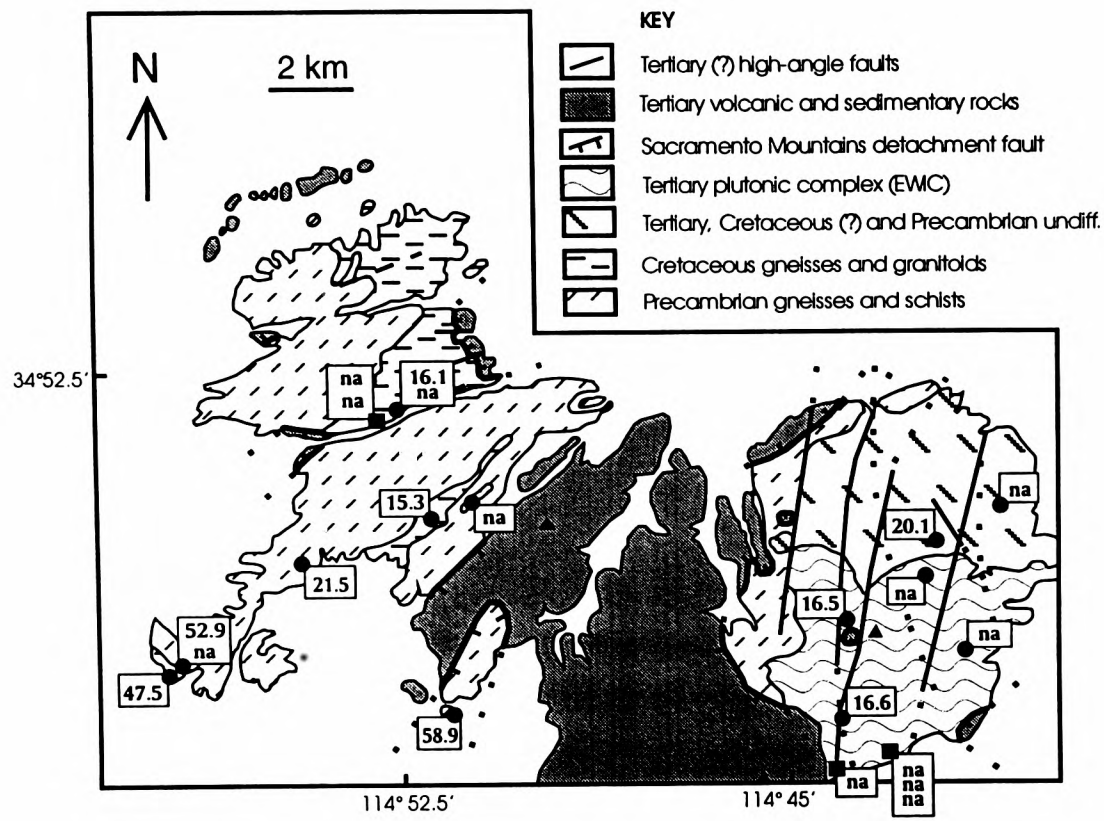


Figure 5.9 - Zircon fission track ages. Circles represent samples in this study, squares published and unpublished data of others (refer to text). Not applicable (na) shown where the mineral is not present in the sample or age data is uninterpretable.

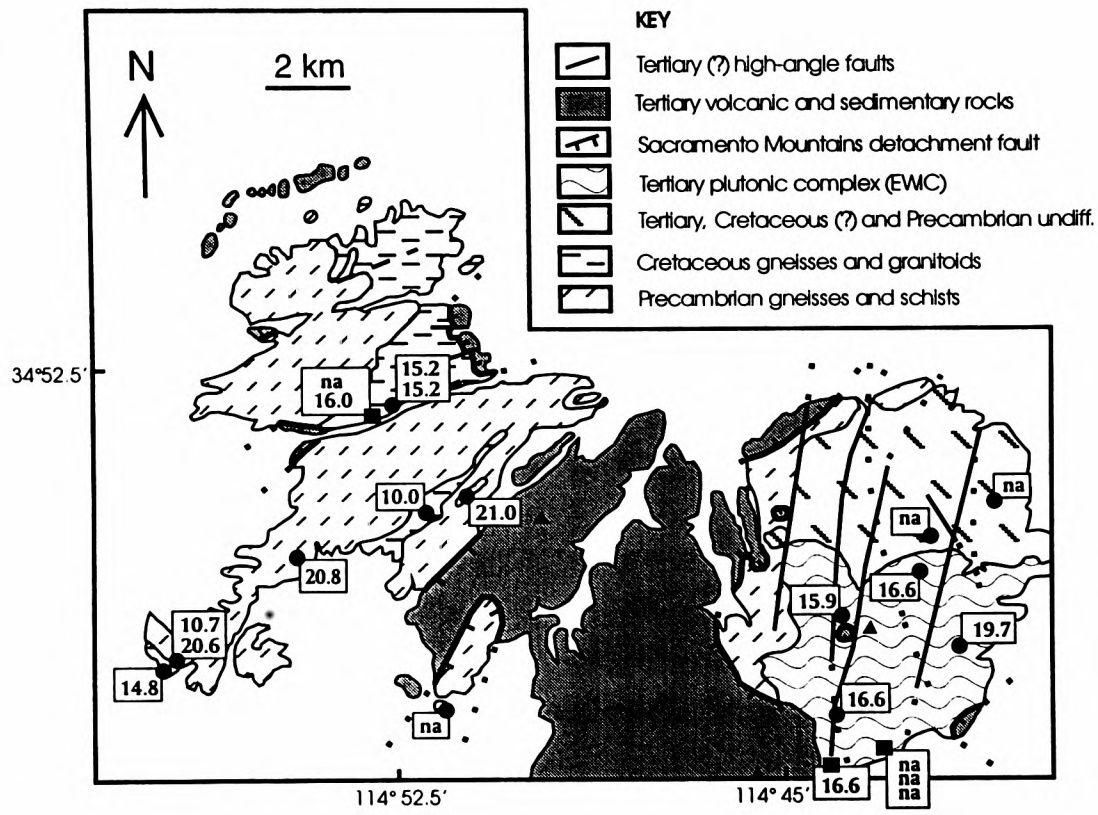


Figure 5.10 - Apatite fission track ages. Circles represent samples in this study, squares published and unpublished data of others (refer to text). Not applicable (na) shown where the mineral is not present in the sample or age data is uninterpretable.

Table 5.6 - Summary of fission track analytical results

Sample No.	Mineral separated	Age (Ma)§ ± 2σ	Distance* (km)	Elevation (m)	Closure† T (°C)
Northeast Sacramento Mountains					
VP94-057b	apatite	19.7 ± 3.3	16.5	583	~100
VP94-127	apatite	16.6 ± 2.7	16.75	802	~100
VP94-129#	zircon	20 1 ± 2.2	17 0	700	~200
VP94-132	zircon	16.6 ± 2.0	12.5	729	~200
	apatite	16 6 ± 3.7	12.5	729	~100
VP94-135	zircon	16.5 ± 2 2	14.25	802	~200
	apatite	15 9 ± 3.5	14.25	802	~100
Northwest Sacramento Mountains					
VP94-138	zircon	15.3 ± 1.3	8 7	775	~200
	apatite	10 0 ± 1.8	8.7	775	~100
VP94-140a	zircon	16.1 ± 1.5	7.6	775	~200
	apatite	15.2 ± 2.5	7.6	780	~100
VP94-140b	apatite	15.2 ± 2.4	7.6	780	~100
VP94-141	zircon	52.9 ± 6.5	0.5	655	~200
	apatite	10.7 ± 3.1	0.5	655	~100
VP94-142	apatite	20.6 ± 6.0	0.5	655	~100
VP94-143	zircon	47.5 ± 6.5	0.4	675	~200
	apatite	14.8 ± 2.0	0.4	675	~100
VP94-144	zircon	21 5 ± 2.9	4 3	750	~200
	apatite	20.8 ± 3.5	4 3	750	~100
VP94-145	zircon	58.9 ± 11.3	7.0	750	~200
VP94-146	apatite	21.0 ± 3.7	10 3	690	~100

Note: See Appendix E, Table E4 for counting statistics associated with each analysis.

§ Pooled ages are quoted; failure of the chi-squared test may indicate non-homogeneous populations, in which case the central age is quoted.

* Distance down-dip from an arbitrary reference line (the NW-SE steel tower transmission line road), perpendicular to the transport direction.

†Closure temperatures from Naeser (1979), Green et al. (1989), Brandon and Vance (1992), and Yamada et al. (1995)

Sample from Precambrian biotite schist at the intrusive contact.

Zircon FT dates from the northwest Sacramento Mountains show younging in the tectonic transport direction (to the NE). Ages vary systematically from ~50 Ma to 15 Ma, with a sharp transition between the Eocene and Miocene ages (Fig. 5.9). Some of the zircon FT ages in the northwest Sacramento Mountains have poor analytical precision, i.e.- VP94-145 (Precambrian upper-plate basement), likely a result of the samples being strongly coloured. The zircons in this investigation display a variety of colours, from clear to violet, with the most coloured varieties being from the older samples. It is difficult to count fission tracks accurately in darker, more coloured grains because this opacity obscures the tracks and dislocations. This problem is further compounded because the older (more coloured) zircons also tend to have higher uranium contents, which is likely to result in more lattice dislocations, which are more difficult to distinguish from fission tracks in coloured grains, and so on... Any bias introduced from zircon colouration is non-

systematic. Grain opacity, in making tracks less visible, may reduce the number of counted tracks, resulting in younger ages. This effect, however, would be offset by the increase in dislocations associated with the higher U contents generally present in strongly coloured grains, which are more likely to be counted as tracks, thus increasing the FT age. The overall result is to produce rather large experimental errors.

The apatite FT data from the northwest Sacramento Mountains, unlike the zircon FT results, define no correlation between age and geographic distribution. Only Miocene ages are recorded, ranging from ~21-10 Ma (Fig. 5.10). Dispersion within the apatite FT data from the northwest Sacramento Mountains is in excess of experimental error. Furthermore, the variation in age displayed at a single location is geologically untenable, e.g, VP94-141 and VP94-142 (both samples of Precambrian metasediment). Consequently, it was expedient to evaluate possible mechanisms to explain this disparity.

As previously stated, FT retention is a function of time, temperature, and composition. FT lengths of ~14 μm suggest that these samples have not been above apatite T_c since the Miocene, therefore mineral composition was considered. FTs in Cl-rich apatites are more resistant to track annealing (shortening) than are fluorine-rich apatites (O'Sullivan and Parrish, 1995; Crowley et al., 1991; Gleadow and Duddy, 1981). F-rich and Cl-poor apatites, being more susceptible to track annealing, may have less tracks, producing systematically younger FT ages. The critical Cl content below which tracks in apatites will anneal relatively quickly appears to be ~0.2-0.3 wt % (P. O'Sullivan, pers. comm., 1996).

Using excess material after FT analysis, eight samples were analysed using the electron microprobe (see Appendix B for a discussion of the electron microprobe analytical technique and associated errors). Electron microprobe apatite analyses are presented in Appendix B, Tables B4 and B5. The results are summarised in figure 5.11, where 60% of the apatites analysed are shown to be F-apatites and the remainder are Cl-apatites. Ideally a correlation between age and Cl-content would be expected in figure 5.11, if track annealing were occurring as a function of Cl-content. The amount of Cl in these apatites, however, is at or below the detection limits of the microprobe (given the operating conditions used, see Appendix B) and such a correlation is not manifest. Consequently, it can only be said that it is probable that the range in apatite compositions contributes to the unexpected variation in apatite FT ages.

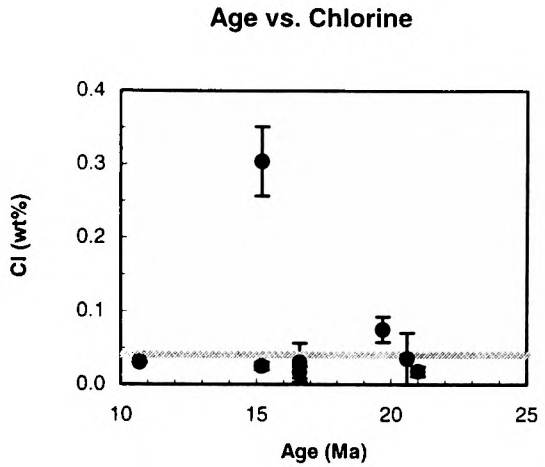


Figure 5.11 Apatite compositions (with 2σ errors). Shaded line denotes the lower limit of Cl-rich apatites which are "age retentive"; below ~0.4 wt.% Cl, apatites become susceptible to track annealing.

5.6 Discussion

The age and thermal evolution of the northern Sacramento Mountains is summarised in figures 5.12 and 5.13. Both figures show the well-defined, contrasting thermal history of the northeast and northwest regions of the Sacramento Mountains. In figure 5.12, age data are plotted against distance down-dip, where distance down-dip is the distance measured along a trend of N60E (the tectonic transport direction) from a fixed, arbitrary point on the power-line road, south of I-40, in the NW Sacramento Mountains. In figure 5.13, time and mineral closure temperature are plotted for each of the analyses presented in this chapter.

Northwest Sacramento Mountains - Younging in the tectonic transport direction is obvious in the northwest Sacramento Mountains, notably in the biotite and zircon (FT) data (Fig. 5.12). This is consistent with normal faulting (see Chapter 6). This region also has a pronounced Cretaceous thermal signature (Figs. 5.12 and 5.13), which may be associated with Late Cretaceous plutonism and/or derive from earlier metamorphism and crustal thickening associated with Cretaceous thrusting. Cretaceous greenschist to amphibolite grade metamorphism, resulting from Laramide compression (thrusting and magmatism), is well documented in the region (Foster et al., 1992; John and Mukasa, 1990; Burchfield and Davis, 1981). Argent (1996) identified a regional amphibolite-facies deformational event thoughout much of the

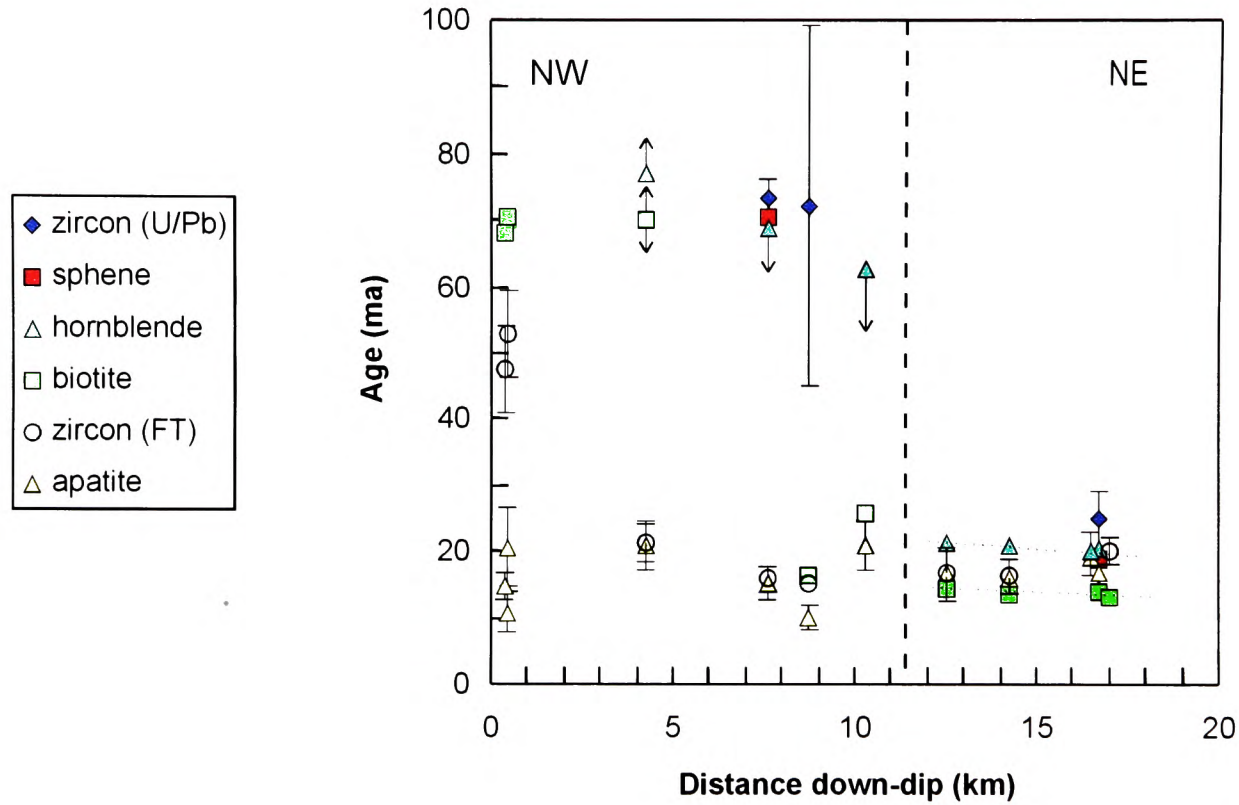


Figure 5.12 - Age plotted against distance down-dip. Samples from both the NE and NW show younging to the NE, in the down-dip, down-section direction. Age error bars are 2 sigma; arrows indicate maximum or minimum, or imprecise ages; symbols may be larger than error bars. Data from the Miocene dike and upper-plate basement in the NW are not included.

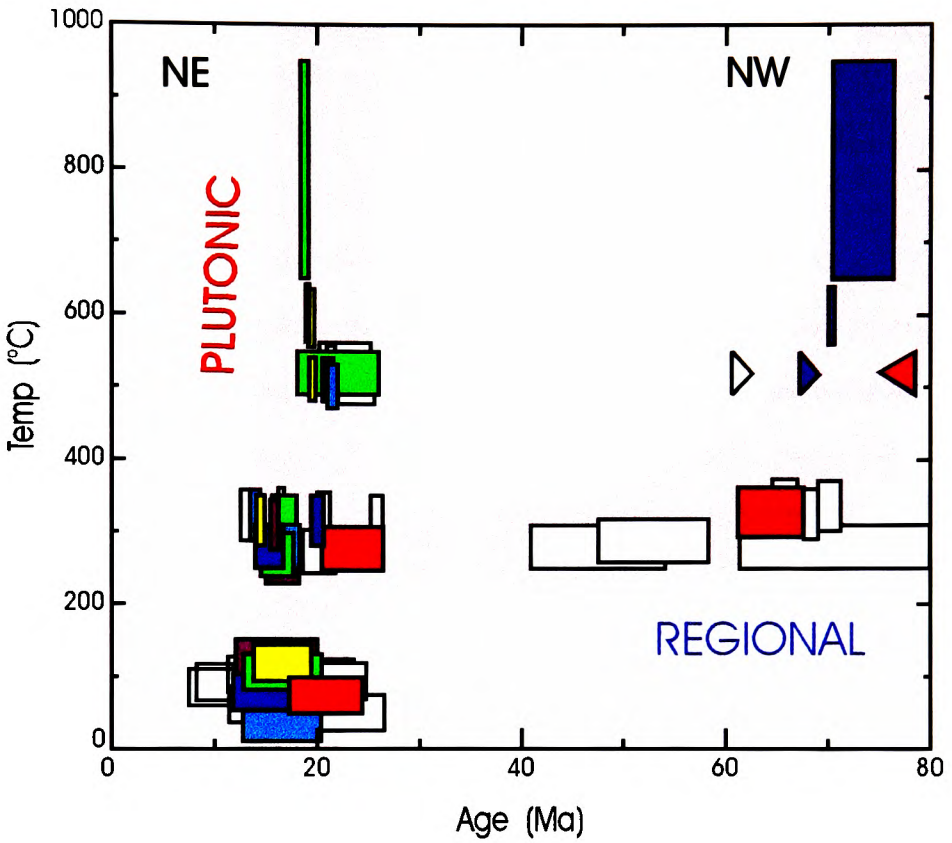


Figure 5.13 - Age versus closure temperature in the northern Sacramento Mountains. The NE region records rapid cooling from magmatic temperatures associated with Miocene plutonism. In the NW, slow cooling dominated since the latest Cretaceous, until the onset of Tertiary detachment faulting. Both regions share the final and nearly instantaneous decrease of ~250°C, through the closure temperatures of biotite, zircon, and apatite. Results have been colour coded when 3 or more minerals have been separated from a sample: dark-blue = VP94-140a; red = VP94-144; pink = VP94-135; light-blue = VP94-132; yellow = VP94-127; green = SCM16 and JW89-140. Error boxes: vertical = range in Tc; horizontal = 2 sigma. Triangles represent argon maxima or minima (refer to text).

northwest Sacramento Mountains of possible Cretaceous age and also noted a lack of pervasive mylonitization.

Late Cretaceous ages in the northwest Sacramento Mountains associated with the T_c of zircon and sphene (≥600°C), as well as with the T_c of biotite (~325 °C), require cooling rates on the order of 100°C/Ma (Fig. 5.12). This figure, consistent with cooling rates associated with Late Cretaceous batholith emplacement in the Old Woman Mountains area just 10 km west of the Sacramento Mountains (Foster et al., 1990) where the argon systematics in hornblendes from Proterozoic rocks have been reset in the Late Cretaceous, suggests that the thermal profile of the northwest Sacramento Mountains may also be dominated by Late Cretaceous plutonism. Rapid Late Cretaceous cooling in the Old Woman Mountains area contrasts with slower rates of 1-10°C/Ma, both immediately prior to, and following, this thermal event (Foster et al., 1990). Post-Late Cretaceous cooling in the northwest Sacramento Mountains slowed to comparable figures, where the difference between biotite and zircon (FT) ages in the southwestern-most region indicate cooling at ~1-6°C/Ma. Lastly, we see that the northeastern-most region of the northwest Sacramento Mountains records very rapid cooling through the T_c associated with biotite, zircon (FT), and apatite to ambient surface temperatures, between ~20 and 15 Ma: 38-53°C/Ma. This figure agrees with previous work by Foster et al. (1992) in the Sacramento and Chemehuevi Mountains. The high temperature portion of the cooling curve for the northwest Sacramento Mountains is consistent with cooling of the crust by thermal conduction (Foster et al., 1992; Harrison and McDougall, 1980; Harrison and Clarke, 1979; Carslaw and Jaeger, 1959), but the sudden increase of the cooling rate to 38-53°C/Ma between 20 and 15 Ma again suggests that tectonic denudation (unroofing) as a result of detachment faulting was the driving mechanism for the final cooling of the northwest Sacramento Mountains.

Northeast Sacramento Mountains - In the NE region, younging in the tectonic transport direction is more subtle, but is recorded in the hornblende and biotite data. The best-fit line to each data set, determined by least squares regression, defines a negative slope (mean -0.23 ± 0.12, 2σ), indicating younging to the NE (Fig. 5.12). This is consistent with normal faulting (see Chapter 6). The thermal regime in the northeast Sacramento Mountains is dominated by the syntectonic Eagle Wash intrusive suite. The initial conditions relating to the intrusion of the EWIC were depths of 7.5-12 km (3.3 ± 0.8 kb) and a crystallisation temperature of 680 ± 19 °C. After intrusion at ~20 Ma, very rapid cooling of the EWIC from

magmatic temperatures to below ~100°C (T_c of apatite) and exposure at the surface occurred by ~15 Ma (Fig. 5.13). This requires cooling rates of >100°C/Ma and exhumation rates of 1.5 - 3 km/Ma. A tabular (sheeted) pluton cooling solely by thermal conduction *in situ* will define a curve with a strongly concave upward appearance (Foster et al., 1992; Harrison and McDougall, 1980; Harrison and Clarke, 1979; Carslaw and Jaeger, 1959), due to the relatively high thermal contrast between the intrusion and the country rock (especially in igneous bodies intruded into the upper crust). Such a cooling path is not defined by the EWIC in the northeast Sacramento Mountains, requiring an additional mechanism of convective heat transfer and/or uplift. Regardless of whether or not convective heat transfer occurred, the exhumation rate of 1.5 to 3 mm/yr clearly necessitates invoking uplift. Given the contemporaneity of detachment faulting with the age of the EWIC, tectonic denudation associated with Miocene detachment faulting is most likely to be the cause of exhumation. Accelerated exhumation from 0.3 to 1.3 -2 mm/yr in the Whipple Mountains (to the south) and Santa Catalina Mountains (southeast Arizona) has also been correlated with tectonic decompression coincident with mid-Tertiary detachment faulting (Anderson et al., 1988).

Summary - The thermal profile, at ~20 Ma, of the footwall in the northern Sacramento Mountains is schematically illustrated in figure 5.14. The "paleoisotherms" are derived from the closure temperatures associated with each of the mineral systems. In as much as these boundaries are likely to be diffuse, given the range in T_c associated with each system, some latitude exists with respect to their locations. For example, all of the apatite ages are Miocene, suggesting that the entire region was above the T_c of apatite prior to this time. The ~210°C paleoisotherm must be located between VP94-141 and VP94-144. All of the zircon samples northeast of, and including, VP94-144 have Miocene ages and must have been above the T_c of zircon (FT) prior to this time. It follows that all of the zircon samples southwest of, and including, VP94-141 record much older ages and would have been below T_c of zircon (FT) prior to the Miocene. Using the same logic, the paleoisotherms associated with ~325°C and ~525°C (T_c of biotite and hornblende, respectively) can be relatively placed.

The ~100°C paleoisotherm is not detected in the region because no older ages are recorded by FTs in apatite. Given that the various mineral data suggest that deeper/hotter portions of the crust are being exposed to the NE, the ~100°C paleoisotherm must be located somewhere to the southwest of the sampling area. The placement of the ~525°C paleoisotherm is derived from similar logic. The location of both the

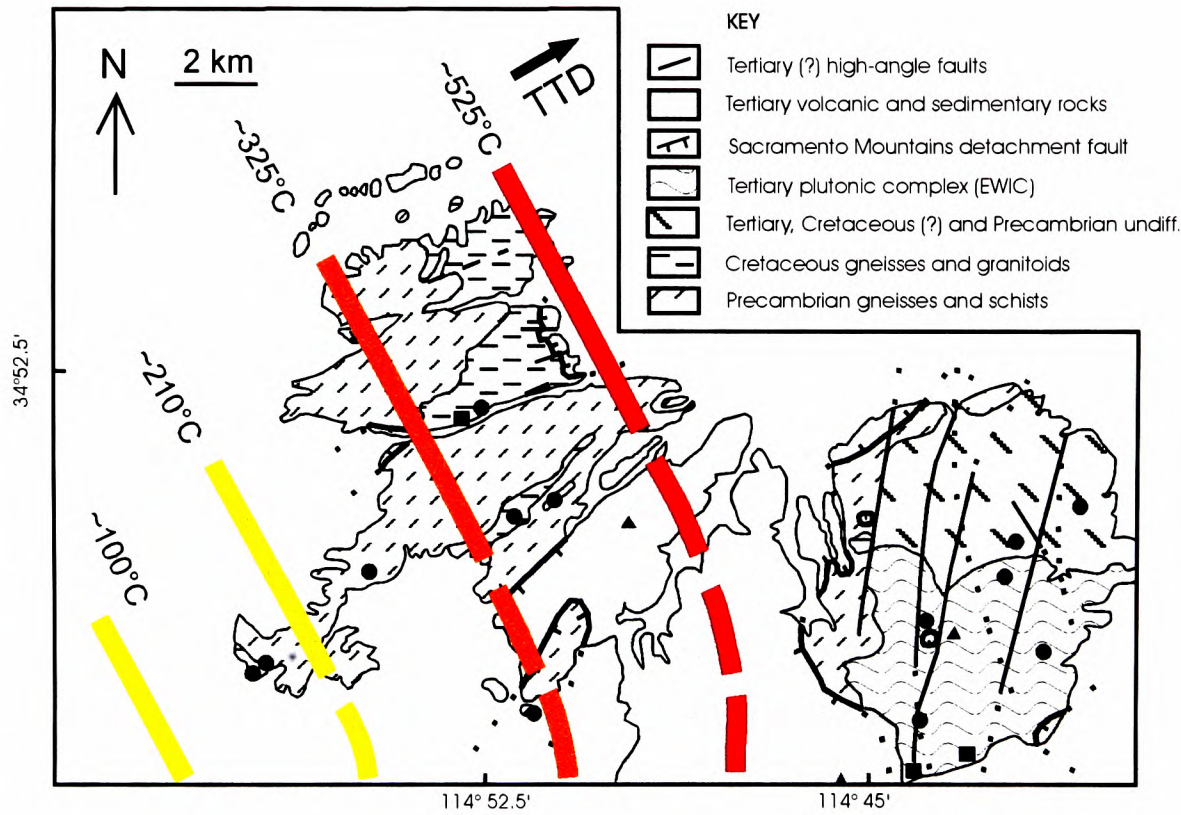


Figure 5.14 - Thermal profile of the northern Sacramento Mountains at ~20 Ma. Schematic paleoisotherms, drawn perpendicular to the tectonic transport direction (TTD), are derived from mineral closure temperatures (refer to text). In the NW, the systematic increase of paleotemperature to the NE is consistent with a tilted block exposing deeper crustal levels as a result of Miocene detachment faulting.

~100°C and the ~525°C paleoisotherms are relatively unconstrained without knowledge of the geothermal gradient at ~20 Ma.

Regarding the final placement of the paleoisotherms: Due to the diffuse nature of these boundaries, it is unlikely that they will be located immediately adjacent to the constraining sample locations, e.g., samples VP94-141 and VP94-144 with respect to the ~210 paleoisotherm. These paleoisotherms have been oriented along a northwesterly trend because i) some lateral control on the orientation of the paleoisotherms is provided by the spatial distribution of sample locations and the zircon (FT) and biotite data have similar ages (within each data-set) along the strike of this trend; also ii) this orientation is perpendicular to the Miocene tectonic transport direction, which might be expected if Miocene detachment faulting was the controlling mechanism for uplift and exhumation of this region (as suggested above).

This thermal profile suggests that the northwest Sacramento Mountains represents a tilted block of crust in which deeper levels of the footwall were exposed as Miocene detachment faulting progressed. The inferred rotation of this block is top-to-the-southwest, consistent with the overall dip of fault blocks within the extensional corridor. As the paleoisotherms increase in temperature to the northeast, the cross-sectional elevation also increases. Assuming that the paleoisotherms were originally horizontal, a minimum amount of tilt of 15-20° can be derived from geometric constraints. The maximum amount of tilt is unconstrained. The rotation of this block must have occurred prior to dyke intrusion, as the dykes are currently near-vertical, but while the block was still relatively hot in its deeper portion because dykes in the northeasternmost region exhibit mylonitic fabrics (Argent, 1996). These dykes are thought to be 19-17 Ma (Spencer, 1985).

In order for block rotation of the northwest Sacramento Mountains to have occurred, it must have been bound by an older (relatively) imbricate splay of the detachment fault system. Merey and Ticken (1989) identified a gently east-dipping reflector at 0.9-1.2 seconds (two-way travel time) on a seismic reflection profile just west of the northwest Sacramento Mountains. This feature is consistent with the interpretation of an underlying detachment fault. Inasmuch as the younging of ages to the northeast suggests that faulting continued longer to the northeast in both the northwest and northeast Sacramento Mountains, the southwest portions of the ranges were at lower temperatures/shallower depths than the

deeper, down-dip, northeast region. This suggests that *differential* uplift and cooling, related to detachment faulting, occurred in the region.

If the northern Sacramento Mountains represented a contiguous section of footwall prior to detachment faulting, the northeast Sacramento Mountains would have been at a similar, or slightly deeper, crustal level compared to the northwest region. The fact that dynamic recrystallization fabrics in the northeast Sacramento Mountains decrease to the north (away from the margin of the EWIC) and that such fabrics are entirely absent from pre-Miocene age rocks in the northwest Sacramento Mountains, supports the idea that the whole of the region was at a similar crustal level. The thermal contribution from synchronous intrusion of the EWIC resulted in a localised and transient, elevated geotherm in the northeast. Consequently, the "regional" paleoisotherms represented by the thermal profile in the northwest were compressed by this thermal event in the northeast Sacramento Mountains (Fig. 5.14).

Chapter 6

Angle of Faulting in the Northern Sacramento Mountains

6.1 Calculating the angle of the fault

The mechanism for the development of low-angle faults is controversial. The question regarding whether or not these structures initiate and are active at low-angles remains of wide interest to geophysicists, geodynamicists, and geologists, and is of global importance, including oceanic as well as continental lithosphere, e.g., Mutter and Karson (1992). The paleothermal profile of the footwall is an important tool for determining the original orientation of crustal-scale normal faults. Geometric and thermal constraints, derived from thermobarometric and thermochronologic data, make it possible to calculate the angle of detachment faulting in the northern Sacramento Mountains. Published applications of these methods are few and are mainly located in the central and southern Basin and Range, e.g., John and Foster (1993), Holm and Dokka (1993), Dokka (1993), and Richard et al. (1990).

Premise - The three techniques presented here (Barometry/Slip rates, Spacing of Isotherms, and Age Variation Down-dip) are based upon the fundamental premise that as normal faulting proceeds, the footwall is progressively unroofed, and minerals from deeper crustal levels in the footwall and along the fault surface pass through their closure temperatures later in time. This results in ages younging down-section/down-dip. This is schematically illustrated in figure 6.1 where, after faulting has progressed, t_1 records an older age

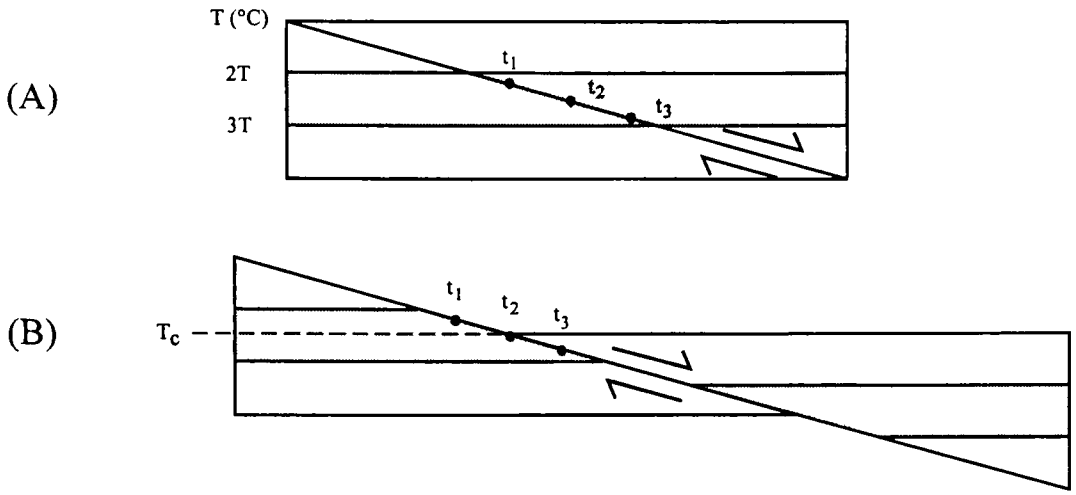


Figure 6.1 Geometric relationship between normal faulting, temperature, and younging down-dip. (A) Pre-faulting condition showing location of three points along the proto-fault surface. Vertical axis is temperature (T°C) and T increases with increasing depth. (B) With initiation of faulting t_1 passes through it's closure temperature (T_c); as faulting continues, t_2 passes through it's T_c; even later, t_3 will pass through its T_c. This results in younging down-dip along the fault, with the associated ages of $t_1>t_2>t_3$.

than t_3 because t_3 passed through its closure temperature later in time. Inasmuch as the thermochronologic data show younging in the direction of tectonic transport (Chapter 5, Fig. 5.14), these samples appear to record the movement of the fault block through the closure temperatures of biotite and zircon (FT) in the NW Sacramento Mountains and through the closure temperatures of hornblende and biotite in the NE Sacramento Mountains.

All of the techniques employed here to calculate the angle of the fault utilize the simple trigonometric relationship, whereby an angle (θ) is expressed

$$\theta = \sin^{-1} \frac{o}{h} \tag{6.1}$$

where o = opposite limb and h = hypotenusal limb. Using the nomenclature of Wernicke (1995), this relationship can be expressed as a function of the paleogeothermal gradient and field paleothermal gradient, with θ as the angle of the fault (Fig. 6.2). The field paleothermal gradient (the pre-unroofing, down-dip thermal gradient of the exposed footwall) between two points with a temperature difference (ΔT) is related

to the paleogeothermal gradient by the average dip of the fault (θ), which from equation 6.1 is

$$\theta = \sin^{-1} \frac{dT / dw}{dT / dz} \tag{6.2}$$

where *dT/dz* is the geothermal gradient just prior to unroofing and *dT/dw* is the measured field paleothermal gradient. In this case, ΔT is defined by the relevant paleoisotherms (the ~525°C and ~325°C paleoisotherms in the NE Sacramento Mountains and the ~325°C and ~210°C paleoisotherms in the NW Sacramento Mountains).

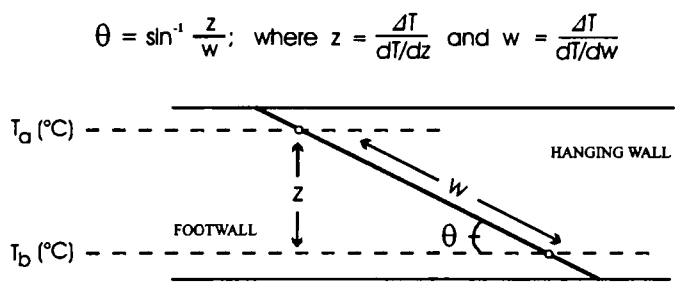


Figure 6.2 Geometric relationship between paleogeothermal gradient (*dT/dz*), field paleothermal gradient (*dT/dw*), and the angle of faulting (θ). Closure temperatures of zircon (FT), biotite, or hornblende (~210°C, ~325°C, and ~525°C, respectively) define the paleoisotherms represented by T_a and T_b.

Assumptions Several assumptions are inherent in combining paleotemperature variations with depth in order to derive the angle of faulting: 1) The paleogeothermal gradient must be known, 2) paleoisotherms should be horizontal and parallel, 3) exhumation of the footwall should be dominantly tectonic, and 4) samples in the footwall should have maintained their relative positions during faulting. Each of these assumptions is evaluated with respect to the northern Sacramento Mountains.

(1) The paleogeothermal gradient must be known. The ambient geothermal gradient prior to Tertiary unroofing has been determined in several areas of the Basin and Range. In these investigations the time-temperature history has been determined from rocks with independently estimated paleodepth. In the region of this investigation, the eastern Mojave Desert, the average geothermal gradient in the upper 10 km of the crust 18 m.y. ago has been estimated to be ~50°C/km (Foster et al., 1991) and 30-50°C/km (John and Foster, 1993). For other regions in the Basin and Range: East-central Nevada (upper 10 km of crust),

~20°C/km at 35 Ma (Dumitru et al., 1991) and 25-35°C/km at 8-10 Ma (Holm and Wernicke, 1990; Holm et al., 1992); and in southern Nevada (upper 3-4 km of the crust), ~25-30°C/km at 15 Ma (Fitzgerald et al., 1991). Given the depth of emplacement associated with the syntectonic EWIC in the northeast Sacramento Mountains (~10 km) and the time of detachment faulting in the northern Sacramento Mountains (23-14 Ma), the paleogeothermal gradient *(dT/dz)* of interest probably ranged from 30-50°C/km.

The derivation of paleogeothermal gradients from the above studies assumes a linear geothermal gradient. Geothermal gradients in the Earth's crust, however, are known to be non-linear and this is likely to have been the case in the Tertiary as well. A non-linear geothermal gradient has been calculated using the following equation (A. Watts, pers. comm., 1997).

$$T(z) = \left(\frac{-A}{2k}\right)z^2 + \left(\frac{Qd + Ad}{k}\right)z \qquad (6.3)$$

where T is temperature (°C), z is thickness of rock column (meters), A is radioactive heat generation (1.25×10^{-6} W/m^3), Ad is the contribution of A to crustal heat flow (6.2×10^{-5} W/m^2), Qd is mantle heat flow (4.2×10^{-2} W/m^2), and k is thermal conductivity (2.5 W/m/°C). For the depths of interest here (~10 km), a geothermal gradient (derivative of equation 6.3) of ~35°C/km is obtained (Appendix E). This suggests that the above experimentally derived range of paleogeothermal gradients is reasonable for a non-linear geotherm as well.

(2) Paleoisotherms should be horizontal and parallel. This must be true in order to make extrapolations over distances/depths, e.g., John and Foster (1993), Dokka (1993), and Foster et al. (1990). For a known duration of faulting, the characteristic distance perpendicular to faulting *(l)* over which the geotherm is perturbed as a result of the juxtaposition of cold hanging wall against warm footwall, is given by the standard diffusion equation of Carslaw and Jaeger (1959)

$$l = \sqrt{kt} \qquad (6.4)$$

where k = thermal diffusivity (10^{-6}m^2/sec) and t = duration of faulting (sec). This is illustrated schematically in figure 6.3, where the temperature on the fault (T°C) is given by $(T_f+T_h)/2$, and T_f and T_h are the temperatures of the footwall and hanging wall, respectively (Molnar and England,

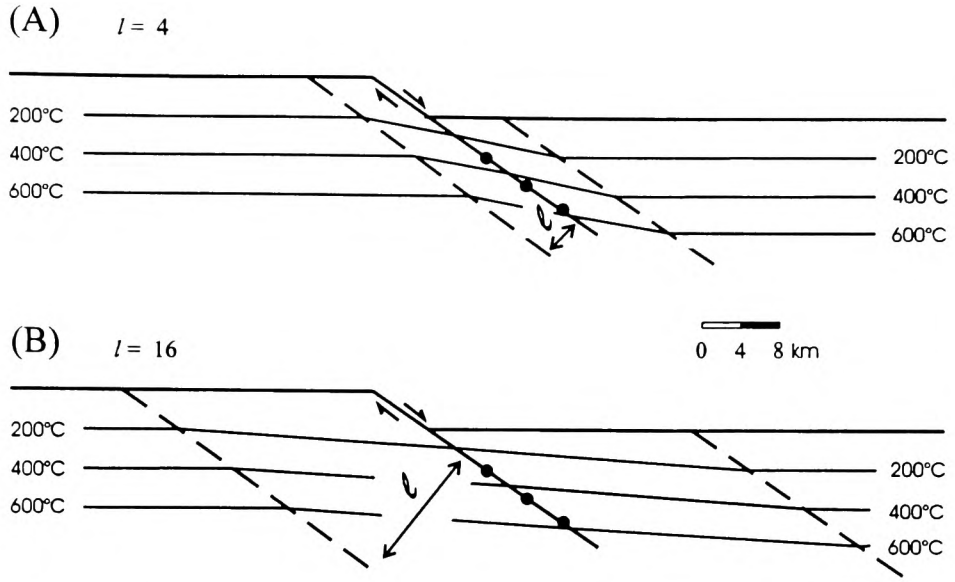


Figure 6.3 Perturbation of the geotherm due to normal faulting. The distance within the crust perpendicular to the fault affected by normal faulting (l) is a function of thermal diffusivity and the duration of faulting. (A) When l is small (arbitrarily = 4 km). (B) When l is large (l = 16 km, the condition for the northeast Sacramento Mountains). Scale is the same in both figures and has no vertical exaggeration. $k = 10^{-6}m^2/sec$.

1990, eq. 4). It can be seen that if l is small, the perturbed isotherms will be relatively steep. This is illustrated in figure 6.3a, where l is arbitrarily set equal to 4 km. If l is large, the isotherms will be shallow, i.e. likely to be near horizontal. In the northern Sacramento Mountains, for $k = 30km^2/Ma$ and $t = 9$ Ma, l = 16 km (Fig. 6.3b). Thus, as l is relatively large, the isotherms are likely to be near horizontal.

(3) If exhumation of the footwall is dominantly tectonic, then the inverse slope of the best-fit line to age data plotted against distance down-dip (Chapter 5, Fig. 5.14) can be used to estimate slip rates for the fault (Foster et al., 1990). Combining geobarometry with thermochronology, rapid exhumation (2-3km/Ma) dominantly controlled by tectonic denudation associated with detachment faulting, was inferred for the northeast Sacramento Mountains (Chapter 5; Pease et al., 1995). Biotite and zircon (FT) data record cooling that is probably due to tectonic denudation, whereas hornblende data, due to it's higher closure temperature, may be recording conditions related to magmatism. Consequently, hornblende age data is excluded from the discussion of the slip rate of the SMDF.

(4) Finally, it is assumed that samples in the footwall have maintained their relative positions during faulting. Geologic mapping suggests that this is true, as the high- and secondary low-angle faults in the range have only minor offsets (10-100m; Chapter 3, Section 3.2).

Within the limits of these assumptions, the angle of faulting and the slip rate associated with the SMDF can be calculated in a number of ways. The calculations to determine the angle of faulting are presented in order of increasing complexity, with the most simplistic first. The parameters which define o and h may vary between techniques and this should be borne in mind.

6.2 Barometry/Slip rates

If tectonic denudation associated with Tertiary detachment faulting is the dominant mechanism responsible for the exhumation of Miocene plutonic rocks, then the angle of faulting can be determined using equation 6.1. Combining the uplift rate (o) with the slip rate along the fault (h), θ can be calculated. Both uplift and slip rates have been derived within the Colorado River extensional corridor.

Several investigations have determined the uplift rates of Miocene plutonic rocks in the extensional corridor using geobarometry: 1.5-3.0 mm/yr, this study; 1.4 mm/yr, Chemehuevi Mountains (Foster et al., 1990); 1.3-2.3 mm/yr, Whipple Mountains (Anderson et al., 1988); and 1.3 mm/yr, Santa Catalina Mountains (Anderson et al., 1988). These estimates define comparable and relatively rapid rates of uplift within the extensional corridor. Furthermore, using thermochronologic and geologic constraints, several investigations have calculated slip rates associated with detachment faulting in the extensional corridor: 7.7 mm/yr, Chemehuevi Mountains (John and Foster, 1993); 7-9 mm/yr, Harcuvar/Buckskin-Rawhide Mountains (Spencer and Reynolds, 1991); and 7.2 mm/yr, Whipple Mountains (Davis, 1988).

Using uplift rates of 1.3-3.0 mm/yr and slip rates of 7-9 mm/yr, the angle of faulting within the extensional corridor is calculated to be in the range of 8° to 25°. Though this determination is by no means rigorous, as a first attempt to constrain the angle associated with Tertiary detachment faulting, this simple calculation which combines data from different authors, different mountain ranges, and data derived using different techniques, provides a degree of reasonable confidence in the final results: *an active, low-angle structure.*

6.3 Spacing of Isotherms

The paleothermal profile now exposed as a result of Tertiary detachment faulting in the northwest Sacramento Mountains can be used to determine the angle of faulting associated with the exhumation of this

region. From equation 6.2, by assuming a reasonable paleogeothermal gradient (*dT/dz*) for the region and using the field paleothermal gradient (*dT/dw*) obtained from the paleoisotherms now exposed, the angle of detachment faulting in the northwest Sacramento Mountains can be calculated.

In this case the field paleothermal gradient (*dT/dw*) is derived from the distance between the two observed paleoisotherms in the northwest Sacramento Mountains. The distance between the ~210°C and ~325°C paleoisotherms (zircon fission track and biotite, respectively) is not well constrained due to the range in closure temperature associated with each system (Chapter 5, Section 5.6). Nevertheless, the apparent distance separating these two paleoisotherms can be reasonably determined to be ~6 km. (A *maximum* separation of 8 km is achieved if the 210°C paleoisotherm is located near VP94-141 and the 325°C paleoisotherm is located near VP94-138, but as previously discussed (Chapter 5, Section 5.6), this is regarded as implausible). A distance of ~6 km separating ~110°C (ΔT) results in a field paleothermal gradient (*dT/dw*) of ~18°C/km.

Using equation 6.2, a paleogeothermal gradient (*dT/dz)* of 30-50°C/km (Section 6.1), and a field paleothermal gradient (*dT/dw*) of ~18°C/km, the angle of faulting is calculated to be 21-37° If the geotherm was non-linear, then a value of 35°C/km may be most appropriate for the value of *dT/dz* (Section 6.1) and the resulting fault angle is 31° This technique lacks precision, a result of poorly constrained closure temperatures and error propagation associated with locating the paleoisotherms and determining the distance between paleoisotherms. Using *reasonable* geologic/thermal constraints, however, an angle of faulting is derived which is at least consistent with that obtained from the "barometric/slip rate" technique above.

6.4 Age Variation Down-dip

Samples were collected from the EWIC (granodioritic phase) along a traverse parallel to the regional transport direction, within 300 m of the detachment fault surface (Fig. 6.4a). The apparent ages from hornblende and biotite mineral separates were plotted against distance in the tectonic transport direction and there is an apparent systematic decrease in age to the NE (Fig. 6.4b). A best-fit line for each data sub-set was calculated by least squares regression. The line fits approximate the time at which the fault passed through the ~325°C and ~525°C paleoisotherms, i.e.- closure temperatures for retention of argon in biotite

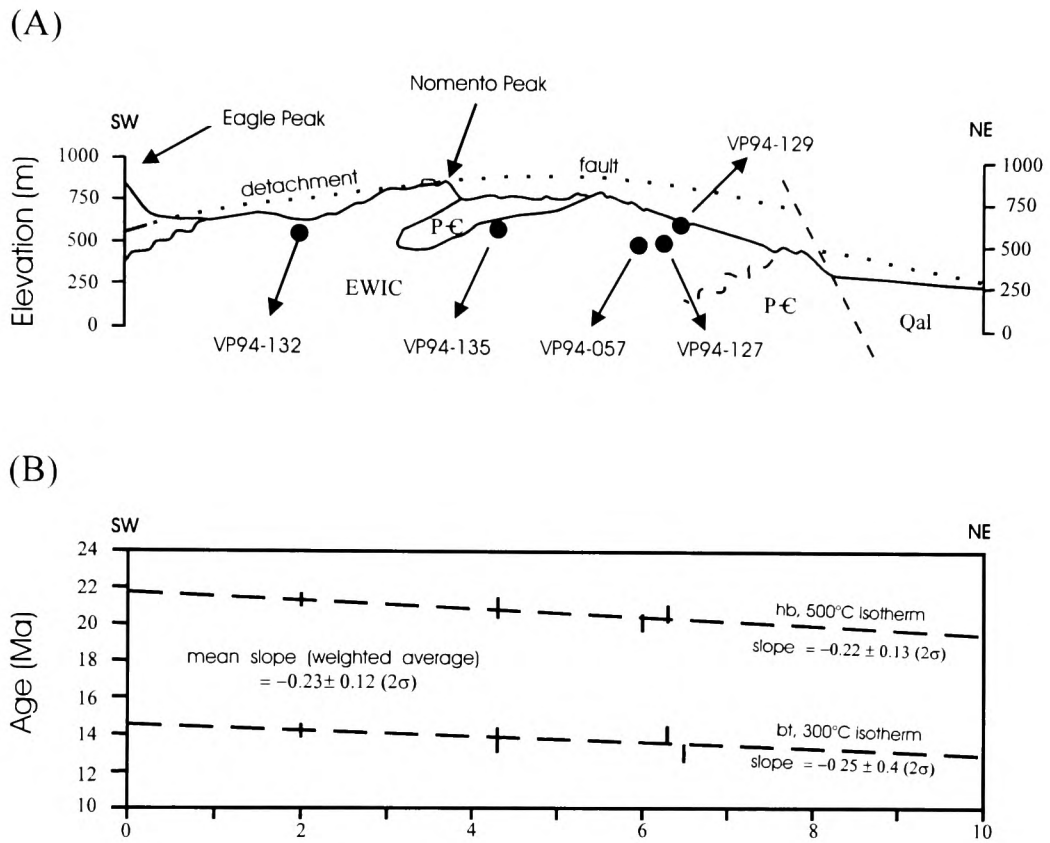


Figure 6.4 (A) Schematic cross-section of the northeast Sacramento Mountains illustrating sample proximity to the detachment fault. Shaded regions represent Tertiary volcanic and sedimentary rocks. (B) Best-fit lines to hornblende and biotite data. Distance down-dip normalized to Eagle Peak.

hornblende, respectively. Using these data the slip rate of the Sacramento Mountains detachment fault can be determined and in combination with equation 6.1, the angle of faulting in the northeast Sacramento Mountains can also be determined.

Slip rate Thermochronologic data from samples collected at, or close to, the paleosurface of the Sacramento Mountains detachment fault can be used to estimate the slip rate for the fault. Foster et al. (1990) have shown that the inverse slope of the best-fit line to thermochronologic data, when plotted against distance in the down-section/down-dip direction, yields the slip rate of the fault. From figure 6.4, sample proximity to the paleofault surface and the distribution of biotite and hornblende $^{40}Ar/^{39}Ar$ data in the down-dip direction are shown. Only the biotite data are used here to determine the slip rate of the SDMF, because the higher T_c of hornblende may reflect transient geothermal gradients related to magmatism (refer to

Section 6.1). The average slip rate for the SMDF recorded by this biotite data is ~4mm/yr (3-9mm/yr within 2σ). The average value is ~50% less than previous estimates of 7-9 mm/yr (Section 6.2) for detachment faulting between 15 and 20 Ma. This suggests that slip along the SMDF at ~14 Ma (biotite ages) in the northeastern Sacramento Mountains could have been slower than elsewhere in the region at this time.

Angle of faulting The variables assigned to the factors which determine the angle of faulting in equation 6.1, i.e.- o and h, are shown in figure 6.5a. The vertical distance between the ~325°C and ~525°C paleoisotherms is given by z (km) and d represents the distance (km) between the paleoisotherms along the fault surface. Using the nomenclature of Wernicke (1995) and equation 6.2, z is a function of the *paleogeothermal gradient* (dT/dz) and d is related to the measured *field paleothermal gradient* (dT/dw). The value of z can be determined using the relationship $z = \Delta T/(dT/dz)$ (Fig. 6.5a), where ΔT is the difference in temperature over the distance z and is expressed in the form

$$\Delta T = T_c\,(hb) - T_c\,(bt) \tag{6.5}$$

where $T_c\,(hb)$ is the closure temperature of hornblende and $T_c\,(bt)$ is the closure temperature of biotite.

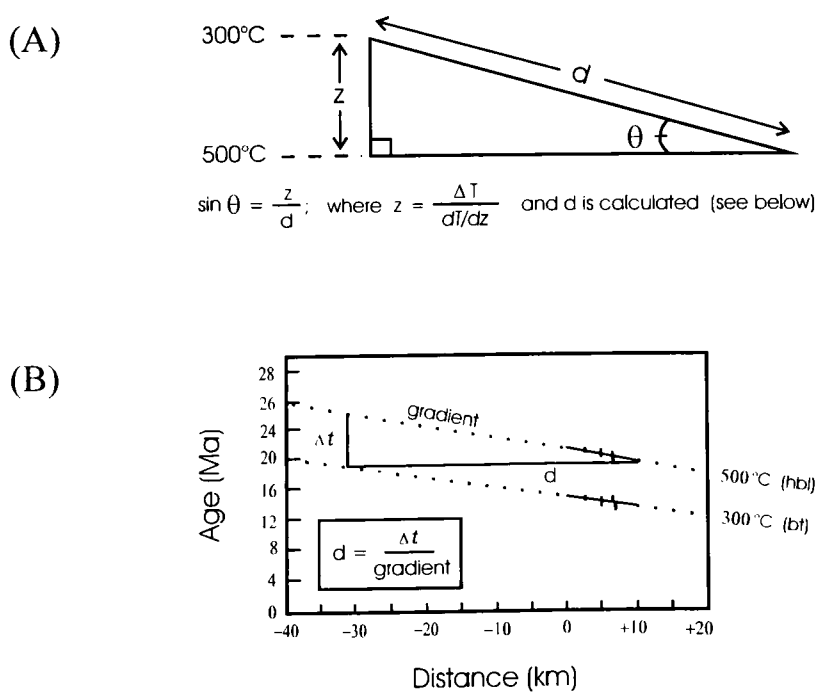


Figure 6.5 (A) Definition of variables assigned to the factors controlling the angle of faulting. (B) Extrapolation of Δt and d from the observed data.

For the rapid cooling rates associated with the northeast Sacramento Mountains (>100°C/Ma for the EWIC; Chapter 5, Section 5.6; Pease et al., 1995), T_c *(hb)* = 550-500°C (Harrison, 1981) and T_c *(bt)* = 345-310°C (Harrison et al., 1985). Harrison (1981) and Harrison et al. (1985) have shown that for mineral compositions similar to those in this study and for rapid cooling rates, the difference in closure temperature between hornblende and biotite (ΔT) is always ≅ 200°C. Thus, the value of ΔT is set equal to 200°C and a *range* of geologically reasonable values are used for *dT/dz*.

The relationship illustrated in figure 6.5b is used to solve for *d*, where

$$d = \Delta t / gradient \qquad (6.6)$$

and Δt and *gradient* are constant if the isotherms are parallel. The difference in age between the ~325°C and ~525°C isotherms is given by Δt, and *gradient* is the age-distance gradient indicated by the slope(s) from figure 6.4b. An average value for Δt is 6.9 ± 1.5(2σ) Ma (Chapter 5, Table 5.5). An average value for *gradient* is the absolute value of the average slope from Fig. 6.4b (0.23 ± 0.12(2σ) Ma/km); consequently *d* = 29.8 ± 16.8(2σ) km.

The results of the calculation for the angle of faulting in the northeast Sacramento Mountains are shown in figure 6.6. Where *d* = 29.8 ± 16.8(2σ) km, ΔT = 200°C, and *dT/dz* = 25-50°C/km, the SMDF was active at an angle between 5-38°. If the limits of the associated errors are considered (shaded region in Fig. 6.6), it is unlikely that the fault was active at angles >30°

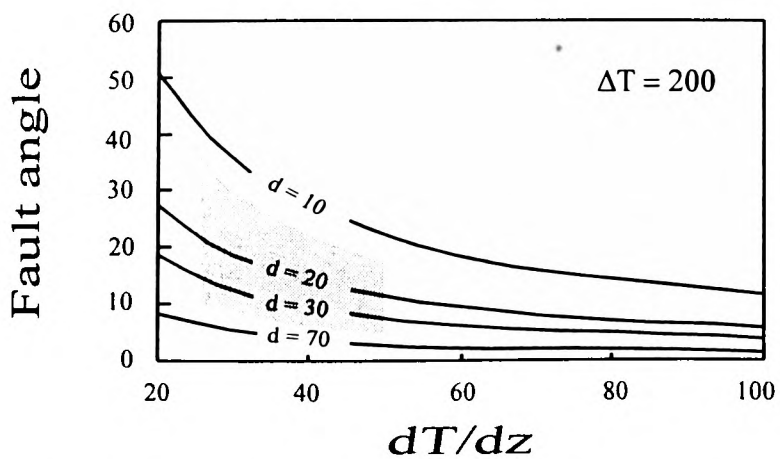


Figure 6.6 The calculated angle of faulting in the northeastern Sacramento Mountains, results indicated by the shaded region. The angle is likely to be <30° (within 2σ limits).

Though this determination of the angle of faulting assumes a *linear* paleogeothermal gradient, the influence of a non-linear paleogeothermal gradient can be assessed. Qualitatively, a non-linear geothermal gradient reduces the vertical distance between the ~325°C and ~525 °C isotherms (z in Fig. 6.5a). It is clear from figure 6.5a that if we hold d constant (e.g., use the extrapolated value based on observed field data) and reduce z, the angle of faulting will be concomitantly reduced. Quantitatively, the geotherm at ~10 km associated with a non-linear gradient was calculated to be ~35°C/km (Section 6.1). Thus, under the more realistic conditions associated with a non-linear geothermal gradient, the angle of faulting in the northeastern Sacramento Mountains would have occurred at even lower angles, between 10° and 25°. The errors associated with this technique for determining the angle of faulting have been rigorously propagated, resulting in a robust solution which is in excellent agreement with the results from both the *Barometry/Slip rate* and *Spacing of Isotherms* techniques.

6.5 Summary

Several techniques have been used to determine the angle of faulting associated with detachment faulting in the Sacramento Mountains region. All three of these techniques use thermochronologic data to combine paleogeothermal gradient with paleotemperature variation, and appear to yield similar results: 8-25° across the extensional corridor (Barometry/Sip rates), 21-37° in the northwest Sacramento Mountains (Spacing of Isotherms), and <30° in the northeast Sacramento Mountains (Age Variation). Furthermore, the calculations suggest that the SMDF in the northern Sacramento Mountains was active between ~20-25° This low-angle solution for the SDMF is robust inasmuch as the angle of faulting is likely to be less than 30°, within error at the 95% confidence level and whether a linear or non-linear geothermal gradient is assumed. A slip rate of ~4mm/yr is obtained for the SMDF in the northeastern Sacramento Mountains, suggesting that faulting was slower here than elsewhere in this region at about 15 m.y. ago. These data contribute to a handful of studies (John and Foster, 1993; Holm and Dokka, 1993; Dokka, 1993; Richard et al., 1990) which suggest that detachment faults initiate and slip at low-angles, i.e.- angles < 30°

Chapter 7

Conclusions and Synthesis

This multi-disciplinary investigation into the timing, distribution, and intensity of tectonothermal events has resulted in an understanding of the tectonic evolution of the northeast Sacramento Mountains, in particular, and of the northern Sacramento Mountains in general. From knowledge of the relative and absolute timing of crustal and tectonic processes, a petrogenetic model for the evolution of the Sacramento Mountains metamorphic core complex can be developed. This model is based on the data presented in the preceding chapters, except where otherwise referenced.

7.1 Tectonogenesis of the northern Sacramento Mountains

The tectonogenetic evolution of the Sacramento Mountains through time (t, Ma) is schematically illustrated in figure 7.1. The ambient, pre-detachment faulting configuration of the crust shows the zone of active mylonitzation (fore-dipping hatchures, \\\\\\) at about 10 km depth (~3.5 kb) and approximately 300°C ($t_{>23}$). The dotted, horizontal line is for structural reference, and the dashed line shows the location of the incipient detachment fault(s). Detachment faulting in the region is known to have been underway at ~22 Ma. Back-dipping hatchures (//////) indicate inactive mylonites. Mylonitization of the EWIC (indicated by wavy lines, ~ ~ ~) occurred as it cooled and passed through the mylonitization zone during exhumation.

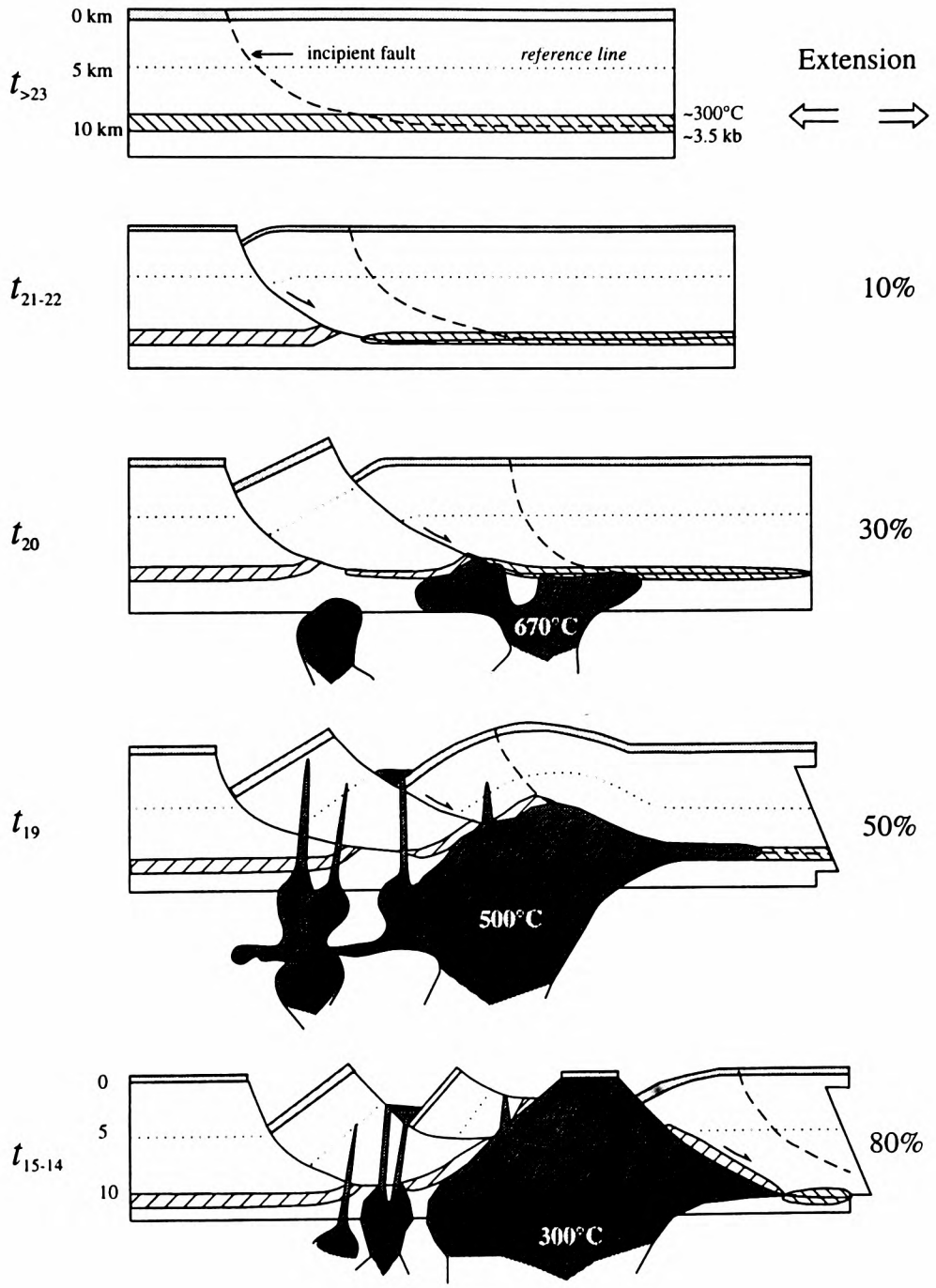


Figure 7.1 - Schematic tectonogenic evolution of the northern Sacramento Mountains. Extension directed NE-SW; time (t) in Ma; displacement indicated on *active* splay only; active mylonites indicated by fore-dipping hatchures (\\\\\); inactive mylonites by back-dipping hatchures (/////). EWIC shown in dark shading, with wavy lines (~~ ~) indicating mylonitized EWIC.

In the northeast Sacramento Mountains, the ~20 Ma EWIC intruded during detachment faulting, into basement which had already been subject to a long and complex sequence of deformation (t_{20}, Fig. 7.1). This calc-alkaline intrusive complex is predominantly granodioritic, with lesser volumes of diorite, granite, and leucogranite. The diorite was probably derived from a "parent" magma not seen in the northern Sacramento Mountains, which was generated from the enriched subcontinental lithospheric mantle. This unseen parent magma ponded at the base of the lower-crust, assimilating old (Proterozoic), mafic (granulitic) material, generating *Td*. The contaminated magma (*Td*) ascended to higher crustal levels and ponded at the base of the detachment shear zone, where it spread laterally, assimilating, mixing, and crystallising, generating magmas of intermediate composition (*Tgd*). This evolutionary stage involved multiple intrusive phases (magma batches), as well as separate magma chambers/conduits. Once emplaced at higher structural levels, small volume partial melts of Proterozoic sialic upper-crust (*Tlg*) were generated. Again, multiple intrusive phases are suggested by the various generations (compositions) of *Tlg*.

Thermobarometry indicates that the granodioritic phase of the EWIC was emplaced at ~3.3 kb and ~680°C, though higher pressure and temperature are indicated at the Eagle Pass quarry site (~4 kb and ~710°C). Barometric data from a two-mica granite in the central Sacramento Mountains (Anderson, 1988), possibly correlative with *Tlg*, suggests that it shared the same emplacement history as *Tgd*. Lower pressures determined from the mylonitic matrix of the two-mica granite suggest that mylonitization occurred while decompression of the footwall was already under way (Anderson, 1988).

The EWIC, while still hot (~500°C) and semi-plastic, continued (?) to deform (t_{19}, Fig. 7.1). Fault motion along the active SMDF system produced the mylonitic fabric of the EWIC. Continued and progressive deformation of the EWIC, from magmatic temperature to low-temperature (~300°C), is thought to have occurred, though textural evidence for syntectonic plutonism (the continuous transition from submagmatic to high-temperature solid-state deformational fabrics; Patterson et al., 1990) is not preserved. The preservation of such fabrics in the EWIC would not be expected, given the duration of deformation in the region and the subsequent rapid cooling and uplift of the northeast Sacramento Mountains (Miller and Paterson, 1994).

The mylonitic fabric associated with the EWIC is notably heterogeneous, reflecting the variations in time, temperature, and strain rate over which it developed. This fabric developed predominantly at sub-

solidus temperatures (~500-300°C), after ~20 but before ~15 million years ago. Rapid cooling from magmatic temperatures also suggests that these fabrics were acquired during uplift and decompression of the range.

During uplift and cooling of the northeast Sacramento Mountains, the dominant compressive stress varied from vertical to N-S horizontal. This variation was apparently due to tectonic denudation, combined with ongoing magmatic intrusion. Exhumation and cooling of the range was complete by ~ 15 Ma on the west side and by ~14 Ma on the east side ($t_{15\text{-}14}$, Fig. 7.1), when the range cooled through the fission track closure temperature of apatite. This diachroneity indicates that detachment faulting continued in the east, after it had ceased in the west.

The variation in orientation of the EWIC's mylonitic fabric across the range is likely to be a primary feature associated with a detachment shear zone. Its back-dipping configuration is consistent with its "capture" by a younger splay of the SMDF system at a later time. Younger, entirely brittle, low-angle faulting indicates that detachment faulting continued during the uplift of the range into the brittle regime. The absent fore-dipping limb was probably transported to the east in the hanging wall of a younger splay of the SMDF system, which is consistent with the existing geometry and timing of detachment faulting in the region.

While the northeast Sacramento Mountains was subject to uplift resulting from both magmatic intrusion and laterally unconfined (one-sided) denudation (detachment faulting), the northwest Sacramento Mountains was tilted along an "older" splay of the SMDF system at ~20 Ma. The thermal profile of the northwest Sacramento Mountains suggests it represents a tilted block of crust in which deeper levels of the footwall are exposed to the northeast. The inferred rotation of this block is top-to-the-southwest, consistent with the overall dip of fault blocks within the extensional corridor. A seismic reflection profile just west of the northwest Sacramento Mountains shows a gently east-dipping reflector at 0.9-1.2 seconds, two-way travel time (Merey and Ticken, 1989), consistent with a shallow, underlying detachment fault.

Dike intrusion in the northwest Sacramento Mountains occurred at 19-17 Ma (Spencer, 1985), synchronous with a later episode of detachment faulting to the east. The dikes show ductile deformation of quartz (Argent, 1996) near the contact with this younger fault splay (currently exposed on the east side on the northwest Sacramento Mountains). This portion of the tilted northwest Sacramento Mountains block

was from the deepest structural level and was at a higher ambient temperature (~400°C) than the southwest region of the northwest Sacramento Mountains (<200°C). This temperature gradient was responsible for the development of localised ductile fabrics in the syntectonic dikes of the northwest Sacramento Mountains.

At this time (19-17 Ma), the northwest Sacramento Mountains experienced NE-SW directed extension of the hangingwall. The "upper plate" footwall, however, was subject to dextral, oblique extension (Argent, 1996). This secondary transtensional regime was probably the result of more rapid rates of extension occurring to the south, rather than to the absence of a subducting slab associated with the retreat of the Pacific plate. The absence of transtensional structures in the surrounding regions further support this interpretation.

Both regions share a rapid cooling and uplift history between ~20 and 15 Ma, which is interpreted to be the result of both exhumation associated with tectonic denudation via detachment faulting and magmatism. Deformational events, recording decreasing temperature and a corresponding change from ductile through brittle behaviour in footwall rocks, are also recognised in the central Sacramento Mountains (Schweitzer, 1991). These events can be correlated across the northwest, northeast, and central Sacramento Mountains on the basis of timing, metamorphic grade, and fabric orientation.

If the northwest and northeast Sacramento Mountains represent a once contiguous section of footwall, the northeast Sacramento Mountains would have been at a similar, or slightly deeper, crustal level compared to the northwest region. The fact that dynamic recrystallization fabrics in the northeast Sacramento Mountains decrease to the north (away from the margin of the EWIC) and that such fabrics are entirely absent from pre-Miocene age rocks in the northwest Sacramento Mountains, supports the idea that the whole of the region was once at a broadly similar crustal level. The thermal contribution from synchronous intrusion of the EWIC resulted in a localised and transient, elevated geotherm in the northeast. The elevated geotherm provided the heat necessary for pervasive mylonitization of country rocks in the immediate vicinity.

7.2 The role of magmatism during detachment faulting

Miocene magmatism helped localise the high degree of crustal extension and core-complex uplift in the extensional corridor. Miocene calc-alkaline volcanic rocks, dike swarms, and scattered coeval plutons focus along the corridor axis (Howard et al, 1996). These rocks are cut by detachment faults, and

their timing shows that magmatism climaxed not long be before the peak of extension. Voluminous unexposed mafic roots to the Miocene intrusions are suggested by the presence of a 200-km-long gravity high (Simpson et al., 1990). In the part of the corridor near the northeast Sacramento Mountains, plutonic rocks and approximate ages include: 17 Ma (K-Ar) diorite from the southern Dead Mountains to the north, 17 Ma (U/Pb) mylonitic granodiorite and cross-cutting 17 Ma (K-Ar) quartz diorite in the northern Dead Mountains, and the 17 Ma (U/Pb) Spirit Mountain and 15 Ma (U/Pb) Mirage plutons in the southern Newberry Mountains further north (Howard et al., 1996). The relative timing of magmatism and extension shows that this magmatism did not result from decompression melting upon crustal thinning. The presence of mafic dykes and dense plutonic roots suggests that magmatism was triggered by rise of basaltic melt from the mantle. The timing and position of plutons suggests that magmatism and consequent crustal softening may have helped to localise hyperextension, tectonic denudation, and core-complex uplift.

7.3 Detachment faulting in the northern Sacramento Mountains

The geometry and mechanism of detachment faulting in the Sacramento Mountains require i) that the detachment fault was initiated and active at low angles, ii) that faulting involved multiple splays, with active faulting generally migrating northeast, iii) that the region uplifted and cooled rapidly, and iv) that the stress field associated with the exhuming footwall varied in both time and space. Published applications of the thermochronologic method used to determine the angle of faulting in this investigation are few and are mainly located in the central and southern Basin and Range (e.g., Richard et al., 1990; John and Foster, 1993; Holm and Dokka, 1993; Dokka, 1993). These results may be geographically biased, but they are in general agreement as to the *low* angle of faulting and the *rapid* cooling of the footwall at the time of unroofing.

Faulting in the Sacramento Mountains and elsewhere in the Basin and Range occurred at angles less than 30° Though theoretical fault mechanics predicts that active normal faults near the Earth's surface should be oriented 45-75° from horizontal (Anderson, 1951), this is not always the case, as is observed from some notable examples of low-angle fault plane solutions (Johnson and Loy, 1992; Abers, 1991; Allmendinger et al., 1983). It seems obvious that active, low-angle faulting does occur, and that fault mechanic theory does not adequately account for this phenomena. The discrepancy between the theoretical and the empirical in this case may have to do with the concept of a rotated stress field. Both Yin (1991) and

Spencer (1982) have shown that the principal stress axes associated with the footwalls of detachment faults can have a range of orientations. The orientation of stress axes is ultimately controlled by the forces acting upon the footwall, which are either buoyant or compressional. In the case of buoyancy, upward pushing force can be generated by uncompensated crustal roots with irregular geometries, isostatic uplift due to tectonic denudation, or synextensional plutonism.

Cooling rates in the northwest Sacramento Mountains during the Late Cretaceous were on the order of 100°C/Ma and are attributed to Cretaceous plutonism. Post-Late Cretaceous cooling in the northwest Sacramento Mountains slowed to about 1-6°C/Ma. Lastly, between ~20 and 15 Ma, the northeastern-most region of the northwest Sacramento Mountains cooled very rapidly from ~300°C to ambient surface temperatures at rates of 38-53°C/Ma. The high-temperature, Late Cretaceous cooling curve for the northwest Sacramento Mountains is consistent with cooling of the crust by thermal conduction (Foster et al., 1992; Harrison and McDougall, 1980; Harrison and Clarke, 1979; Carslaw and Jaeger, 1959), but the sudden increase of the cooling rate to 38-53°C/Ma between 20 and 15 Ma suggests that tectonic denudation (unroofing) as a result of detachment faulting was the driving mechanism for the final cooling of the northwest Sacramento Mountains.

The thermal regime in the northeast Sacramento Mountains is dominated by the syntectonic Eagle Wash intrusive complex. After intrusion at ~20 Ma, the EWIC cooled rapidly from magmatic temperatures to below ~100°C and was exposed at the surface by ~15 Ma. This requires cooling rates of >100°C/Ma and exhumation rates of 1.5 3 km/Ma. The cooling path defined by the EWIC cannot be explained by convective heat transfer and/or uplift alone. Given the contemporaneity of detachment faulting with the intrusion of the EWIC, tectonic denudation associated with Miocene detachment faulting is likely to have facilitated exhumation and cooling.

The ambient temperature of most footwalls (excluding syn-rift plutons) is usually 300-400°C and their deeper portions appear to cool to <100°C rapidly (in 1-10 million years). $^{40}Ar/^{39}Ar$ and fission track thermochronologic data indicate that mid-crustal mylonitic rocks associated with metamorphic core complexes have cooled quickly as a result of tectonic exhumation. Cooling rates as high as 100°C/m.y., but generally around 50°C/m.y., have been documented in the Sacramento Mountains (this study), Chemehuevi, Whipple, and Ruby Mountains (John and Foster, 1993; Foster et al., 1990; Davis, 1988; Dallmeyer et al.,

1986; Dokka et al., 1986). Assuming a constant geothermal gradient of 30°C/km, upward rates of motion of 4 km/m.y. are implied. Additionally, barometric studies on syn- and post-tectonic intrusive rocks indicate exhumation rates of 1.3-2.3 km/m.y. (Anderson, 1988). This suggests that the exhumation and rapid cooling of most core complexes must be due to similar mechanisms as those which are proposed for the Sacramento Mountains, namely buoyancy forces. The uplift and cooling of metamorphic core complexes must be primarily facilitated by the combination of magmatism and tectonic denudation via detachment faulting.

In a regime dominated by E-W horizontal extension, the dominant stress in the northeast Sacramento Mountains alternated between σ_1 and σ_3, i.e.- between $\sigma_3 < \sigma_2 \approx \sigma_1$ and $\sigma_1 > \sigma_2 \approx \sigma_3$. Rapid variations of the state of stress in the crust have been called upon to explain the relatively contemporaneous intrusion of both horizontal and vertical dikes in metamorphic core complexes (John, 1987; Spencer, 1985). Three dimensional strain can be partitioned in space, or oscillate in time, in such a way so as to produce such variations in the state of stress. Mechanisms which would produce strain variation include differential tectonic unroofing (i.e. - single-sided denudation), buoyant forces associated with an uncompensated crustal root, and magmatic inflation. Inasmuch as the younging of ages to the northeast suggests that normal faulting in the northeast Sacramento Mountains continued longer in the northeast than in the southwest part of the range, differential tectonic unroofing (if not single-sided denudation) occurred. Differential uplift and cooling is a by-product of differential tectonic unroofing, as the southwest would have been at lower temperatures/shallower depths than the northeast region of the northeast Sacramento Mountains for any point in time during faulting. Magmatic inflation resulting from the intrusion of the EWIC would also have contributed to the buoyant forces acting during the uplift of the northeast Sacramento Mountains. The combined effects of syntectonic plutonism and differential tectonic denudation in the northeast Sacramento Mountains suggests that a heterogeneous vertical stress could have developed. Certainly, the *episodicity* associated with both magmatism and detachment faulting would have contributed to the effects associated with a three dimensional strain. For example, when the vertical stress is reduced as a result of denudation or magmatism, horizontal compression perpendicular to σ_3 is facilitated; however, as the denuded footwall is isostatically compensated, or as plutons solidify, the vertical stress is restored and vertical compression

dominates. This alternation of the dominant stress is facilitated by the episodic nature of magmatic intrusion and detachment faulting in space and time.

7.4 Future investigations

An investigation such as this is never really finished, because the answer to one question always promotes several others. Future investigations in the Sacramento Mountains can illuminate a number of issues. Certainly, more U/Pb geochronologic work (especially ion-probe techniques) in the northern part of the northeast Sacramento Mountains would be beneficial in identifying pre-Tertiary lithologies, i.e.-inheritance, and evaluating the apparent absence of Cretaceous lithologies. The geochemistry of the Miocene volcanics in the region is relatively unevaluated and investigations into the possible correlations between syntectonic plutons and their extrusive equivalents would undoubtedly yield much useful information regarding mixing processes, magma chamber dynamics/structure, etc. The geologic mapping can always be improved by providing more detail than time allowed during the initial investigation. For example, mapping at a finer scale than 1:24,000. Micro-structural investigations into the genesis of mylonitic shear zones, both geochronological/thermobarometric (using mylonitic minerals) and geochemical (looking at compositional changes associated with mylonite formation), could increase our understanding of these processes.

Abers, G., 1991, Possible seismogenic shallow-dipping normal faults in the Woodlark-D'Entrecasteaux extensional province, Papua New Guinea: Geology, v. 19, p. 1205-1208.

Allmendinger, R., Sharp, J., VonTish, D., Serpa, L., Brown, L., Kaufman, S., Oliver, J., and Smith, R. B., 1983, Cenozoic and Mesozoic structure of the eastern Basin and Range province, Utah, from COCORP seismic-reflection data: Geology, v. 11, p. 532-536.

Anderson, E., 1951, The dynamics of faulting (second edition): Edinburgh, Scotland, Oliver and Boyd, 191p.

Anderson, J., 1983, Proterozoic anorogenic granite plutonism of North America: Geological Society of America Memoirs, v. 161, p. 133-154.

Anderson, J., 1996, Status of thermobarometry in granitic batholiths: Transactions of the Royal Society of Edinburgh, v. 87, p. 125-138.

Anderson, J. , 1988, Core complexes of the Mojave-Sonoran Desert: Conditions of plutonism, mylonitization, and decompression, in Ernst, W.G., editor, Metamorphism and crustal evolution of the western United States, Rubey Volume VII: Prentice Hall, Englewood Cliffs, New Jersey, p. 503-525.

Anderson, J., and Bender, E., 1988, Nature and origin of Proterozoic A-type granitic magmatism in the southwestern United States: Lithos, v. 23, p. 19-52.

Anderson, J., and Cullers, R., 1990, Middle to upper crustal plutonic construction of a magmatic arc; an example from the Whipple Mountains metamorphic core complex: in Anderson, J., editor, The Nature and Origin of Cordilleran Magmatism, p. 47-69.

Anderson, J., and Smith, D., 1995, The effects of temperature and fo_2 on the Al-in-hornblende barometer: American Mineralogist, v. 80, p. 549-559.

Anderson, J. , Barth, A., and Young, E., 1988, Mid-crustal Cretaceous roots of Cordilleran metamorphic core complexes: Geology, v. 16, p. 366-369.

Argent, J., 1996, The geology and Tertiary structural evolution of the northwest Sacramento Mountains footwall core complex, sourtheast California, USA: University of Oxford, England (D. Phil. thesis), 200p.

Argent, J., and Pease, V., 1994, Tectonic and crustal evolution of the Sacramento Mountains, southeast California: the footwall of a metamorphic core complex: Geological Society of London, Tectonic Studies Group Annual Meeting, p. 5.

Armstrong, R., 1982, Cordilleran metamorphic core complexes from Arizona to southern Canada: Annual Review of the Earth and Planetary Sciences, v. 10, p. 12-154.

Armstrong, R. , and Ward, P., 1991, Evolving geographic patterns of Cenozoic magmatism in the North American Cordillera: The temporal and spatial association of magmatism and metamorphic core complexes: Journal of Geophysical Research, v. 96, p. 13,201-13,224.

Atwater, T., 1970, Implications of plate tectonics for Cenozoic tectonic evolution of western North America: Geological Society of America Bulletin, v. 81, p. 3513-3536.

Axen, G., 1992, Pore pressure, stress increase, and fault weakening in low-angle normal faulting: Journal of Geophysical Research, v. 97, p. 8979-8991.

Axen, G., 1993, Ramp-flat detachment faulting and low-angle normal reactiviation of the Tule Springs thrust, southern Nevada: Geological Society of American Bulletin, v. 105, p. 1076-1090.

Axen, G., Taylor, W., and Bartley, J., 1993, Space-time patterns and tectonic controls of Tertiary extension and magmatism in the Great Basin of the western United States: Geological Society of America Bulletin, v. 105, p. 56-76.

Bartley, J., Fletcher, J., Glazner, A., 1990, Tertiary extension and contraction of lower-plate rocks in the Central Mojave metamorphic core complex, southern California: Tectonics, v. 9, p. 521-534.

Bell, T., and Etheridge, M., 1973, Microstructure of mylonites and their descriptive terminology: Lithos, v. 6, p. 337-348.

Bell, T., and Hammond, R., 1984, On the internal geometry of mylonite zones: Journal of Geology, v. 92, p. 667-686.

Bender, E., Anderson, J., Wooden J., and Miller, C., 1990, The Fenner Gneiss and associated units: An early Proterozoic composite batholith, Piute and Old Woman Mountains, California: Geological Society of America Abstracts with Programs (Codilleran Section), v. 22, p. 7.

Bennett, V., and DePaolo, D., 1987, Proterozoic crustal history of the western lUnited States as determined by neodymium isotopic mapping: Bulletin of the Geological Society of America, v. 99, p. 674-685.

Beratan, K., 1989, Basin development during Miocene detachment faulting, Whipple Mountains, southeastern California, Ph. D. dissertation, University of Southern California, 320p.

Bishop, C. (compiler), 1963, Geologic Map of California, Needles (1 degree x 2 degree) sheet: California Division of Mines and Geology, scale 1:250,000.

Block, L., and Royden, L. H., 1990, Core complex geometries and regional scale flow in the lower crust: Tectonics, v. 9, p. 557-567.

Blumenfeld, P. and Bouchez, J. -L., 1988, Shear criteria in granite and migmatite deformed in the magmatic and solid states: Journal of Structural Geology, v. 10, p. 361-372.

Blundy, J., and Holland, T., 1990, Calcic amphibole equilibria and a new amphibole-plagioclase gothermometer: Contributions to Mineralogy and Petrology, v. 104, p. 208-224.

Bonham, H., 1960, Geology and mineral resources of T.9N., R.21-22E, San Bernardino base and meridian, San Bernardino county, California: Southern Pacific Land Company unpublished report, 29p.

Bradshaw, G., and Zoback, M., 1988, Listric normal faulting, stress refraction, and the state of stress in the Gulf Coast basin: Geology, v. 16, p. 271-274.

Bradshaw, T., Hawksworth, C., and Gallagher, K., 1993, Basaltic volcanism in the Southern Basin and Rnage: no role for a mantle plume: Earth and Planetary Science Letters, v. 116, p. 45-62.

Brandon, M., and Vance, J., 1992, Tectonic evolution of the Cenozoic Olympic subduction complex, Washington State, as deduced from fission-track ages for detrital zircons: American Journal of Science, v. 292, p.565-636.

Brodie, K., and Rutter, E., 1985, On the relationship between deformation and metamorphism, with special reference tothe behavior of basic rocks, in Thompson, A., and Rubie, D., Metamorphic reactions: Kinetics, Textures, and Deformation: Springer-Verlag Inc., New York, p. 138-179.

Brooks, W. , and Martin, R. , 1985, Discordant isotopic ages and potassium metasomatism in volcanic rocks, Yavapai County, Arizona: Geological Society of America Abstracts with Programs, v. 17, p.344.

Buck, W. , 1988, Flexural rotation of normal faults: Tectonics, v. 7, p. 959-973.

Buising, A., 1990, The Bouse Formation and bracketing units, southeastern California and western Arizona: Implications for the evolution of the proto-Gulf of California and the lower Colorado River: Jounal of Geophysical Reasearch, v. 95, p. 20,111-20,132.

Burchfiel, B., and Davis, G., 1981, Mojave Desert and environs: in The Geotectonic Development of California (Rubey Volume 1), Prentice-Hall, New Jersey, p. 217-252.

Burchfiel, B., Zhiliang, C., Hodges, K., Yuping, L., Royden, L., Changrong, D., and Jiene, X., 1992, The South Tibetan detachment system, Himalayan orogen: Extension comtemporaneous with and parallel to shortening in a collisional mountain belt: Special Paper of the Geological Society of America, no. 269, p. 1-41.

Carr, W., and Dickey, D., 1976, Cenozoic tectonics of the eastern Mojave Desert: U.S.Geological Survey Professional Paper 1000, 75p.

Carslaw, H., and Jaeger, J., 1959, Conduction of heat in solids (2nd. edition): Clarendon Press, Oxford.

Choukroune, P., and Smith, E., 1985, Detachment faulting and its relatinship to older structural events on Saddle Island, River Mountains, Clark County, Nevada: Geology, v. 13, p. 421-424.

Christiansen, R., and Lipman, P., 1972, Cenozoic volcanism and plate-tectonic evolution of the western United States. II. Late Cenozoic: Philosophical Transactions of the Royal Society of Londan, A271, p. 249-284.

Collier, J. T., 1960, Geology and mineral resources of T.8N., R.21-22E., San Bernardino base and meridian, San Bernardino county, California: Southern Pacific Land Company unpublished report, 32p.

Coney, P., 1979, Tertiary evolution of Cordilleran metamorphic core complexes, in Armentrout, J. W., et al. (editors), Cenozoic paleogeography of the western United States: Sociey of Economic Paleontologists and Mineralogists, Pacific Section III, p. 15-28.

Copeland, P., Parrish, R., and Harrison, T., 1988, Identification of inherited radiogenic Pb in monazite and implications for U-Pb systematics: Nature, v. 333, p.760-763.

Cosca, M., Essene, E., and Bowman, J., 1991, Complete chemical analyses of metamorphic hornblendes: Implications for normalizations, calculated H_2O activities, and thermobarometry: Contributions to Mineralogy and Petrology, v. 108, p. 472-484.

Crittenden, M., Coney, P., and Davis, G. (editors), 1980, Cordilleran metamorphic core complexes: Geological Society of America Memoir 153, 490p.

Crowley, K., Cameron, M., and Schaefer, R., 1991, Experimental studies of annealing of etched fission tracks in fluorapatite; Geochimica et Cosmochimica Acta, v. 55, p. 1449-1465.

Dallmeyer, R., Snoke, A., and McKee, E., 1986, The Mesozoic-Cenozoic tectonothermal evolution of the Ruby Mountains, East Humboldt Range, Nevada: A Cordilleran metamorphic core complex: Tectonics, v. 5, p.931-954.

Dalrymple, G., and Lanphere, M., 1969, Potassium-argon dating: Principles, techniques, and applications to geochronology: Freeman and Company Publishers, San Francisco, 258p.

Darton, N., 1915, Guidebook of the western United States, Part C, The Santa Fe Route: United States Geological Survey Bulletin, v. 613, p. 146-148.

Davis, G., 1988, Rapid upward transport of midcrustal mylonitic gneisses in the footwall of a Miocene detachment fault, Whipple mountains, southeastern California: Geologische Rundschau, v. 77, no. 1, p.191-209.

Davis, G., and Lister, G., 1988, Detachment faulting in continental extension; perspectives from the southwest U. S. Cordillera: Geological Society of America Special Publication 218, p. 133-159.

Davis, G.., Anderson, J., Frost, E., and Shackelford, T., 1980, Mylonitization and detachment faulting in the Whipple-Buckskin-Rawhide Mountains terrane, southeastern California and western Arizona: in Crittenden, M. D., Jr., Coney, P. J., and Davis, G. H., editors, Cordilleran Metamorphic Core Complexes, Geological Society of America Memoir 153, p. 79-130.

Davis, G., Anderson, J., Martin, D., Krummenacher, D., Frost, E. and Armstrong, R., 1982, Geologic and geochronologic relations in the lower plate of the Whipple detachment fault, Whipple Mountains, southeastern California: a progress report: in Frost, E. and Martin, D., editors, Mesozoic-Cenozoic Tectonic Evolution of the Colorado River Region California, Arizona and Nevada, Cordilleran Publishers, San Diego, California, p. 409-432.

Deer, W., Howie, R., and Zussman, J., 1966, An introduction to the rock forming minerals: Longman Group Limited, London, England, 528p.

DeJongh, W., 1973, X-ray flourescence analysis applying theorectical matrix corrections. Stainless steel: X-ray spectrometry, v. 2, p. 151-158.

DePaolo, D., 1988, Neodymium Isotope Geochemistry An Introduction: Springer-Verlag, Berlin, 187p.

DePaolo, D., Linn, A., and Schubert, G., 1991, The continental crustal age distribution: methods of determining mantle separation ages from Sm-Nd isotopic data and application to the southwestern United States: Journal of Geophysical Research, v. 96, p. 2071-2088.

Dickenson, W., 1979, Cenozoic plate tectonic setting of the Cordilleran region in the United states: in Armentrout, J., Cole, M, and TerBest, H., (editors), SEPM Pacific Cenozoic Paleogeography of the Western United States, SEPM Pacific Coast Paleogeography Symposium, v. 3, p. 1-13.

Dodson, M., 1973, Closlure temperature in cooling geochronological and petrological systems: Contributions to Mineralogy and Petrology, v. 40, p. 259-274.

Dokka, R., 1993, Original dip and subsequent modification of a Cordilleran detachment fault, Mojave extensional belt, California: Geology, v. 21, p. 711-714.

Dokka, R., Mahaffie, M., and Snoke, A., 1986, Thermochronologic evidence of major tectonic denudation associated with detachment faulting, Northern Ruby Mountains East Humboldt Range, Nevada: Tectonics, v. 5, p. 995-1006.

Duebendorfer, E., and Simpson, D., 1994, Kinematics and timing of Tertiary extension in the Lake Mead region, Nevada: Geological Society of America Bulletin, v. 106, p.1057-1073.

Dumitru, T., Gans, P., Foster, D., and Miller, E., 1991, Refrigeration of the western Cordilleran lithosphere during Laramide shallow-angle subduction: Geology, v. 19, p. 1145-1148.

Eaton, 1982, The Basin and Range province: Origin and tectonic significance: Annual Review of Earth and Planetary Sciences, v. 10, p. 409-440.

Elston, D., McKee, T., 1982, Age and correlation of the late Proterozoic Grand Canyon disturbance, northern Arizona: Bulletin of the Geological Society of America, v. 93, p. 681-699.

Falkner, C., Miller, C., Wooden, J., and Heizler, M., 1995, Petrogenesis and tectonic significance of the calk-alkaline, bimodal Aztec Wash pluton, El Dorado Mountains, Colorado River Extensional Corridor: Journal of Geophysical Research, v. 100, p. 10453-10476.

Farmer, G.,Perry, F., Semken, S., Crowe, B., Curtis, D., and DePaolo, D., 1989, Isotopic evidence of the structure and origin of subcontinental lithospheric mantle in southern Nevada: Journal of Geophysical Research, v. 94, p. 7885-7898.

Faure, G., 1986, Principles of isotope geology (*second edition*): John Wiley & Sons, Inc., New York, 589 p.

Fisher, R., 1953, Dispersion on a sphere: Royal Society of London Proceedings, v. 217, p. 295-305.

Fitzgerald, P., and Gleadow, A., 1988, Fission-track geochronology, tectonics and structure of the Transantarctic Mountains in Northern Victoria Land, Antarctica: Chemical Geology (Isotope Geoscience Section), v. 73, p. 169-198.

Fitzgerald, P., and Gleadow, A., 1990, New approaches in fission track geochronology as a tectonic tool: Examples from the Transantarctic Mountains, Nuclear Tracks Radiation Measurement, v. 17, p.351-357.

Fitzgerald, P., Fryxell, J., and Wernicke, B., 1991, Miocene crustal extension and uplift in southeastern Nevada: Constraints from fission track analysis: Geology, v. 19, p. 1013-1016.

Fleck, R., Sutter, J., and Elliot, D., 1977, Interpretation of discordant 40Ar/39Ar age spectra of Mesozoic tholeiites from Antarctica: Geochimica et Cosmochimica Acta, v. 41, p.15-32.

Fleet, M., and Barnett, R., 1978, Aliv/Alvi partitioning in calciferous amphiboles from the Frood mine, Sudbury, Ontario: Canadian Mineralogist, v. 16,p. 527-532.

Fletcher, J., Bartley, J., Martin, M., Glazner, A., Walker, J., 1995, Large-magnitude continental extension: An example from the central Mojave metamorphic core complex: Geological Society of America Bulletin, v. 107, p. 1468-1483.

Fletcher, J., and Bartley, J., 1994, Constrictional strain in a non-coaxial shear zone: Implications for fold and rock fabric development, central Mojave metamorphic core complex, California: Jounral of Structural Geology, v. 16, p. 555-570.

Forsyth, D., 1992, Finite extension and low-angle normal faulting: Geology, v. 20, p. 27-30.

Foster, D., and Fanning, C., 1997, Geochronology of the Idaho-Bitterroot batholith and Bitterroot Dome: An example of magmatism preceeding and contemporaneous with metamorphic core complex extension: Geological Society of America Bulletin, in press.

Foster, D., and Gleadow, A., 1992, The morphotectonic evolution of rift-margin mountains in central Kenya, Constraints from apatite-fission track thermochronology: Earth and Planetary Science Letters, v. 113, p. 157-171.

Foster, D., Harrison, T., Miller, C., and Howard, K., 1990, The 40Ar/39Ar thermochronology of the eastern Mojave Desert, California, and adjacent western Arizona with implications for the evolution of metamorphic core complexes: Journal of Geophysical Research, v. 95, p. 20,005-20,024.

Foster, D., John, B., Campbel, E., and Fanning, C., 1996, The timing and role of sytectonic plutonism in the development of the Colorado River extensional corridor: Sacramento Mountains example: Geological Society of America Abstracts with Programs, p. A450.

Foster, D., Miller, C., Harrison, T., and Hoisch, T., 1992, $^{40}Ar/^{39}Ar$ thermochronology and thermobarometry of metamorphism, plutonism,and tectonic denudation in the Old Woman Mountains area, California: Geological Society of America Bulletin, v. 104, p. 176-191.

Foster, D., Miller, D., and Miller, C., 1991, Tertiary extension in the Old Woman Mountains area, California: Evidence from apatite fission track analysis: Tectonics, v. 10, p. 875-886.

Frey, F., Green, D., Roy, S., 1978, Integrated models of basalt petrogenesis: a study of quartz tholeiites to olivine melilites from southeastern Australia utilizing geochemical and experimental petrologic data: Journal of Petrology, v. 19, p. 463-513.

Frost, E., and Martin, D., 1982, Comparison of Mesozoic compressional tectonics with mid-Tertiary detachment faulting in the Colorado River area, California, Arizona, and Nevada, in Cooper, J. D., editor, Geologic excursions in the California desert: Geologic Society of America, Cordilleran Section, 78th Annual Meeting (Field Trip Guide), p. 113-159.

Gaber, J., Foland, K., and Corbato, C., 1988, On the significance of argon release from biotite and amphibole during $^{40}Ar/^{39}Ar$ vacuum heating: Geochimica et Cosmochimica Acta, v. 10, p. 2457-2465.

Ganguly, J., and Saxena, S., 1984, Mixing properties of aluminosilicate garnets - Constraints from natural and experimental data, and applications to geothermobarometry: American Mineralogist, v. 69, p. 88-97.

Gans, P., and Miller, E., 1983, Style of mid-Tertiary extension in east-central Nevada, in Geologic excursions in the overthrust belt and metamorphic core complexes of the Intermountain Region: Utah Geology and Mineral Survey, Special Study 59, p. 108-139.

Gans, P., Miller, E., McCarthy, J., and Ouldcott, M., 1985, Tertiary extensional faulting and evolving ductile-brittle transition zones in the northern Snake Range and vicinity: New insights from seismic data: Geology, v. 13, p. 189-193.

Gans, P., Mahood, G., and Schermer, E., 1989, Synextensional magmatism in the Basin and Range Province: Geological Society of America Special Paper, v. 233, 53 p.

Ghent, E., and Stout, M., 1981, Geobarometry and geothermometry of plagioclase-biotite-garnet-muscovite assemblages: Contributions to Mineralogy and Petrology, v. 76, p. 92-97.

Gill, J., 1981, Orogenic Andesites and Plate Tectonics: Springer-Verlag, Berlin, 390p.

Glazner, A., 1990, Recycling of continental crust in Miocene volcanic rocks from the Mojave block, southern California: in Anderson, J. (editor) The Nature and Origin of Cordilleran Magmatism, Geological Society of America Memoir 174, p. 147-168.

Glazner, A., and Bartley, J., 1991, Volume loss, fluid flow and state of strain in extensional mylonites from the central Mojave Desert, California: Journal of Structural Geology, v. 13, p. 587-595.

Glazner, A., Walker, J., Bartley, J., and Dent, S., 1988, Distribution and relations of Precambrian and Paleozoic rocks in the central Mojave Desert, California: Geological Society of America Abstracts with Programs, v. 20, p. 163.

Gleadow, A., Duddy, I., 1981, A natural long term annealing experiment for apatite; Nuclear Tracks, v. 5, p. 169-174.

Gleadow, A., Duddy, I., Green, P., and Lovering, J., 1986, Confined fission track lengths in apatite: A diagnostic tool for thermal history analysis: Contributions to Mineralogy and Petrology, v. 94, p. 405-415.

Green, P., Duddy, I., Laslett, G., Hegarty, K., Gleadow, A., and Lovering, J., 1989, Thermal annealing of fission tracks in apatite 4. Quantitative modelling techniques and extension to geological time scales: Chemical Geology (Isotope Geoscience Secion), v. 79, p. 155-182.

Hamilton, W., 1988, Detachment faulting in the Death Valley region, California and Nevada: U.S. Geological Survey Bulletin 1790, p.51-85

Hammarstrom, J., and Zen, E., 1986, Aluminum in hornblende: An empirical igneous geobarometer: American Mineralogist, v. 71, p. 1297-1313.

Hanmer and Passchier, 1991, Shear-sense indicators: A review: Geological Survey of Canada Paper 90-17, 72p.

Harrison, T., 1983, Some observations on the interpretation of 40Ar/39Ar age spectra: Isotope Geoscience, v. 1, p. 319-338.

Harrison, T., 1981, Diffusion of 40Ar in hornblende: Contributions to Mineralogy and Petrology, v. 78, p. 324-331.

Harrison, T., and Clarke, G., 1979, A model of the thermal effects of igneous intrusion and uplift as applied to Quottoon Pulton, British Columbia: Canadian Journal of Earth Science, v. 16, p. 411-420.

Harrison, T., and McDougall, I., 1980, Investigations of an intrusive contact, northwest Nelson, New Zealand - I. Thermal, chronological and isotopic constraints: Geochimica et Cosmochimica Acta, v. 44, p. 1985-2003.

Harrison, T., and McDougall, I., 1981, Excess 40Ar in metamorphic rocks from Broken Hill, New South Wales: Implications for 40Ar/39Ar age spectra and the thermal history of the region: Earth and Planetary Science Letters, v. 55, p. 123-149.

Harrison, T., Duncan, I., and McDougall, I., 1985, Diffusion of 40Ar in biotite: Temperature, pressure, and compositional effects: Geochimica et Cosmochimica Acta, v. 49, p. 2461-2468.

Harrison, T., McKeegan, K., and LeFort, P., 1995, Detection of inherited monazite in the Manaslu leucogranite by 208Pb/232Th ion microprobe dating: Crystallization age and tectonic implications: Earth and Planetary Science Letters, v. 133, p. 271-282.

Hazzard, J., and Dosch, E., 1936, Archean rocks in the Old Woman and Piute Mountains, San Bernardino County, California: Proceedings of the Geological Society of America, p. 308-309.

Heaman, L., and Parrish, R., 1991, U-Pb geochronology of accessory minerals *in* Mineralogical Association of Canada Short Course Handbook on Applications of Radiogenic Isotope Systems to Problems in Geology, v. 19, p. 59-102.

Heimann, A., Steinitz, G., and Zafrir, H., 1992, Irradiation of samples for 40Ar/39Ar dating using the Soreq Nuclear Research Center IRR-1 reactor: Israelly Nuclear Geophysics, v. 6, p. 273-286.

Heizler, M., and Harrison T., 1988, Multiple trapped argon isotope components revealed by 40Ar/39Ar isochron analysis: Geochimica et Cosmochimica Acta, v. 52, p. 1295-1303.

Hetzel, R., Ring, U., Akal, C., and Troesch, M., 1995, Miocene NNE-directed extensional unroofing in the Menderes Massif, southwestern Turkey: Journal of the Geological Society Of London, v. 152, p. 639-654.

Hoisch, T., Miller C., Heizler, M., Harrison, T, and Stoddard, E., 1988, Late Cretaceous regional metamorphism in southeastern California, in Ernst, W.G., editor, Metamorphism and crustal evolution in the western Cordillera, conterminous United States (Rubey Volume 7): Englewood Cliffs, New Jersey, Prentice-Hall, p. 538-571.

Hoisch, T., 1990, Empirical calibration of six geobarometers for the mineral assemblage quartz + muscovite + biotite + plagioclase + garnet: Contributions to Mineralogy and Petrology, v. 104, p. 225-234.

Holland, T., and Blundy, J., 1994, Non-ideal interactions in calcic amphiboles and their bearing on amphibole-plagioclase thermometry: Contributions to Mineralogy and Petrology, v. 116, p. 433-447.

Hollister, L., Grissom, G., Peters, E., Stowell, H., and Sisson, V., 1987, Confirmation of the empirical correlation of Al in hornblende with pressure of solidification of calc-alkaline plutons: American Mineralogist, v. 72, p. 231-239.

Holm, D., and Dokka, R., 1993, Interpretation and tectonic implications of cooling histories: An example from the Black Mountains, Death Valley extended terrane, California: Earth and Planetary Science Letters, v. 116, p. 63-80.

Holm, D., and Wernicke, B., 1990, Black Mountains crustal section, Death Valley extended terrain, California: Geology, v. 18, p. 520-523.

Holm, D., Snow, J., and Lux, D., 1992, Thermal and barometric constraints on the intrusive and unroofing history of the Black Mountains: Implications for timing, initial dip, and kinematics of detachment faulting in the Death Valley region, California: Tectonics, v. 11, p. 507-522.

Howard, K., 1991, Intrusion of horizontal dikes: Tectonic significance of Middle Proterozoic diabase sheets widespread in the upper crust of the southwestern United States: Journal of Geophysical Research, v. 96, p. 12,461-12,478.

Howard, K., and Foster, D., 1996, Thermal and unroofing history of a thick, tilted Basin and Range crustal section in the Tortilla Mountains, Arizona, Journal of Geophysical Research, v. 101, p. 511-522.

Howard, K., and John, B., 1987, Crustal extension along a rooted system of imbricate low-angle faults: Colorado River extensional corridor, California and Arizona, in Coward, M. P., Dewey, J. F., and Hancock, P. L., editors, Continental extensional tectonics: Geological Society Special Publication No. 28, p. 229-311.

Howard, K., John, B., and Miller, C., 1987, Metamorphic core complexes, Mesozoic ductile thrusts, and Cenozoic detachments: Old Woman Mountains-Chemehuevi Mountains transect, California and Arizona, in Davis, G., and Van den Dolder, E., (editors), Geologic diversity of Arizona and its margins: Excursions to choice ares: Arizona Bureau of Geology and Mineral Technology Special Paper, v. 5, p. 365-382.

Howard, K., McCaffrey, K., Wooden, J., Foster, D., and Shaw, S., 1995, Jurassic thrusting of Precambrian basement over Paleozoic cover in the Clipper Mountains, southeastern California: in Miller, D., and Busby, C. (editors), Jurassic Magmatism and Tectonics of the North American Cordillera, Geological Society of America Special Paper 299, p. 375-392.

Howard, K., Stone, P., Pernokas, M., and Marvin, R., 1982, Geologic and geochronologic reconnaissance of the Turtle Mountains area, California: West border of the Whipple detachment terrane, in Frost, E.G., and Martin, D.L., editors, Mesozoic-Cenozoic tectonic evolution of the Colorado River region, California, Arizona, and Nevada (Anderson-Hamilton volume): San Diego, California, Cordilleran Publishers, p. 341-354.

Howard, K., Wooden, J., Simpson, R., and Pease, V., 1996, Extension-related plutonism along the Colorado River extensional corridor: Geological Society of America Abstracts with Programs, p. A450.

Hurford, A., and Green, P., 1983, The zeta age calibration of fission track dating, Chemical Geology (Isotope Geoscience Section), v. 1, p. 258-317.

Hyndman, D., and Myers, S., 1988, The transition from amphibole-facies mylonite to chloritic breccia and role of the mylonite in formation of Eocene epizonal plutons, Bitterroot dome, Montana: Geologische Rundschau, v. 77, p. 211-226.

Irvine, T., and Baragar, W., 1971, A guide to chemical classification of the common igneous rocks: Canadian Journal of Earth Sciences, v. 8, p. 523-548.

Jackson, J., 1987, Active normal faulting and crustal extension, in Coward, M.P., Dewey, J.F., and Hancock, P.L., editors., Continental extensional tectonics: Geological Society of London Special Publication 28, p. 3-17.

Jackson, J., and McKenzie, D., 1983, The geometrical evolution of normal fault systems: Journal of Structural Geology, v. 5, p. 471-482.

Jackson, J., and White, N., 1989, Normal faulting in the upper continental crust: Journal of Structural Geology, v. 11, p. 15-36.

Jacobsen, S., and Wasserburg, G., 1984, Sm-Nd isotopic evolution of chondrites and achondrites, II: Earth and Planetary Science Letters, v. 67, p. 137-150.

John, B., 1982, Geologic framework of the Chemehuevi Mountains, southeastern California, in Frost, E.G., and Martin, D.L., editors., Mesozoic-Cenozoic tectonic evolution of the Colorado River region, California, Arizona, and Nevada (Anderson-Hamilton volume): San Diego, California, Cordilleran Publishers, p. 317-325.

John, B., 1986, Structural and intrusive history of the Chemehuevi Mountains area, southeastern California and western Arizona: University of Californiz, Santa Barbara, Ph. D. thesis, 295p.

John, B., and Mukasa, S., 1990, Footwall rocks of the mid-Tertiary Chemehuevi detachment fault: A window into the middle crust in the southern Cordillera: Journal of Geophysical Research, v. 95, p. 463-475.

John, B., and Wooden, J., 1990, Petrology and geochemistry of the metaluminous to peraluminous Chemehuevi Mountains Plutonic Suite, southeastern California: in Anderson,J., editor, The Nature and Origin of Cordilleran Magmatism, Geological Society of America Memoir 174, p. 71-98.

John, B., and Foster, D., 1993, Structural and thermal constraints on the initiation angle of detachment faulting in the southern Basin and Range: The Chemehuevi Mountains case study: Geological Society of America Bulletin, v. 105, p. 1091-1108.

Johnson, R., and Loy, K., 1992, Seismic reflection evidence for seismogenic low-angle faulting in southeastern Arizona: Geology, v. 20, p. 597-600.

Jolivet, L., Daniel, J., and Fournier, M., 1991, Geometry and kinematics of extension in Alpine Corsica: Earth and Planetary Science Letters, v. 104, p. 278-291.

Karlstrom, K., Miller, C., Kingsbury, J., Wooden, J., 1993, Pluton emplacement along an active ductile thrust zone, Piute Mountains, southeastern California: Interaction between deformational and solidification processes: Geological Society of America Bulletin, v. 105, p. 213-230.

Kerrich, R., 1988, Detachment zones of Cordilleran metamorphic core complexes: Thermal, fluid and metasomatic regimes: Geologische Rundschau, v. 77, p. 157-181.

Kerrich, R., and Hyndman, D., 1986, Thermal and fluid regimes in the Bitterroot lobe-Sapphire block detachment zone, Montana: Evidence from $^{18}O/^{16}O$ and geologic relations: Geological Society of America Bulletin, v. 97, p. 147-155.

Kohler, S., Loyd, R., Burnett, J., 1985, Mineral land classification-northeast quarter of the Needles 1 x 2 degree quadrangle, San Bernardino county, California: California Department of Conservation, Division of Mines and Geology, Open File Report 85-18 SAC.

Krabbendam, M, and Leslie, A., 1996, Folds with vergence opposite to the sense of shear: Journal of Structural Geology, v. 18, p. 777-781.

Langmuir, C., Vocke, R., Hanson, G., and Hart, S., 1978, A general mixing equation with applications to Icelandic basalts: Earth and Planetary Science Letters, v. 37, p. 380-392.

Lanphere, M. and Dalrymple, G., 1976, Identification of excess ^{40}Ar by the $^{40}Ar/^{39}Ar$ age spectrum technique: Earth and Planetary Science Letters, v. 32, p. 141-148.

Lapworth, C., 1885, The Highland controversy in British history: Its causes, course, and consequences: Nature, v. 32, p. 558-559.

Leake, B., 1978, Nomenclature of amphiboles: Canadian Mineralogist, v. 16, p. 501-520.

Lee, R., and McConchie, D., 1982, Comprehensive major and trace element analysis of geological material by X-ray fluorescense using low dilution fusions: X-ray Spectrometry, v. 11, p. 55-63.

Leeman, W., and Hawksworth, C., 1986, Open magma systems: Trace element and isotopic constraints: Journal of Geophysical Research, v. 91, p. 5901-5912.

LeMaitre, R., Bateman, P., Dudek, A., Keller, J., Lameyre Le Bas, M., Sabine, P., Schmid, R., Sorensen, H., Streckeisen, A., Woolley, A., and Zanettin, B., 1989, A classification of igneous rocks and glossary of terms: Blackwell, Oxford.

Lister, G., and Baldwin, S., 1993, Plutonism and the origin of metamorphic core complexes: Geology, v. 21, p. 607-610.

Lister, G., and Davis, G., 1989, The origin of metamorphic core complexes and detachment faults formed during Tertiary continental extension in the northern Colorado River region, U.S.A.: Journal of Structural Geology, v. 11, p. 65-94.

Lister, G., and Snoke, A., 1984, S-C mylonites: Journal of Structural Geology, v. 6, p. 617-638.

Lucchitta, I., and Suneson, N., 1993, Stratigraphic section of the Castaneda Hills - Signal area, Arizona: U.S. Geological Survey Bulletin 2053, p. 139-144.

Ludwig, K. and Silver, L., 1977, Lead isotopic inhomogeneity in Precambrian igneous -feldspars: Geochimeca et Cosmochimeca Acta, v. 41, p. 1457-1471.

Lugmair, G., and Marti, K., 1978, Lunar initial 143Nd/144Nd: Differential evolution of the lunar crust and mantle: Earth and Planetary Science Letters, v. 35, p. 273-84.

Naney, M., 1983, Phase equilibria of rock-forming ferromagnesian silicates in granitic systems: American Journal of Science, v. 283, p. 993-1033.

Neumann, T., and Leszcykowski, A., 1993, Identified mineral resources of the Needles 1 x 2 degree quadrangle, California: U. S. Bureau of Mines Mineral Land Assessment Open File Report, 14-93.

Manning, A., and Bartley, J., 1994, Postmylonitic deformation in the Raft River metamorphic core complex, northwestern Utah: Evidence of a rolling hinge: Tectonics, v. 13, p. 596-612.

Marsal, D., 1987, Statistics for geoscientists: Pergamon Press, New York, 176p.

McCarthy, J., Larkin, S., Fuis, G., Simpson, R., and Howard, K., 1991, Anatomy of a metamorphic core complex: Seismic refraction/wide-angle reflection profiling in southeastern California and western Arizona: Journal of Geophysical Research, v. 96, p. 12,259-12,292.

McClelland, W., 1982, Structural geology of the central Sacramento Mountains, San Bernardino County, California, in Frost, E. G., and Martin, D. L., editors, Mesozoic-Cenozoic tectonic evolution of the Colorado River region, California, Arizona, and Nevada: Cordilleran Publishers, San Diego, California, p. 401-406.

McClelland, W., 1984, Low-angle Cenozoic faulting in the central Sacramento Mountains, San Bernardino County, California: MSc Thesis, University of Southern California, 94 p.

McDougall, I., and Harrison, T., 1988, Geochronology and thermochronology by the $^{40}Ar/^{39}Ar$ method: Oxford University Press, New York, 212 p.

McDougall, I., and Roksandic, Z., 1974, Total fusion 40Ar/39Ar ages using HIFAR reactor: Journal of the Geological Society of Australia, v. 21, p. 81-89.

McGarr, A., 1988, On the state of lithospheric stress in the absence of applied tectonic forces: Journal of Geophysical Research, v. 93, p. 13,609-13,617.

McKenzie, D., 1978, Some remarks on the development of sedimentary basins: Earth and Planetary Science Lettters, v. 40, p. 25-32.

Mellosh, H., 1990, Mechanical basis for low-angle faulting in the Basin and Range province: Nature, v. 343, p. 331-335.

Menzies, M., Leeman, W., and Hawksworth, C., 1983, Isotope geochemistry of Cenozoic volcanic rocks reveals mantle heterogeneity below the western USA: Nature, v. 303, p. 205-209.

Merey, C., and Ticken, E., 1989, Geophysical investigation, California low-level waste disposal project, Ward Valley, California: U.S. Ecology: California low-level waste disposal facility Licence Application, Appendix 2320B.

Metzger, D., and Loeltz, O., 1973, Geohydrology of the Needles area, Arizona, California, and Nevada: U.S. Geological Survey Professional Paper 486-J, 54p.

Miller, C., and Wooden, J., 1993, Anatexis, hybridization, and the modification of ancient crust: Mesozoic plutonism in the Old Woman Mountains area, California: Lithos, v. 32, p. 111-133.

Miller, C., Wooden, J., Bennett, V., Wright, J., Solomon, G., and Hurst, R., 1990, Petrogenesis of the composite peraluminous-metaluminous Old Woman-Piute Range batholith, southeastern California; Isotopic constraints: in Anderson,J., editor, The Nature and Origin of Cordilleran Magmatism, Geological Society of America Memoir 174, p. 99-109.

Miller, C., Watson, E., and Harrison, T., 1988, Perspectives on the source, segregation, and transport of granitoid magmas: Transactions of the Royal Society of Edinburgh, v. 79, p. 135-156.

Miller, E., Gans, P., and Garing, J., 1983, The Snake Range decollement: an exhumed mid-Tertiary brittle-ductile transition: Tectonics, v. 2, p. 239-263.

Miller, R., and Paterson, S., 1994, The transition from magmatic to high-temperature solid-state deformation: implications from the Mount Stuart batholith, Washington: Journal of Structural Geology, v. 16, n. 6, p. 853-865.

Miyashiro, A., 1974, Island arc volcanic rock series: a critical review: Petrologie, v. 1, p. 177-187.

Molnar, P., and England, P., 1990, Temperatures, heat flux, and frictional stress near major thrust faults: Journal of Geophysical Research, v. 95, p.4833-4856.

Molnar, P., and Lyon-Caen, H., 1989, Fault plane solutions of earthquakes and active tectonics of the Tibetan Plateau and its margins: Geophysical Journal International, v. 99, p. 123-153.

Moorbath, S., and Taylor, P., 1986, Geochronology and related isotope geochemistry of high-grade metamorphic rocks from the lower continental crust, in The Nature of the Lower Continental Crust (J. Dawson et al., editors), Geological Society of London Special Publication No. 24, p. 211-220.

Mutter, J., and Karson, J., Structural processes at slow-spreading ridges: Science, v. 257, p. 627-634.

Naeser, C., 1979, Fission-track dating and geologic annealing of fission tracks, in Lectures in Isotope Geology (edited by E. Jäger and J. Hunziker), Springer-Verlag, New York, p. 145-169.

Nakata, J., Pernokas, M., Howard, K., Nielson, J., and Shannon, J., 1990, K-Ar and fission-track ages (dates) of volcanic, intrusive, altered,and metamorphic rocks in the Mojave Mountains area, west-central Arizona: Isochron/West, no. 56, p. 8-20.

Naney, M., 1983, Phase equilibria of rock-forming ferromagnesian silicates in granitic systems: American Journal of Science, v. 283, p. 993-1033.

Nielson, J., and Beratan, K., 1995, Stratigraphic and structural systhesis of a Miocene extensional terrane, southeast California and west-central Arizona: Geological Society of America Bulletin, v. 107, p. 241-252.

Nielson, J., and Beratan, K., 1990, Tertiary basin development and tectonic implications, Whipple detachment system, Colorado River extensional corridor, California and Arizona: Journal of Geophysical Research, v. 95, p. 599-614.

Norton, M., 1987, The Nordfjord-Sogn detachment, W. Norway: Norsk Geologisk Tiddskrift, v. 67, p. 93-106.

O'Hara, K., and Blackburn, W., 1989, Volume-loss model for trace element enrichments in mylonites: Geology, v. 17, p. 524-527.

O'Sullivan, P., and Parrish, R., 1995, The importance of apatite composition and single-grain ages when interpreting fission track data from plutonic rocks: a case study from the Coast Ranges, British Columbia: Earth and Planetary Science Letters, v. 132, p. 213-224.

Otton, J., 1982, Tertiary extensional tectonics and associated volcanism in west-central Arizona, in Frost, E., and Martin, D. (editors), Mesozoic-Cenozoic tectonic evolution of the Colorado River region, California, Arizona, and Nevada: San Diego, California, Cordilleran Publishers, p. 41-54.

Pankhurst, R., and O'Nions, R., 1973, Determination of Rb/Sr and 87Sr/86Sr ratios of some standard rocks and evaluation of x-ray fluorescence spectrometry in Rb-Sr geochemistry: Chemical Geology, v. 12, p. 127-136.

Parrish, R., 1990, U-Pb dating of monazite and its application to geological problems: Canadian Journal of Earth Sciences, v. 27, p. 1431-1450.

Parsons, T, and Thompson, G., 1993, Does magmatism influence low-angle normal faulting? Geology, v. 21, p. 247-250.

Passchier, C., and Simpson, C., 1986, Porphyroclast systems as kinematic indicators: Journal of Structural Geology, v. 8, p. 831-843.

Patterson, S., Vernon, R., Tobisch, O., 1989, A review of criteria for the identificatin of magmatic and tectonic foliations in granitoids: Journal of Structural Geology, v. 11, p. 349-363.

Pearce, J., 1982, Trace element characteristics of lavas from destructive plate boundaries: in Thorpe, R., editor, Andesites: Wiley, chichester, p. 525-548.

Pearce, J., Harris, N., and Tindle, A., 1984, Trace element discrimination diagrams for the tectonic interpretation of granitic rocks: Journal Of Petrology, v. 25, p. 956-983.

Pease, V., Foster, D., Wooden, J., O'Sullivan, P., Argent, J., 1995, Tertiary Plutonism and extension in the Sacramento Mountains, SE California: EOS Transactions, v. 76, p. 639.

Pierce, W., 1973, Principle features of the Heart Mountain fault and the mechanism problem, in DeJong, K., and Scholten, R., editors, Gravity and Tectonics: New York, John Wiley and Sons, Inc., p. 457-471.

Potts, P., 1987, Handbook of silicate rock analysis (Chapter 8), Blackie and Son Ltd., London, England, 622p.

Potts, P., Tindle, A., Isaacs, M., 1983, On the precision of electron microprobe data: A new test for the homogeneity of mineral standards, American Mineralogist, v. 68, p. 1237-1242.

Proffett, J., 1977, Cenozoic geology of the Yerington district, Nevada, and implications for the nature and origin of Basin and Range faulting: Geological Society of America Bulletin, v. 88, p. 247-266.

Rehrig, W., and Reynolds, S., 1980, Geologic reconnaissance of a northwest trending zone of metamorphic core complexex in southern and western Arizona, in M. Crittendan, P. Coney, and G. Davis, editors, Cordilleran Metamorphic Core Complexes, Memoir of the Geological Society of America, Boulder, Colorado, p. 131-157.

Reynolds, S., and Lister, G. S., 1990, Folding of mylonitic zones in Cordilleran metamorphic core complexes: Evidence from near the mylonitic front: Geology, v. 18, p. 216-219.

Reynolds, S., and Spencer, J., 1985, Evidence for large-scale transport on the Bullard detachment fault, west-central Arizona: Geology, v. 13, p. 353-356.

Richard, S., Fryxell, J., and Sutter, J., 1990, Tertiary structure and thermal history of the Harquahala and Buckskin Mountains, west central Arizona: Implications for denudation by a major detachment fault system: Journal of Geophysical Research, v. 95, p. 19,973-19,987.

Roddick, J., 1978, The application of isochron diagrams in $^{40}Ar/^{39}Ar$ dating: A discussion: Earth and Planetary Science Letters, v. 41, p. 233-244.

Rollinson, H., 1993, Using Geochemical Data: Evaluation, Presentation, Interpretation: Longman Scientific and Technical, Essex, England, 352p.

Saunders, A., and Tarney, J., 1984, Geochemical characteristics of basaltic volcanism within back-arc basins: in Kokelaar, B., and Howells, M. (editors), Marginal basin geology, Special Publication of the Geological Society of London No. 16, p. 59-76.

Scott, R., and Lister, G., 1992, Detachment faults: Evidence for a low-angle origin: Geology, v. 20, p. 833-836.

Schweitzer, J., 1991, Structural evolution of crystalline lower plate rocks, central Sacramento Mountains, southeastern California: Virginia Polytechnic Institute and State University (Ph. D. Thesis), 180p.

Sibson, R., 1977, Fault rocks and fault mechanisms: Journal of the Geological Society of London, v. 133, p. 191-213.

Silver, L., 1963, The use of cogenetic uranium-lead isotope systems in zircons in geochronology: Radioactive Dating, International Atomic Energy Agency Symposium, Athens, p. 279-287.

Silver, L., and Deutsch, S., 1963, Uranium-lead isotopoic variations in zircon: a case study: Journal of Geology, v. 71, p.721-758.

Simpson, C., 1985, Deformation of granitic rocks across the brittle-ductile transition: Journal of Structural Geology, v. 7, p. 503-511.

Simpson, C., Schweitzer, J., and Howard, K., 1991, A reinterpretation of the timing, position, and significance of part of the Sacramento Mountains detachment fault, southeastern California: Geological Society of America Bulletin, v. 103, p. 751-761.

Simpson, R., Howard, K., Jachens, R., and Mariano, J., 1990, A positive gravity anomaly along the Colorado River extensional corridor: Evidence for new crustal material?: EOS (American Geophysical Union Transactions), v. 71, p. 1594.

Smith, E., Feuerbach, D., and Naumann, T., 1990, Mid-Miocene volcanic and plutonic rocks in the Lake Mead area of Nevada and Arizona: Production of intermediate igneous rocks in an extensional environment: in Anderson, J. (editor), The Nature and Origin of Cordilleran Magmatism, Geological Society of America Memoir 174, p. 169- 194.

Smith, E., 1982, Geology and geochemistry of the volcanic rocks in the River Mountains, Clark County, Nevada, and comparisons with volcanic rocks in the nearby areas, in Frost, E., and Martin, D. (editors), Mesozoic-Cenozoic tectonic evolution of the Colorado River region, California, Arizona, and Nevada: San Diego, California, Cordilleran Publishers, p. 41-54.

Smith, R., and Bruhn, R., 1984, Intraplate extensional tectonics of the eastern Basin and Range: Inferences on structural style from seismic reflection data, regional tectonics, and thermal-mechanical models of brittle-ductile deformation: Journal of Geophysical Research, v. 89, p. 5,733-5,762.

Spear, F., and Kimball, K., 1984, RECAMP- A Fortran IV program for estimating Fe^{3+} contents in amphiboles: Computers and Geoscences, v. 10, p. 317-325.

Spencer, J., 1985, Miocene low-angle normal faulting and dike emplacement, Homer Mountain and surrounding areas, southeastern California and southernmost Nevada: Geological Society of America Bulletin, v. 96, p. 1140-1155.

Spencer, J., 1984, Role of tectonic denudation in warping and uplift of low angle normal faults: Geology, v. 12, p. 95-98.

Spencer, J., 1982, Origin of folds of Tertiary low-angle fault surfaces, southeastern California and western Arizona: in Frost, E. G., and Martin, D. L., editors, Mesozoic-Cenozoic tectonic evolution of the Colorado River region, California, Arizona, and Nevada: Cordilleran Publishers, San Diego, California, p. 123-134.

Spencer, J., and Chase, C., 1989, Role of crustal flexure in initiation of low-angle normal faults and implications for structural evolution of the Basin and Range province: Journal of Geophysical Research, v. 94, p. 1765-1775.

Spencer, J., and Reynolds, S., 1986, Some aspects of the middle Tertiary tectonics of Arizona and southeastern California: Arizona Geological Society Digest, v. 16, p. 102-107.

Spencer, J., and Reynolds, S., 1991, Tectonics of mid-Tertiary extension along a transect through west-central Arizona: Tectonics, v. 10, p. 1204-1221.

Spencer, J., Richard, S., Reynolds, S., Miller, R., Shafiqullah, M., Gilbert, W., and Grubenshy, M., 1995, Spatial and temporal relationships between mid-Tertiary magmatism and extension in southwestern Arizona: Journal of Geophysical Research, v. 100, p. 10.321-10,351.

Spencer, J., and Turner, R., 1982, Dike swarms and low-angle faults, Homer Mountain and the northwestern Sacramento Mountains, in Frost, E. G., and Martin, D. L., editors, Mesozoic-Cenozoic tectonic evolution of the Colorado River region, California, Arizona, and Nevada: Cordilleran Publishers, San Diego, California, p. 97-108.

Spencer, J., and Turner, R., 1983, Geologic map of part of the northwestern Sacramento Mountains, southeastern California: U. S. Geological Survey Open-File Report 83-614.

Stacey, J, and Kramers, J., 1975, Approximation of terrestrial lead isotope evolution by a two-stage model: Earth and Planetary Science Letters, v. 26, p. 207-221.

Staudigel, J., 1979, Chemical analysis of interlaboratory standards, Initial Reports, Deep Sea Drilling Project, v. 51-53, Part 2, p. 1331-1333.

Steiger, R., and Jäger, E., 1977, Subcommission on geochronology: Conventions on the use of decay constants in geo- and cosmochronology: Earth and Planetary Science Letters, v. 36, p. 359-362.

Stewart, J., 1980, Regional tilt patterns of late Cenozoic basin-range fault blocks, western United States: Bulletin of the geological society of America, v. 91, p. 460-464.

Stone, P., Howard, K., and Hamilton, W., 1983, Correlation of metamorphosed Paleozoic strata of the southeastern Mojave Desert region, California and Arizona: Geological Society of America Bulletin, v. 94, p. 1135-1147.

Suneson, N., and Lucchitta, I., 1983, Origin of bimodal volcanism, southern Basin and Range province, west central Arizona, Geological Society of America Bulletin, v. 94, p. 1005-1019.

Thatcher, W., and Hill, D., 1991, Fault orientations in extension and conjugate strike-slip environments and their implications: Geology, v. 19, p. 1116-1120.

Thomas, W., Clark, H., Young, E., Orrell, S., and Anderson, J., 1988, Proterozoic high-grade metamorphism in the Colorado River region, Nevada, Arizona, and California, in Ernst, W., (editor), Metamorphism and crustal evolution of the western United States (Rubey Volume 7): Prentice-Hall, Englewood Cliffs, New Jersey, p. 526-537.

Thompson, R., 1982, British Tertiary volcanic province: Scottish Journal of Geology, v. 18, p. 49-107.

Tilton, G., and Barreiro, B., 1980, Origin of lead in Andean calc-alkaline lavas southern Peru: Science, v. 210, p. 1245-1247.

Tosdal, R., Haxel, G., and Wright, J., 1989, Jurassic geology of the Sonoran Desert region, southern Arizona, southeastern California, and northernmost Sonora: Construction of a continental-margin magmatic arc, in Jenny, J., and Reynolds, S., (editors), Geologic evolution of Arizona: Tucson, Arizona; Arizona Geological Digest 17, p. 397-434.

Tullis, J., 1983, Deformation of feldspars: in P. Ribbe (editor), Feldspar Mineralogy, Reviews of Mineralogy, v. 2, p. 297-323.

Tullis, J., Snoke, A., and Todd, V., 1982, Penrose Conference report on significance and petrogenesis of mylonitic rocks: Geology, v. 10, p. 227-230.

Turnbull, M., Whitehouse, M., Moorbath, S., 1996, New isotopic age determinations for the Torriconian, NW Scotland: Journal of the Geological Society of London, v. 153, p. 955-964.

Vaniman, D. Crowe, B., Gladney, E., 1982, Petrology and geochemistry of hawaiite lavas from Crater Flat, Nevada: Contributions to Mineralogy and Petrology, v. 80, p. 341-357.

Wagner, G., and Van den Haute, P., 1992, Fission-Track Dating: Ferdinand Enke Verlag, Stuttgart, Germany, 285p.

Waters, F., and Erlank, A., 1988, Assessment of the vertical extent and distribution of mantle metasomatism below Kimberly, South Africa: Journal of Petrology Special Lithosphere Issue, p. 185-204.

Wernicke, B., 1981, Low-angle normal faults in the Basin and Range province: Nappe tectonics in an extending orogen: Nature, v. 291, p. 645-647.

Wernicke, B., 1985, Uniform-sense normal simple shear of the continental lithosphere: Canadian Journal of Earth Sciences, v. 22, p. 108-125.

Wernicke, B., 1995, Low-angle normal faults and seismicity: A review: Journal of Geophysical Research, v. 100, p. 20,159-20,174.

Wernicke, B., and Axen, G., 1988, On the role of isostacy in the evolution of normal fault systems: Geology, v. 16, p. 848-851.

Wernicke, B., and Burchfiel, B., 1982, Modes of extensional tectonics: Journal of Structural Geology, v. 4, p. 105-115

Whitehouse, M., Stacey, J., and Miller, F., 1992, Age and nature of the basement in northeastern Washington and northern Idaho: Isotopic evidence from Mesozoic and Cenozoic granitoids: The Journal of Geology, v. 100, p. 691-701.

Whitehouse, M., Fowler, M, and Friend, C., 1996, Conflicting mineral and whole-rock isochron ages from the Late-Archaean Lewisian Complex of northwestern Scotland: Implications for geochronology in polymetamorphic high-grade terrains: Ceochimica et Cosmochimica Acta, v. 60, p. 3085-3102.

Wise, D., Dunn, D., Engelder, J., Geiser, P., Hatcher, R., Kish, S., Odom, A., Schamel, S., 1984, Fault-related rocks: Suggestions for terminology: Geology, v. 12, p. 391-394.

Wilson, M., 1989, Igneous petrogenesis: Unwin Hyman, London.

Wilson, J., McCarthy, J., Johnson, R., and Howard, K., 1991, An axial view of a metamorphic core complex: Crustal Structure of the Whipple and Chemehuevi Mountains, southeastern California: Journal of Geophysical research, v. 96, p. 12,293-12,311.

Wooden, J., and Miller, D., 1990, Chronologic and isotopic framework of Early Proterozoic evolution in the eastern Mojave Desert region, SE California: Journal of Geophysical Research, v. 95, p. 20,133-20,146.

Wooden J., Stacey, J., Doe, B., Howard, K., and Miller, D., 1988, Pb isotopic evidence for the formation of Proterozoic crust in the southwestern United States, in Ernst, W. (editor), Metamorphism and crustal evolution of the western United States, Rubey Volume 7: Englewood Cliffs, New Jersey, Prentice-Hall, p. 69-86.

Yamada, R., Tagami, T., Nishimura, S., and Ito, H., 1995, Annealing kinetics of fission tracks for zircon: An experimental study: Chemical Geology, v. 122, p. 249-258.

Yin, A., 1989, Origin of regional rooted low-angle normal faults: A mechanical model and its tectonic implications: Tectonics, v. 8, p. 469-482.

Yin, A., 1991, Mechanism for the formation of domal and basinal detachment fault: A three dimensional analysis: Jounal of Geophysical Research, v. 96, B9, p. 14,577-14,594.

Yin, A., and Dunn, J., 1992, Structural and stratigraphic development of the Whipple-Chemehuevi detachment fault systems, southeastern California: Implications for the geometrical evolution of domal and basinal low-angle normal faults: Geological Society of America Bulletin, v. 104, p. 659-674.

Young, E., Wooden, J., Shieh, Y., and Farber, D., 1992, Geochemical evolution of jurrassic diorites from the Bristol Lake region, California, USA, and the role of assimilation: Contributions to Mineralogy and Petrology, v. 110, p. 68-86.

Young, E., Anderson, J., Clark, H., and Thomas, W., 1989, Petrology of biotite-cordierite-garnet gneiss of the McCullough Range, Nevada I. Evidence for Proterozoic low-pressure fluid-absent granulite grade matamorphism in the southern Cordillera: Journal of Petrology, v. 30, p. 39-60.

York, D., 1969, Least squares fitting of a straight line with correlated errors: Earth and Planetary Science Letters, v. 5, p. 320-324.

Zartman, R., and Doe, B., 1981, Plumbotectonics: The model: Tectonophysics, v. 75, p. 135-162.

Zeitler, P., Johnson, N., Naeser, C., and Tahirkheli, R., 1982, Fission-track evidence for Quaternary uplift of the Nanga Parbat region, Pakistan: Nature, v. 298, p. 255-257.

Zindler, A., and Hart, S., 1986, Chemical geodynamics: Annual Review of Earth and Planetary Science, v. 14, p. 493-571.

Zoback, M., 1989, State of stress and modern deformation of the northern Basin and Range province: Jounal of Geophysical Research, v. 94, p. 7105-7128.

Zoback, M., Anderson, R., and Thompson, G., 1981, Cainozoic evolution of the state of stress and style of tectonism of the Basin and Range Province of the western United States: Philosophical Transactions of the Royal Society of London, A300, p. 407-434.

APPENDIX A: X-Ray Flourescence Analytical Techniques And Analyses

Specifications and operating conditions

Major and trace element analyses were performed on a Philips PW1400 X-ray fluorescence (XRF) wavelength-dispersive spectrometer in the Department of Earth Sciences at Oxford. The X-rays were generated using a Rh tube. The analyzing crystals used were LiF(220), LiF(200), PE, and PX(1). The machine was calibrated using international geostandards. Major element analyses were corrected by the Phillips X14 software package which utilized the formula of De Jongh (1973). Trace element mass absorption was determined using the Rh compton scatter peak. The elements Co, Cr, V, and Ba were corrected for the Fe, Mn, and Ti absorption edges and line overlaps.

Major element specimen preparation

The major elements were obtained on fused glass disks. The disks contained 1 g of whole-rock powder and 5 g of flux. The rock powder was heated at 120°C for 12 hours to remove all H_2O- (non-structurally bound H_2O). The powders were then weighed, heated to 1000°C for 12 hours, and then reweighed. The weight difference was taken to be H_2O+ (structurally bound H_2O). The disks were made with Spectroflux (100B) and were dried at 60°C for 12 hours. The dried rock powder and flux were mixed and fused for five minutes at 1200°C in a zirconia grained Pt-5% Au alloy crucible. The mixture was swirled after 2.5 minutes to homogenize the liquid. The melt was poured into a Pt-Au alloy casting mould and quenched over a jet of air. A milligram or two of lithium borate (LiBO4) was added to several samples after several unsuccessful attempts to cool the disks without cracking; it turned out that these samples had particularly high silica contents (>75 wt.%). The crucible and mould were cleaned between each fusing in boiling 6M HCl.

The XRF is calibrated for a flux-to-rock powder ratio of 1:5 and major element totals are sensitive to this ratio. Other factors affecting oxide totals include the incorrect loading of beads into the spectrometer and contamination on bead surfaces, e.g.- finger prints. Consequently, oxide totals of 98.5-101.5% (prior to the determination of structurally bound H_2O) were considered acceptible and values outside this range were reanalyzed.

Trace element specimen preparation

Trace elements analyses were measured on pressed powder pellets composed of 10g of whole-rock powder and 1 ml of Moviol glue. The rock powder and Moviol were mixed using an agate mortar and pestle. The mixture was put into a steel piston and subjected to 10^5 Pa of pressure for thirty seconds. The pellets were subsequently dried at 60°C for 12 hours.

Limit of determination, precision, and accuracy

XRF measurements are based on the X-ray count rates at the relevant X-ray spectra lines. In order to detect an element in a specimen, the counting peak must be distinguishable from background radiation. Consequently, the time spent counting X-rays must be sufficiently large, and/or the concentration of the element must be sufficiently high. Potts (1987) provides an extensive discussion on the problems associated with determining the errors involved with XRF analyses.

Limit of determination - Potts (1987) defines a "limit of determination" as the lowest concentration which can be quantitatively determined at the operating conditions of the machine. This value is dependent on the composition of the rock and time spent counting X-rays. Table A1 below provides the limit of determination (ld) at typical routine operating conditions. Major element oxides are not normally given in ppm, and therefore the ppm lds were converted into wt% equivalents for international standards AVG-1, G-2, NIM-G, PCC-1, and W-2. These international standards represent a wide range of rock compositions, subsuming those in this thesis, and yield comparable results.

Precision - "The precision of XRF data is usually extremely high and is easily verified from replicate analyses..." (Potts, 1987). This has been confirmed on the Oxford XRF spectrometer by replicate analyses of a specimen subsumed within the compositonal range of the EWIC. The mean analyses and coefficients of variation (CV = 100 × standard deviation / mean analysis) are presented below in Table A2. These results compare very well with those of Lee & McConchie (1982), though it should be noted that their data was obtained using an XRF spectrometer with different specifications than the Oxford machine.

Accuracy Accuracy is a measure of how close the measured value is to the "true" value. The accuracy of the XRF technique is determined by comparing measurements of international rock standards to

Table A1. Limit of determination (ld)

Element	SiO2	TiO	Al2O3	Fe2O3	MnO	MgO	CaO	Na2O	K2O	P2O5	Ga	Zn	Cu	Ni	Co	Cr	V	Ba	Rb	Sr	Y	Zr	Nb	Pb	Th	U
ppm	1000	240	600	260	240	1200	140	2400	140	140	6	9	6	6	6	10	10	24	3	3	3	6	6	6	9	6
wt%	0.032	0.001	0.078	0.004	0.001	0.075	0.012	0.233	0.021	0 031																

Note: The ppm data (Potts, 1987) represents the limit of determination for a wide variety of rock types under routine operating conditions. Glass disk values have been used for major elements and powder pellet values for trace elements. Major element oxides are typically expressed as a wt%, consequently ppms have been converted.

Table A2. Precision

	Argent (pers. com)		Lee & McConchie (1982)	
Element	Mean	CV%	Mean	CV%
SiO2	64.70	0.07	59.25	0.13
TiO	0.65	0.34	1.05	0.19
Al2O3	16.04	0.1	16.99	0.16
Fe2O3	4.03	0.15	6.81	0.16
MnO	0.06	1.1	0.095	2.1
MgO	2.21	0.85	1.54	0.78
CaO	3.84	0.16	4.89	0.12
Na2O	4.12	0.49	4.3	1.4
K2O	3.19	0.14	2.95	0.14
P2O5	0.16	1.15	0.49	0.1
Total	99.01		98.37	
Ga	20.6	1.5	82	2.4
Zn	62.3	1 2	63	3
Cu	21.2	3.8	22	12.7
Ni	36.2	1.7		
Co	23.3	9.4		
Cr	54.0	3.4		
V	72.1	2.4	121	4.3
Ba	1138.3	0.6	1200	0 5
Rb	62.7	0.6	64	4.5
Sr	175.7	0.3	646	1
Y	12.6	4.5	26	13
Zr	174.4	0 3	260	2.2
Nb	8.8	4.1		
Pb	21.1	4.5	34	9.1
Th	6.4	4.8		
U	ld	ld		

Note: Unpublished data from J. Argent specimen 9553155BM, measured 10 times; Lee & McConchie data on AGV-1, measured 10 times, obtained with a flux:rock powder ratio of 2:1 using a Cr or Mo tube.

Table A3. Accuracy

	Gladney et al. (1983)		Oxford (pers. coms.)
Element	Mean	CV%	Mean RD%
SiO2	59.25	0.49	0.22
TiO	1.06	2.40	2.08
Al2O3	17.15	0.99	0.83
Fe2O3	6.76	2.80	0.9
MnO	0.10	4.20	1 7
MgO	1.53	3.30	1.41
CaO	4.94	1.40	1.39
Na2O	4.25	1.40	1.73
K2O	2.90	1.70	1.18
P2O5	0.48	3.10	2.51
Total	98.42		
Ga	20	7.5	1.41
Zn	88	1.1	2.43
Cu	60	5.0	15.12
Ni	17	12.0	3.1
Co	15	4.0	13 16
Cr	12	13.0	12.39
V	123	4.8	3.04
Ba	1221	0.7	4.79
Rb	67	0.7	3.06
Sr	662	0.7	2.63
Y	12	14.0	8.97
Zr	225	4.0	4.86
Nb	15	10.0	6.68
Pb	36	6.9	10.98
Th	6.5	2.8	2.14
U	1.89	6.6	ld

Note: Gladney et al. (1983) data on AGV-1, outliers discarded, unpublished Oxford major element data from K. Parish on BHVO-1, BR, G-2, GH, SiO2, SY-2 and trace element data from J. Haynes on AGV-1, BCR-1, DTS-1, G-1, G-2, W-1.

the international consensus compositions. Given that the consensus values for international rock standards are compilations of analyses from multiple sources, and not the true compositions of the rocks, the accuracy of the XRF technique can only be estimated. An estimate of accuracy was obtained by choosing geostandards representing a wide range of rock types (AGV-1, BCR-1, BHVO-1, BR, DTS-1, G-1, G-2, GH, SiO2, SY-2, W-1), and measuring them as unknowns on the XRF spectrometer. The mean of the relative deviation (RD%= 100×(measured-consensus)/consensus) of the analyses are presented in Table A3. The data of Gladney et al. (1983) is a consensus, or true value, obtained by compiling analyses from different techniques and laboratories (discarding outliers). Although the mean RD% for the Oxford spectrometer is not directly comparable to the CV% values of Gladney et al. (1983), they both give an indication of the uncertainty in the accuracy of the measurements and compare well. The salient feature demonstrated by Gladney et al. (1983) is the uncertainty in a so-called "true" composition of one of the most extensively analyzed georeferences upon which rests the determination of the accuracy of the technique.

Data

XRF analyses made during the course of this investigation are presented in Table A4 (major elements) and Table A5 (trace elements). Theoretical normative mineralogies (CIPW) are also included in Table A4. CIPW norms were calculated following the procedure of Cox et al. (1979) with the following addition: The oxidation state of iron varies with silica content; using mathmatical iteration, FeO and Fe_2O_3 were calculated from Fe_2O_3T in order to converge on the recommended values of LeMaitre et al. (1989) for a given silica content. The conversion from Fe2O3T measured with the XRF to FeO was made using the molecular weight conversion factor of 1.1113. The CIPW norm calculation was written as a spreadsheet using Microsoft Excell 5.0 and a copy for PC is available free of charge from the author upon request. These analyses represent the regional variation of the EWIC (all compositional phases), as well as the surrounding country rocks, in the NE Sacramento Mountians.

NOTE: Major elements are given as weight percent oxide (wt%) and trace elements as parts per million (ppm). All data generated are in these tables, including analyses which are not used in data synthesis, e.g., those with exceptionally high H_2O+ and those below the ld of the XRF. Sample locations are given relative to Universal Transverse Mercator coordinates (Northerly and Easterly) for Zone 11, in meters.

Table A4. XRF analyses, CIPW norms, and UTM locations

	Cretaceous and Precambrian lithologies									
Sample	VP94-140b	VP94-140a	VP94-144	VP94-146	VP94-139b	VP94-142	VP94-141	VP94-129	VP94-143	VP94-138
Major Elements										
SiO2	45.14	61.44	61.45	63.02	64.23	69.11	70.73	71.98	73.76	74.03
TiO2	1.51	0.66	0.74	1.28	1 20	0.29	0.44	0.48	0.10	0.08
Al2O3	13.34	17.92	17.22	13.85	13.62	16.16	15.50	14.27	14.27	14.39
Fe2O3T	9.87	5.92	6.19	7.92	7.57	2.98	3 24	4.44	0.97	1.15
MnO	0.16	0.11	0.14	0.13	0.12	0.05	0.05	0.06	0.04	0.03
MgO	12.13	2.15	2.25	1.20	1.06	1.03	1.07	1.18	0.16	0.15
CaO	10.70	5.46	5.83	3.69	3.71	1.82	3.15	1.81	1.14	1.37
Na2O	2.73	3.86	3.21	2.53	2.59	2.85	3.91	2.68	4.00	4.02
K2O	2.08	2.13	2.42	4.77	4.67	5.43	2.32	3.36	4.56	4.19
P2O5	1.18	0.25	0.37	0.62	0.59	0.03	0.07	0.02	0.02	0.01
H2O-	0.29	0.40	0.23	0.13	0.22	0.19	0.20	0.18	0.13	0.24
H2O+	1.73	1.06	1.15	0.50	0.34	0.77	0.72	0.89	0.38	0.52
Totals	100.86	101.36	101.19	99.64	99.92	100.71	101.40	101.35	99.53	100.17
CIPW Norms										
q	0.00	14.26	16.43	20.20	21.81	25.39	29.81	36.49	30.10	31.08
c	0.00	0.00	0.00	0.00	0.00	2.34	0.98	2.97	0.71	0.76
or	12.30	12.60	14.31	28.21	27.62	32.12	13.72	19.87	26.97	24.78
ab	8.28	32.62	27.13	21.38	21.89	24.09	33.05	22.65	33.81	33.98
an	17.97	25.23	25.38	12.30	11.70	8.84	15.18	8.85	5.53	6.74
lc	0.00	0.00	0.00	0.00	0.00	0.00	0.00	0.00	0.00	0.00
ne	8.02	0.00	0.00	0.00	0.00	0.00	0.00	0.00	0.00	0.00
ac	0.00	0.00	0.00	0.00	0.00	0.00	0.00	0.00	0.00	0 00
di	21.99	0.20	0.95	1.67	2.43	0.00	0.00	0.00	0.00	0.00
wo	0.00	0.00	0.00	0.00	0.00	0.00	0 00	0.00	0.00	0.00
hy	0.00	10.65	10.74	7.27	6.34	4.82	5.26	6.18	1.16	1 31
ol	21.67	0.00	0 00	0.00	0.00	0 00	0.00	0.00	0.00	0.00
mt	2 18	2.06	2 15	3.56	3.41	1 34	1.24	2.00	0.44	0.52
il	2.87	1.25	1.41	2.43	2.28	0.55	0.84	0.91	0.19	0.15
ap	2.58	0.55	0.81	1.35	1.29	0.07	0.15	0.04	0.04	0.02
Trace Elements										
Ga	16.8	22.4	18.4	21.2	20.2	15.9	17.2	15.6	17.3	15 4
Zn	101.7	82.5	79.8	127.4	115.6	47.7	50.7	59.1	31.8	32.1
Cu	47.7	1.6	3.6	15.8	22.3	1.9	1 1	5.9	3.5	3.3
Ni	307.6	3.8	5.5	7.2	7.5	9.9	10.8	15.5	1.7	2.1
Co	55.2	26.5	21.3	25.2	30.7	15.5	23.0	27.0	27.9	24.2
Cr	577.2	6.3	11.7	7.5	4.4	10 4	27.6	37.6	4.0	3.0
V	213.3	95.1	86.2	77.1	66.2	19.5	47.6	51.0	6.0	4.7
Ba	1404.7	1016.9	1043.0	2255.5	3001.8	770.9	714.2	856.7	634.6	1474.1
Rb	32.9	66.0	59.0	114.2	94.2	110.5	70.1	97.4	136.1	87.3
Sr	1109.2	810.2	520.4	277.0	330.9	348.1	375.2	223.2	233.9	319.9
Y	33.1	19.4	28.8	62.4	57.4	37.2	6.9	36.0	21.7	14.3
Zr	253.1	168.5	193.5	664.8	720.5	239.6	99.2	171.6	75.6	74.2
Nb	18.4	8.4	12.6	26.4	18.4	11.4	7.8	10.9	11.5	7.8
Pb	6.1	12.6	9.7	25.4	25.5	37.8	15.2	24.4	29.6	27.6
Th	13.1	6.8	3 7	3.1	1.8	18.9	5.4	11.6	5.9	4.6
U	3.3	-0.3	-0.2	0.5	0.8	2.5	0.0	1.4	1.6	0 4
North	3859258	3859258	3855653	3857722	3858497	3853405	3853405	3856006	3853352	3857082
East	694215	694215	693110	698120	698129	689919	689919	708917	689761	696608

Table A4..

	Cret. & Precam.		*Td*						
Sample	VP94-145	VP95-242	VP95-256	VP94-130a	VP94-124	VP94-123b	VP94-123c	VP94-123a	VP94-135
Majors									
SiO2	74.04	74.64	49.66	51.33	52.66	53.24	54.83	54.96	56.73
TiO2	0.36	0.08	1.72	1.65	1.06	0.95	1.12	0.97	1.24
Al2O3	14.08	13.87	10.09	15.39	12.72	17.97	19.28	19.64	15.93
Fe2O3T	2.44	0.91	9.85	8.96	8.19	6.86	6.91	6.06	7.92
MnO	0.03	0.02	0.16	0.10	0.14	0.10	0.09	0.09	0.09
MgO	0.36	0.14	11.89	7.32	9.63	6.05	3.90	4.00	5.75
CaO	1.25	1.31	12.36	8.61	9.95	8.69	6.52	8.66	6.98
Na2O	2.65	3.73	1.87	3.21	2.47	3.77	4.61	4.49	3.63
K2O	5.48	4.77	1.17	2.35	2.33	1.41	2.44	1.28	1.99
P2O5	0.08	0.00	1.08	0.63	0.46	0.24	0.31	0.20	0.25
H2O-	0.27	0.23	0.20	0.21	0.19	0.22	0.14	0.23	0.34
H2O+	0.78	0.19	2.51	1.93	1.45	1.60	0.73	1.09	0.76
Totals	101.83	99.89	102.56	101.70	101.25	101.09	100.88	101.67	101.61
Norms									
q	33.94	31.38	0.00	0.00	0.00	0.00	0.00	0.34	4.50
c	1.69	0.17	0.00	0.00	0.00	0.00	0.00	0.00	0.00
or	32.41	28.21	6.92	13.90	13.78	8.34	14.43	7.57	11.77
ab	22.40	31.52	15.80	27.13	20.88	31.86	38.96	37.95	30.68
an	5.68	6.50	15.66	20.60	16.70	27.90	24.66	29.61	21.26
lc	0.00	0.00	0.00	0.00	0.00	0.00	0.00	0.00	0.00
ne	0.00	0.00	0.00	0.00	0.00	0.00	0.00	0.00	0.00
ac	0.00	0.00	0.00	0.00	0.00	0.00	0.00	0.00	0.00
di	0.00	0.00	30.94	14.47	23.74	11.00	4.62	9.76	9.51
wo	0.00	0.00	0.00	0.00	0.00	0.00	0.00	0.00	0.00
hy	2.51	1.06	13.70	6.76	12.74	12.58	7.42	10.25	16.80
ol	0.00	0.00	8.05	8.29	5.53	2.58	4.15	0.00	0.00
mt	1.10	0.41	2.18	3.11	2.52	2.11	2.40	2.10	2.44
il	0.68	0.15	3.27	3.14	2.01	1.81	2.13	1.84	2.36
ap	0.17	0.00	2.36	1.38	1.00	0.52	0.68	0.44	0.55
Traces									
Ga	16.6	14.4	15.1	22.5	17.0	18.5	25.7	19.3	23.0
Zn	38.3	16.5	113.7	86.6	83.0	53.7	95.1	50.9	98.9
Cu	1 1	6.2	0.0	0.2	3.3	9.5	7.0	9 4	1.0
Ni	4.5	3.3	247.0	53.7	165.5	80.8	52.0	36.9	59.0
Co	23.4	27.6	50.6	49.0	48.6	39.5	30.4	31.4	39.9
Cr	7 7	0.8	843.5	25.6	359.2	235.8	41.5	84.3	116.8
V	20.8	8.1	174.2	272.9	167.6	126.9	141 7	115.4	204.3
Ba	712.1	1286.5	1128.7	808.6	1349.4	471.1	1463.6	471.8	828.8
Rb	184.9	92.4	20.8	51.8	34.8	34.2	60 5	29 1	48.5
Sr	132.3	395.1	706.6	1044.2	771.6	850.4	1358.4	1066.9	912.3
Y	43.9	13.5	31.7	28 6	23.8	19.4	25.7	17.8	22 3
Zr	227.6	59.8	202.0	119.3	176.1	121.5	283.2	113.8	85.3
Nb	16.9	5.9	20.2	8.0	9.9	6.9	9.3	6.4	7.5
Pb	31 5	29.9	3.3	4.9	9.0	6.8	12.9	11.5	6.8
Th	39.4	4.5	7.5	4.8	6.3	4.7	5.9	4.1	1.8
U	1.9	0.6	1.3	1.3	0.3	-0.3	0.1	1.0	1.0
North	3854729	3854525	3856923	3856202	3851505	3851556	3851556	3851556	3855544
East	696565	706963	707057	709038	707814	707915	707915	707915	706893

Table A4..

	Td			*Tgd*					
Sample	VP94-057b	VP94-020c	VP95-198	VP94-137	VP94-119b	VP94-130b	VP94-139a	VP94-127	VP94-132
Majors									
SiO2	57.34	57.75	57.79	59.79	60.21	62.67	64.88	65.52	66.14
TiO2	1.17	1.06	1.04	1.06	0.79	0.77	0.65	0.55	0.53
Al2O3	16.92	17.55	17.88	17.57	18.18	17.77	16.50	16.58	16.78
Fe2O3T	7.21	6.26	6.56	5.80	4.92	4.96	3.94	3.51	3.39
MnO	0.10	0.08	0.08	0.08	0.07	0.06	0.06	0.06	0.05
MgO	3.84	3.92	3.35	2.67	2.70	2.00	2.18	1.58	1.43
CaO	6.62	5.73	5.69	5.29	4.80	4.63	3.84	3.69	3.69
Na2O	4.20	4.43	4.09	3.86	4.86	4.16	4.33	4.32	4.60
K2O	2.18	2.52	2.87	3.19	2.76	2.65	3.15	3.13	3.13
P2O5	0.47	0.37	0.34	0.36	0.23	0.27	0.20	0.18	0.16
H2O-	0.18	0.24	0.56	0.29	0.19	0.20	0.38	0.22	0.17
H2O+	0.70	0.78	0.52	0.70	0.82	1.15	1.37	0.71	0.81
Totals	100.93	100.69	100.77	100.66	100.53	101.30	101.49	100.04	100.88
Norms									
q	5.45	4.35	5.43	9.54	6.63	14.49	15.92	17.76	17.06
c	0.00	0.00	0.00	0.00	0.00	0.26	0.00	0.00	0.00
or	12.89	14.91	16.98	18.87	16.33	15.67	18.63	18.51	18.51
ab	35.50	37.44	34.57	32.62	41.07	35.16	36.60	36.51	38.88
an	20.84	20.52	21.90	21.14	19.60	21.22	16.24	16.56	15.85
lc	0.00	0.00	0.00	0.00	0.00	0.00	0.00	0.00	0.00
ne	0.00	0.00	0.00	0.00	0.00	0.00	0.00	0.00	0.00
ac	0.00	0.00	0.00	0.00	0.00	0.00	0.00	0.00	0.00
di	7.27	4.45	3.35	2.25	2.22	0.00	1.23	0.47	1.16
wo	0.00	0.00	0.00	0.00	0.00	0.00	0.00	0.00	0.00
hy	11.49	12.27	11.70	9.75	9.39	8.77	7.37	6.02	5.40
ol	0.00	0.00	0.00	0.00	0.00	0.00	0.00	0.00	0.00
mt	2.77	2.40	2.52	2.23	1.89	1.90	1.77	1.58	1.42
il	2.22	2.01	1.98	2.01	1.50	1.46	1.24	1.05	1.01
ap	1.03	0.81	0.74	0.79	0.50	0.59	0.44	0.39	0.35
Traces									
Ga	22.5	23.3	24.2	22.5	24.2	22.9	21.7	21.7	21.9
Zn	85.3	79.7	90.8	85.7	79.1	73.7	71.0	69.1	56.7
Cu	17.6	4.6	36.2	19.7	38.9	12.1	30.4	9.1	5.7
Ni	36.4	64.0	32.9	16.8	41.6	16.0	40.6	13.9	9.4
Co	35.6	32.2	27.3	31.1	27.6	25.9	27.4	25.2	22.6
Cr	40.0	91.4	33.4	10.8	40.8	12.4	46.7	21.4	17.4
V	138.3	122.6	129.5	107.7	90.6	80.2	71.6	58.4	57.0
Ba	985.2	1476.3	1258.7	1328.0	1322.1	1656.3	1278.3	1355.4	1549.2
Rb	50.0	54.2	65.3	83.4	69.9	60.8	67.2	71.0	55.9
Sr	1257.2	1188.0	1108.3	1098.7	1156.0	1074.6	960.5	1045.0	1072.6
Y	19.2	21.0	19.9	18.6	15.6	17.4	13.1	13.6	11.6
Zr	152.5	226.4	276.5	118.0	218.6	208.7	198.1	185.3	172.2
Nb	13.4	10.9	10.9	9.5	7.4	10.3	7.9	9.2	7.8
Pb	15.6	13.3	15.6	12.7	21.0	15.5	20.9	21.7	20.6
Th	4.9	4.7	7.3	2.4	6.4	4.1	5.7	5.1	3.5
U	0.9	0.3	0.3	0.4	1.0	0.4	1.2	0.1	0.8
North	3853884	3852503	3852142	3853661	3851008	3856748	3858497	3855745	3851955
East	710016	706696	705823	708703	708287	709910	698129	708756	706696

Table A4..

	Tgd									
Sample	VP94-020a	VP95-185	VP95-249	VP94-016b	VP94-002	VP94-020b	VP95-251	VP94-119a	VP95-159	VP94-128
Majors										
SiO2	66.51	66 84	66.99	67 00	67.35	67.42	67.98	69 58	69.58	71.02
TiO2	0.53	0.53	0.50	0.52	0.57	0.46	0.37	0.37	0.33	0 30
Al2O3	15.95	15.77	16.38	15.77	16.34	16.41	16.38	15.51	15.53	15.18
Fe2O3T	3 42	3.40	3.58	3.16	3.30	3.00	2.57	2.41	2.36	2.11
MnO	0.06	0.05	0.05	0.05	0.04	0.04	0.04	0.03	0.06	0.05
MgO	1.48	1.58	1.19	1 32	1 26	1.28	0.86	1.01	0.74	0.75
CaO	3.30	3.35	3.26	2.86	3.58	3 53	2.88	2 69	2.28	2.37
Na2O	4.49	4.22	4.51	3.99	4.72	4.80	4.71	4.21	4.11	4.01
K2O	3.94	3.38	3 24	4.38	2.14	2.46	3.14	3.67	4.32	4.09
P2O5	0.17	0.14	0.16	0.14	0.14	0.13	0.08	0.09	0.10	0.08
H2O-	0.23	0.35	0.22	0.31	0.29	0.22	0.21	0.14	0.31	0.15
H2O+	0 51	0.85	0.64	0.72	0 69	0.61	0.38	0.60	0.35	0.62
Totals	100.60	100.46	100.72	100.22	100.43	100.36	99.60	100.31	100.07	100.72
Norms										
q	16.29	19.50	18.95	18.67	21.48	20.21	20.58	23.39	22.71	25.43
c	0.00	0.00	0.00	0.00	0.07	0.00	0.17	0.00	0.17	0.02
or	23.30	19.99	19.16	25.91	12.66	14.55	18.57	21.71	25.55	24.19
ab	37.95	35.67	38.12	33.72	39.89	40.57	39.81	35.58	34.74	33.89
an	11.69	14.06	14.84	12.14	16.86	15.93	13.78	12.54	10.67	11.24
lc	0.00	0.00	0.00	0.00	0.00	0.00	0.00	0.00	0.00	0.00
ne	0.00	0.00	0.00	0.00	0.00	0.00	0.00	0.00	0.00	0.00
ac	0.00	0.00	0.00	0.00	0.00	0.00	0.00	0.00	0.00	0.00
di	2.92	1.35	0.25	0.93	0.00	0.61	0.00	0.18	0 00	0.00
wo	0.00	0.00	0.00	0.00	0 00	0.00	0.00	0.00	0 00	0.00
hy	4.53	5.70	5.47	4.87	5.57	5.03	3.88	4.01	3.50	3.33
ol	0.00	0.00	0.00	0.00	0.00	0 00	0.00	0.00	0.00	0.00
mt	1.54	1.42	1.50	1.42	1.27	1.25	1.16	1.08	1.06	0.95
il	1.01	1.01	0.95	0.99	1.08	0.87	0 70	0.70	0.63	0.57
ap	0 37	0.31	0.35	0.31	0 31	0.28	0.17	0 20	0.22	0.17
Traces										
Ga	19.2	20.0	23.0	18.6	20.6	19 8	20.3	19.1	19 1	18.9
Zn	53.2	45.2	60.2	38.7	49.7	49.9	47.3	37.6	37.3	45.9
Cu	2.7	8.2	14.3	3.5	7.9	6.3	4.8	2.3	3.0	3 7
Ni	12.0	20.1	6.5	13.6	7.3	11.6	5.9	13.3	6.1	10.9
Co	30.2	27.9	27.4	24.2	27.2	28.9	25 4	37 2	23.1	27.1
Cr	14 8	27.0	10.8	17.2	6 1	9.4	9.4	16 9	6.6	7.0
V	50.8	54.1	53.7	46 2	60.2	50.4	32.7	39.5	23 7	30.8
Ba	1215.2	1255.4	1428.2	1403.4	939 9	992.8	1175.7	1401.6	1213.8	1194 0
Rb	93.6	64.0	61.9	91 4	49.3	55.9	68 5	62.0	80.4	77.4
Sr	765.8	737.8	878.7	677.6	886.1	830.0	904.0	750.0	582.7	652.3
Y	14.6	13.5	13.2	16.2	8.7	11.2	10.2	9.7	12.5	9.9
Zr	152.1	160.8	209.4	182.9	149.3	140.9	166.6	121.9	158.2	112.9
Nb	11.5	11.0	7.9	14.2	8.9	6.9	7 1	6 5	10.7	7.2
Pb	24.0	16.3	19.2	15.8	17.4	19.4	21.5	25 1	26.5	27 3
Th	8.0	7.8	6.3	8.3	4 6	3.8	8 9	4 1	6.0	5 2
U	2.6	0.9	1.3	0.7	1.7	0.5	0.3	0.6	0.7	1.8
North	3852503	3849376	3855413	3852113	3850543	3852503	3855724	3851008	3857607	3855475
East	706696	705359	707081	706520	706799	706696	706280	708287	706472	708071

Table A4..

	Tlg								
Sample	VP94-060b	VP95-160	VP94-069b	VP95-234	VP94-133	VP95-243	VP95-252	VP95-258	VP94-136
Majors									
SiO2	72.51	73.33	73.57	73.93	74.16	74.24	74.26	74.39	74.84
TiO2	0.26	0.11	0.09	0.13	0.07	0.05	0.17	0.08	0.07
Al2O3	14.50	14.38	14.13	14.46	15.05	14.74	14.13	14.51	14.49
Fe2O3T	1.54	1.22	1.08	1.25	0.91	0.68	1.32	1.04	0.96
MnO	0.02	0.01	0.02	0.01	0.01	0.02	0.03	0.02	0.02
MgO	0.32	0.22	0.18	0.25	0.10	0.10	0.28	0.15	0.13
CaO	1.62	1.50	1.30	1.60	1.29	0.97	1.49	1.24	1.47
Na2O	3.53	4.34	3.91	3.87	4.91	4.04	4.10	4 25	4.12
K2O	5.48	3.95	4.82	4.38	3.96	4.98	3.95	4.48	4.37
P2O5	0.03	0.01	0.01	0.00	0.02	0.04	0.01	0.03	0.01
H2O-	0.16	0.26	0.16	0.38	0.23	0.14	0.16	0.12	0.17
H2O+	0.30	0.13	0.42	0.34	0.15	0.37	0.24	0.41	0.17
Totals	100.26	99.45	99.69	100.59	100.86	100.37	100.14	100.72	100.82
Norms									
q	26.80	29.07	29.00	30.47	27.31	29.34	31.31	29.38	30.52
c	0.00	0.25	0.12	0.43	0.37	1.02	0.41	0.47	0.32
or	32.41	23.36	28.51	25.91	23.42	29.46	23.36	26.50	25.85
ab	29.83	36.68	33.05	32.71	41.50	34.14	34.65	35.92	34.82
an	7.48	7.38	6.39	7.94	6.27	4.55	7.33	5.96	7.23
lc	0.00	0.00	0.00	0.00	0.00	0.00	0.00	0.00	0.00
ne	0.00	0.00	0.00	0.00	0.00	0.00	0.00	0.00	0.00
ac	0.00	0.00	0.00	0.00	0.00	0.00	0.00	0.00	0.00
di	0.30	0.00	0.00	0.00	0.00	0.00	0.00	0.00	0.00
wo	0.00	0.00	0.00	0.00	0.00	0.00	0.00	0.00	0.00
hy	1.62	1.46	1.29	1.53	0.96	0.80	1.64	1.20	1.09
ol	0.00	0.00	0.00	0.00	0.00	0.00	0.00	0.00	0.00
mt	0.69	0.55	0.49	0 56	0.41	0.31	0.59	0.47	0.43
il	0.49	0.21	0.17	0.25	0.13	0.10	0.32	0.15	0.13
ap	0.07	0.02	0.02	0.00	0.04	0.09	0.02	0.07	0.02
Traces									
Ga	14.7	14.4	15.3	14.6	17.1	17.6	16.5	16.7	16.5
Zn	17.5	13.1	26.0	7.5	11.8	17.9	22.1	26.0	11.9
Cu	9.4	4.3	3.8	3.8	5.0	3.3	4.6	2.7	4.0
Ni	8.4	1.7	2.5	4.9	3.0	3.9	2.9	2.4	3.9
Co	25.0	23.2	24.7	25.4	24.2	23.3	31 5	20.8	27.5
Cr	-0.1	4.3	3.4	4.6	1.2	4.8	6.7	3.7	1.7
V	15 7	7.4	4.5	9.3	7.7	3.8	12.7	6.7	7.2
Ba	1390.8	1491.9	1232.9	1386.7	759.7	464.7	2171.5	971.5	1143.0
Rb	90.6	84.1	93.1	62.1	87.3	127.0	71.5	113.7	76.4
Sr	357 3	451.0	308.9	400.4	247.5	178.0	564.2	280.4	344.0
Y	16.1	9.8	13.2	11.2	23.3	15.0	8.7	13.7	11.4
Zr	191.2	62.2	63.3	86.8	53.0	39.8	92.0	55.9	62.0
Nb	10.3	6.0	7.8	5.5	7.9	10.1	6.9	8.1	8.0
Pb	19.5	22.4	30.1	26.5	26.2	30.8	27.9	23.9	23 7
Th	12.2	4.0	5.0	6.8	5.2	3.0	7 2	3.0	3.5
U	0 3	0.0	-0.2	0.0	1.2	0.1	0.0	0.4	-0.3
North	3853884	3854444	3857370	3852970	3855934	3854793	3855899	3856621	3853661
East	710016	708518	711526	708727	705660	705366	706088	705922	708703

Table A4..

	Tlg		*Banded unit*						
Sample	VP95-214	VP95-250	VP95-240	VP95-253	VP95-254	VP95-247	VP95-246	VP95-238	VP95-237
Majors									
SiO2	75.83	75.95	54.85	55.69	55.71	63.47	64.50	65.16	65.99
TiO2	0.05	0.08	1.22	1.16	1.17	0.72	0.75	0.70	0.53
Al2O3	12.86	13.87	16.41	16.58	16.56	16.36	16.44	16.08	16.37
Fe2O3T	0.52	0.66	7.50	7 24	7.23	4.50	4.65	4.37	3.51
MnO	0.01	0.01	0.13	0.09	0.09	0.07	0.07	0.07	0.05
MgO	0.02	0.12	5.12	5.42	5.41	2.48	2.86	2.52	1.80
CaO	0.77	1.74	7.08	6.90	6.89	4.19	4.18	3.79	3.61
Na2O	3.26	4.13	3.55	4.06	4.07	4.07	3.55	4.14	4.52
K2O	5.92	3.53	2.93	2.37	2.36	3.13	3.00	3.07	2.98
P2O5	0.00	0.00	0.53	0.44	0.45	0.20	0.19	0.19	0.15
H2O-	0.20	0.20	0.69	0.14	0.13	0.22	0.28	0.53	0.35
H2O+	0.18	0.25	0.96	0.79	0.41	0.98	0.80	0.47	0.41
Totals	99.62	100.54	100.97	100.87	100.48	100.39	101.27	101.08	100.27
Norms									
q	32.56	34.33	1.35	1.14	1.21	14.91	18.09	16.90	17.48
c	0.00	0.08	0.00	0.00	0.00	0.00	0.19	0.00	0.00
or	35.02	20.88	17.33	14.02	13.96	18.51	17.74	18.16	17.63
ab	27.55	34.91	30.00	34.31	34.40	34.40	30.00	34.99	38.20
an	2.92	8.64	20.14	19.97	19.91	17.08	19.51	16.18	15.54
lc	0.00	0.00	0.00	0.00	0 00	0.00	0.00	0.00	0.00
ne	0.00	0.00	0.00	0.00	0.00	0 00	0.00	0.00	0.00
ac	0.00	0.00	0.00	0.00	0.00	0.00	0.00	0.00	0.00
di	0.79	0.00	9.33	9.19	9 15	1.95	0.00	1.13	1.14
wo	0.00	0.00	0.00	0.00	0.00	0.00	0.00	0.00	0.00
hy	0.03	0.77	14.45	15.03	14.99	8.17	10.67	8.82	6.45
ol	0 00	0.00	0.00	0.00	0.00	0.00	0.00	0.00	0.00
mt	0.23	0.30	2.60	2.51	2 51	2.02	1.78	1.83	1.47
il	0.10	0.15	2.32	2 20	2.22	1.37	1.43	1.33	1.01
ap	0.00	0.00	1.16	0.96	0.98	0.44	0.41	0.41	0.33
Traces									
Ga	19.9	15.3	21.0	22.4	20.0	21.4	21.0	20.5	20.3
Zn	8.5	16.4	86.1	88.0	48.3	67.0	67.2	64.2	57.3
Cu	4.7	3.2	28.4	15.3	5.6	2.7	9.1	12.2	5.0
Ni	1.9	2.0	57.3	112.9	6.7	38.7	42.6	37.6	26.8
Co	28.7	31.6	32.5	34.5	27.0	27 4	27.6	26.0	26.2
Cr	5.4	5.9	137 6	114 8	14.8	57 3	50 4	51.3	34.6
V	4.1	7.6	152.1	155.8	34.6	79.0	82.1	83.6	59.7
Ba	127.1	1137 5	1295.6	1094.2	1177.9	1295.7	1219.0	1050.7	1243.0
Rb	105.0	57.0	66 3	44.9	71.6	72.6	72.0	69.6	61.8
Sr	79.1	370.3	1028.8	1094.8	538.7	834.8	822.3	748.9	930.1
Y	0.9	5.0	23.5	19.6	3.5	18.6	15.0	16.1	12.5
Zr	42.0	80.3	267.7	159.8	139.6	198.8	188.6	188.4	165.8
Nb	4.5	4.8	14.6	10.0	4.4	12.9	11.9	11.2	8.8
Pb	40.4	31 3	10.9	10.5	24.6	14.9	24 1	17.1	17.9
Th	13.8	4.3	8.9	6.2	4.0	7.8	6.0	8.6	6.5
U	1.8	0.5	0 8	0.7	0.1	0.0	0.1	1.3	0.9
North	3853209	3855449	3854472	3856707	3856707	3855355	3855355	3854472	3854472
East	704412	706912	707045	706939	706939	707198	707198	707045	707045

Table A4..

	Banded unit			*Young dikes, Tu*				
Sample	VP95-255	VP95-239	VP95-248	VP95-164	VP95-168	VP95-165	VP95-163	VP95-170
Majors								
SiO2	73.24	74.36	74.92	49.36	51.72	53.04	53.37	53 43
TiO2	0.10	0.10	0.08	1.77	1.57	1.55	1.34	1.75
Al2O3	14.54	14.16	14.35	17.24	16.76	16.67	16.57	16.47
Fe2O3T	1.21	0.91	1.17	11.33	9.67	10.14	9.90	11.29
MnO	0.03	0.01	0.03	0.15	0.13	0.16	0.14	0.11
MgO	0.21	0.19	0.15	5.46	6.99	5.14	5.80	5.00
CaO	1.47	1.29	1.20	7.14	7.47	6.36	8.44	6.02
Na2O	4.22	3.72	3.47	3.86	3.78	4.64	2.89	5.92
K2O	4.10	4.81	4.79	2.53	1.48	2.53	1.28	0.39
P2O5	0.01	0.01	0 01	0.54	0.48	0.37	0.26	0 43
H2O-	0.10	0.36	0.13	1.19	1.22	1.19	1.10	1.43
H2O+	0.30	0.26	0.40	4.98	5.99	3.56	3.29	4.96
Totals	99.53	100.18	100.71	105.55	107.26	105.35	104.38	107.21
Norms								
q	29.16	31.02	33.22	0.00	0.00	0.00	4.01	0.00
c	0.49	0.49	1.28	0.00	0.00	0.00	0.00	0.00
or	24.25	28.45	28.33	14.96	8.75	14.96	7.57	2.31
ab	35.67	31.44	29.33	28.56	31.95	37.78	24.43	50.03
an	7.23	6.34	5.89	22.20	24.35	17.15	28.42	17.19
lc	0.00	0.00	0.00	0.00	0.00	0.00	0.00	0.00
ne	0.00	0.00	0.00	2.20	0.00	0.78	0.00	0.00
ac	0.00	0.00	0.00	0.00	0.00	0.00	0.00	0.00
di	0.00	0.00	0 00	7.96	7.76	9.79	9.60	8.09
wo	0.00	0.00	0.00	0.00	0.00	0.00	0.00	0.00
hy	1.48	1.13	1.33	0.00	11.97	0.00	18.99	4.04
ol	0.00	0.00	0.00	14.50	7.44	12.05	0.00	10.05
mt	0.54	0.41	0.53	3.49	2.98	3.52	3.05	3.92
il	0.19	0.19	0.15	3.36	2.98	2.95	2.55	3.33
ap	0.02	0.02	0 02	1.18	1.05	0.81	0.57	0.94
Traces								
Ga	16.5	15.1	15.5	20.0	18.0	18 6	18.1	19.6
Zn	22.8	13.5	25.1	64.9	76.2	75.4	73.3	53.8
Cu	4.0	4.6	3 2	31.4	9.8	35 8	51.7	0 0
Ni	4.5	4.0	5.8	26.6	119 1	31 2	75.5	21.8
Co	21.2	27 7	19.4	40.2	35.6	30.8	53.2	31 5
Cr	7.8	5.9	6.3	21.6	166 1	77 4	58.9	26.9
V	11.0	8.8	5 2	223.7	163.2	193.4	173.1	215.5
Ba	1169.9	1346.7	1303.7	2944.9	960 0	673.2	1709.1	204.9
Rb	81.7	77.3	94 7	61.2	26.0	64 5	22 8	9.8
Sr	302.5	369.5	290.3	645.0	456.9	577.5	496.1	367.4
Y	10.9	9.2	14.3	41.1	27.8	38.1	29.5	39.8
Zr	66.8	67.1	64.7	319.5	278.7	248 9	190.4	283.4
Nb	7.8	5.6	8.2	16.4	28.5	14.4	10.1	15.0
Pb	31.2	27.5	30.8	0.0	0.9	2.2	3.4	0.2
Th	3.7	8.3	6.1	6.3	8.8	5.7	5.0	7 6
U	0.2	0.1	0.9	0.0	0.4	0 0	0.0	1.2
North	3856707	3854472	3855355	3851761	3851371	3851838	3851594	3851594
East	706939	707045	707198	708552	708970	708530	708648	708648

APPENDIX B: Electron Microprobe Analytical Techniques And Analyses

Specifications and operating conditions

Minerals were analyzed on 30μm thick, polished thin sections. The sections were coated with 20nm of carbon to prevent charge build-up. The mineral analyses were performed using a Cambridge Instruments Microscan 9 electron microprobe. The microprobe has two wavelength dispersive spectrometers and is controlled by a Cambridge Instruments Microscan 9 software package. The microprobe was calibrated by running standards before each session of mineral analysis. Once the elements were measured, a ZAF correction was applied to the apparent weight percent values to correct for differences between the matrix of the unknown and the standards.

Operating conditions during analyses were: beam diameter, 0.5μm; beam current, 40nA; accelerating potential, 20kV. Under these operating conditions the excitation volume of the target, which varies from element to element, had maximum diameter of 3μm. The X-ray counting times were routine for this technique: 10 to 30 seconds, depending on the element. Counting times were increased to 50 seconds for apatite analyses in order to improve the limit of determination for chlorine. Background counting times were typically 5 seconds, but were increased to 50 seconds for Cl in apatite analyses.

Limit of determination, precision, and accuracy

Electron microprobe measurements are based on the X-ray count rates at the relevant X-ray spectra lines. In order to detect an element in a mineral, the counting peak must be distinguishable from background radiation. Consequently, the time spent counting X-rays must be sufficiently large, and/or the concentration of the element must be sufficiently high. Potts (1987) provides an extensive discussion on the problems associated with determining the errors involved with electron microprobe analyses.

Limit of determination - Potts (1987) defines the "limit of determination" as the lowest concentration which can be quantitatively determined at the operating conditions of the machine. Table B1 provides the limit of determination (ld) for a wide range of mineral standards obtained under routine operating conditions. Though ld values for most oxides have been taken from Potts (1987), those for phosphate, fluorine, and chlorine were calculated using data from this study with the following equation:

$$Ld\ (wt\%) = 6/m\sqrt{Rb/Tb}$$

where m = count rate on the standard / concentration in the standard

Rb = background counts/second on specimen

Tb = time on background

Precision Precision is defined by the ability of the electron microprobe to reproduce a measurement. The precision of the electron microprobe technique is summarized in Table B2. Using replicate analyses of DSDP basaltic glass, Potts et al. (1983) have calculated coefficients of variation (CV = 100 × standard deviation / mean analysis). In general, the CVs range from 0.5-2.0%. The exceptions are MnO and K_2O, whose unfavorably large CV's are the result of concentrations at, or approaching, the ld (cf. Table C1) of the microprobe and, therefore, are not representative of the technique overall.

As stated previously, the microprobe calculates the concentrations of elements in a specimen from the peak X-ray count rates. X-ray emission is a random process and the 2σ variation in the counting rate over the counting time (converted to wt% by the software package) gives an estimate of the uncertainty of each measurement. Also shown in Table B2 are representative mineral analyses from this study, their associated 2σ variations, and the 2σ variations expressed as a percentage of the mineral analysis. These percentages are generally less than 2%. Large percentages, e.g.- Fe2O3, are generally due to low oxide concentrations which are at, or are approaching, the ld (cf. Table B1) of the microprobe. These values can be directly compared with the CVs from the DSDP analyses. It should be noted that these values are similar and indicative of the precision of Oxford electron microprobe analyses.

Accuracy Accuracy is a measure of how close the measured value is to the "true" value. The accuracy of the electron microprobe is determined by comparing measurements of international rock standards to the international consensus compositions. Given that the consensus values for these standards are compilations of analyses from multiple sources, and not the true compositions of the rocks, the accuracy of the electron microprobe can only be estimated. Staudigel (1979) compiled the consensus value for DSDP basaltic glass using chemical analyses generated at different laboratories. Table B3 compares Staudigel's

Table B1. Limit of determination (ld)

Oxide	SiO2	TiO2	Al2O3	Fe2O3	MnO	MgO	CaO	Na2O	K2O	P2O5	F	Cl
ld wt%	0.05	0.05	0.06	0.060	0 060	0.07	0.03	0.07	0.04	0.04	0.04	0.04

Note: Ld for most oxides from Potts (1987), ld for P2O5, F, and Cl calculated using data from this study, refer to text.

Table B2. Precision

Oxide	Potts et al , 1983		Hornblende			Plagioclase			Biotite			Apatite		
	DSDP	CV%	VP94-130b	2σ	%	VP94-130b	2σ	%	VP94-130b	2σ	%	VP94-127	2σ	%
SiO2	51.53	0.47	41.48	0.09		61.22	0.11	0.18	36.72	0.08	0.22			
TiO2	1.32	1.90	1.73	0.02					2.36	0.03	1.27			
Al2O3	15.01	0.65	11.64	0.05		24.65	0.08	0.32	15.24	0.06	0.39			
Fe2O3	9.05	0.74	0.22	0.14		0.09	0.01	11 11	0.19	0.14	73.68	0.01	0.01	100.00
MnO	0.18	7.20	16.48	0.03					16.94	0.03	0.18	0.04	0.02	50.00
MgO	7.96	1.00	10.71	0.06					13.54	0.07	0.52			
CaO	11.15	0.68	11.64	0.06		5.16	0.04	0.78	0.00	0.01		55.51	0.15	0.27
Na2O	2.76	1.60	1.64	0 03		8.23	0.07	0.85	0.12	0.01	8.33			
K2O	0.07	7.10	0.97	0.02		0.21	0.01	4.76	9.48	0.07	0.74			
P2O5	nd											42.11	0.18	0.43
F	nd											2.42	0.02	0.83
Cl	nd											0.02	0.01	50.00
Total	99.03		96.51			99.56			94.59			100.11		

Note: DSDP=mean of 54 analyses; results expressed as wt%; 2σ variations from samples VP94-130b and VP94-127 expressed as % of analysis for camparison with CV%; nd, not determined.

Table B3. Accuracy, using DSDP basaltic glass

Oxide	SiO2	TiO2	Al2O3	Fe2O3	MnO	MgO	CaO	Na2O	K2O	P2O5	F	Cl
Potts et al.	51.53	1.32	15.01	9.05	0 18	7.96	11.15	2.76	0.07	nd	nd	nd
CV%	0.47	1.90	0.65	0.74	7.20	1.00	0.68	1.60	7.10			
Staudigel	51.52	1.3	15.390	9.120	0.17	8.12	11.31	2.48	0.09	nd	nd	nd
RD%	0.02	1.54	2.470	0.770	5.88	1.97	1.41	11.29	22.22			

Note: Data from Potts et al. (1983) and Staudigel (1979); relative deviations (RD%) between Staudigel and Potts et al. are estimates of accuracy; nd, not determined.

consensus values with the mean analysis of Potts et. al (1983). The relative deviation (RD%= 100 x (measured-consensus)/consensus) between the two data sets is generally 1-2%, except where the concentration of the element is at, or near, the ld for the microprobe, e.g. MnO and K2O. Factors which may influence the overall ability of the microprobe to generate accurate analyses include: counting times, volatile loss, beam focus loss, inhomogeneous samples, etc.

Data

Analyses made during the course of this thesis are presented in Table B4 and are listed in the order in which the analyses were run. The data include analyses of the following minerals: hornblende, plagioclase, biotite, and apatite. Apatite analyses were made on a grain mount of the remaining mineral separates after fission track analyses. A summary of average apatite compositions is presented in Table B5. These analyses represent a regional sampling of the EWIC (dioritic and granodioritic phases) in the NE Sacramento Mountains.

NOTE: Where elements were analysed, the concentration of the oxide is given as a weight percent, otherwise the column is left blank. All data generated is in this table, including analyses which are not used in data synthesis, i.e.- the occasional mislocation due to errors of the automated tracking stage, results below the limit of determination specified in Table B1, non-stoichiometric mineral compositions, and analyses with unacceptable totals (wt. %). In general, the following totals were considered acceptable: amphibole, 95-97, apatite, 97-101 (large range due to element volatility), and feldspar, 97-99. The last batch of feldspars had higher totals (99-101, probe numbers A5-DO5 in Table C4), but because they have a balanced stoichiometry these analyses are regarded as acceptable. Data not used in final syntheses have been indicated with an asterisk in Table B4.

Table B4. Microprobe analyses

Probe no.	Sample no.	Grain no.	core/rim	SiO2	TiO2	Al2O3	MnO	FeO	MgO	CaO	Na2O	K2O	P2O5	F	Cl	Total
A-1	VP94-001	Hbl-1	c	43.61	1.45	10.52	0.23	11.02	14.26	11.37	1.98	0.77				95.21
B-1	VP94-001	Hbl-1	r	46.68	0.31	5.20	0.15	8.49	13.62	9.80	0.53	0.32				85.10*
C-1	VP94-001	Hbl-1	r	51.64	0.37	4.47	0.19	8.77	17.18	12.57	0.60	0.18				95.97
D-1	VP94-001	Hbl-2	c	47.13	0.63	8.16	0.24	10.57	15.39	11.80	1.37	0.61				95.90
E-1	VP94-001	Hbl-2	r	49.60	0.48	6.04	0.18	9.94	16.25	12.00	1.08	0.45				96.02
F-1	VP94-001	Hbl-2	i	50.69	0.44	5.27	0.25	8.92	17.06	12.05	1.00	0.34				96.02
Q-1	VP94-001	Hbl-3	c	41.52	2.03	12.88	0.11	9.83	14.55	11.24	2.21	0.98				95.35
R-1	VP94-001	Hbl-3	c	41.41	2.62	12.59	0.15	9.63	14.55	11.10	2.37	0.86				95.28
S-1	VP94-001	Hbl-3	r	42.76	1.77	11.57	0.18	11.04	13.61	11.59	1.93	0.78				95.23
T-1	VP94-001	Hbl-3	r	50.83	0.56	5.27	0.19	9.06	17.05	12.12	0.91	0.40				96.39
W-1	VP94-001	Hbl-4	c	41.93	1.75	12.18	0.19	11.24	14.11	11.16	2.31	0.79				95.66
X-1	VP94-001	Hbl-4	r	49.05	0.35	6.76	0.18	8.69	17.14	11.51	1.27	0.48				95.43
Y-1	VP94-001	Hbl-5	c	41.44	2.79	12.93	0.16	10.81	13.68	11.47	2.32	0.87				96.47
Z-1	VP94-001	Hbl-5	c	41.48	2.28	12.67	0.22	10.26	14.39	11.41	2.21	0.90				95.82
AA-1	VP94-001	Hbl-5	r	51.49	0.52	4.83	0.22	7.89	18.10	12.26	0.85	0.24				96.13
AB-1	VP94-001	Hbl-5	r	46.03	0.52	9.99	0.22	10.19	15.07	11.92	1.69	0.50				96.40
AH-1	VP94-001	Hbl-6	c	41.00	3.06	13.32	0.14	9.81	13.81	11.54	2.17	0.93				95.78
AI-1	VP94-001	Hbl-6	r	50.90	0.59	4.45	0.16	7.97	17.68	12.31	0.76	0.23				95.05
AJ-1	VP94-001	Hbl-7	c	40.89	3.04	13.04	0.18	10.36	13.34	11.59	2.01	0.86				95.31
AK-1	VP94-001	Hbl-7	r	45.64	1.05	9.19	0.18	11.28	14.65	11.86	1.50	0.53				95.88
AP-1	VP94-011c	Hbl-1	c	47.69	0.90	7.62	0.19	11.55	14.88	12.23	0.90	0.62				96.58
AQ-1	VP94-011c	Hbl-1	r	45.55	0.73	9.38	0.23	13.42	13.13	12.00	1.06	0.72				96.22
AR-1	VP94-011c	Hbl-2	c	49.57	0.65	5.28	0.00	10.82	15.88	11.77	0.83	0.41				95.21
AS-1	VP94-011c	Hbl-2	r	47.67	0.22	7.60	0.20	14.13	13.19	11.93	0.84	0.43				96.21
BB-1	VP94-011c	Hbl-3	c	47.58	1.23	7.44	0.20	12.21	14.53	11.97	0.83	0.54				96.53
BC-1	VP94-011c	Hbl-3	r	47.01	0.81	7.79	0.24	11.70	14.67	11.97	1.11	0.64				95.94
BE-1	VP94-011c	Hbl-4	c	39.27	6.02	10.57	0.24	13.44	10.50	12.56	0.97	0.75				94.32*
BF-1	VP94-011c	Hbl-4	r	47.32	1.16	7.32	0.27	12.20	14.33	11.79	0.95	0.54				95.88
BI-1	VP94-011c	Hbl-5	c	43.11	1.85	10.74	0.24	13.84	12.70	11.77	1.51	0.73				96.49

Table B4. Microprobe analyses

Probe no.	Sample no.	Grain no.	core/rim	SiO2	TiO2	Al2O3	MnO	FeO	MgO	CaO	Na2O	K2O	P2O5	F	Cl	Total
BJ-1	VP94-011c	Hbl-5	r	49.97	0.68	5.23	0.24	10.99	15.75	12.03	0.73	0.42				96.04
BL-1	VP94-019	Hbl-1	c	48.00	0.70	6.19	0.24	13.79	14.05	11.81	0.94	0.64				96.36
BM-1	VP94-019	Hbl-2	c	48.74	0.48	5.42	0.30	13.37	14.81	12.02	0.67	0.45				96.26
BQ-1	VP94-019	Hbl-3	c	50.42	0.40	4.67	0.28	12.66	14.70	11.79	0.76	0.44				96.12
BU-1	VP94-019	Hbl-4	c	47.84	0.88	6.40	0.28	13.80	13.88	11.82	1.11	0.68				96.69
BV-1	VP94-019	Hbl-4	r	48.28	0.68	6.14	0.27	13.76	14.01	11.75	1.11	0.59				96.59
BY-1	VP94-019	Hbl-5	c	49.44	0 66	4.99	0.26	13.32	13.88	11.82	0.41	0.38				95.16
BZ-1	VP94-019	Hbl-5	r	48.44	0.51	5.88	0.26	13.24	14.29	11.76	0.94	0.53				95.85
DC-1	VP94-019	Hbl-6	c	49.36	0.59	5.30	0.31	13.22	14.72	11.89	0.88	0.49				96.76
DD-1	VP94-019	Hbl-6	r	50 93	0.29	4.28	0.30	12.14	15.48	12.15	0.64	0 34				96.55
G-1	VP94-001	Plg-1	r	60.77		23.42		0.12		5.38	8.23	0.17				98.09
I-1	VP94-001	Plg-1	c	61.84		23.24		0.06		4.63	8.60	0.18				98.55
J-1	VP94-001	Plg-1	c	62.79		21.98		0.04		3.51	9.18	0.23				97.73
K-1	VP94-001	Plg-1	r	65.09		20.87		0.07		2.05	10.27	0.16				98.51
L-1	VP94-001	Plg-2	c	60.99		23.76		0.12		5.45	8.15	0.16				98.63
M-1	VP94-001	Plg-2	r	64.49		21.08		0.10		2.47	9.90	0.16				98.20
N-1	VP94-001	Plg-3	c	60.08		22.50		0.09		4.92	8.23	0.18				96.00*
P-1	VP94-001	Plg-3	r	60.32		23.57		0 14		5.40	8.15	0.15				97.73
U-1	VP94-001	Plg-4	c	58.96		24.54		0.20		6.50	7.48	0.17				97.85
V-1	VP94-001	Plg-4	r	61.66		23.34		0.09		5.12	8.39	0.22				98.82
AC-1	VP94-001	Plg-5	c	58.23		25.52		0.06		7.46	7.00	0.16				98.43
AD-1	VP94-001	Plg-5	c	56.65		22.50		0.17		5.27	7.28	0.20				92.07*
AE-1	VP94-001	Plg-5	r	55.19		23.32		0.27		5.65	7.29	0.38				92.10*
AF-1	VP94-001	Plg-6	c	61.92		22.57		0.09		4.25	8.69	0.56				98.08
AG-1	VP94-001	Plg-6	r	61.44		21.66		0.10		3.07	6.10	5.54				97.91
AM-1	VP94-011c	Plg-1	c	55.29		27.03		0.13		9.28	5.81	0.13				97.67
AN-1	VP94-011c	Plg-1	r	51.20		29.20		0.12		12.67	4.09	0.11				97.39
AT-1	VP94-011c	Plg-2	c	48.63		4.90		12.37		11.86	0.56	0 23				78.55*
AU-1	VP94-011c	Plg-2	r	60.66		24.19		0.14		5.94	8.07	0.21				99 21

Table B4. Microprobe analyses

Probe no.	Sample no.	Grain no.	core/rim	SiO2	TiO2	Al2O3	MnO	FeO	MgO	CaO	Na2O	K2O	P2O5	F	Cl	Total
AW-1	VP94-011c	Plg-3	c	56.11		26.41		0.07		8.71	6.25	0.17				97.72
AX-1	VP94-011c	Plg-3	r	59.51		23.96		0.06		6.01	7.95	0.16				97.65
AY-1	VP94-011c	Plg-4	c	56.33		26.13		0.07		8.11	6.04	0.29				96.97*
AZ-1	VP94-011c	Plg-4	r	56.02		26.47		0.20		8.85	6.28	0.16				97.98
BG-1	VP94-011c	Plg-5	c	54.27		27.52		0.09		10.34	5.41	0.12				97.75
BH-1	VP94-011c	Plg-5	r	52.47		25.58		1.99		8.49	5.39	1.28				95.20*
BO-1	VP94-019	Plg-1	c	66.15		25.00		0.19		5.38	8.20	0.19				105.11*
BP-1	VP94-019	Plg-2	c	62.66		23.20		0.09		4.43	8.70	0.27				99.35
BT-1	VP94-019	Plg-3	c	60.99		23.66		0.13		5.68	7.97	0.19				98.62
BX-1	VP94-019	Plg-4	c	61.48		23.14		0.13		4.83	8.47	0.21				98.26
DA-1	VP94-019	Plg-5	c	60.50		22 69		0.16		5.72	8.24	0.28				97.59
DE-1	VP94-019	Plg-6	c	62.04		23.28		0.20		4.83	8.42	0.27				99.04
DH-2	VP94-119b	Hbl-1	c	43.54	0.67	8.92	0.32	18.21	10.49	11.53	1.13	1.00				95.81
DK-2	VP94-119b	Hbl-2	c	44.70	0.96	8.45	0.36	17.71	10.80	11.42	1.27	0.97				96.64
DN-2	VP94-119b	Hbl-3	c	44.46	1.00	8.23	0.38	17.68	11.17	11.49	1.32	1.00				96.73
DU-2	VP94-119b	Hbl-4	c	36.05	2.89	14.65	0.31	18.77	12.08	0.01	0.11	9.67				94.54*
DV-2	VP94-119b	Hbl-4	r	44.68	1 38	13.10	0.23	15.92	11.30	2.54	0.35	7.57				97.07
DY-2	VP94-119b	Hbl-5	c	43.95	1.07	8.14	0.39	17.42	11.04	11.38	1.39	1.01				95.79
DZ-2	VP94-119b	Hbl-5	r	43.79	0.76	8.30	0.43	17.34	11.20	11.62	1.30	0.97				95.71
EC-2	VP94-061	Hbl-1	c	45.65	0.47	7.81	0.38	17.50	10.74	11.79	0.84	0.65				95.83
ED-2	VP94-061	Hbl-2	c	46.10	0.82	8.66	0.31	16.02	12.03	11.82	1.17	0.63				97.56*
EE-2	VP94-061	Hbl-3	c	49.11	0.42	5.72	0.32	14.17	14.00	11.77	0.84	0.33				96.68
EK-2	VP94-061	Hbl-4	c	44.71	0.87	9.00	0.30	16.12	11.61	11.81	1.04	0.70				96.16
EL-2	VP94-061	Hbl-4	r	45.91	0.73	8.14	0.31	15.71	12 19	11.66	1.03	0.51				96.19
EQ-2	VP94-061	Hbl-5	c	44.75	0.97	8.96	0.34	16.00	11.72	11.49	1.14	0.66				96.03
ER-2	VP94-061	Hbl-5	r	46.63	0.44	7.95	0.32	16.22	12.11	11.93	0.79	0.56				96.95
EX-2	VP94-020c	Hbl-1	c	46.08	1.02	7.15	0.39	15.52	12.39	11.90	1.02	0.70				96.17
FA-2	VP94-020c	Hbl-2	c	42.84	1.74	9.19	0.38	17.01	10.64	11.38	1.32	0.84				95.34
FB-2	VP94-020c	Hbl-2	r	47.25	0.35	6.73	0.34	15.37	12.18	11.22	0.75	0.57				94.76*

Table B4. Microprobe analyses

Probe no.	Sample no	Grain no.	core/rim	SiO2	TiO2	Al2O3	MnO	FeO	MgO	CaO	Na2O	K2O	P2O5	F	Cl	Total
FG-2	VP94-020c	Hbl-3	c	42.54	1.80	9.61	0.38	16.43	11.05	11.52	1.44	0 79				95.56
FH-2	VP94-020c	Hbl-3	r	38.21	0.29	6.57	0.28	15.04	12.80	11.82	0.73	0.50				86.24*
FO-2	VP94-020c	Hbl-4	c	39.99	1.16	7.66	0.26	15.92	12.71	11.84	1.17	0.65				91.36*
FP-2	VP94-020c	Hbl-4	r	44.23	0.89	5.40	0.43	14.05	10.62	9.84	1.01	0.44				86.91*
DF-2	VP94-119b	Plg-1	r	61.69		22.77		0.20		4.86	8.22	0 33				98.07
DG-2	VP94-119b	Plg-1	c	60.43		23.46		0.14		5.68	7.95	0.34				98.00
DL-2	VP94-119b	Plg-2	c	56.83		23.91		0.61		5.91	5.93	0.42				93.61*
DM-2	VP94-119b	Plg-2	r	61.98		22.88		0.07		4.86	8.43	0.30				98.52
DP-2	VP94-119b	Plg-3	c	61.40		22.99		0.12		5.03	8.47	0.16				98.17
DQ-2	VP94-119b	Plg-3	r	60.04		24.04		0.13		6.14	7.72	0.22				98.29
DR-2	VP94-119b	Plg-4	c	59.60		24.39		0.14		4.69	8.19	0.19				97.20
DS-2	VP94-119b	Plg-4	r	61.41		22.91		0.16		4.83	8.46	0.34				98.11
DW-2	VP94-119b	Plg-5	c	59.14		23.52		0.17		5.98	7.59	0.35				96.75*
DX-2	VP94-119b	Plg-5	r	60.37		22.35		0.20		4.65	8.54	0.35				96.46*
EB-2	VP94-061	Plg-1	c	56.24		23.30		0.12		6.20	7.38	0.14				93.38*
EF-2	VP94-061	Plg-2	c	56.82		23.64		0.13		6.13	7.62	0.16				94.5*
EG-2	VP94-061	Plg-3	c	59.47		24.50		0.60		6.70	7.45	0.06				98.32
EH-2	VP94-061	Plg-3	r	59.85		24 02		0.19		5.97	7.77	0.19				97.99
EI-2	VP94-061	Plg-4	c	59.57		23.88		0.10		6.09	7.65	0.18				97.47
EJ-2	VP94-061	Plg-4	r	60.70		23.93		0.20		5.84	7.92	0.22				98.81
EM-2	VP94-061	Plg-5	c	60 38		23.93		0.12		6.08	7.88	0.21				98.60
EN-2	VP94-061	Plg-5	r	60.49		24.18		0.12		6.16	7.92	0.22				99.09
EO-2	VP94-061	Plg-6	c	58.74		24.27		0.12		6.58	7.55	0.16				97 42
EP-2	VP94-061	Plg-6	r	56.83		23.14		0.10		5.97	7.29	0.14				93.47*
ES-2	VP94-020c	Plg-1	c	61.00		23.58		0.14		5.42	8.17	0.29				98.60
ET-2	VP94-020c	Plg-1	r	61.53		23.64		0.16		5.31	8.29	0.31				99.24
EU-2	VP94-020c	Plg-2	c	60.13		23.75		0.06		5.75	8.02	0.27				97.98
EY-3	VP94-020c	Plg-3	c	61.22		24.12		0 07		5.83	6.95	0.17				98.36
EZ-3	VP94-020c	Plg-3	r	61.58		23.45		0.06		5.29	8.36	0.29				99.03

Table B4. Microprobe analyses

Probe no.	Sample no.	Grain no.	core/rim	SiO2	TiO2	Al2O3	MnO	FeO	MgO	CaO	Na2O	K2O	P2O5	F	Cl	Total
FM-3	VP94-020c	Plg-4	c	60.40		23.38		0.06		5.48	8.13	0.18				97.63
FN-3	VP94-020c	Plg-4	r	60.59		23.40		0.13		5.64	8.16	0.24				98.16
FQ-3	VP94-020c	Plg-5	c	60.89		23.53		0.09		5.67	8.02	0.31				98.51
FR-3	VP94-020c	Plg-5	r	61.59		23.05		0.16		5.02	8.55	0.18				98.55
C-4	VP94-123b	Hbl-1	c	46.54	0.95	7.52	0.27	13.80	13.18	11.69	0.95	0.68				95.58
D-4	VP94-123b	Hbl-1	r	47.83	0.75	6.73	0.22	13.51	14.00	11.94	0.80	0.62				96.40
E-4	VP94-123b	Hbl-2	c	47.75	0.75	6.49	0.26	13.07	13.96	11.94	0.84	0.62				95.68
F-4	VP94-123b	Hbl-2	r	48.55	0.57	5.79	0.28	12.86	14.30	11.94	0.70	0.47				95.46
I-4	VP94-123b	Hbl-3	c	47.53	0.92	6.80	0.20	12.78	14.32	11.90	0.90	0.57				95.92
J-4	VP94-123b	Hbl-3	r	49.73	0.37	5.03	0.27	12.52	14.90	12.01	0.64	0.35				95.82
M-4	VP94-123b	Hbl-4	c	47.98	0.79	6.37	0.27	12.37	14.48	11.85	0.71	0.54				95.36
N-4	VP94-123b	Hbl-4	r	47.94	0.51	6.46	0.28	13.16	13.79	11.45	0.67	0.72				94.98
U-4	VP94-123b	Hbl-5	c	49.41	0.46	5.23	0.23	11.94	15.02	11.85	0.51	0.40				95.05
V-4	VP94-123b	Hbl-5	r	46.36	0.86	6.93	0.22	13.06	13.42	11.72	0.84	0.64				94.05*
AE-4	VP94-123c	Hbl-1	c	42.31	1.09	8.21	0.37	9.96	10.88	11.28	1.24	0.89				86.23*
AF-4	VP94-123c	Hbl-1	r	44.91	0.40	7.89	0.32	15.87	11.71	11.52	1.06	0.67				94.35*
AK-4	VP94-123c	Hbl-2	c	42.21	1.29	9.49	0.31	17.29	10.46	11.58	1.23	1.06				94.92*
AM-4	VP94-123c	Hbl-2	r	40.98	1.08	11.93	0.26	19.12	10.80	7.60	0.67	3.27				95.71
AN-4	VP94-123c	Hbl-3	c	43.40	1.25	9.61	0.36	17.43	10.38	11.46	1.21	1.05				96.15
AO-4	VP94-123c	Hbl-3	r	44.37	0.98	8.88	0.38	17.16	11.07	11.40	1.21	0.95				96.40
AV-4	VP94-123c	Hbl-4	c	44.06	0.82	9.10	0.30	16.48	10.78	11.58	0.89	0.89				94.90
AW-4	VP94-123c	Hbl-4	r	44.39	0.95	8.66	0.31	16.64	11.17	11.61	1.17	0.93				95.83
AY-4	VP94-123c	Hbl-5	c	45.44	0.93	8.15	0.36	16.67	11.48	11.36	1.17	0.79				96.35
AZ-4	VP94-123c	Hbl-5	r	43.71	0.80	9.52	0.39	17.29	10.55	11.30	1.16	0.99				95.71
BD-4	VP94-124	Hbl-1	c	48.38	0.55	6.09	0.24	12.00	14.57	11.97	0.83	0.57				95.20
BE-4	VP94-124	Hbl-1	r	49.69	0.44	5.51	0.26	11.94	15.23	12.15	0.67	0.49				96.38
BH-4	VP94-124	Hbl-2	c	42.00	11.39	5.42	0.16	8.77	9.47	17.24	0.47	0.39				95.31
BI-4	VP94-124	Hbl-2	r	47.07	0.66	6.21	0.22	10.90	14.83	11.61	0.97	0.00				92.47*
BL-4	VP94-124	Hbl-3	c	48.64	0.57	6.11	0.23	12.19	14.69	11.92	0.74	0.62				95.71

Table B4. Microprobe analyses

Probe no.	Sample no.	Grain no.	core/rim	SiO2	TiO2	Al2O3	MnO	FeO	MgO	CaO	Na2O	K2O	P2O5	F	Cl	Total
BM-4	VP94-124	Hbl-3	r	52.80	0.18	3.52	0.29	10.74	16.40	12.34	0.38	0.23				96.88
BP-4	VP94-124	Hbl-4	c	50.01	0.57	5.04	0.20	10.86	15.66	12.10	0.65	0.47				95.56
BQ-4	VP94-124	Hbl-4	r	47.83	0.61	5.59	0.22	11.07	15.42	11.85	0.84	0.51				93.94*
BU-4	VP94-124	Hbl-5	c	48.10	0.55	5.97	0.26	11.53	14.93	11.77	0.67	0.57				94.35*
BV-4	VP94-124	Hbl-5	r	48.82	0.57	5.86	0.19	10.48	15.85	11.18	0.79	0.59				94.33*
A-4	VP94-123b	Plg-1	c	57.90		25.17		0.07		7.43	6.94	0.23				97.74
B-4	VP94-123b	Plg-1	r	60.83		24.58		0.12		6.49	7.57	0.33				99.92
G-4	VP94-123b	Plg-2	c	59.64		24.35		0.12		6.33	7.58	0.37				98.39
H-4	VP94-123b	Plg-2	r	59.98		24.27		0.09		6.32	7.50	0.27				98.43
K-4	VP94-123b	Plg-3	c	59.05		23.93		0.09		6.08	7.63	0.17				96.95
L-4	VP94-123b	Plg-3	r	59.16		24.62		0.09		6.77	7.34	0.24				98.22
P-4	VP94-123b	Plg-4	c	54.61		27.40		0.09		10.20	5.33	0.16				97.79
Q-4	VP94-123b	Plg-4	r	59.14		24.51		0.10		6.72	7.39	0.25				98.11
R-4	VP94-123b	Plg-5	c	52.09		28.55		0.36		11.36	4.54	0.17				97.07
S-4	VP94-123b	Plg-5	r	60.04		23.66		0.13		5.58	8.04	0.33				97.78
AB-4	VP94-123c	Plg-1	c	59.60		24.29		0.06		6.33	7.52	0.23				98.03
AC-4	VP94-123c	Plg-1	r	59.65		23.88		0.26		5.75	7.74	0.21				97.49
AG-4	VP94-123c	Plg-2	c	58.41		24.76		0.10		6.83	7.05	0.40				97.55
AH-4	VP94-123c	Plg-2	r	60.20		23.94		0.12		5.80	7.72	0.35				98.13
AR-4	VP94-123c	Plg-3	r	58.80		25.14		0.09		6.89	7.15	0.28				98.35
AS-4	VP94-123c	Plg-4	c	56.47		26.42		0 12		8.55	6.20	0.24				98.00
AT-4	VP94-123c	Plg-4	r	57.01		25.90		0.07		7.92	6.46	0.20				97 56
BB-4	VP94-123c	Plg-5	c	59.55		24.18		0.09		6.18	7.74	0.16				97.90
BC-4	VP94-123c	Plg-5	r	59.00		24.15		0.13		6.43	7.46	0.25				97 42
BF-4	VP94-124	Plg-1	c	56.24		26.48		0.09		8.74	6.14	0.22				97.91
BG-4	VP94-124	Plg-1	r	60.25		23.70		0.09		5.74	7.90	0.23				97.91
BJ-4	VP94-124	Kspar	c	62.85		18.32		0.07		0.01	1.53	14.12				96.90
BK-4	VP94-124	Kspar	r	62.99		18.21		0.03		0.00	0.90	15.18				97.31
BN-4	VP94-124	Plg-3	c	58.82		25.42		0.09		7.38	7.06	0.20				98.97

Table B4. Microprobe analyses

Probe no.	Sample no.	Grain no.	core/rim	SiO2	TiO2	Al2O3	MnO	FeO	MgO	CaO	Na2O	K2O	P2O5	F	Cl	Total
BO-4	VP94-124	Plg-3	r	59.58		24.66		0.07		6.21	7.72	0.19				98.43
BR-4	VP94-124	Plg-4	c	58 72		25.12		0.09		6.99	7.11	0.29				98.32
BS-4	VP94-124	Plg-4	r	58 56		25.04		0.13		7.10	7.17	0.25				98.25
BW-4	VP94-124	Plg-5	c	59.14		24.54		0.06		6.47	7.41	0.49				98.11
E-5	VP94-125	Hbl-1	c	44.95	0.93	8.86	0.22	13.80	12.65	11.65	1.15	0.88				95.09
F-5	VP94-125	Hbl-1	r	44.16	0.86	9.63	0.18	14.40	12.33	11.71	1.31	0.90				95.48
G-5	VP94-125	Hbl-2	c	45.02	1.26	8.61	0.23	13.63	12.98	11.58	1.24	0.95				95.50
H-5	VP94-125	Hbl-2	r	45.57	0.44	8.97	0.23	13.60	13.02	11.86	1.15	0.63				95.47
M-5	VP94-125	Hbl-3	c	44.52	0.99	10.63	0.20	14.20	13.42	9.01	0.79	2.68				96.44
U-5	VP94-125	Hbl-4	c	46.40	0 99	8.56	0.16	13.62	12.81	11.37	1.03	1.00				95.94
V-5	VP94-125	Hbl-4	r	45.99	0.88	8.27	0 22	13.26	13.25	11.79	1.11	0.80				95.57
Z-5	VP94-125	Hbl-5	c	46 28	1.08	8.29	0.20	13.35	13.66	11.90	1.12	0.86				96.74
AA-5	VP94-125	Hbl-5	r	45 87	0 73	8.79	0 23	14.05	12.90	11.78	1.01	0.83				96.19
AI-5	VP94-130b	Hbl-1	c	47.87	0.29	6.79	0.19	14.41	13.24	12.18	0.66	0.45				96.08
AJ-5	VP94-130b	Hbl-1	r	47.50	0.64	7.31	0.20	13.75	13.62	11.85	0.80	0.63				96.30
AP-5	VP94-130b	Hbl-2	c	47.86	0.68	7.16	0.22	13.34	13.81	11.63	0.84	0.65				96.19
AQ-5	VP94-130b	Hbl-2	r	46.40	0.81	7.80	0.19	13.88	13.28	11.53	1.12	0.73				95.74
AV-5	VP94-130b	Hbl-3	c	47.50	0.68	6.69	0.20	13.33	14.08	11.71	0.87	0.63				95.69
AW-5	VP94-130b	Hbl-3	r	46.29	0.68	7.82	0.16	13.97	13.26	11.83	0.95	0.73				95.69
AY-5	VP94-130b	Hbl-4	c	41.48	1.73	11.64	0 22	16.48	10.71	11.64	1.64	0.97				96.51
AZ-5	VP94-130b	Hbl-4	r	41.46	1.75	11.78	0.20	16.63	10.61	11.64	1.70	1.00				96.77
BD-5	VP94-130b	Hbl-5	c	46.65	0.81	7.90	0 23	14.43	13.12	11.85	0.95	0.77				96.71
BE-5	VP94-130b	Hbl-5	r	47.47	0.66	7.12	0 16	13.69	13.72	11.92	0.79	0.66				96.19
BN-5	VP94-246	Hbl-1	c	46.29	0.66	7.64	0 47	15.14	12.31	11.66	0.86	0.72				95.75
BO-5	VP94-246	Hbl-1	r	44.11	0.62	9.51	0.43	16.32	11.30	11.63	1.08	0.93				95.93
BP-5	VP94-246	Hbl-2	c	44.09	0.82	9.14	0.45	16.07	11.50	11.56	1.07	0.96				95.66
BQ-5	VP94-246	Hbl-2	r	44.13	0.62	9.61	0.44	16.59	11.25	11.71	1.15	0.92				96.42
BT-5	VP94-246	Hbl-3	c	45.12	0.71	8.70	0 50	16.17	11.68	11.46	0.99	0.87				96.20
BU-5	VP94-246	Hbl-3	r	44.24	0.56	9.48	0 38	16.55	10.99	11.57	0.97	0.88				95.62

Table B4. Microprobe analyses

Probe no.	Sample no.	Grain no.	core/rim	SiO2	TiO2	Al2O3	MnO	FeO	MgO	CaO	Na2O	K2O	P2O5	F	Cl	Total
DA-5	VP94-246	Hbl-4	c	42.17	1.05	11.25	0.44	17.22	10.32	11.47	1.16	1.30				96.38
DB-5	VP94-246	Hbl-4	r	45.07	0.67	8.78	0.39	15.85	11.65	11.74	0.93	0.85				95.93
DF-5	VP94-246	Hbl-5	c	45.67	0.77	7.60	0.42	15.24	12.26	11.88	1.01	0.79				95.64
DG-5	VP94-246	Hbl-5	r	44.75	0.56	9.21	0.47	16.34	11.42	11.63	1.11	0.86				96.35
A-5	VP94-125	Plg-1	c	57.65		26.90		0.10		7.49	6.77	0.24				99.15
B-5	VP94-125	Plg-1	r	60.04		25.13		0.03		5.88	7.90	0.24				99.22
J-5	VP94-125	Plg-2	c	60.62		25.35		0.14		5.67	7.86	0.31				99.95
K-5	VP94-125	Plg-2	r	58 60		26.50		0.17		7.15	7.09	0.18				99.69
P-5	VP94-125	Plg-3	c	60 61		24.96		0.09		5.44	7.93	0.35				99.38
Q-5	VP94-125	Plg-3	r	58.81		26.67		0.19		7.17	7.14	0.19				100.17
R-5	VP94-125	Plg-4	c	59 50		25.81		0.06		6.10	7.63	0.16				99.26
S-5	VP94-125	Plg-4	r	59 73		25.72		0.10		6.04	7.80	0.16				99.55
W-5	VP94-125	Plg-5	c	59.86		25.58		0.14		6.01	7.79	0.24				99.62
X-5	VP94-125	Plg-5	r	59.94		25.84		0.13		6.17	7.71	0.28				100.07
AB-5	VP94-130b	Plg?-1	c	59.64		27.59		0.12		2.57	6.94	2.83				99.69
AC-5	VP94-130b	Plg-1	r	61.23		24.66		0.09		5.15	8.30	0.24				99 67
AK-5	VP94-130b	Plg-2	c	61.22		24.65		0.09		5.16	8.23	0.21				99.56
AM-5	VP94-130b	Plg-2	r	60.91		24.42		0.06		4.97	8.36	0.19				98.91
AR-5	VP94-130b	Plg-3	c	53.07		30.44		0.10		10.96	4.80	0.32				99.69
AS-5	VP94-130b	Plg-3	r	53.82		30.28		0.12		10.83	4.98	0.13				100.16
BB-5	VP94-130b	Plg-4	c	59.46		25.96		0.12		6.12	7.42	0.29				99.37
BC-5	VP94-130b	Plg-4	r	61.54		24.64		0.10		5.06	8.26	0.33				99.93
BG-5	VP94-130b	Plg-5	c	61.38		24.45		0.13		5.10	8.01	0.59				99.66
BH-5	VP94-130b	Plg-5	r	61.28		24.42		0.04		5.05	8.16	0.35				99.30
BI-5	VP94-246	Plg-1	c	58.95		26.45		0.16		6.97	7.07	0.40				100.00
BJ-5	VP94-246	Plg-1	r	60.38		26.16		0.04		6.52	7.70	0.24				101.04
BK-5	VP94-246	Plg-2	c	57.46		27.80		0.16		8.10	6.42	0.25				100.19
BM-5	VP94-246	Plg-2	r	59.11		26.04		0.14		6.19	7.05	0.27				98.80
BR-5	VP94-246	Plg-3	c	59.36		26.46		0.09		6.88	7.34	0.17				100.30

Table B4. Microprobe analyses

Probe no.	Sample no.	Grain no.	core/rim	SiO2	TiO2	Al2O3	MnO	FeO	MgO	CaO	Na2O	K2O	P2O5	F	Cl	Total
BS-5	VP94-246	Plg-3	r	59.83		26.30		0.06		6.53	7.46	0.16				100.34
BY-5	VP94-246	Plg-4	c	60.85		25.41		0.12		5.93	7.73	0 45				100.49
BZ-5	VP94-246	Plg-4	r	58.87		26.56		0.10		7.11	7.16	0.17				99.97
D-5	VP94-246	Plg-5	c	57.62		27.24		0.09		7.51	6.87	0.23				99.56
DE-5	VP94-246	Plg-5	r	59.42		26.39		0.09		6.75	7.36	0.16				100.17
DJ-5	VP94-246	Plg-1	gmass	58.66		26.97		0.10		7.24	7.08	0.20				100.25
DK-5	VP94-246	Plg-2	gmass	58.23		27.13		0.10		7.60	7.01	0.11				100.18
DL-5	VP94-246	Plg-3	gmass	57.93		27.67		0.10		8.07	6.71	0.18				100.66*
DM-5	VP94-246	Plg-4	gmass	59.05		25.77		0.09		6.03	7.47	0.46				98.87
DN-5	VP94-246	Plg-5	gmass	59.41		26.28		0.04		6.81	7.32	0.16				100.02
DO-5	VP94-246	Plg-6	gmass	58.29		26.07		0.09		6.88	7.31	0.20				98.84
A	VP94-146	Ap-1					0.01	0.04		52.89			40.30	2.54	0.01	95.79*
B	VP94-146	Ap-2					0.06	0.03		54.47			42.31	2 71	0.01	99.59
C	VP94-146	Ap-3					0.00	0.03		53.69			40.44	2 56	0.02	96.74
D	VP94-146	Ap-4					0.06	0.09		54.70			41.97	2.73	0.02	99.57
E	VP94-146	Ap-5					0.06	0.06		53.88			41.44	2.33	0.02	97.79
F	VP94-146	Ap-6					0.01	0.03		53.43			40.11	2.37	0.03	95.98*
G	VP94-146	Ap-7					0.01	0.00		51.67			39.06	2.48	0.02	93.24*
I	VP94-146	Ap-8					0.06	0.07		54.06			40.68	2.48	0.02	97.37
J	VP94-146	Ap-9					0.00	0.03		53.63			40.82	2.65	0.01	97.14
K	VP94-132	Ap-1					0.04	0.01		54.99			41.61	2.59	0.02	99.26
L	VP94-132	Ap-2					0.06	0.03		54.85			42.31	2.90	0.01	100.16
M	VP94-132	Ap-3					0.01	0.00		54.11			41 17	2.58	0.06	97.93
P	VP94-140a	Ap-1					0.01	0.01		55.00			42.03	2 25	0.02	99.32
Q	VP94-140a	Ap-2					0.03	0.01		54.45			42.01	2 37	0.03	98.90
R	VP94-140a	Ap-3					0.08	0.00		54.55			42.28	2.32	0.02	99.25
S	VP94-140a	Ap-4					0.00	0.01		54.10			41.86	2.45	0.02	98.44
T	VP94-140a	Ap-5					0.08	0.01		54.58			42.21	2.44	0.03	99.35
U	VP94-140a	Ap-6					0.01	0.06		54.99			42.61	2.39	0.02	100.08

Table B4. Microprobe analyses

Probe no.	Sample no.	Grain no.	core/rim	SiO2	TiO2	Al2O3	MnO	FeO	MgO	CaO	Na2O	K2O	P2O5	F	Cl	Total
V	VP94-140a	Ap-7					0.07	0.00		55.06			42.50	2.39	0.02	100.04
W	VP94-140a	Ap-8					0.06	0.07		55.22			42.38	2.22	0.03	99.98
X	VP94-140a	Ap-9					0.07	0.01		54.88			42.74	2.17	0.03	99.90
Y	VP94-140a	Ap-10					0.06	0.01		54.98			41.58	2.30	0.03	98.96
Z	VP94-140b	Ap-1					0.04	0.25		51.94			40.48	1.79	0.22	94.72*
AA	VP94-140b	Ap-2					0.01	0.16		53.57			40.37	1.76	0.34	96.21*
AB	VP94-140b	Ap-3					0.06	0.01		53.79			40.54	1.84	0.37	96.61*
AC	VP94-140b	Ap-4					0.01	0.01		54.02			41.12	1.76	0.34	97.26
AD	VP94-140b	Ap-5					0.04	0.00		54.67			42.01	1 87	0.24	98.83
AE	VP94-140b	Ap-6					0.00	0.04		54.66			41.31	1.80	0.30	98.11
AF	VP94-140b	Ap-7					0.04	0.03		53.73			39.38	1.69	0.28	95.15*
AG	VP94-140b	Ap-8					0.03	0.07		53.50			40.52	1.76	0.34	96.22*
AH	VP94-140b	Ap-9					0.07	0.03		56.45			42.65	2.01	0.31	101.52*
AI	VP94-140b	Ap-10					0.04	0.07		54.08			41.75	1.85	0.30	98.09
AJ	VP94-142	Ap-1					0.30	0.10		54.46			42.27	2.61	0.06	99.80
AK	VP94-142	Ap-2					0.07	0.01		54.57			42.06	2.54	0.01	99.26
AM	VP94-057b	Ap-1					0.03	0.04		54.92			41.98	2.49	0.07	99.53
AN	VP94-057b	Ap-2					0.07	0.04		55.05			42.09	2 37	0.08	99.70
AO	VP94-057b	Ap-3					0.01	0.01		54.57			41.27	2.50	0.06	98.42
AP	VP94-057b	Ap-4					0.10	0.07		55.12			41.83	2.32	0.07	99.51
AQ	VP94-057b	Ap-5					0.04	0.06		55.59			41.64	2 59	0 06	99.98
AR	VP94-057b	Ap-6					0.06	0.01		55.28			41.98	2.34	0 06	99 73
AS	VP94-057b	Ap-7					0.08	0.00		55.47			41.95	2.44	0.10	100.04
AT	VP94-057b	Ap-8					0.10	0.06		54.81			41.83	2.47	0.07	99.34
AU	VP94-057b	Ap-9					0.04	0.04		55.22			42.00	2.37	0.07	99.74
AV	VP94-057b	Ap-10					0.00	0.06		53.85			39.89	2.32	0.11	96.23*
AW	VP94-127	Ap-1					0.04	0.01		55.51			42.11	2 42	0 02	100.11
AX	VP94-127	Ap-2					0.01	0 00		56.00			42.79	2.46	0.01	101 27*
AY	VP94-127	Ap-3					0.11	0.07		55.29			41.72	2.44	0.03	99.66

Table B4. Microprobe analyses

Probe no.	Sample no.	Grain no	core/rim	SiO2	TiO2	Al2O3	MnO	FeO	MgO	CaO	Na2O	K2O	P2O5	F	Cl	Total
AZ	VP94-127	Ap-4					0.10	0.01		55.30			41.98	2.30	0.01	99.70
BB	VP94-127	Ap-5					0.10	0.01		54.91			42.01	2.47	0.02	99.52
BC	VP94-127	Ap-6					0.08	0.06		55.16			42.27	2.34	0.02	99.93
BD	VP94-127	Ap-7					0.06	0.03		54.96			41.90	2.59	0.03	99.57
BE	VP94-127	Ap-8					0.10	0.00		54.71			41.72	2.40	0.01	98.94
BF	VP94-127	Ap-9					0.01	0 01		55.02			41.67	2.49	0.01	99.21
BG	VP94-127	Ap-10					0.06	0.04		54.84			39.06	2.47	0 02	96.49
BH	VP94-141	Ap-1					0.01	0.03		56.93			43.60	2.40	0.03	103.00*
BI	VP94-141	Ap-2					0.08	0.04		55.32			42.27	2.24	0.03	99.98

APPENDIX C: Mineral Separation Techniques

Minerals separated from fresh, whole-rock samples include zircon (zrn), monazite (mnz), sphene (spn), apatite (ap), feldspar (fspar), hornblende (hbl), and biotite (bt). Ten samples were originally collected for U/Pb analyses, i.e.- zrn + mnz or zrn + spn mineral pairs, and one of these was recollected in an attempt to verify the initial analytical results. These samples were analysed using the "conventional" population-technique, thus requiring ≈25 kilograms of whole-rock sample. For the other mineral separates, 2-3 kilograms of whole-rock sample would have been suffcient. The whole-rock samples were "coarse crushed" to pea-size in a jaw-crusher. Some of this material was set aside for later chemisty. The remaining pea-sized gravel was reduced to "fine crush" using a BICO disk-mill. The milled disaggregate was sluiced across a Wilfey table, which roughly segregates material by density. Aggregate grains and grains with inclusions cause the division between high-, medium-, and low-density material to overlap slightly. The low-density material (rock dust/flour) was discarded. The remaining material was used to obtain mineral separates, with hbl, fspar,and bt in the medium-density material, and zrn, mnz, sph, and apatite in the high-density material. The jaw crusher, disk mill, and Wilfey table were cleaned between samples.

The mineral separation procedure generally involves sieving to the size fraction desired, removing magnetite with a hand magnet (as it congests the equipment used later in finer-scale magnetic separation), an initial "coarse" magnetic separation into felsic and mafic minerals using a Carpco, a "fine" magnetic separation into sub-populations of mafic minerals using a Frantz, density separation using heavy liquids (in this case methylene iodide, MI), and hand-picking under a binocular microscope for >99% purity. The order in which these steps are done can be modified to suit each sample and the mineral separate desired. In some cases Frantzing and the heavy liquid stage needed to be repeated. It takes approximately 3 hours to crush 25 kg of rock (through "coarse" and "fine crush" stages). The mineral separation stage takes approximately 1 day per zrn, mnz, or sph, with an additional day of hand-picking for each. Hbl, bt, and ap take about 1 day each for heavy liquid separation. These mineral separates then each also require an additional day of hand-picking. The separation of 5 minerals, each from 10 samples, requires approximately 2.5 - 3 months of labor.

Zrn ± mnz, zrn ± sph, and fspar were separated for U/Pb analyses, while hbl and bt were separated for $^{40}Ar/^{39}Ar$ analyses, and zrn, spn, and ap were separated for fission track analyses. The values in Table D1 are the specific gravities used to calibrate the heavy liquid for each mineral separation. In order to get the purest separates possible, these values have been restricted from the wider range existing for most minerals. Mineral separation procedures unique to each of these minerals are itemized below.

Table C1. Specific gravity of minerals used in this study

Zrn	Mnz	Spn	Hbl	Bt	Ap	MI
4.68	5.2	3.52	2.8-3.15	2.85-3.2	3.15-3.20	3.32

Feldspar - The medium-density material was sieved for the <355 µm size fraction (45 mesh Tyler or US size standard). After separation through the Frantzing stage, the resulting, magnetically clean, material was generally >50% fspar. Approximately 1 gram of this material was rinsed in a 5% HF (hydrofluoric acid) solution for 15-20 minutes, removing external surfaces and labile Pb (Ludwig and Silver, 1977).

Zircon & Sphene -The high-density material was sieved for the <250 µm size fraction (50 mesh Tyler or US size standard). A rigorous, multi-step, Frantzing procedure was followed with the ramp initially at the maximum slope (15°). After progressing to the maximum amperage in 9 - 10 steps, and repeating this procedure, the ramp incline was reduced to 10°. Progressing to maximum amperage in 9 10 steps was repeated, and the whole procedure repeated at 5°, 3°, and 1° ramp inclines. This procedure generated ≥ 50 mg of impure, variably colored zrn (clear, pink, and smoky), and ≥ 50 mg of impure, golden-yellow spn separates. Zrn samples were then sieved into 4 - 6 size populations: <63µm, <80µm, <100µm, <130µm, <163µm, and ≥163 µm (230 to 100 mesh Tyler or US size standard). The amount of sample used for analysis varied with the inferred age of the sample. Inferred Tertiary samples used twice as much sample as Cret (?) or Precambrian (?) samples: Zrn 10-20 mg , spn ≈20 mg, versus 5-10 mg for pre-Tertiary samples.

Monazite - Mineral separation procedure is the same as for zrn and spn except that mnz is separated on the Frantz at lower amps (0.4 1.0 amps). Mnz separates off the Frantz are generally very impure because many other minerals with inclusions, etc., will also separate at 0.4-1.0 amps. This

procedure generated ≈49 mg of impure, greenish-yellow mnz from each sample, with the exception of the recollected sample. Mnz is then sieved into the same size populations as zrn (see above). Mnz is easily recognized by it's monoclinic crystal habit, but samples were quickly scanned under the SEM to confirm phosporus and rare earth element peaks. Only about 2 mg of sample is necessary for analysis because mnz is thorium-rich.

Hornblende Sieve fraction used: 105 to 200μm (150 to 80 mesh Tyler or US size standard); coarser fraction had composite grains and was not used. Every sample required hand-picking. A total of 20-50 mg of pure separate was obtained. About 2 mg of sample was used for each laser fusion analysis and ≈10 mg was used for incremental heating analysis.

Biotite - Sieve fraction used: 200 to 300 μm (80 to 35 mesh Tyler or US size fraction); coarser fraction had composite grains and was not used. A total of 20-40 mg of pure separate was obtained and about ≈2 mg was used for each laser fusion analysis.

Apatite - Sieve fraction used: 100-200 μm (150 to 80 mesh Tyler or US size fraction). For fission track analyses, because samples to be analyzed are visually selected under the microscope, sample puriety is acceptible at ≥50%. This puriety was attained using heavy liquids and no further cleaning of ap samples was necesssary. Some samples were reletively ap-poor, yielding only tens of grains. The amount of material mounted was typically 20 - 50 grains. This was also true for both spn and zrn grain mounts for fission track analyses. Excess apatite, after fission track analyses, was used for electron microprobe analyses. In some samples, there was no excess ap to use for microprobe work.

APPENDIX D: Isotopic Analytical Techniques And Analyses

U/Pb and common lead analytical techniques

U/Pb age determinations are based on the following radioactive decay schemes:

$$^{238}_{92}U \rightarrow ^{206}_{82}Pb + 8^{4}_{2}He + 6\beta^{-} + Q \qquad \lambda(^{238}\text{U}) = 1.55125 \times 10^{-10}\ \text{a}^{-1} \qquad (1)$$

$$^{235}_{92}U \rightarrow ^{207}_{82}Pb + 7^{4}_{2}He + 4\beta^{-} + Q \qquad \lambda(^{235}\text{U}) = 9.8485 \times 10^{-10}\ \text{a}^{-1} \qquad (2)$$

$$^{232}_{90}Th \rightarrow ^{208}_{82}Pb + 6^{4}_{2}He + 4\beta^{-} + Q \qquad \lambda(^{232}\text{Th}) = 4.9475 \times 10^{-11}\ \text{a}^{-1} \qquad (3)$$

where Q = decay energy and half-lives are from Steiger and Jäger (1977).

Once the minerals are separated from the whole-rock sample, weighed aliquots of the various size fractions are washed, dissolved, spiked, and the U and Pb is separated by anion exchange chromatography. This general procedure is mineral dependent, and the relevant modifications are outlined below. All U/Pb chromatographic procedures use pre-cleaned Biorad AG1x8, 200-400 mesh, resin (chloride form).

Mass spectrometry for the conventional data was performed using a Finnigan MAT262 multi-collector mass spectrometer at the United States Geological Survey, Menlo Park. Pb (zircon, monazite, sphene, and common Pb in feldspar) was loaded onto single Re filaments with silica-gel activator. U was loaded onto the evaporation filament of a double Re filament assembly. Repeated analysis of NBS981 and NBS982 standards indicated a reproducible mass fractionation of -0.12% per atomic mass unit. Overall 2σ analytical errors for the feldspar analyses are 0.1% on all ratios to ^{204}Pb. Measured uncertainties in the ^{206}Pb/^{204}Pb ratios of the zircon fractions range from 0.6 5.2% (2σ); uncertainties in ^{238}U/^{235}U are 0.1% (2σ). The uncertainties associated with monazite and sphene are equal to, or better than, these values.

Zircon Using Teflon beakers, all zrn samples are washed in 1cc of 1N HNO3 and left on a hotplate set to 60-80°C for about a 1/2 hour. The HNO3 is pipetted off and the samples are rinsed 3x with distilled H2O. Samples are then dried on the hotplate at 100°C (about 20 minutes). High-pressure, stainless steel bombs with teflon inner sleeves are used for dissolution. 1cc 14N HNO3 and 5 cc HF are added to samples in Teflon beakers, which are then placed in high-pressure bombs. Samples are left to dissolve in an oven set at 210°C for 10-14 days. The dissolution is then split into 2/3:1/3 aliquots for concentration (IC) and identification (ID), respectively. The ID split is then spiked and both IC and ID are put though the columns.

U/Pb Zircon Chromatography

(using 0.15 cc columns filled with pre-cleaned resin)

wash	1cc of 2x distilled 6N HCl
wash	1cc 3x distilled H2O
wash	1cc of 2x distilled 6N HCl
wash	1cc 3x distilled H2O
prep.	0.5cc 3N HCl
load	all ID or IC onto column
prep.	0.1cc 3N HCl by drip
prep.	0.1 cc 3N HCl
prep.	0.1 cc 3N HCl
prep.	0.5cc 3N HCl (removes zirconium)
collect Pb	0.5cc of 2x distilled 6N HCl (from ID or IC)
collect Pb	0.5cc of 2x distilled 6N HCl (from ID or IC)
collect Pb	0.1cc of 2x distilled 6N HCl (from ID or IC)

(add drop of H3PO4 to Pb collection)

collect U	0.5cc 3x distilled H2O (U from ID)
collect U	0.5cc 3x distilled H2O (U from ID)
collect U	0.5cc 3x distilled H2O (U from ID)

(add a drop conc. HNO3, ie.- 14N, to U for stability)

Sphene and monazite - The procedure is similar to that of zrn, but Savillex beakers are used, the time dissolving spn is usually ≈1 day, and dissolution occurs on a hotplate at 130°C (high-pressure bombs are not usually necessary). Dissolved material is evaporated to dryness on a hotplate and 0.1 cc of 14N HNO3 is added; this is dried and repeated 3x, insuring the absence of insoluble fluorides. Splitting and spiking procedures are the same (see zrn above). Evaporated split and spiked samples are re-dissolved each in 1.2 cc of 1 part 6N HCl and 2 parts 1N HBr, capped, and left overnight on a hotplate at 130°C. Cooled samples are ready for chromatography. Chromatography is more complicated, involving more steps.

U/Pb Sphene and Monazite Chromatography
(using 0.15 cc columns filled with pre-cleaned resin)

equil.	0.5 cc of 1N HBr
load	1.2 cc of re-dissolved sample
collect U	0.1 cc of 1N HBr by drip (U for ID)
collect U	0.1 cc of 1N HBr (U for ID)
collect U	0.2 cc of 1N HBr (U for ID)
collect U	0.6 cc of 1N HBr (U for ID)

(remove and evaporate for later U Chromatography A; see below)

collect Pb	0.5 cc of 6N HCl
collect Pb	0.5 cc of 6N HCl
collect Pb	0.1 cc of 6N HCl

(add 1 drop 14N HNO3 to ID and IC and evaporate; add 1 drop 6N HCl to each and evaporate)
(dissolve in 0.5 cc 3N HCl and later use zrn chromatography to extract Pb ID and IC)

U Chromatography A
(using 0.5 cc columns filled with pre-cleaned resin)
(dissolve U bearing evaporate with 1.0 cc of 7N HNO3 and evaporate)
(dissolve U bearing evaporate from above with 1.0 cc 7N HNO3, warm and cool for loading onto columns)

load	0.1 cc re-dissolved sample
wash	0.1 cc of 7N HNO3 by drip
wash	0.1 cc of 7N HNO3
wash	0.1 cc of 7N HNO3
wash	0.1 cc of 7N HNO3
wash	0.5 cc of 7N HNO3
collect U	3.0 cc 3x distilled H2O

(add a drop of 14N HNO3 and evaporate; re-dissolve in 0.5 cc 7N HNO3 for U Chromatography B, see below)

U Chromatography B (for sphene)
(using 0.15 cc columns filled with pre-cleaned resin)

equil.	0.5 cc of 7N HNO3
load	0.5 cc re-dissolved sample from U Chromatography A above)
wash	0.1 cc of 7N HNO3
wash	0.1 cc of 7N HNO3
wash	0.1 cc of 7N HNO3
wash	0.2 cc of 7N HNO3
collect U	0.5 cc 3x distilled H2O
collect U	0.5 cc 3x distilled H2O

(add a drop of 14 N HNO3 and evaporate for mass spectrometry)

^{40}Ar/ ^{39}Ar analytical techniques and analyses

The principal reaction involved in the ^{40}Ar/ ^{39}Ar method of dating is:

$$^{39}_{19}K(n,p)^{39}_{18}Ar\,, \qquad (4)$$

where the formation of ^{39}Ar is the result of irradiation of K-bearing samples in a nuclear reactor. But there are several interferring reactions resulting from interactions of neutrons with the isotopes of calcium, potassium, and chlorine, and these also produce argon isotopes (Table D1).

Table D1. Interfering nuclear reactions associated with ^{40}Ar/ ^{39}Ar dating

Argon Produced	Calcium	Potassium	Argon	Chlorine
^{36}Ar	^{40}Ca(n, $n\alpha$)			
^{37}Ar	^{40}Ca(n, α)	^{39}K(n, $n\,d$)	^{36}Ar(n, γ)	
^{38}Ar	^{42}Ca(n, $n\alpha$)	^{39}K(n, d)	^{40}Ar(n, $n\,d$, β)	^{37}Cl(n, γ, β)
	^{41}K(n, α, β)			
^{39}Ar	^{42}Ca(n, α)	^{39}K(n, p)$^{\alpha}$	^{38}Ar(n, γ)	
	^{43}Ca(n, $n\alpha$)	^{40}K(n, d)	^{40}Ar(n, d, β)	
^{40}Ar	^{43}Ca(n, α)	^{40}K(n, p)		
	^{44}Ca(n, $n\alpha$)	^{41}K(n, d)		

Ca is the most important interferring reaction because it involves ^{36}Ar, which will affect the atmospheric Ar correction. Ca is also primarily responsible for the production of ^{37}Ar, thus the abundance of ^{37}Ar is an indication of the extent of Ca interference. Correction factors for interferring isotopes were determined by analyzing K_2SO^4 and CaF_2 salts irradiated with the samples and the following values were used: (^{40}Ar/^{39}Ar)K = 0.0105, (^{36}Ar/^{37}Ar)Ca = 0.000298, and (^{39}Ar/^{37}Ar)Ca = 0.000712. For complete discussions on these interactions and correcting for them, the reader is referred to Faure (1986) and McDougall and Harrison (1988).

The number of radiogenic ^{40}Ar atoms present in the sample due to decay of ^{40}K during its lifetime is given by

$$^{40}Ar^{*} = \frac{\lambda e}{\lambda}{}^{40}K(e^{\lambda t} - 1)\,, \qquad \text{where } \lambda(^{40}\text{K}) = 5.5430 \times 10^{-10}\ \text{a}^{-1}$$
$$\text{and } \lambda e(^{40}\text{K}) = 0.581 \times 10^{-10}\ \text{a}^{-1} \qquad (5)$$

The neutron flux (J) associated with each irradiation is calculated with the use of monitor minerals (minerals of a known age), in this case GA1550 biotite. Samples and flux monitors were wrapped in Al foil and placed in a quartz vial with the flux monitors spaced at 0.5 - 1.0 cm intervals over the length of the tube. The vials were sealed and irradiated at the Soreq Nuclear Research Centre, IRR-1 reactor, Israel. For the biotite samples, single grains or small numbers of grains were loaded into milled pits in a copper plate and placed into a gas extraction line fitted with a glass viewport. Gas was extracted from these samples using a defocussed 6 Watt argon ion laser with stepwise heating accomplished by varying the power output of the laser. Gas extraction for the hornblende samples was performed in a computer controlled double vacuum resistance furnace. Extracted gas was expanded into a stainless steel clean-up line and purified for about 10 minutes with Zr-Ti getters.

Once J is determined and the 40Ar*/39Ar ratios of unknowns are measured, the dates can be calculated using the equation

$$\frac{1}{\lambda}\ln\left(\frac{^{40}Ar^{*}}{^{39}Ar}J + 1\right) \qquad (6)$$

and errors are propagated using the method of Dalrymple and Lanphere (1971). This assumes that all the ^{40}Ar in the irradiated sample is either radiogenic or atmospheric, that all the ^{36}Ar is atmospheric, and that ^{39}Ar produced by interferring reactions is corrected for so that the resulting ^{39}Ar is solely produced by equation 4 above.

$^{40}Ar/^{39}Ar$ analyses were performed at La Trobe University, Melbourne, Australia. Ar isotopes were measured using a VG3600 mass spectrometer operating at a sensitivity of 1 x 10^{-3} amps/torr, using a Daly photomultiplier set at a gain of 100 over the Faraday cups. The data were corrected for machine background, line blank, and mass discrimination. Extraction line blanks of atmospheric composition were typically 9 x 10^{-17} to 1 x 10^{-16} moles ^{40}Ar for the laser and 2 x 10^{-16} for the furnace. The value for mass discrimination determined by analyzing atmospheric Ar was 1.0105 for 1 amu. Biotite and hornblende samples were analyzed using the laser fussion technique and only hornblende samples were also analyzed using the incremental heating technique. The results of $^{40}Ar/^{39}Ar$ analyses are presented in Table D2 (below). Plots of release spectra and isochrons are presented in Table D3 (below).

Fission track analytical techniques and analyses

The fisson track (FT) age and FT length distribution can be used to reveal the time-temperature path experienced by the mineral. The principal reaction involved in FT analysis is the natural, spontaneous radioactive decay (fission) of ^{238}U. The fisson fragments fly apart at 180° to each other, creating a single fission damage zone (track) in the crystal lattice. The resulting linear, damage zone is typically 10-20μ long and a few Å in width. Such tracks can be observed by transmission electron microscopy. Using an etchant, the density of these *spontaneous* fission tracks in a mineral (the quantitative daughter product of the FT method) can be measured with an optical microscope. Fission tracks are annealed (shortened) by a diffusion mechanism that is not yet completely understood, but is a function of temperature, time, and mineral composition. Slight annealing occurs even at room temperature and total annealing occurs over geologic time scales at temperatures greater than the mineral closure temperature. Annealing reduces the density of fission tracks in the crystal. In a very simplistic view: The fewer the tracks, the younger the FT age.

To determine the "parent" isotopic abundance (U concentration), the sample is irradiated in a nuclear reactor. Using a well-thermalized site in the reactor where only slow, thermal neutrons exist, fission is induced in only a small fraction of the atoms of the less abundant U isotope, ^{235}U. In this way a set of *induced* fission tracks is produced, which are etched and counted in a similar way to *spontaneous* tracks. The ^{235}U abundance is related to the ^{238}U concentration using the isotopic abundance ratio of natural uranium. Determination of the parent and daughter abundances in FT dating essentially involves measuring densities of induced and spontaneous fission tracks that originated in the same location in the mineral. This procedure includes sample preparation (mineral separation, mounting and polishing), etching, irradiation of the sample and monitor standards, track counting, and age calculation.

The dating procedure used for this investigation is known as the "external dectector method": A U-free mica plate is placed in contact with the polished and etched mineral surface prior to irradiation. Induced tracks register in the mica during irradiation (as a result of neutron bombardment in the reactor) in the one-way passage of fission fragments from the mineral into the external mica detector. In contrast, the measured spontaneous tracks result from the passage of fission fragments across the internal surface (now polished) from both above and below are unrealated to the irradiation process. Standards of known age and dosimeter glasses are usually included in the irradiation package in order to monitor neutron flux in the reactor. The age equation has the following form:

$$T = \frac{1}{\lambda_D} \ln\left[1 + \lambda_D \quad \xi \frac{\rho_s}{\rho_i} \rho_d \right] \qquad (7)$$

where T = time (age)

λ_D = total decay constant for ^{238}U (1.55125×10^{-10}/yr)

ρ_s/ρ_i = spontaneous/induced FT density ratio in sample

and ζ, the personal mean zeta value is given by,

$$\xi = \frac{\left(e^{\lambda_D T_{STD}} - 1\right)}{\lambda_D \left(\rho_s / \rho_i\right)_{STD} g \rho_d} \qquad \text{where} \quad T_{STD} = \text{age of standard} \tag{8}$$

$(\rho_s/\rho_i)_{STD}$ = spontaneous/induced track density ratio in standard
g = geometry factor (0.5)
ρ_d = induced FT density of a standard glass with known U content

The zeta parameter eliminates the need for accurate knowledge of the total thermal neutron flux in the reactor (which is not readily measurable) and the spontaneous fission decay constant for ^{238}U (which is poorly known). Large, unexplained errors beyond that predicted by conventional error analysis tend to occur in each zeta value determined: Averaging zeta parameters from successive irradiations in the same laboratory, measured by the operator, is absolutely necessary for a well-defined personal mean zeta value.

FT analyses of zircon and apatite were performed at La Trobe University, Melbourne, Australia, following the procedures described in Foster and Gleadow (1992) and Fitzgerald and Gleadow (1998). FT ages were calculated using the zeta calibration method (Hurford and Green, 1983) and errors were calculated using the conventional method of Green (1981), which assumes a Poisson distribution. The "Chi-squared" statistic is used to determine the probability that all grains counted belong to a single population of ages (Galbraith, 1981). A probability of <5% is evidence of an asymmetric, i.e. non-Poisson, spread of single-grain ages. Central ages have been reported where the pooled data result in a marginal Chi-squared probability, i.e. - 10-15%, which may indicate a non-homogenoeous age population.

Zrn and ap grains were mounted in epoxy resin on glass slides and were ground and polished to reveal internal surfaces of grains. Zrn samples were etched in a mixture of KOH:NaOH:LOH, at a ratio of 14:6:1 respectively, at 200-220°C for up to 4 hours to reveal fossil fission tracks. The amount of time in the etchant bath is dependant upon the amount of radiation damage in the grains, which is a function of the U content and the sample age. Ap samples were etched in 5N HNO3 at room temperture for 20 seconds to reveal fossil fission tracks. All samples were irradiated in the X-7 position of the Australian HIFAR Research Reactor. Thermal neutron fluences were monitored using a muscovite detector. A summary of the zrn and ap FT results are presented in Table D4 and the counting statistics associated with each sample are included in Table D5 (below).

Table D2. 40Ar/39Ar analytical data

T (°C) (or Watts)	^{36}Ar (mol)	^{37}Ar (mol)	^{39}Ar (mol)	^{40}Ar (mol)	% $^{40}Ar^*$	$^{40}Ar^*/^{39}Ar(K)$	Cumulative ^{39}Ar (%)	Calculated age (Ma ± 1σ)	Ca/K
VP94-057b	hornblende	J =	1.0572E-2						
0.5W	4.717E-18	2.799E-15	6.070E-16	1.725E-15	33.1	0.943	29.25	17.90 ±4.35	8.79E+0
1.0W	6.739E-18	7.695E-15	1.469E-15	2.222E-15	40.2	0.610	100.00	11.61 ± 0.64	9.99E+0
Total	1.146E-17	1.049E-14	2.076E-15	3.947E-15		0.708		13.45 ± 1.72	
VP94-057b	hornblende	J =	1.0572E-2						
4.0W	2.085E-17	2.791E-14	5 253E-15	1 040E-14	63.8	1.268	100.00	24.03 ± 0.47	1.01E+1
Total	2.085E-17	2.791E-14	5.253E-15	1.040E-14		1.268		24.03 ± 0.47	
VP94-057b	hornblende	J =	1.0572E-2						
800	6.453E-17	4.418E-15	4.565E-15	3.323E-14	3.179	3.32	43.6	59.6 ± 40.79	1.84E+0
900	4.289E-17	8.851E-15	3.310E-15	1.584E-14	24.7	1.183	5.73	22.42 ± 0.82	5.09E+0
980	9.810E-17	1.034E-13	1.830E-14	4.406E-14	54.4	1.316	19.01	24.93 ± 0.58	1.08E+1
1010	1.153E-16	1.892E-13	3.378E-14	5.802E-14	69.4	1.196	43.52	22.67 ± 0.35	1.07E+1
1040*	7.640E-17	1.164E-13	2.180E-14	3.712E-14	66.2	1.131	59.34	21.45 ± 0.23	1.02E+1
1070*	5.209E-17	5.144E-14	9.328E-15	2.218E-14	50.6	1.208	66.11	22.89 ± 0.41	1.05E+1
1100*	6.081E-17	4.561E-14	7.704E-15	2.383E-14	41.1	1.277	71.70	24.18 ± 1.17	1.13E+1
1130*	4.596E-17	3.382E-14	5.672E-15	1.795E-14	40.6	1.289	75.81	24.43 ± 1.32	1.14E+1
1170*	5.016E-17	3.189E-14	5.483E-15	1.938E-14	37.7	1.338	79.79	25.34 ± 1.10	1.11E+1
1450	2.904E-16	1.534E-13	2.785E-14	1.308E-13	44.5	2.100	100.00	39.62 ± 0.50	1.05E+1
Total	8.967E-16	7.384E-13	1.378E-13	4.024E-13		1.465		27.72 ± 0.54	
VP94-069b	biotite	J =	1.0647E-2						
0.3	6.783E-21	6.928E-20	2.105E-15	2.013E-14	99.9	9.549	29.04	174.88 ± 2.44	6.25E-5
0.5	4.833E-18	4.359E-17	2.068E-15	2.524E-14	94.3	11.508	57.55	208.75 ± 3.71	4.01E-2
0.7	4.959E-18	1.366E-17	1.335E-15	2.750E-14	94.6	19.486	75.97	340.47 ± 5.97	1.94E-2
1.0	3.626E-18	4.519E-17	1.028E-15	2.660E-15	59.5	1.538	90.15	29.34 ± 1.46	8.35E-2
4.0	1.363E-18	6.186E-17	7.140E-16	4.112E-15	90.2	5.192	100.00	97.17 ± 3.53	1.65E-1
Total*	1 479E-17	1.644E-16	7.251E-15	7.964E-14		10.373		189.20 ± 3.42	

Table D2. Con't.

T (°C) (or Watts)	^{36}Ar (mol)	^{37}Ar (mol)	^{39}Ar (mol)	^{40}Ar (mol)	% $^{40}Ar^*$	$^{40}Ar^*/^{39}Ar(K)$	Cumulative ^{39}Ar (%)	Calculated age (Ma ± 1σ)	Ca/K
VP94-069b	biotite	J =	1.0647E-2						
0.3	1.194E-17	7.016E-18	3.013E-15	9.829E-15	63.8	2.081	23.54	39.53 ± 0.90	4.42E-3
0.5	3.438E-19	4.919E-17	3.059E-15	8.983E-15	98.6	2.895	47.44	54.76 ± 1.03	3.06E-2
0.8	6.783E-21	6.665E-18	2.147E-15	1.070E-14	99.8	4.973	66.22	93.07 ± 1.11	5.90E-3
4.0	4.827E-18	6.141E-17	4.580E-15	1.115E-14	86.8	2.114	100.00	40.15 ± 1.04	255E-2
Total*	1.712E-17	1.243E-16	1.280E-14	4.067E-14		2.772		52.48 ± 1.01	
VP94-127	biotite	J =	1.0659E-2						
0.3W	4.608E-17	4.657E-16	9.469E-15	2.078E-14	34.2	0.751	23.61	14.36 ± 0.24	9.34E-2
0.5W	6.497E-18	1.050E-16	8.294E-15	7.682E-15	74.0	0.685	44.29	13.12 ± 0.64	2.40E-2
0.8W	4.568E-18	4.351E-16	1.166E-14	1.036E-14	86.2	0.766	73.36	14.65 ± 0.15	7.09E-2
4.0W	6.298E-18	7.182E-16	1.068E-14	9.799E-15	80.5	0.738	100.00	14.13 ± 0.17	1.28E-1
Total	6.344E-17	1.724E-15	4.010E-14	4.862E-14		0.738		14.13 ± 0.28	
VP94-127	biotite	J =	1.0659E-2						
0.25W	6.783E-21	8.450E-18	1.130E-17	7.442E-17	98.1	6.469	0.09	120.30 ± 12.66	1.42E+0
0.5W*	4.071E-18	2.200E-16	3.054E-15	3.225E-15	62.3	0.658	24.68	12.60 ± 0.67	1.37E-1
0.7W*	5.42E-18	1.079E-15	5.485E-15	5.498E-15	71.5	0.717	68.84	13.74 ± 0.50	3.74E-1
4.0W*	3.899E-18	6.795E-16	3.871E-15	3.889E-15	70.9	0.712	100.00	13.64 ± 0.35	3.34E-1
Total	1.340E-17	1.987E-15	1.242E-14	1.269E-14		0.706		13.53 ± 0.51	
VP94-127	hornblende	J =	1.0584E-2						
0.25W	1.029E-17	1.817E-16	9.041E-17	3.556E-15	14.9	5.882	2.42	108.96 ± 19.96	3.82E+0
0.5W	5.695E-18	6.865E-16	2.241E-16	1.028E-15	-58.0	0.001	8.42	0.019 ± 5.846	5.83E+0
0.8W	7.910E-18	9.014E-15	1.968E-15	3.197E-15	51.1	0.832	61.06	15.82 ± 0.85	8.73E+0
4.0W	5.056E-18	6.892E-15	1.456E-15	2.223E-15	59.4	0.910	100.00	17.29 ± 1.16	9.02E+0
Total	2.895E-17	1.677E-14	3.739E-15	1.000E-14		0.935		17.77 ± 1.73	

Table D2. Con't.

T (°C) (or Watts)	^{36}Ar (mol)	^{37}Ar (mol)	^{39}Ar (mol)	^{40}Ar (mol)	% $^{40}Ar^*$	$^{40}Ar^*/^{39}Ar(K)$	Cumulative ^{39}Ar (%)	Calculated age (Ma ± 1σ)	Ca/K
VP94-127	hornblende	J =	1.0584E-2						
800	2.153E-16	7.031E-15	7.314E-15	7.968E-14	20.8	2.271	4.55	42.85 ± 0.88	1.83E+0
900	2.728E-17	4.617E-15	3.217E-15	1.032E-14	25.5	0.819	6.55	15.57 ± 1.01	2.73E+0
980	5.672E-17	4.693E-14	1.324E-14	2.593E-14	50 8	0.997	14.77	18.93 ± 0.25	6.75E+0
1020	9 169E-17	1.362E-13	3 092E-14	4.796E-14	67.8	1.056	33.95	20.04 ± 0.32	8.39E+0
1040	6.614E-17	1.180E-13	2 582E-14	3.499E-14	73 0	0.993	49.97	18.87 ± 0.27	8.71E+0
1060	lost								
1090*	6.194E-17	7.182E-14	1.482E-14	2.829E-14	57.1	1.094	59.16	20.77 ± 0.55	9.24E+0
1110*	5 006E-17	5.736E-14	1 133E-14	2.205E-14	55.3	1.080	66.18	20.51 ± 0.45	9 66E+0
1140*	5.395E-17	5.616E-14	1.156E-14	2 361E-14	52.9	1.084	73.35	20.58 ± 0.53	9.26E+0
1170*	5.578E-17	3 019E-14	6.188E-15	2.052E-14	32 3	1.075	77.19	20.41 ± 0.74	9.30E+0
1450	8.630E-16	1.723E-13	3.678E-14	3.020E-13	20.5	1.685	100.00	31.90 ± 1.69	8.93E+0
Total	1.542E-15	7.006E-13	1.612E-13	5.953E-13		1.243		23.58 ± 0.72	
VP94-129	biotite	J =	1 0692E-2						
0.2W*	6.416E-18	1.592E-17	2 911E-15	3.987E-15	51.7	0.708	11.79	13.61 ± 0.90	1.04E-2
0.4W*	4.664E-18	5.955E-18	5.803E-15	5.403E-15	73.4	0.683	35.29	13.13 ± 0.42	1.95E-3
0.6W*	3.918E-18	5.870E-17	4 874E-15	4 456E-15	73 0	0.667	55.02	12.83 ± 0.32	2.29E-2
4.0W	9.417E-19	9.956E-17	1 111E-14	9.828E-15	96.1	0.850	100.00	16.32 ± 0.19	1.70E-2
Total	1.594E-17	1.801E-16	2.470E-14	2.367E-14		0.758		14.56 ± 0.35	
VP94-129	biotite	J =	1 0692E-2						
0.3W	7.643E-19	4.428E-17	1 499E-15	1.715E-15	86.1	0.985	35.83	18.91 ± 0.59	5.61E-2
0.6W	1.825E-18	5.847E-18	1 615E-15	1.646E-15	66.2	0.675	74.41	12.98 ± 0.82	6.88E-3
0.8W	6.783E-21	7.498E-20	5.743E-16	6.604E-16	98.8	1.136	88.13	21.78 ± 0.21	2.48E-4
4.0W	6.783E-21	7.498E-20	4.970E-16	6.488E-16	98.9	1.291	100.00	24.73 ± 0.26	2.87E-4
Total	2.603E-18	5.027E-17	4 185E-15	4.670E-15		0.923		17.71 ± 0.59	

Table D2. Con't.

T (°C) (or Watts)	^{36}Ar (mol)	^{37}Ar (mol)	^{39}Ar (mol)	^{40}Ar (mol)	% $^{40}Ar^*$	$^{40}Ar^*/^{39}Ar(K)$	Cumulative ^{39}Ar (%)	Calculated age (Ma ± 1σ)	Ca/K
VP94-132	hornblende	J =	1.0766E-2						
0.5W	4.864E-18	1.226E-15	3.158E-16	1.531E-15	12.9	0.629	11.56	12.18 ± 4.16	7.40E+0
0.75W	3.738E-18	6.649E-15	1.252E-15	1.800E-15	70.4	1.017	57.34	19.65 ± 0.79	1.01E+1
1.0W	3.449E-18	4.384E-15	8.392E-16	1.205E-15	46.7	0.673	88.04	13.02 ± 1.71	9.96E+0
4.0W	3.657E-18	1.754E-15	3.270E-16	6.267E-16	-48.4	0.001	100.00	0.019 ± 4.209	1.02E+1
Total	1.571E-17	1.401E-14	2.734E-15	5.162E-15		0.745		14.41 ± 1.87	
VP94-132	hornblende	J =	1.0766E-2						
800	4.408E-16	5.711E-15	4.811E-15	1.482E-13	12.4	3.835	3.01	72.99 ± 3.30	2.26E+0
900	3.131E-17	5.748E-15	2.977E-15	1.268E-14	30.8	1.311	4.88	25.29 ± 0.82	3.67E+0
980	4.902E-17	3.677E-14	8.340E-15	2.141E-14	47.0	1.211	10.09	23.38 ± 0.59	8.40E+0
1010*	7.952E-17	1.111E-13	2.098E-14	3.720E-14	62.5	1.113	23.20	21.49 ± 0.37	1.01E+1
1040*	1.235E-16	2.543E-13	4.708E-14	6.515E-14	77.6	1.078	52.60	20.82 ± 0.35	1.03E+1
1070*	3.600E-17	3.458E-14	6.411E-15	1.485E-14	48.4	1.126	56.61	21.73 ± 0.74	1.03E+1
1100*	7.596E-17	1.087E-13	1.932E-14	3.462E-14	62.2	1.120	68.67	21.62 ± 0.46	1.07E+1
1130*	5.647E-17	5.425E-14	9.877E-15	2.297E-14	47.7	1.114	74.84	21.50 ± 0.60	1.05E+1
1170	6.914E-17	5.070E-14	9.227E-15	2.747E-14	41.5	1.241	80.61	23.95 ± 0.96	1.05E+1
1450	6.565E-16	1.608E-13	3.105E-14	2.624E-13	31.3	2.658	100.00	50.89 ± 0.97	9.88E+0
Total	1.618E-15	8.227E-13	1.601E-13	6.469E-13		1.502		28.94 ± 0.66	
VP94-132	biotite	J =	1.0713E-2						
4.0W	1.049E-17	5.085E-16	5.912E-15	8.274E-15	62.3	0.872	100.00	16.78 ± 0.66	1.63E-1
Total	1.049E-17	5.085E-16	5.912E-15	8.274E-15		0.872		16.78 ± 0.66	
VP94-132	biotite	J =	1.0713E-2						
0.3W*	6.030E-18	8.281E-17	4.820E-15	5.491E-15	66.8	0.761	25.93	14.64 ± 0.43	3.26E-2
0.5W*	5.634E-18	1.838E-16	5.059E-15	5.431E-15	68.7	0.737	53.15	14.19 ± 0.27	6.90E-2
0.7W*	4.640E-18	1.314E-15	4.168E-15	4.271E-15	69.6	0.713	75.58	13.73 ± 0.56	5.99E-1
4.0W	3.171E-18	1.934E-15	4.540E-15	4.615E-15	82.4	0.837	100.00	16.11 ± 0.45	8.10E-1
Total	1.947E-17	3.515E-15	1.859E-14	1.981E-14		0.762		14.67 ± 0.42	

Table D2. Con't.

T (°C) (or Watts)	^{36}Ar (mol)	^{37}Ar (mol)	^{39}Ar (mol)	^{40}Ar (mol)	% $^{40}Ar^*$	$^{40}Ar^*/^{39}Ar(K)$	Cumulative ^{39}Ar (%)	Calculated age (Ma ± 1σ)	Ca/K
VP94-135	hornblende	J =	1.0597E-2						
4.0W	4.025E-17	4.111E-14	3.655E-15	1.537E-14	45.9	1.947	100.00	36.85 ± 1.76	2.15E+1
Total	4.025E-17	4.111E-14	3.655E-15	1.537E-14		1.947		36.85 ± 1.76	
VP94-135	hornblende	J =	1.0597E-2						
0.3W	5.440E-18	9.894E-17	7.568E-17	1.335E-15	-19.8	0.001	2.81	0.019 ± 30.293	2.49E+0
0.6W	2.447E-18	3.938E-15	6.840E-16	1.660E-15	76.9	1.875	28.11	35.49 ± 2.34	1.10E+1
1.0W	5.892E-18	7.009E-15	1.177E-15	1.977E-15	42.5	0.717	71.65	13.66 ± 0.57	1.14E+1
4.0W	4.898E-18	5.012E-15	7.667E-16	1.333E-15	23.9	0.418	100.00	7.97 ± 3.08	1.25E+1
Total	1.868E-17	1.606E-14	2.703E-15	6.305E-15		0.905		17.22 ± 2.57	
VP94-135	hornblende	J =	1.0597E-2						
800	3.311E-16	5.574E-15	5.278E-15	1.103E-13	11.6	2.435	5.11	45.95 ± 2.21	2.01E+0
900	6.338E-17	6.073E-15	3.532E-15	2.168E-14	15.9	0.976	8.52	18.56 ± 1.34	3.27E+0
980	7.942E-17	6.184E-14	1.196E-14	3.310E-14	45.2	1.254	20.06	23.82 ± 0.84	9.86E+0
1020*	1.914E-16	2.472E-13	3.763E-14	7.695E-14	54.3	1.115	56.31	21.20 ± 0.39	1.25E+1
1040*	4.977E-17	4.063E-14	6.714E-15	1.786E-14	37.3	0.996	62.78	18.95 ± 0.99	1.15E+1
1070*	5.235E-17	3.485E-14	5.273E-15	1.783E-14	30.1	1.024	67.86	19.47 ± 0.83	1.26E+1
1100*	8.627E-17	6.586E-14	9.651E-15	3.038E-14	34.8	1.102	77.16	20.94 ± 0.86	1.30E+1
1130*	1.068E-16	5.335E-14	7.869E-15	3.598E-14	25.1	1.155	84.74	21.95 ± 0.53	1.29E+1
1170*	7.910E-17	4.804E-14	7.111E-15	2.697E-14	28.8	1.096	91.59	20.83 ± 1.37	1.29E+1
1450	1.893E-16	5.606E-14	8.727E-15	6.709E-14	23.8	1.840	100.00	34.84 ± 0.83	1.23E+1
Total	1.229E-15	6.195E-13	1.037E-13	4.381E-13		1.243		23.61 ± 0.79	
VP94-135	biotite	J =	1.0734E-2						
0.4W	1.069E-17	7.647E-20	6.905E-15	8.381E-15	61.4	0.746	33.44	14.38 ± 0.23	2.10E-5
0.7W	2.356E-18	3.162E-17	7.073E-15	6.693E-15	88.5	0.838	67.69	16.15 ± 0.23	8.49E-3
4.0W	3.123E-18	1.239E-16	6.671E-15	6.230E-15	84.2	0.787	100.00	15.17 ± 0.28	3.53E-2
Total	1.617E-17	1.556E-16	2.065E-14	2.130E-14		0.790		15.24 ± 0.24	

Table D2. Con't.

T (°C) (or Watts)	^{36}Ar (mol)	^{37}Ar (mol)	^{39}Ar (mol)	^{40}Ar (mol)	% $^{40}Ar^*$	$^{40}Ar^*/^{39}Ar(K)$	Cumulative ^{39}Ar (%)	Calculated age (Ma ± 1σ)	Ca/K
VP94-135	biotite	J =	1.0734E-2						
0.25W	1.153E-18	1.944E-17	1.007E-15	1.698E-15	79.4	1.338	16.91	25.73 ± 0.80	3.67E-2
0.4W	6.783E-21	6.793E-20	1.040E-15	1.197E-15	98.9	1.139	34.36	21.93 ± 0.15	1.24E-4
0.6W	6.783E-21	6.793E-20	1.242E-15	1.370E-15	98.9	1.091	55.21	21.01 ± 0.10	1.04E-4
4.0W*	2.525E-18	6.022E-17	2.668E-15	2.623E-15	70.7	0.695	100.00	13.40 ± 0.70	4.29E-2
Total	3.691E-18	7.980E-17	5.957E-15	6.888E-15		0.964		18.57 ± 0.50	
VP94-138	biotite	J =	1 0755E-2						
0.25W	1.130E-17	2.119E-17	9.297E-15	1.168E-14	70.6	0.887	30.21	17.13 ± 0.38	4.33E-3
0.35W	1 589E-18	3.972E-17	4.102E-15	4.217E-15	87.9	0.904	43.54	17.45 ± 0.33	1.84E-2
0.6W	4.010E-18	1.668E-16	9.990E-15	9.708E-15	86.9	0.844	76.00	16.30 ± 0.26	3 17E-2
4.0W	2.739E-18	6.281E-17	7.387E-15	7.189E-15	87.7	0.854	100.00	16.49 ± 0.27	1.62E-2
Total*	1.964E-17	2.905E-16	3.078E-14	3.280E-14		0.867		16.75 ± 0.31	
VP94-138	biotite	J =	1.0755E-2						
0.2W	1.325E-17	1.035E-16	8.513E-15	1.120E-14	64.3	0.846	16.45	16.35 ± 0.29	2.31E-2
0.5W	5.564E-18	1.609E-16	1.723E-14	1.659E-14	89.1	0.858	49.73	16.57 ± 0.23	1.77E-2
0.7W	5.365E-18	1.987E-16	1.550E-14	1.472E-14	88.2	0.838	79.67	16.19 ± 0.10	2.44E-2
4.0W	4.034E-18	6.666E-17	1 052E-14	9.935E-15	86.9	0.821	100.00	15.86 ± 0.13	1.20E-2
Total*	2.821E-17	5.298E-16	5.176E-14	5 244E-14		0.843		16.27 ± 0.18	
VP94-140a	hornblende	J =	1.0609E-2						
0.3W	8.222E-18	1.504E-16	8.121E-17	4 663E-15	48.2	27.689	0.69	464.65 ± 14.04	3.52E+0
0.7W	9.622E-18	1.493E-14	4 239E-15	1.817E-14	91.3	3.926	36.59	73.62 ± 0.96	6.71E+0
4.0W*	1.229E-17	2.711E-14	7.488E-15	2.909E-14	95.5	3.718	100.00	69.80 ± 1.50	6.90E+0
Total	3.014E-17	4.220E-14	1.181E-14	5.193E-14		3.958		74.21 ± 1.39	

Table D2. Con't.

T (°C) (or Watts)	^{36}Ar (mol)	^{37}Ar (mol)	^{39}Ar (mol)	^{40}Ar (mol)	% $^{40}Ar^*$	$^{40}Ar^*/^{39}Ar(K)$	Cumulative ^{39}Ar (%)	Calculated age (Ma ± 1σ)	Ca/K
VP94-140a	hornblende	J =	1.0609E-2						
0.3W	1.206E-17	3.703E-16	2.730E-16	7.754E-15	54.4	15.472	1.68	274.20 ± 5.77	2.58E+0
0.4W	4.807E-18	1.455E-15	3.810E-16	2.104E-15	38.4	2.126	4.01	40.24 ± 4.97	7.28E+0
0.7W	1.855E-17	4.196E-14	1.181E-14	4.675E-14	95.9	3.806	76.46	71.41 ± 0.37	6.77E+0
4.0W*	6.124E-18	1.378E-14	3.839E-15	1.471E-14	95.7	3.675	100.00	69.00 ± 0.31	6.84E+0
Total	4.155E-17	5.757E-14	1.631E-14	7.132E-14		3.932		73.72 ± 0.55	
VP94-140a	biotite	J =	1.0775E-2						
0.2W	2.004E-17	2.260E-16	7.866E-15	1.069E-14	44.0	0.598	47.20	11.59 ± 0.25	5.46E-2
0.6W	9.717E-18	1.647E-16	6.688E-15	9.671E-15	69.7	1.008	87.34	19.50 ± 0.21	4.68E-2
4.0W	5.640E-18	1.376E-16	2.111E-15	3.185E-15	47.4	0.715	100.00	13.84 ± 0.24	1.24E-1
Total*	3.540E-17	5.283E-16	1.666E-14	2.355E-14		0.778		15.05 ± 0.23	
VP94-140a	biotite	J =	1.0775E-2						
0.3W	8.561E-18	8.854E-17	5.004E-15	6.586E-15	60.9	0.802	45.02	15.52 ± 0.44	3.36E-2
0.5W	6.054E-18	1.238E-17	3.295E-15	4.259E-15	57.2	0.739	74.67	14.32 ± 0.58	7.14E-3
0.7W	1.685E-18	7.207E-20	1.186E-15	1.617E-15	68.4	0.933	85.34	18.05 ± 0.73	1.15E-4
4.0W	1.871E-18	7.347E-17	1.630E-15	2.038E-15	72.3	0.905	100.00	17.50 ± 0.82	8.56E-2
Total*	1.817E-17	1.744E-16	1.111E-14	1.450E-14		0.812		15.72 ± 0.57	
VP94-140b	hornblende	J =	1.0622E-2						
0.3W	5.023E-18	5.849E-17	1.403E-16	2.848E-15	48.0	9.752	2.76	177.81 ± 10.52	7.93E-1
0.5W	5.891E-19	4.421E-17	3.437E-16	1.575E-15	89.0	4.077	9.51	76.48 ± 6.09	2.44E-1
0.85W	8.863E-18	1.073E-14	2.689E-15	6.002E-15	71.6	1.603	62.24	30.47 ± 0.69	7.60E+0
4.0W*	6.624E-18	7.611E-15	1.926E-15	3.591E-15	63.6	1.189	100.00	22.64 ± 1.24	7.53E+0
Total	2.110E-17	1.844E-14	5.099E-15	1.402E-14		1.839		34.90 ± 1.54	

Table D2. Con't.

T (°C) (or Watts)	^{36}Ar (mol)	^{37}Ar (mol)	^{39}Ar (mol)	^{40}Ar (mol)	% $^{40}Ar^*$	$^{40}Ar^*/^{39}Ar(K)$	Cumulative ^{39}Ar (%)	Calculated age (Ma ± 1σ)	Ca/K
VP94-140b	hornblende	J =	1 0622E-2						
0.3W	7.720E-18	1.420E-16	1.557E-16	3.819E-15	40.6	9.955	3.05	181.33 ± 13.39	1.73E+0
0.5W	6.393E-18	1.220E-15	3.865E-16	2.246E-15	20.5	1.195	10.62	22.75 ± 12.87	6.01E+0
0.65W	4.144E-18	4.023E-15	1 016E-15	2.659E-15	66.9	1.756	30.49	33.34 ± 1.91	7.55E+0
0.85W	4.977E-18	6.634E-15	1.703E-15	3.552E-15	74.5	1.559	63.81	29.63 ± 0.87	7.42E+0
4.0W	5.352E-18	7.405E-15	1.850E-15	3.384E-15	72.0	1.320	100.00	25.12 ± 0.59	7.63E+0
Total	2.859E-17	1.942E-14	5.111E-15	1.566E-14		1.740		33.05 ± 2.27	
VP94-141	biotite	J =	1.0796E-2						
0.3W	7.999E-18	4.021E-17	3.342E-15	3.978E-14	94.0	11.187	40.96	205.71 ± 2.69	2.29E-2
0.5W	1.162E-18	2.325E-17	1.331E-15	5.310E-15	93.3	3.723	57.28	71.09 ± 0.56	3.32E-2
0.7W	6.783E-21	3.502E-17	1.623E-15	6.420E-15	99.8	3.947	77.16	75.29 ± 0.85	4 10E-2
4.0W	3.735E-18	1.071E-16	1.863E-15	7.316E-15	84.8	3.329	100.00	63.70 ± 1.08	1 09E-1
Total	1.290E-17	2.056E-16	8.159E-15	5 883E-14		6.735		126.63 ± 1.61	
VP94-141	biotite	J =	1.0796E-2						
0.2W	7.279E-18	1.257E-16	4.410E-15	1.735E-14	87.4	3.438	15.89	65.76 ± 0.61	5.42E-2
0.4W*	3.795E-18	1.315E-16	8.002E-15	3.074E-14	96.1	3.692	44.72	70.52 ± 0.60	3.12E-2
0.6W*	3.702E-18	1.216E-16	5.324E-15	2.055E-14	94.5	3.647	63.90	69.67 ± 0.72	4 34E-2
4.0W*	5.206E-18	6.053E-16	1.002E-14	3.839E-14	95.9	3.672	100.00	70.14 ± 0.45	1 15E-1
Total	1.998E-17	9.841E-16	2.776E-14	1.070E-13		3.636		69.47 ± 0.57	
VP94-142	biotite	J =	1.0818E-2						
0.3W	7.564E-18	1.307E-16	2.782E-15	1.197E-14	81.2	3.494	27.18	66.92 ± 1.53	8.93E-2
0.5W	1.697E-18	7.067E-20	3.037E-15	1.300E-14	95.9	4.104	56.86	78.36 ± 0.83	4.42E-5
0 7W	7.587E-19	7.067E-20	1.850E-15	8.653E-15	97.2	4.545	74.94	86.59 ± 1.35	7.26E-5
4 0W	4.325E-18	1.800E-17	2.565E-15	2.763E-14	95.3	10.265	100.00	189.97 ± 3.09	1 33E-2
Total	1 434E-17	1.489E-16	1.023E-14	6.125E-14		5.562		105.40 ± 1.68	

Table D2. Con't.

T (°C) (or Watts)	^{36}Ar (mol)	^{37}Ar (mol)	^{39}Ar (mol)	^{40}Ar (mol)	% $^{40}Ar^*$	$^{40}Ar^*/^{39}Ar(K)$	Cumulative ^{39}Ar (%)	Calculated age (Ma ± 1σ)	Ca/K
VP94-142	biotite	J =	1.0818E-2						
0.3W	3.813E-17	4.101E-16	2.461E-14	9.564E-14	88.0	3.420	34.94	65 53 ± 0.66	3.17E-2
0.5W*	5.181E-18	1.454E-16	1.820E-14	6.894E-14	97.5	3.694	60.78	70.70 ± 0.28	1.52E-2
0.75W*	4.202E-18	4.066E-17	1.210E-14	4.585E-14	97.0	3.677	77.96	70.37 ± 0.27	6.39E-3
4.0W*	4.744E-18	8.781E-20	1.552E-14	5.900E-14	97.3	3.701	100.00	70.82 ± 0.31	1.08E-5
Total	5.226E-17	5.962E-16	7.042E-14	2.694E-13		3.597		68.87 ± 0.42	
VP94-143	biotite	J =	1 0839E-2						
0.3W	1.685E-17	9.225E-18	4 797E-15	2.583E-14	80.5	4.336	42.45	82.84 ± 1.03	3.65E-3
0.5W	2.475E-18	1.916E-17	2.253E-15	9.475E-15	92.1	3.872	62.39	74.17 ± 1.37	1.62E-2
4.0W	7.579E-18	4.418E-17	4.250E-15	1.801E-14	87.3	3.700	100.00	70.94 ± 1.86	1.98E-2
Total	2.691E-17	7.256E-17	1.130E-14	5.331E-14		4.004		76.64 ± 1.41	
VP94-143	biotite	J =	1.0839E-2						
0.2W	2 770E-17	1.495E-16	4 039E-15	1.929E-14	57.4	2.741	7.91	52.82 ± 0.37	7.03E-2
0.5W*	9 107E-18	1.323E-17	1.655E-14	6.134E-14	95.3	3.534	40.32	67.82 ± 0.18	1.52E-3
0.7W*	5.669E-18	1.409E-16	1.219E-14	4.500E-14	96.0	3.545	64.20	68.02 ± 0.55	2.20E-2
4.0W*	6.130E-18	1.175E-16	1.828E-14	6.734E-14	97.0	3.575	100.00	68.58 ± 0.34	1.22E-2
Total	4.860E-17	4.211E-16	5.105E-14	1.930E-13		3.489		66.96 ± 0.34	
VP94-144	hornblende	J =	1.0757E-2						
0.3W	7.085E-18	6.341E-16	1.686E-16	2.399E-15	15.0	2.137	2.76	41.01 ± 9.94	7.16E+0
0.6W*	7.966E-18	1.661E-14	4.525E-15	1.924E-14	95.1	4.055	76.73	77.03 ± 1.05	6.99E+0
0.8W	2.621E-19	2.530E-15	6.059E-16	2.697E-15	105.2	4.695	86.63	88.90 ± 1.90	7.96E+0
4.0W	2.182E-18	3.338E-15	8.180E-16	3.516E-15	89.8	3.870	100.00	73.58 ± 1.27	7.78E+0
Total	1.749E-17	2.311E-14	6.117E-15	2.785E-14		4.041		76.76 ± 1.41	

Table D2. Con't.

T (°C) (or Watts)	^{36}Ar (mol)	^{37}Ar (mol)	^{39}Ar (mol)	^{40}Ar (mol)	% $^{40}Ar^*$	$^{40}Ar^*/\ ^{39}Ar(K)$	Cumulative ^{39}Ar (%)	Calculated age (Ma ± 1σ)	Ca/K
VP94-144	hornblende	J =	1.0757E-2						
0.3W	8.437E-18	1.140E-15	2.956E-16	2.555E-15	6.2	0.540	2.84	10.46 ± 4.67	7.35E+0
0.5W	1.554E-17	9.281E-15	2.565E-15	1.127E-14	66.3	2.920	27.52	55.79 ± 1.11	6.89E+0
0.7W	1.151E-17	1.927E-14	5.149E-15	2.156E-14	91.8	3.855	77.06	73.31 ± 0.39	7.13E+0
4.0W	1 214E-17	9.645E-15	2.385E-15	1.018E-14	72.9	3.120	100.00	59.55 ± 0.88	7.70E+0
Total	4.762E-17	3.934E-14	1.039E-14	4.556E-14		3.361		64.08 ± 0.80	
VP94-144	biotite	J =	1 0850E-2						
0.3W	1.097E-17	1.895E-16	7.234E-15	2.651E-14	87.6	3.208	32.05	61.74 ± 0.88	4.98E-2
0.5W	3.657E-18	1.798E-16	6.835E-15	2.386E-14	95.2	3.325	62.34	63.94 ± 0.95	5.00E-2
0.7W*	6.026E-18	2.075E-16	4.302E-15	1.853E-14	90.2	3.887	81.40	74.53 ± 0.65	9.16E-2
4.0W	4.583E-18	3.739E-16	4.199E-15	1.670E-14	91.8	3.653	100.00	70.12 ± 1.19	1.69E-1
Total	2.523E-17	9.508E-16	2.257E-14	8.561E-14		3.456		66.41 ± 0.91	
VP94-144	biotite	J =	1.0850E-2						
0.3W	5.103E-18	9.764E-17	2 953E-15	1.028E-14	85.1	2.963	31.21	57.08 ± 1.03	6.28E-2
0.5W	3.506E-18	7.852E-17	2.493E-15	8.316E-15	87.3	2.912	57.56	56.12 ± 0.96	5.98E-2
0.7W	4.579E-18	1.508E-16	1.308E-15	4.439E-15	69.5	2.360	71.39	45.61 ± 0.50	2.19E-1
4.0W	2.043E-18	1.067E-16	2.707E-15	9.091E-15	93 1	3.128	100.00	60.22 ± 0.95	7.49E-2
Total	1.523E-17	4.337E-16	9.461E-15	3.212E-14		2.913		56.14 ±0.91	
VP94-146	hornblende	J =	1.0634E-2						
0.5W	2.303E-18	4.546E-15	1.599E-15	1.158E-14	97.4	7.072	52.23	130.81 ± 2.01	5.41E+0
1.0W	3.933E-18	3.120E-15	1.092E-15	4.705E-15	80.9	3.491	87.92	65.77 ± 1.66	5.44E+0
4.0W	1.754E-18	1.001E-15	3.696E-16	1.523E-15	71.5	2.953	100.00	55.78 ± 3.53	5.15E+0
Total	7.990E-18	8.666E-15	3.060E-15	1.781E-14		5.297		98.86 ± 2.07	

Table D2. Con't.

T (°C) (or Watts)	^{36}Ar (mol)	^{37}Ar (mol)	^{39}Ar (mol)	^{40}Ar (mol)	% $^{40}Ar^*$	$^{40}Ar^*/^{39}Ar(K)$	Cumulative ^{39}Ar (%)	Calculated age (Ma ± 1σ)	Ca/K
VP94-146	hornblende	J =	1 0634E-2						
0.2W	4.285E-18	1.362E-16	1.552E-16	6.137E-15	79.5	31.465	2.64	520.71 ± 7.93	1.67E+0
0.5W	3.701E-18	5.673E-15	2.097E-15	1.043E-14	94.1	4.687	38.22	87.74 ± 0.70	5.15E+0
0.8W	3.289E-18	6.145E-15	2.186E-15	9.111E-15	95.0	3.968	75.31	74.57 ± 0.56	5.35E+0
4.0W*	2.700E-18	4.069E-15	1.455E-15	5.290E-15	91 4	3.329	100.00	62.76 ± 0.52	5.32E+0
Total	1.397E-17	1.602E-14	5.894E-15	3.096E-14		4.791		89.65 ± 0.80	
VP94-146	biotite	J =	1 0841E-2						
0.2W	7.888E-18	1.199E-16	2.274E-15	4 442E-15	47 2	0.922	13.17	17.95 ± 1.63	1.00E-1
0.4W	5.535E-18	1.631E-16	4.291E-15	5.853E-15	71.5	0.976	38.01	18.98 ± 0.89	7.22E-2
0.6W*	5.733E-18	1.850E-15	8.340E-15	1.246E-14	87.0	1.300	86.31	25.26 ± 0.38	4.21E-1
4.0W	6.796E-18	3.239E-16	2 365E-15	3.504E-15	42.8	0.634	100.00	12.35 ± 0.67	2.60E-1
Total	2.595E-17	2.457E-15	1.727E-14	2.626E-14		1.079		20.97 ± 0.71	
VP94-146	biotite	J =	1.0841E-2						
0.25W*	5.794E-18	7.067E-20	3.465E-15	6.445E-15	72.9	1.356	20.08	26.32 ± 1.24	3.88E-5
0.35W*	3.175E-18	7.067E-20	2.969E-15	5.021E-15	80.7	1.365	37.29	26.50 ± 0.43	4.52E-5
0.6W*	3 837E-18	3.271E-17	6.384E-15	9.496E-15	87.4	1.300	74.29	25.25 ± 0.39	9.74E-3
4.0W	1 193E-18	1 254E-16	4 436E-15	7 357E-15	94.7	1.571	100.00	30.47 ± 0.57	5 37E-2
Total	1 400E-17	1.583E-16	1 725E-14	2.832E-14		1.392		27.02 ± 0.61	

Note: $^{40}K\lambda = 5\ 5430^{-10}$, * = step used in plateau, isochron, weighted mean, or maximum age determinations; $^{40}Ar/^{39}Ar$ analyses were performed at La Trobe University. Samples and flux monitor GA1550 biotite (97 9 Ma, McDougall and Roksandic, 1974) were wraped in Al foil and placed in a quartz vial. Flux monitors were spaced every 0.5 - 1.0 cm over the length of the tube Vials were sealed and irradiated at Soreq Nuclear Research Centre, IRR-1 reactor, Israel (Heimann et al., 1992). Biotite samples, single grains or small numbers of grains, were loaded into milled pits in a copper plate and placed into a gas extraction line fitted with a glass viewport. Gas was extracted using a defocussed 6W argon ion laser. Step-wise heating was accomplished by varying the power output of the laser. Gas extraction from hornblende was performed in a computer controled double-vacuum resistance furnace. Extrated gas was expanded into a stainless steel clean up line and purified for about 10 minutes with Zr-Ti getters. Argon isotopes were measured using a VG3600 mass spectrometer operating at a sensitivity of 1×10^{-3} amps/torr, using a Daly photomultiplier set at a gain of 100 over the Faraday cups. Data was corrected for machine background, line blank, and mass discrimination. Extraction line blanks of atmospheric composition were typically 9×10^{-17} to 1×10^{-16} mole ^{40}Ar (laser) and 2×10^{-16} (furnace). Mass discrimination, determined by analyzing atmospheric argon, was 1.0105 for 1 amu. Correction factors for interfering isotopes were determined by analysing K_2SO_4 and CaF_2 salts irradiated with the samples and the following values were used: $(^{40}Ar/^{39}Ar)K = 0.0105$, $(^{36}Ar/^{37}Ar)Ca = 0.000298$, and $(^{39}Ar/^{37}Ar)Ca = 0.000712$.

Table D3. %39Ar release spectra and isochron plots

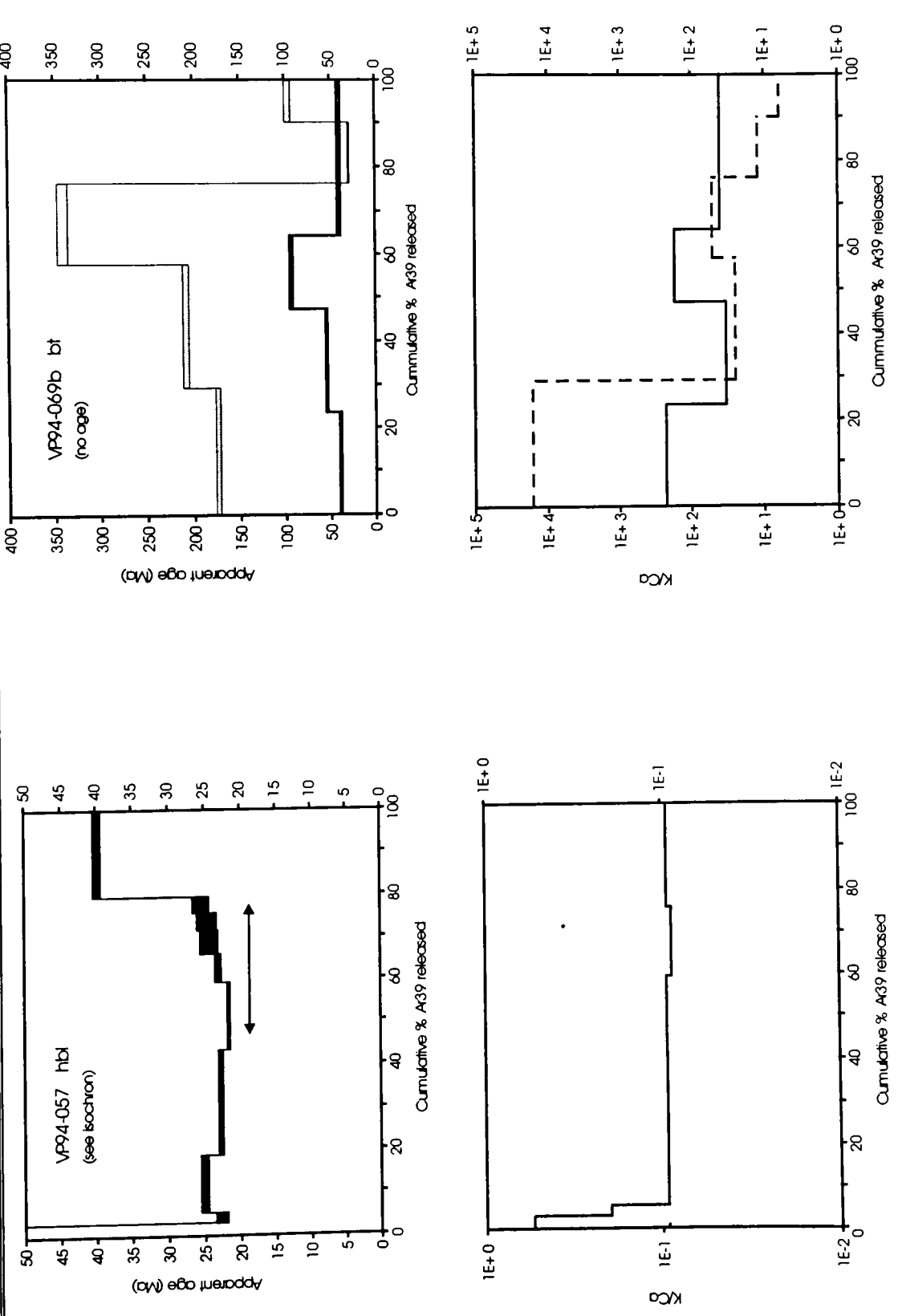


Table D3. Con't.

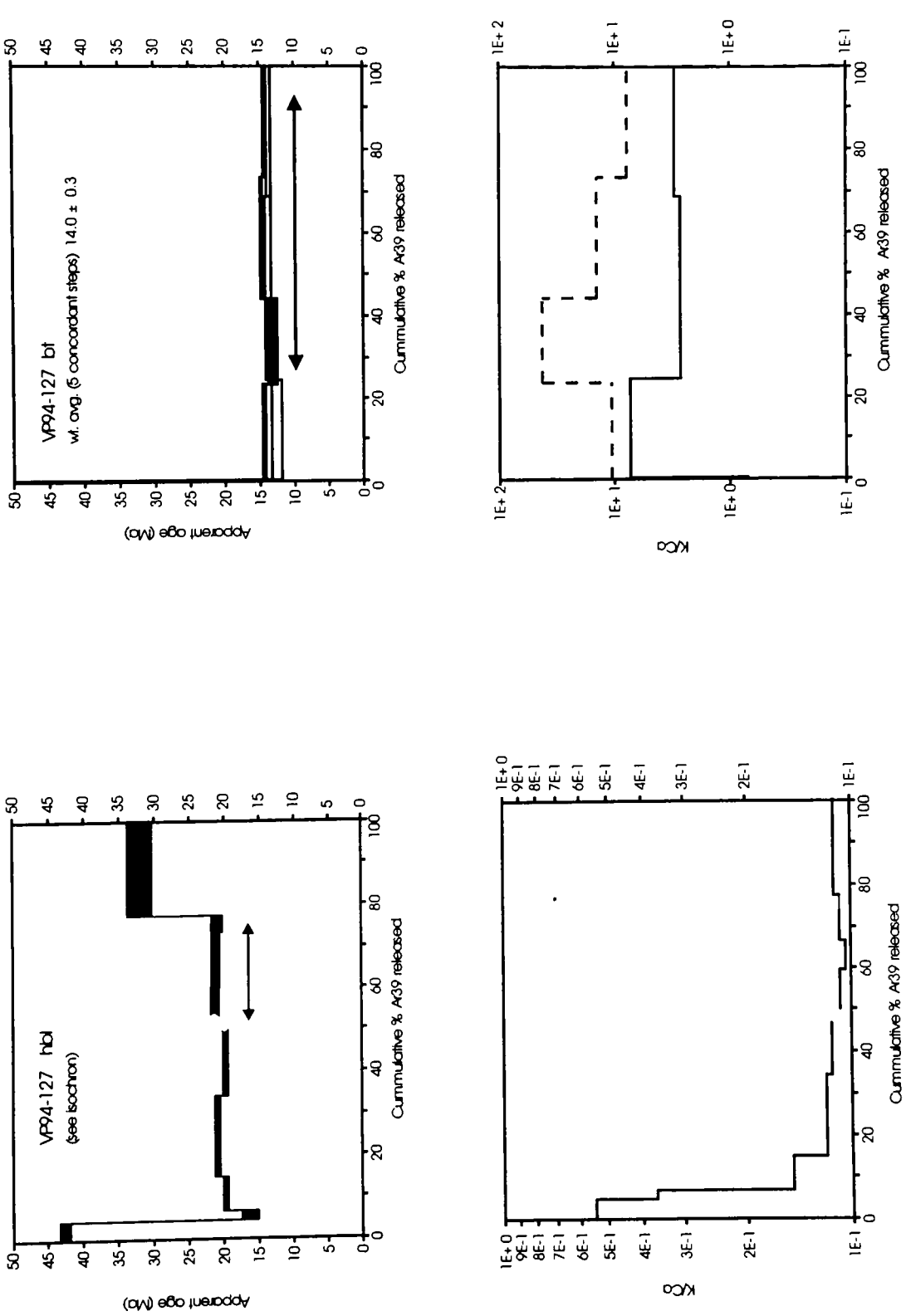
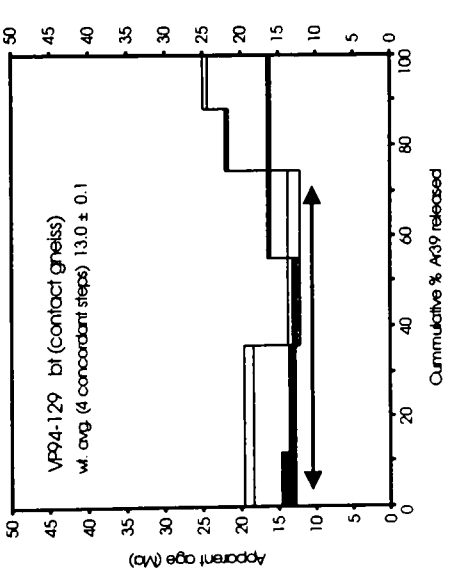


Table D3. Con't.



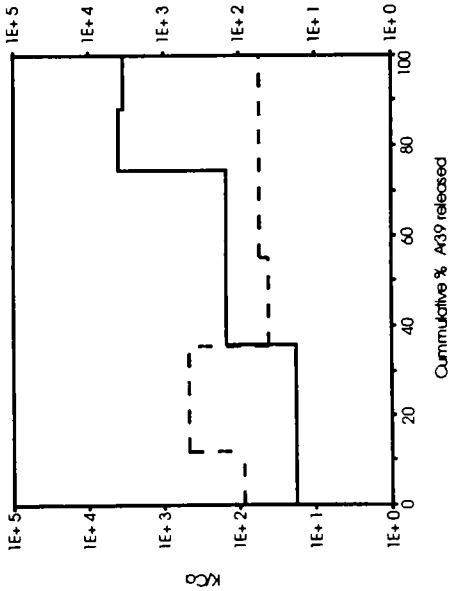
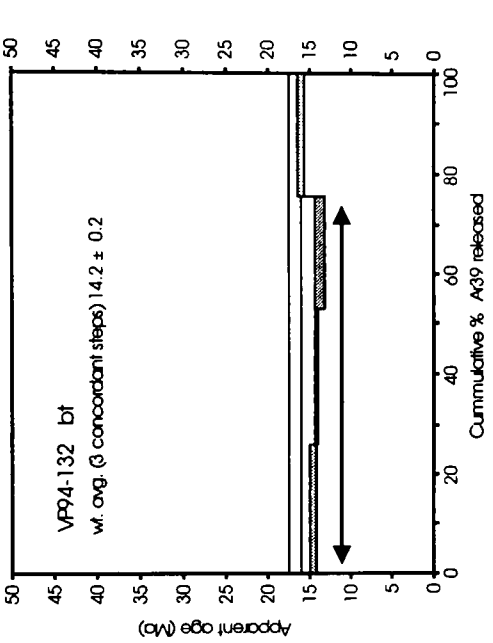
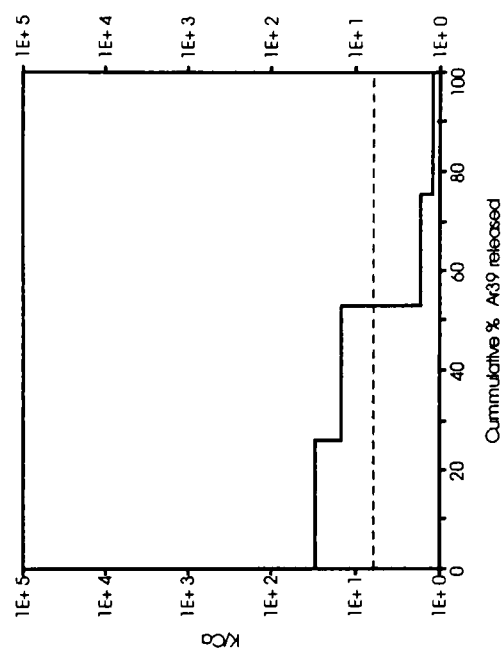
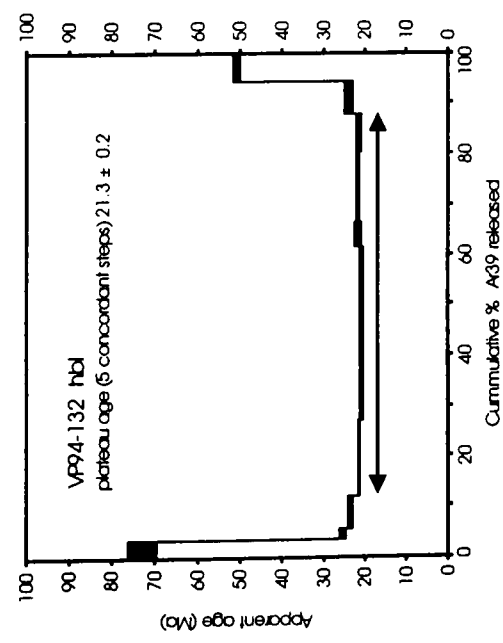


Table D3. Con't.







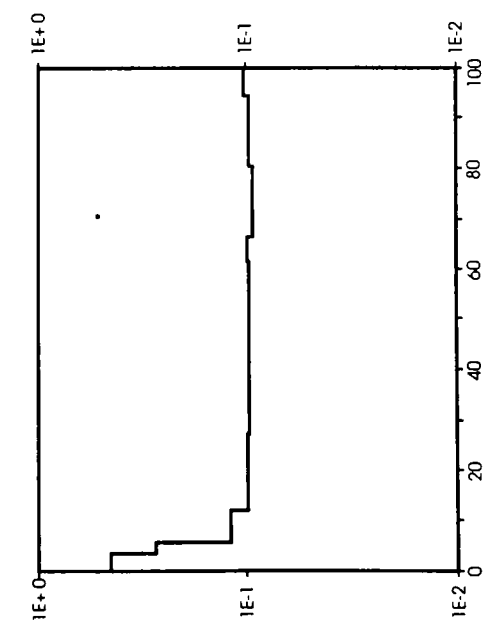
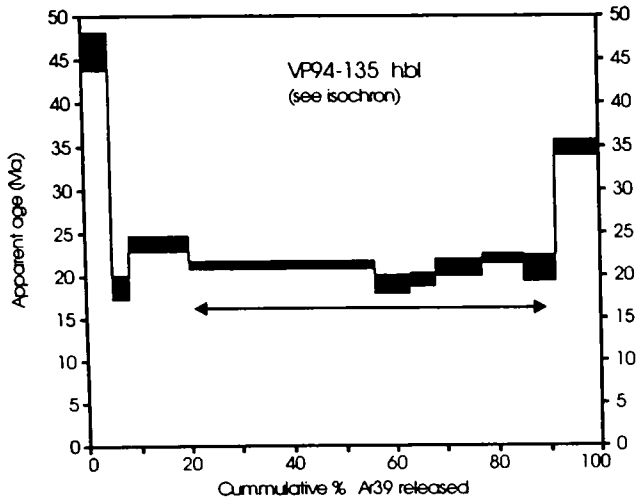
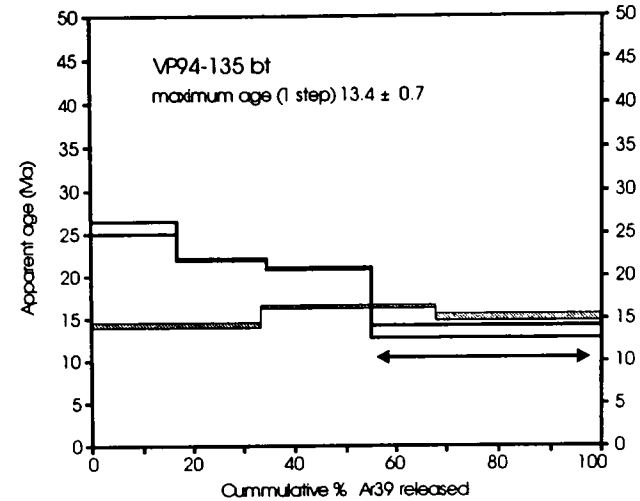
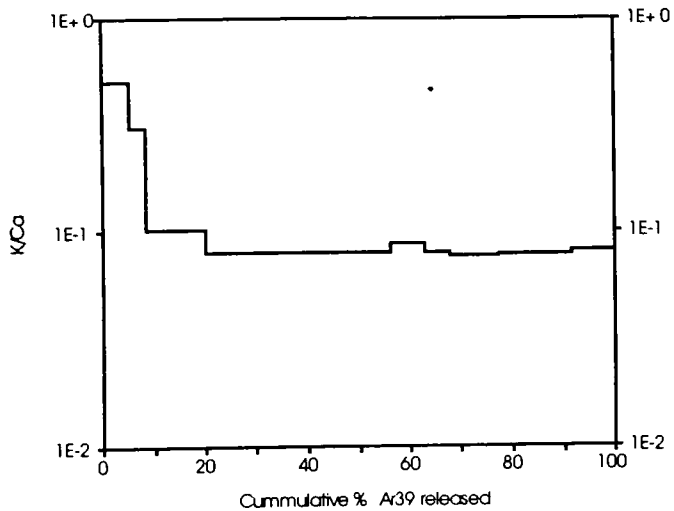


Table D3. Con't.







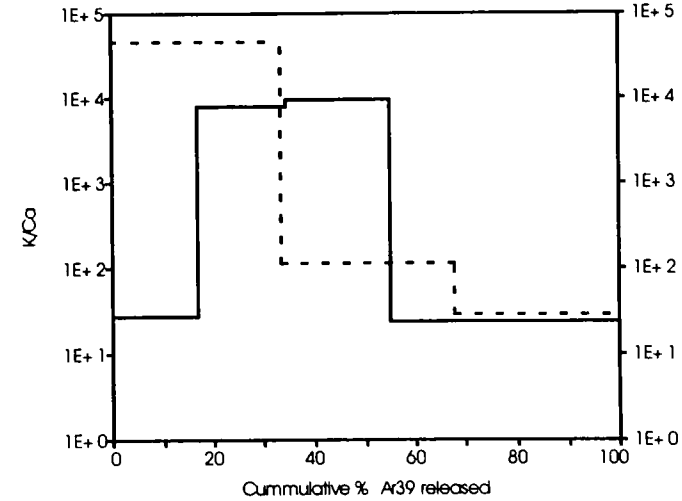


Table D3. Con't.

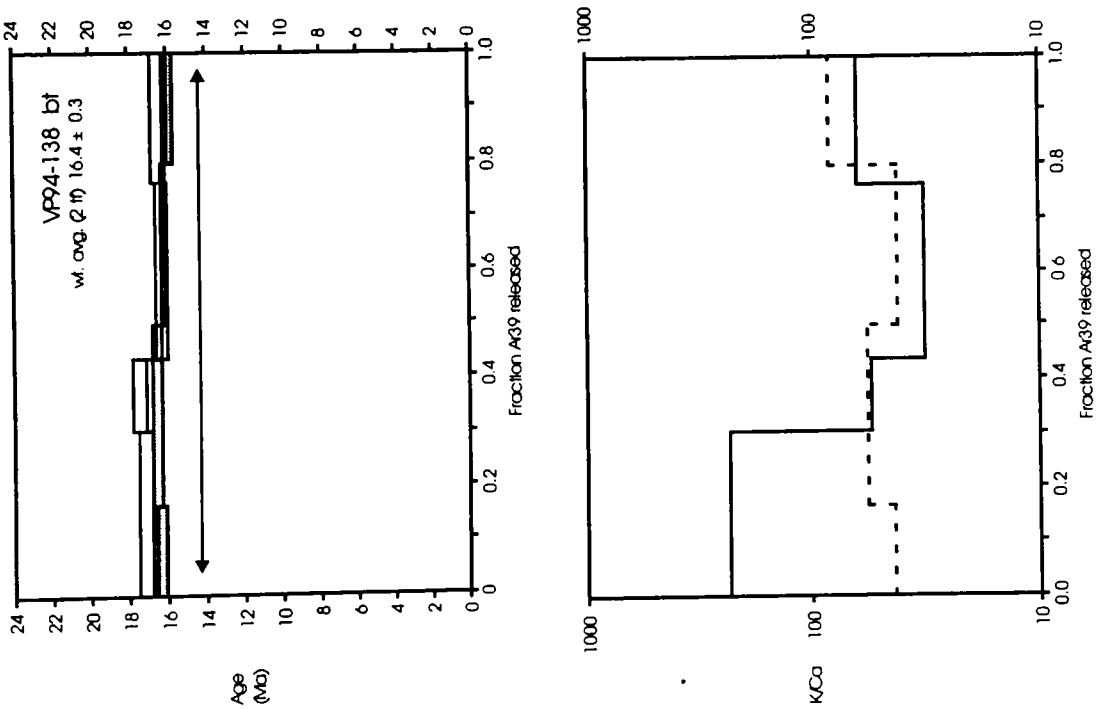
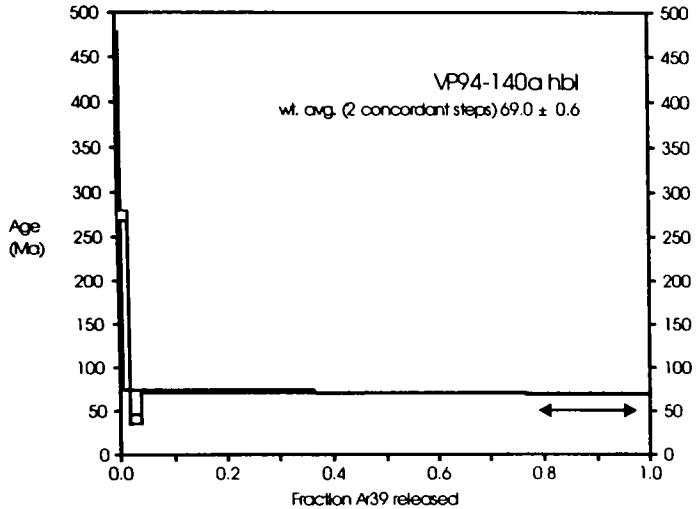
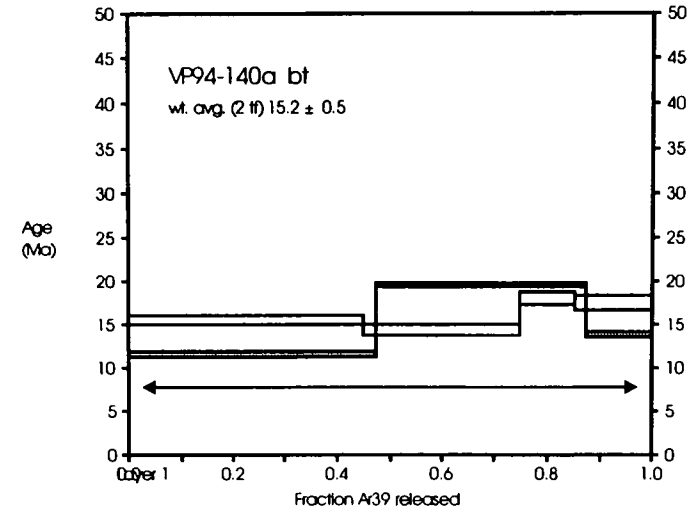
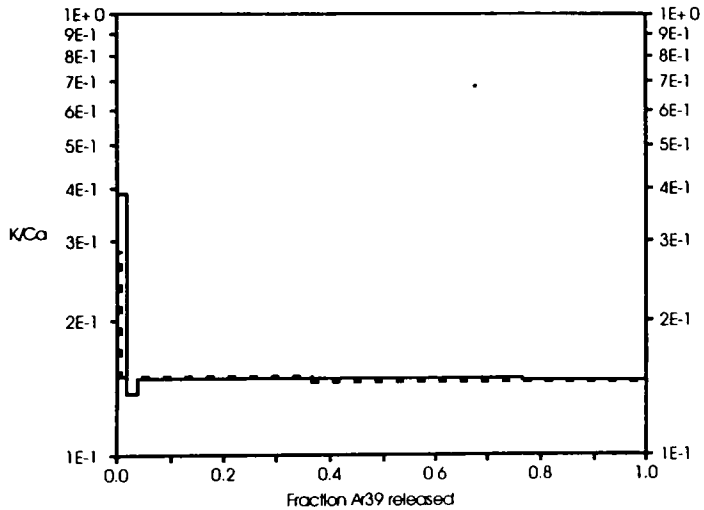


Table D3. Con't.







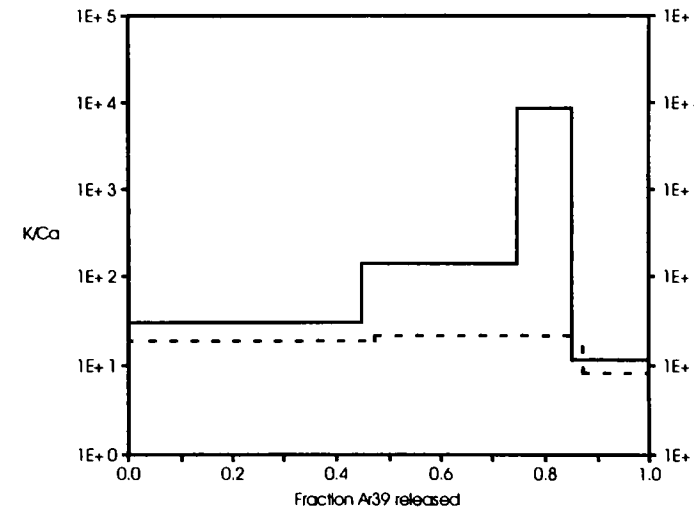
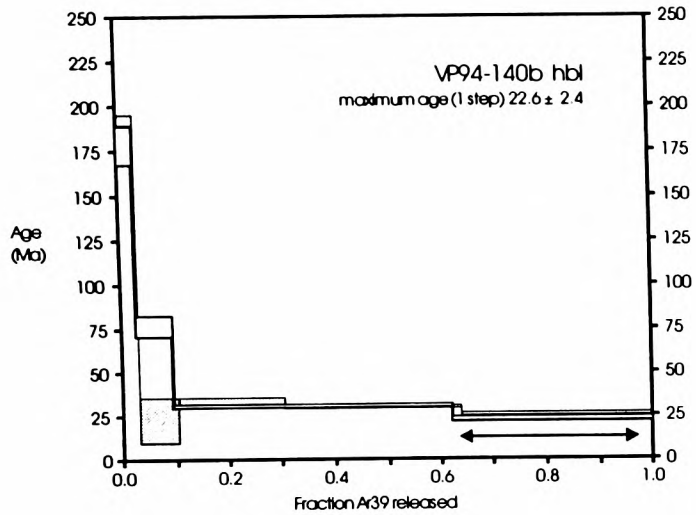
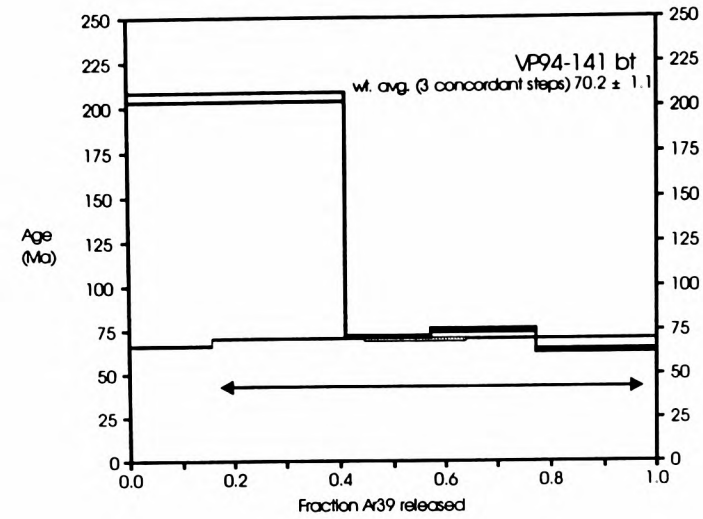
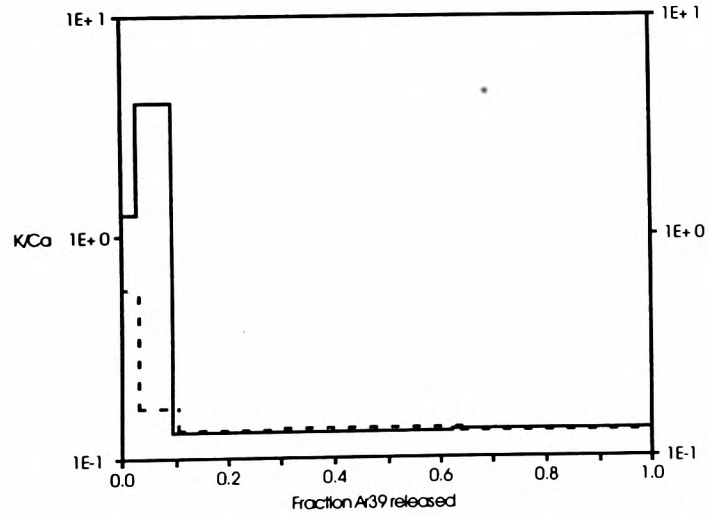


Table D3. Con't.







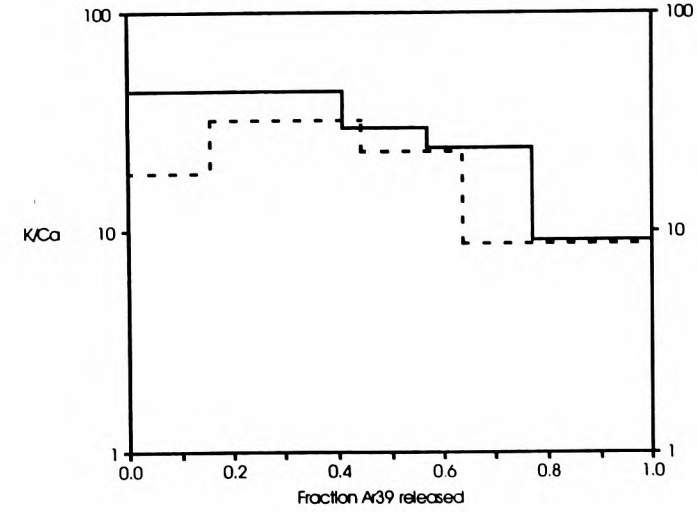
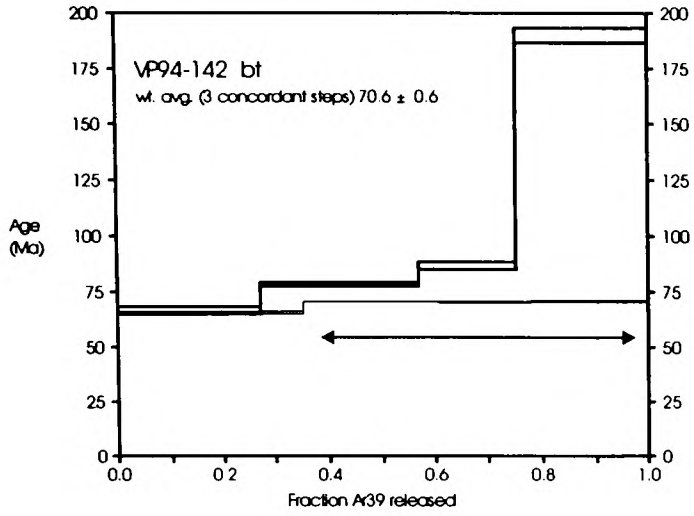
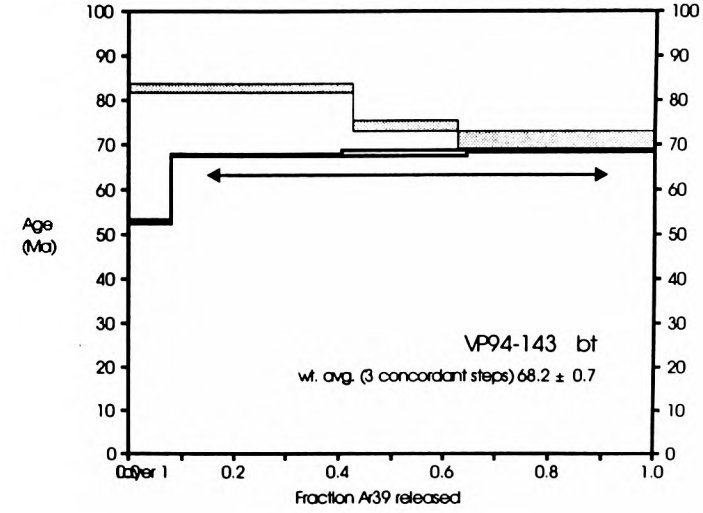
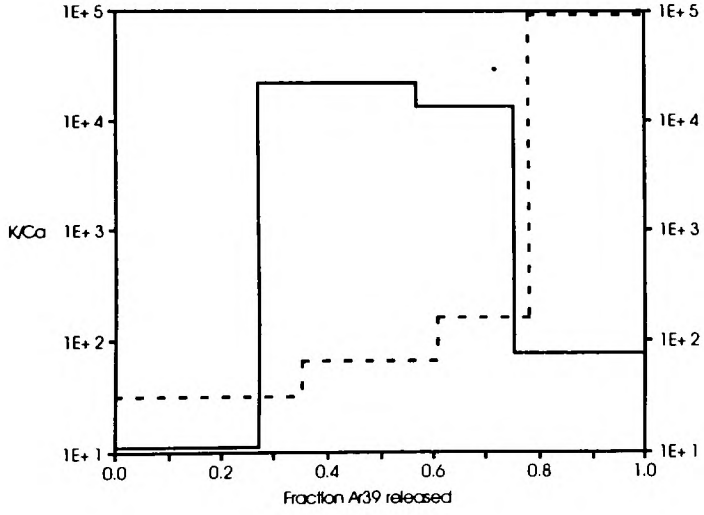


Table D3. Con't.







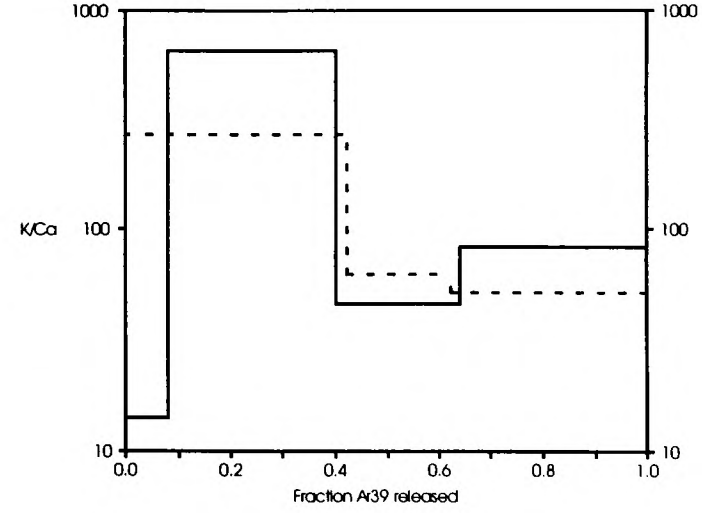


Table D3. Con't.

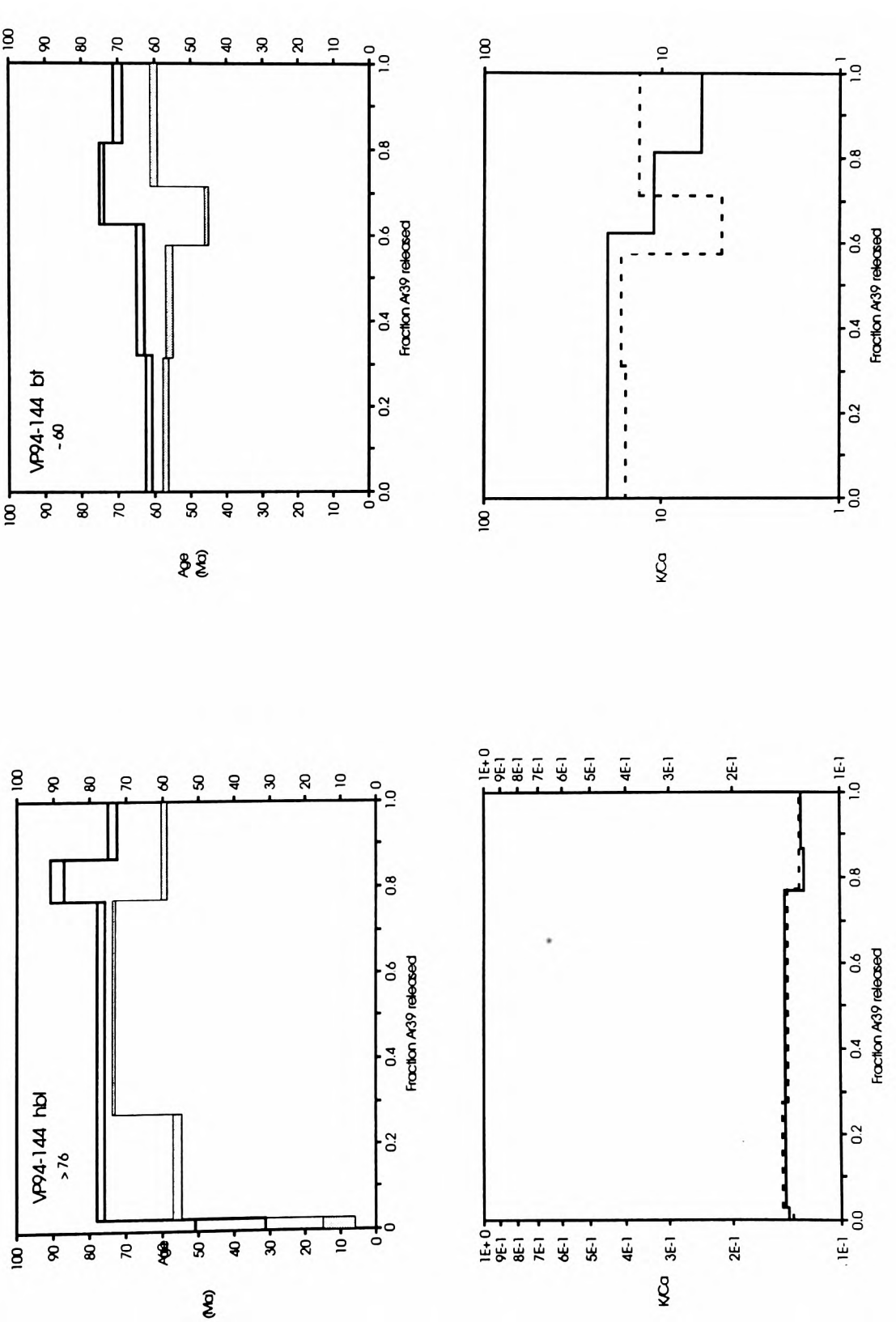


Table D3. Con't.

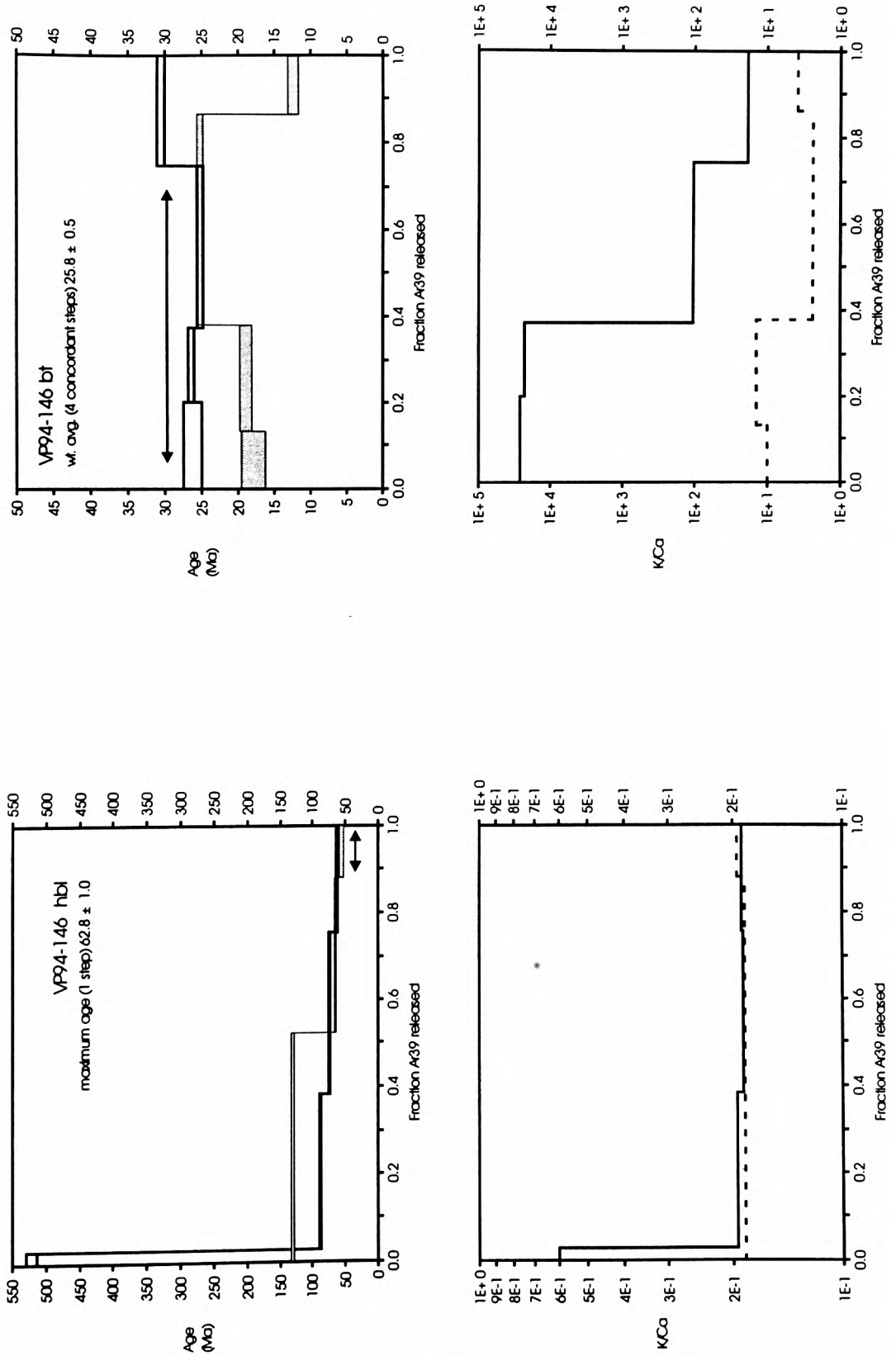


Table D3. Con't.

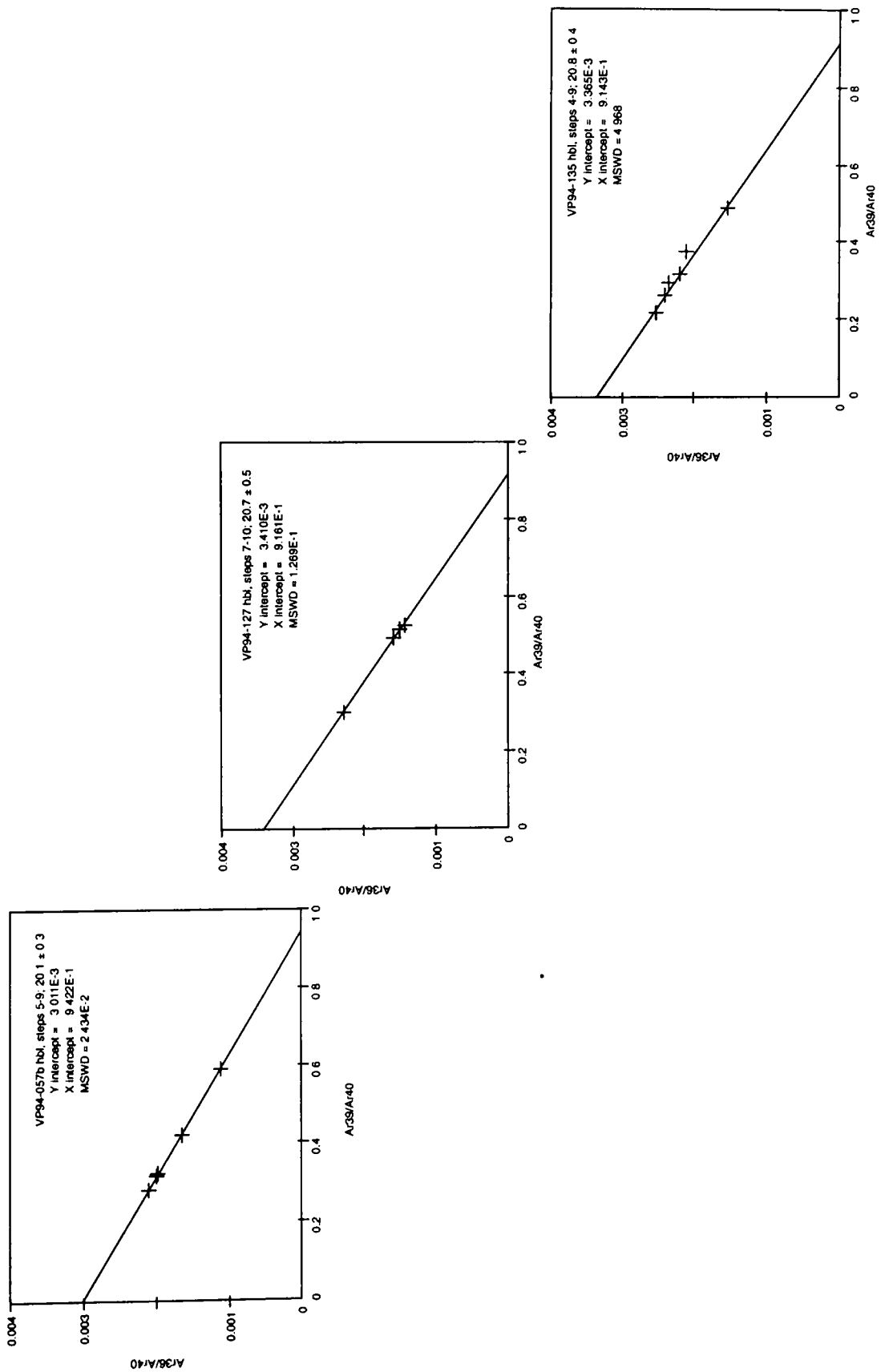


Table D4. Summary of fission track analytical results

Sample No.	Elevation (m)	No. of grains	Spontaneous track density ($x10^5 cm^{-2}$)	Induced track density ($x10^6 cm^{-2}$)	Standard track density ($x10^6 cm^{-2}$)	Mean track length (μm)	Standard deviation (μm)	Uranium (ppm)	Chi square probability (%)	Fission track age (Ma ± 1σ)*	
Zircons											
VP94-129	700	13	35.45 (1397)	4.284 (1688)	0.5541 (2266)	---	---	402	93.6	20.1	1.1
VP94-132	729	15	15.63 (1005)	2.292 (1474)	0.556 (2266)	---	---	214.4	76.3	16.6	1.0
VP94-135	802	15	8.129 (588)	1.203 (870)	0.5579 (2266)	---	---	112.1	98.6	16.5	1.1
VP94-138	775	15	34.58 (1781)	7.371 (3796)	0.5204 (2007)	---	---	566.6	99.7	15.3	0.7
VP94-140a	780	12	15 (1147)	3.017 (2307)	0.5178 (2007)	---	---	233.1	94.2	16.1	0.8
VP94-141	655	12	43.96 (1444)	2.033 (668)	0.5598 (2266)	---	---	188.9	92.9	52.9	3.3
VP94-143	675	12	20.93 (1130)	1.104 (596)	0.5617 (2266)	---	---	102.2	12.1	47.5	3.3
VP94-144	750	15	31.67 (513)	3.654 (592)	0.5636 (2266)	---	---	337.1	28.8	21.5	1.5
VP94-145	750	10	25.29 (446)	1.06 (187)	0.5655 (2266)	---	---	97.5	92	58.9	5.7
Apatites											
VP94-057b	583	25	0.9639 (156)	1.301 (2105)	1.403 (2736)	14.15 (100)	1.1	10.3	57.2	19.7	1.7
VP94-127	802	25	0.8944 (152)	1.43 (2431)	1.403 (2736)	13.84 (100)	1.3	11.3	95.3	16.6	1.4
VP94-132	729	25	0.7012 (87)	1.131 (1403)	1.403 (2736)	13.97 (20)	1.4	10.1	83.2	16.6	1.9
VP94-135	802	25	0.5252 (90)	0.8754 (1500)	1.403 (2736)	14.3 (9)	0.93	6.9	48.5	15.9	1.8
VP94-138	775	25	0.8393 (141)	2.228 (3743)	1.403 (2736)	14.5 (100)	0.95	17.6	96.6	10.0	0.9
VP94-140a	780	25	0.9236 (161)	1.618 (2820)	1.403 (2736)	14.4 (90)	1.1	14.4	63.1	15.2	1.3
VP94-140b	780	20	0.6186 (85)	1 084 (1489)	1.403 (2736)	14.31 (54)	1.07	9.7	97.9	15.2	1.7
VP94-141	655	25	0.3605 (62)	0.9088 (1563)	1.403 (2736)	13.95 (78)	1.15	8.1	12.1	10.7	1.6
VP94-142	655	20	0.3469 (51)	0 4483 (659)	1.403 (2736)	14.23 (2)	0.85	4	47.7	20.6	3.0
VP94-143	675	25	1.348 (245)	2 426 (4410)	1.403 (2736)	13.82 (38)	1.16	21.6	56.3	14.8	1.0
VP94-144	750	25	0.7792 (130)	0.995 (1660)	1.403 (2736)	13.96 (36)	1.56	8.9	71.3	20.8	1.9
VP94-146	690	20	1.114 (139)	1.41 (1759)	1.403 (2736)	14.03 (74)	1.32	12.6	94.3	21.0	1.9

Note: * Age calculation using the zeta method (after Green, 1981): dosimeter glass U3 for zircon (zeta 88) and glass CN5 for apatite (zeta 379). Central ages are reported where pooled data result in low probability from the Chi-squared test, i.e.- ~12%, which may suggest a non-homogeneous age population. Number of tracks counted in parentheses. Standard and induced track densities measured on external detectors (g = 0.5), spontaneous (fossil) track densities on internal mica surfaces.

Table D5. Fission track counting statistics

VP94-129 Zircon
Irradiation LU355-01

No.	Ns	Ni	Na	RATIO	U(ppm)	RHOs	RHOi	F.T.AGE(Ma)
1	147	166	25	0.886	798.6	7.536E+06	8.510E+06	21.5 ± 2.6
2	134	156	40	0.859	469.0	4.293E+06	4.998E+06	20.9 ± 2.6
3	62	87	30	0.713	348.8	2.649E+06	3.717E+06	17.3 ± 3.0
4	76	106	50	0.717	255.0	1.948E+06	2.717E+06	17.4 ± 2.7
5	68	86	24	0.791	431.0	3.631E+06	4.592E+06	19.2 ± 3.2
6	168	192	40	0.875	577.3	5.383E+06	6.151E+06	21.2 ± 2.4
7	192	217	60	0.885	435.0	4.101E+06	4.635E+06	21.5 ± 2.3
8	86	114	50	0.754	274.2	2.204E+06	2.922E+06	18.3 ± 2.7
9	16	18	30	0.889	72.2	6.835E+05	7.689E+05	21.6 ± 7.5
10	197	260	60	0.758	521.2	4.208E+06	5.553E+06	18.4 ± 1.9
11	91	104	36	0.875	347.4	3.239E+06	3.702E+06	21.2 ± 3.2
12	92	96	30	0.958	384.9	3.930E+06	4.101E+06	23.3 ± 3.5
13	68	86	30	0.791	344.8	2.905E+06	3.674E+06	19.2 ± 3.2
	1397	1688			402.0	3.545E+06	4.284E+06	

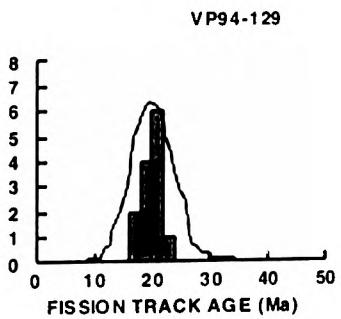
Area of basic unit = 7.803E-07 cm-2

CHI SQUARED = 2.786273 WITH 12 DEGREES OF FREEDOM
P(chi squared) = 93.6 %
CORRELATION COEFFICIENT = 0.984
VARIANCE OF SQR(Ns) = 8.012218
VARIANCE OF SQR(Ni) = 9.267975

Ns/Ni = 0.828 ± 0.030
MEAN RATIO = 0.827 ± 0.021

Pooled Age = 20.1 ± 1.1 Ma
Mean Age = 20.1 ± 1.0 Ma
Central Age = 20.1 ± 0.8Ma
% Variation = 0.00%

Ages calculated using a zeta of 87.8 ± 3 for U3 glass 52 ppm
RHO D = 5.541E+05cm-2; ND = 2266



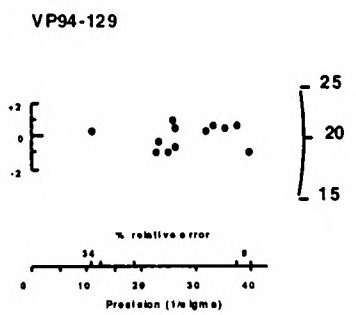


Table D5. Con't.

VP94-132 Zircon
Irradiation LU355-02

No.	Ns	Ni	Na	RATIO	U(ppm)	RHOs	RHOi	F.T.AGE(Ma)
1	46	73	40	0.630	218.7	1.474E+06	2.339E+06	15.4 ± 3.0
2	16	28	100	0.571	33.6	2.050E+05	3.588E+05	13.9 ± 4.4
3	37	50	24	0.740	249.7	1.976E+06	2.670E+06	18.0 ± 4.0
4	64	82	50	0.780	196.6	1.640E+06	2.102E+06	19.0 ± 3.3
5	100	167	40	0.599	500.4	3.204E+06	5.350E+06	14.6 ± 1.9
6	164	259	60	0.633	517.4	3.503E+06	5.532E+06	15.4 ± 1.7
7	43	63	40	0.683	188.8	1.378E+06	2.018E+06	16.6 ± 3.4
8	20	32	40	0.625	95.9	6.408E+05	1.025E+06	15.2 ± 4.4
9	97	133	60	0.729	265.7	2.072E+06	2.841E+06	17.8 ± 2.5
10	54	70	40	0.771	209.8	1.730E+06	2.243E+06	18.8 ± 3.5
11	67	74	60	0.905	147.8	1.431E+06	1.581E+06	22.1 ± 3.8
12	66	110	80	0.600	164.8	1.057E+06	1.762E+06	14.6 ± 2.4
13	63	102	50	0.618	244.5	1.615E+06	2.614E+06	15.1 ± 2.5
14	125	157	60	0.796	313.6	2.670E+06	3.353E+06	19.4 ± 2.5
15	43	74	80	0.581	110.9	6.888E+05	1.185E+06	14.2 ± 2.8
	1005	1474			214.4	1.563E+06	2.292E+06	

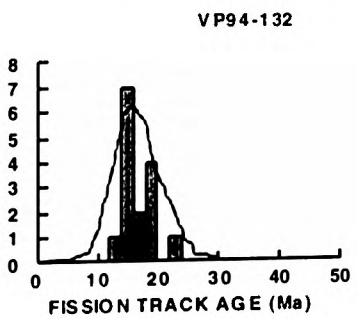
Area of basic unit = 7.803E-07 cm-2

CHI SQUARED = 4.994711 WITH 14 DEGREES OF FREEDOM
P(chi squared) = 76.3 %
CORRELATION COEFFICIENT = 0.972
VARIANCE OF SQR(Ns) = 5.612754
VARIANCE OF SQR(Ni) = 8.190194

Ns/Ni = 0.682 ± 0.028
MEAN RATIO = 0.684 ± 0.025

Pooled Age = 16.6 ± 1.0 Ma
Mean Age = 16.7 ± 0.9 Ma
Central Age = 16.6 ± 0.8Ma
% Variation = 0.38%

Ages calculated using a zeta of 87.8 ± 3 for U3 glass 52 ppm
RHO D = 5.560E+05cm-2; ND = 2266



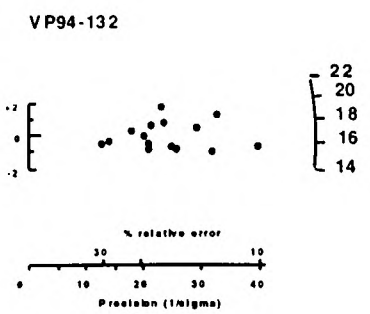


Table D5. Con't.

VP94-135 Zircon
Irradiation LU355-03

No.	Ns	Ni	Na	RATIO	U(ppm)	RHOs	RHOi	F.T.AGE(Ma)
1	27	39	60	0.692	77.6	5.767E+05	8.330E+05	16.9 ± 4.3
2	19	25	80	0.760	37.3	3.044E+05	4.005E+05	18.6 ± 5.7
3	32	53	70	0.604	90.4	5.859E+05	9.703E+05	14.8 ± 3.4
4	24	41	49	0.585	99.9	6.277E+05	1.072E+06	14.3 ± 3.7
5	44	62	60	0.710	123.4	9.398E+05	1.324E+06	17.4 ± 3.5
6	54	89	60	0.607	177.2	1.153E+06	1.901E+06	14.8 ± 2.6
7	36	46	80	0.783	68.7	5.767E+05	7.369E+05	19.1 ± 4.3
8	89	119	50	0.748	284.3	2.281E+06	3.050E+06	18.3 ± 2.7
9	28	49	50	0.571	117.1	7.177E+05	1.256E+06	14.0 ± 3.4
10	64	107	32	0.598	399.4	2.563E+06	4.285E+06	14.6 ± 2.4
11	41	55	60	0.745	109.5	8.757E+05	1.175E+06	18.2 ± 3.8
12	17	27	36	0.630	89.6	6.052E+05	9.612E+05	15.4 ± 4.8
13	44	60	80	0.733	89.6	7.049E+05	9.612E+05	17.9 ± 3.6
14	37	61	100	0.607	72.9	4.742E+05	7.818E+05	14.8 ± 3.1
15	32	37	60	0.865	73.7	6.835E+05	7.903E+05	21.1 ± 5.2
	588	870			112.1	8.129E+05	1.203E+06	

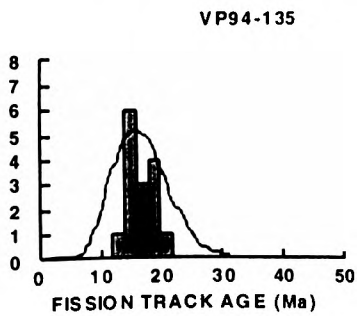
Area of basic unit = 7.803E-07 cm-2

CHI SQUARED = 2.501891 WITH 14 DEGREES OF FREEDOM
P(chi squared) = 98.6 %
CORRELATION COEFFICIENT = 0.963
VARIANCE OF SQR(Ns) = 1.942662
VARIANCE OF SQR(Ni) = 2.917598

Ns/Ni = 0.676 ± 0.036
MEAN RATIO = 0.683 ± 0.023

Pooled Age = 16.5 ± 1.1 Ma
Mean Age = 16.7 ± 0.9 Ma
Central Age = 16.5 ± 0.9Ma
% Variation = 0.00%

Ages calculated using a zeta of 87.8 ± 3 for U3 glass 52 ppm
RHO D = 5.579E+05cm-2; ND = 2266



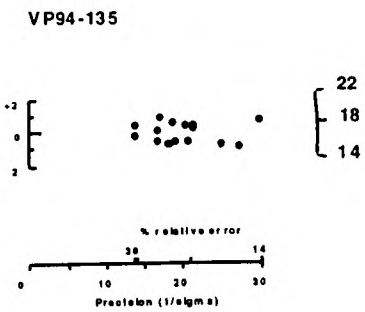


Table D5. Con't.

VP94-138 Zircon
Irradiation LU359-18

No.	Ns	Ni	Na	RATIO	U(ppm)	RHOs	RHOi	F.T.AGE(Ma)
1	75	139	48	0.540	285.3	2.002E+06	3.711E+06	17.6 ± 2.6
2	111	231	36	0.481	632.1	3.951E+06	8.223E+06	15.7 ± 1.9
3	153	323	24	0.474	1325.7	8.170E+06	1.725E+07	15.4 ± 1.6
4	63	154	56	0.409	270.9	1.442E+06	3.524E+06	13.3 ± 2.0
5	367	769	54	0.477	1402.8	8.710E+06	1.825E+07	15.6 ± 1.1
6	202	383	40	0.527	943.2	6.472E+06	1.227E+07	17.2 ± 1.6
7	44	106	40	0.415	261.0	1.410E+06	3.396E+06	13.5 ± 2.5
8	88	296	60	0.297	486.0	1.880E+06	6.322E+06	9.7 ± 1.2
9	17	36	45	0.472	78.8	4.841E+05	1.025E+06	15.4 ± 4.6
10	57	126	25	0.452	496.5	2.922E+06	6.459E+06	14.8 ± 2.4
11	48	109	30	0.440	357.9	2.050E+06	4.656E+06	14.4 ± 2.5
12	231	469	60	0.493	770.0	4.934E+06	1.002E+07	16.1 ± 1.4
13	187	379	50	0.493	746.7	4.793E+06	9.714E+06	16.1 ± 1.5
14	67	139	12	0.482	1141.0	7.155E+06	1.484E+07	15.7 ± 2.4
15	71	137	80	0.518	168.7	1.137E+06	2.195E+06	16.9 ± 2.5
	1781	3796			566.6	3.458E+06	7.371E+06	

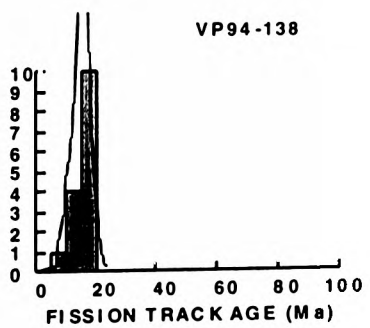
Area of basic unit = 7.803E-07 cm-2

CHI SQUARED = 9.965546 WITH 14 DEGREES OF FREEDOM
P(chi squared) = 13.2 %
CORRELATION COEFFICIENT = 0.986
VARIANCE OF SQR(Ns) = 15.78281
VARIANCE OF SQR(Ni) = 31.23567

Ns/Ni = 0.469 ± 0.013
MEAN RATIO = 0.465 ± 0.015

Pooled Age = 15.3 ± 0.7 Ma
Mean Age = 15.2 ± 0.7 Ma
Central Age = 15.2 ± 0.7Ma
% Variation = 7.60%

Ages calculated using a zeta of 125.5 ± 3 for CN 1 glass 40 ppm
RHO D = 5.204E+05cm-2; ND = 2007



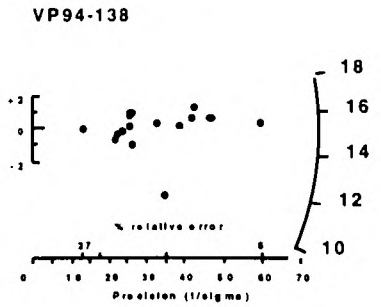


Table D5. Con't.

VP94-140a Zircon
Irradiation LU359-15

No.	Ns	Ni	Na	RATIO	U(ppm)	RHOs	RHOi	F.T.AGE(Ma)
1	38	67	80	0.567	82.9	6.087E+05	1.073E+06	18.4 ± 3.8
2	96	159	100	0.604	157.4	1.230E+06	2.038E+06	19.6 ± 2.6
3	71	180	80	0.394	222.8	1.137E+06	2.884E+06	12.8 ± 1.8
4	69	187	100	0.369	185.1	8.843E+05	2.397E+06	12.0 ± 1.7
5	63	138	60	0.457	227.7	1.346E+06	2.948E+06	14.8 ± 2.3
6	79	147	100	0.537	145.5	1.012E+06	1.884E+06	17.4 ± 2.5
7	51	95	100	0.537	94.0	6.536E+05	1.217E+06	17.4 ± 3.1
8	67	130	60	0.515	214.5	1.431E+06	2.777E+06	16.7 ± 2.6
9	83	213	60	0.390	351.4	1.773E+06	4.550E+06	12.6 ± 1.7
10	87	181	80	0.481	224.0	1.394E+06	2.900E+06	15.6 ± 2.1
11	355	623	100	0.570	616.8	4.550E+06	7.984E+06	18.5 ± 1.4
12	88	187	60	0.471	308.6	1.880E+06	3.994E+06	15.3 ± 2.0
	1147	2307			233.1	1.500E+06	3.017E+06	

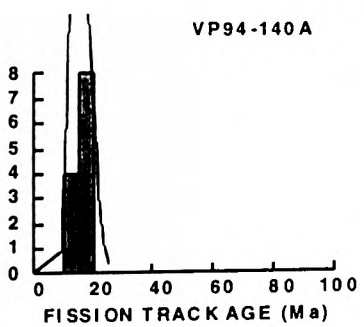
Area of basic unit = 7.803E-07 cm-2

CHI SQUARED = 9.422443 WITH 11 DEGREES OF FREEDOM
P(chi squared) = 6.4 %
CORRELATION COEFFICIENT = 0.984
VARIANCE OF SQR(Ns) = 10.0764
VARIANCE OF SQR(Ni) = 16.78243

Ns/Ni = 0.497 ± 0.018
MEAN RATIO = 0.491 ± 0.022

Pooled Age = 16.1 ± 0.8 Ma
Mean Age = 15.9 ± 0.9 Ma
Central Age = 15.8 ± 0.8Ma
% Variation = 10.11%

Ages calculated using a zeta of 125.5 ± 3 for CN 1 glass 40 ppm
RHO D = 5.178E+05cm-2; ND = 2007



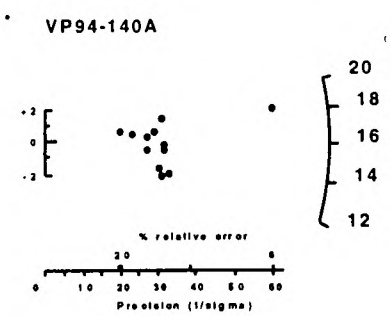


Table D5. Con't.

VP94-141 Zircon
Irradiation LU355-04

No.	Ns	Ni	Na	RATIO	U(ppm)	RHOs	RHOi	F.T.AGE(Ma)
1	168	72	36	2.333	238.1	5.981E+06	2.563E+06	57.1 ± 8.4
2	104	48	24	2.167	238.1	5.553E+06	2.563E+06	53.0 ± 9.5
3	48	28	20	1.714	166.7	3.076E+06	1.794E+06	42.0 ± 10.1
4	130	46	25	2.826	219.0	6.664E+06	2.358E+06	69.1 ± 12.2
5	145	78	32	1.859	290.2	5.807E+06	3.124E+06	45.5 ± 6.6
6	84	38	60	2.211	75.4	1.794E+06	8.117E+05	54.1 ± 10.8
7	127	60	40	2.117	178.6	4.069E+06	1.922E+06	51.8 ± 8.4
8	110	52	25	2.115	247.6	5.639E+06	2.666E+06	51.8 ± 9.0
9	125	56	24	2.232	277.8	6.675E+06	2.990E+06	54.6 ± 9.1
10	160	74	40	2.162	220.2	5.126E+06	2.371E+06	52.9 ± 7.7
11	132	64	60	2.062	127.0	2.819E+06	1.367E+06	50.5 ± 8.0
12	111	52	35	2.135	176.9	4.064E+06	1.904E+06	52.2 ± 9.0
	1444	668			188.9	4.396E+06	2.033E+06	

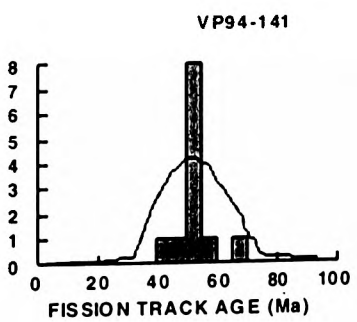
Area of basic unit = 7.803E-07 cm-2

CHI SQUARED = 2.524794 WITH 11 DEGREES OF FREEDOM
P(chi squared) = 92.9 %
CORRELATION COEFFICIENT = 0.919
VARIANCE OF SQR(Ns) = 2.635132
VARIANCE OF SQR(Ni) = 1.073414

Ns/Ni = 2.162 ± 0.101
MEAN RATIO = 2.161 ± 0.077

Pooled Age = 52.9 ± 3.3 Ma
Mean Age = 52.9 ± 2.8 Ma
Central Age = 52.9 ± 2.7Ma
% Variation = 0.00%

Ages calculated using a zeta of 87.8 ± 3 for U3 glass 52 ppm
RHO D = 5.598E+05cm-2; ND = 2266



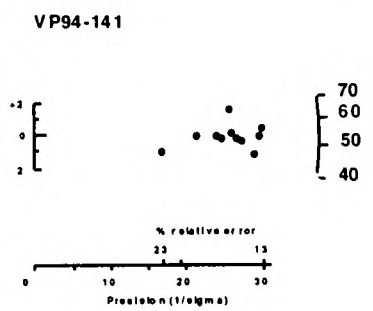


Table D5. Con't.

VP94-143 Zircon
Irradiation LU355-05

No.	Ns	Ni	Na	RATIO	U(ppm)	RHOs	RHOi	F.T.AGE(Ma)
1	54	16	60	3.375	31.6	1.153E+06	3.417E+05	82.7 ± 23.8
2	117	59	16	1.983	437.5	9.371E+06	4.726E+06	48.7 ± 8.0
3	211	116	60	1.819	229.4	4.507E+06	2.478E+06	44.7 ± 5.5
4	164	113	50	1.451	268.1	4.204E+06	2.896E+06	35.7 ± 4.6
5	22	14	50	1.571	33.2	5.639E+05	3.588E+05	38.6 ± 13.3
6	19	8	40	2.375	23.7	6.087E+05	2.563E+05	58.3 ± 24.7
7	100	35	60	2.857	69.2	2.136E+06	7.476E+05	70.1 ± 14.0
8	37	21	100	1.762	24.9	4.742E+05	2.691E+05	43.3 ± 12.0
9	78	50	100	1.560	59.3	9.996E+05	6.408E+05	38.4 ± 7.1
10	237	124	60	1.911	245.2	5.062E+06	2.649E+06	47.0 ± 5.5
11	67	28	60	2.393	55.4	1.431E+06	5.981E+05	58.7 ± 13.4
12	24	12	36	2.000	39.5	8.544E+05	4.272E+05	49.1 ± 17.5
	1130	596			102.2	2.093E+06	1.104E+06	

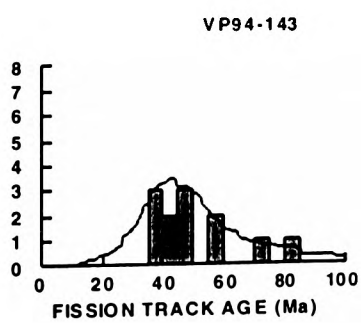
Area of basic unit = 7.803E-07 cm-2

CHI SQUARED = 8.291399 WITH 11 DEGREES OF FREEDOM
P(chi squared) = 12.1 %
CORRELATION COEFFICIENT = 0.970
VARIANCE OF SQR(Ns) = 14.4615
VARIANCE OF SQR(Ni) = 9.133731

Ns/Ni = 1.896 ± 0.096
MEAN RATIO = 2.088 ± 0.165

Pooled Age = 46.6 ± 3.0 Ma
Mean Age = 51.3 ± 4.5 Ma
Central Age = 47.5 ± 3.3Ma
% Variation = 12.44%

Ages calculated using a zeta of 87.8 ± 3 for U3 glass 52 ppm
RHO D = 5.617E+05cm-2; ND = 2266



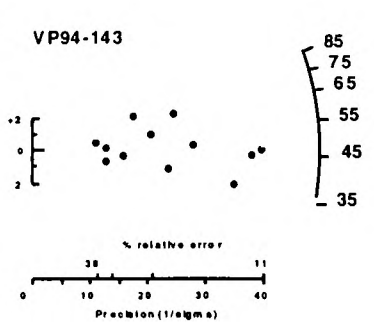


Table D5. Con't.

VP94-144 Zircon
Irradiation LU355-06

No.	Ns	Ni	Na	RATIO	U(ppm)	RHOs	RHOi	F.T.AGE(Ma)
1	148	157	40	0.943	952.2	9.729E+06	1.032E+07	23.3 ± 3.0
2	14	24	30	0.583	194.1	1.227E+06	2.104E+06	14.4 ± 4.9
3	18	17	21	1.059	196.4	2.254E+06	2.129E+06	26.2 ± 9.0
4	26	28	35	0.929	194.1	1.953E+06	2.104E+06	23.0 ± 6.4
5	138	188	70	0.734	651.6	5.184E+06	7.062E+06	18.2 ± 2.3
6	42	50	50	0.840	242.6	2.209E+06	2.630E+06	20.8 ± 4.5
7	69	59	50	1.169	286.3	3.629E+06	3.103E+06	28.9 ± 5.4
8	37	40	60	0.925	161.7	1.622E+06	1.753E+06	22.9 ± 5.4
9	21	29	70	0.724	100.5	7.888E+05	1.089E+06	17.9 ± 5.3
	513	592			337.1	3.167E+06	3.654E+06	

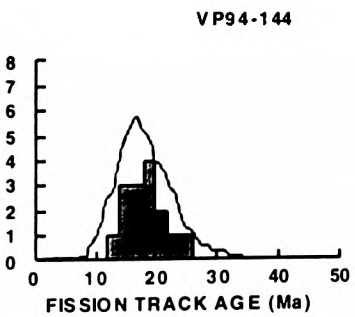
Area of basic unit = 3.803E-07 cm-2

CHI SQUARED = 3.967444 WITH 8 DEGREES OF FREEDOM
P(chi squared) = 44.0 %
CORRELATION COEFFICIENT = 0.975
VARIANCE OF SQR(Ns) = 9.960232
VARIANCE OF SQR(Ni) = 11.62152

Ns/Ni = 0.867 ± 0.052
MEAN RATIO = 0.878 ± 0.060

Pooled Age = 21.5 ± 1.8 Ma
Mean Age = 21.7 ± 2.0 Ma
Central Age = 21.5 ± 1.5Ma
% Variation = 5.84%

Ages calculated using a zeta of 88 ± 5 for U3 glass 52 ppm
RHO D = 5.636E+05cm-2; ND = 2266



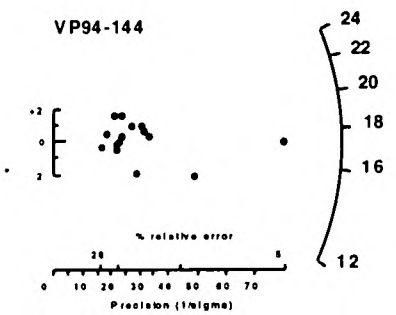


Table D5. Con't.

VP94-145 Zircon
Irradiation LU355-07

No.	Ns	Ni	Na	RATIO	U(ppm)	RHOs	RHOi	F.T.AGE(Ma)
1	56	20	8	2.800	294.6	8.971E+06	3.204E+06	69.1 ± 18.2
2	39	15	24	2.600	73.7	2.083E+06	8.010E+05	64.2 ± 19.7
3	35	13	21	2.692	73.0	2.136E+06	7.933E+05	66.5 ± 21.8
4	44	16	16	2.750	117.8	3.524E+06	1.282E+06	67.9 ± 20.0
5	50	20	16	2.500	147.3	4.005E+06	1.602E+06	61.8 ± 16.5
6	24	12	20	2.000	70.7	1.538E+06	7.689E+05	49.5 ± 17.6
7	69	25	40	2.760	73.7	2.211E+06	8.010E+05	68.2 ± 16.1
8	60	34	36	1.765	111.3	2.136E+06	1.210E+06	43.7 ± 9.5
9	36	18	25	2.000	84.8	1.845E+06	9.227E+05	49.5 ± 14.4
10	33	14	20	2.357	82.5	2.115E+06	8.971E+05	58.3 ± 18.7
	446	187			97.5	2.529E+06	1.060E+06	

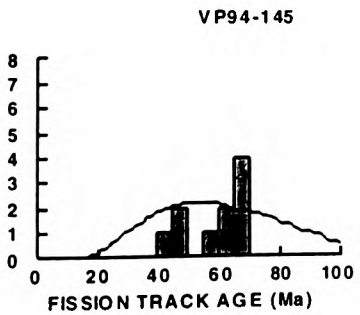
Area of basic unit = 7.803E-07 cm-2

CHI SQUARED = 1.934565 WITH 9 DEGREES OF FREEDOM
P(chi squared) = 92.0 %
CORRELATION COEFFICIENT = 0.823
VARIANCE OF SQR(Ns) = 1.089762
VARIANCE OF SQR(Ni) = .5169542

Ns/Ni = 2.385 ± 0.208
MEAN RATIO = 2.422 ± 0.119

Pooled Age = 58.9 ± 5.7 Ma
Mean Age = 59.9 ± 3.8 Ma
Central Age = 58.9 ± 5.3Ma
% Variation = 0.01%

Ages calculated using a zeta of 87.8 ± 3 for U3 glass 52 ppm
RHO D = 5.655E+05cm-2; ND = 2266



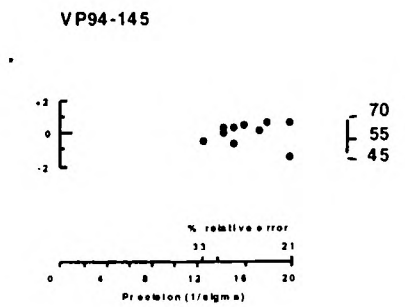


Table D5. Con't.

VP94-057b Apatite
Irradiation LU330-01

No.	Ns	Ni	Na	RATIO	U(ppm)	RHOs	RHOi	F.T.AGE(Ma)
1	7	87	100	0.080	8.8	8.971E+04	1.115E+06	21.4 ± 8.4
2	6	76	90	0.079	8.6	8.544E+04	1 082E+06	21.0 ± 8.9
3	2	32	70	0.062	4.6	3.662E+04	5.859E+05	16.6 ± 12.1
4	13	118	100	0.110	12.0	1.666E+05	1.512E+06	29.2 ± 8.6
5	4	85	90	0.047	9.6	5.696E+04	1.210E+06	12.5 ± 6.4
6	6	50	50	0.120	10.1	1.538E+05	1.282E+06	31.8 ± 13.8
7	12	115	60	0.104	19.4	2.563E+05	2.456E+06	27.7 ± 8.4
8	5	71	80	0.070	9.0	8.010E+04	1.137E+06	18.7 ± 8.7
9	4	68	90	0.059	7.7	5.696E+04	9.683E+05	15.6 ± 8.0
10	1	42	80	0.024	5.3	1.602E+04	6.728E+05	6.3 ± 6.4
11	3	78	100	0.038	7.9	3.845E+04	9.996E+05	10.2 ± 6.0
12	6	62	100	0.097	6.3	7.689E+04	7.946E+05	25.7 ± 11.0
13	0	41	70	0.000	5.9	0.000E+00	7.506E+05	0.0 ± 0.0
14	11	149	100	0.074	15.1	1.410E+05	1.910E+06	19.6 ± 6.1
15	3	106	100	0.028	10.7	3.845E+04	1.358E+06	7.5 ± 4.4
16	9	92	100	0.098	9.3	1.153E+05	1.179E+06	26.0 ± 9.1
17	11	131	100	0.084	13.3	1.410E+05	1.679E+06	22.3 ± 7.0
18	4	82	50	0.049	16.6	1.025E+05	2 102E+06	13.0 ± 6.6
19	9	79	100	0.114	8.0	1.153E+05	1.012E+06	30.2 ± 10.7
20	6	90	80	0.067	11.4	9.612E+04	1.442E+06	17.7 ± 7.5
21	2	69	100	0.029	7.0	2.563E+04	8.843E+05	7.7 ± 5.5
22	8	83	50	0.096	16.8	2.050E+05	2.127E+06	25.6 ± 9.5
23	9	143	80	0.063	18.1	1.442E+05	2.291E+06	16.7 ± 5.8
24	9	75	80	0.120	9.5	1.442E+05	1.201E+06	31.8 ± 11.3
25	6	81	54	0.074	15.2	1.424E+05	1.922E+06	19.7 ± 8.3
	156	2105			10.3	9.639E+04	1.301E+06	

Area of basic unit = 7.803E-07 cm-2

CHI SQUARED = 11.06167 WITH 24 DEGREES OF FREEDOM
P(chi squared) = 57.2 %
CORRELATION COEFFICIENT = 0 742
VARIANCE OF SQR(Ns) = .7075488
VARIANCE OF SQR(Ni) = 2.69722

Ns/Ni = 0.074 ± 0.006
MEAN RATIO = 0.071 ± 0.006

Pooled Age = 19.7 ± 1.7 Ma
Mean Age = 19.0 ± 1.8 Ma
Central Age = 19.7 ± 1.7Ma
% Variation = 2.33%

Ages calculated using a zeta of 379.2 ± 3 for CN 5 glass 12.5 ppm
RHO D = 1.403E+06cm-2; ND = 2736

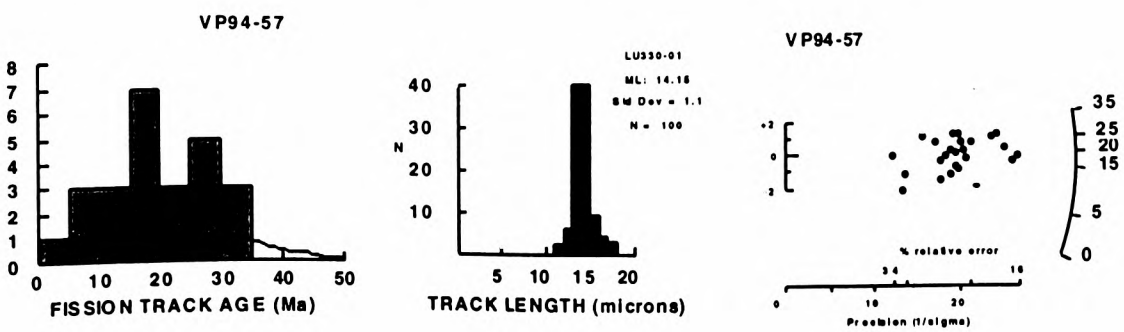


Table D5. Con't.

VP94-127 Apatite
Irradiation LU330-02

No.	Ns	Ni	Na	RATIO	U(ppm)	RHOs	RHOi	F.T.AGE(Ma)
1	3	38	42	0.079	9.2	9.154E+04	1.160E+06	21.0 ± 12.6
2	6	99	100	0.061	10.0	7.689E+04	1.269E+06	16.1 ± 6.8
3	7	147	60	0.048	24.8	1.495E+05	3.140E+06	12.7 ± 4.9
4	5	93	100	0.054	9.4	6.408E+04	1.192E+06	14.3 ± 6.6
5	18	291	100	0.062	29.5	2.307E+05	3.729E+06	16.4 ± 4.0
6	2	62	80	0.032	7.9	3.204E+04	9.932E+05	8.6 ± 6.2
7	6	78	100	0.077	7.9	7.689E+04	9.996E+05	20.4 ± 8.7
8	2	61	70	0.033	8.8	3.662E+04	1.117E+06	8.7 ± 6.3
9	5	67	100	0.075	6.8	6.408E+04	8.586E+05	19.8 ± 9.2
10	18	222	80	0.081	28.1	2.884E+05	3.556E+06	21.5 ± 5.3
11	5	108	100	0.046	11.0	6.408E+04	1.384E+06	12.3 ± 5.6
12	3	39	100	0.077	4.0	3.845E+04	4.998E+05	20.4 ± 12.2
13	6	137	100	0.044	13.9	7.689E+04	1.756E+06	11.6 ± 4.9
14	6	127	36	0.047	35.8	2.136E+05	4.521E+06	12.6 ± 5.3
15	4	37	100	0.108	3.8	5.126E+04	4.742E+05	28.7 ± 15.1
16	9	97	90	0.093	10.9	1.282E+05	1.381E+06	24.6 ± 8.6
17	3	42	100	0.071	4.3	3.845E+04	5.383E+05	19.0 ± 11.3
18	8	88	70	0.091	12.7	1.465E+05	1.611E+06	24.1 ± 8.9
19	1	16	100	0.062	1.6	1.282E+04	2.050E+05	16.6 ± 17.1
20	4	101	80	0.040	12.8	6 408E+04	1.618E+06	10.5 ± 5.4
21	5	87	100	0.057	8.8	6.408E+04	1.115E+06	15.3 ± 7.0
22	8	140	80	0.057	17.7	1.282E+05	2.243E+06	15.2 ± 5.5
23	3	37	100	0.081	3.8	3.845E+04	4.742E+05	21.5 ± 12.9
24	2	76	100	0.026	7.7	2.563E+04	9.740E+05	7.0 ± 5.0
25	13	141	90	0 092	15.9	1.851E+05	2.008E+06	24.5 ± 7.1
	152	2431			11.3	8.944E+04	1.430E+06	

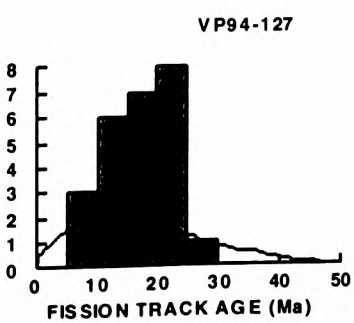
Area of basic unit = 7.803E-07 cm-2

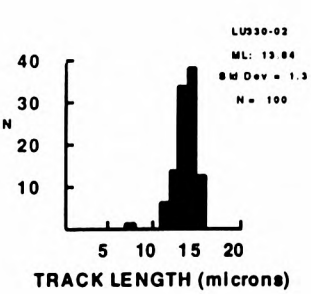
CHI SQUARED = 6.855989 WITH 24 DEGREES OF FREEDOM
P(chi squared) = 95.3 %
CORRELATION COEFFICIENT = 0.895
VARIANCE OF SQR(Ns) = .6672497
VARIANCE OF SQR(Ni) = 8.59792

Ns/Ni = 0.063 ± 0.005
MEAN RATIO = 0.064 ± 0.004

Pooled Age = 16.6 ± 1.4 Ma
Mean Age = 16.9 ± 1.2 Ma
Central Age = 16.6 ± 1.4Ma
% Variation = 0.08%

Ages calculated using a zeta of 379.2 ± 3 for CN 5 glass 11.1 ppm
RHO D = 1.403E+06cm-2; ND = 2736





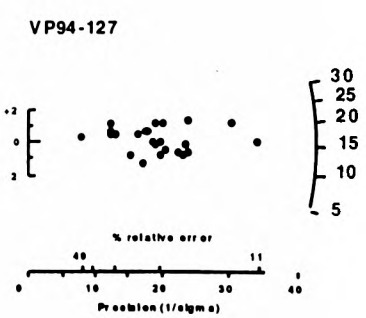


Table D5. Con't.

VP94-132 Apatite
Irradiation LU330-3

No.	Ns	Ni	Na	RATIO	U(ppm)	RHOs	RHOi	F.T.AGE(Ma)
1	8	83	60	0.096	15.8	1.709E+05	1.773E+06	25.8 ± 9.6
2	1	25	80	0.040	3.6	1.602E+04	4.005E+05	10.7 ± 11.0
3	3	36	60	0.083	6.8	6.408E+04	7.689E+05	22.4 ± 13.4
4	2	17	60	0.118	3.2	4.272E+04	3.631E+05	31.5 ± 23.6
5	5	82	50	0.061	18.7	1.282E+05	2.102E+06	16.4 ± 7.5
6	6	53	100	0.113	6.1	7.689E+04	6.792E+05	30.3 ± 13.1
7	2	33	60	0.061	6.3	4.272E+04	7.049E+05	16.3 ± 11.8
8	1	35	50	0.029	8.0	2.563E+04	8.971E+05	7.7 ± 7.8
9	5	108	60	0.046	20.6	1.068E+05	2.307E+06	12.4 ± 5.7
10	0	61	80	0.000	8.7	0.000E+00	9.772E+05	0.0 ± 0.0
11	9	163	100	0.055	18.6	1.153E+05	2.089E+06	14.8 ± 5.1
12	5	37	60	0.135	7.0	1.068E+05	7.903E+05	36.2 ± 17.3
13	3	68	70	0.044	11.1	5.492E+04	1.245E+06	11.8 ± 7.0
14	2	56	100	0.036	6.4	2.563E+04	7.177E+05	9.6 ± 6.9
15	2	31	80	0.065	4.4	3.204E+04	4.966E+05	17.3 ± 12.6
16	7	161	80	0.043	23.0	1.121E+05	2.579E+06	11.7 ± 4.5
17	6	65	70	0.092	10.6	1.098E+05	1.190E+06	24.8 ± 10.6
18	2	34	90	0.059	4.3	2.848E+04	4.841E+05	15.8 ± 11.5
19	11	107	100	0.103	12.2	1.410E+05	1.371E+06	27.6 ± 8.8
20	3	36	80	0.083	5.1	4.806E+04	5.767E+05	22.4 ± 13.4
21	4	112	100	0.036	12.8	5.126E+04	1.435E+06	9.6 ± 4.9
	87	1403			10.1	7.012E+04	1.131E+06	

Area of basic unit = 7.803E-07 cm-2

CHI SQUARED = 9.558635 WITH 20 DEGREES OF FREEDOM
P(chi squared) = 51.4 %
CORRELATION COEFFICIENT = 0.710
VARIANCE OF SQR(Ns) = .6039795
VARIANCE OF SQR(Ni) = 6.042944

Ns/Ni = 0.062 ± 0.007
MEAN RATIO = 0.067 ± 0.007

Pooled Age = 16.6 ± 1.9 Ma
Mean Age = 17.9 ± 2.0 Ma
Central Age = 16.7 ± 1.9Ma
% Variation = 8.00%

Ages calculated using a zeta of 383 ± 5 for Other glass 12.5 ppm
RHO D = 1.403E+06cm-2; ND = 2736

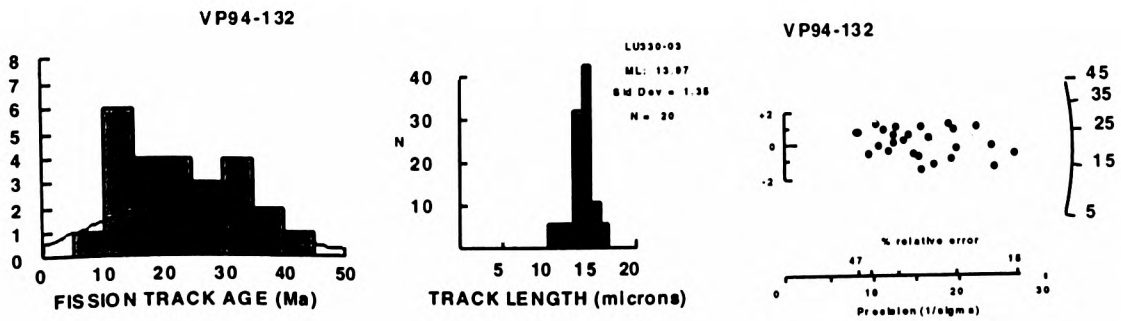


Table D5. Con't.

VP94-135 Apatite
Irradiation LU330-04

No.	Ns	Ni	Na	RATIO	U(ppm)	RHOs	RHOi	F.T.AGE(Ma)
1	7	52	100	0.135	5.3	8.971E+04	6.664E+05	35.7 ± 14.4
2	2	67	100	0.030	6.8	2.563E+04	8.586E+05	7.9 ± 5.7
3	3	38	100	0.079	3 9	3.845E+04	4.870E+05	21.0 ± 12.6
4	2	43	80	0.047	5.4	3.204E+04	6.888E+05	12.4 ± 8.9
5	5	49	80	0.102	6.2	8.010E+04	7.850E+05	27.1 ± 12.7
6	7	45	100	0.156	4.6	8.971E+04	5.767E+05	41.2 ± 16.8
7	2	44	80	0.045	5.6	3.204E+04	7.049E+05	12.1 ± 8.7
8	2	50	100	0.040	5.1	2.563E+04	6.408E+05	10.6 ± 7.7
9	1	25	100	0.040	2.5	1.282E+04	3.204E+05	10.6 ± 10.8
10	0	25	100	0.000	2.5	0.000E+00	3.204E+05	0.0 ± 0.0
11	16	303	80	0.053	38.4	2.563E+05	4.854E+06	14.0 ± 3.6
12	2	56	100	0.036	5.7	2.563E+04	7.177E+05	9.5 ± 6.8
13	2	65	100	0.031	6.6	2.563E+04	8.330E+05	8.2 ± 5.9
14	12	183	100	0.066	18.6	1.538E+05	2.345E+06	17.4 ± 5.2
15	2	55	100	0.036	5.6	2.563E+04	7.049E+05	9.7 ± 7.0
16	0	9	80	0.000	1.1	0.000E+00	1.442E+05	0.0 ± 0.0
17	5	50	25	0.100	20.3	2.563E+05	2.563E+06	26.5 ± 12.5
18	1	42	90	0.024	4.7	1.424E+04	5.981E+05	6.3 ± 6.4
19	3	25	100	0.120	2.5	3.845E+04	3.204E+05	31.8 ± 19.5
20	2	70	100	0.029	7.1	2.563E+04	8.971E+05	7.6 ± 5.4
21	3	60	100	0.050	6.1	3.845E+04	7.689E+05	13.3 ± 7.9
22	7	83	81	0.084	10.4	1.108E+05	1.313E+06	22.4 ± 8.8
23	2	26	100	0.077	2.6	2.563E+04	3.332E+05	20.4 ± 15.0
24	2	30	80	0.067	3.8	3.204E+04	4.806E+05	17.7 ± 12.9
25	0	5	20	0.000	2.5	0.000E+00	3.204E+05	0.0 ± 0.0
	90	1500			6.9	5.252E+04	8.754E+05	

Area of basic unit = 7.803E-07 cm-2

CHI SQUARED = 11.79694 WITH 24 DEGREES OF FREEDOM
P(chi squared) = 48.5 %
CORRELATION COEFFICIENT = 0.882
VARIANCE OF SQR(Ns) = .919316
VARIANCE OF SQR(Ni) = 9.089757

Ns/Ni = 0.060 ± 0.007
MEAN RATIO = 0.058 ± 0.008

Pooled Age = 15.9 ± 1.8 Ma
Mean Age = 15.4 ± 2.2 Ma
Central Age = 15.9 ± 1 8Ma
% Variation = 3.09%

Ages calculated using a zeta of 379.2 ± 3 for CN 5 glass 11 1 ppm
RHO D = 1.403E+06cm-2; ND = 2736

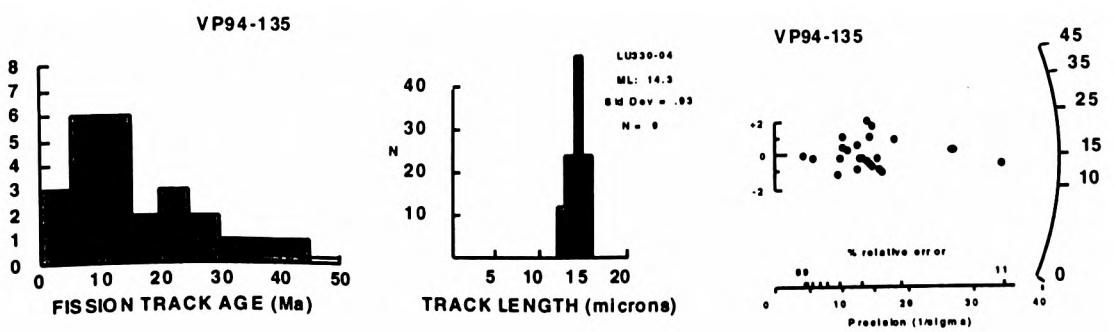


Table D5. Con't.

VP94-138 Apatite
Irradiation LU330-05

No.	Ns	Ni	Na	RATIO	U(ppm)	RHOs	RHOi	F.T.AGE(Ma)
1	2	108	40	0.019	27.4	6.408E+04	3.460E+06	4.9 ± 3.5
2	4	66	100	0.061	6.7	5.126E+04	8.458E+05	16.1 ± 8.3
3	16	407	100	0.039	41.3	2.050E+05	5.216E+06	10.4 ± 2.7
4	0	15	100	0.000	1.5	0.000E+00	1.922E+05	0.0 ± 0.0
5	11	223	90	0.049	25.1	1.566E+05	3.175E+06	13.1 ± 4.1
6	9	161	100	0.056	16.3	1.153E+05	2.063E+06	14.9 ± 5.1
7	2	56	81	0.036	7.0	3.164E+04	8.860E+05	9.5 ± 6.8
8	2	52	100	0.038	5.3	2.563E+04	6.664E+05	10.2 ± 7.4
9	2	67	80	0.030	8.5	3.204E+04	1.073E+06	7.9 ± 5.7
10	11	354	100	0.031	35.9	1.410E+05	4.537E+06	8.3 ± 2.5
11	3	114	100	0.026	11.6	3.845E+04	1.461E+06	7.0 ± 4.1
12	9	267	100	0.034	27.1	1.153E+05	3.422E+06	9.0 ± 3.0
13	5	157	80	0.032	19.9	8.010E+04	2.515E+06	8.5 ± 3.8
14	6	177	100	0.034	17.9	7.689E+04	2.268E+06	9.0 ± 3.7
15	9	156	60	0.058	26.4	1.922E+05	3.332E+06	15.3 ± 5.3
16	8	209	100	0.038	21.2	1.025E+05	2.678E+06	10.2 ± 3.7
17	4	123	63	0.033	19.8	8.137E+04	2.502E+06	8.6 ± 4.4
18	10	208	80	0.048	26.4	1.602E+05	3.332E+06	12.8 ± 4.1
19	4	57	30	0.070	19.3	1.709E+05	2.435E+06	18.6 ± 9.6
20	8	161	100	0.050	16.3	1.025E+05	2.063E+06	13.2 ± 4.8
21	3	127	100	0.024	12.9	3.845E+04	1.628E+06	6.3 ± 3.7
22	2	114	100	0.018	11.6	2.563E+04	1.461E+06	4.7 ± 3.3
23	2	47	100	0.043	4.8	2.563E+04	6.023E+05	11.3 ± 8.2
24	7	216	100	0.032	21.9	8.971E+04	2.768E+06	8.6 ± 3.3
25	2	101	49	0.020	20.9	5.231E+04	2.642E+06	5.3 ± 3.8
	141	3743			17.6	8.393E+04	2.228E+06	

Area of basic unit = 7.803E-07 cm-2

CHI SQUARED = 6.494443 WITH 24 DEGREES OF FREEDOM
P(chi squared) = 96.6 %
CORRELATION COEFFICIENT = 0.906
VARIANCE OF SQR(Ns) = .8062935
VARIANCE OF SQR(Ni) = 14.84447

Ns/Ni = 0.038 ± 0.003
MEAN RATIO = 0.037 ± 0.003

Pooled Age = 10.0 ± 0.9 Ma
Mean Age = 9.7 ± 0.8 Ma
Central Age = 10.0 ± 0.9Ma
% Variation = 0.01%

Ages calculated using a zeta of 379.2 ± 3 for CN 5 glass 11.1 ppm
RHO D = 1.403E+06cm-2; ND = 2736

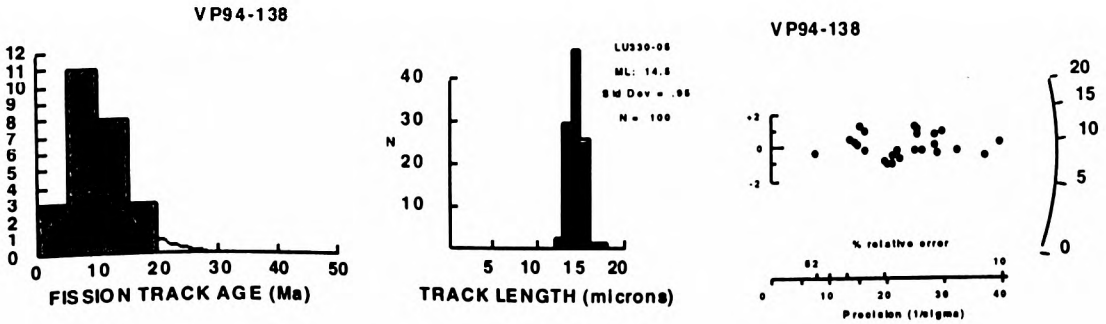


Table D5. Con't.

VP94-140a Apatite
Irradiation LU330-06

No.	Ns	Ni	Na	RATIO	U(ppm)	RHOs	RHOi	F.T.AGE(Ma)
1	4	74	80	0.054	10.6	6.408E+04	1.185E+06	14.4 ± 7.4
2	1	60	100	0.017	6.8	1.282E+04	7.689E+05	4.4 ± 4.5
3	18	254	100	0.071	29.0	2.307E+05	3.255E+06	18.8 ± 4.6
4	8	114	80	0.070	16.3	1.282E+05	1.826E+06	18.6 ± 6.8
5	0	57	100	0.000	6.5	0.000E+00	7.305E+05	0.0 ± 0.0
6	12	167	100	0.072	19.1	1.538E+05	2.140E+06	19.1 ± 5.7
7	1	56	80	0.018	8.0	1.602E+04	8.971E+05	4.7 ± 4.8
8	4	61	100	0.066	7.0	5.126E+04	7.818E+05	17.4 ± 9.0
9	19	196	40	0.097	55.9	6.087E+05	6.280E+06	25.7 ± 6.2
10	7	103	100	0.068	11.8	8.971E+04	1.320E+06	18.1 ± 7.1
11	5	79	100	0.063	9.0	6.408E+04	1.012E+06	16.8 ± 7.8
12	3	127	70	0.024	20.7	5.492E+04	2.325E+06	6.3 ± 3.7
13	12	151	100	0.079	17.2	1.538E+05	1.935E+06	21.1 ± 6.3
14	9	238	100	0.038	27.2	1.153E+05	3.050E+06	10.1 ± 3.4
15	3	40	70	0.075	6.5	5.492E+04	7.323E+05	19.9 ± 11.9
16	5	125	90	0.040	15.9	7.120E+04	1.780E+06	10.6 ± 4.9
17	5	97	100	0.052	11.1	6.408E+04	1.243E+06	13.7 ± 6.3
18	3	75	100	0.040	8.6	3.845E+04	9.612E+05	10.6 ± 6.3
19	4	56	64	0.071	10.0	8.010E+04	1.121E+06	19.0 ± 9.8
20	3	51	80	0.059	7.3	4.806E+04	8.170E+05	15.6 ± 9.3
21	7	107	100	0.065	12.2	8.971E+04	1.371E+06	17.4 ± 6.8
22	8	155	80	0.052	22.1	1.282E+05	2.483E+06	13.7 ± 5.0
23	2	31	100	0.065	3.5	2.563E+04	3.973E+05	17.1 ± 12.5
24	12	263	100	0.046	30.0	1.538E+05	3.370E+06	12.1 ± 3.6
25	6	83	100	0.072	9.5	7.689E+04	1.064E+06	19.2 ± 8.1
	161	2820			14.4	9.236E+04	1.618E+06	

Area of basic unit = 7.803E-07 cm-2

CHI SQUARED = 10.56948 WITH 24 DEGREES OF FREEDOM
P(chi squared) = 63.1 %
CORRELATION COEFFICIENT = 0.841
VARIANCE OF SQR(Ns) = 1.015825
VARIANCE OF SQR(Ni) = 9.057719

Ns/Ni = 0.057 ± 0.005
MEAN RATIO = 0.055 ± 0.005

Pooled Age = 15.2 ± 1.3 Ma
Mean Age = 14.6 ± 1.2 Ma
Central Age = 15.1 ± 1.3Ma
% Variation = 8.04%

Ages calculated using a zeta of 379.2 ± 3 for CN 5 glass 12.5 ppm
RHO D = 1.403E+06cm-2; ND = 2736

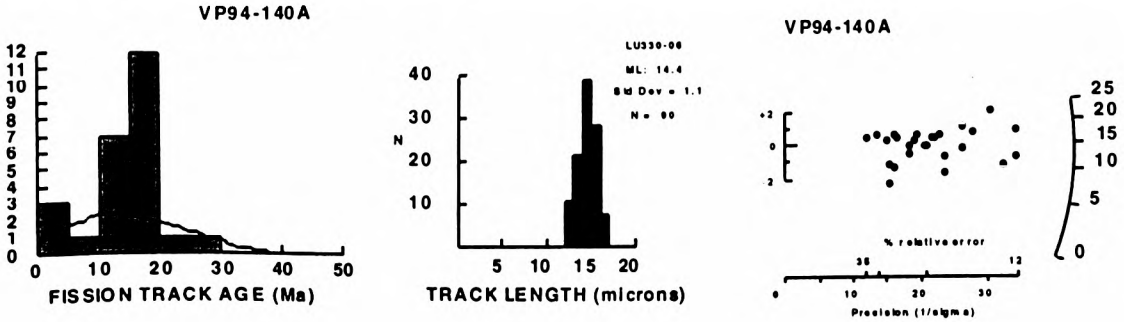


Table D5. Con't.

VP94-140b Apatite
Irradiation LU330-07

No.	Ns	Ni	Na	RATIO	U(ppm)	RHOs	RHOi	F.T.AGE(Ma)
1	2	30	80	0.067	4.3	3.204E+04	4.806E+05	17.7 ± 12.9
2	1	10	100	0.100	1.1	1.282E+04	1.282E+05	26.5 ± 27.8
3	3	23	80	0.130	3.3	4.806E+04	3.684E+05	34.6 ± 21.3
4	2	20	90	0.100	2.5	2.848E+04	2.848E+05	26.5 ± 19.7
5	3	35	80	0.086	5.0	4.806E+04	5.607E+05	22.8 ± 13.7
6	1	30	100	0.033	3.4	1.282E+04	3.845E+05	8.9 ± 9.0
7	2	34	80	0.059	4.9	3.204E+04	5.447E+05	15.6 ± 11.4
8	0	21	81	0.000	3.0	0.000E+00	3.323E+05	0.0 ± 0.0
9	3	41	100	0.073	4.7	3.845E+04	5.254E+05	19.4 ± 11.6
10	8	123	90	0.065	15.6	1.139E+05	1.751E+06	17.3 ± 6.3
11	9	127	80	0.071	18.1	1.442E+05	2.034E+06	18.8 ± 6.5
12	10	250	100	0.040	28.5	1.282E+05	3.204E+06	10.6 ± 3.4
13	1	16	70	0.062	2.6	1.831E+04	2.929E+05	16.6 ± 17.1
14	6	84	70	0.071	13.7	1.098E+05	1.538E+06	19.0 ± 8.0
15	1	17	100	0.059	1.9	1.282E+04	2.179E+05	15.6 ± 16.1
16	11	227	100	0.048	25.9	1.410E+05	2.909E+06	12.9 ± 4.0
17	8	173	100	0.046	19.8	1.025E+05	2.217E+06	12.3 ± 4.5
18	2	56	80	0.036	8.0	3.204E+04	8.971E+05	9.5 ± 6.8
19	4	64	80	0.062	9.1	6.408E+04	1.025E+06	16.6 ± 8.6
20	8	108	100	0.074	12.3	1.025E+05	1.384E+06	19.7 ± 7.2
	85	1489			9.7	6.186E+04	1.084E+06	

Area of basic unit = 7.803E-07 cm-2

CHI SQUARED = 4.301865 WITH 19 DEGREES OF FREEDOM
P(chi squared) = 97.9 %
CORRELATION COEFFICIENT = 0.934
VARIANCE OF SQR(Ns) = .8189344
VARIANCE OF SQR(Ni) = 14.59524

Ns/Ni = 0.057 ± 0.006
MEAN RATIO = 0.064 ± 0.006

Pooled Age = 15.2 ± 1.7 Ma
Mean Age = 17.1 ± 1.7 Ma
Central Age = 15.2 ± 1.7Ma
% Variation = 0.01%

Ages calculated using a zeta of 379.2 ± 3 for CN 5 glass 12.5 ppm
RHO D = 1.403E+06cm-2; ND = 2736

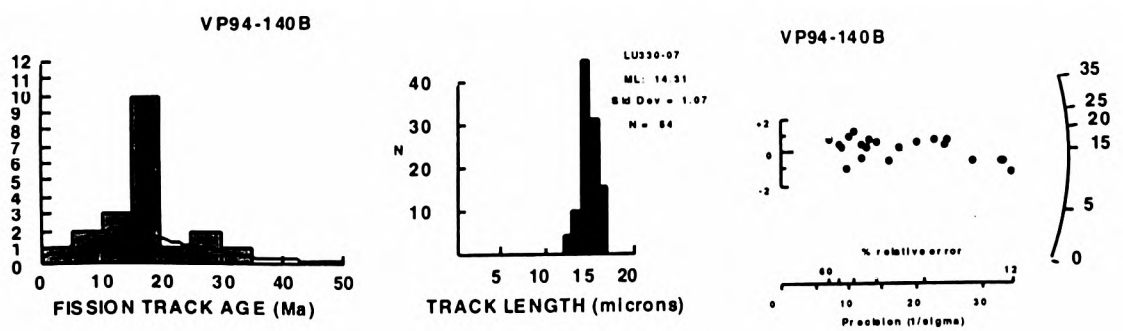


Table D5. Con't.

VP94-141 Apatite
Irradiation LU330-08

No.	Ns	Ni	Na	RATIO	U(ppm)	RHOs	RHOi	F.T.AGE(Ma)
1	3	43	90	0.070	5.5	4.272E+04	6.123E+05	18.5 ± 11.1
2	6	198	100	0.030	22.6	7.689E+04	2.537E+06	8.1 ± 3.3
3	3	87	70	0.034	14.2	5.492E+04	1.593E+06	9.2 ± 5.4
4	4	73	100	0.055	8.3	5.126E+04	9.355E+05	14.6 ± 7.5
5	3	107	100	0.028	12.2	3.845E+04	1.371E+06	7.5 ± 4.4
6	2	55	80	0.036	7.8	3.204E+04	8.811E+05	9.7 ± 7.0
7	0	31	70	0.000	5.1	0.000E+00	5.675E+05	0.0 ± 0.0
8	5	64	80	0.078	9.1	8.010E+04	1.025E+06	20.7 ± 9.6
9	2	21	100	0.095	2.4	2.563E+04	2.691E+05	25.3 ± 18.7
10	6	71	100	0.084	8.1	7.689E+04	9.099E+05	22.4 ± 9.6
11	1	98	90	0.010	12.4	1.424E+04	1.395E+06	2.7 ± 2.7
12	4	70	100	0.057	8.0	5.126E+04	8.971E+05	15.2 ± 7.8
13	5	40	80	0.125	5.7	8.010E+04	6.408E+05	33.2 ± 15.7
14	2	94	100	0.021	10.7	2.563E+04	1.205E+06	5.7 ± 4.0
15	0	28	100	0.000	3.2	0.000E+00	3.588E+05	0.0 ± 0.0
16	4	46	100	0.087	5.3	5.126E+04	5.895E+05	23.1 ± 12.0
17	0	61	64	0.000	10.9	0.000E+00	1.221E+06	0.0 ± 0.0
18	3	55	48	0.055	13.1	8.010E+04	1.468E+06	14.5 ± 8.6
19	0	28	100	0.000	3.2	0.000E+00	3.588E+05	0.0 ± 0.0
20	0	22	100	0.000	2.5	0.000E+00	2.819E+05	0.0 ± 0.0
21	1	40	80	0.025	5.7	1.602E+04	6.408E+05	6.6 ± 6.7
22	2	58	100	0.034	6.6	2.563E+04	7.433E+05	9.2 ± 6.6
23	4	52	72	0.077	8.2	7.120E+04	9.256E+05	20.4 ± 10.6
24	1	83	100	0.012	9.5	1.282E+04	1.064E+06	3.2 ± 3.2
25	1	38	80	0.026	5.4	1.602E+04	6.087E+05	7.0 ± 7.1
	62	1563			8.1	3.605E+04	9.088E+05	

Area of basic unit = 7.803E-07 cm-2

CHI SQUARED = 16.12021 WITH 24 DEGREES OF FREEDOM
P(chi squared) = 12.1 %
CORRELATION COEFFICIENT = 0.476
VARIANCE OF SQR(Ns) = .6616311
VARIANCE OF SQR(Ni) = 4.430685

Ns/Ni = 0.040 ± 0.005
MEAN RATIO = 0.042 ± 0.007

Pooled Age = 10.5 ± 1.4 Ma
Mean Age = 11.1 ± 1.9 Ma
Central Age = 10.7 ± 1.6Ma
% Variation = 28.72%

Ages calculated using a zeta of 379.2 ± 3 for CN 5 glass 12.5 ppm
RHO D = 1.403E+06cm-2; ND = 2736

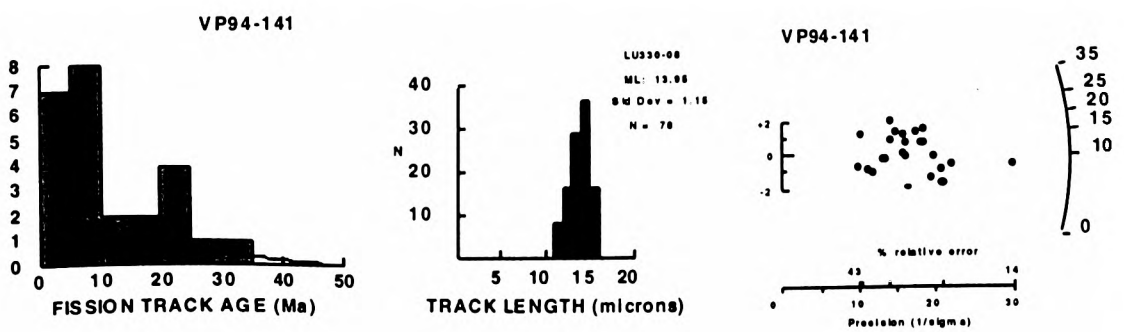


Table D5. Con't.

VP94-142 Apatite
IRRADIATION LU330-09

No.	Ns	Ni	Na	RATIO	U(ppm)	RHOs	RHOi	F.T.AGE(Ma)
1	3	19	80	0.158	2.7	4.806E+04	3.044E+05	41.9 ± 26.0
2	0	44	100	0.000	5.0	0.000E+00	5.639E+05	0.0 ± 0.0
3	3	42	100	0.071	4.8	3.845E+04	5.383E+05	19.0 ± 11.3
4	5	62	100	0.081	7.1	6.408E+04	7.946E+05	21.4 ± 10.0
5	2	36	80	0.056	5.1	3.204E+04	5.767E+05	14.8 ± 10.7
6	13	89	100	0.146	10.2	1.666E+05	1.141E+06	38.7 ± 11.5
7	2	41	100	0.049	4.7	2.563E+04	5.254E+05	13.0 ± 9.4
8	1	10	64	0.100	1.8	2.002E+04	2.002E+05	26.5 ± 27.8
9	2	15	100	0.133	1.7	2.563E+04	1.922E+05	35.4 ± 26.6
10	3	32	100	0.094	3.7	3.845E+04	4.101E+05	24.9 ± 15.0
11	3	19	100	0.158	2.2	3.845E+04	2.435E+05	41.9 ± 26.0
12	5	62	100	0.081	7.1	6.408E+04	7.946E+05	21.4 ± 10.0
13	1	8	80	0.125	1.1	1.602E+04	1.282E+05	33.2 ± 35.2
14	0	37	100	0.000	4.2	0.000E+00	4.742E+05	0.0 ± 0.0
15	2	24	80	0.083	3.4	3.204E+04	3.845E+05	22.1 ± 16.3
16	2	41	100	0.049	4.7	2.563E+04	5.254E+05	13.0 ± 9.4
17	0	11	100	0.000	1.3	0.000E+00	1.410E+05	0.0 ± 0.0
18	2	17	100	0.118	1.9	2.563E+04	2.179E+05	31.2 ± 23.3
19	0	23	100	0.000	2.6	0.000E+00	2.948E+05	0.0 ± 0.0
20	2	27	100	0.074	3.1	2.563E+04	3.460E+05	19.7 ± 14.4
	51	659			4.0	3.469E+04	4.483E+05	

Area of basic unit = 7.803E-07 cm-2

CHI SQUARED = 9.344374 WITH 19 DEGREES OF FREEDOM
P(chi squared) = 47.7 %
CORRELATION COEFFICIENT = 0.766
VARIANCE OF SQR(Ns) = .7792115
VARIANCE OF SQR(Ni) = 2.984356

Ns/Ni = 0.077 ± 0.011
MEAN RATIO = 0.079 ± 0.012

Pooled Age = 20.6 ± 3.0 Ma
Mean Age = 20.9 ± 3.1 Ma
Central Age = 20.2 ± 3.2Ma
% Variation = 24.28%

Ages calculated using a zeta of 379.2 ± 3 for CN 5 glass 12.5 ppm
RHO D = 1.403E+06cm-2; ND = 2736

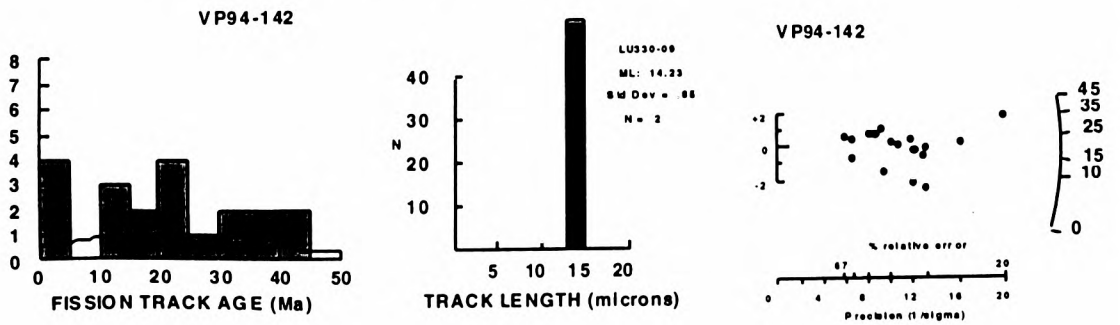


Table D5. Con't.

VP94-143 Apatite
Irradiation LU330-10

No.	Ns	Ni	Na	RATIO	U(ppm)	RHOs	RHOi	F.T.AGE(Ma)
1	8	169	50	0.047	38.6	2.050E+05	4.332E+06	12.6 ± 4.6
2	11	176	100	0.062	20.1	1.410E+05	2.256E+06	16.6 ± 5.2
3	1	49	80	0.020	7.0	1.602E+04	7.850E+05	5.4 ± 5.5
4	0	9	100	0.000	1.0	0.000E+00	1.153E+05	0.0 ± 0.0
5	15	223	80	0.067	31.8	2.403E+05	3.572E+06	17.9 ± 4.8
6	10	156	100	0.064	17.8	1.282E+05	1.999E+06	17.0 ± 5.6
7	1	67	90	0.015	8.5	1.424E+04	9.540E+05	4.0 ± 4.0
8	9	216	100	0.042	24.7	1.153E+05	2.768E+06	11.1 ± 3.8
9	11	241	100	0.046	27.5	1.410E+05	3.089E+06	12.1 ± 3.7
10	7	163	100	0.043	18.6	8.971E+04	2.089E+06	11.4 ± 4.4
11	10	86	80	0.116	12.3	1.602E+05	1.378E+06	30.9 ± 10.3
12	19	289	100	0.066	33.0	2.435E+05	3.704E+06	17.5 ± 4.2
13	20	332	100	0.060	37.9	2.563E+05	4.255E+06	16.0 ± 3.7
14	6	130	100	0.046	14.8	7.689E+04	1.666E+06	12.3 ± 5.1
15	6	163	60	0.037	31.0	1.282E+05	3.482E+06	9.8 ± 4.1
16	3	51	100	0.059	5.8	3.845E+04	6.536E+05	15.6 ± 9.3
17	17	318	100	0.053	36.3	2.179E+05	4.075E+06	14.2 ± 3.5
18	2	46	100	0.043	5.3	2.563E+04	5.895E+05	11.6 ± 8.3
19	4	137	90	0.029	17.4	5.696E+04	1.951E+06	7.8 ± 3.9
20	17	316	100	0.054	36.1	2.179E+05	4.050E+06	14.3 ± 3.6
21	18	267	100	0.067	30.5	2.307E+05	3.422E+06	17.9 ± 4.4
22	20	254	100	0.079	29.0	2.563E+05	3.255E+06	20.9 ± 4.9
23	1	70	100	0.014	8.0	1.282E+04	8.971E+05	3.8 ± 3.8
24	6	161	100	0.037	18.4	7.689E+04	2.063E+06	9.9 ± 4.1
25	23	321	100	0.072	36.7	2.948E+05	4.114E+06	19.0 ± 4.1
	245	4410			21.6	1.348E+05	2.426E+06	

Area of basic unit = 7.803E-07 cm-2

CHI SQUARED = 11.13878 WITH 24 DEGREES OF FREEDOM
P(chi squared) = 56.3 %
CORRELATION COEFFICIENT = 0.928
VARIANCE OF SQR(Ns) = 1.714696
VARIANCE OF SQR(Ni) = 17.30942

Ns/Ni = 0.056 ± 0.004
MEAN RATIO = 0.050 ± 0.005

Pooled Age = 14.8 ± 1.0 Ma
Mean Age = 13.2 ± 1.3 Ma
Central Age = 14.8 ± 1.0Ma
% Variation = 0.81%

Ages calculated using a zeta of 379.2 ± 3 for CN 5 glass 12.5 ppm
RHO D = 1.403E+06cm-2; ND = 2736

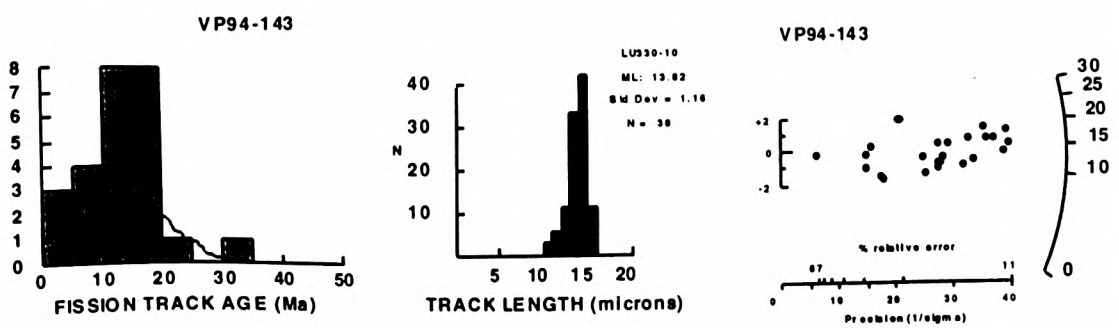


Table D5. Con't.

VP94-144 Apatite
Irradiation LU330-11

No.	Ns	Ni	Na	RATIO	U(ppm)	RHOs	RHOi	F.T.AGE(Ma)
1	1	17	80	0.059	2.4	1.602E+04	2.723E+05	15.6 ± 16.1
2	2	50	80	0.040	7.1	3.204E+04	8.010E+05	10.6 ± 7.7
3	1	30	100	0.033	3.4	1.282E+04	3.845E+05	8.9 ± 9.0
4	5	34	100	0.147	3.9	6.408E+04	4.357E+05	39.0 ± 18.7
5	6	42	100	0.143	4.8	7.689E+04	5.383E+05	37.9 ± 16.6
6	23	309	90	0.074	39.2	3.275E+05	4.400E+06	19.8 ± 4.3
7	0	15	80	0.000	2.1	0.000E+00	2.403E+05	0.0 ± 0.0
8	2	43	80	0.047	6.1	3.204E+04	6.888E+05	12.4 ± 8.9
9	2	51	80	0.039	7.3	3.204E+04	8.170E+05	10.4 ± 7.5
10	4	48	64	0.083	8.6	8.010E+04	9.612E+05	22.1 ± 11.5
11	2	18	100	0.111	2.1	2.563E+04	2.307E+05	29.5 ± 22.0
12	13	256	100	0.051	29.2	1.666E+05	3.281E+06	13.5 ± 3.8
13	3	20	70	0.150	3.3	5.492E+04	3.662E+05	39.8 ± 24.6
14	1	19	90	0.053	2.4	1.424E+04	2.706E+05	14.0 ± 14.4
15	1	30	80	0.033	4.3	1.602E+04	4.806E+05	8.9 ± 9.0
16	2	44	100	0.045	5.0	2.563E+04	5.639E+05	12.1 ± 8.7
17	1	11	64	0.091	2.0	2.002E+04	2.203E+05	24.1 ± 25.2
18	7	56	100	0.125	6.4	8.971E+04	7.177E+05	33.2 ± 13.3
19	3	16	60	0.188	3.0	6.408E+04	3.417E+05	49.7 ± 31.3
20	3	40	100	0.075	4.6	3.845E+04	5.126E+05	19.9 ± 11.9
21	2	21	100	0.095	2.4	2.563E+04	2.691E+05	25.3 ± 18 7
22	25	297	70	0.084	48.4	4.577E+05	5.437E+06	22.4 ± 4.7
23	11	87	100	0.126	9.9	1.410E+05	1.115E+06	33.5 ± 10.8
24	6	67	70	0.090	10.9	1.098E+05	1.227E+06	23.8 ± 10.1
25	4	39	80	0.103	5.6	6.408E+04	6.248E+05	27.2 ± 14.3
	130	1660			8.9	7.792E+04	9.950E+05	

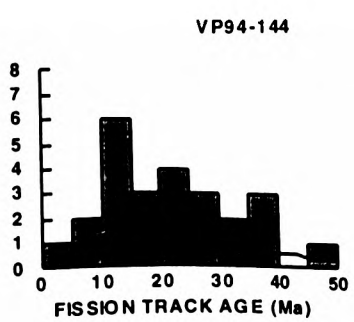
Area of basic unit = 7.803E-07 cm-2

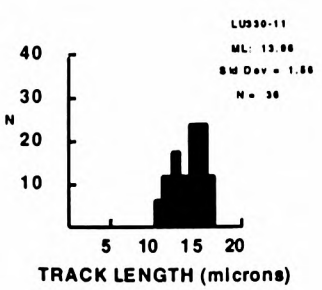
CHI SQUARED = 9.855512 WITH 24 DEGREES OF FREEDOM
P(chi squared) = 71.3 %
CORRELATION COEFFICIENT = 0.945
VARIANCE OF SQR(Ns) = 1.385507
VARIANCE OF SQR(Ni) = 15.79831

Ns/Ni = 0.078 ± 0.007
MEAN RATIO = 0.083 ± 0.009

<u>Pooled Age = 20.8 ± 1.9 Ma</u>
Mean Age = 22.1 ± 2.4 Ma
Central Age = 20.8 ± 1.9Ma
% Variation = 1.96%

Ages calculated using a zeta of 379.2 ± 3 for CN 5 glass 12.5 ppm
RHO D = 1.403E+06cm-2; ND = 2736





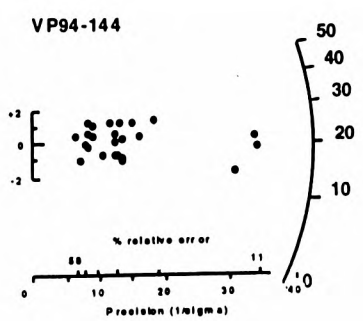


Table D5. Con't.

VP94-146 Apatite
Irradiation LU330-12

No.	Ns	Ni	Na	RATIO	U(ppm)	RHOs	RHOi	F.T.AGE(Ma)
1	2	22	60	0.091	4.2	4.272E+04	4.699E+05	24.1 ± 17.8
2	2	45	100	0.044	5.1	2.563E+04	5.767E+05	11.8 ± 8.5
3	1	18	100	0.056	2.1	1.282E+04	2.307E+05	14.8 ± 15.2
4	6	65	70	0.092	10.6	1.098E+05	1.190E+06	24.5 ± 10.5
5	3	18	60	0.167	3.4	6.408E+04	3.845E+05	44.2 ± 27.6
6	4	39	90	0.103	4.9	5.696E+04	5.553E+05	27.2 ± 14.3
7	7	61	35	0.115	19.9	2.563E+05	2.234E+06	30.5 ± 12.2
8	2	47	64	0.043	8.4	4.005E+04	9.411E+05	11.3 ± 8.2
9	8	69	70	0.116	11.3	1.465E+05	1.263E+06	30.8 ± 11.5
10	25	315	100	0.079	36.0	3.204E+05	4.037E+06	21.1 ± 4.4
11	9	87	100	0.103	9.9	1.153E+05	1.115E+06	27.5 ± 9.6
12	4	71	100	0.056	8.1	5.126E+04	9.099E+05	15.0 ± 7.7
13	1	15	100	0.067	1.7	1.282E+04	1.922E+05	17.7 ± 18.3
14	4	86	100	0.047	9.8	5.126E+04	1.102E+06	12.4 ± 6.3
15	10	103	90	0.097	13.1	1.424E+05	1.467E+06	25.8 ± 8.6
16	19	287	40	0.066	81.9	6.087E+05	9.195E+06	17.6 ± 4.2
17	3	47	50	0.064	10.7	7.689E+04	1.205E+06	17.0 ± 10.1
18	7	55	70	0.127	9.0	1.282E+05	1.007E+06	33.8 ± 13.6
19	1	10	100	0.100	1.1	1.282E+04	1.282E+05	26.5 ± 27.8
20	21	299	100	0.070	34.1	2.691E+05	3.832E+06	18.7 ± 4.2
	139	1759			12.6	1.114E+05	1.410E+06	

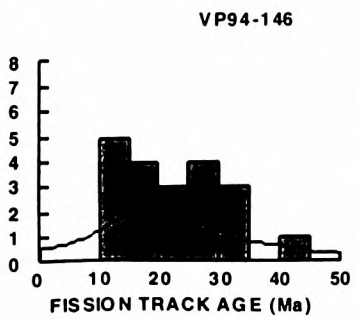
Area of basic unit = 7.803E-07 cm-2

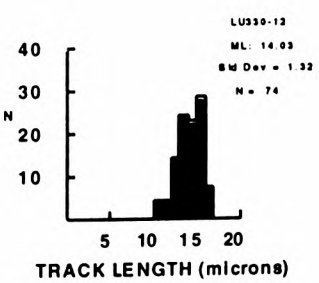
CHI SQUARED = 5.197206 WITH 19 DEGREES OF FREEDOM
P(chi squared) = 94.3 %
CORRELATION COEFFICIENT = 0.969
VARIANCE OF SQR(Ns) = 1.408273
VARIANCE OF SQR(Ni) = 18.63404

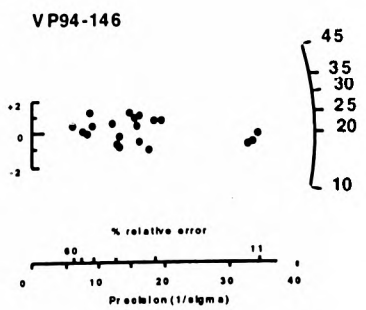
Ns/Ni = 0.079 ± 0.007
MEAN RATIO = 0.085 ± 0.007

Pooled Age = 21.0 ± 1.9 Ma
Mean Age = 22.6 ± 2.0 Ma
Central Age = 21.0 ± 1.9Ma
% Variation = 0.01%

Ages calculated using a zeta of 379.2 ± 3 for CN 5 glass 12.5 ppm
RHO D = 1.403E+06cm-2; ND = 2736







APPENDIX E: Non-linear Geothermal Gradient

Calculation of a non-linear geothermal gradient

A non-linear geothermal gradient was calculated using the following equation, assuming an equilibrium geotherm:

$$T(z) = -A*z*z/2k + ((Qd + Ad)/k)*z \qquad (1)$$

where T is temperature (°C), z is thichness of rock column (meters), A is radioactive heat generation (1.25×10^{-6} W/m^3), Ad is the contribution of A to crustal heat flow of z*A (6.2×10^{-5}W/m^2), Qd is mantle heat flow (42×10^{-3} W/m^2), *k* is thermal conductivity (2.5 W/m/°C). Numbers in parentheses at 10 km use 1/2 and 2x the mantle heat flow, respectively.

depth (km)	T (°C)		
3	100.2		
5	200.8		
10	389.4	(305)	(557)
15	565.6		
20	729.6		
25	881.2		
30	1020.6		
35	1147.6		
40	1262.4		
45	1346.8		
50	1455.0		

The above quadratic equation was used to solve for the depth and geothermal gradient (instantaneous slope) associated with T = 300°C and 500°C: 7.6 km and 37.7 °C/km versus 13.1 km and 34.9°C/km, respectively.

Calculation of the apparent distance separating non-linear geotherms

The apparent distance, i.e.- the distance separating two points on the hypotenusal limb with respect to a trigonometric sine relationship, is assumed to be proportional to the vertical separation (refer to Chapter 6, Fig. 6.2). Given the vertical separation (defined above) and using the apparent distance measured from the data in the northwest Sacramento Moutains, the angular relationship can be determined. This angle is then used with the vertical separation (defined above) to solve for the proportionally equavalent apparent distances not measurable from the data alone. This calculation is performed in order to determine whether a non-linear gradient can produce the observed distribution of paleoisotherms in the northwest Sacramento Mountains.

	Vertical distance (*z*)	Apparent distance (*w*)	Angular relationship (θ)
a)	2	**4.6**	26°
b)	2.6	6	**26°**
c)	5.5	**12.7**	26°

Note: *z* and *w* known in b), solve for θ; substitute θ in a) and c) and solve for *w*. Results in **bold**.

The results suggest that the observed paleoisotherms are consistent with a non-linear geotherm in as much as the observed distribution can be modeled.